Fluid Power *and* Motion Control

FPMC 2010

**Dr D N Johnston
and Professor A R Plummer**
Editors

UNIVERSITY OF BATH

ASME
SETTING THE STANDARD

Fluid Power and Motion Control

Fluid Power and Motion Control
(FPMC 2010)

Edited by

Dr D N Johnston
Symposium Organiser

Professor Andrew Plummer
Director

Centre for Power Transmission and Motion Control
University of Bath, UK

Front cover picture: The Market Cross, Castle Combe
Back cover picture: Temperature distribution in a cylinder block and piston

Preface

The Fluid Power and Motion Control Symposium took place on 15-17 September 2010. It was the 22nd in the series of Symposia held at the University of Bath, and was co-organised by the American Society of Mechanical Engineers (ASME). It was co-sponsored by the Network of Fluid Power Centres in Europe (FPCE). The Symposium was truly international, with authors from fifteen countries. Thirty-eight fully refereed papers were presented with particular emphasis on efficiency in fluid power systems and components. A Keynote speech was presented by Dr Win Rampen of Artemis Intelligent Power Ltd on 'The development of Digital Displacement® technology'. The event included a visit to the beautiful Cotswold village of Castle Combe, during which two of the world's most prestigious fluid power awards were presented, the Bramah and Koski Medals.

The FPMC Symposia now alternate each year between Bath and the USA. In 2009 the Symposium took place in the USA for the first time, in Hollywood, California. We are honoured that ASME is collaborating with us in this venture, and look forward to a long and fruitful partnership. In 2011 the event will take place in Washington DC.

Without the continued support and enthusiasm of authors, reviewers, delegates and staff, it would not be possible to sustain such a long-running and successful series of events. Heartfelt thanks are due to all who have contributed. Special thanks are due to Gillian Elsworth for her considerable effort in compiling the material for this book, and for organizing and ensuring the smooth running of the event. We are also grateful for the support from Hadleys Ltd.

<div align="right">

Professor A R Plummer, Director
Dr D N Johnston, Symposium Organiser
Centre for Power Transmission and Motion Control
Bath, September 2010

</div>

Contents

Noise and Vibration

Pumps and Motors

Modelling and simulation

Control

Sealing, friction and leakage

IC engines and automotive applications

Valves, orifices and stability

Efficient applications of fluid power

KEYNOTE ADDRESS

The Development of Digital Displacement® Technology

Dr. Win Rampen
Managing Director
Artemis Intelligent Power Limited

THE PRE-HISTORY OF ARTEMIS

In the early 1970s the planet hit its first global oil crisis. Although this turned out to be largely a politically driven event, it sparked a lot of action around the world, some of it in the UK.

Professor Stephen Salter was feeling sorry for himself with a bout of flu when his wife instructed him to buck up and solve the energy crisis. His attempt at doing this resulted first, in an appreciation of the high power density of ocean waves and, second, in his solution, the Salter Duck.

The Duck was a long buoyant device which lay across the waves, its non-circular profile presenting a "beak" which rose and fell with each wave, so generating a huge force which was resisted by a torque exerted between the Duck and its internal spine, as it rotated with the wave. Salter realised at an early stage that the challenge of coupling this irregular, slow, high-force motion to the constant, fast-rotation needed to drive a conventional generator was at least as difficult as solving many of the other issues required to make a functioning wave power device. Accordingly he formed a team and recruited Robert Clerk, an engineer who had been developing advanced hydraulic machines over the previous decade, to lead and mentor it. The author was privileged to be part of that small team at its inception in 1980.

Although Salter had systematically evaluated all practical forms of power take-off, and then eliminated all but the hydraulic solution, he was still left with three serious shortcomings. His power take-off needed to handle megawatts. Conventional hydraulics were generally an order of magnitude too small. He needed to efficiently and directly control machine displacements at a moderately high band-width. Electro-hydraulics of that era needed several hardware layers to interface with digital computers. Finally, although full power efficiencies of conventional machines were not too discouraging, his device (along with most other renewable plant) needed to operate with a load factor of around 35%. In this regard the part-load efficiency of conventional hydrostatic transmissions was demoralising in the extreme.

The team's brief was simply to solve these three problems, which meant a fundamental reassessment of conventional hydraulic equipment. The outcome of this work is both Digital Displacement® technology and Artemis Intelligent Power Ltd., an R&D company in Edinburgh with 30 employees.

DIGITAL DISPLACEMENT® FUNDAMENTALS

The technology comes from a radical reassessment of fluid power machines. The loss sources of conventional piston machines were investigated at Edinburgh, first in the context of the design of the Clerk Tri-link, an axial piston pump/motor with many advances over contemporary commercial offerings, then, in the radial format poppet-valve machines often used in small industrial applications. It was realised that the losses of conventional machines remain relatively constant, independent of stroke and power throughput, leading to poor part-load efficiency. The concept devised for Digital Displacement® machines was to create a mechanism for off-loading working chambers altogether, so that their power-handling capacity, whilst almost instantly available, created very little parasitic loss.

This was done by providing actively-controlled poppet valves for each pumping cylinder, effectively replacing the mechanically commutated ports normally used in variable machines. The low pressure poppet valve, so called because it links the pumping cylinder to the low-pressure manifold in all circumstances, is normally open and defaults to leave the cylinder in an idle mode. Oil is sucked into and expelled from the cylinder during each stroke, with attendant flow losses, but no pressure related loads, leakages or compressibility losses. An idling cylinder typically imposes a parasitic power loss of less than one percent of an active one at full pressure. Cylinders are actuated in pumping mode by closing the electro-magnetically actuated low-pressure valve at bottom dead centre. This allows the pumping stroke to generate pressure and deliver a defined amount of fluid to the high-pressure manifold, through the high-pressure valve. In the case of a pump, this valve can be a passive check whilst, for a motor, it must also be electro-magnetically actuated. Poppet valve pumps in the radial format are extremely efficient due to the small diameter of the eccentric, which drives the pistons, and due to the potential for large valves, to provide for ingress and egress of the fluid into the pumping chamber, with minimal pressure drop.

In this way a pump, with a peak overall efficiency above 97%, can be made but more importantly, due to the off-loading mechanism, can operate over a broad speed and torque map whilst still exceeding 95%. This opens up a lot of applications historically closed to fluid-power drives as a result of poor efficiency.

Poppet valves have two important characteristics: they are asymmetric in nature and they are difficult to open against pressure. In the case of the Artemis machines, where the actuators must be very fast, the hydraulic forces are potentially two orders of magnitude greater than any practical electro-magnetic actuator could oppose. The Artemis motoring cycle arose after realising that these problems of actuation could be resolved through timing the valves in conjunction with the piston motion, such that the cylinder pressure could be made to rise and fall to equalise with manifold levels. By this means the cylinder pressure could be brought up to the level of the high-pressure manifold and the HP valve could be

opened.   Equally the pressure could be dropped to allow the low-pressure poppet to reopen. Motoring constituted a third mode of operation, giving the machine two quadrant capability.

By working out how to start and reverse the machines, full four-quadrant operation became possible and the pump/motors could be used to effect vehicle propulsion by directly driving the wheels.

Because the mechanical components in the machine are always following the same prescribed motion with every shaft rotation, and only the very low-mass poppets are being externally controlled, the response is very fast. It takes milliseconds to actuate the valves, with the consequent pumping or motoring cycle always completing in half of a shaft revolution. It should be obvious that the response time is, in fact, almost entirely linked to shaft speed.

Variable flow is synthesised through the choosing of cylinders to actuate as the associated pistons near each end of their stroke. The actuation sequence can be visualised as a bit-stream of digital decisions. The consequent output flow will have a displacement error never greater than half a cylinder (in a constant flow demand). At low flow demands, a smoother output can be created through the use of more frequent, small, part-stroke cylinder actuations.

The full controllability of the machines allows the formation of extremely efficient hydraulic drive circuits with open-circuit architectures. It also permits the incorporation of energy storage accumulators.

THE BIRTH OF ARTEMIS INTELLIGENT POWER

The road between the early days of the wave power and the Artemis of today was anything but straight. At the risk of putting off young entrepreneurs, I will describe at least a few of the more important events along the way.

After the demise of the UK's wave power initiative, Salter applied to the SERC (now EPSRC) for funding to work on selectable inlet valves for digitally controllable hydraulic machines. The application was initially rejected.   Perhaps for the first time, due to rather extraordinary circumstances, the rejection was withdrawn and the grant awarded. The new technology was on its way. Given the massive change of landscape from the early 80s, when there had been universal concern about energy supply, to the latter part of the decade where everyone was once again convinced that the oil would never run out, a new purpose for these hydraulic machines had to be found. A principal realisation was that the technology, initially intended for very large systems, could also be made smaller and turned around - in order to convert constant rotational motion into operator-controlled work functions and vehicle propulsion.

This refocusing allowed the Edinburgh team to target the mobile hydraulics industry and its various applications. Unfortunately, at that stage there was little awareness of either fuel

conservation or the need to reduce emissions of engines.   The only thing which manufacturers could engage with was the prospect of greatly shrinking or even eliminating the expensive, vulnerable and difficult to mount cooling systems.

During this time we conducted flow experiments on a purposely design poppet valve rig, built individual selectable valves, got them running at induction motor speeds, built them into pumps and worked out primitive control algorithms.   The SERC funding came to an end and wasn't renewed in 1989.   The SERC had taken the view that fluid power was a sunset industry!   Fortunately at that time   J.H. Fenner had begun to work on water hydraulics and was looking for a route to a variable pump.   They took a license for the technology from the University and supported the team for the following four years.   During this time the first pumps and pump/motors were made at 18 cc/rev scale.   Two fundamental patents were also lodged.   Four papers outlining the principles of the new technology were also written for BHRA and, later, for the Bath Fluid Power Workshops of the early 1990s.

A large fraction of Fenner's business was related to coal mining. The virtual closure of that industry, and the accompanying recession, forced them to relinquish their license. With no-one on staff to assist in commercialising the nascent Digital Displacement® technology, the University agreed to give the patents back to the inventors. April 1st 1994 marked the start of Artemis Intelligent Power ltd., jointly owned by its founders, Salter and Rampen, and with an employee, Jon Almond. Another useful by-product of the Bath workshops was an introduction to the late Bob Koski, who very kindly mentored me through the challenges of starting a fluid power company.

At the very beginning, because there was no money to support further R&D work on the technology, our efforts were entirely focussed on consulting. Some successful hydraulic components for car body hardware and vehicle suspension arose from these activities, as did enough cash to support the initial Artemis radial piston machine, which was designed from a clean sheet of paper.

Fresh from roles in the university, we adopted a strategy of developing a niche product that we felt we could manufacture in modest quantities to get the business off the ground. The product we had in mind was a hydraulic power-pack which could be plugged into a single-phase, 13 A, socket and provide controlled hydraulic output – with electronic flow, pressure and power limiting – very much the hydraulic analogue of a bench-top regulated electrical power supply. This used a 2cc pumping module in a radial configuration, with the pump completely submerged in the integral reservoir.

Our attempt to raise funds for this venture corresponded exactly with the growing dot-com bubble.   Investors were completely without interest in hardware products with the accompanying cost of producing real components.

Fortunately at this time we were introduced to Waverley Cameron, who had been involved with licensing technology for the better part of his career. His immediate reaction was that R&D engineers should not try to be manufacturers and that we needed to focus on a different business model. This was based on technology licensing in different application fields, bringing in different and complimentary licensees who did not compete head on,

giving some level of exclusivity, and ensuring that all of the members of the licensee-club could share the improvements to the technology so that all of them got the best technology as it was developed. For the most part this strategy has been very successful and has allowed Artemis to grow year on year without taking in external equity from VCs or angels.

MAJOR APPLICATIONS OF DIGITAL DISPLACEMENT® TECHNOLOGY

The first licensee was Danfoss Hydraulics, a company led by Jorgen Clausen, who perhaps was alone in the hydraulics industry in realising the importance of energy efficiency in hydraulics. Artemis has worked with Danfoss, later Sauer-Danfoss, from the late 1990s until the present day on mobile applications. Perhaps this demonstrates the benefits of having a small, agile, skunk-works attached to a large company, with its completely different priorities of manufacturing quality, product support and logistics.

The automotive driveline components company Dana became involved with Artemis around 1999, with a view to developing hydraulic hybrid vehicle transmissions. From a business point of view this worked for Artemis because Dana could access all of the global vehicle manufacturers. Transmissions were not part of their product range, they were in fact complementary to their driveshafts and axle businesses and so the addition of a new product range, that did not in any way cannibalise their existing sales, seemed like a perfect fit. Unfortunately the upheavals in Detroit through the mid-2000s left Dana in Chapter 11. It sold the Intelligent Hydraulic Drive group and the Artemis license to Bosch-Rexroth in 2006, with whom we have worked since that time. Bosch-Rexroth USA have a light military vehicle equipped with a Digital Displacement transmission and are aiming to market the transmission for hybrid commercial vehicles. In parallel with their activities Artemis has developed a series hybrid car, based on a BMW 530i, with a 3.0 litre petrol engine. The vehicle was first tested at Millbrook unmodified, then retested after the complete hybrid system was incorporated into its driveline. The results showed a 50% fuel saving in the urban part of the NEDC test and 27% fuel saving through the entire cycle. The new driveline attained this remarkable level of fuel conservation through recapturing braking energy, turning the engine off when not needed, and by operating the engine along an optimum curve. The required power was typically delivered at a maximum torque, minimum speed point. The driveability, which would normally have been unacceptable due to the lack of torque headroom, was enhanced by feeding in energy from the accumulator during the time the engine was being sped up to a more powerful operating point.

The self-timing aspect of poppet valves ensure that the expected hydraulic whining noise is entirely absent in the car, the only sound being a slightly percussive one that is completely hidden underneath the engine noise.

Artemis was awarded a TSB grant in 2009 to work on Kinetic Energy Recovery Systems – or KERS – and so we continue to focus on propel systems, at ever larger scales.

After a bit of a false start in 2000, Artemis began working on much larger wind turbine transmissions in 2007 with support from the Carbon Trust. In 2009 we completed a 1.5 MW transmission: a 1 MNm Digital Displacement® ring-cam pump, driven at rotor speed,

feeding oil into two 800 kW Artemis motors, rotating at a synchronous speed of 1500 RPM. The transmission weighs in at around 6 Tonnes, which is about 40% of the original gearbox that it replaces. Artemis is currently working to put this transmission into a wind turbine nacelle with funding from DECC.

The transmission has many advantages over the gearbox that it replaces. The input torque is spread into 68 active pumping modules, half of which are active at any time, with the maximum Hertzian stresses of their rolling contacts absolutely limited by the relief valve in the high pressure manifold. This can be contrasted with the five or so meshing teeth of a planetary gear stage, where a few teeth take all of the load (while the others go on an extended holiday), and where there is no effective way to limit maximum load because of the rigid coupling to large inertias at both ends. The complete decoupling of the rotor and the generator, achieved by placing a large gas accumulator between them, also allows rejection of resonant phenomena, effortlessly manages grid fault ride-through and generally improves turbine controllability. The technology is scalable to above 10 MW and so can handle the largest offshore turbines yet envisaged.

FUTURE GOALS

Beyond the three application areas mentioned above, Artemis has been working on several smaller projects. These have involved active suspension for vehicles, hydraulics for injection moulding machines, transmissions for rail-cars, compressed-air energy storage and marine and tidal energy devices. We fully expect that at least some of these will grow to absorb more of our attention over the next year or two.

We view the direct electronic control of hydraulic power transmission as the optimal, and lasting, engineering solution for many high-power/high-force applications. The thought that fluid power is in some way in decline is not accepted at Artemis. We totally reject the Sunset image.

We feel that we are at the start of a wave of technological developments in fluid power – much like the beginning of common-rail diesel engines two decades ago.

There is much to do and a lot that can be gained.

Fluids

Viscosity measurement device for tailor made fuels under high pressure conditions

Drumm, Sebastian; Wohlers Alexander; Fatemi, Arshia; Murrenhoff, Hubertus
RWTH Aachen University,
Institute for Fluid Power Drives and Controls (IFAS),
Steinbachstraße 53, 52074 Aachen, Germany

ABSTRACT

The Cluster of Excellence "Tailor made fuels from biomass", funded by the German research foundation (DFG), is an interdisciplinary collaboration of about 15 institutes and 50 researchers. The aim of the project is to find an optimised process to synthesise new fuels based on biomass. Furthermore the combustion and injection system shall be optimised by reconsidering the new fuel as a design element. The task of the authors is to develop a guideline for designing an injection system adapted to these fuels. The focus is on high pressure pumping of the new fuels within common rail systems.

In this paper investigations to characterise the tribological behaviour of the new fuels will be presented. A test rig to measure the viscosity under high pressure conditions of up to 500 MPa has been built. The design of the test rig and the measuring principle for these extreme conditions will be shown. To detect the viscosity of the fluids under high pressure conditions the falling body principle is used. Furthermore measurement results for the first tailor made fuels will be presented.

These data are needed to parameterise simulation models of the injection system which are set up parallel to the experiments.

Keywords: viscosity measurement, high pressure, ethanol, fuel, falling body viscometer

1. INTRODUCTION

In the Cluster of Excellence "Tailor-Made Fuels from Biomass" new fuels from biomass are being developed and the combustion process is also being optimised. At the Institute for Fluid Power Drives and Controls (IFAS) the tribology of the injection system for combustion engines is the main focus of the investigation. The intention is to gain the hydraulic and tribological characteristics of the fluids. Therefore the viscosity and the bulk modulus of the fluids have to be measured in the possible operating pressure and

temperature range of an injection system. The suggested fuels in cluster might have lower viscosity than conventional diesel fuels. This will cause higher leakage in the injection system especially in the pump in the gap between piston and bushing which requires attention [1]. The test rig to analyse the fuels and results of first measurements are shown in this paper.

2. THE HIGH PRESSURE TEST RIG

The high pressure test rig is structured in two main parts: The pressing piston and the high pressure vessel as shown in **Fig. 1**. The pressing piston is able to generate a force of up to 1200 kN. This force is transferred to the piston of the high pressure vessel. The sealed fluid volume in the vessel is compressed in order to generate pressures of up to 500 MPa.

The high pressure vessel is the main part of the test rig, shown in **Fig. 2**. It is filled with the fluid, which is to be analysed under high pressure.

Pressing Piston

High Pressure Vessel
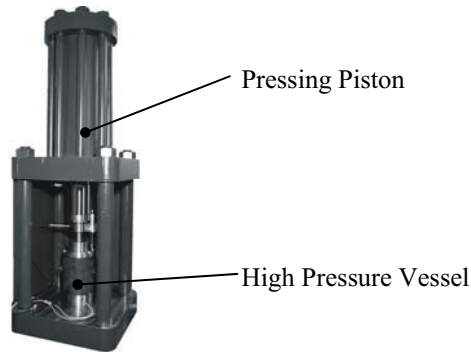
Figure 1: High pressure test rig, overall height 1990 mm

Position Sensor

Pressure Sensor

High Pressure Piston
Sealing

Ultrasonic Sensor

Viscometer

Temperature Sensor
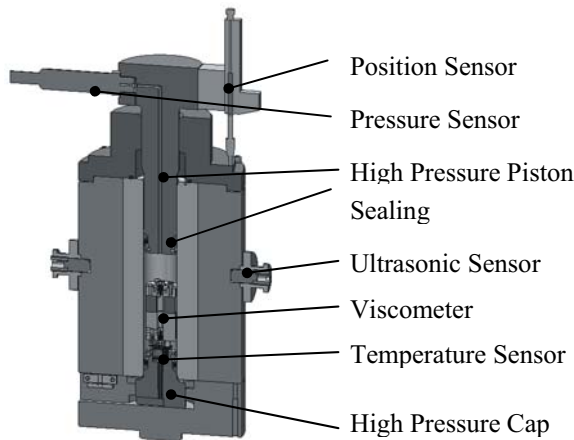
High Pressure Cap

Figure 2: High pressure vessel, inner diameter 40 mm

The high pressure piston is equipped with a position sensor to determine the piston stroke. Furthermore a pressure sensor is attached to the piston, which is connected to the high pressure through a bore in the piston. The bore is also used as the vessels air bleed. In the housing of the vessel two ultrasonic sensors are installed to measure the speed of sound in the test fluid. In the lower high pressure cap of the vessel a temperature sensor is integrated to analyse the fluid's temperature directly inside the vessel. Additionally, an electric cable feed through is placed in the cap to connect the falling body viscometer, which can be installed in the pressure vessel. To heat the test rig an electric heating cable is wrapped around the vessel.

3. FALLING BODY VISCOMETER

To analyse the viscosity under high pressure conditions a falling body viscometer is used, see **Fig. 3**. It is installed in the high pressure vessel. Using a solenoid the falling body is lifted to the upper position which is detected by the upper electric contact. After this the falling body is set free and starts to fall through the falling tube until it reaches the lower electric contact. The time the falling body needs to fall is detected by the lower electric contact. This time is the reference signal for the viscosity. To accelerate the lift of the falling body a check valve is installed at the bottom of the falling tube. During the recording of the falling time, pressure and temperature of the test fluid are measured continuously. [2]
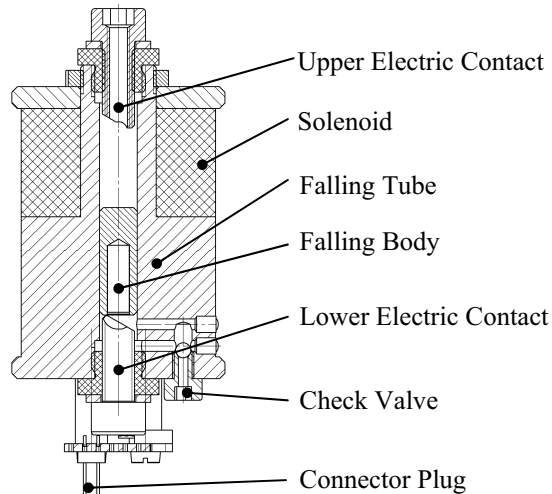
Figure 3: Falling body viscometer
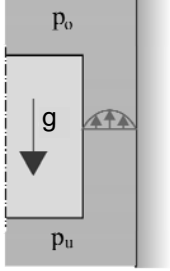
4. VISCOSITY MEASUREMENTS

To measure the viscosity with the falling body viscometer a correlation between falling time and viscosity has to be established. There are two effects that determine the falling time. First there is the gap flow rate Q of the fluid. The fluid has to pass through the gap

between the falling body and the wall of the falling tube, as shown in **Fig. 4**. This flow rate is caused by the displacement of the fluid beneath the falling body. For the variables see the nomenclature at the end of the paper.

Eq. 1 shows the flow rate Q in the gap between the falling body and the falling tube which depends on the diameter of the tube d, the gap width s, the length of the gap l, the pressure difference Δp between the upper and the lower side of the falling body and the dynamic viscosity η. The pressure difference Δp between the lower pressure p_u and the upper pressure p_o depends on the gravity force on the falling body and the lifting force caused by the density difference between the falling body and the fluid, see **Eq. 2**. **Eq. 3** describes the volume V_{fb} of the falling body. **Eq. 4** shows the flow rate Q depending on the speed of the falling body v and the cross section of the falling body. Eq. 1 to 4 can be transformed into **Eq. 5**. This equation shows that the dynamic viscosity η depends on the falling time t, the density of the fluid ρ and other values that are absolute terms.

The second aspect is the shear stress of the fluid in the gap between the falling body and the wall of the falling body caused by the movement of the falling body, see **Fig. 5**. The shear stress τ depends on the dynamic viscosity η, the speed of the falling body v and the gap width s, see **Eq. 6**. **Eq. 7** shows the shear stress τ described by the boundary conditions described by gravity force and densities. **Eq. 8** gives the speed of the falling body v. Eq. 6 to 8 and 3 can be transformed into **Eq. 9**, which again shows that the dynamic viscosity η depends on the falling time t, the density of the fluid ρ and other values that are absolute terms. [3]

$$Q = \frac{\pi \cdot d \cdot s^3}{12 \cdot l \cdot \eta} \Delta p \qquad \text{Eq. 1}$$
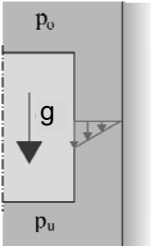
$$\Delta p = \frac{(\rho_{fb} - \rho) \cdot V_{fb} \cdot g}{\pi \cdot r^2} \qquad \text{Eq. 2}$$

$$V_{fb} = \pi \cdot r^2 \cdot l \qquad \text{Eq. 3}$$

$$Q = v \cdot A_{fb} = \frac{L}{t} \pi \cdot r^2 \qquad \text{Eq. 4}$$

$$\eta = \frac{s^3 \cdot g}{6 \cdot L \cdot r} (\delta_{fb} - \delta) \cdot t \qquad \text{Eq. 5}$$

Figure 4: Flow rate between falling body and wall

$$\tau = \eta \frac{v}{s} \qquad \text{Eq. 6}$$

$$\tau = \frac{(\rho_{fb} - \rho) \cdot V_{fb} \cdot g}{\pi \cdot d \cdot l} \qquad \text{Eq. 7}$$

$$v = \frac{L}{t} \qquad \text{Eq. 8}$$

$$\eta = \frac{r \cdot g \cdot s}{2 \cdot L} (\rho_{fb} - \rho) \cdot t \qquad \text{Eq. 9}$$

Figure 5: Speed difference between falling body and wall

Eq. 5 and 9 both show that the dynamic viscosity η depends on the falling time t, the difference of the density of the falling body ρ_{fb} and the density of the fluid ρ and absolute terms although they are based on two different effects. Eq. 5 and 9 are combined in **Eq. 10**. The factor K has to be determined by a calibration measurement in accordance with DIN 53015. [5]

$$\eta = K \cdot \left(\rho_{fb} - \rho\right) \cdot t \qquad \text{Eq. 10}$$

To define the factor K measurements under atmospheric pressure have been undertaken with ethanol as a reference fluid. The data used for the calibration is shown in **Tab. 1**. The dynamic viscosity η is determined with a conventional Ubbelohde-Viscometer at different temperatures. Parallel to that the falling time t with ethanol is measured with the falling body viscometer for these temperatures at atmospheric pressure. The density of the fluid is measured using the volume change of the vessel. During the tests the fluid is sealed in the vessel. Using the position sensor of the pressing piston the change of the volume in the vessel can be determined and so the change of the density can be calculated. The density of the falling body made from 1.4305 is taken from Stahlschlüssel. [6]

Using these data, the calibration factor K is calculated with Eq. 10. This is done for 30 °C and 50 °C. For further analysis of the viscosity measurements the arithmetic mean of these two factors is calculated, thus the calibration factor K equals $2.988 \cdot 10^{-8}$ m²/s².

Temperature	T	[°C]	30	50
Dynamic viscosity	η	[Pa s]	0.000980	0.000698
Falling time	t	[s]	4.517	3.352
Density of falling body	ρ_{fb}	[kg/m³]	7897	7883
Density of ethanol	ρ	[kg/m³]	782	768
Calibration factor	K	[m²/s²]	$3.049 \cdot 10^{-8}$	$2.927 \cdot 10^{-8}$

Tab. 1: Calibration data for ethanol

In **Fig. 6** measured falling times for ethanol are plotted over temperature and pressure. Each dot stands for a single measurement, so a wide range of data is available. The single measurements where done in single rows after the test rig was heated. One can recognise that there is nearly no measurement noise in the single measurement rows but the temperature is not constant. Using Eq. 10 the falling times are converted to dynamic viscosities. Therefore the change of density over pressure and temperature is considered. In **Fig. 7** the dynamic viscosity of ethanol is plotted over temperature and pressure. The viscosity rises with increasing pressure. For rising temperatures the viscosity decreases as expected.
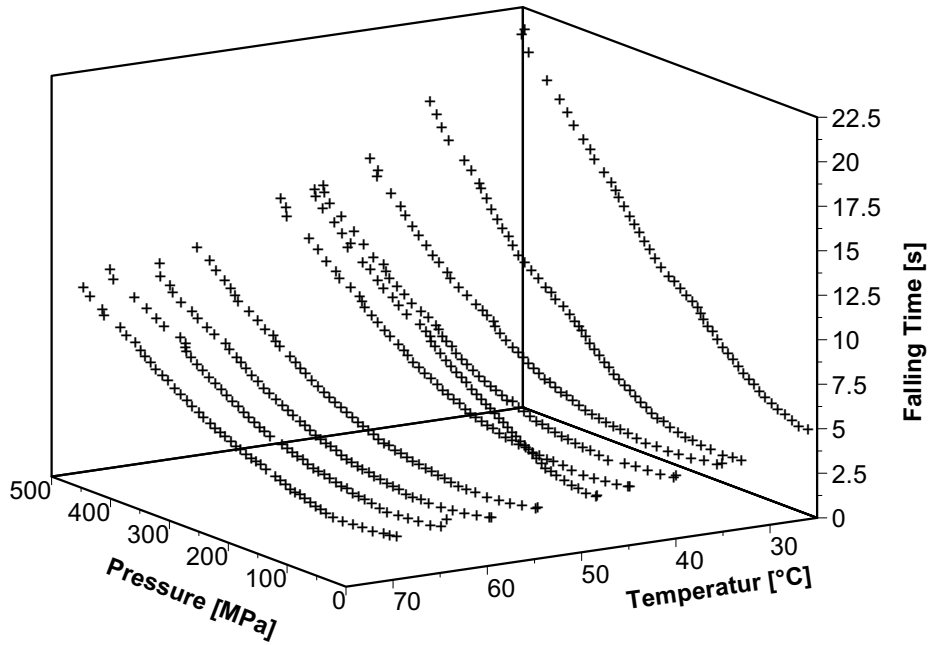
Figure 6: Falling time over pressure and temperature for ethanol
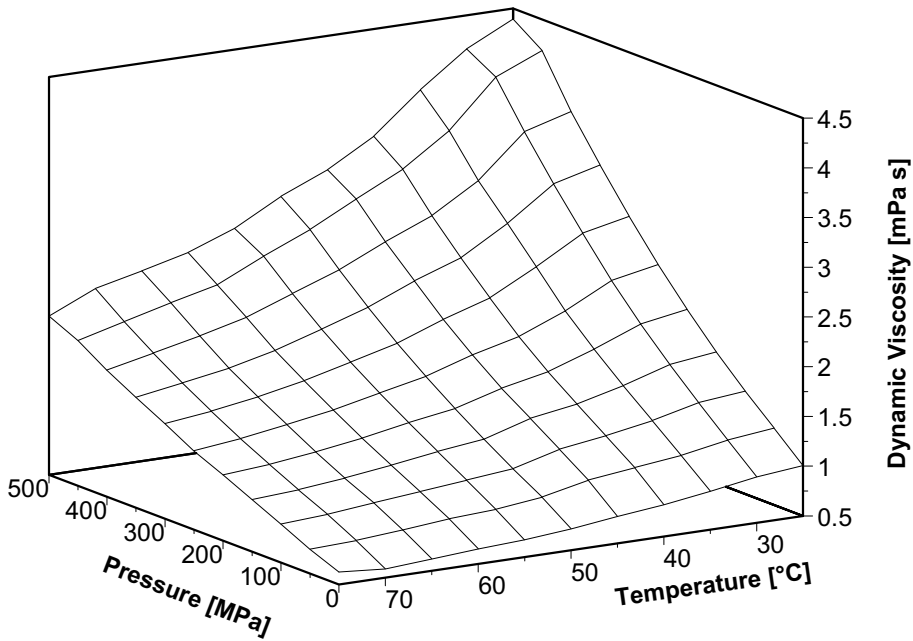
Figure 7: Dynamic viscosity over pressure and temperature for ethanol

5. CONCLUSION

The determination of the viscosity under pump like conditions are essential for the design of injection systems as well as for parameterisation of hydraulic simulation models of injection systems within the Cluster of Excellence "Tailor-Made Fuels from Biomass". The first test measurements with ethanol as a reference fluid have proved the functionality of the viscometer. Already with the first measurement results one can see the influence of the pressure on the dynamic viscosity. As expected the results show the logarithmic correlation of the viscosity to the pressure. Since the injection pressures in the Cluster of Excellence "Tailor-Made Fuels from Biomass" shall reach a level over 200 MPa it is imported to know the properties of the new fuels also under this high pressure conditions. In the next step measurements with the first proposed group of tailor made fuels will be carried out. Furthermore the test rig can be used to measure every kind of fluid, which is used in hydraulic systems or tribological contacts.

NOMENCLATURE

A_{fb}	Area of falling body	[m²]
d	Diameter of falling tube	[m]
g	Gravity	[m/s²]
K	Calibration factor	[m²/s²]
l	Length of falling body	[m]
L	Falling length	[m]
p_o	Upper pressure	[Pa]
p_u	Lower pressure	[Pa]
Q	Flow rate in gap	[m³/s]
r	Radius of falling body	[m]
s	Gap width	[m]
t	Falling time	[s]
T	Temperature	[°C]
v	Velocity of falling body	[m/s]
V_{fb}	Volume of falling body	[m³]
Δp	Pressure difference	[MPa]
η	Dynamic viscosity	[mPa s]
ρ	Density	[kg/m³]
ρ_{fb}	Density of falling body	[kg/m³]
τ	Shear stress	[N/m²]

ACKNOWLEDGMENTS

REFERENCES

[1]   Constantine Arcoumanis, The potential of di-methyl ether (DME) as an alternative fuel for compression-ignition engines: A review, Fuel, Volume 87 (2008) 1014–1030

[2]   Blume, Jochen; Druck- und Temperatureinfluss auf Viskosität und Kompressibilität von flüssigen Schmierstoffen. Dissertation, RWTH Aachen (1987)

[3]   Murrenhoff, Hubertus; Grundlagen der Fluidtechnik, Shaker Verlag (2005)

[4]   Mustafa E. Tata, The Speed of Sound and Isentropic Bulk Modulus of Biodiesel at 21°C from Atmospheric Pressure to 35 MPa, Journal of the American Oil Chemists' Society Vol. 77, No. 3 (2000)

[5]   DIN 53015, Messung der Viskosität mit dem Kugelfallviskosimeter nach Höppler; (2001)

[6]   Stahlschlüssel, Verlag Stahlschlüssel Wegst GmbH, (2007)

Dynamic Modeling of a Magnetorheological Rotation Rheometer

Esa Kostamo, Jari Kostamo, Jyrki Kajaste, Matti Pietola
Department of Engineering Design and Production
Aalto University School of Science and Technology, Finland

ABSTACT

Magnetorheological (MR) fluids are widely utilized in applications requiring good dynamic performance. When striving to apply the magnetorheological technology in high frequency devices and to define the dynamic range of the MR fluids there is a need to develop new methods to study the response time of MR fluids. Although the dynamics of the MR fluids has been proven to be fast, the precise measurement of the fluid's response time has turned out to be a challenging task. To achieve more reliable results, attention needs to be paid to the selection of the measurement method and all the functional components of the measurement set-up need to be modeled.

The contribution of this study is to publish a new construction and a simulation model of a magnetorheological rotation rheometer. The research device is designed to be used in the study of the response time of the MR fluid and in the fluid model development. The constitutive idea of the designed rotation rheometer is to be able to directly detect the change in the fluids apparent yield stress by measuring the transmitted torque between the rotor and stator of the rheometer. To eliminate the influence of the mechanical construction of the rheometer a simulation model will be developed based on the CAD-model and validated by impulse measurements. Applicability of the developed rheometer in response time measurements of the MR fluid will be discussed and the procedure of the future measurements will be outlined.

1. INTRODUCTION

Magnetorheological (MR) fluids are classified in the group of smart materials in which one or more characteristic properties of a material can be varied by an external stimulus. In the case of magnetorheological fluids by controlling the electric current, magnetic field-induced increase in the yield stress of the fluid can be varied in a wide range. The alteration in the rheological characteristics of MR fluids is caused by micron-sized ferromagnetic particles mixed into a low viscosity Newtonian fluid. When the external magnetic field is applied the particles align parallel to the magnetic flux lines forming chain-like structures. The fact that this mechanism can reversibly convert the MR medium from free flowing

fluid to semi-solid material in a fraction of a millisecond makes the MR technology an interesting candidate for today's dynamic fluid power applications.

However, quantification of the pure response time of the magnetorheological fluid has turned out to be a challenging task. The response time of a magnetorheological device can be considered to consist of the performance of the power electronics, the reluctance of the magnetic circuit, stiffness of the hydraulic circuit, strength of the mechanical structure and the delay of the MR fluid. When striving to define the fastest possible response and the highest boundary frequency, the pure delay of the fluid should be studied. Other MR device performance limiting factors can be considered as design parameters whose optimization may have a great influence on the final performance of the device.

Many publications related to studying the response time of magnetorheological fluids have been documented in the literature. The research methods and developed test setups have varied considerably and so far no generally accepted procedure has been developed. Also the reported response times have covered a wide range from a fraction of a millisecond to the several tens of milliseconds. However it should also be taken into a consideration that in many cases the response time of the experimental device has been determined rather than the response time of the fluid.

In the study of Laun et al. (1) the response of a magnetorheological fluid to a change of magnetic flux density has been investigated by using a commercial plate-plate magnetorheometer MCR501 (Anton Paar GmbH) at a constant shear rate. The instrument was modified with a firmware allowing access to unfiltered torque signal with higher sampling rate. The results showed the measured switching time was much shorter compared to the result from the original filtered signal. However, the main contribution of the study done by Laun et al. (1) appears to have focused notably on the modification of the used magnetorheometer.

Electrorheological (ER) fluids can be considered similar from the operating point of view to magnetorheological fluids. The basic mechanism increasing apparent viscosity is the same with MR fluids, but the activation of the ER fluids is excited by external electric field. Ulrich S. et al. (2) measured the response time of electrorheological fluid with a hydraulic test setup where two identical flow channels are switched in-line that are alternately stressed by an electric field. The pressure of the fluid is measured before, between and after the flow channels. The dynamic performance of the valve is estimated by a set of two linear first order differential equations that are fitted to the measured transient pressure data by parameter optimization. As a result response time of 0.9ms is reported. Also strong relation between fluid temperature and response time has been noted. However, in this study the measured response time can be understood to depict the dynamic performance of the total experimental device rather than the ER fluid itself.

Kostamo J. et al. (3) investigated the performance of a magnetorheological damper by combining a symmetric hydraulic cylinder with an external magnetorheological valve. The valve used in the experiment was specially designed for high frequency applications and enabled fast magnetic field transients in the fluid gap. The main contribution of this study was to demonstrate that it is possible to construct a MR damper with considerable better dynamic performance compared to commercially available semi active dampers.

Documented results showed that a kilonewton scale response in damping force was reached within a response time of one millisecond.

In a study done by Concalves (4) the time dependence of MR effect was investigated at high shear rates. An experimental slit rheometer was manufactured in which the fluid was activated in a constant magnetic field at a certain length of the rheometer. The pressure difference over the rheometer was measured as a function of the dwell time which was defined as the amount of time the fluid spent in the active part of the slit rheometer. By increasing the flow velocity the dwell time was decreased until no pressure difference caused by the MR effect was observed. The results indicated that the magnetic field strength has an influence on the response time of the fluid by decreasing the response time at higher strengths of the magnetic field. Reported response time ranged from 0.24ms to 0.19ms.

The scope of this study is to present a new method to estimate the response time of the magnetorheological fluid. This will be carried out by developing experimental MR rotation rheometer. The functional principle and the mechanical construction of the rheometer will be introduced in the following section. The compliance and dynamics of the mechanical construction will be taken into account by formulating a dynamic model for the design and by simulating the essential parts of the rheometer. The model of the mechanics will be validated by impulse measurements. The applicability of the developed rheometer in the response time measurements of the MR fluid will be discussed and the procedure for the future measurements will be outlined.

2. ROTATION RHEOMETER

In simplicity the magnetorheological rotation rheometer developed in this study consists of a servo motor driving a rotating cup (rotor) and a bearing-mounted stationary core part (stator) that is fastened to the frame of the device by a cantilever and a force transducer. The diameter difference between the rotor and stator is approximately 1.2mm forming a volume that is filled with the MR fluid. When measuring the response of the fluid the servo drive is driven at a constant speed of rotation and transient current excitations are controlled to the stator coil wings. A magnetic field induces an increase in the yield stress of the MR fluid and tends to rotate the stator that can be measured as an increased force between the cantilever and frame of the rheometer. In short, the constitutive idea of the rotation rheometer is to directly detect the change in the fluid's apparent yield stress by measuring the transmitted torque of the rheometer.

Figure 1 shows an exploded view of the CAD-model of the designed rotation rheometer. In addition, the functional parts are pointed out. The rotor of the device consists of the inertial mass and the square shaped cup. During the measurements the rotor is rotated at a constant angular velocity and the function of the inertial mass is to diminish the fluctuations in the speed of rotation while the magnetizing current is switched on and off. The cup for the MR fluid and the stator is manufactured of aluminium and magnetic steel and it is permanently mounted to the inertial mass. To ensure the exact fluid gap between the rotor and stator the lower aluminium part in the rotating cup has a bearing housing for the stator. The magnetic

steel core located in the middle of the aluminium parts will take part in the activation of the MR fluid.
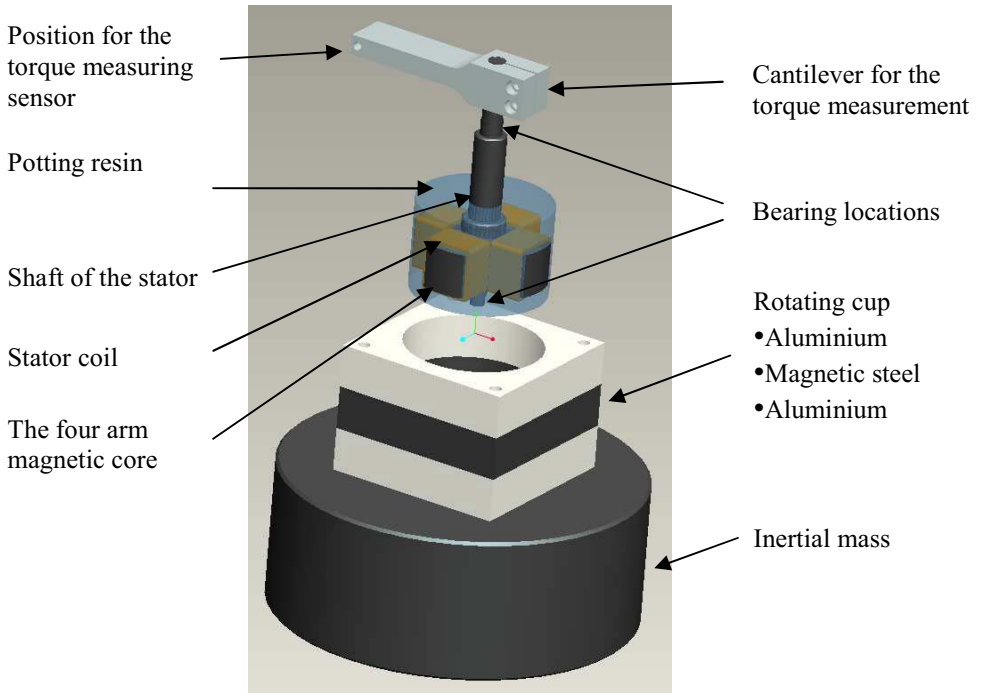
Figure 1, CAD-model of the rotation rheometer

The core of the stator consists of a four arm magnetic steel part. Both rotor and stator magnetic core parts are manufactured of magnetic high frequency material to avoid eddy currents and enabling transient changes in the field strength. The separate coils around every arm are used to generate the MR fluid activating magnetic field. The activation of the fluid happens between the rotor and stator in the rectangular area of every arm. The four arm core part and the coils are potted in resin to give a cylindrical shape to the stator. The shaft of the stator and on the shaft tightened cantilever transmits the torque variations to the force transducer. As the force transducer a piezo sensor is used to ensure fast response, high resolution and inelastic measurement.

In Figure 2 the manufactured magnetorheological rotation rheometer is presented. The frame of the rheometer consists of steel plates that are separated by levelling rods. The rotor part of the rheometer is bearing mounted to the middle plate and the upper plate supports the torque measurement and the upper end of the stator. From the lower plate the device is rigidly mounted to the T slot floor of the laboratory hall. The total height of the rheometer is approximately 80cm, width of the front side 32cm and depth 20cm.
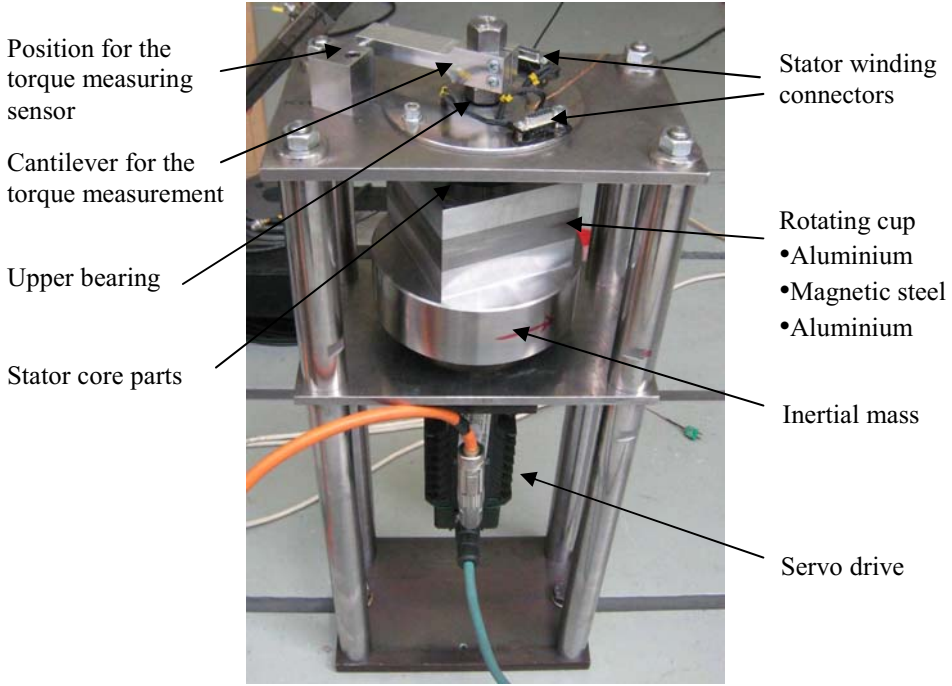
Figure 2, Experimental MR rotation rheometer

3. DYNAMIC MODEL

Mechanical construction of the rotation rheometer has been modelled based on the equation of the damped torsion oscillator. In this case the oscillator consists of a shaft and a torsional mass of inertia which is mounted to the lower end of the shaft. The other end of the shaft is rigidly fixed to the frame of the device by the cantilever. The effective torsional mass of inertia consists of the magnetic core parts of the stator that are pointed out in the Figure 1. The general differential equation for the system can be written as (5),

$$J_{tot}\frac{d^2\varphi}{dt^2} = M_t - c\frac{d\varphi}{dt} + M_{MR} \qquad\qquad 1$$

where J_{tot} is the total torsional moment of inertia of the system, φ is the torsion angle of the shaft, M_t is the torsional moment caused by the torsional angle of the shaft, c is the damping coefficient and M_{MR} is the excitation moment generated by MR effect.

On the other hand, if the torsional moment is constant between two cross sections of the shaft with the distance difference of l, the equation between the torsional moment and the torsional angle can be represented as,

$$M_t = \frac{-GI_p}{l}\varphi \qquad\qquad 2$$

where G is the material specific shear modulus, l is the length of the shaft and I_p is the torsion constant of the shaft. The shear modulus of the material can be calculated by the elastic modulus E and Poisson's constant υ of the material as presented in the Equation 3.

$$G = \frac{E}{2(1+\upsilon)} \qquad\qquad 3$$

The torsion constant for the round shaft with the constant diameter of d can be calculated as shown in the following equation.

$$I_p = \frac{\pi d^4}{32} \qquad\qquad 4$$

By combining Equations 1 and 2 the analytic expression of the magnetorheological rotation rheometer can be formulated as,

$$\frac{d^2\varphi}{dt^2} + \frac{c}{J_{tot}}\frac{d\varphi}{dt} + \frac{GI_{ptot}}{J_{tot}l}\varphi = M_{MR} \qquad\qquad 5$$

where I_{ptot} is the total torsion modulus of the device. When calculating the total torsion modulus for the shaft of the stator it must be taken into account that the shaft consists of several parts with different diameters and lengths. To combine the torsion constants of different parts of the shaft to the following equation of the total torsion constant can be used.

$$\frac{1}{I_{ptot}} = \frac{1}{l_{tot}}\left(\frac{l_1}{I_{p1}} + \frac{l_2}{I_{p2}} + \dots + \frac{l_n}{I_{pn}}\right) \qquad\qquad 6$$

In the Equation 6 l_{tot} is the total length of the stator shaft, $l_1 + l_2 + \dots + l_n$ and $I_{p1} + I_{p2} + \dots + I_{pn}$ are the lengths and the torsion constant of the different parts of the shaft respectively.

However, before calculating the total torsion constant of the rheometer the effect of the cantilever must also be taken into account. In this study the cantilever has been reduced to a shaft that has the same length with the shaft of the stator. The diameter of the reduced shaft has been calculated by assuming the same angle of torsion for the cantilever and the

reduced shaft with the same torsional moment. The cantilever has been approximated as a simply supported beam in which case the torsion angle can be evaluated with equation 7

$$\varphi = \frac{-M_t l_c}{3EI_c}$$

7

where l_c is the length of the cantilever and I_c is the second moment of area. The second moment of area for the rectangular beam is defined as,

$$I_c = \frac{w_c h_c^3}{12}$$

8

where w_c is the width and h_c is the height of the cantilever. By rearranging the Equation 2 the rotation angle of the round shaft is formulated below where l_{red} is the length of the reduced shaft.

$$\varphi = \frac{-M_t l_{red}}{GI_p}$$

9

Inserting Equations 4 to 9 and 8 to 7 followed by the combination of the Equations 7 and 9 the diameter of the reduced shaft can be calculated from the Equation 10. In consequence the reduced shaft has the same torsion modulus with the cantilever and this can be added into the Equation 6.

$$d_{red} = \left(\frac{8Ew_c h_c^3 l_{red}}{\pi Gl_c} \right)^{\frac{1}{4}}$$

10

The torsional moment of inertia for the reduced shaft is simply calculated by the following equation,

$$J_{red} = \frac{1}{2} \rho_c \pi \left(\frac{d_{red}}{2} \right)^4$$

11

where ρ_c is the density of the cantilever. The total torsional moment of inertia for the Equation 5 can be calculated by summing up all the torsional moments of inertia of the subcomponents in the stator. By using the correct material properties these values can be collected directly from the CAD-model. When adding the torsional moments of inertia of the shaft of the stator and the reduced shaft, one third of the total value is assumed to have an effect to the dynamics of the stator.

4. RESULTS

The dynamics of the rheometer was analyzed by creating a simulation model based on the equations presented in the previous section. The physical dimensions of the manufactured rheometer were used to describe real dynamics of the stator. As a result the torsional natural frequency of the stator of the rheometer was calculated to be 312.6Hz. To validate this result an impulse measurement for the rheometer was carried out. In this experiment the torsion mode of the stator was excited by an impulse force and the resulting oscillation was measured by the torque measuring sensor. The frequency content of the acquired data was then analyzed by FFT algorithm and the resulted spectrum is presented in the Figure 3. It can be seen that the natural frequency of the manufactured device meets the calculated natural frequency with a good accuracy.
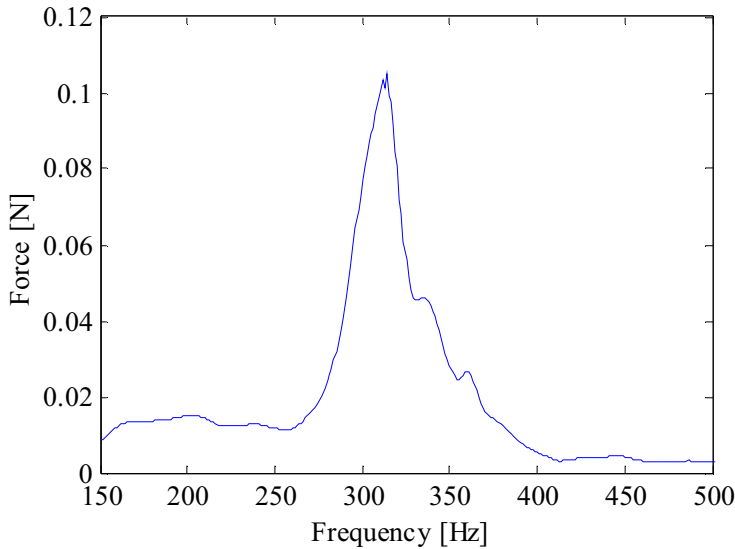
Figure 3, FFT spectrum of the impulse excitation of the stator

The damping in this case of rotation rheometer is mainly caused by the MR fluid, wiring of the stator coils, friction of the bearings and material internal friction of the deflecting parts. In consequence the analytical definition of the damping factor may be quite challenging and hence in this study the damping is estimated experimentally.

The simulated response and the impulse measurement of the rheometer were also compared in the time domain. The comparison of these results is shown in Figure 4 where the oscillation at the natural frequency can be seen to dominate the response. The model of damped torsion oscillator can also be found to depict the rotation rheometer with a satisfactory accuracy. Immediately after the impulse a slight difference in the measured and simulated amplitudes of the oscillation can be observed. One reason for this is suggested to be the other oscillation modes of the stator. However, after a couple of oscillation cycles the

influence of additional modes can be seen to fade out and the simulation corresponds to the measured response.
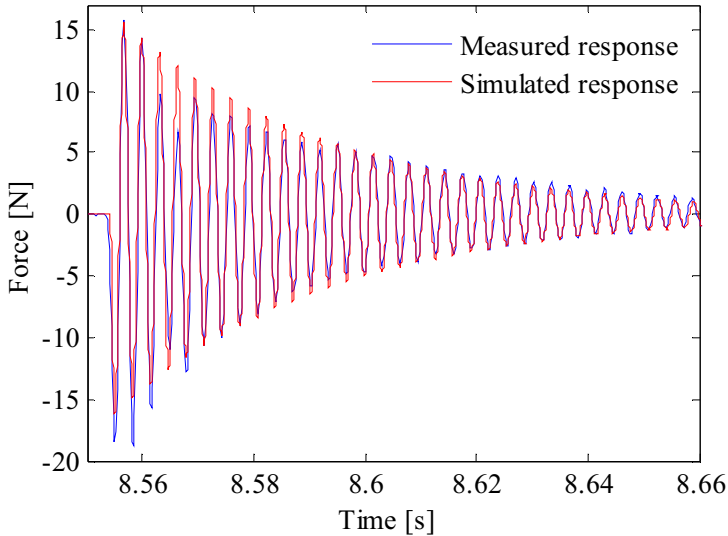
Figure 4, Comparison of the measured and simulated impulse response of the stator

5. DEFINING THE MR FLUID RESPONSE TIME

In this section the method for defining the response time of magnetorheological fluid by using the developed rotation rheometer will be outlined. Perhaps the most important question is the dynamics of the rotation rheometer. As reviewed in section 1 the response time of the magnetorheological fluid has been reported to be in range of 0.2ms. This would roughly correspond to the maximal frequency bandwidth of 1700Hz for the technology. On the other hand in the previous section the natural frequency of the rheometer has been measured to be only 312Hz. Based on this it is clear that the rheometer cannot directly depict the dynamic characteristics of the MR fluid in the case of step excitation because the rheometer is used in the supercritical range.

However, the key idea in defining the response time of MR fluid is to utilize the developed simulation model to compare the simulated step response with the measured response from the device. This procedure is illustrated in the Figure 5 where two step responses are simulated and the measured data representing blue curve is delayed for couple of time steps. Now the simulated red curve contains only the analytic model of the stator of the rheometer. In comparison the "measured" blue curve includes the pure response time of the MR fluid, dynamics of the fluid and the dynamics of the rheometer. As an assumption the effect of the dynamics of the MR fluid to the measured response could be negligible. This is because the dynamics of the fluid can be considered to be in a range of one decade faster than the dynamics of the rheometer when the response is dominated by the slower

dynamics of the components. In short by this assumption the response of the rheometer could be estimated to consist of the pure response time of the fluid and the dynamics of the stator. In Figure 5 this response time of the MR fluid is pointed out with arrows and t_{MR} notation. When analyzing the results the simulated curve will be postponed an amount of time until it gives the best possible match to the measured curve resulting the response time of the MR fluid. These results will be analyzed and documented in more detail in the future.
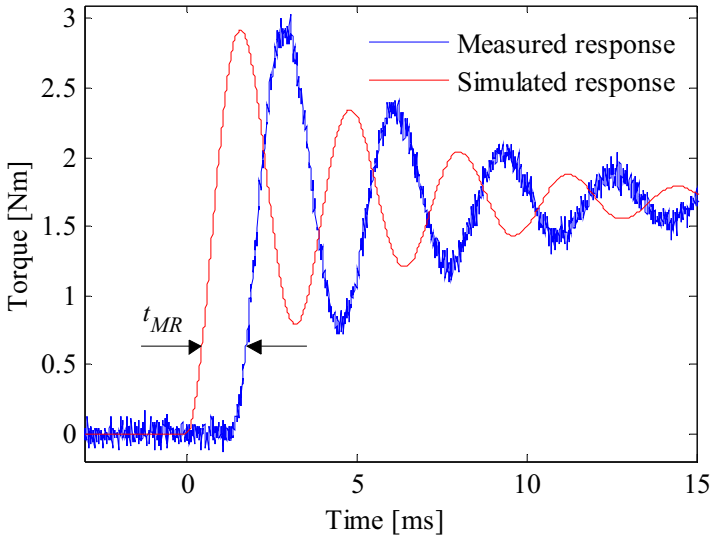
Figure 5, Illustrative graph of the defining the MR fluid response time

6. CONCLUSIONS

The contribution of this paper was to propose a new design and a simulation model of a magnetorheological rotation rheometer that will be used in studying the response time of MR fluids. As an introduction to the subject a literature review of some studies discussing about the response time of the MR fluid was given and the applied methods and results were summarized. According to the recent publications the response time of the MR fluid was proposed to be in range of 0.2ms.

The construction of the developed rotation rheometer was presented by the CAD-model and picture of the manufactured device. The functional components were pointed out and operational principle was described. The model of the rheometer was implemented by deriving the analytic equations of the damped torsion oscillator. The effect of the torque measuring cantilever to the dynamics of the stator was taken into account by reducing the moment of inertia of the cantilever to an appended shaft by assuming the same angular torsion for the cantilever and the reduced shaft. The simulated model was validated by impulse response measurements from the manufactured research device. The results were

analyzed in the frequency and time domain and a good equivalency between simulated and measured responses was found out.

This publication was concluded by an introduction to the method that is intended to be used in the further study of the response time of the magnetorheological fluid. Using this method the simulated and measured responses are analyzed together enabling the elimination of the effect of the stator dynamics to the results. As a result the pure response time of the MR fluid can be estimated.

REFERENCES

(1) H. Laun and C. Gabriel, "Measurement modes of the response time of a magneto-rheological fluid (MRF) for changing magnetic flux density", Rheologica Acta, vol. 46, pp. 665-676, 2007.

(2) Ulrich, S., Böhme, G. and Bruns, R., "Measuring the response time and static rheological properties of electrorheological fluids with regard to the design of valves and their controllers", Journal of Physics: Conference Series, vol. 149, 2009.

(3) J. Kostamo, E. Kostamo, J. Kajaste and M. Pietola, "Magnetorheological (MR) damper with a fast response time," Bath/ASME Symposium on Fluid Power and Motion Control, FPMC 2008, pp. 169-182.

(4) F. D. Goncalves and J. D. Carlson, "Investigating the Time Dependence of the MR Effect", vol. 21, pp. 4832-4840, 2007.

(5) A. Ylinen, *Kimmo- Ja Lujuusoppi.* , vol. 2, 1970, pp. 1010.

Experimental investigation and theoretical prediction of the lubricity of biofuel components

A. Fatemi[1], K. Masuch[2], H. Murrenhoff[1], K. Leonhard[2]
1- RWTH Aachen University, Institute for Fluid Power Drives and Controls (IFAS)
2- RWTH Aachen University, Chair of Technical Thermodynamics (LTT)

ABSTRACT

In the design of fuel supply pumps and injection units, the tribological properties of the fuel are an essential concern. This is because the majority of high-pressure injection systems are fuel-lubricated and rely on the lubrication ability of the fuel itself. Therefore the lubricity of biobased pure compounds is investigated via high-frequency reciprocating rig (HFRR). A novel method employing COSMO-RS and theory of adsorption is adopted in order to find a correlation between molecular structure and tribological properties of fuel components. From a more general perspective, this concept can be used for the analysis of the tribological characteristics of components of biodegradable hydraulics fluids.

Keywords: fuel injection systems, lubricity, biofuels, COSMO-RS, prediction models

1. INTRODUCTION

Biofuels as a possible alternative to fossil fuels have gained a huge research interest in the last decades. The first generation of biofuels applied in the transport sector, including the class of fatty acid methyl esters (FAME, e.g. rapeseed methyl ester, RME), bioethanol and others is now used in conventional diesel and gasoline motors as pure fuel or blended with hydrocarbon based fuels. Due to their competition with food and their partly undesired combustion properties, several research groups are now focusing on the next generation of biofuels.

Among these, the cluster of excellence "Tailor-Made Fuels from Biomass" (TMFB) adopts an interdisciplinary approach including aspects of the production and of the utilization of the fuel in the engine. The long-term goal is to determine the optimal composition of fuel taking into account its economical production including aspects of the renewable feedstock as well as its injection, ignition and combustion properties relevant for the engine's efficiency and emissions. Therefore this approach offers an opportunity to reconsider the fuel as a design element in the optimization of combustion and injection systems.

Beside the combustion performance and emission considerations, the lubricating ability of the fuel has a high significance in the fuel design. This issue has received much attention after the introduction of low sulfur diesel fuels and failure reports in injection systems operating with these fuels (1). These reports originate mainly from countries in which a higher level of hydro-treatment to reduce sulfur content was prescribed due to environmental concerns. The process of hydro-treatment removes not only sulfur but also other polar oxygenates and nitrogen containing contaminants which are essentially the naturally lubricating, surface active components responsible for protecting the sliding surfaces in fuel injection pumps against wear (1).

After the introduction of the first generation of biofuels, the tribological characteristics of these fuels were reported in various publications (2). The ester-based biofuels like fatty acid methyl ester or biodiesel are well known to have an excellent lubricity performance. These compounds are conventionally used as lubricity enhancers for diesel fuels.

A contrasting example is Dimethylether (DME) which is an outstanding clean and a non-toxic alternative for diesel fuel, but due to its low lubricity and viscosity cannot be supplied at high pressures. It is still an open question how an economical selection of additives and materials for a durable injection of this fuel can be made (3).

In this study we discuss a conventional experimental method for the assessment of the lubricating ability of fuels. Subsequently the results of these experiments for compounds proposed for future bio-based fuels within the TMFB cluster are presented. Finally we adopt a predictive model for the lubricity, as recently proposed by the authors (4). Such a model is a prerequisite for a future screening or even design of an optimized fuel with respect to multiple criteria as it is targeted in the cluster of excellence TMFB.

2. THE ISSUE OF TRIBOLOGY IN THE DESIGN OF INJECTION SYSTEMS

The majority of high-pressure injection systems are fuel-lubricated and rely on the lubricating ability of the fuel itself. Fuel injection equipments (FIE) according to European emission standard (Euro 5 and above) have to supply extremely high fuel pressures and have to be equipped with a precise injection control to meet the new stringent emission specifications. It is imperative for these systems to maintain their top performance during their entire life ranging from 150 to 500 thousand kilometres (5).

Modern diesel engine cars are mostly equipped with Common Rail (CR) injection pumps. This concept of injection can supply a higher pressure than conventional distribution type injection systems and is hereby able to improve the injection, spray and ignition processes. These changes result in the reduction of environmentally harmful emissions. Both alternative fuels and environmentally legislations can stipulate higher injection pressures. From the design point of view, a higher injection pressure is associated with higher contact pressures and contact temperatures in injection pumps, leading to more severe tribological conditions (5).

Fig. 1 shows critical tribological contacts in a commercial Common Rail injection pump (CP1 series) and the fuel injector (6). The polygon part, mounted on the eccentric shaft

forces the plungers to perform a reciprocal motion in the piston and draw and deliver the fuel via embedded valves. The illustrated critical tribological contacts subjected to wear are the contacts between hexagon and plunger bottom, valve balls imbedded in the pump and the injector ball which closes the flow throttle (6). In the more recent series of injection pumps (CP3 series) which are designed for higher pressures, a special design of the barrel tappet lowers the subjection of the very critical and fine machined contacts with the plunger to wear. This is done by redirecting the lateral forces caused by friction of the plunger bottom and hexagon to a larger area (7).
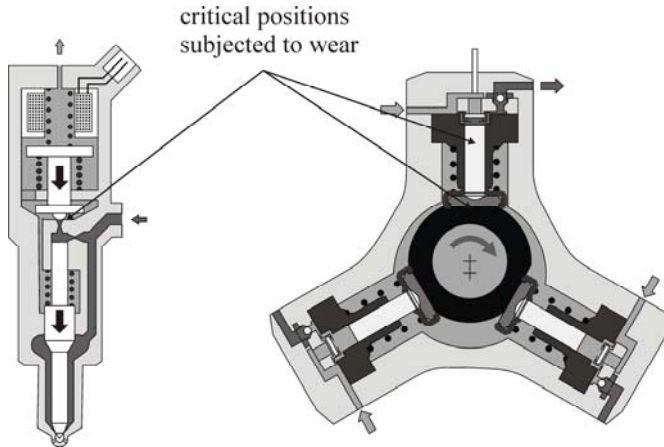
Figure 1: critical tribological contacts in injector and CR-Pump (CP1 type) (6)

3. LABARATORY SCALE TEST BENCHES FOR PREDICTION OF THE FUEL LUBRICITY

Although bulk characteristics like viscosity of a fuel are important for a better lubrication in injection systems, the lubricating ability of the fuels is determined by different physical and chemical mechanisms between different fuel components and the surface (1). However, testing a fuel injection pump over a period of 2000 hours or running a car for 150000 km is not feasible. Consequently designers of fuel injection systems together with developers of the fuel industry have developed different laboratory scale test rigs that simulate the most critical tribological conditions in fuel pumps for the assessment of the desired, however not scientifically defined quality, "lubricity"(8).

The HFRR method was selected in a round-robin evaluation of several lubricity-testing methods as an ISO standard for diesel fuels (9). Since there is no standard method for biofuels, the HFRR is adopted in this study since this apparatus is able to distinguish between different types of additive-like molecules and shows a better reproducibility compared to other methods (10).

The configuration of the HFRR is depicted in **Fig. 2**. In a standard HFRR measurement, a 6 mm ball loaded with 2 N reciprocates on a steel plate with a frequency of 50 Hz and a

stroke of 1 mm for 75 minutes. The diameter of the wear scar (WSD) on the ball is determined at the end of the measurement. The smaller the wear scar diameter, the better the lubricity. According to ISO 12156-1 (9), this value has to be corrected depending on the bulk temperature and the humidity via correction factors. The humidity factor widely used in fuel industry is questioned within the investigations of Shaver et al. (11). Therefore, only the average WSD of the ball is presented in this study and not the corrected values. The HFRR experiments are performed in a closed box in order to exclude variations of temperature and humidity during the test to improve the repeatability.
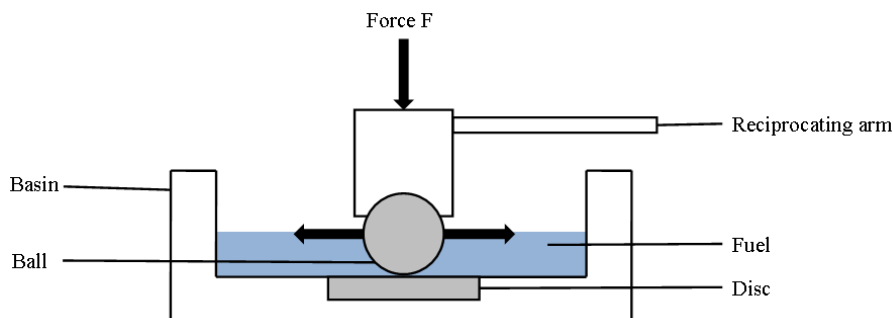
Figure 2: High frequency reciprocating rig (HFRR)

As mentioned before, in order to meet future environmental standards, higher injection pressures than the ones currently applied are needed. Therefore it is necessary to verify that the HFRR test results still can be applied to these more severe tribological conditions, as this method has been initially designed for conventional diesel injection systems. For this reason developers of fuel injection systems have developed a concept (HiTOM) to simulate more severe tribological contacts (5). This test is designed to reproduce the main contacts present in Common-Rail pumps. In this test a cylinder oscillates against a plate exhibiting a line contact and the normal force can be increased up to 10000 N by a hydraulic actuator. The cylinder specimen is an original part of a Common-Rail pump and the plate represents the raceway of a pump camshaft, made of the same bearing steel. These materials are the ones conventionally used in Common Rail systems and are very likely to be the preferred choice for future fuel injection equipments. The very tedious HiTOM test provides data for load carrying capacity (LCC), but a comparative study (5) shows that the HFRR has still the ability to differentiate between the lubricity of different compounds and compositions relevant to next-generation of injection pumps.

4. EXPERIMENTAL RESULTS

In order to derive a correlation between molecular structure and lubricity of fuel components, a variation of chemical structures of candidates of TMFB fuels is given in Table 1. In this structure variation we are interested in the impact of the carbonyl group in levulinic acid and its derived esters comparing with valeric acid and esters based on it.

The histogram in Fig 3 illustrates the average wear scar diameter for the above mentioned compounds. The squares represent the kinematic viscosity at 40°C. A pronounced

difference is apparent in the lubricity of levulinates and levulinic acid in comparison with valerates and valeric acid. Ethyl levulinate and butyl levulinate provide a better resistance against wear compared to ethyl valerate and butyl valerate. The carboxylic acids in this study do not possess a better performance in the pure state. This can be possibly ascribed to their corrosive character (12) (23). In the following diagrams it is shown that they are more effective as additive in low concentrations.

Ethyl levulinate
(EL)

Butyl levulinate
(BL)

Ethyl Valerate
(EV)

Butyl Valerate
(BV)

Levulinic acid
(LA)

Valeric acid
(VA)

2- Nonanone
(2N)
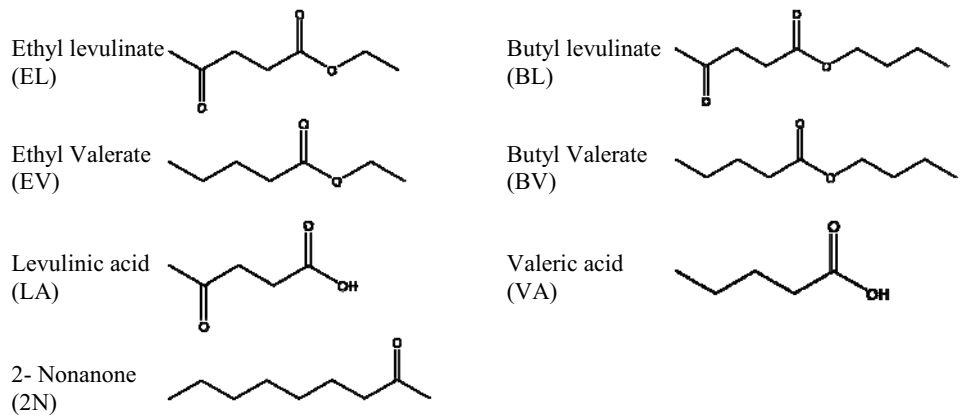
Table 1: Proposed candidates for diesel fuel and similar structures (group A)
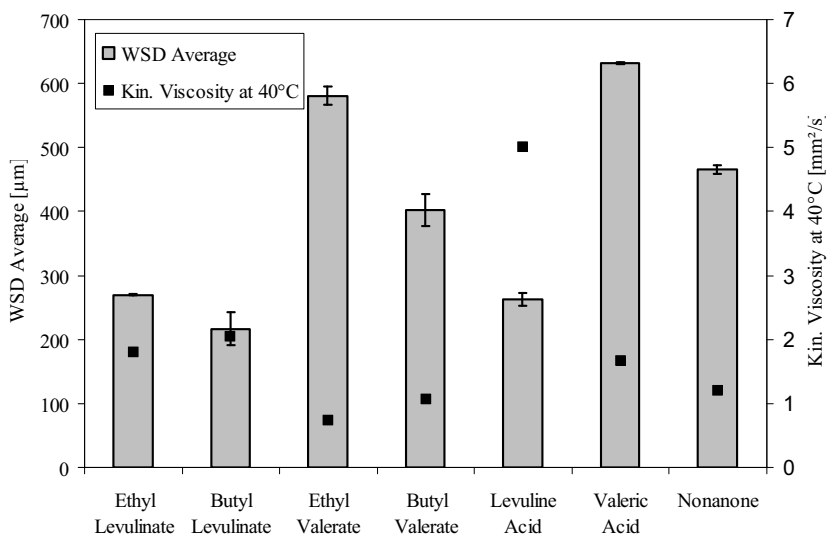
Figure 3: Lubricity of TMFB candidates for diesel fuel under investigation and similar structures

Fig. 4 illustrates the lubricity of the mentioned compounds as additives in dodecane as a model for low-lubricity diesel fuel. The impact of esters and fatty acids on the lubricity of

the model fuel can be taken from this illustration. There is a considerable difference in the impact of carboxylic acids compared to esters. In blends of 0.1% levulinic acid and valeric acid in dodecane, the lubricity requirement ($WSD_{max} = 460$ µm) for diesel fuel is fulfilled.
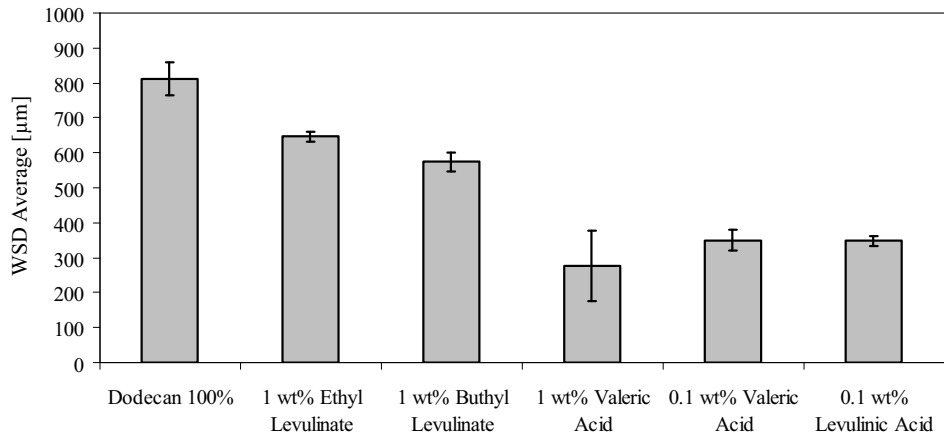
Figure 4: The impact of TMFB candidates on the lubricity of dodecane as a model for a low lubricity diesel fuel

Table 2 illustrates bio-based candidates for gasoline fuel. The compounds of this group have cyclic ester (=lactone), hemiacetal and ether functional groups.

Gamma Valerolactone **(GVL)**	
Tetrahydrofufuryl Alcohole **(THFA)**	
2 Methyl Tetrahydrofuran **(2-MTHF)**	

)
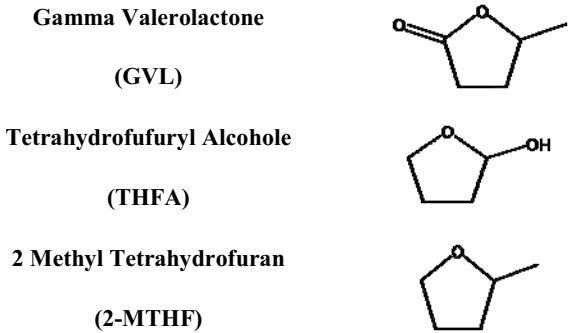
The lubricity of the fuels presented in Table 2 is given in Fig 5, showing that a fuel with the hydroxyl group has a better lubricity than those with an ester group (e.g. Gamma Valerolactone). The 2-Methyl-Tetrahydrofuran (2-MTHF, an ether) has the worst lubricity for reasons discussed below.
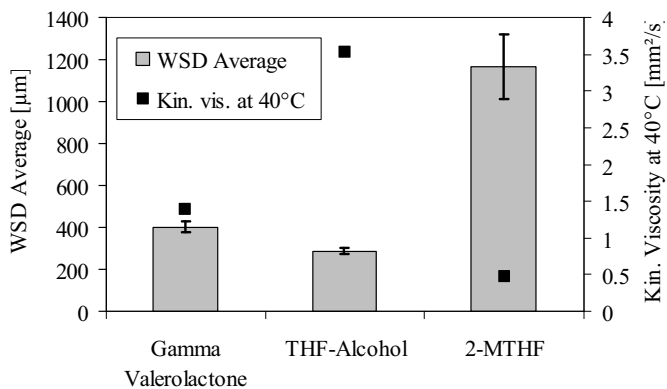
Figure 5: Lubricity of compounds proposed for bio-based gasoline fuels (group B)

The presented results and the error bars show a good repeatability within the presented experiments. However comparing the same compounds between different test benches from different groups does not necessarily yield a good agreement. Fig. 6 shows the measurements performed by Knothe et al. (2) versus our experiments. The deviations of the lubricity values are ranging up to 26%. This issue has to be considered in the next sections regarding the theoretical predicted WSD's. These deviations may originate from different sources like impurities, details of soaking and cleaning of the specimens, oxidation of compounds exposed to air, and above all, the impact of humidity on the lubricity. The correction factor (9) for an impact of humidity on diesel fuel can not be used here since the response of oxygenated bio-based fuels to the air humidity is not comparable with diesel blends. Furthermore, this correction factor does not present a reliable prediction even for conventional diesel fuels, as stated by Shaver et. al. (11).
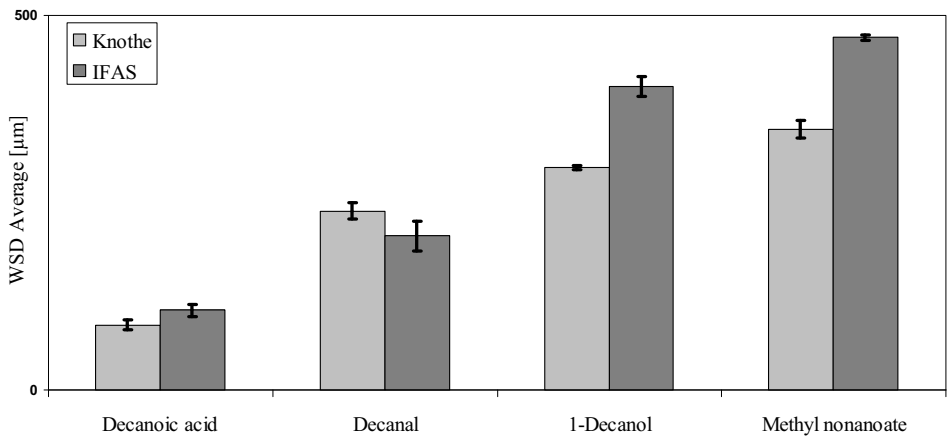
Figure 6: Comparison of the lubricity of C10 molecules in this study with measurements of Knothe et. al. (2)

5. THEORETICAL MODELS FOR PREDITION OF THE FUEL LUBRICITY

Predicting a very application-oriented property like the wear rate of a point contact for different lubricants is not an easy task. The same applies to the wear rate representing values given by HFRR. One has to keep in mind that the HFRR was not designed as a scientific experiment in the first place, but as a pragmatic test for practical applications. In a scientific experiment, normally the factors influencing the result are reduced to a minimum in order to find a physically profound explanation.

In contrast tests fulfilling ANSI-standards or DIN-norms are usually designed to include numerous and complex influences. These influences are subsumed in one single value like the wear scar (HFRR). The individual influences on this quantity are far from being fully understood, and a resulting holistic model is not yet available (13). Proposed influence factors are chemisorption, physisorption, reactive polymerization, hydrodynamic contribution, tribochemical reactions, catalytic reactions and etc. (13), (14).

As stated above, the long-term objective of the presented model is an application for a screening and design of an optimized fuel, according to multiple criteria.

For the lubrication part of this screening process, however, it is not essential to explain exactly why a molecule lubricates or why it does not lubricate. In fact the goal is to have a preselection tool in order to reduce a diversity of possible fuel candidates to a number accessible to the time-consuming lubrication experiments.

This can be done by quantitative structure-property relationship (QSPR) models. QSPR-models relate the desired quantity to descriptors that are characteristic for a given molecule. QSPR model development can be seen as some kind of data mining. If the physics of a problem is not fully understood, an empirical correlation is built between the target value and descriptors thought to be relevant for that regarded phenomenon. Presented lubrication-related descriptors in the literature are e.g. conductivity, density, viscosity (15) or infrared absorbances (16).

We recently presented a model (4) not only fulfilling the criteria for screening purposes, but having even the potential to suggest promising candidates for synthesis for a further design of an optimized fuel. This is done by using solely descriptors that can be computed from the molecular structure.

The applied model providing the molecular descriptors is the 'Conductor-Like-Screening-Model' (17) (COSMO) and the sigma-moment-QSPR approach (18), based on the 'Conductor- Like-Screening-Model-for-Real-Solvents' (COSMO-RS) (19).

The basic idea is that the lubricity, defined as the inverse HFRR-wear-scar, is somehow related to the surface screening charge distribution (SCDD) of a molecule when placed in a cavity in an ideal conducting continuum. The cavity in which the molecule is placed, is built of slightly modified Van-der-Waals spheres around the atoms (20). The screening charge density of the molecule at the surface of the cavity is taken from quantum mechanical density functional theory calculations.

The distribution function of the SCDD can be approximated by its statistical moments, the 'sigma-moments'. To take hydrogen bonding capabilities of a molecule into account, for SSCD exceeding a given threshold, additional functions are used to provide 'hydrogen bonding moments'. The sigma- (M) and hydrogen-bond-moments (M_{acc}/M_{don}) have shown to describe adsorption phenomena to poorly defined matrices like activated carbon (18) or even soil (21).

The lubricated surface is a similarly poorly defined structure. It consists of blank, oxidized and hydroxylated patches in unknown quantities. So we applied the sigma moment approach to describe the lubrication, as described in detail in (4). Deviations from the ideal linear molecular shape reduce the lubrication performance of an adsorbate, so we additionally included the sphericity (Ψ) (22) of a molecule as a rough shape parameter, calculated from the COSMO volume and surface. The correlation of theses descriptors to wear scar data from literature (2) leads to the following equation:

$$\frac{1}{WSD} = 1.836 \frac{1}{mm} + 1.600.10^{-2} \frac{1}{A^{*2}.mm}\left(\frac{A^{*2}}{e}\right)^4 .M_4^{x} - 1.342.10^{-1} \frac{1}{A^{*2}.mm}\left(\frac{A^{*2}}{e}\right).M_{acc2}^{x}$$

$$-1.623.10^{-1} \frac{1}{A^{*2}.mm}\left(\frac{A^{*2}}{e}\right).M_{don2}^{x} - 7.416.10^{-4} \frac{1}{A^{*2}.mm}.A_{COSMO}^{x} - 9.726.10^{-1} \frac{1}{mm}\Psi$$

Eq. 1

This equation allows a good categorization into good, mediocre and poor lubricants. However, outliers are possible, mainly for multi-functional molecules and carboxylic acids that can form two coupled hydrogen bonds and are therefore also multi-functional. This is why the predicted, preselected candidates have to be validated by HFRR measurements.

6. RESULT AND DISCUSSION OF THE PREDICTION MODEL

We used the correlation presented above to predict the lubricity of esters in order to verify our model for this group of compounds. The results of the prediction in comparison with the measured WSD are shown in Fig.7.

In most cases the prediction gives a good estimation of the experimental values and can differentiate the ranking of the compounds. Excluding the outliers valeric-acid, levulinic-acid, and 2-methyltetrahydrofuran (2-MTHF) the wear scar is predicted with only 15% mean deviation. However the outliers show that the results have to be treated with care. In general, measurement uncertainties have to be separated from model limitations.

As our predictive model is parameterized for a given experimental setup (2), errors are inherent when transferring the results to another setup (as done here). As can be taken from fig. 6, our experiments revealed a lower WSD compared to the results of Knothe on whose data our model was parameterized. This might be the reason for the underestimation of the wear scar in all cases.
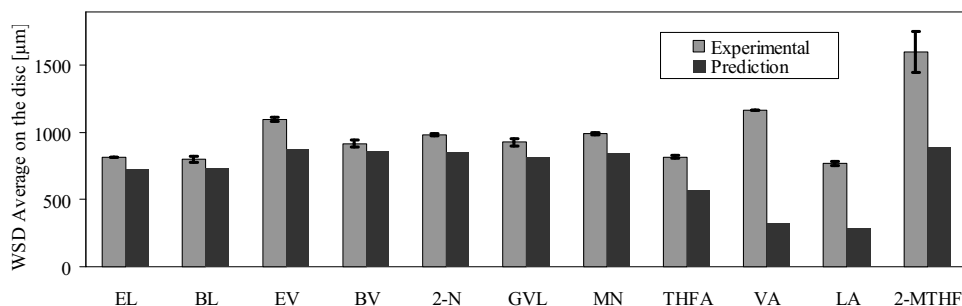
Figure 7: Prediction of the wear scar diameter on the disc for components in group A and B

A further source of error is a varying humidity of the surrounding atmosphere, which has been shown to have an impact on the WSD as stated in chapter 4. Finally additives can reduce the WSD significantly when present in the PPM region, so influences of impurities in the sample are difficult to account for. All these factors are somewhat relevant, but for the three outliers it is more likely that these deviations are caused by model limitations.

For valeric-acid and levulinic-acid, the overestimation of their lubricant performance is severe. In general acids tend to dimerize at their polar headgroup. Consequential those polar groups taking part in the dimerization are not free to interact with surface they ought to protect. In addition and more severe is the corrosive effect of those acids on the metal surface. As this corrosion is a chemical reaction it can not be captured by a model that has no information about the exact molecular structure of the reaction products. For fatty acids in general, chemisorption on the metal surface and formation of metal soaps have been reported (23). Consequently, SSCD information is not sufficient to predict such reactions, further the composition of the final products is not known.

For 2-MTHF we suppose that the steric hindrance due to the methyl group prevents a good surface coverage that is needed for wear prevention. A known issue of COSMO-RS that applies even more to the sigma-moment approach is that all geometric information about the shape of the molecule and the location of the different screening charge densities is lost by using solely the SSCD histogram. As mentioned above, our shape parameter can only give a rough estimation of the sphericity/linearity but does not explain these more complicated shape influences. As a result the lubricity is overestimated when mainly considering charges.

Subsuming our model is able to do effectively what it is made for: Reduce the number of promising candidates to those that are supposed to fulfill the lubrication criterion. But the results should not be taken 'as is' and manual post-processing is not dispensable. This is especially the case if a fuel is found that fulfills most of the other criteria which an optimized fuel has to be designed towards.

7. CONCLUSION AND OUTLOOK

In this paper the experimental investigation on the lubricity of the first proposed candidates for TMFB has been presented. The esters and acids with an additional carbonyl functional group reveal an enhanced lubricity compared to esters and carboxylic acids without carbonyl group. The lubricity performance of these compounds in dodecane as a model for a low lubricity diesel fuel shows however the favorable impact of fatty acids compared to esters. In the group 2 the fuels showed the ranking of alcohol > ester > ether.

The HFRR operates at atmospheric pressure, with temperatures limited by fuel boiling temperature. None of the existing conventional laboratory scale lubricity tests can predict the lubricity at temperatures approaching the boiling point of the fuel at atmospheric pressure. This is however in contrast with the fact that many fuel injection systems operate at temperatures approaching 100°C and are expected to rise temperatures in the near future (24). Since the most of tribological contacts in fuel injection equipment are under category of mixed lubrication, one has to consider the importance of viscosity as the major influencing parameter beside lubricity duo to elastohydrodynamic (EHL) fraction of the contact pressure (12).

Concerning pressure, the situation is quite different. The increasing of the viscosity of the fuel under pressure leads to enhancement of the EHL fraction and consequently less wear. The boundary lubrication fraction is also examined by HFRR with underestimation of the positive effect of adsorbability on wear protection. According to Langmuire's theory of adsorption, elevated pressure increases the fraction of adsorbate on the surface at any given temperature which however is beneficial for boundary lubrication and wear protection (25). Nevertheless this effect is included in the statistical analysis which correlates the amount of wear in injection pumps with pass-fail criteria of the HFRR test.

The correlative model proposed in previous work has good predictive power for most of the studied molecules and has proven its applicability as a preselection tool. However, the existence of outliers shows that the results have to be treated with care. Particularly for molecules for which chemical reactions or sterical hindrances have dominant effects, the results should be verified experimentally.

An even more application oriented pre-selection tool would be one for the evaluation of the impact of blending polar oxygenate fuels into low lubricity fuels. Such a tool is presently under development in our groups.

REFERENCES:

(1) Barbour, R.H., Rickeard D.J., Elliott N.G: Understanding Diesel Lubricity, SAE Technical Paper 2000-01-1918 (2000)

(2) Knothe G., Steidley KR.: Lubricity of components of biodiesel and petrodiesel. The origin of biodiesel lubricity, Energy & Fuels 19:1192–1200, (2005)

(3) Biorefinery, The worldwide status at the beginning of 2006

(4) Masuch. K., Fatemi A., Murrenhoff H., Leonhard K., A COSMO-RS based QSPR model for the lubricity of bio- and petrodiesel components, submitted to "Lubrication Science" in 18.03.2010

(5 Matzke, M., Litzow, U., Jess, A., Caprotti, R. and Balfour, G.: Diesel Lubricity Requirements of Future Fuel injection Equipment, SAE Paper 2009-01-084 (2009)

(6) Wichmann V., Pressure K., Abschlussbericht zum Vorhaben: Auswirkung des Zusatzes von RME auf Schmierfähigkeit von schwefelarmem Dieselkraftstoff, Rostock, (2001)

(7) Diesel Speicher-einsprizsysteme, Landhäußer et al., Robert Bosch GmbH Series, Fachwissen Kfz-Technik, (2007)

(8) Appledorn, J.K., Dukek, W.G.: Lubricity of Jet Fuel, SAE Technical Paper 660712, (1966)

 (9) DIN EN ISO 12156-1: Dieselkraftstoff – Methode zur Bestimmung der Schmierfähigkeit unter Verwendung eines Schwingungsverschleiß-Prüfgerätes (HFRR)

(10) Blizard, N.C., Bennett P.A.: A Comparison of Modified Elevated Temperature HFRR Test Data with Scuffing BOCLE Results, SAE Paper 961946 (1996)

(11) Shaver D.B., Giannini R.M., P.I. Lacey J. Erwin: Efects of Water on Distillate Fuel Lubricity, SAE Technical Paper Series 982568, (1998)

(12) Stachowiak G.W., Batchelor, A.W,: Engineering Tribology, 3.rd edition (2005)

(13) Hsu SM., Gates RS., Boundary Lubrication and boundary lubricating films, in: B. Bhushan, Modern tribology handbook, vol. I, CRC Press, Boca Raton, 2001, pp. 455492

(14) Furey MJ., Kajdas C., Kemplnski R., Applications of the Concept of Tribopolymerisation in Fuels, Lubricants, metalworking, and minimalist Lubrication, Lubrication Science (2002); 15(1), pp. 73-82,

(15) Korres DM., Anastopoulos G., Lois E., Alexandridis A., Sarimveis H., Bafas G., A neural network approach to the prediction of diesel fuel lubricity, Fuel (2002); 81, pp. 1243-1250

(16) Lodrigueza EA., Method for Prediction of High Frequency Reciprocating Rig Wear Scar Diameter for Hydrocarbon Mixtures 2008, United States Patent Application Publication, Pub. No.: US 2008/0090302 A1

(17) Klamt A., Schürmann G., COSMO: A New Approach to Dielectric Screening in Solvents with Explicit Expressions for the Screening Energy and its Gradient, J. Chem. Soc. Perkin Trans. (1993); 2, pp. 799-805

(18) Mehler C., Klamt A., Peukert W., Use of COSMO-RS for Prediction of Adsorption Equilibria, AIChE Journal 2002; 48(5), pp 1093-1099

(19) Klamt A., Eckert F., COSMO-RS: A novel and efficient method for the a priori prediction of thermophysical data of liquids, Fluid Phase Equilibria (2000); 172(1), pp. 43-72,

(20) Klamt A., Jonas V., Bürger T., Lohrenz J.C.W., Refinement and Parametrization of COSMO-RS, J. Phys. Chem. A (1998); 102, pp. 5074- 5085

(21) Klamt A., Diedenhofen M., Prediction of Soil Sorption Coefficients with COSMO-RS, J. Chem. Environmental Toxicology and Chemistry, (2002); 21, pp. 2562-2566

(22) Wadell H., Volume, shape and round- ness of quartz particles, Journal of Geology (1935); 43, pp. 250-280

(23) Bowden, F.P, Tabor, D.: The friction and lubrication of Solids (1954)

(24) Lacey P.I., Naegeli D.W., Da Le Cruz J.L, M. V. Wahlen, Lubricity of Volatile fuels for compression ignition engines, SAE Paper 2000-01-1804, (2000)

(25) Spikes H.A. and Cameron A., A Comparison of Adsorption and Boundary Lubricant Failure, Proc. Roy. Soc., London, Series A, Vol. 336, (1974), pp. 407-419.

Digital hydraulics

A Compact Hydraulic Switching Converter for Robotic Applications

Helmut Kogler*, Rudolf Scheidl*, Michael Ehrentraut*, and Emanuele Guglielmino, Claudio Semini, Darwin G. Caldwell**
* Johannes Kepler University Linz
Institute of Machine Design and Hydraulic Drives
Altenbergerstraße 69, 4040 Linz, Austria
** Italian Institute of Technology
Department of Advanced Robotics
Via Morego 30, 16163 Genoa, Italy

ABSTRACT

This paper is concerned with the application of switching technology to hydraulic actuation. Classical proportional flow control employing servo/proportional valves is dissipative and inefficient. By analogy it can be seen as the equivalent of resistive (rheostatic) motor control.

In mobile outdoor robotic applications where high power density, ruggedness and reliability are key requirements, the low efficiency of proportional control can be a limitation and it is necessary to go beyond the paradigm of proportional flow/pressure control.

One response to this challenge is to revisit traditional on-off hydraulic technology and develop systems and devices that behave in analogous manner to their power electronic counterparts. A prototype hydraulic switching converter, inspired by the electric DC-DC Buck converter, is presented. Its design, sizing and performance relative to a classical proportional valve-controlled system are assessed in the different operation modes. Pros and cons of the current design are identified.

1. Introduction

The reconsideration of hydraulic actuators in robotics particularly in mobile robots in particular for outdoor, high dynamic and heavy-duty applications is at the forefront of robotic research. An application is reported in [1]. Combustion engines are the preferred prime movers of such robots since they offer higher autonomous operation range than electrical drives powered by batteries. Nonetheless, an efficient use of energy is an important issue also for combustion engine powered mobile robots, since smaller power consumption saves weight of engines and tank for higher payload or other performance improvements. A simulation study in [1] compares proportional valve controlled robotic leg actuation with hydraulic switching converters, in particular a hydraulic Buck converter, and shows a significant energy saving potential of the latter. The benchmark for this comparative study was the actuation of a small pony sized quadruped robot's leg. The

encouraging simulation results showed energy savings far beyond 50% and motivated the development a corresponding switching converter prototype.

So far, hydraulic switching control is studied and developed only by a small number of research groups. The first studies known to the authors from USA [3, 4] were published in the late 80s. Publications of European research groups [5 to 13] started in the early 90s and presented different principles for this new class of hydraulic control technologies. Most of these papers are concept presentations, simulation studies, or first prototypal realizations. In [14] a hydraulic buck converter (HBC) design is presented in which the switching and check valves and the accumulators of the supply lines are already integrated in a block but the hydraulic inductance and the consumer side accumulator are externally mounted. The basis for an integrated design are compact switching and check valves, and also compact accumulators or other fluid pulsation damping devices. An overall compact design not only helps the integration into a machine or vehicle but is also important for enhanced efficiency and noise reduction. These aspects are discussed in [15, 16]. Motion control of hydraulic switching controlled linear actuator is presented in [17, 18].

The development of a compact HBC for a robotic leg as was presented in [2] and is subject of this paper. Its design and design rationale are presented in section 2, the preliminary experimental work on the steady state performance in section 3, a direct experimental energy consumption comparison with a proportional control in section 4, and an extensive outlook on improvement potentials for applications in mobile robots in section 5.

2.   Design of a compact HBC

2.1 HBC schematic and steady state characteristics

The HBC (which can also recuperate energy driving a linear actuator) is given by its schematic in Figure 1. Its functioning principle is described in [14, 18] and corresponds fully to the electrical buck converter, (see e.g., [19]). To extend the piston, the system pressure (p_S) side switching valve is operated, and to retract it the tank side valve. The actuation intensity is adjusted by the duty cycle κ of the PWM signal of the switching valves. The steady state performance characteristic of such a HBC according to a simple model is given in Figure 2. A HBC in the configuration shown in Figure 1 using check valves to suck oil from the tank line in 'forward mode' and to refill oil to the pressure line in 'recuperation mode' has two characteristic modes: i) the so called 'flow-control mode' for small flow rates and consumer pressures p_C that are in the middle of the tank and system pressure; ii) the 'pressure control mode' for high flow rates and for low or high pressures, respectively (see Figure 2). The boundary between 'flow control mode' and 'pressure control mode' is defined by the dashed line of Figure 2. Corresponding formulas of these curves of the idealized model and of extended models which take viscous friction and wave propagation in the inductance pipe into account can be found in [18].
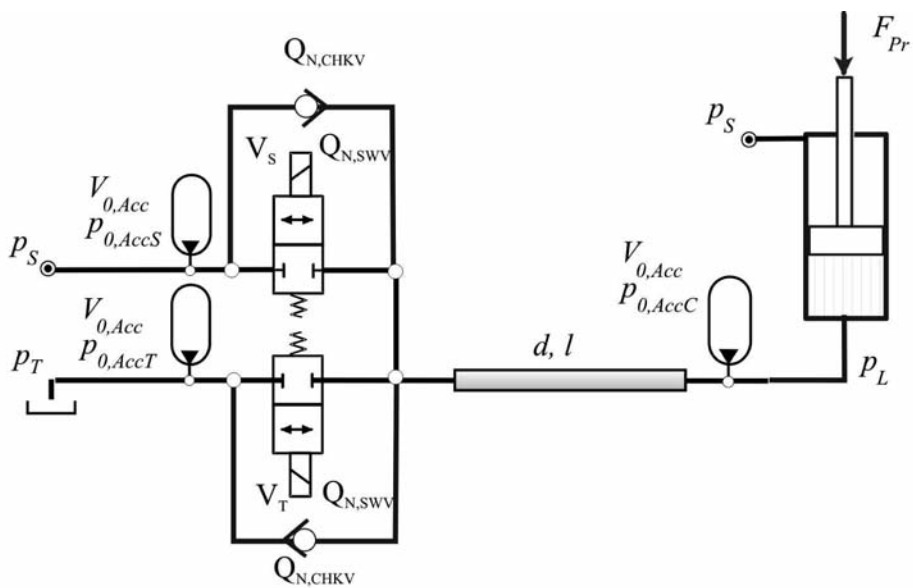
Figure 1 schematic of a hydraulic buck converter controlled linear drive
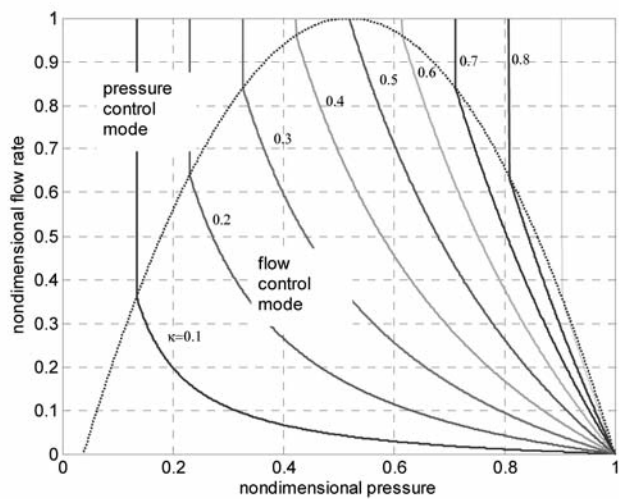
Figure 2 nondimensional performance characteristic of a HBC in forward mode neglecting the inductance pipe resistance

2.2 Design rationale

The requirements and constraints on the HBC for the robotic application are

System pressure p_S	*160 bar*	Aluminium components shall be applied for light weight design; that limits the system pressure
Tank pressure p_T	*5 bar*	A HBC requires an increased tank pressure to avoid cavitation; the minimum tank pressure necessary to meet this constraint depends on the response dynamics and nominal flow rate ($Q_{N,CHKV}$) of the tank side check valve and on a compact design featuring very low parasitic inductances; see [15, 16, 22] for physical background and details.
Nominal flow rate of the HBC	*3 l/min*	The study [1] revealed 1 l/min as typical nominal flow rate; in order to have some reserve and to balance the nominal flow rate of the available fast switching valves (see below) to some degree a higher flow rate was chosen
Switching valve	LCM 3/2 way switching valve	The study [1] showed that control accuracy is improved if switching frequencies are rather 100 Hz than 70 Hz; currently, there is only one valve available that can run such frequencies; its nominal flow rate $Q_{N,SWV}$ is 10 l/min @ 5 bar pressure loss; further data on this valve can be found in [20, 21]
Check valve	LCM plate valve design	A fast response high flow rate check valve is a must to achieve high efficiency and to avoid cavitation even if the tank line is only moderately increased; a plate valve design following the outline of [23] was chosen and optimized for this HBC.
Compact design		A compact design should facilitate the integration of the HBC in the robot and eases the overall modular design; it also helps to keep the noise level low which is an important aspect in switching control
Lightweight design		Light weight is important for mobile robots; the first HBC design focused on compactness rather than on light weight: aluminum as lightweight material would be preferred on steel for the hydraulic block; but it is damageable at threads and fits which makes a frequent manipulation complicated in testing and tuning of the system; redesign in aluminum and a further block shaping to avoid unneeded masses can be done

		straightforward in a second step
Pressure ripple damping		Damping devices for both supply lines and for the consumer lines are required. It was decided to use gas filled hydraulic accumulator technology because of their compactness; previous work showed inadequate dynamical response of conventional diaphragm accumulators because of their high in- and outflow hydraulic impedances and lifetime problems due to the high frequent operation.

2.3 Sizing

A simulation model in Matlab Simulink as described in [1] was employed to size first the hydraulic inductance. A first finding for an optimal size of the inductance pipe was an inner diameter of 2 mm and a length of 0.5 m. But it turned out that for the nominal flow rate of 3 l/min turbulent flow occurred which increased friction dramatically and, hence, deteriorates efficiency. Considering the turbulence avoidance constraint and taking the availability of pipe dimensions into account, optimization yielded a pipe of 3 mm x 1.05 m.

The nominal flow rate requirements on the check valve $Q_{N,CHKV}$ were set to be 20 l/min @ 5 bar pressure loss, to safely avoid cavitation also for the peak flow rates under worst conditions. An oversized check valve also facilitates a good recuperation performance of the HBC.

To overcome impedance and lifetime problems of diaphragm accumulators light weight aluminum piston accumulators were designed. In simulation studies a nominal accumulator volume $V_{0,Acc}$ of 0.04 l was found to yield acceptable attenuation results.

2.4 Mechanical design

A critical aspect of a compact HBC design is the arrangement of the inductance pipe. A straight pipe provides the best efficiency but is lengthy and impacts on the overall compactness of the system. A compromise is a large loop that brings the pipe end close to its beginning. This facilitates an integration of all components also of the consumer side accumulator into one block.

Different arrangements of the components and the inner connecting lines have been studied. The prototypal realization of the most compact design of all these trials is shown in Figure 3.

The design allows a very compact arrangement of more than one HBC. The supply lines go through the block. An additional block needs to be attached at the back side and gets in this way automatically connected to the supply lines. All connected HBCs have parallel access to all accumulators of the pressure line and tank line. If the switching of the different HBCs is properly phase shifted, pulsation of the total in- and outflow from and to the pressure and tank line, respectively, can be minimized such that accumulator volume can be saved. This is somehow analogous to multi-level electronic converters. See [24] for info.

The HBC block was manufactured in steel and not in aluminum, although lightweight design is an important issue for mobile robots. But this is the first prototype and during experimental testing frequent mounting and dismounting of components may damage threads if these are made of soft material, like aluminum. Since in this stage of development the functional performance is key, weight optimization by lightweight materials and design modifications will be done later.

Three piston accumulators were realized for reducing pulsations in the two supply lines and in the consumer line. A connection is provided in the block of the HBC to add a second accumulator to the consumer line to improve the damping performance further. Each accumulator has a volume of 0.04 l.
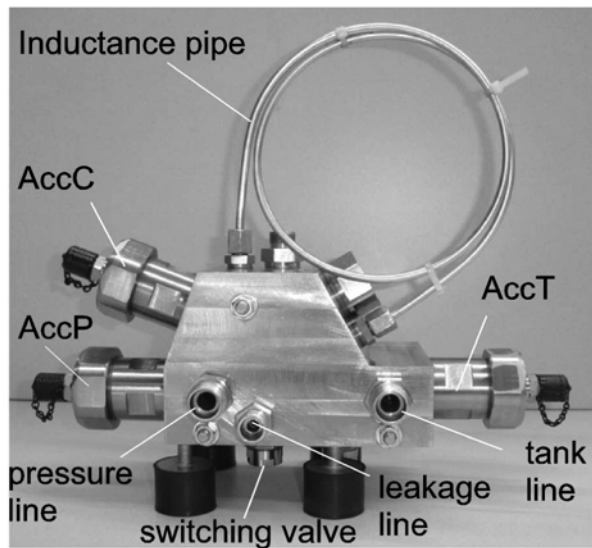
Figure 3 prototypal realization of a compact HBC

Simulations showed that for the very small diameter of the converter inductance pipe a low viscosity oil (15 cSt nominal kinematic viscosity at 40°C) increases efficiency considerably compared to typical viscosity values (32 or 46 cSt). Therefore, such a low viscosity oil has been selected (Shell Tellus T15).

3.   Experimental results

3.1 Steady state performance characteristics in forward mode

The schematic of the experimental setup is shown in Figure 4. A small 1.5 kW supply unit (SU) provides the hydraulic power. A nominally constant pressure is realized by a relief valve (RVS). The lower supply (tank side) pressure is raised to 5 bar by a pressure relief valve (RVT) and a small throttle valve (THT). That throttle can be removed if the backflow

is fed to the accumulator AccR and not to the tank directly. AccS, AccT, and AccC are the piston accumulators mounted on the HBC. Pressure sensors PS1, PS2, and PS3 measure the system, tank, and consumer line pressures. FM1 and FM2 are flow meters connected to the system and consumer line. The flow from the tank line is computed from the difference of consumer and system line flow rates. The proportional valve PV realizes different consumer resistances to determine the performance of the HBC in a wide operating range of pressure and flow rate. In stage 1 of this valve the forward mode is controlled, in stage 2 the recuperation mode (see next section). Control of the HBC, recording of measurement signals, computation of efficiency, and the automated execution of the whole measurement procedure was done with dSpace control hardware and the corresponding software. Control and measurement signals are sketched in Figure 5.
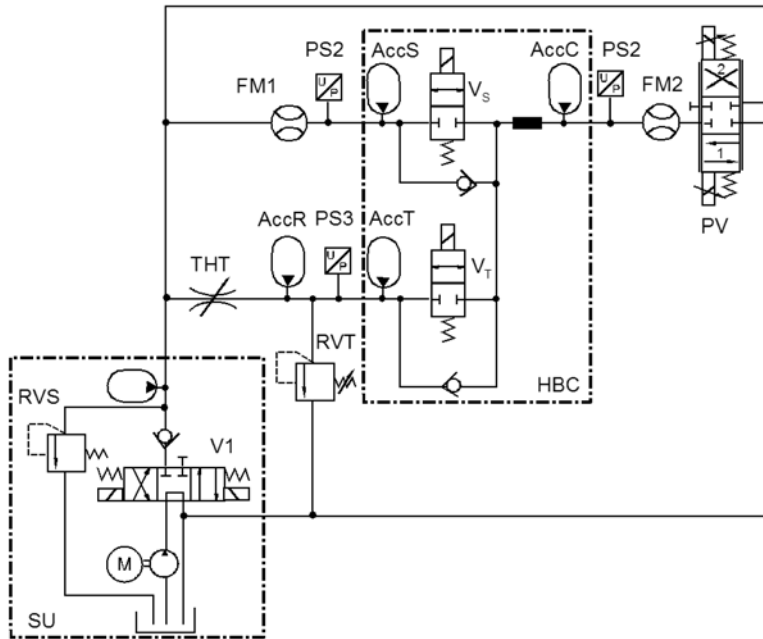
Figure 4 hydraulic schematic of the experimental set-up for steady state HBC performance tests
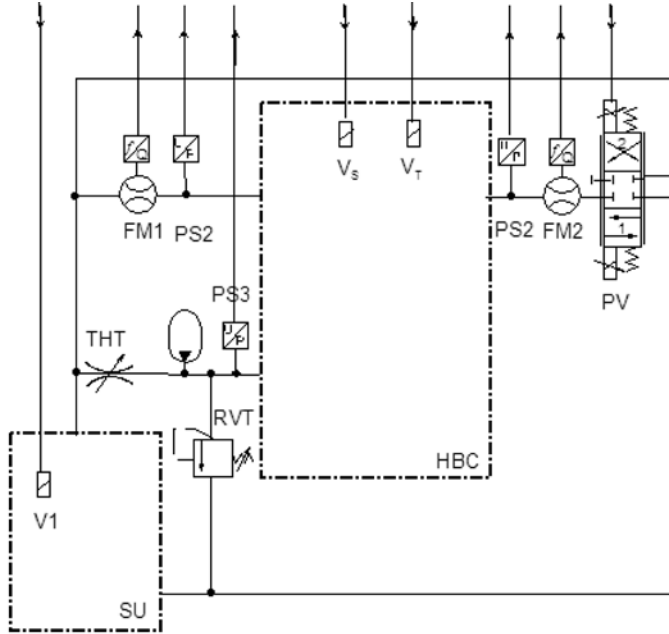
Figure 5 schematic of the control and measurement arrangement for steady state HBC performance tests

In an outer loop of the automated test sequence the duty cycle κ was varied between 20% and 60% in steps of 5% and in an inner loop the proportional valve (PV in Figure 4) was adjusted to obtain average flow rates Q_L ranging from 0.5 to 3 l/min in steps of 0.25 l/min for each κ. The pressures p_S, p_T, and p_L and the flow rates Q_S and Q_L were measured and recorded with a 10 kHz sampling rate. From these signals the hydraulic power flows at these three lines were computed and integrated over one full switching cycle to derive the efficiency in forward mode according to the following formula:

$$\eta = \frac{\int\limits_0^T p_L Q_L \, dt}{\int\limits_0^T p_S Q_S \, dt + \int\limits_0^T p_T (Q_L - Q_S) \, dt} \tag{1}$$

Figure 6 shows the graphs of the measured pressures and efficiencies and the efficiency improvement to a proportional drive that provides same pressure and flow rate and works with the same supply pressure p_S.
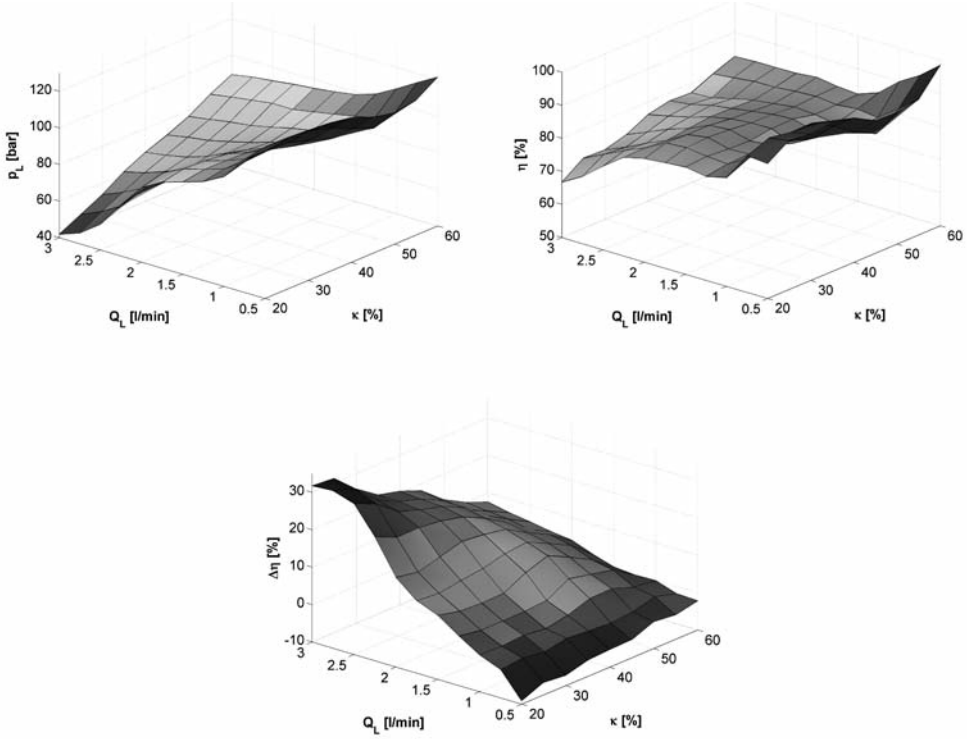
Figure 6   measured load pressures p_L , **efficiencies** η, **and efficiency improvements over resistance control** $\Delta\eta$ **of a HBC for different duty cycles** κ **and flow rates** Q_L **for a switching frequency 100 Hz.**

The HBC has quite a constant efficiency profile in a large operating range. The improvements over resistance control are higher for low operating pressures when resistance control has high pressure losses.

3.2 Steady state performance characteristics in recuperation mode

Basically, the hydraulic scheme and the control and measurement setup described in Section 3.1 and shown in Figure 4 and Figure 5, respectively are used. To provide a backflow of oil from the consumer line it is connected with the pressure line by the proportional valve operating in position 2 to control the pressure p_L. In this mode only the tank side valve is operated in PWM mode. The efficiency in this mode is given by the following formula

$$\eta = \frac{\int_0^T p_S Q_S dt + \int_0^T p_T (Q_L - Q_S) dt}{\int_0^T p_L Q_L dt} \tag{2}$$

Obviously, this is the inverse of (1). The measured performance characteristics for 100 Hz switching frequency and at nominal oil operation temperatures of 40°C are presented in Figure 7.

In contrast to the 'forward mode' results of Figure 6, no comparison with resistance control is given, since no energy recuperation is possible in conventional resistance control.
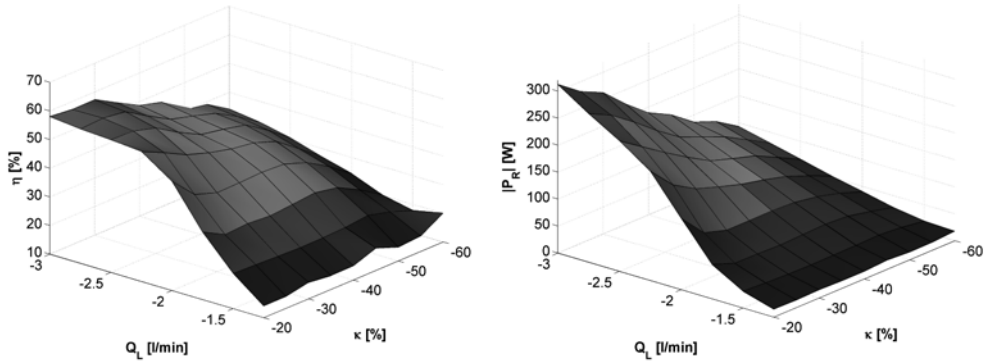
Figure 7   measured efficiencies η and recuperated power a HBC in 'recuperation mode' for different duty cycles κ and flow rates Q_L for a switching frequency 100 Hz.

There is a considerable recuperation efficiency and power, taking into account that this is a low power (< 1 kW) application where hydraulic efficiencies are often relatively poor. The peak recuperated power is 300 W which is 66% of the rated power in forward mode (450W).

3.3 Direct energy consumption comparison of HBC and resistance control

In the efficiency comparison of HBC with resistance control shown in Figure 4 the latter efficiency is computed from the actual consumer pressure and the system pressure of the HBC values. Furthermore, only steady state results are shown. To get a direct experimental comparison for an unsteady operation the loading and unloading of a hydraulic accumulator is taken as benchmark. The scheme of the test setup corresponds largely to the previous cases. Instead of a resistive load realized by a proportional valve the accumulator of 0.32 l volume and a filling pressure of 40 bar is placed. The flow to this accumulator and the pressure at its port are measured. A sinusoidal rising and falling of the pressure is controlled via a feedback loop.
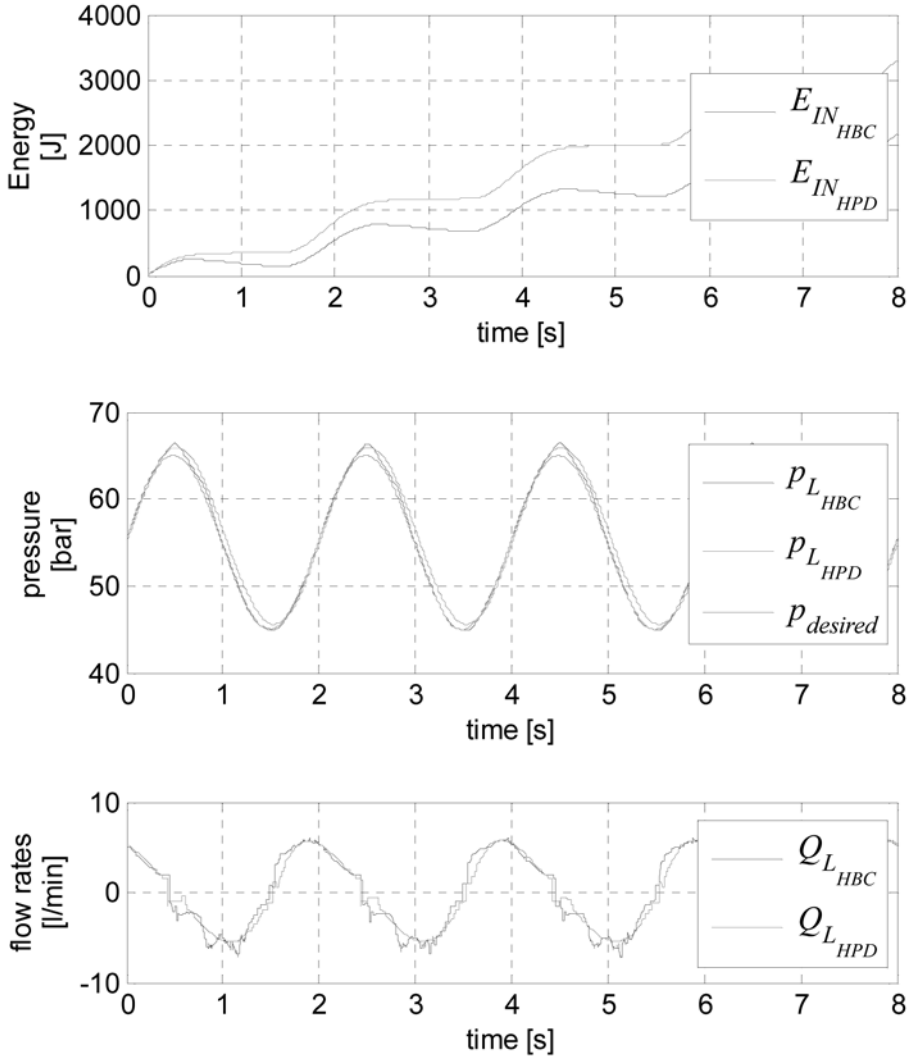
Figure 8 measured power consumptions, accumulator pressures, and flow rates of a HBC and hydraulic proportional control for the periodic charging and discharging of a hydraulic accumulator.

4.   Conclusion and outlook

A hydraulic buck converter for a mobile robotic application can be designed in a compact way. High efficiency values also for these small power applications in the sub-kilowatt range were obtained. The converter can also recuperate energy. In a direct energy consumption comparison with hydraulic resistance control by a proportional valve for the periodic charging and discharging of an accumulator the buck converter achieved a 34% reduced average energy consumption.

This converter will be applied to the control of a hydraulic leg for a quadruped robot and its operating performance in terms of motion control precision and efficiency will be experimentally tested.

Acknowledgement

REFERENCES

(1)   Guglielmino E., Semini C., Yang Y., Caldwell D., Scheidl R., Kogler H., Energy Efficient Fluid Power in Autonomous Legged Robots, Proc. 2009 ASME Dynamic Systems and Control Conference, Renaissance Hollywood Hotel, October 12-14, 2009, Hollywood, California.

(2)   Ehrentraut M., Auslegung und Realisierung eines kompakten, energieeffizienten hydraulischen Antriebes für kleine Leistungen, Diploma thesis, Johannes Kepler University, 2010.

(3)   Brown, F.T., 1987, "Switched reactance hydraulics: a new approach to the control of fluid power", Proc. National Conference on Fluid Power, Chicago, Feb-Mar, pp25-34

(4)   Brown, F.T., Tentarelli, S.C., Ramachandran, S., 1988, "A hydraulic rotary switched-inertance servo-transformer", Trans. ASME, J. Dyn. systems, meas. & cont., 110(2), pp144-150.

(5)   H. Gall, K. Senn. Freilaufventile – Ansteuerungskonzept zur Energieeinsparung bei hydraulischen Linearantrieben. Ölhydraulik und Pneumatik 38, 1994, pp. 38-43.

(6)   R. Scheidl, A.S. Abo El Lail, D. Schindler. On Fluid Power Control by Switching Techniques. In Acar, Makna, Penney (Eds.): Proc. Joint Hungarian-British Int. Mechatronics Conf., Sept. 21-23, Budapest, Computational Mechanics Publishers, Southampton, Boston, 1994, pp. 551-556.

(7)   R. Scheidl. Realisierung von Schalttechniken für hydraulische Antriebe. e&i Elektrotechnik und Informationstechnik, 113, 1996, pp. 553-558.

(8)   R. Scheidl, D. Schindler, G. Riha, W. Leitner. Basics for the Energy-Efficient Control of Hydraulic Drives by Switching Techniques. In J. Lückel (ed.): Proc. 3rd Conference on Mechatronics and Robotics, Oct. 4-6, Paderborn, Teubner, Stuttgart, 1995.

(9)   R. Scheidl, G. Riha. Energy Efficient Switching Control by a Hydraulic 'Resonance-Converter'. In C.R. Burrows, K., A. Edge (Eds.): Proc. Workshop on Power Transmission and Motion Control (PTMC'99), Sept. 8-11, Bath, 1999, pp. 267-273.

(10)   J. Dantlgraber. Hydro-Transformer. European patent application (PCT) Intern. Publication No. WO 00/08339, 2000.

(11)   R. Scheidl, M. Garstenauer, B. Manhartsgruber. Switching Type Control of Hydraulic Drives – a Promising Perspective for Advanced Actuation in Agricultural Machinery. SAE-Technical paper series 2000-01-2559, Society of Automotive Engineers, 2000.

(12)   Kogler, H., Scheidl, R. 2008. Two Basic Concepts of Hydraulic Switching Converters. The First Workshop on Digital Fluid Power, 3rd October 2008, Tampere, Finland.

(13)   Johnston D. N., A Switched Inertance Device for Efficient Control of Pressure and Flow, Proc. ASME/Bath Fluid Power Symposium at 2nd Annual Dynamic Systems and Control Conference, October 12-14, 2009, Hollywood, CA, USA.

(14)   Scheidl, R., Manhartsgruber, B., Kogler, H., Winkler, B., Mairhofer M., The Hydraulic Buck Converter - Concept and Experimental Results, Proc. 6th IFK, 6. International Fluid Power Conference, Dresden, 31.3.-2.4. 2008.

(15)   Scheidl R., Manhartsgruber B., Mikota G., and Winkler B., State of the Art in Hydraulic Switching Control – Components, Systems, Applications, Proc. Ninth Scandinavian International Conference on Fluid Power (SICFP'05), June 1.3, 2005, Linköping, Sweden.

(16)   Scheidl R., Steiner B., Winkler B., Mikota G., Basic problems in fast hydraulic switching valve technology; Proc. Sixth Internat. Conference on Fluid Power Transmission and Control (ICFP05), April 5-8, Hangzhou, China.

(17)   Kogler, H., Winkler, B. and Scheidl, R. 2006. Flatness Based Control of a Fast Switching Hydraulic Drive. 2nd International Conference on Computational Methods in Fluid Power, FPNI'06, Aalborg, Denmark.

(18)   Kogler H. and Manhartsgruber B., Simulation Tools and Control Design for Fast Switching Hydraulic Systems, Proc. 2nd Workshop on Digital Fluid Power (DFP09), Linz, Nov. 12-13, 2009.

(19)   Tietze U., Schenk Ch., Halbleiter-Schaltungstechnik, 9th Edition, ISBN 0-387-19475-4, Springer Verlag, 1990.

(20)   Plöckinger A, Scheidl R., Winker B., Development and Prototyping of a Compact, Fast 3/2 Way Switching Valve with Integrated Onboard Electronics, Proc. 11th Scandinavian International Conference on Fluid Power, SICFP'09, June 2-4, 2009, Linköping, Sweden.

(21)   Plöckinger A, Scheidl R., Winker B., Performance, durability and applications of a Fast Switching Valve, Proc. 2nd Workshop on Digital Fluid Power (DFP09), Linz, Nov. 12-13, 2009.

(22)   Scheidl R., Kogler H., Manharstgruber B., A Cavitation Avoidance Strategy in Hydraulic Switching Control Based on a Nonlinear Oscillator, Proc. Of the 10th Scandinavian International Conference on Fluid Power, SICFP'07, May 21-23, 2007, Tampere, Finland.

(23)   Plöckinger A., Scheidl R., Development and Laboratory Tests of a Cheap, Robust, and Fast Check Valve for Industrial Applications, Proc. 9th Scandinavian International Conference on Fluid Power, SICFP05, June 1, 2005, Linköping, Sweden.

(24)   http://leiwww.epfl.ch/publications/schibli_nguyen_rufer_ieee_98.pdf

Characteristics of digital hydraulic pressure reducing valve

Teemu Lähteenmäki
Mika Ijas
Esa Mäkinen
Tampere University of Technology
Department of Hydraulics and Automation
Tampere, Finland
Phone +358 2 823 4970, Fax +358 2 823 4974
E-mail: teemu.lahteenmaki@tut.fi

ABSTRACT

Development in the field of digital hydraulics has been very fast lately. Some of the main focuses of the research have been in developing faster acting valves, more energy efficient systems and developing digital actuators. However the area of pressure control is still relatively uncharted territory.

In this study a digital hydraulic pressure reducing valve system was developed and its characteristics were measured and compared to a high-quality analog pressure reducing valve. The goal was to improve linearity, hysteresis and to reduce dependence of the pressure on the volume flow, which typically are disadvantages of normal analog pressure reducing valves.

The studied digital hydraulic pressure reducing valve system consists of two six-valve DFCUs (Digital Flow Control Units) and a controller with a separate pressure feedback sensor of the control volume. Common, rather slow, on/off –cartridge valves were used with a separate fixed orifice plates to get binary coded nominal flow rates. For controller a basic PID –controller was chosen in order to make it easy to tune and with low demand for computing power. The controller was realized with a dSPACE real-time system.

The study introduces a few ways to improve the performance of the digital hydraulic pressure reducing valve system. Delay compensation can be used to reduce pressure peaks in state changing situations, antiwindup –system was adopted to ease problems in flow saturation situations and booster circuits was used for faster valve actuation. Measured results are shown and some still remaining problems and the need for the future research are discussed.

Keywords: Digital hydraulics, digital valve, DFCU, pressure control, pressure reducing valve

1   INTRODUCTION

During 21st century there has been a boom in the development of digital hydraulics. Maybe the most completely researched application area of digital hydraulics is control valves. Recently also other applications, like digital hydraulic cylinders, have been researched. However, there is so far very little research available in pressure control.
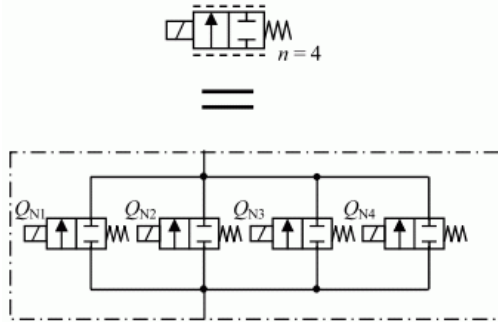
Figure 1 the drawing symbol of DFCU that consists of several parallel connected on/off-valves (1)

Figure 1 depicts a drawing symbol of digital hydraulic valve (upper picture) that consists of one or more (in this case four, lower picture) parallel connected on/off-valves. This parallel connected valve system is commonly called Digital Flow Control Unit (DFCU)(1). A DFCU can be thought as a variable orifice with fixed amount of different flow areas. The flow area can be changed by opening a combination of differently sized valves. More valves give a better resolution and/or bigger maximum opening area. If external pressure sensor is added to the system it is possible to use the variable valve opening area to control pressure.

In this study some of the measured characteristics of developed digital hydraulic pressure reducing valve are introduced. The developed valves system used common, rather slow, on/off –cartridge valves and simple PID-controller. To make the valves change states faster an analog booster circuitry was used and its effectiveness measured and evaluated.

The introduced characteristics need to be kept in mind while developing and measuring the performance of similar valve systems. The measurements shown also point some pros and cons of this technique when applied to pressure control.

2   KNOWN CHARACTERISTICS OF PRESSURE CONTROL

The well known good characteristics of the digital hydraulics apply also in the field of pressure control. The valves are more fault tolerant because of the redundancy offered by the parallel connection and also because the use of reliable on/off valves (2, 3). The energy efficiency is boosted by the non-leaking valves (4). Furthermore, the valve system is highly flexible and easily configurable just by changing the controller software or its parameters according to the circumstances (1).

However, there are a couple of characteristics that should be considered before designing a digital hydraulic pressure valve. One of them is the variable bulk modulus. The hoses in the system and the oil used to transfer the energy have a highly pressure dependent bulk modulus. This means that fixed amount of oil passed to the controlled volume changes the pressure differently depending on the pressure level already in the controlled volume. This characteristic changes the systems integral pressure gain.
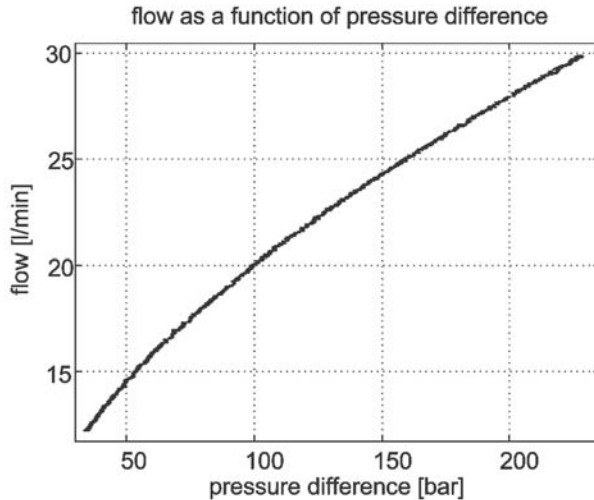
Figure 2 flow through the biggest valve of the system as a function of pressure difference over the measured valve system

Another characteristic is also linked to pressure dependent pressure gain. A certain control value represents a combination of opened valves. The opened valve combination can be thought as a fixed orifice and so the flow through it depends on the pressure difference over the valves (figure 2). This means that a certain control value has variable flow rate depending on the pressure difference over the valves. (5) This makes it difficult to get the controlled pressure down to zero and up to the level of inlet pressure as in both these cases the pressure difference over the valve system is low. These two properties combined make the high pressure operation difficult and the operation near zero even more difficult.

In conclusion, the pressure gain is highly variable and depends on the effective bulk modulus of the system and on the current pressure difference over the active valve system. This sets a demand for the controller to vary gain according to the conditions. A fixed gain controller can also be used but its performance is always weaker at the other end of the controlled pressure band. This is a common characteristic to all pressure valves (6, 7).

Common difficulty to all digital valve systems is the variable valve delays and the pressure peaks they produce. The problem can be minimized with cleverer valve coding, by carefully compensating the variances in delays in the control system or by faster valves. (1) The binary valve coding chosen for this paper gives the widest range of flow values through a DFCU, but it is the most sensitive to pressure peaks caused by variable valve delays. Compensation of the delays requires a lot of knowledge on the individual valve delays and their behavior in different situations so it was left for future research. This decision was also made because one of the goals of this paper was to study possibilities to

utilize low-end hardware and simple control method. However, to make the chosen common valves to work faster, an analog booster circuit was used and the performance of this upgrade was measured and presented in this paper.

3   DEVELOPED VALVE SYSTEM
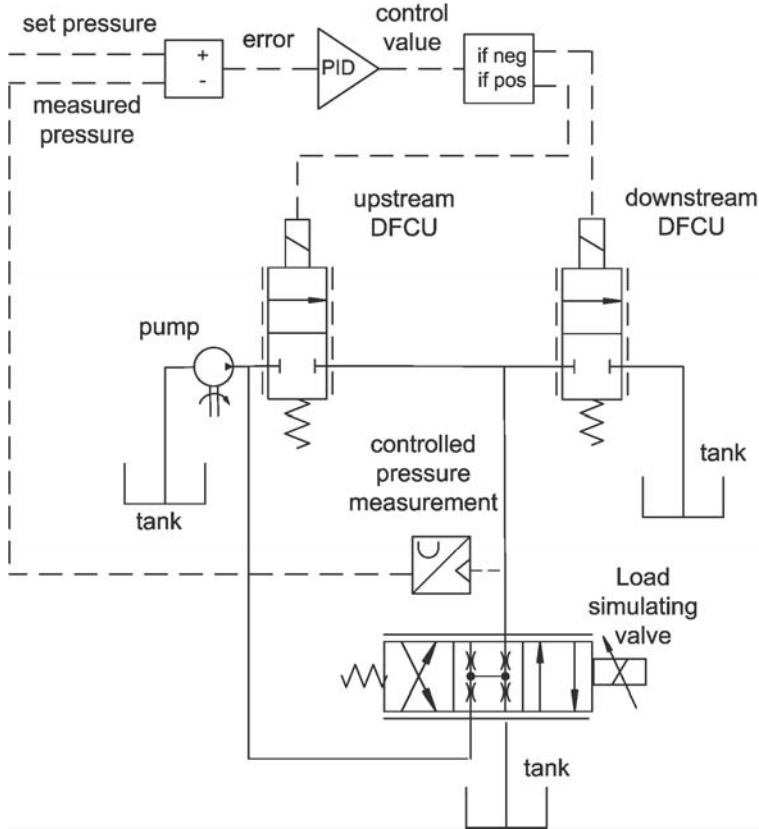
Figure 3 conceptual schema of the developed valve system

The studied valve system (figure 3) consists of two six valve DFCUs, external pressure sensor and a controller unit. The general idea is that the controller opens some of the upstream valves if the measured pressure is too low and the downstream valves if the pressure is too high. The greater the difference between set pressure and measured pressure the higher flow rate valves the controller needs to open. The developed system is based on ISO 10770-3 standard (8) with minor modifications. It is the same system Ijas used in his research (5). The two DFCUs are actually situated in one valve block and the coding of the flow rates is done with orifice plates placed between the valve and the valve block. The coding is done according to PCM–type binary system. The PCM (Pulse Code Modulation) means that every valve is differently sized and binary sizing system means that the smallest valve has half the flow rate of the second smallest and so on (1). In this case the orifice

sizes from the smallest to the biggest are 0.3 mm, 0.4 mm, 0.6 mm, 0.9 mm, 1.3 mm and 1.8 mm. The sizing is not actually ideal and is restricted by the drill sizes found for the task. A Hydac WS08W-01 cartridge valve was chosen for the task for its suitable specs, wide availability and reasonable price. The manufacturer promised delay for the valves is 35 ms and maximum recommended pressure is 250 bar.

4   BOOSTER MEASUREMETS

The goal of this study was to find out what kind of performance is it possible to get with modern valves and other easily accessible hardware. It is well known that with faster valves the DFCU's generally perform better. Pressure peaks caused by the variable delays between the valves in the DFCU are smaller, the controlled pressure can be more accurately achieved and the system can react faster to changes. One way to achieve this while keeping the cost down is to boost the operation of valve control.
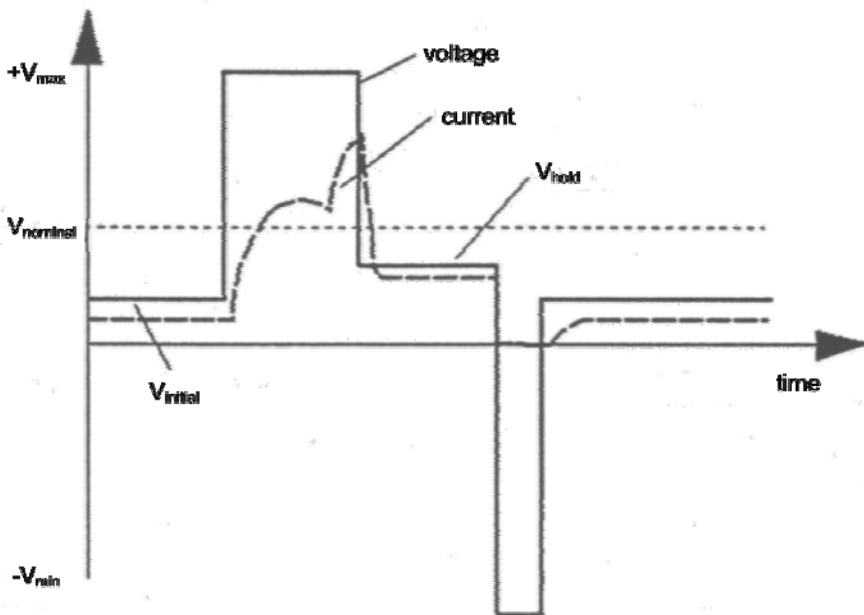
Figure 4 behavior of voltage and current with booster circuit (10)

The principle of booster circuit is to use several more suitable voltages to control the valve spool instead of the usual one constant operating voltage ($V_{nominal}$, figure 4). To boost the opening of the valve a higher operation voltage can be used. This higher voltage ($+V_{max}$) should be applied only for the time it takes for the spool to move into fully open position. Different technologies could be used to realize a booster circuit. In a simple analog electric circuit used in this paper, the boost length can be set by sizing of a capacitor. (10)

After the initial boost the voltage is dropped to as low as possible while keeping the valve opened (V_{hold}). This way it is faster to shut the valve and damaging of the solenoid can be

avoided. Also the energy consumption and heating of the valve is reduced. In some designs even a short negative voltage can be applied for faster valve closing. (10)
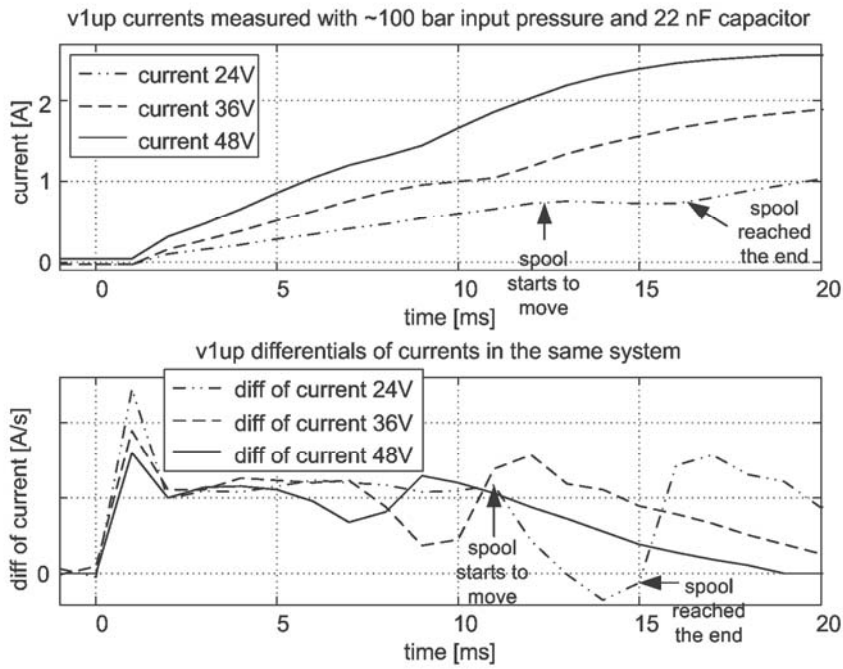
Figure 5 current along with its derivative with three input voltages

In figure 5 the drop in current in the middle of the rising trend is caused by the moving spool. From the calculated differentials (MatLabs diff function) the drop in current is easier to detect. The diff function calculates the difference of two following samples and puts the result to the point of time of the earlier sample. Because of this, the delay read from the differentials of current seem a bit optimistic. The diff function practically forms a derivative of the current from which changes are easier to detect. The results of the diff function have been scaled to fit the same figure. When the differential of current starts to decline the spool starts to move and when the differential starts to rise the spool has reached the end of its movement. The measured spool delays are presented in the table 1. The drop in the current seems to get smaller and harder to detect with higher operation voltages.

The measurements are done from the upstream valve 1 (abbreviated v1up, 0.3 mm flow diameter). For this experiment a bigger 22 nF capacitor is used for longer than necessary current boost. The valves are installed in a system with inlet pressure of a 100 bar and the sampling time of the measurement system was 1 ms. The current were measured with LEM LTS 15-NP current sensor and they are electronically filtered.

Table 1 measured spool delays in system with 100 bar pressure difference

Operational voltage [V]	spool starts moving [ms]	spool moved to the end [ms]
24	11	15
36	7	10
48	5	8

It is expected that the operation voltage influences the time used by the valve to fully open. In table 1 are presented opening delays for some operation voltages. The main trend is that higher voltage shortens the time needed for the spool to start moving. The influence of raising the operation voltage from 24 to 36 Volts is much bigger so it can be assumed that the impact of even higher voltages will be smaller.
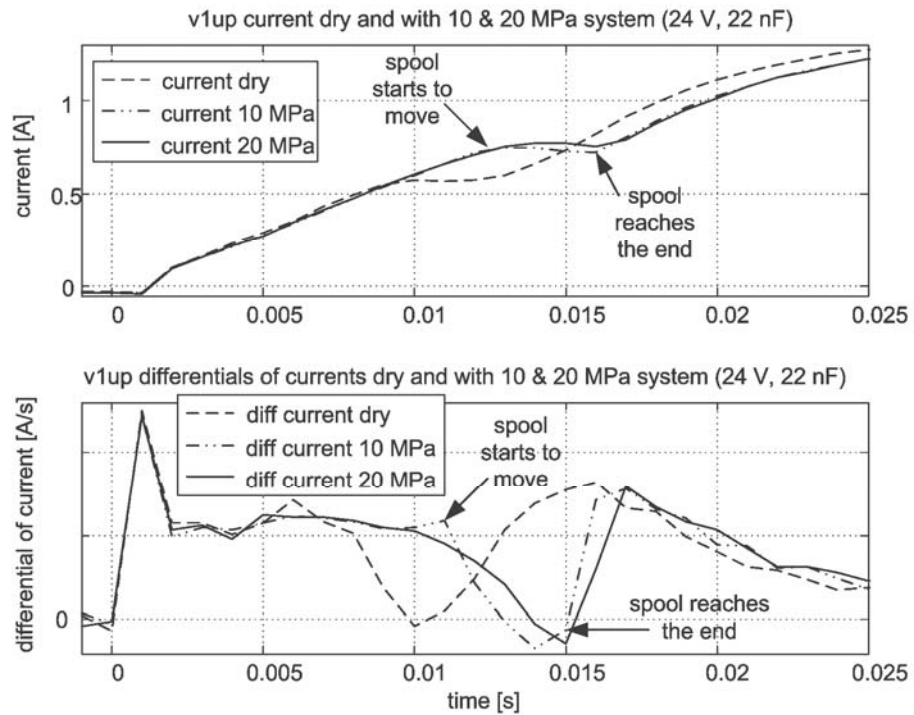
Figure 6 the behavior of current with the valve plugged in a hydraulic system and with the valve on dry

In figure 6 the currents and their differentials measured from the upstream valve 1 are shown in different situations. The currents are measured in three different cases: in a system with nearly 100 bar pressure difference over the measured DFCU, in a system with 200 bar pressure difference and in a dry system where the valve is not connected to any hydraulic

fluid at all. The drop in the current interpreted as the spool movement happens earlier in measurement done with the valve not connected to hydraulic system. This way it is possible to prove that the spool moves slower in real life system than in measurements done with the valves on the dry. The measurements also show that the higher pressure slows the spool down, but the impact of higher pressure is only minor. The measured delays for the spool to finish its movement are 10 ms in the dry, 14 ms in the 100 bar system and 15 ms in the 200 bar system.
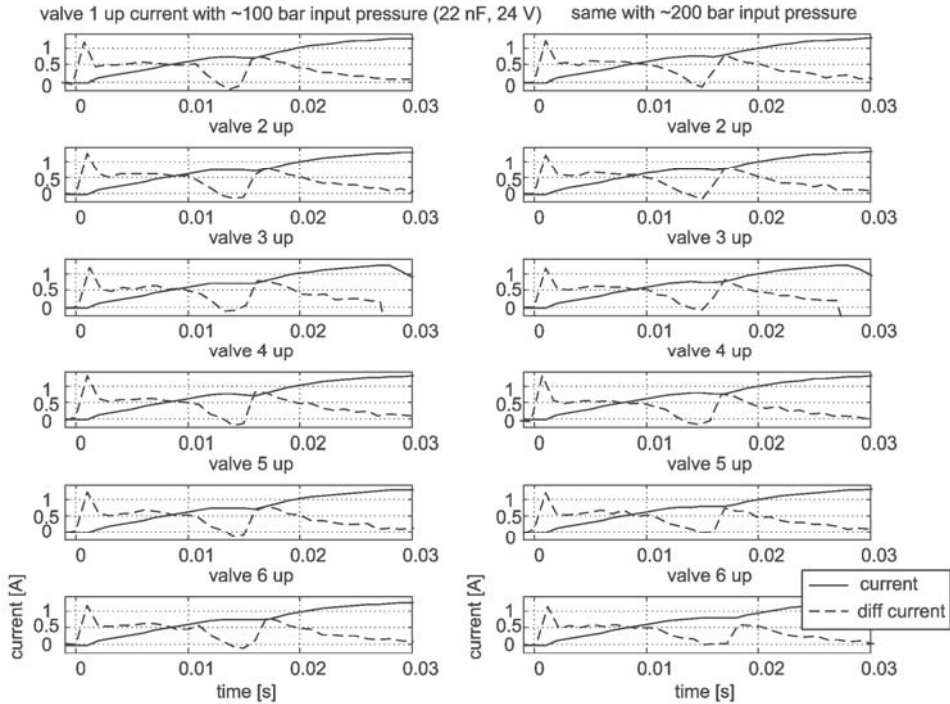
Figure 7 Currents and their differentials for all valves in two input pressures

From figure 7 currents and their differentials (scaled to fit) are presented for each valve with two input pressures. Different valves are stacked above each other in the figure. The delay for spool movement is virtually same for every differently sized valve. On the right side the same measurements have been repeated with higher 200 bar input pressure. By comparing these it is safe to say that the pressure compensation of the chosen valve type works and the pressure difference has only small (about 1-2 ms) influence on the spool delays.
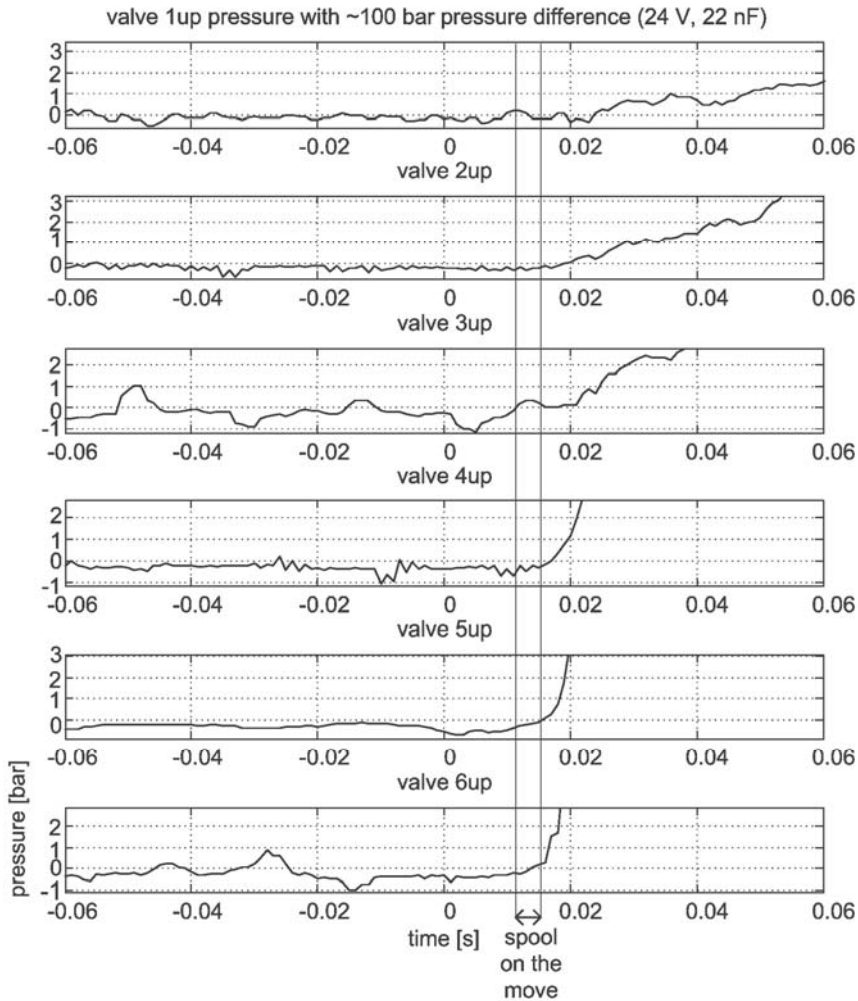
Figure 8 development of pressure during valve opening

In figure 8 depicts the pressure curve when each of the valves on upstream DFCU are manually opened in turn while the similarly sized valve on the downstream DFCU is kept opened the whole time. The below zero pressures are caused by slight calibration error and pressure ripples caused by interference. The spool movement time determined from the current is also shown. The measurement implies that the smallest valve is also the slowest, but both the pressure and the valve size have an influence on the pressure rise rate making it difficult to accurately detect the valve opening time from the measured pressure. There are also pressure ripples that make the determination of valve delays even harder. The measurement done from the current on the other hand, only represents the spool movement and does not take the dynamics of the fluid into account. The fluid movement time is often considered to be insignificantly small.

In conclusion the current measurement is accurate and easy way to determine valve opening delays. Pressure measurement on the other hand is a bit pessimistic and inaccurate, but especially with high pressure difference and higher flow rate valves can be used for estimation.
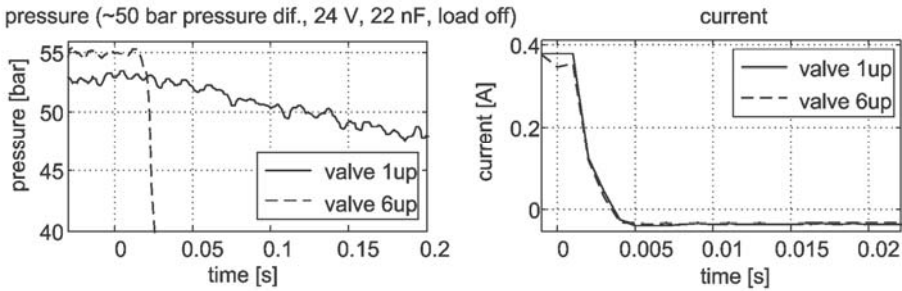
Figure 9 the current and pressure measured during valve closing

The determination of closing delays is more difficult. The spool movement is not detectable (figure 9) from the current measurement and estimation from the pressure measurement has the same problems as when determining the opening delay.

For a rapid closing of the valve it is necessary to set the holding current to as low level as possible while still able to keep the valve opened. This current level is characteristic to each valve type. Higher operating voltage would reduce the closing delay further, but not as significantly as in the case of the opening delay. In this study the closing was tested only with the 24 V. With the studied booster circuit a manual readjustment of the holding current would have been required for every voltage level.

5   COMPARISON TO CONVENTIONAL VALVE

The digital pressure valve is designed to give an alternative for analog pressure reducing valves. The performance is here compared against a high quality analog valve in dynamic and static tests to get idea of the performance levels. Some characteristics of each technique can also be seen from these measurements.

The analog valve has integrated electronics and is hard to tune. The PID –controller found in the digital valve on the other hand is relatively easy to tune and its tuning methods are comparatively common knowledge. For these tests the parameters for the digital valve controller were searched with few test runs and they are not optimal. The used parameters are K=1.1, T_i=0.3 and T_d=0.0005.

The measurement and controller refresh frequency was 1000 Hz, but the control to the valves was refreshed only at 50 Hz according to the measured valve delays. The used operating voltage of the booster circuits was 36 V. The supply pressure was around 205 bars.
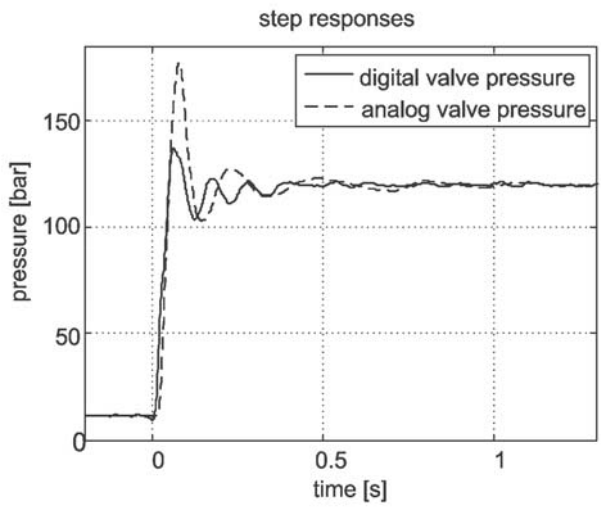
Figure 10 the step responses of studied digital valve system and comparative analog valve

The comparison of the step responses (figure 10) reveals the aggressiveness of the tuning and the overall gain of the system. The step used in this test was from 11.5 to 120 bars. During the measurement the valve simulating load was set at 0V control but still leaking internally.

It is understandable that the analog valve is tuned for a bigger system so the gain of the controller needs to be high. This is why the overshoot of the analog valve is higher (57.3 bar). The digital valve can however reach the set pressure as fast as the analog valve (48 ms) with smaller overshoot (16.9 bar) and pressure ripples. The settling time within 2 bars for the digital valve is 361 ms and for the analog valve 736 ms. The pressure delays of both valves are small.
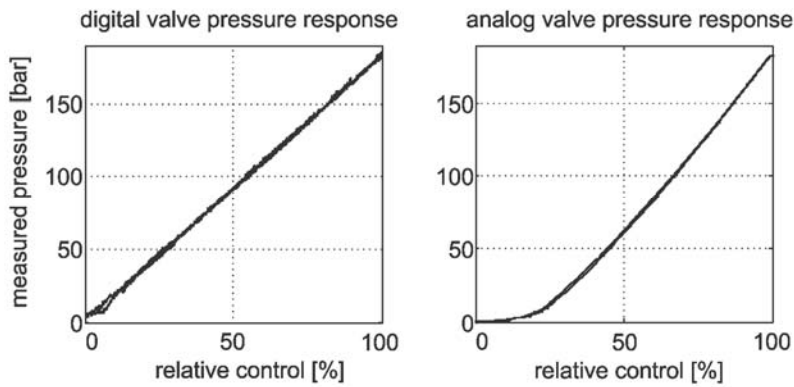
Figure 11 the pressure response while raising the set pressure with a ramp

The digital valve system has a variable delay caused by the refresh rate of the controller (max 20 ms). Regardless of that in the measurement the digital valve has even slightly smaller delay than the comparison valve. Both of the valves have a good steady-state accuracy and stability.

In another test the valves set pressure, or in the analog valves case the control voltage, was ramped up to 182.5 bars, kept there for a while and then reduced back to 11.5 bars. The whole sequence took place in 80 seconds. During this time the load valve was kept leaking at 0 V control.

From the measurements shown in figure 11 the nonlinearity of the analog valves can be seen compared to the digital valves remarkable linearity. For analog valve this can be compensated by control software but this causes some extra work. The hysteresis of both valves is very small. The digital valve has problems achieving zero pressure with this controller and settings. Digital valve also starts to raise the pressure late because of the winding up of the controller. There also seem to be little pressure ripples during the raising and lowering of the pressure. They are probably caused by asynchronous valve operation.
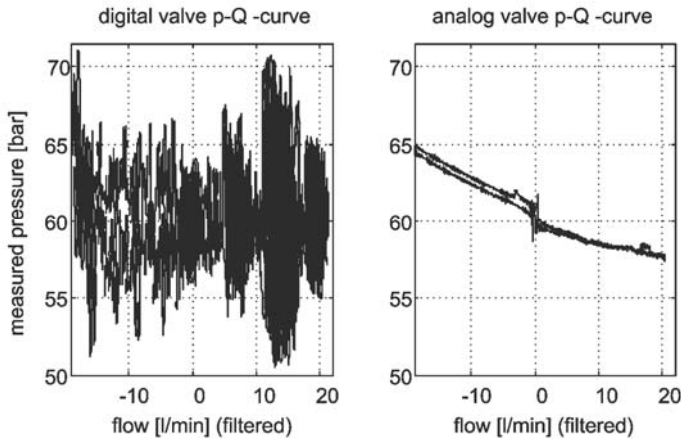
Figure 12 the pressure response while using a ramp control to the flow through the load valve

This measurement (figure 12) shows how well the valves manage to keep the set pressure when the amount and direction of flow to the load changes. This was realized by ramping up and down the control voltage of the valve that simulates load. The negative flow here means that the flow direction is reversed and now the flow goes back from the load. Both figures have been digitally filtered twice with 2th order low pass filter with natural frequency of 200 rad/s and damping factor of 0.7. Filtering has been done in both cases with identical settings.

The analog valves have problems with the changing flow direction that can be seen also in this measurement (11). Overall the analog valve manages to keep the pressure within 5 bars of the set value (60 bars) while the error becomes bigger towards higher flow rates (6, 7). The digital valve system keeps the pressure around the set value, but generates pressure ripples throughout the tested flow range.

6   CONCLUSIONS AND DISCUSSION

The studied valve system consisted of two six valve DFCUs, external pressure sensor and a controller unit. The sizing of the valves was done according to PCM–type binary system and relatively affordable prized cartridge valves were selected for the DFCUs. A booster circuit was used to reduce switching times of the valves. This system was measured and compared to conventional high quality analog pressure reducing valve.

The measured currents can be used to determine the movement of the valve spool. Pressure measurement is not as accurate, but it can be used for rough estimate of the delay. Delays estimated from the pressure are a bit bigger compared to delays determined from the current, especially on smaller valves.

The booster circuit cuts the opening delay roughly by half compared to manufacturers info. The use of higher operating voltage of the booster circuit reduces the delay even further. The hydraulic system slows spool movement by as much as 5 ms. The pressure level of the system has no significant influence on the delays and the spool movement times between differently sized valves are almost identical. For smaller closing delays the holding current should be set as low as possible, so this was left to the future studies.

The pressure behavior with a ramp input is linear and hysteresis of the valve is insignificantly small. Zero pressure is problematic for the digital valve to achieve. The pressure keeps fairly constant while ramping up and down the flow through the load valve, but big pressure ripples occur.

This study shows that digital valve corrects many of the analog valves flaws (12) but introduces a couple of new ones. The behavior is very linear and the hysteresis is small. Also there are no pressure peaks when the load flow changes the direction (11). New problems are difficulties near zero pressure and the constant pressure peaks probably caused by the imprecise valve operation. The former is caused by the DFCUs pressure difference dependent flow ratios that make it difficult for a fixed gain controller to control the pressure near the ends of the pressure band. The pressure level dependent bulk modulus also makes the tuning of the controller always a compromise. Solving these problems should be the main focus of future research.

The study shows that despite of the relatively slow valves and the simple control the digital valve system achieves good performance results. In addition, the digital hydraulic pressure valve shows great potential by improving the fault tolerance, linearity of response and tuning possibilities beyond conventional valves.

REFERENCES

1. Linjama, M., Laamanen, A. and Vilenius, M. 2003. Is it Time for Digital Hydraulics?. The 8th Scandinavian International Conference on Fluid Power, SICFP'03. Tampere, Finland. 7.−9.5.2003

2. Siivonen, L., Linjama, M. & Vilenius, M. 2005. Analysis of Fault Tolerance of Digital Hydraulic Valve System. Power Transmission and Motion Control. Bath, Great Britain. s.133−145

3. Lauttamus, T., Linjama, M., Nurmia, M. & Vilenius, M. 2006. A novel seat valve with reduced axial forces. Power Transmission and Motion Control. University of Bath, Great Britain. s.415−427

4. Linjama, M., Tamminen, P., Andersson, B. & Vilenius, M. 2005. Performance of The Valvistor with Digital Hydraulic Pilot Control. The Ninth Scandinavian International Conference on Fluid Power, SICFP'05. 1.−3.6.2005, Linköping, Sweden.

5. Ijas, M., Mäkinen, E. & Linjama, M. 2009. Digital Hydraulic Pressure Control. The 11th Scandinavian International Conference on Fluid Power, SICFP'09. Linköping, Sweden. 2.−4.6.2009

6. Parker Hanifin catalogue, read 30.6.2010, downloadable from: http://www.parker.com/literature/Hydraulic%20Controls%20Europe/HY11-3500UK%2004/PEW-R4R_UK.pdf

7. Bosch Rexroth catalogue, read 30.6.2010, downloadable from: http://www.boschrexroth.com/modules/BRMV2PDFDownload.dll?db=brmv2&lvid=1146319&mvid=3057&clid=1&sid=ED5F30A671404BCBD1075E3829C74BE6&sch=M

8. International Standard. 2008. ISO-10770-3, Hydraulic Fluid Power – Electrically Modulated Hydraulic Control Valves, Part: Test Method for Pressure Control Valves. 38s.

9. Karjalainen, J-P., Karjalainen, R., Huhtala, K. & Vilenius, M. 2005. The dynamics of hydraulic fluids – significance, differences and measuring. Power Transmission and Motion Control. Bath, Great Britain. s. 437−450.

10. Mäkinen, E., Virvalo, T., Tuominen, P. & Mattila, J., 1994. The comparison of different booster circuits used to improve characteristics of on/off-valves. International Conference of Machine Automation (ICMA '94). Tampere, Finland. 15.−18.2.1994

11. Virvalo, T. 2003. Comparing pressure control methods. Proceedings of the Fourth International Symposium on Fluid Power Transmission and Control, ISFP'2003, 8.−10.4.2003, Wuhan, China.

12. Dirk Linden, Design principles for proportional pressure reducing valves in mobile applications, The Tenth Scandinavian International Conference on Fluid Power, SICFP'07, 21-23.5.2007, Tampere, Finland

Experimental Evaluation of a Piston-Type Digital Pump-Motor-Transformer with Two Independent Outlets

Mikko Heikkilä, Jyrki Tammisto, Mikko Huova, Kalevi Huhtala, Matti Linjama
Tampere University of Technology
Department of Intelligent Hydraulics and Automation
P.O. BOX 589, FI-33101 Tampere, Finland

ABSTRACT

The digital pump-motor-transformer is a new energy-efficient alternative to the fluid power system. Based on digital (stroke to stroke) control of each piston of the pumping unit, its functionality consisted of (1) an arbitrary number of independent outlets, (2) service of each outlet at arbitrary pressure levels, (3) energy recovery from each outlet back to the prime mover, (4) power transfer from one outlet to another at arbitrary pressure levels, and (5) energy storage in and recovery from a hydraulic accumulator independent of pressure. Theoretical analysis and simulations show that the principle works and is highly efficient. This paper reports the first experimental results on the principle. The prototype pump-motor-transformer consisted of a six-piston inline pump, fast on/off control valves, and two independent outlets. The system was measured for its efficiency, controllability, energy transformation, and flow sharing functionality. The results are encouraging but show also that more pistons are needed for smooth flow rates.

Keywords: Digital pump-motor-transformer, efficiency, independent outlets

1. INTRODUCTION

The digital pump-motor-transformer is a solution based on digital pump-motor technology, in which Artemis Intelligent Power Ltd. is the leading pioneer (1). Like traditional pumps, this digital technology uses reciprocating pump elements with the exception that the check valves or the valve plate are replaced with active on/off control valves.

An important difference between digital and traditional pump technology is programmability. In the former, the operating mode of each piston can be selected independently of each other. In addition, the pre-compression can be optimized according to the load pressure without compromises. Valve delays can be compensated for, which is not possible with passive check valves. Moreover, the pressure release function allows recovery of the energy stored in the compressibility of the fluid. The main drawback is that

the flow rate fluctuates considerably at partial displacement (2). Another challenge is that the technology sets high requirements for the durability, flow capacity, and accuracy of the control valves. And, of course, digital machines are also more difficult to control because they come with more control options.

The concept and theoretical study of the digital pump-motor-transformer with independent outlets have been published before (3). The idea behind the concept is to multiply control valves (a simple digital pump-motor-transformer with two independent outlets is shown in figure 1). Additional valves are introduced between the pumping chambers and the new outlet B with each piston then having six modes, if we ignore the pre-compression and pressure release phases:

- Pump into outlet A (Pump A)

- Pump into outlet B (Pump B)

- Pump into tank (Pump T)

- Receive fluid from outlet A (Motor A)

- Receive fluid from outlet B (Motor B)

- Suck fluid from tank (Suck T)

Neither the number of independent outlets nor the pressure at the outlets have to be limited, because each piston is connected to exactly one outlet or to the tank. Thus the pump-motor-transformer in figure 1 can serve two actuators with arbitrary pressure levels and flow direction.
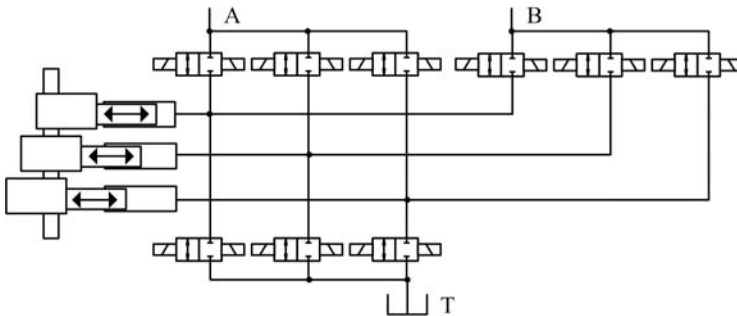
Figure 1. Three-piston digital pump-motor-transformer with two independent outlets

This paper is the first report of experimental results on a prototype digital pump-motor-transformer with two independent outlets. The pump we studied was a six-piston inline pump equipped with fast prototype valves, and we measured it for its efficiency and controllability. Furthermore, we examined the system's capability to transfer power between actuator lines.

2. CONTROL METHOD

2.1 Angle measurement

To control each individual on/off valve at the right moment, we must know as accurately as possible the rotation angle and angular velocity of the pump-motor-transformer. This is done by measuring the absolute rotation angle of the pump axis using a Hall sensor and a 144-tooth gear in the system. However, since the 144 resolution was too small to time accurately the on/off valves, we used more advanced method to accurately estimate the angle and angular velocity of the pump.

Filtering was realized by the exponential moving average method to filter out the measured time between two pulses using the previous filtered value and the most recent measured time interval to achieve the filtered output:

$$out(k) = out(k\text{-}1) + \alpha*(in(k)\text{-}out(k\text{-}1)), \qquad \text{Eq. 1}$$

where the weight term $\alpha \in (0,1]$ defines the rate at which previous values were forgotten. The weight term 1 means that only the last measured interval was used as output, and that the smaller the value, the slower the dynamics of the filter became. With accurate enough data on the time interval between two pulses, we could calculate the angular velocity in deg/s with the following equation:

$$\omega_{est} = 1/T_{pulses}/N_{pulses}*360°, \qquad \text{Eq. 2}$$

where T_{pulses} is filtered time between pulses and N_{pulses} number of pulses per revolution. Simulations showed that the values 0.2 – 0.3 yielded good accuracy and fast enough dynamics.

For accurate measurement of the angle of the pump-motor-transformer, a method must be used to avoid errors also in the long run. Therefore, the measurement error should be reset regularly by using a separate zero pulse that occurs once per revolution. The individual piston angles a_1, a_2, a_3, a_4, a_5, a_6, (values: [0, 360), where 0 is the bottom dead center and 180 approximately the top dead center) used by the controller, are always calculated based on the zero pulse. In this way, a potential measurement error may only briefly lower the performance of the pump-motor-transformer.

2.1 Selection of operation mode

The six-piston boxer pump we studied had three piston pairs, and in each pair the pistons were in opposite phases, resulting in six working mode decision instants during one pump revolution. At each mode decision instant, pumping mode was chosen for one piston and suction mode for the other.

The above mode choice was to keep the actuator supply pressure within user-given threshold values, as shown in figure 2. In the figure, the pressure in actuator line B remains constantly within the threshold values so that only actuator A is focused on supply pressure control. This mode choice logic initiated pumping into actuator line A whenever the measured pressure was below the threshold value at a mode choice instant. When the actuator pressure exceeded the threshold value, as it did during the third last and the second

last mode choice instants in the figure, the piston in the suction phase was connected to the actuator line to lower the pressure. The accuracy of this pressure control depends on the chosen threshold values in that the tighter the thresholds, the more accurate the pressure control. However, there are certain minimum limits to threshold values, since the flow rate can be controlled only piecewise.
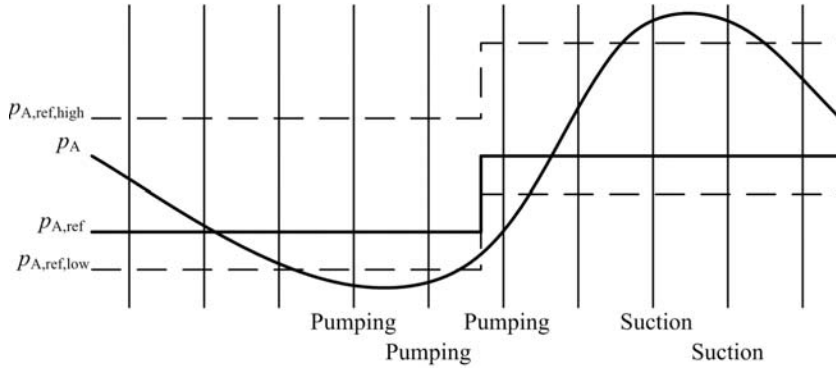
Figure 2. Examples of selecting the operation mode

Because the pump must feed two actuator lines, situations may arise when both actuator line pressures are outside the threshold values. If in one actuator the supply pressure is too low and in the other too high, mode choice is straightforward. The pumping piston connects to the low-pressure actuator line and in the suction phase to the high-pressure line. If both pressures are too low, the pumping piston connects to the line with the highest undershoot. The motoring mode is chosen in the same way if both pressures are too high. If no pumping or suction is needed, the pistons connect to the tank line.

2.3 Control of valve timing
To operate smoothly, the digital pump-motor-transformer must accurately time the valve switching. To avoid excessive pressure peaks and oscillation, pressures at valve inlet and outlet ports must be close in value when the valve opens. Incorrect valve timing lowers efficiency as well. Therefore, pre-compression time, pressure release time, and valve delays must all be taken into account in valve control.

Table 1 shows the method we used to calculate the optimal switching angle with $\theta_{\Delta p}$ representing the pre-compression time or pressure release time in degrees and θ_{valve} the valve delay in degrees. The variables $p_{current\_mode}$ and $p_{upcoming\_mode}$ are port pressures measured on the pump-motor-transformer. For example, if fluid was currently received from actuator line B and the next pumping stroke was directed to actuator line A, $p_{current\_mode}$ was the pressure for port B and $p_{upcoming\_mode}$ that for port A. The piston movement Δx during pre-compression or pressure release was calculated using the equation

$$\Delta x = \Delta p \frac{V}{BA} K_{cf} ,$$ Eq. 3

where Δp is the pressure difference ($| p_{current\_mode} - p_{upcoming\_mode} |$), V the overall volume, B the bulk modulus of the fluid, A the piston area, and K_{cf} the correction factor.

Table 1. Determination of optimal valve switching angles

	$p_{current\_mode} \geq p_{upcoming\_mode}$	$p_{current\_mode} < p_{upcoming\_mode}$
Opening at BDC	$\theta_{open} = 360° - \theta_{valve}$	$\theta_{open} = \theta_{\Delta p} - \theta_{valve}$, if $\theta_{\Delta p} \geq \theta_{valve}$ $\theta_{open} = 360° - \|\theta_{\Delta p} - \theta_{valve}\|$, if $\theta_{\Delta p} < \theta_{valve}$
Closing at BDC	$\theta_{close} = 360° - \theta_{\Delta p} - \theta_{valve}$	$\theta_{close} = 360° - \theta_{valve}$
Opening at TDC	$\theta_{open} = 180° + \theta_{\Delta p} - \theta_{valve}$	$\theta_{open} = 180° - \theta_{valve}$
Closing at TDC	$\theta_{close} = 180° - \theta_{valve}$	$\theta_{close} = 180° - \theta_{\Delta p} - \theta_{valve}$

In timing calculations at top dead center (TDC), the overall volume V equals the size of the cylinder dead volume. At bottom dead center (BDC), the parameter V equals the sum of the dead volume and cylinder displacement. The bulk modulus B is estimated in relation to pressure level and temperature. With a correction factor K_{cf}, the slope can be further adjusted. When the trajectory of the piston is sinusoidal, pre-compression time or pressure release time in degrees can be calculated from

$$\cos(\theta_{\Delta p}) = \frac{-2\Delta x}{s} + 1 \text{ ,}$$ Eq. 4

where the fixed parameter s is the piston stroke. Eventually, the valves are controlled based on a measured piston angle, and a valve command is executed when the piston angle reaches the optimal calculated switching angle.

3. TEST SYSTEM

3.1 Pump modification
We modified the digital pump-motor-transformer from a six-piston boxer pump by replacing the check valves with actively controlled, fast two-way prototype on-off valves. Their opening and closing delays were about 1 ms and their flow rate about 23 l/min at a 5-bar pressure difference. The hydraulic circuit of our pump-motor-transformer is shown in figure 3.

Each cylinder had a tank valve, two actuator valves, and a pressure relief valve, and pressure was measured in each cylinder. The actuator lines are marked A and B and the tank line T. The tank line had two accumulators and was constructed with low pressure hoses to minimise pressure oscillation. Tank and both actuator line pressures and temperatures were measured from the valve blocks.
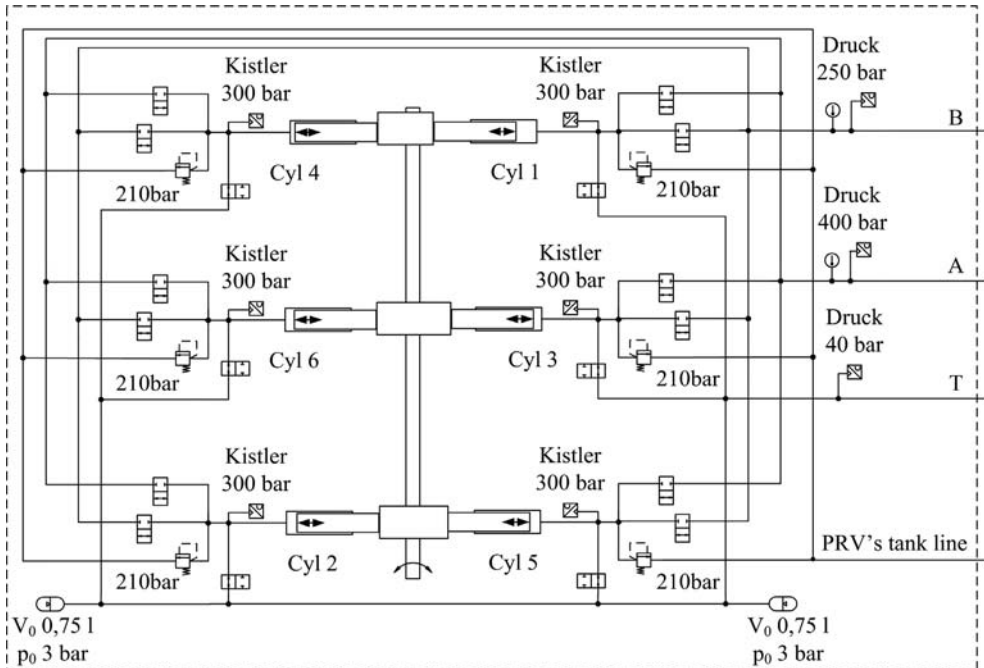
Figure 3. Hydraulic circuit of the digital pump-motor-transformer

3.2 Measurement system

Figure 4 shows the measurement system of our digital pump-motor-transformer, marked with an oval next to the torque sensor. Both actuator lines had flow and pressure sensors near the accumulators.

The flow in actuator line A was measured after the accumulator, whereas that in line B was measured before the accumulator. The accumulator in actuator line A was 0.75 litres and was used to smooth flow and pressure oscillations. Line B had a 4-litre accumulator, which was used for energy storage. Both accumulators could be switched off the circuit. Different loadings were realised using an electrically controlled proportional directional control valve in line A and a manual throttle valve in line B. For safety reasons, pressure relief valves were mounted on the actuator lines.

Because the flow capacity of the on-off valves was less than that of the original check valves, a pressurized tank line was used to avoid cavitation in the pump. Therefore, an auxiliary pump had to be used. The inlet pressure was about 10 bar and was controlled with a pressure relief valve.
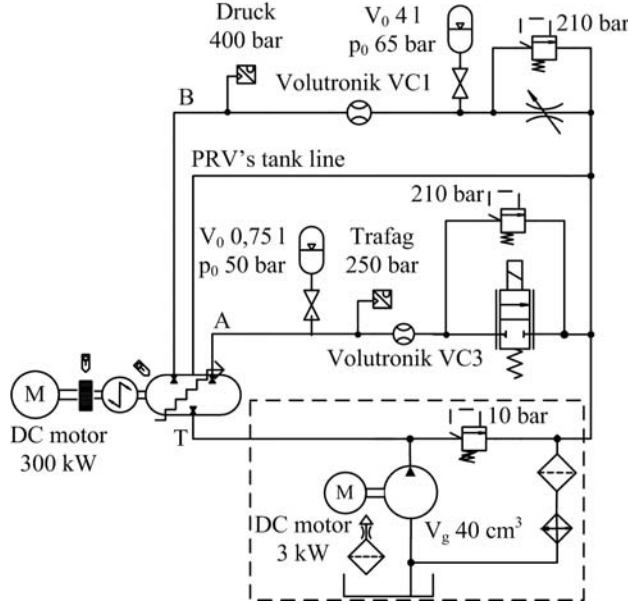
Figure 4. Measurement system of the digital pump-motor-transformer

4. EXPERIMENTAL RESULTS

4.1 Efficiency measurements

Pumping efficiency at full displacement was measured at 500, 750, and 1000 rpm angular velocities without the actuator line accumulator. The oil temperature was about 40 °C, and the pressure differences applied were 20 to 180 bar. The system's volumetric and hydromechanical efficiencies are shown in figure 5. Volumetric efficiency of a pump can be calculated from

$$\eta_{vol} = \frac{Q}{nV_g},$$

Eq. 5

where Q is the flow, n the angular velocity, V_g the geometrical volume. Accuracy of volumetric measurement mainly depended on accuracy of Volutronik. Therefore maximum error in volumetric efficiency was ±0.3 percentage units. Hydromechanical efficiency of a pump can calculated from

$$\eta_{hm} = \frac{\Delta p \, V_g}{2\pi T},$$

Eq. 6

where Δp is the pressure difference and T the torque. Accuracy of pressure and torque sensors limited the accuracy. Accuracy of hydromechanical measurement was the lowest (±5.3 percentage units), when pressure difference and angular velocity were small. On the

contrary, measurement error was the lowest, ±1.5 percentage units, at maximum pressure difference and angular velocity.
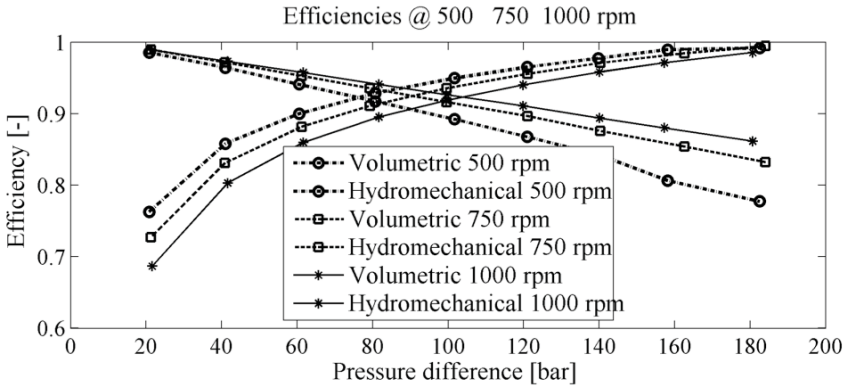
Figure 5. Volumetric and hydromechanical efficiencies of the pump-motor-transformer as pump at full displacement

The volumetric efficiency clearly dropped when the pressure difference was increased, mainly because of leaks in the on/off valves. Hence the volumetric efficiency increased along with the angular velocity.

The hydromechanical efficiency was high but dropped when the angular velocity was increased mainly because of the low flow capacity of the on-off valves. Increasing the pressure difference improved the hydromechanical efficiency.
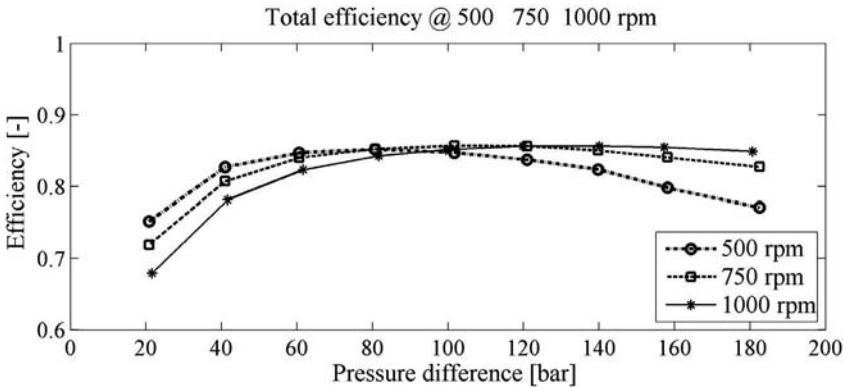
Figure 6. Total efficiencies of the pump-motor-transformer as pump at full displacement

Total efficiencies are shown in figure 6. The system's total efficiency was low at low pressures when the angular velocity was increased, whereas at high pressures it increased with increasing angular velocity. The total efficiency was 80 % over most of the measurement range. Total efficiencies were defined as product of volumetric and hydromechanical efficiencies thus accuracy of measurement was lower than in case of hydromechanical measurement.

Total efficiencies with partial displacements are shown in figure 7. We used an angular velocity of 500 rpm and an oil temperature of 30 °C. The actuator line accumulator was used to smooth the flow.
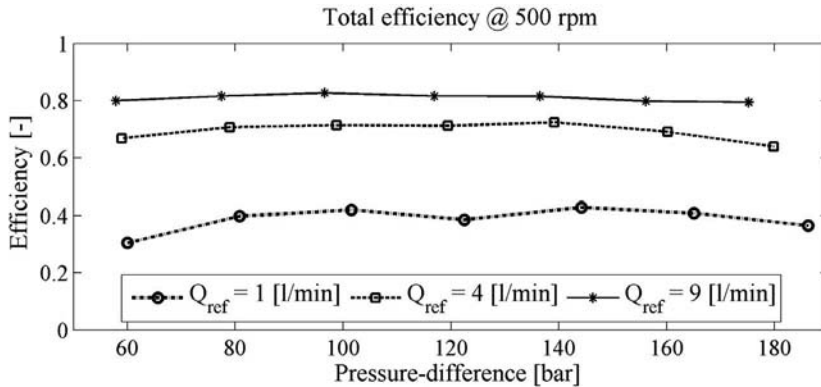
Figure 7. Total efficiencies of the pump-motor-transformer as pump at partial displacements

The total efficiency dropped when flow was decreased. At flows over 4 l/min, the efficiency was almost consistently above 70 %, whereas at small flow, it was poor owing to idle losses of the pump-motor-transformer.

The efficiencies of the digital pump-motor-transformer were also measured as motor (figure 8). We used an angular velocity of 500 rpm and an oil temperature of 30 °C and did the measurements on actuator line B with the accumulator engaged. The pressure in the accumulator was raised to its maximum, and the pressure reference then changed to 60 bar. Since the reference was lower than the measured pressure in the actuator line, motoring started. Efficiencies were calculated at designated times to obtain efficiency at a certain pressure difference. The accumulator pre-charge pressure was about 65 bar, yielding a minimum pressure difference of 60 bar. The maximum pressure difference measured 150 bar.
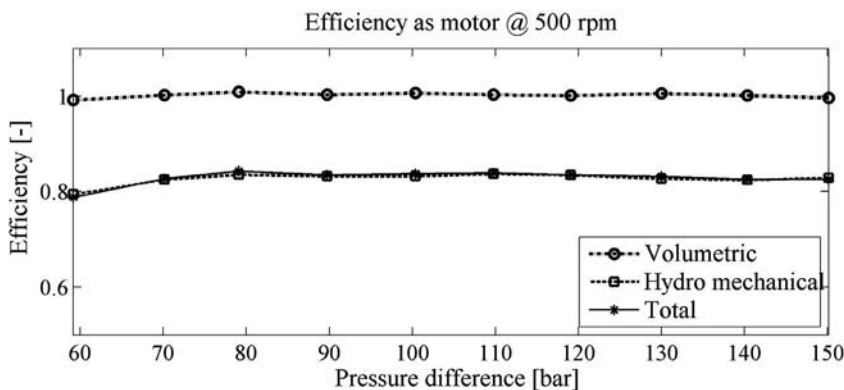
Figure 8. Efficiencies of the pump-motor-transformer as motor at full displacement

Because the volumetric efficiency was defined as the ratio of the motor geometrical volume and the measured flow into the motor multiplied by angular velocity (cf. Eq. 5), it was at best slightly over 100 %. At a motoring stroke, the pressure valve was closed before BDC (pressure release), and therefore the motor sucked oil from the actuator line less than the geometric volume. The hydromechanical efficiency was over 80 % over most of the pressure range. At some points (for instance 80 bar), the total efficiency was better than the hydromechanical efficiency, because the volumetric efficiency was over 100 %.

4.2 Idle losses

Idle losses signify the power the digital pump-motor-transformer consumed while idling, and they are shown at different angular velocities in figure 9. We used an inlet pressure of 10 bar and a temperature of 40 °C and measured idle losses at 200 to 1400 rpm angular velocity.

Idle losses increased rapidly when the angular velocity was increased mainly because of increased pressure losses in the on/off valves. The idle losses fit well the third order fitting curve.
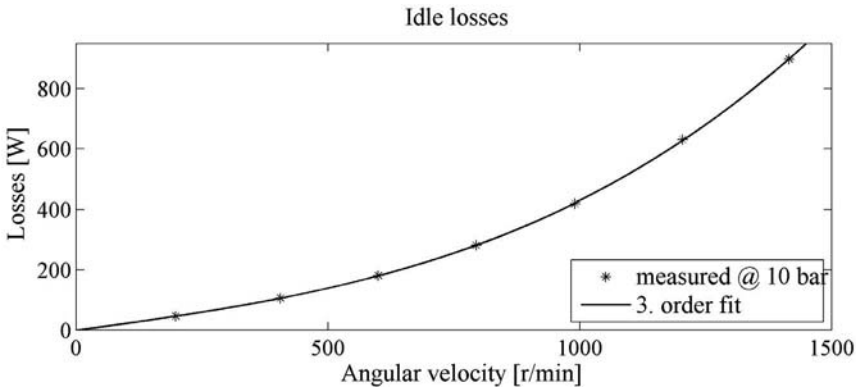
Figure 9. Idle losses of the pump-motor-transformer at different angular velocities

4.3 Pressure response

Pressure responses with different actuator flows are shown in figure 10. We used an angular velocity of 500 rpm, a temperature of 30 °C, and a step of 70 to 100 bar. Responses were measured on actuator line A with the accumulator engaged. An angular velocity of only 500 rpm was used with the actuator line accumulator, because 1000 rpm produces too much pressure oscillation due the natural frequency of the actuator line and accumulator. The flow out of the accumulator was controlled with a proportional valve. Before a pressure step, flows were set at zero, 3 l/min, and 7 l/min.

When the flow out of the accumulator was increased, pressure rose more slowly. Because the start of the step was not fixed at any particular angle, initial pressures varied slightly at the step time. In addition, the system pressure dropped more rapidly with bigger flows.
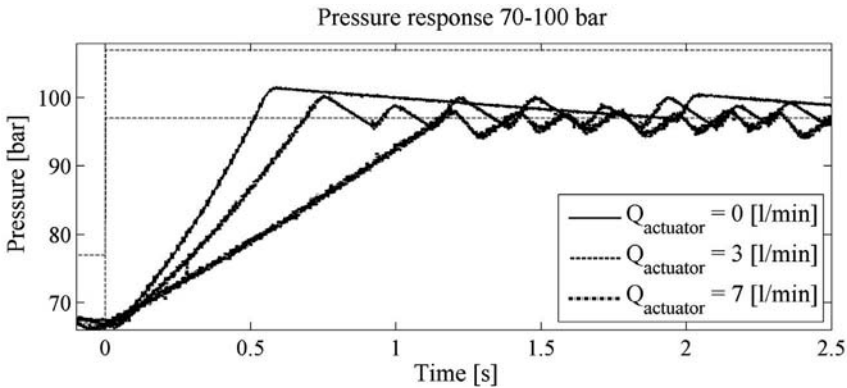
Figure 10. Pressure response with different actuator flows at an angular velocity of 500 rpm

The effect of the pressure level on the pressure step with the accumulator engaged is shown in figure 11, where a pressure step of 30 bar is evident from 70 and 150 bar. Various pressure steps were tested because of the non-linearity of the gas accumulator. We used an angular velocity of 500 rpm and a temperature of 30 °C. The flow out of the accumulator was zero.
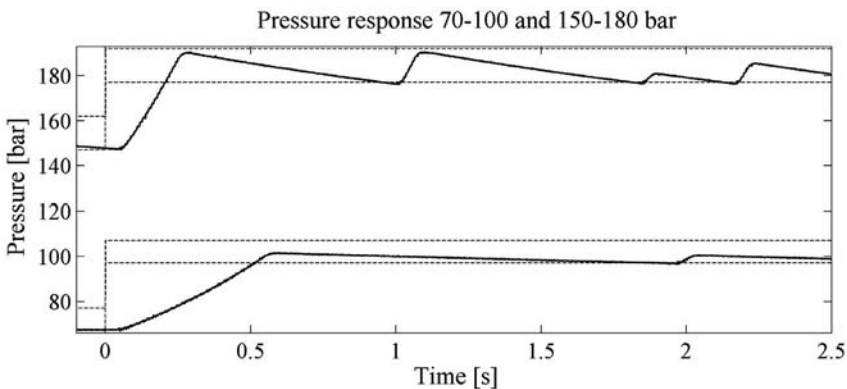
Figure 11. Pressure responses at different pressure levels at 500 rpm angular velocity

Because the pressure increased much faster at higher pressure, wider thresholds had to be used. The pressure also varied widely. Three different overshoots occurred in step response from 150 to 180 bar, as the controller engaged the pump each time the system pressure dropped below the lower reference limit. The controller could have used one, two, or three strokes depending on the measured system pressures. Moreover, pumping occurred more often at high pressure because of increased leakage and a smaller gas volume in the accumulator.

4.4 Response to flow disturbance
Besides pressure response, also response to flow disturbance was measured. A disturbance was produced with a proportional valve in actuator line A, and the controller sought to maintain constant pressure. When the proportional valve opening was increased, flow out

of the accumulator increased, simulating an actuator with increasing speed (response shown in figure 12). We used an angular velocity of 500 rpm, a temperature of 30 °C, and a 0.75-litre accumulator.

The flow out of the accumulator increased as the proportional valve opening was increased. Because of increased flow, pressure in the actuator line dropped rapidly, and pumping strokes became more frequent. However, the pressure did not significantly change even at changing flow.
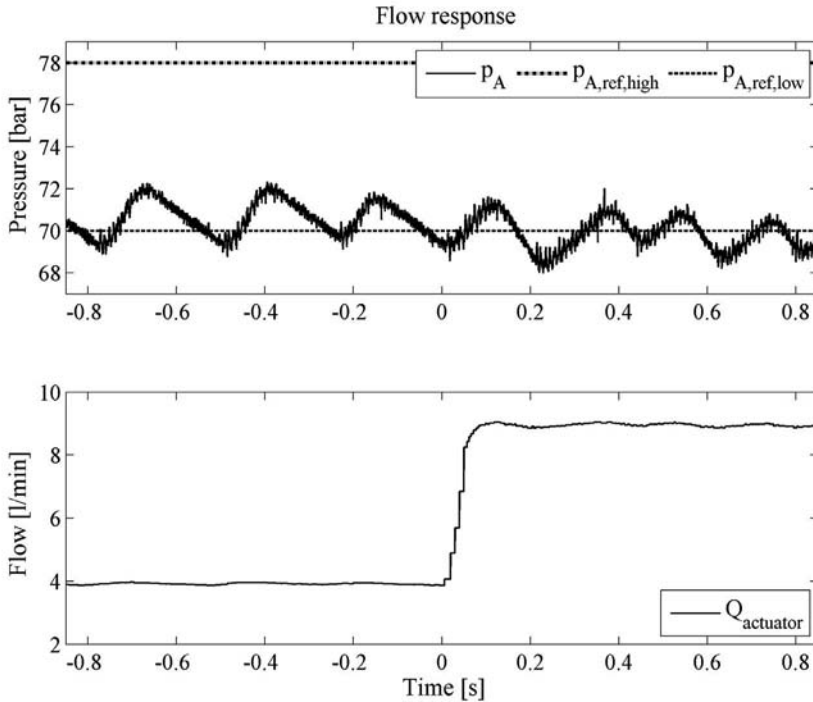
Figure 12. Response to flow disturbance

4.5 Power transfer

Power transfer was studied with fluid being received from actuator line B and pumped to actuator line A, accomplished by charging the accumulator in line B to 150 bar and then applying reference steps. The reference for actuator line A was changed from 1 to 100 bar, while concurrently that for line B was changed from 150 to 70 bar.

The above power transfer is shown in figure 13 with actuator pressures in the upper part of the figure and below that flows in the actuator lines. We used an angular velocity of 500 rpm and a temperature of 30 °C. The proportional valve in actuator line A was open to maintain a pressure of less than 100 bar at full displacement. The throttle valve in actuator line B was closed.

After the steps, pumping strokes were executed in actuator line A and suction strokes from actuator line B; that is, fluid was received from line B and pumped into line A. It should be noted that pumping and motoring take place in parallel at full displacement. The hydraulic power taken from actuator line B was about 2.61 kW and that pumped into line A was 1.67 kW. In addition, the shaft power transferred to the electric motor was about 0.43 kW. Hence losses were about 0.51 kW (2.61-1.67-0.43) and the efficiency of power transfer 80 %. Powers were defined from 0.1 seconds to the end of the measurement, that is, at full displacement.
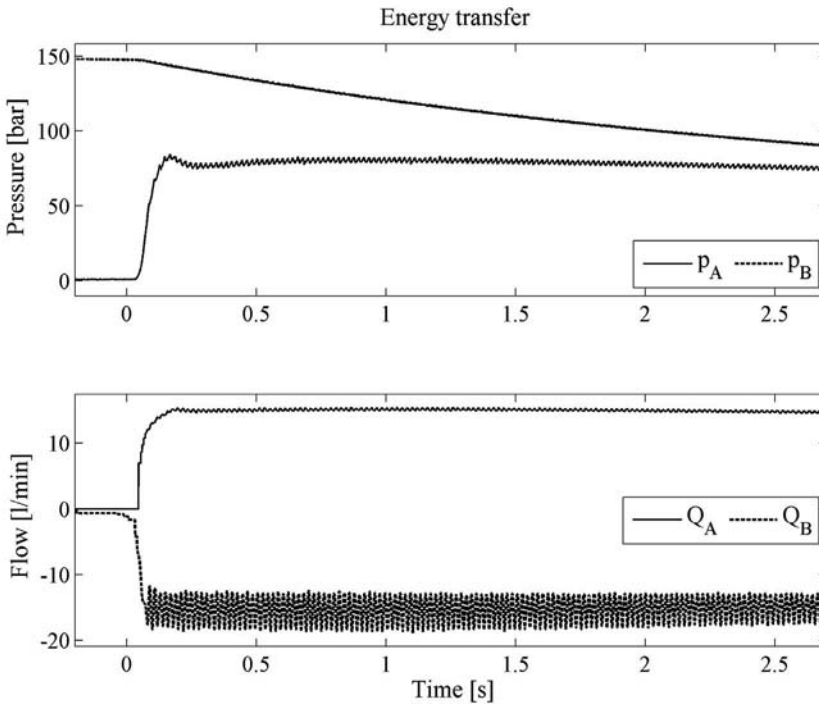
Figure 13. Energy transfer between actuator lines

5. CONCLUSIONS

Our results prove that the digital pump-motor-transformer works both as pump and motor. Moreover, it is capable of transferring power between actuator lines. Because pressures can differ at outlets, the pump-motor-transformer executes a hydraulic transformer function as well. The power transfer efficiency of our system was 80 %. Consequently, its efficiency did not decrease in the transformer mode.

Total efficiencies were between 65 and 85 % when pumping at full displacement. At partial displacements, they were lower due to idle losses in the pump-motor-transformer. At full displacement motoring, total efficiencies were 80 to 85 %. At some points, the volumetric

efficiency was even beyond 100 %, owing to the definition of the term. It would have been even better if the valves had leaked less.

Response measurements show that pressures in actuator lines could be controlled even if actuator flows changed. It took 0.25 to 0.5 seconds for pressure in the actuator line to rise 30 bar when the 0.75-litre accumulator was used, for pressurising time depends on pressure level. For pressure control, nonlinearity is an undesirable feature in accumulators, and a rigid volume might well be the better option. In addition, more advanced control methods should be considered. For example, an accumulator model added to the controller would make for more accurate pressure control.

Electrical losses in valves were not included in this research because of the prototype valves used. However, the pump-motor-transformer should consume electrical power no more than a few percent of its maximum power, which is challenging for existing valve technology.

In summary, this first prototype digital pump-motor-transformer was not as efficient as traditional machines mainly because of the prototype valves used in it. However, our results show that the system's efficiency can be significantly improved by using the digital pump-motor-transformer approach because of its extended functionality.

NOMENCLATURE

A	Piston area [m]
B	Bulk modulus [Pa]
K_{cf}	Correction factor
n	Angular velocity [1/s]
N_{pulses}	Number of pulses per revolution
$p_{current\_mode}$	Port pressure (p_T, p_A or p_B) [Pa]
$p_{upcoming\_mode}$	Port pressure (p_T, p_A or p_B) [Pa]
Δp	Pressure difference [Pa]
Q	Flow [m^3/s]
s	Piston stroke [m]
T	Torque [Nm]
T_{pulses}	Time between two pulses [s]
V	Overall volume [m^3]
V_g	geometrical volume [m^3]
Δx	Piston movement during pre-compression or pressure release [m]
η_{hm}	Hydromechanical efficiency
η_{vol}	Volumetric efficiency
θ_{close}	Closing angle of valve [deg]
θ_{open}	Opening angle of valve [deg]
θ_{valve}	Valve delay [deg]
$\theta_{\Delta p}$	Pre-compression time or pressure release time [deg]
ω_{est}	Estimated angular velocity [deg/s]

REFERENCES

1   Ehsan, Md., Rampen, W., Salter, S. Modeling of Digital-Displacement Pump-Motors and Their Application as Hydraulic Drives for Nonuniform Loads. ASME Journal of Dynamic Systems, Measurement, and Control, March 2000, Vol. 122, pp. 210 – 215.

2   Tammisto, J., Huova, M., Heikkilä, M., Linjama, M., Huhtala, K. Measured Characteristics of an In-line Pump with Independently Controlled Pistons. The 7 th International Fluid Power Conference, IFK'10, Aachen, Germany, 2010.

3   Linjama, M., Huhtala, K. Digital Pump-Motor with Independent Outlets. The 11 th Scandinavian International Conference on Fluid Power, SICFP'09, Linköping, Sweden, 2009.

Improving Characteristic of Switching Hydraulic System Based on High-speed On/off Valves

Feng Wang

State Key Laboratory of Fluid Power Transmission and Control
Zhejiang University, Hangzhou 310027, China

Center for Compact and Efficient Fluid Power
University of Minnesota, Minneapolis, MN 55455, USA

Linyi Gu

State Key Laboratory of Fluid Power Transmission and Control
Zhejiang University, Hangzhou 310027, China

ABSTRACT

Switching hydraulic techniques have been greatly developed due to lower throttling losses, intelligent control and low cost. The main benefits of the Pulse Width Modulation (PWM) switching technique are continuous output and simple hydraulic hardware. The biggest challenge of this switching technique is the development of extremely fast, reliable and energy efficient on/off valves. The slow response of the valves aggravates hydraulic fluctuation greatly.

Therefore in this paper, the hydraulic fluctuation which is caused by the switching of high-speed on/off valve is studied. The case studied is a hydraulic motor rotary speed control system using high-speed on/off valves. Hydraulic fluctuation occurs as the hydraulic motor is periodically accelerated and decelerated.

Other than adding a hydraulic accumulator or hydraulic damper to attenuate the fluctuation, this paper seeks the reason why fluctuation occurs and the ways to attenuate it. It is shown that fluctuation is related to many parameters such as switching frequency, switching chamber volume, moment of inertia on the motor shaft, viscous friction and so on. The study is conducted with various parameters to evaluate the influence of proposed parameters on the fluctuation. Results show that fluctuation can be attenuated greatly through the proper design of those parameters.

KEYWORDS: Switching hydraulic system, Pulse Width Modulation (PWM), high-speed on/off valve, hydraulic fluctuation.

1. INTRODUCTION

Digital hydraulic systems have been considered as a competitive alternative to traditional control with servo or proportional valves. Important benefits of digital hydraulic systems are lower throttling losses, low sensitivity to contamination, intelligent control, good repeatability and low cost.

Generally, digital technologies in hydraulic systems can be divided into three classes. The simplest one is traditional on/off technology in which the output of the system has only two discrete values, such as pump/motor rotating or stopped, cylinder moving or stopped, pressure high or low. Traditional on/off technology is not studied much nowadays as it is considered as old-fashioned. However, it is the best solution for cases in which the control characteristics can be tolerated, and the approach is very popular in pneumatic systems.

The second class is the utilization of parallel-connected hydraulic components. The systems are truly digital as the output has only discrete values (Linjama, 2003). Parallel-connected on/off valve system has seldom been applied in 20th century (Tanaka, 1988). The development of valves and control techniques has resulted in extensive research and development of this technology since 2000. Digital hydraulic valve systems can significantly save energy similarly as analogue distributed valve systems (Siivonen, 2005). The valve system is fault tolerant and failure in single valve does not prevent the use of the actuator (Laamanen, 2004). However, in case of non-synchronous switching of the valves a rather complicated controller is required. Moreover, large numbers of valves are needed to obtain high flow capacity resolution (Linjama, 2005).

The third class is switching technique which imitates principle of electric switching systems. The typical form is to use Pulse Width Modulation (PWM) on/off valves to produce an analog output through high-frequency switching (Dantlgraber, 2000). The switching technique relies on fast switching and the main benefits of this technique are continuous output and simple hydraulic hardware (Scheidl, 2005). The most important commercial applications of this switching technique are ABS brakes and fuel injection systems of modern cars (Johnson, 2001). It has also found its application in the fan drive cooling system of the mobile machinery in recent years (Hettrich, 2009).

The biggest challenge of switching techniques is the development of extremely fast, reliable and energy efficient on/off valves. Traditional valve technology seems not to be able to satisfy these requirements. The slow response of the valves aggravates the hydraulic fluctuation greatly.

Therefore in this paper, one of characteristics of switching hydraulic system, hydraulic fluctuation, is studied. The case studied in this paper is a hydraulic motor rotary speed control system using high-speed on/off valves. Fluctuation occurs as the hydraulic motor is periodically accelerated and decelerated. Other than adding a hydraulic accumulator or hydraulic damper to attenuate the fluctuation, this paper studies some parameters such as switching frequency, duty ratio, switching chamber volume, moment of inertia and viscous friction to evaluate the influence of these parameters on the fluctuation.

2. ANALYTICAL MODEL

The schematic diagram of hydraulic motor rotary speed control system using high-speed on/off valves is shown in Fig. 1. The system consists of a high-speed on/off valve, a high-speed check valve and a hydraulic motor. The high-speed on/off valve is controlled by a PWM signal. The high-speed check valve is hydraulically driven according to the state of the high-speed on/off valve. The backing pressure is set a little higher than the cracking pressure of the high-speed check valve.

The switching chamber in Fig. 1 is designed as small as possible to make the pressure build-up dynamics faster than the high-speed on/off valve (Gu, 2003). Assume the high-speed on/off valve works at a frequency of 10 Hz and the duty ratio is 50%. Suppose the flow rate through the hydraulic motor is 3.75 l/min, the bulk modulus of the oil is 17000 bar and the chamber volume is 5.65 ml (a pipeline with inner diameter of 6 mm and length of 200 mm). Then the resulting pressure transient time from 0 to 200 bar would be 0.0012 s, which is much shorter than the open time of the high-speed on/off valve (0.05s).
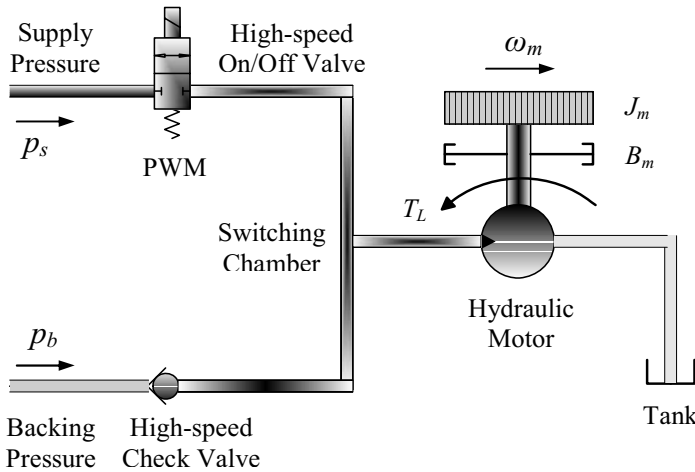
Fig. 1 Schematic diagram of the hydraulic motor rotary speed control system using high-speed on/off valves

The principle of operation of the switching hydraulic system will now be explained. When the PWM signal is high, the high-speed on/off valve opens. The inlet pressure of the hydraulic motor increases rapidly and the high-speed check valve closes quickly under the reversed pressure. The hydraulic motor speeds up. When the PWM signal is low, the high-speed on/off valve closes. Due to the moment of inertia of the load, the rotary speed of the hydraulic motor will not decrease rapidly and the flow through it will not be discontinuous (Cao, 2005, 2006). The continuous flow leads to rapid pressure decrease at the inlet of the hydraulic motor as no additional oil flows into the chamber. When this pressure decreases to a value which is lower than the backing pressure minus cracking pressure of the high-speed check valve, the high-speed check valve opens and the oil in the pressurized tank flows into the switching chamber. The hydraulic motor slows down.

The theoretical analysis is based on some simplifications. Since the pressure losses across the valves and pipelines only have influence on system efficiency while having minor impact on the fluctuation, they have been ignored in the following analysis for simplicity.

The dynamic equation of a hydraulic motor can be formulated as below when the high-speed on/off valve opens (Lu, 1988):

$$p_s D_m = T_L + B_m \omega_m + J_m \frac{d\omega_m}{dt} \tag{1}$$

Since it is a first order linear differential equation, the rotary speed of the hydraulic motor in the acceleration stage can be expressed as:

$$\omega_{m+} = \frac{p_s D_m - T_L}{B_m} + C_1 e^{-\frac{B_m}{J_m}t} \tag{2}$$

where C_1 is a constant.

Similarly, the dynamic equation of the hydraulic motor when the high-speed on/off valve closes can be expressed as follows since the backing pressure is set only a little higher than the cracking pressure of the check valve:

$$0 = T_L + B_m \omega_m + J_m \frac{d\omega_m}{dt} \tag{3}$$

The rotary speed of the hydraulic motor in the deceleration stage can be expressed as:

$$\omega_{m-} = -\frac{T_L}{B_m} + C_2 e^{-\frac{B_m}{J_m}t} \tag{4}$$

where C_2 is a constant.

The rotary speed of the hydraulic motor at time 0 and DT in the acceleration stage can be formulated from Eq. (2):

$$\omega_{m+}(0) = \frac{p_s D_m - T_L}{B_m} + C_1 \tag{5}$$

$$\omega_{m+}(DT) = \frac{p_s D_m - T_L}{B_m} + C_1 e^{-\frac{B_m}{J_m}DT} \tag{6}$$

Similarly, the rotary speed of the hydraulic motor at time DT and T in the deceleration stage can be formulated from Eq. (4):

$$\omega_{m-}(DT) = -\frac{T_L}{B_m} + C_2 e^{-\frac{B_m}{J_m}DT}$$

(7)

$$\omega_{m-}(T) = -\frac{T_L}{B_m} + C_2 e^{-\frac{B_m}{J_m}T}$$

(8)

The steady state condition for the hydraulic motor rotary speed is that the rotary speed at the start of the period is equal to the rotary speed at the end of the period:

$$\omega_{m+}(0) = \omega_{m-}(T)$$

(9)

Furthermore, the rotary speed of the hydraulic motor at time DT must be continuous:

$$\omega_{m+}(DT) = \omega_{m-}(DT)$$

(10)

Therefore the following equations can be established according to Eq. (5) ~ Eq. (10):

$$\frac{p_s D_m - T_L}{B_m} + C_1 = -\frac{T_L}{B_m} + C_2 e^{-\frac{B_m}{J_m}T}$$

(11)

$$\frac{p_s D_m - T_L}{B_m} + C_1 e^{-\frac{B_m}{J_m}DT} = -\frac{T_L}{B_m} + C_2 e^{-\frac{B_m}{J_m}DT}$$

(12)

Thus the constants C_1 and C_2 in Eq. (2) and Eq. (4) can be solved:

$$C_1 = \frac{p_s D_m}{B_m} \frac{1 - e^{\frac{B_m}{J_m}(DT-T)}}{e^{-\frac{B_m}{J_m}T} - 1}$$

(13)

$$C_2 = \frac{p_s D_m}{B_m} \frac{1 - e^{\frac{B_m}{J_m}DT}}{e^{-\frac{B_m}{J_m}T} - 1}$$

(14)

The rotary speed fluctuation of the hydraulic motor can be defined as the rotary speed increase in the acceleration stage or the rotary speed decrease in the deceleration stage:

$$\Delta\omega_m = \omega_{m+}(DT) - \omega_{m+}(0) = \omega_{m-}(DT) - \omega_{m-}(T)$$

(15)

According to Eq. (5) ~ Eq. (15), the rotary speed fluctuation of hydraulic motor is:

$$\Delta\omega_m = \frac{p_s D_m}{B_m} \frac{1 - e^{-\frac{B_m}{J_m}DT}}{e^{-\frac{B_m}{J_m}T} - 1}(e^{-\frac{B_m}{J_m}DT} - e^{-\frac{B_m}{J_m}T}) \qquad (16)$$

It is shown from Eq. (16) that the rotary speed fluctuation of the hydraulic motor is determined by many parameters such as hydraulic motor displacement, switching frequency of high-speed on/off valve, duty ratio and so on. Four of all these parameters have been carefully studied to evaluate the influence on the rotary speed fluctuation. These are: switching frequency, duty ratio, moment of inertia and coefficient of viscous friction.

3. SIMULATION

To study the influence of different parameters on the rotary speed fluctuation as well as to verify the theoretical analysis, simulations have been carried out in AMESim which is shown in Fig. 2. An elementary hydraulic fluid model is used. The density, bulk modulus, viscosity are defined in fluid model. Pipe friction and pipe compliance have not been taken into account because it is assumed that they have no significant influence on the fluctuation for the envisaged system.
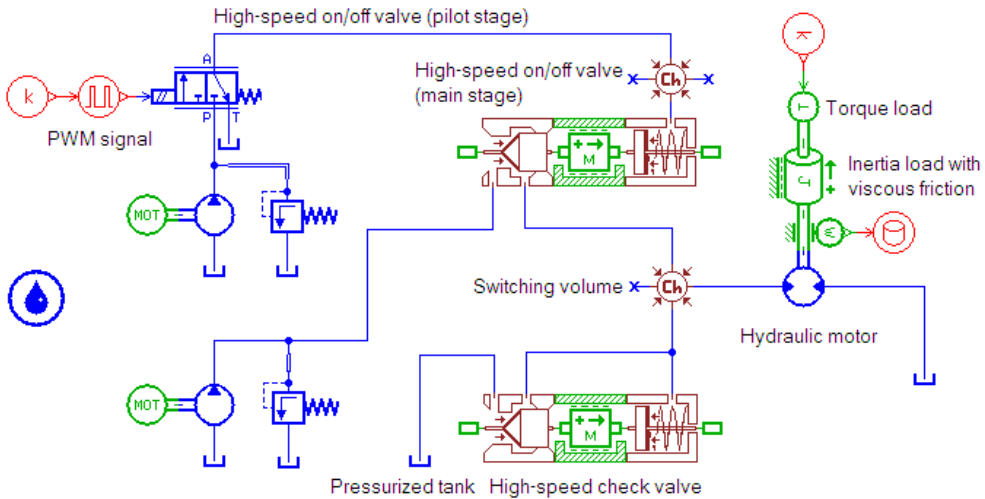
Fig. 2 Hydraulic motor rotary speed control system model in AMESim

In the simulation model, the high-speed on/off valve is designed as a two-stage valve since such valves enable large flow rates (Lu, 2002). The main stage of the valve is a conical poppet type valve with sharp edge seat. The pilot stage is a 3w2p high-speed on/off valve. Parameters of the 3w2p pilot valve are assumed to be the same as commercially available high-speed on/off valves. The limit frequency of this pilot valve is 80 Hz and nominal flow

rate is 2 L/min. The high-speed check valve in the model is also a conical poppet valve with sharp edge seat.

The compressibility of the fluid is taken into consideration in the simulation. This is the biggest difference between the theoretical analysis and the simulation. The switching chamber (see Fig. 1) does have an influence on the acceleration and deceleration of the hydraulic motor. Due to the compressibility of the fluid, the hydraulic motor can not be accelerated instantaneously when the high-speed on/off valve opens as it takes time for the chamber pressure to increase to the desired value (Wu, 1993). Although it is a very short time, it becomes important at higher switching frequencies.

To simplify the simulation model, a fixed displacement hydraulic motor with constant mechanical and volumetric efficiency has been assumed. The torque load, viscous friction load and moment of inertia of the hydraulic motor are taken into consideration in the model.

Properties of the simulation model are listed in Table 1.

Table 1 Properties of the simulation model

Property	Value	Unit
Density of hydraulic fluid	850	[kg/m^3]
Bulk modulus of hydraulic fluid	1700	[MPa]
Absolute viscosity of hydraulic fluid	51	[cP]
Limit frequency of pilot valve	80	[Hz]
Nominal flow rate of pilot valve	2	[L/min]
Piston diameter of poppet valve	16	[mm]
Hole diameter of poppet valve	14.5	[mm]
Rod diameter of poppet valve	9	[mm]
Spool mass of poppet valve	0.028	[kg]
Spool displacement limit of poppet valve	6	[mm]
Switching chamber volume	15.7	[cm^3]
Supply pressure	21	[MPa]
Pilot pressure	25	[MPa]
Backing pressure	1	[MPa]
Duty ratio	0.5	[---]
Switching frequency	5	[Hz]
Displacement of hydraulic motor	10	[ml/r]
Load torque on the motor shaft	8	[N·m]
Moment of inertia on the motor shaft	0.25	[kg·m^2]
Coefficient of viscous friction	0.01	[N·m/rpm]

Fig. 3 shows the rotary speed of the hydraulic motor at various switching frequencies. The switching frequency varies from 5 to 20 Hz with a step size of 5 Hz while other parameters such as duty ratio, load torque, moments of inertia etc remain unchanged. It is shown that the rotary speed fluctuation decreases greatly as the switching frequency increases.
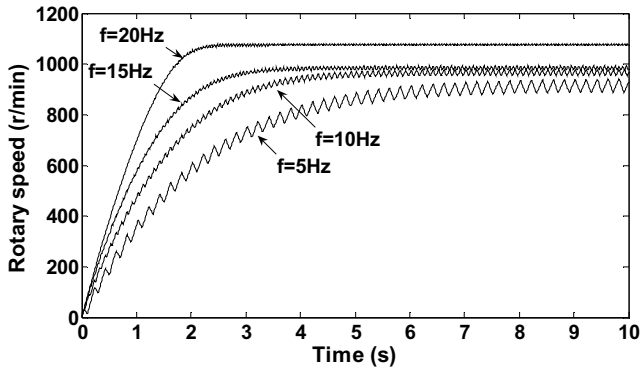
Fig. 3 Rotary speed of the hydraulic motor at different switching frequencies
($D = 0.5$, $B_m = 0.01 N \cdot m /(r / \min)$, $J_m = 0.25 kg \cdot m^2$)

Fig. 4 shows the rotary speed fluctuation of the hydraulic motor at various switching frequencies. The rotary speed fluctuation decreases from 52 to 10 rpm when the switching frequency increases from 5 to 20 Hz. The figure also shows the fluctuation comparison between theoretical analysis and the simulation. Although the fluctuation in the simulation is slightly lower than that in the theoretical analysis, the two curves change very similarly when the switching frequency varies.
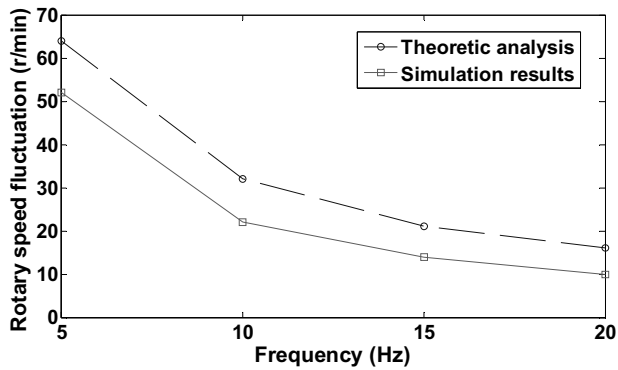
Fig. 4 Rotary speed fluctuation of the hydraulic motor at different switching frequencies ($D = 0.5$, $B_m = 0.01 N \cdot m /(r / \min)$, $J_m = 0.25 kg \cdot m^2$)

The rotary speed of the hydraulic motor at various duty ratios is shown in Fig. 5. Although the rotary speed increases as the duty ratio increases, the rotary speed fluctuation remains almost unchanged when the duty ratio varies from 0.4 to 0.7. Fig. 6 shows that the fluctuation in the simulation is about 50 rpm while it is a little higher in the theoretical analysis.
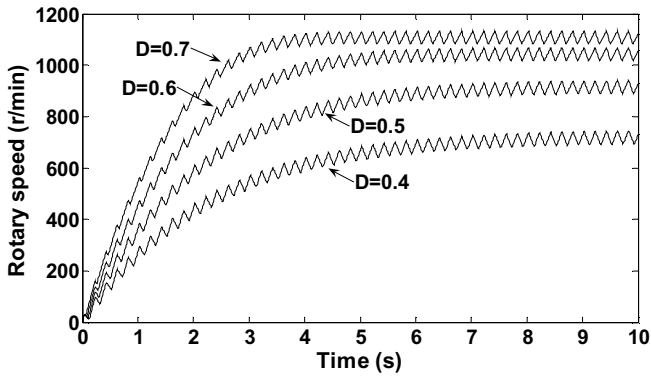
Fig. 5 Rotary speed of the hydraulic motor at different duty ratios
($f = 5Hz$, $B_m = 0.01 N \cdot m /(r / \min)$, $J_m = 0.25 kg \cdot m^2$)
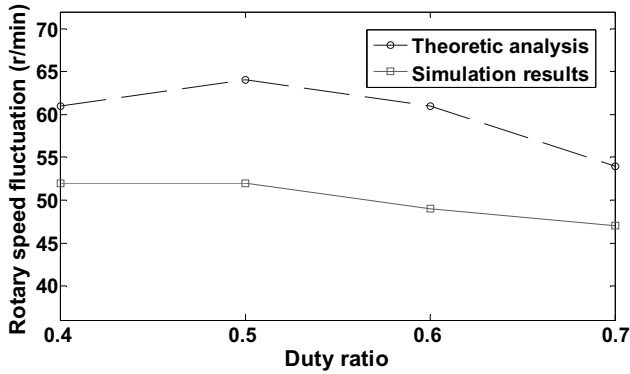
Fig. 6 Rotary speed fluctuation of the hydraulic motor at different duty ratios
($f = 5Hz$, $B_m = 0.01 N \cdot m /(r / \min)$, $J_m = 0.25 kg \cdot m^2$)

Fig. 7 shows the rotary speed of the hydraulic motor at various moments of inertia. Although the average rotary speed remains unchanged when the moment of inertia varies, the rotary speed fluctuation decreases greatly when the moment of inertia increases.

The fluctuation comparison at various moments of inertia between theoretical analysis and the simulation is shown in Fig. 8. The fluctuation in the simulation decreases from 126 to 52 rpm as the moment of inertia increases from 0.1 to 0.25 kg·m^2, which is lower than that in the theoretical analysis.

Fig. 9 shows the rotary speed of the hydraulic motor at various coefficients of viscous friction. The average rotary speed decreases greatly when the coefficient of viscous friction increases from 0.005 to 0.02 N·m/rpm.
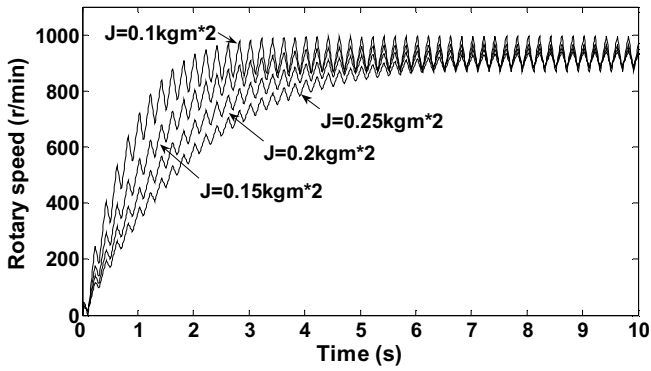
Fig. 7 Rotary speed of the hydraulic motor at different moments of inertia
($D = 0.5$, $f = 5Hz$, $B_m = 0.01 N \cdot m /(r / \min)$)
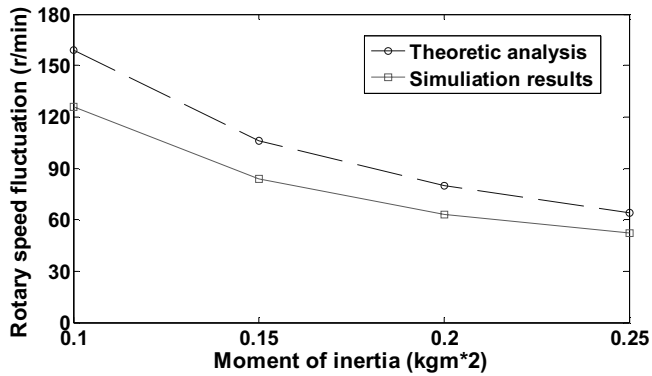
Fig. 8 Rotary speed fluctuation of the hydraulic motor at different moments of inertia
($D = 0.5$, $f = 5Hz$, $B_m = 0.01 N \cdot m /(r / \min)$)
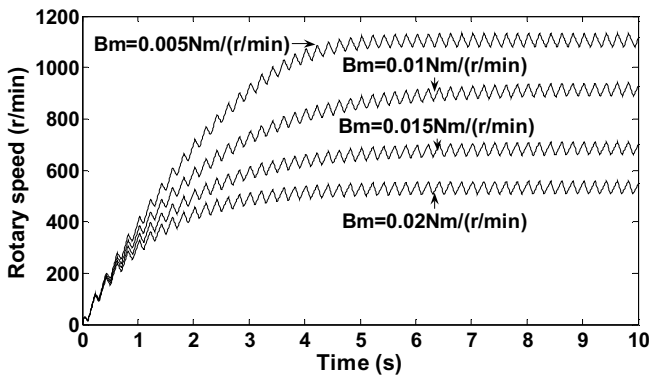
Fig. 9 Rotary speed of the hydraulic motor at different coefficients of viscous friction ($D = 0.5$, $f = 5Hz$, $J_m = 0.25 kg \cdot m^2$)

Although the average rotary speed decreases when the coefficient of viscous friction increases, the fluctuation in the simulation remains about 50 rpm which is shown in Fig. 10.
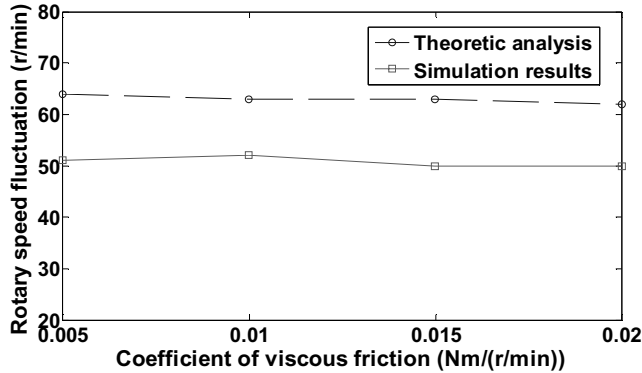
Fig. 10 Rotary speed fluctuation of the hydraulic motor at different coefficients of viscous friction ($D = 0.5$, $f = 5Hz$, $J_m = 0.25 kg \cdot m^2$)

Simulation results show the influence of the proposed four parameters on the rotary speed fluctuation. It is shown that the rotary speed fluctuation of a hydraulic motor is greatly influenced by the switching frequency and moment of inertia on the motor shaft. The fluctuation decreases greatly when the switching frequency increases or the moment of inertia increases. Simulations results also show that the duty ratio and coefficient of viscous friction have almost no influence on the fluctuation.

4. DISCUSSIONS AND CONCLUSIONS

As a promising digital hydraulic technique, switching techniques have been considered as a competitive alternative to traditional control with servo or proportional valves. The biggest challenge of switching techniques is the development of fast, reliable and energy efficient on/off valves. The slow response of the valves increases the hydraulic fluctuation greatly.

In this paper, one of characteristics of the switching system, hydraulic fluctuation, is studied. The case studied is a hydraulic motor rotary speed control system using high-speed on/off valves. The flow through the hydraulic motor not only comes from supply side but also from pressurized tank side. Fluctuation thus occurs as hydraulic motor is periodically accelerated and decelerated.

Other than adding a hydraulic accumulator or hydraulic damper to attenuate the fluctuation, this study seeks the inherent relationship between system parameters and the fluctuation. Some parameters are studied to evaluate their influence on the fluctuation. These are:

switching frequency, duty ratio, moment of inertia of the hydraulic motor and coefficient of viscous friction.

Simulation results show that the hydraulic fluctuation is greatly influenced by the switching frequency and the moment of inertia of the hydraulic motor. The fluctuation decreases greatly when the switching frequency increases or moment of inertia increases. Simulation results also show that the duty ratio and coefficient of viscous friction have almost no influence on the fluctuation.

It should be mentioned that although the simulation results accord with theoretical analysis well, the rotary speed fluctuations in the simulation are a little lower (10%~20%) than those in the theoretical analysis. This is due to the fact that the simulation has taken the switching chamber volume into consideration while it is neglected in the theoretical analysis. This is the biggest difference between the simulation and theoretical analysis. Due to the existence of the switching chamber, both the acceleration and deceleration time are shortened, which is equivalent to increasing the switching frequency and thus the fluctuation decreases.

NOMENCLATURE

Symbol	Property	Unit
p_s	Supply pressure	[MPa]
p_b	Backing pressure	[MPa]
D_m	Displacement of hydraulic motor	[ml/r]
T_L	Load torque on the motor shaft	[N·m]
B_m	Coefficient of viscous friction of hydraulic motor	[N·m/rpm]
J_m	Total moment of inertia on the motor shaft	[kg·m^2]
ω_m	Rotary speed of hydraulic motor	[rpm]
ω_{m+}	Rotary speed of hydraulic motor in the acceleration stage	[rpm]
ω_{m-}	Rotary speed of hydraulic motor in the deceleration stage	[rpm]
T	Periodicity of PWM signal	[s]
f	Switching frequency	[Hz]
D	Duty ratio of PWM signal	[---]
$\Delta\omega_m$	Rotary speed fluctuation of hydraulic motor	[rpm]

ACKNOWLEDGEMENTS

REFERENCES

M. Linjama, A. Laamanen & M. Vilenius, 2003. Is it time for digital hydraulics? *Proceedings of the Eighth Scandinavian International Conference on Fluid Power,* Tampere, Finland, pp. 347–366.

H. Tanaka, 1988. Electro-Hydraulic PCM Control. *Journal of Fluid Control*, Vol. 18, No 1, pp. 34-46.

L. Siivonen, M. Linjama & M. Vilenius, 2005. Analysis of fault tolerance of digital hydraulic valve system. *Power Transmission and Motion Control, PTMC2005*, pp. 133–146.

A. Laamanen, L. Siivonen, M. Linjama & M. Vilenius, 2004. Digital Flow Control Unit – an Alternative for a Proportional Valve? *Power Transmission and Motion Control, PTMC2004*, pp. 297–308.

M. Linjama, M. Vilenius, 2005. Improved Digital Hydraulic Tracking Control of Water Hydraulic Cylinder Drive. *International Journal of Fluid Power*, Vol. 6, No 1, pp. 29–39.

M. Linjama, M. Vilenius, 2005. Digital Hydraulic Tracking Control of Mobile Machine Joint Actuator Mockup. *Proceedings of the Ninth Scandinavian International Conference on Fluid Power,* Linköping, Sweden, 16 p.

J. Dantlgraber. Hydro-Transformer. *European patent application (PCT) International.* Publication No. WO 00/08339, 2000.

R. Scheidl, B. Manhartsgruber, 2005. State of the Art in Hydraulic Switching Control – Components, Systems, Applications. *Proceedings of the Ninth Scandinavian International Conference on Fluid Power,* Linköping, Sweden, 12 p.

B. Johnson, S. Massey & O. Sturman, 2001. Sturman Digital Latching Valve. *Proceedings of the Seventh Scandinavian International Conference on Fluid Power,* Linköping, Sweden, pp. 299–314.

H. Hettrich, F. Bauer, F. Fuchshumer, 2009. Speed controlled, energy efficient fan drive within a constant pressure system. *The Second Workshop on Digital Fluid Power*, Linz, Austria.

Linyi Gu, Minxiu Qiu, Bo Jin, Jianwei Cao, 2003. New hydraulic systems made up of hydraulic power bus and switchmode hydraulic power supplies. *Chinese Journal of Mechanical Engineering*, 39(1), 84-88.

Jianwei Cao, Linyi Gu, Feng Wang, Minxiu Qiu, 2005. Switchmode hydraulic power supply theory. *Proceedings of 2005 ASME International Mechanical Engineering Congress and Exposition,* Orlando, FL, USA, No.79019.

Jianwei Cao, Linyi Gu, Feng Wang and Ying Chen, 2006. Research on the principle and characteristic of compound switchmode hydraulic power supply. *Proceedings of 2006 ASME International Mechanical Engineering Congress and Exposition,* Chicago, IL, USA, No. 13453.

Yongxiang Lu, Dahong Hu, 1988. *Electro-hydraulic Proportional Control Technique.* China Machine Press, Beijing, China.

Yongxiang Lu, 2002. *Technical Manual of Hydraulics and Pneumatics*. China Machine Press, Beijing, China.

Genmao Wu, Minxiu Qiu, Qingfeng Wang, 1993. *Practical electro-hydraulic proportional control technique*. Zhejiang University Press, Hangzhou, China.

High performance valves

Robustness Analysis of Models for Hydraulic Servo Valve by Using a Statistical Method

J Liu, H Wu, H Handroos, and H Haario
Faculty of Technology, Lappeenranta University of technology
P.O. Box 20, FIN-53851 Lappeenranta, Finland
junhong.liu@lut.fi

ABSTRACT

Proportional valves have gained a large number of applications because of their low cost, easy maintenance, and high performance. They generally operate nonlinearly. It is important to evaluate their models in order to improve the overall system performance. The aim of this work is modeling of a proportional servo solenoid valve using a statistical method — the Markov chain Monte Carlo approach. Several dynamic models of the valve are presented; their ordinary differential equations with unknown parameters are formed. The noise-corrupted physical data are used for parameter estimation. The analysis and predictions take into account all the uncertainties in the models and the data. The model structures are developed until acceptable statistical results have achieved. The identifiability of model parameters is quantified by probability distributions. Model predictions are obtained. New situations are taken for verification. Results indicate that the third order model has the most excellent agreement between the measured and simulated results in wide operating range and is most robust, and the second order system is a reasonable candidate for simplification purpose. The validity of models and the successfulness of parameter identification in hydraulic component and system model development can be quantified with this statistical method.

1. INTRODUCTION

Hydraulic systems have been the center of research for decades [1, 2, 3, 4]. Hydraulic component and systems operate nonlinearly. Besides the system identification, it is crucial to preview behavior in order to discovery the relevant and irrelevant factors of models, to improve the controllers and the overall system performance, to optimize the structure, and to apply suitably simplified models to real-time control.

Valve models have been studied [2, 4, 5, 6]. Dynamic performance of hydraulic systems has improved due to the use of electronics and microprocessors. Proportional servo solenoid valves have high dynamic performance and have gained closed-loop applications

since they cost low and require easy maintenance. The typical input to a proportional servo solenoid valve is a voltage to solenoid, which produces a force input to a servo-hydraulic control system. This force causes the spool to change position and thereby will change the orifice areas, which control system flow and pressure. Disturbances to the spool motion are highly undesirable and can be due to frictional forces between valve spool and sleeve, static pressure forces due to the spool geometry, or flow-induced inertial forces. Control strategies, employing the closed-loop position control, have been developed to achieve good spool dynamic characteristics over the whole valve operation conditions. This leads to the possibility of using simple models of spool motion, neglecting the non-linear hysteresis, friction or flow forces effects.

In this work, the modeling work is performed by a statistical method — the Markov chain Monte Carlo (MCMC) approach, which has become a commonly used technique for analyzing nonlinear models in different applications. The dynamic models are represented as ordinary differential equations (ODE) systems with unknown parameters, and the noise-corrupted measurement data is used for fitting models. The reliability of the parameters as well as the model predictions are quantified as probability distributions. The model structures are developed until acceptable statistical results have achieved.

This paper is structured as follows. Section 2 describes the models of a proportional servo solenoid valve with position feedback control and the on-board trigger electronics (OBE). Section 3 describes the modeling method; among a large variety of the MCMC algorithms, the delayed rejection adaptive Metropolis method (DRAM) [7, 8, 9] is chosen for the modeling task. Results are given in Section 4 and conclusions in Section 5.

2. HYDRAULIC SYSTEM DESCRIPTION

The directly operated proportional servo solenoid valve with the position control and the OBE under study is shown in Fig. 1. The main spool of the valve is the key component of the flow divider and is highly responsible for the outcome of the transfer function.

A first order model can be applied in the case of a high-bandwidth valve without response peaks or overshoots in the responses, while the second order model can also describe these un-idealities [10]. A linearized model for an electrohydraulic servo system has revealed that the higher order model fits closer to the experimental data because of the reduced unmodeled dynamics [11].

Three mathematical models will be described as the valve models, involving parameters that may be completely unknown or only known within certain ranges.

Voltage u (V) is the valve input. When the input is applied to the valve, the spool is shifted and openings are produced. The shift of the spool, namely position displacement x_s (mm), is in both directions. The spool is connected to the linear variable differential transformer (LVDT) that gives a testable voltage output u_s (V) proportional to the spool displacement x_s. Voltage u_s, with its range as ± 10 V ($\pm u_{s,max}$), is measured and directly used for providing information of the spool displacement for an input u of ± 10 V. Another option is to use the normalized valve spool position $\bar{x}_s = x_s / x_{s,max}$, and $\bar{x}_s \in [-1,1]$, which is the same as the

normalized spool displacement by $\bar{x}_s = \bar{u}_s$, and $\bar{u}_s = u_s/u_{s,\max}$ .The difference between two options is only one coefficient $u_{s,\max}$ in the representation formula. The straight representation u_s is kept using throughout the work.
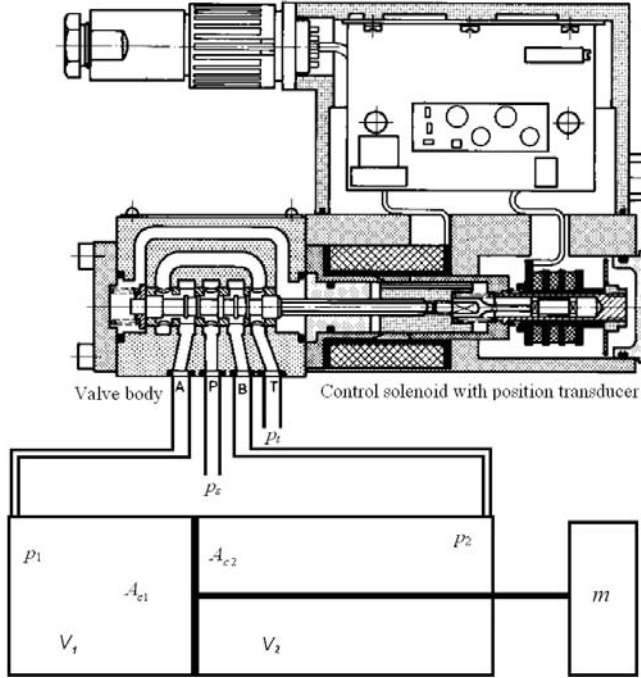
Figure 1 Schematic diagram of experimental configuration

2.1 First order model
The relationship of u_s and u can simply be of a first order model as in [11]:

$$G_1(s) = \frac{U_s(s)}{U(s)} = \frac{K_1}{T_1 s + 1}.$$ (1)

2.2 Second order model
The valve model can be represented by a second order transfer function [2, 11] as:

$$G_2(s) = \frac{U_s(s)}{U(s)} = \frac{K_2 \omega_2^2}{s^2 + 2\zeta_2 \omega_2 + \omega_2^2}.$$ (2)

2.3 High order model
Valve chambers are small and the compressible flows are lumped to the line and chamber actuator models. Assume a positive spool displacement (it would lead to the same solution if taking the negative spool displacement). The valve volumetric flowrate are then modeled by algebraic equations.

2.3.1 Flowrate models

The load pressure is defined as the pressure difference between ports 1 and 2:

(a)   (b)
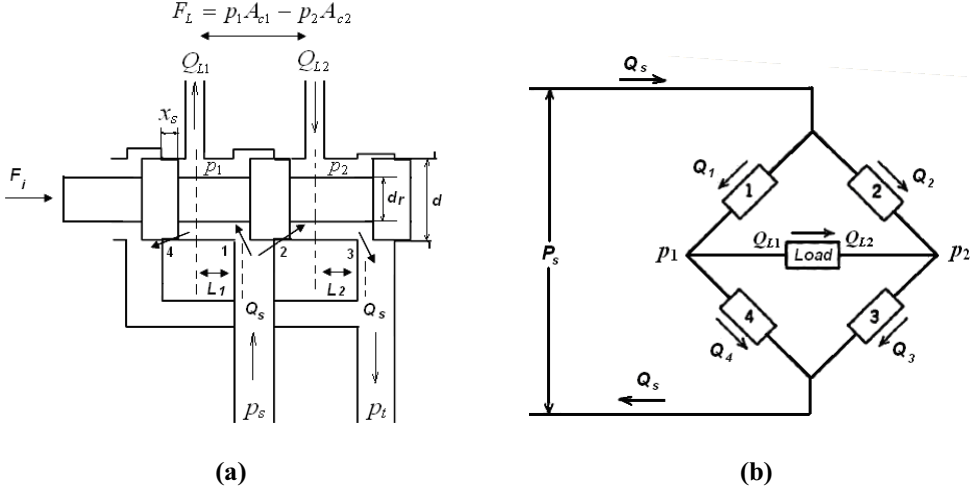
Figure 2 (a) Three-land-four-way valve; (b) Wheatstone bridge system

$$F_L = p_1 A_{c1} - p_2 A_{c2}. \tag{3}$$

The volumetric flowrate is always assumed turbulent, the governing nonlinear equations describing the fluid flow distributions in the valve are written as [1, 2], where the discharge coefficient α_d depends on the valve spool position by $\alpha_d = \alpha_{d0}\left[1 - K_{d,corr} \cdot |x_s| / x_{s,\max}\right]$:

$$Q_1 = \alpha_d A_1(x_s)\sqrt{\frac{2}{\rho}(p_s - p_1)}, \ x_s \geq 0 \ \text{(extension)}, \tag{4}$$

$$Q_2 = \alpha_d A_2(-x_s)\sqrt{\frac{2}{\rho}(p_s - p_2)}, \ x_s \geq 0 \ \text{(retraction)}, \tag{5}$$

$$Q_3 = \alpha_d A_3(x_s)\sqrt{\frac{2}{\rho}(p_2 - p_t)}, \ x_s \geq 0 \ \text{(extension)}, \tag{6}$$

$$Q_4 = \alpha_d A_4(-x_s)\sqrt{\frac{2}{\rho}(p_1 - p_t)}, \ x_s \geq 0 \ \text{(retraction)}. \tag{7}$$

2.3.2 Relationship between pressures

The orifices are matched and symmetrical for an ideal critical center valve, so the orifice areas and flows have the following relationship:

$$A_1 = A_3, \ Q_1 = A_{c1}v, \ Q_3 = A_{c2}v, \tag{8}$$

$$A_2 = A_4, \ Q_2 = A_{c2}v, \ Q_4 = A_{c1}v. \tag{9}$$

If p_t is considered as datum pressure for other pressures, the port pressures are related. Combining (4), (6), and (8) in extension situation, yields:

$$p_s = p_1 + \left(A_{c1}^2 / A_{c2}^2\right) \cdot p_2 - \left(A_{c1}^2 / A_{c2}^2\right) \cdot p_t = p_1 + k_c^2 p_2 - k_c^2 p_t, \tag{10}$$

where $k_c = A_{c1} / A_{c2}$. Using (3) and (10), the following relations are then obtained:

$$p_1 = \frac{p_s + k_c^2 p_t + \left(k_c^2 / A_{c2}\right) \cdot F_L}{1 + k_c^3}, p_2 = \frac{k_c p_s + k_c^3 p_t - \left(1 / A_{c2}\right) \cdot F_L}{1 + k_c^3}. \tag{11}$$

Or combining (3), (5), (7), and (9) in retraction condition yields $p_s = p_1 / k_c^2 + p_2 - p_t / k_c^2$,

$$p_1 = \frac{k_c^2 p_s + p_t + \left(k_c^2 / A_{c2}\right) \cdot F_L}{1 + k_c^3}, \text{ and } p_2 = \frac{k_c^3 p_s + k_c p_t - \left(1 / A_{c2}\right) \cdot F_L}{1 + k_c^3}.$$

The pressure in port 1 is k_c times of the pressure in port 2 for a matched and symmetrical valve with no load ($F_L = 0$). As load is applied, the pressure in p_1 increases and the pressure in p_2 decreases while the absolute change reads $\Delta p_1 = k_c^2 \cdot \Delta p_2$.

2.3.3 Open-loop transfer function
For representation simplicity, the subscripts of orifice area and volumetric flowrate are omitted. The steady-state axial flow force on the spool (Fig. 3) can be calculated by [1, 2]:
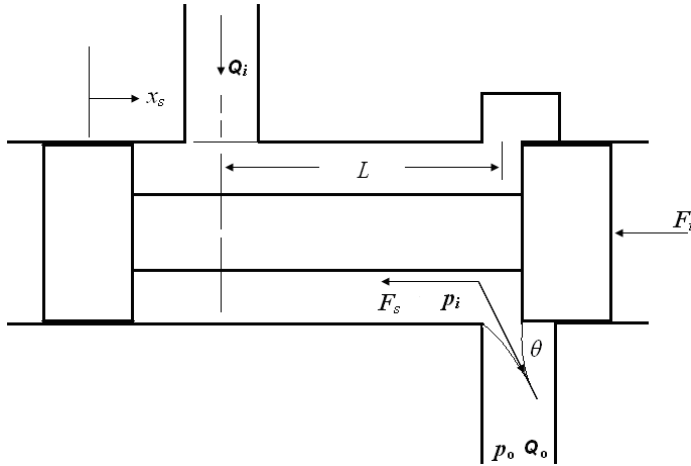
Figure 3 Axial flow force on a spool valve due to flow leaving a valve chamber

$$F_s = \rho Q v(\cos\theta) = \rho Q \left(\frac{Q}{A(x_s)}\right)(\cos\theta) = 2\alpha_d^2 A(x_s)\Delta p(\cos\theta) = 2\alpha_d^2 W x_s \Delta p(\cos\theta), \tag{12}$$

where pressure drop $\Delta p = p_i - p_o$ (p_i and p_o the pressures in places fluid flows from and to).

Two orifices (1 and 3 for $+x_s$; 2 and 4 for $-x_s$) are active at one time in an ideal critical center valve (Fig. 2). When the valve has a positive spool displacement, the steady-state axial flow forces on the spool are:

$$F_{Rss\_1} = 2\alpha_d^2 W x_s (p_s - p_1)(\cos\theta), F_{Rss\_3} = 2\alpha_d^2 W x_s (p_2 - p_t)(\cos\theta). \tag{13}$$

And the transient flow force is due to the acceleration of the fluid in the annular valve chamber. The direction of this force is such that it tends to close the valve port. The magnitude of the transient flow force is given by Newton's second law as

$$F_{Rts\_1} = Ma = \rho L_1 A_v \frac{d(Q_1/A_v)}{dt} = \rho L_1 \frac{dQ_1}{dt},$$

$$F_{Rts\_3} = Ma = \rho L_2 A_v \frac{d(Q_3/A_v)}{dt} = \rho L_2 \frac{dQ_3}{dt}. \tag{14}$$

Using (4), (6), (11-14), the flow force opposing the spool motion is obtained:

$$F_R = F_{Rss\_1} - F_{Rts\_1} + F_{Rss\_3} + F_{Rts\_3}$$

$$= 2\alpha_d^2 W x_s (p_s - p_1)(\cos\theta) - \rho L_1 \frac{dQ_1}{dt} + 2\alpha_d^2 W x_s (p_2 - p_t)(\cos\theta) + \rho L_2 \frac{dQ_3}{dt}$$

$$= 2\alpha_d^2 W \cdot \frac{k_c^3 p_s - k_c^2 (p_t + (1/A_{c2}) \cdot F_L)}{1 + k_c^3} (\cos\theta) x_s$$

$$- L_1 \alpha_d W \sqrt{2\rho \frac{k_c^3 p_s - k_c^2 (p_t + (1/A_{c2}) \cdot F_L)}{1 + k_c^3}} \cdot \frac{dx_s}{dt}$$

$$- L_1 \alpha_d W x_s \cdot \frac{1}{\sqrt{\dfrac{k_c^3 p_s - k_c^2 (p_t + (1/A_{c2}) \cdot F_L)}{\rho(1 + k_c^3)/2}}} \cdot \frac{d\left(\dfrac{k_c^3 p_s - k_c^2 (p_t + (1/A_{c2}) \cdot F_L)}{1 + k_c^3}\right)}{dt}$$

$$+ 2\alpha_d^2 W \frac{p_s k_c - p_t - (1/A_{c2}) \cdot F_L}{1 + k_c^3} (\cos\theta) x_s$$

$$+ L_2 \alpha_d W \sqrt{2\rho \frac{p_s k_c - p_t - (1/A_{c2}) \cdot F_L}{1 + k_c^3}} \cdot \frac{dx_s}{dt}$$

$$+ L_2 \alpha_d W x_s \cdot \frac{1}{\sqrt{\dfrac{p_s k_c - p_t - (1/A_{c2}) \cdot F_L}{\rho(1 + k_c^3)/2}}} \cdot \frac{d\left(\dfrac{p_s k_c - p_t - (1/A_{c2}) \cdot F_L}{1 + k_c^3}\right)}{dt}. \tag{15}$$

Neglecting the return line pressure p_t (it is usually much smaller than the other pressures involved) and the pressure rate terms [1], the following equation is obtained:

$$F_R = 2\alpha_d^2 W(1+k_c^2)\frac{k_c p_s - (1/A_{c2})\cdot F_L}{1+k_c^3}(\cos\theta)x_s$$

$$+ \alpha_d W(L_2 - L_1 k_c)\sqrt{2\rho\frac{k_c p_s - (1/A_{c2})\cdot F_L}{1+k_c^3}}\frac{dx_s}{dt} \tag{16}$$

$$= K_f x_s + B_f \frac{dx_s}{dt},$$

where $K_f = 2\alpha_d^2 W\left(1+\dfrac{1}{k_c}\right)\dfrac{p_s A_{c1} - F_L}{A_{c1}+A_{c2}/k_c}(\cos\theta)$ and $B_f = \alpha_d W\left(\dfrac{L_2}{\sqrt{k_c}}-L_1\right)\cdot\sqrt{2\rho\dfrac{p_s A_{c1}-F_L}{A_{c1}+A_{c2}/k_c}}$.

Both K_f and B_f are related to not only F_L but also the valve spool position, and their values reach individual maxima when $F_L = 0$.

The force of electric solenoid is described by the following equation:

$$F_i = K_i i^2, \tag{17}$$

where the relationship of the voltage input and current is:

$$u = \frac{d(Li)}{dt} + Ri. \tag{18}$$

Finally, the dynamic equation of the spool motion is:

$$F_i = M_v \frac{d^2 x_s}{dt^2} + (B_v + B_f)\frac{dx_s}{dt} + (K_v + K_f)x_s. \tag{19}$$

Linearizing on (17) and taking the Laplace transformation on (19) lead to the following:

$$\frac{X_s(s)}{U(s)} = \frac{2K_i i_0/RM_v}{\left(\dfrac{L}{R}s+1\right)\left[s^2 + \dfrac{B_v+B_f}{M_v}s + \dfrac{K_v+K_f}{M_v}\right]}. \tag{20}$$

Equation (20) is rewritten using u_s and the open-loop transfer function is obtained:

$$G_O(s) = \frac{U_s(s)}{U(s)} = \frac{u_{s,max}}{x_{s,max}}\cdot\frac{X_s(s)}{U(s)} = \frac{k_3 c_3^3}{s^3 + 3c_1 s^2 + 3c_2^2 s + c_3^3}, \tag{21}$$

where $c_1 = \dfrac{1}{3}\left(\dfrac{R}{L}+\dfrac{B_v+B_f}{M_v}\right)$, $c_2 = \sqrt{\dfrac{1}{3}\left(\dfrac{R}{L}\cdot\dfrac{B_v+B_f}{M_v}+\dfrac{K_v+K_f}{M_v}\right)}$, $c_3 = \sqrt[3]{\dfrac{R}{L}\cdot\dfrac{K_v+K_f}{M_v}}$, and

$$k_3 = \frac{2\cdot K_i \cdot i_0 \cdot u_{s,max}}{R\cdot x_{s,max}\cdot(K_v+K_f)}.$$

2.3.4 Closed-loop model

The valve has closed-loop position control. Representing the control unit as a proportional controller with k_P a non-negative value (Fig. 4).
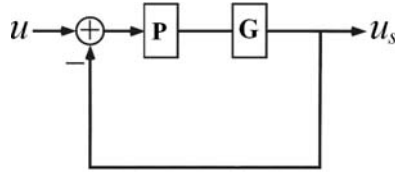
Figure 4 Block diagram of a standard feedback control with proportional controller

When the open-loop transfer function is represented in (21), the close-loop transfer function of valve can be rewritten as:

$$G_F(s) = \frac{U_s(s)}{U(s)} = \frac{C(s)G_o(s)}{1 + C(s)G_o(s)} = \frac{k_P \cdot \dfrac{k_3 \cdot c_3^3}{s^3 + 3c_1 s^2 + 3c_2^2 s + c_3^3}}{1 + k_P \cdot \dfrac{k_3 \cdot c_3^3}{s^3 + 3c_1 s^2 + 3c_2^2 s + c_3^3}}$$

$$= \frac{k_3 c_3^3 \cdot k_P}{s^3 + 3c_1 s^2 + 3c_2^2 s + c_3^3\left(1 + k_3 k_P\right)} = \frac{K_3 a_3^3}{s^3 + 3a_1 s^2 + 3a_2^2 s + a_3^3}, \quad (22)$$

where $a_1 = c_1, a_2 = c_2, a_3 = c_3\sqrt[3]{1 + k_3 k_P}$, and $K_3 = k_3 k_P / \left(1 + k_3 k_P\right)$.

Adding the proportional controller does not change the transfer function formula, as seen from (21) to (22), which actually have the same formula except some constant transformation. So, omitting the time delay in (20), the open-loop transfer function $G_O(s)$ in become s a second order function, and the related close-loop model $G_F(s)$ also turns out to be a second order function, both can be represented by (2) with constant transformation similar to that used for obtaining (22) from (21).

3. METHOD

3.1 Overall equation of a system model

A model is a mathematical description of the process that generates the states and the observations. The model can depend on a set of model parameters and it can be driven externally by control parameters. A dynamical model can be written as:

$$s = f(x, \theta, c),$$
$$y = g(x, \theta) + \varepsilon, \quad (23)$$

where, θ denotes the parameters to be estimated, c the known constants, x control variables, s the system states, y the observations, ε the unsystematic observation errors, and the relationship functions g and f.

The sum of squared residuals (*SS*) is used in the MCMC algorithm and the objective is to minimize *SS*; the applied mean of the sum, the objective function, being *N* the number of observations and y_i the observed responses at x_i, is written in the form:

$$\iota = \frac{1}{N} \sum_{i=1}^{N} \left(y_i - g(x_i) \right)^2 = \frac{1}{N} \cdot SS \cdot \tag{24}$$

3.2 ODE systems
The ODE system of each valve model has control variable $x = u$ and observations $y = u_s$.

The ODE system of the first order model in (1), having state u_s and an initial state u_{s0} with the unknown parameters, K_1 and T_1, has the following form,

$$\frac{du_s(t)}{dt} = (K_1 u - u_s)/T_1 \cdot \tag{25}$$

The ODE system of the second order model in (2), being states $[u_s \ \dot{u}_s]$ and the initial states $[u_{s0} \ 0]$ with three unknowns, K_2, ζ_2, and ω_2, is written as,

$$\frac{du_s(t)}{dt} = \dot{u}_s,$$
$$\frac{d\dot{u}_s(t)}{dt} = k_2 \omega_2^2 u - 2\zeta_2 \omega_2 \dot{u}_s - \omega_2^2 u_s. \tag{26}$$

The ODE system of the third order model in (22), containing states $[u_s \ \dot{u}_s \ \ddot{u}_s]$ and the initial states $[u_{s0} \ 0 \ 0]$ with unknowns, K_3, a_1, a_2, and a_3, has the form of:

$$\frac{du_s(t)}{dt} = \dot{u}_s,$$
$$\frac{d\dot{u}_s(t)}{dt} = \ddot{u}_s,$$
$$\frac{d\ddot{u}_s(t)}{dt} = K_3 a_3^3 u - 3a_1 \ddot{u}_s - 3a_2^2 \dot{u}_s - a_3^3 u_s. \tag{27}$$

3.3 Applying Bayesian modeling
Unidentifability of the estimated parameters can be caused by limited availability of observational data or by the structure of the nonlinear model equations. This can sometimes be solved with the better design of experiments and reparameterizing the model. Bayesian approach is a powerful way to quantify the uncertainties in the whole modeling procedure, and the unknowns' unidentifiability is detected by inspecting their posterior distributions.

The MCMC simulation of values from the posterior distribution of the parameters is a computational method that can be applied to a wide variety of modeling problems. To use the models in Bayesian settings we need to specify a prior distribution for the parameters. As an example, take the term valve gain in each model corresponds to valve output, i.e., the

amount of spool displacement transformed into voltage, at the valve input. We have the manufacture's information about this value, which however is subjected to some doubt. If no such prior is known (other than positivity and some large upper bounds), we also can assume non-informative priors for each unknown parameters in MCMC calculations constraints. The value of MCMC sampling methods is that they provide 'all' the parameter values that reasonably well fit the data, instead of a single 'best fit'. Note, anyway, that we routinely first perform a standard LSQ fitting to provide a good starting point for subsequent parameter sampling.

Calculating the models, given the data and the unknown parameters, requires solving the differential equations using numerical methods. To solve the equations, we specify an initial condition for the observations of the valve output, i.e., the values of u_s and its derivatives at the initial time point 0 for each physical experiment. However these values are themselves observations subject to errors, and solving the equations with the initial values fixed will cause bias. In the classical least squares estimation, the control variables x are assumed to be precise or at least with error that is negligible compared with the observational error in the dependent variables. An observation with error is considered as an extra parameter.

4. RESULTS

4.1 Experimental setup

A Bosch Rexroth servo solenoid valve with position control and on-board electronics (4WRPEH 6) is under study. The data acquisition system was a dSPACE digital signal processor. The sampling frequency was 1000 (Hz). The control program was the c/c^{++} language program [12]. Input voltage u was fed to the valve using a DS 1103 I/O card; u_s was collected from the valve's LVDT signal.

For studying the valve dynamics, eight physical experiments were independently carried out with null load or with different load and varied supply pressure. In each experiment, a step signal was fed as the valve input, while the valve input u and the valve's LVDT signal u_s were directly collected along with time. Eight sets of physical data were obtained. The obtained physical data are noise corrupted and clustered into nine groups featuring null load, loaded, negative and positive input, different combinations of load conditions and input types, and hybrid (Table 1). The nine groups were individually used as tests to fit the three models of the valve.

The unknown parameters of a model are optimized by the least square fitting using the software package *modest* [13]. The DRAM algorithm [7] is applied to modeling. When a model is fitted with data, the MCMC chain is produced by the algorithm and the chain is a matrix, having order (the number of simulations) × (the number of parameters), of samples from the posterior distribution of the multi-dimensional parameter vector. All statistical reasoning on a fitted model and its parameters can be based on the obtained matrix. The obtained chain is commonly used to: (*i*) calculate the posterior means, the standard deviations, and correlations; and (*ii*) to obtain illustrative plots, e.g., histograms and density estimation. Any model-derived values, such as predictive posterior distributions, are given by calculating the respective values using parameter samples from the chain. The posterior

correlations and two-dimensional marginal posterior plots of the parameter combinations can be used as diagnostics of parameter identifiability. The variance of the predictive distribution reflects the predictive power of the model. A large variance may be due to uncertainty in the model, effects not taken into account in the model, or noise in the measurement. The uninformative prior is used for each parameter.

Table 1 Data for fitting models

Test	Experiment		Number of data sets
	Step input	Load	
1	Mixed	Null load	4
2	Negative	Null load	2
3	Positive	Null load	2
4	Mixed	Loaded	4
5	Negative	Loaded	1
6	Positive	Loaded	3
7	Negative	Mixed	3
8	Positive	Mixed	5
9	Mixed	Mixed	8

4.2 Posterior distributions

The nine groups of original physical data were used for fitting the three models of the studied valve. The model parameters are estimated generally for each test (Table 1) that contains data obtained from individual experiments. Among the nine tests, the test 4, consisting four independent data sets, is taken for demonstration. The third model with four parameters generally estimated for the four data sets gives the best agreement with the observations compared to the first order model and the second order model; and the second order model performs a little bit worse than the third order model.

Figure 5 shows the data used together with the fit obtained by the MCMC method. The model predicted spool position 95% posterior limits are shown by gray area around the median estimate. Figure 6 shows the posterior corrections of the parameters in the third-order model. The objective function values according to (24) from nine tests are plotted in Fig. 7a, from which it can be concluded that the third-order model best suits the data for fitting, and the curve of the second order model is quite close to that of the third order model, compared to the first order model.

4.3 Verification

The found models were further verified with new situations. Eight physical experiments were carried out separately, having varied pulse input to valve, load, and supply pressure. The models with parameters found by test 9 were applied. The objective function values in (24) from eight tests are plotted in Fig. 7b. As observed from the plots, the third-order model performs superiorly over the other two models; and the results from the second order model are very close to those of the third order model and much better than those of the first order model.

(a) First order model;   (b) second order model;   (c) third order model
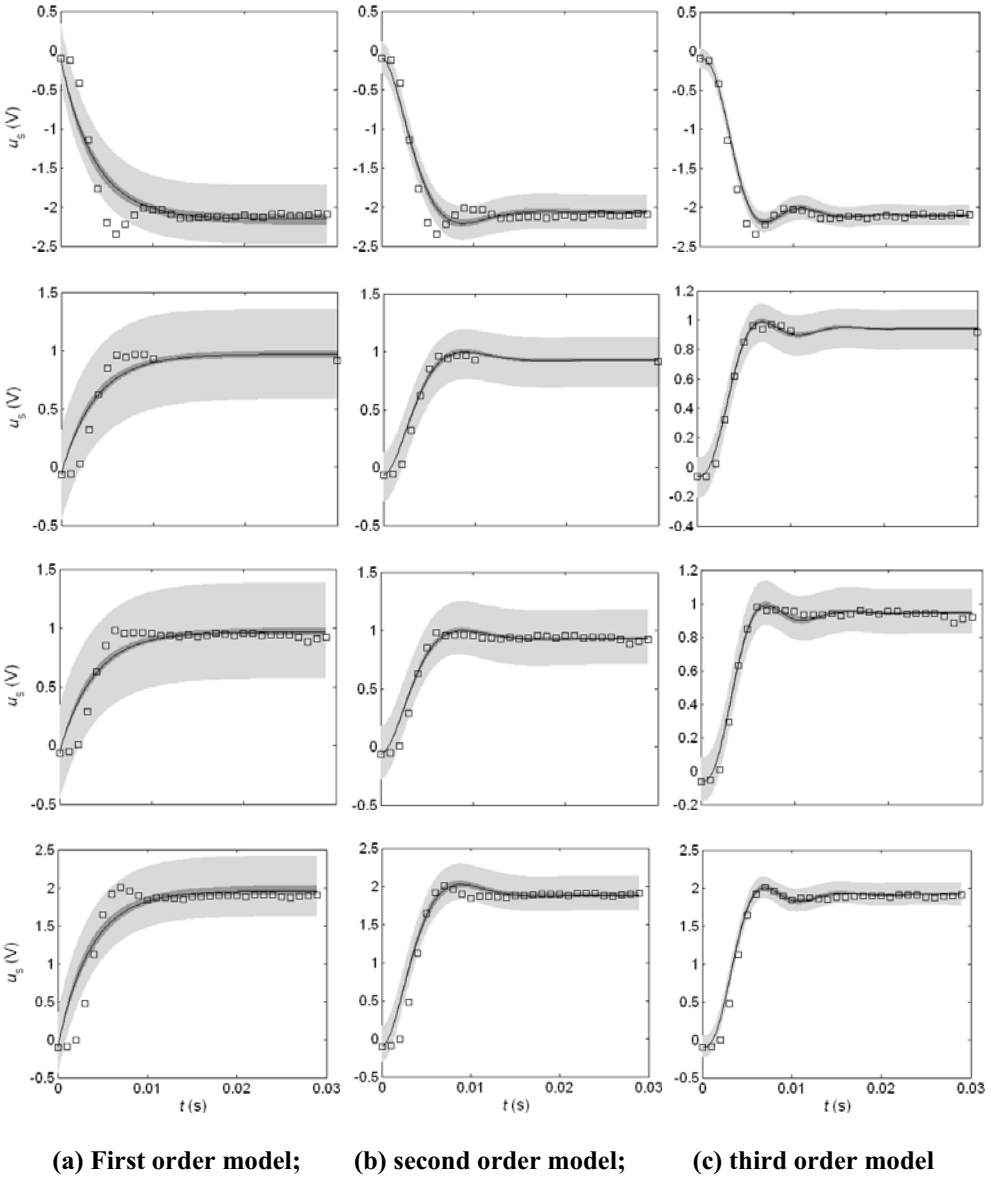
Figure 5 Plots of the fitted models and uncertainties in Test 4. (Legends: Solid lines show the median fits obtained; darker areas correspond to the 95% posterior limits of the model uncertainties; lighter areas illustrate the 95% bounds of the uncertainties in predicting new observations; and squares present observations)
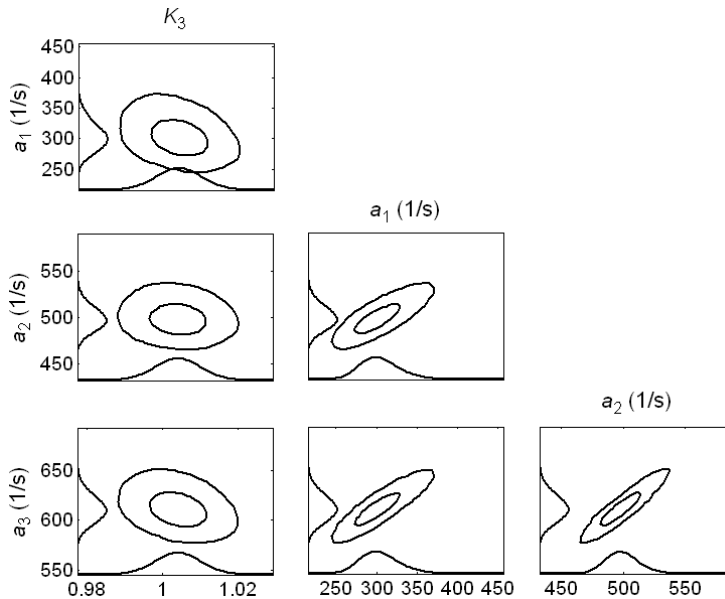
Figure 6 Two-dimensional marginal posterior distributions of K_3, a_1, a_2, and a_3. The two contour lines correspond to 50% and 90% regions; distributions along axes are one-dimensional marginal densities

| (a) | (b) |
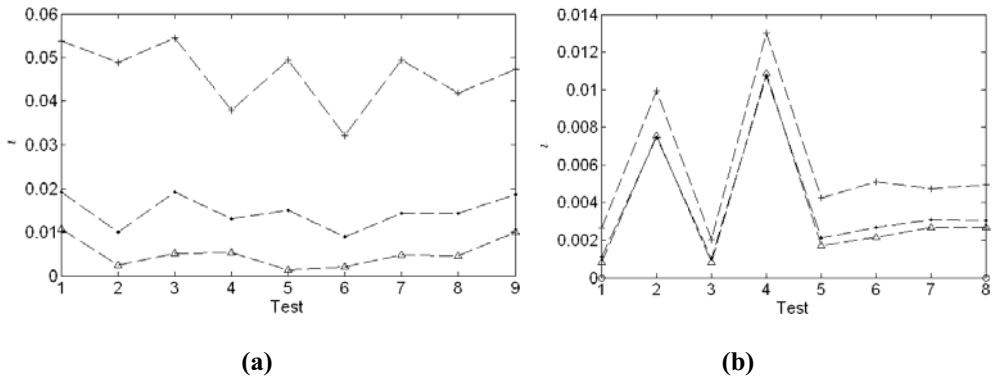
Figure 7 (a) Means of the squared residual sums from fitting tests; (b) the values of ι of the verification tests (Figure legends: + first order, ● second order, ∆ third order)

5. DISCUSSION AND SUMMARY

The paper evidently shows the strength of the MCMC method in hydraulic component and system model development. The analysis and predictions take into account all the uncertainties in models and data; and the uncertainties are quantified using a full statistical approach. The coefficients of each model prove to be uncorrelated and identifiable with the given data. New situations are also taken for verification. The results indicate that the third

order model has the most excellent agreement between the measured and simulated results in wide operating range and is most robust, but the second order system is a reasonable candidate for simplification purpose since it noticeable performs very close to the third order model revealed by the fitting results and the verifications.

Notation

A_i, A	valve orifice areas (m^2)
A_{ci}	piston areas (m^2)
B_f	viscous damping coefficient (Ns/m)
F_L	load force (N)
K_f	flow force spring rate (N/m)
K_i	valve gains (no physical unit)
L_i	damping length (m) (the axial length between incoming and outgoing flows)
Q_i, Q	volumetric flowrate through orifice (m^3/s)
T	time constant (s)
V_i	chamber volumes (m^3)
W	area gradient of orifice (m^2/m)
a_i	constants (1/s)
m_v	spool mass weight (kg)
p_L	load pressure (Pa)
p_1, p_2	input and output line pressures (Pa) (pressures at valve ports 1 and 2)
p_s, p_t	pump and tank pressures (Pa) (supply and return pressures)
u	input voltage to valve (V)
u_s	voltage corresponding to spool position displacement (V)
v	flow speed (m/s)
x_s	valve spool displacement (m)
α_d	discharge coefficient (no physical unit)
θ	angle at which fluid jet leaves spool chamber (°)
ρ	mass density of fluid (Ns^2/m^4)
ζ	damping ratio (no physical unit)
ω_n	natural angular frequency (rad/s)

References

1. Merritt H E. "Hydraulic control systems", John Wiley, New York; 1967.
2. Jelali M, Kroll A. "Hydraulic servo-systems — modeling, identification, and control," Springer; 2003.
3. Lyshevski S E. "Identification of nonlinear systems with noisy data: a nonlinear mapping-based concept in time domain," in Proc. American Control Conf., Arlington, VA, USA 2001; 2:1634-1635.
4. Ferreira J A, Gomes Almeida F, Quintas M R. "Semi-empirical model for a hydraulic servo-solenoid valve," Journal of Systems & Control Engineering, 2002; **216**(3):237-248.
5. Yousefi H, Handroos H, Soleymani A. Application of differential evolution in system identification of a servo-hydraulic system with a flexible load. Mechatronics 2008; 18(9):513-528.
6. P. La Hera, U. Mettin, I. R. Manchester, A. Shiriaev, Identification and Control of a Hydraulic Forestry Crane, Proceedings of the 17th IFAC World Congress, pages 2306-2311, Seoul, Korea, July 6-11 2008.
7. Haario H, Laine M, Mira A, Saksman E. "DRAM: Efficient adaptive MCMC," Stat. Comput 2006; **16**:339-354.
8. Liu J, Handroos H, Haario H, Wu H. "Reliability analysis of a model for servo hydraulic system by utilizing Markov chain Monte Carlo method," in Proc. 7th Int'l Conf. on Fluid Power Transmission and Control, Apr 7-10, 2009, Hangzhou, China; 783-787.
9. Liu J, Handroos H, Haario H, Nishiumi T. "Improving the robustness of simulation models for hydraulic components and circuits by a statistical method," in Proc. 11th Scandinavian Int'l Conf. on Fluid Power, Jun 2-4, 2009, Linköping, Sweden.
10. Thayer W J. "Transfer Functions for moog Servovalves," Technical Bulletin #103, Moog Inc., Controls division, East aurora, NY, 1965; 1-11.
11. Kim D M, Tsao T C. "A linearized electrohydraulic servovalve model for valve dynamics sensitivity analysis and control system design," ASME J. Dyn. Syst., Meas., Control, 2000; **122**:179-187.
12. Mathworks Inc. "Users guide of real time workshop", 2005.
13. Haario H. "MODEST user guide", ProfMath Company, 1995.

Reluctance Networks for Simulation of Proportional Solenoids in Fluid Power Valve Systems

Dirk Wehner, Siegfried Helduser, Jürgen Weber
Institut für Fluidtechnik, TU Dresden, Germany

Georg Schoppel
Bosch Rexroth AG, Lohr am Main, Germany

ABSTRACT

Methods for virtual product development become more and more popular. Simulation tools like Lumped parameter, FEM or CFD are used to determine system performance in the early phase of design process. That saves development costs and development time. Electrohydraulic valve systems are characterized by mechatronic properties and a lot of complex nonlinear relations. That makes the development of electrohydraulic valve systems to an substantial challenge. Model approaches with lumped parameters offer good opportunities to describe the entire valve consisting of valve electronics, proportional solenoid, mechanical and hydraulic effects. The proportional solenoid is an important subsystem of such a valve. While FEM-model enables a detailed design a holistic analysis of the entire valve is not possible. Modell approaches are needed that can describe the solenoid performance in a holistic model (e.g. a lumped parameter model). One possibility to describe the proportional solenoid in such a way is the reluctance network. To date there is no approach available to describe the performance of a proportional solenoid in an acceptable precision with lumped parameters.

The paper presents a new approach to derive an appropriable reluctance model for proportional solenoids like they are used today. This new approach is characterized by two attributes: First the structure of the reluctance network conforms to the structure of the magnetic flux. That leads to a physically based model approach which enables a better understanding of the functionality and a purposeful optimization in order to meet valve requirements. The second attribute is the parametrization of the model done by FEM-results. 2D FEM-calculations allow a view inside the solenoid and the abolition of experimental work for determining model parameters. The paper shows the idea of that approach as well as the way of development and parametrization of the reluctance network. The obtained results are compared to experimental investigations.

1   INTRODUCTION

Electrohydraulic valve systems are important components in modern fluid power applications. Based on an electrical command value, they control hydraulic power (pressure and / or flow) to provide fast and accurate drive solutions. The mechatronic properties of such valves are characterised by the use of electric, electromagnetic, mechanical and fluid mechanical disciplines. That mechatronic character as well as the increasing requirements on functionality, robustness and sound emission causes a lot of efforts in development time and costs.

In order to improve the development process, simulation based methods were established in the past years (1), (2), (3) and (4). In comparison to design models (Pro-E, Catia, Solid Works, etc.) the fundamental idea here is to establish model approaches that are able to describe the static and dynamic behavior of a product in the early phase of the development process. Tools like Matlab, ITI-SimulationX (5), ANSYS or Fluent are often used to solve selected topics within the development process. A holistic modelling of the entire system is more complex and not that widely used.
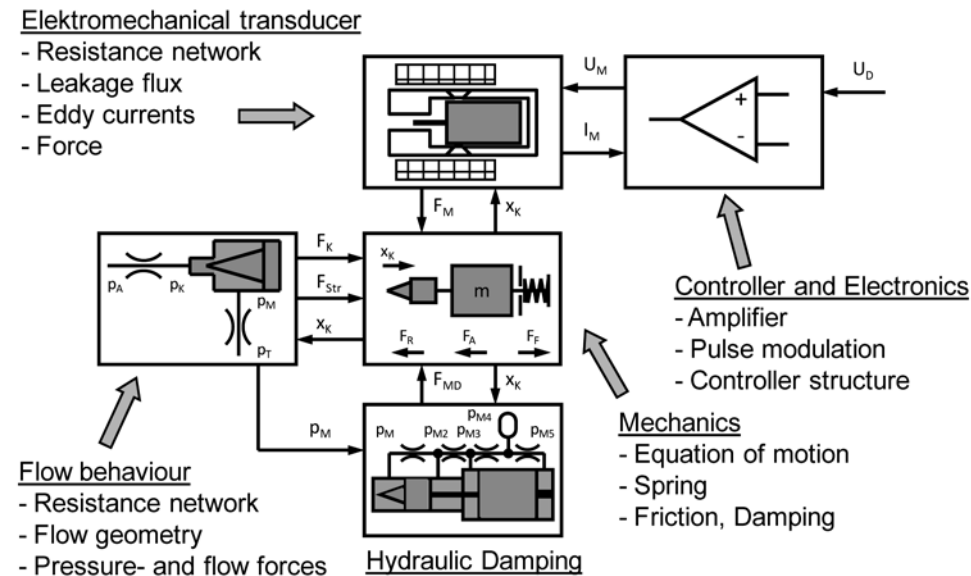
Figure 1   Holistic model of a proportional pressure relief valve

Figure 1 illustrates exemplary the model structure of a holistic model of a proportional pressure relieve valve. That model is divided in several sub models in order to describe the behaviour of each sub system in an appropriate way, see (6) and (7). That kind of holistic modelling allows for example the analysis of the behaviour of the pressure p_A depending on the set value U_D given as an input on the valve electronics, like it is presented in (8).

In order to enable such investigations each submodel has to provide a precise and manageable model with lumped parameters. Subsystems like the proportional solenoid are characterised by a high complexity which makes it difficult to find an appropriate model description, see (9) and (10).

2   MODELLING APPROACHES

In order to describe the static and dynamic behaviour of a proportional solenoid multiple model approaches such as inductance models or FE-models can be utilized, see (1). The question is which approach fits best into a holistic valve model. To answer this question first of all the model requirements have to be specified. Next the available approaches need to be compared. In order to be able to integrate a solenoid model in a holistic model of a valve the following specifications need to be fulfilled:

Possibility for integration. The model for the solenoid needs to be used as a submodel for the entire valve model. So it should be able to be integrated into a simulation tool were the holistic valve model can be calculated. **Reduced calculation effort.** In order to realize acceptable development times the simulation time should be as short as possible. Large and detailed submodels like FE-models may lead into extensive calculation effort. Even the time for model set up needs to be considered. **Parametrization by design data.** The philosophy of virtual product development requires models which can be parametrized only by design data. That means there are no experimental results required to get a suitable, realistic and precise model. According to that it is possible to get information in an early phase of the development. **Traceability of model parameters.** The entire valve model allows a description of the static and dynamic performance of the actual design. In order to optimize this design model parameters can be changed as long as the required performance occurs. The new set of parameters has to be transferred into a new design of the product. Not every model type allows that traceability of parameters.
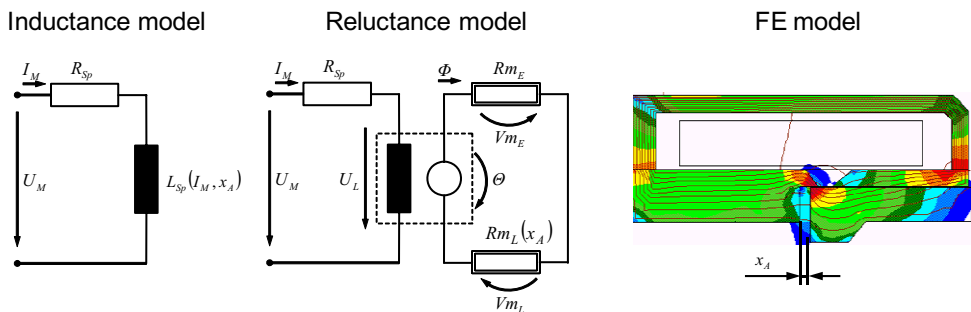
Figure 2   Three different types of solenoid models

Figure 2 illustrates three different types of solenoid models. The simplest type is the **Inductance model**. The static and dynamic behavior of the solenoid is characterized by two electrical elements the ohmic resistance and the inductance of the coil. The nonlinear

inductance L_{Sp} depends on the current I_M and the air gap x_A and can only be considered by a measured characteristic diagram. The solenoid force F_M is defined proportional to the current I_M. Because of its simple structure the model can easly be integrated into a holistic simulation model by keeping the calculation effort low. The determination of the model parameters using measurements or FEM calculations is possible. But the achievable model accuracy is due to the simple approach quite small.

The basic idea of the **Reluctance model** follows the idea of network models, were the magnetic flux is specified by a circuit of different magnetic resistances with lumped parameters. So the paths of the magnetic flux can be modeled more detailed. Particular effects like stray fluxes or eddy currents can be investigated much better with such reluctance networks. Basically it is possible to define a magnetic resistance by geometrical data. The solenoid force F_M is calculated by the magnetic flux pervading the air gap. That more realistic approach enables to consider the dynamic magnetic effects much better. The calculation effort is compared to a FE-model much lower and the model can be easly integrated in a holistic model.

The **FE-model** is the most common used tool to determine a suitable solenoid design. The static and dynamic behavior is calculated by a discretized field of elements where the Maxwell equations are solved. The model set up only requires the design and the magnetic material data. In particular the force-stroke-characteristic of a proportional solenoid can be represented very well by a FE-model. Due to the amount of the model size the calculation effort is relatively high although the latest software tools are equipped with capable solvers. One disadvantage in terms of the holistic valve development is that the FE-model is difficult to be integrated in an entire valve model. An integration of the FE-model in the system model via simulator coupling is generally possible. But that causes a considerably longer simulation time.

The question remains which model fits best in order to consider all relevant physical effects of a valve as they are shown in Figure 1. First of all a simulation tool is required were the relevant physical domains (electrics, magnetics, mechanics, hydraulics) can be considered. Software tools like ITI SimulationX, Matlab, AMESim offer such capabilities. A reluctance model of the solenoid can be integrated into such a tool and offers enough possibilities to describe specific qualities. By using that model approach a way has to be found to determine an applicable model structure and a set of parameters by avoiding experimental investigations. In order to achieve this the FE-model should be used to look more detailed into the solenoid and to achieve the required information which otherwise would be derived from measurement results.The following chapters are illustrating a way how to develop and how to parameterize a reluctance model for a proportional solenoid using FE-model results.

3   FINITE ELEMENT ANALYSIS

Modelling and simulation of proportional solenoids by finite element methods is a well investigated research field (11) and (3). In this chapter an already existing proportional solenoid is used to show the model quality.
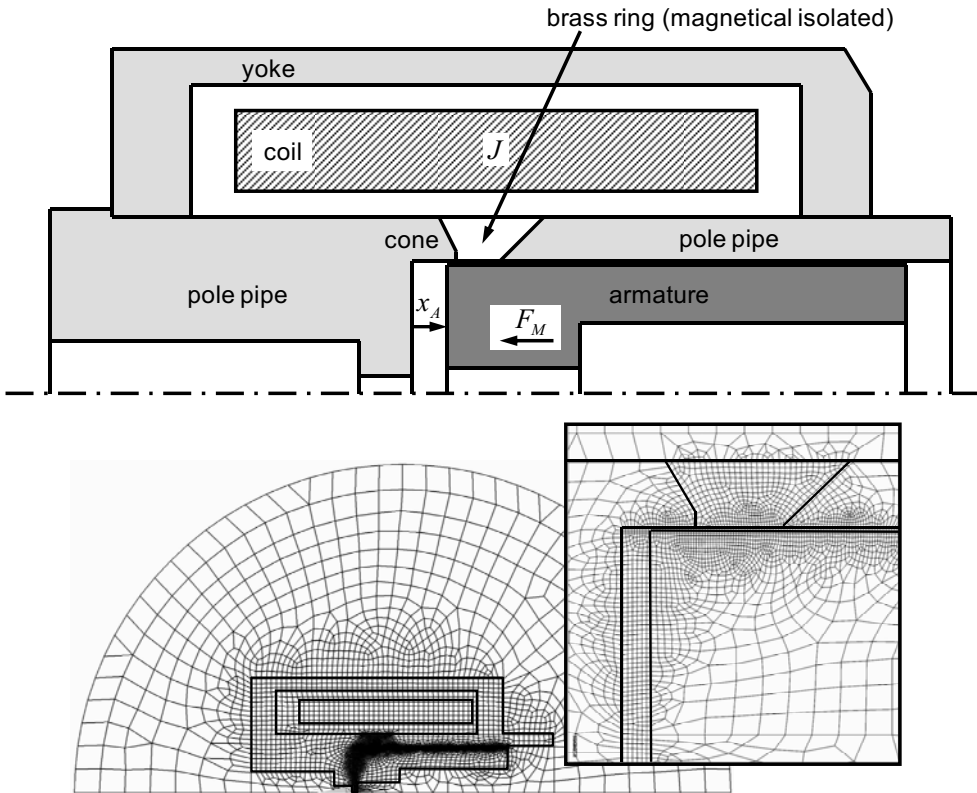
Figure 3   Exemplary design and FE-mesh of a proportional solenoid

Figure 3 shows the design of a solenoid which represents the geometrical basis for the model set up. Because of the rotational symmetry a 2-dimensional FE-model is sufficient. The coil impresses a current density J which can be determined from the current I_M, the number of windings n_{Sp} and the cross section of the winding area A_W.

The position of the armature is defined by the air gap x_A. The resulting armature force is F_M. Yoke, pole pipe and armature get the nonlinear properties (B-H-curve) of the used ferromagnetic materials. Magnetic hysteresis is not considered.

The simulation results are shown in figure 4. An acceptable model quality can be determined in comparison to the measurements. Only at high currents and large armature positions the deviations are remarkable. In general it can be derived that the quality of the FE-model is good enough in order to be used to develop a reluctance network.
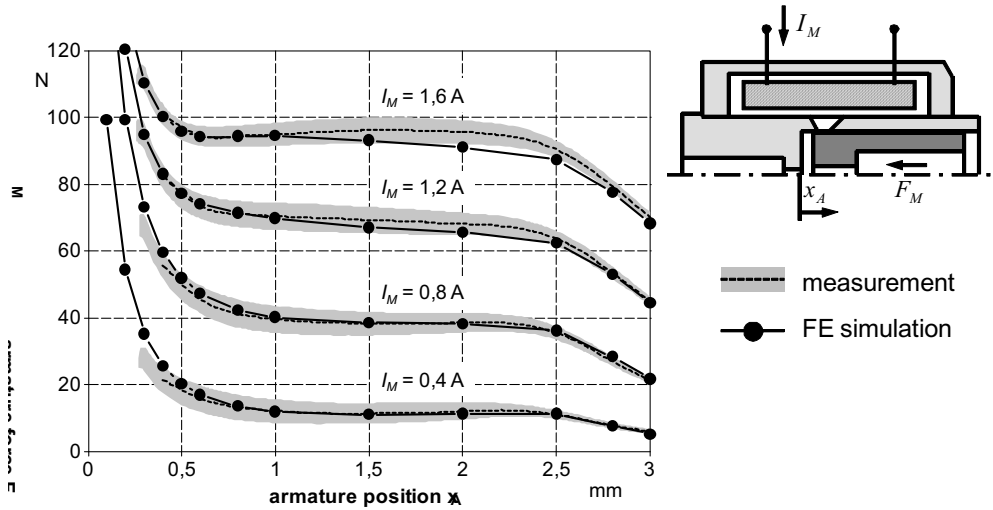
Figure 4   Measured and FEM-simulated force-stroke-relation

In addition to the force F_M more information is available. Figure 5 illustrates the force vectors acting on the surface of the armature as well as the direction and density of the magnetic flux (flux lines). Both information can be used to derive the reluctance network.
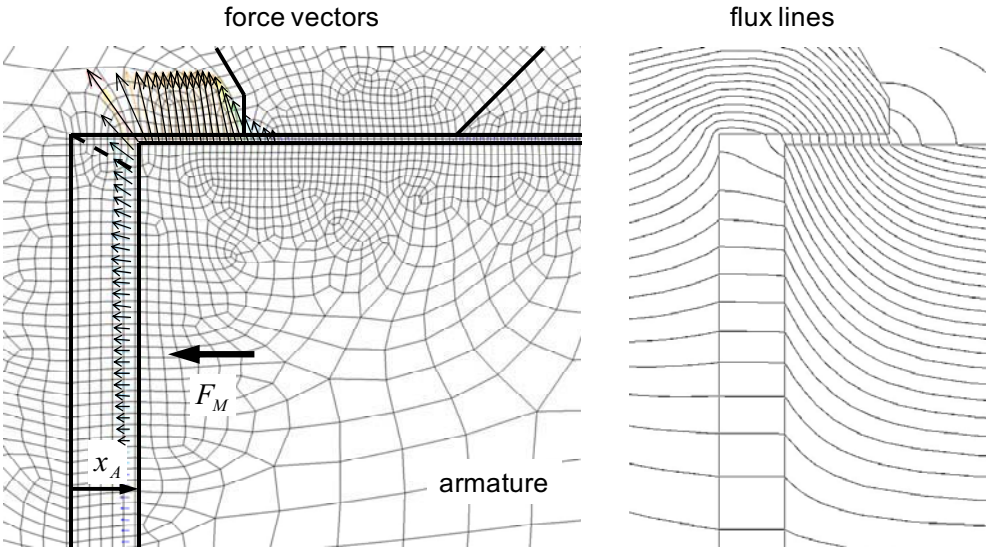
Figure 5   Force vectors and flux lines determined by the FE-model

4   STRUCTURE OF THE RELUCTANCE NETWORK

In order to get a realistic model the network structure should be oriented to the flux distribution. Figure 6 shows the flux lines of the analysed solenoid for a current of I_M=1,6A and an armature position of x_A=1mm. Analysing the flux paths four zones (A, B, C and D) can be differentiated. Zone A represents the major of the ferromagnetic material. Here the flux density B is due to the large cross-section relatively low. The magnetic flux in zone A penetrates also the air gap (zone B) as well as the cone (zone C). The magnetic resistance will strongly depend on the armature position x_A. Zone D represents the stray fluxes inside the coil and outside the yoke.
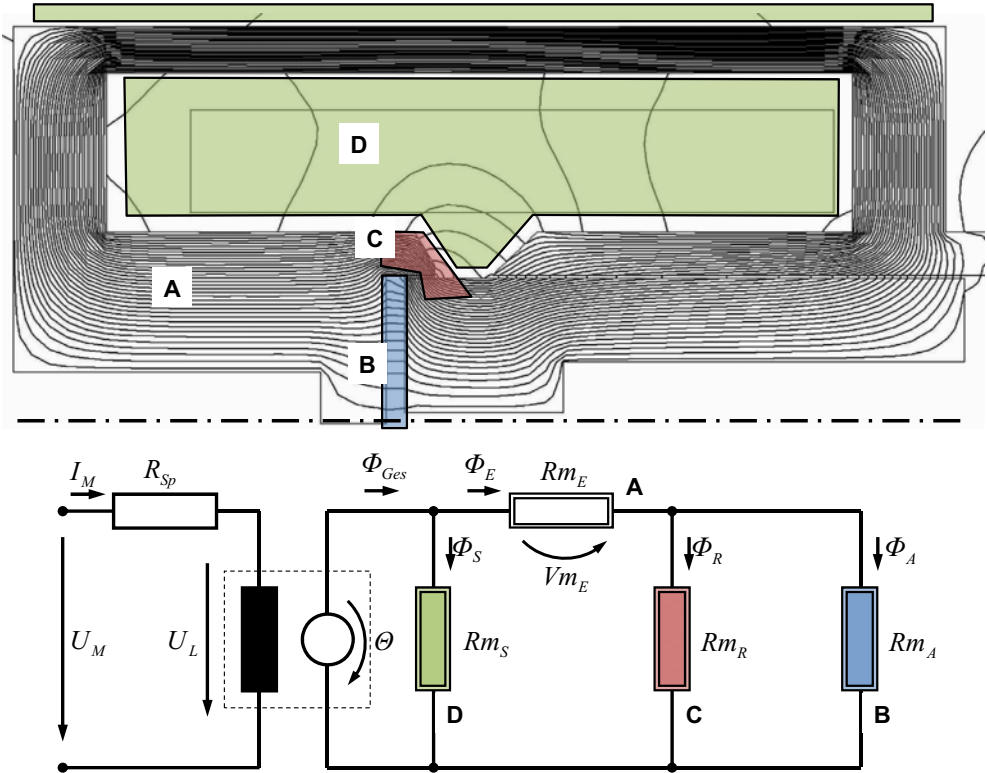
Figure 6   Force vectors and flux lines determined by the FE-model

According to that flux distribution a model structure for the reluctance network has been developed and is shown in figure 6. The magnetomotive force Θ causes a magnetic flux Φ_{Ges} that can be divided into two parts. The stray flux Φ_S and the iron flux Φ_E. It is assumed that the iron flux Φ_E is penetrating the entire zone A. That flux will be divided according to the two zones B and C into an axial flux Φ_A and a radial flux Φ_R. According to the force calculation of an ideal air gap (11):

$$F = \frac{\Phi^2}{2\mu_0 A} \qquad (1)$$

the resulting armature force F_M should be a function of the two magnetic fluxes Φ_A and Φ_R.

5   PARAMETRIZATION BY FEM RESULTS

5.1   Quantification of the magnetic flux

After defining the model structure the parameters of the network elements have to be found by means of FEM results. Therefore it is necessary to quantify the magnetic flux distribution. This is possible by means of well defined flux paths. Figure 7 illustrates a path definition which may be applicable on any proportional solenoid.
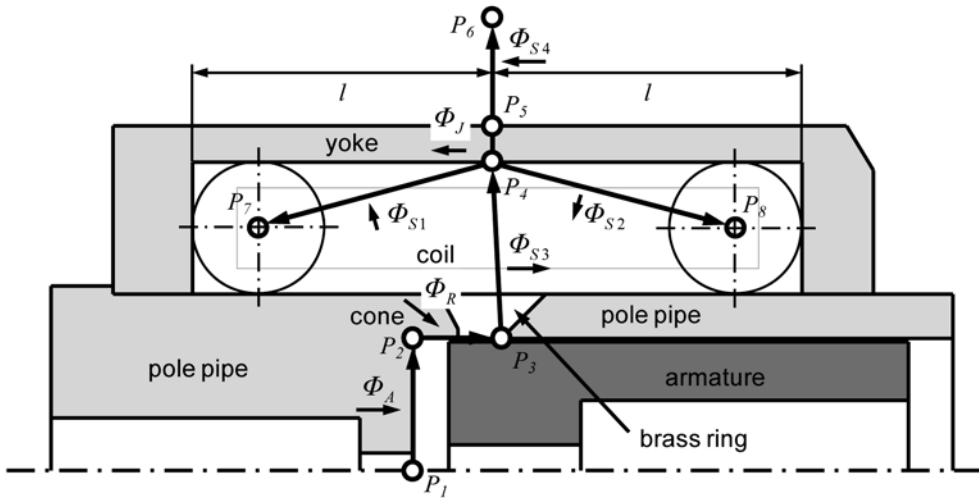
Figure 7   Definition of paths to analyse the flux distribution

Each path $\overline{P_i P_j}$ describes an area A that is penetrated by a certain amount of magnetic flux Φ. The flux is due to the integration of the flux density B over the area A:

$$\Phi = \int_A \vec{B} d\vec{A}. \qquad (2)$$

According to the shown paths seven different fluxes can be derived. The axial flux Φ_A is penetrating the axial air gap between pole pipe and armature. The radial flux Φ_R is going though the cone into the armature. The stray flux Φ_{S3} goes from one side of the pole pipe over the brass ring and the coil area to the other side of the pole pipe. That flux is not penetrating the armature. Φ_{S1} and Φ_{S2} are stray fluxes going through the coil area. Φ_J represents the flux going through the yoke. The stray fluxes outside the yoke are characterized by Φ_{S4}.

Figure 8 shows exemplary the several fluxes for a current of I_M=1,6A depending on the armature position x_A. Increasing of the air gap x_A causes an increase of the overall magnetic resistance. That is why the entire flux Φ_{Ges} decreases on rising armature positions. The fluxes Φ_A and Φ_R are changing significantly at low values of x_A. The specific design of the cone affects the ratio of those two values as well as the resulting force-stroke-characteristic. The stray fluxes Φ_{Si} have a significant proportion of the entire flux Φ_{Ges} and can not be neglected.

$$\Phi_{Ges} = \Phi_A + \Phi_R + \Phi_{S3} + \Phi_{S12}$$

$$\Phi_{S12} = \Phi_{S1} + \Phi_{S2}$$

$$I_M = 1,6\,A$$

$$\Theta = 1142\,A$$
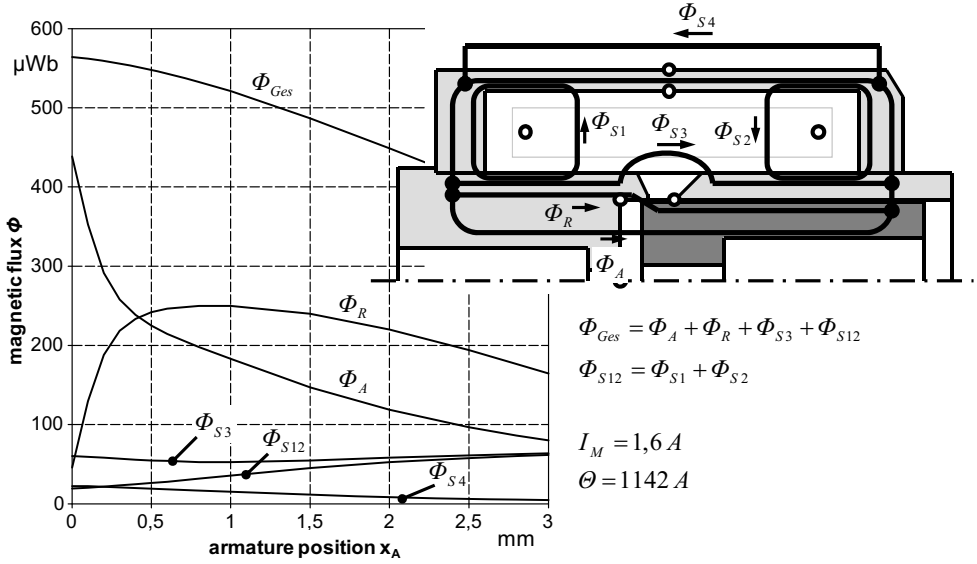
Figure 8   FEM simulated flux distribution

5.2   Parametrization of the magnetic resistances

As shown in Figure 6 four magnetic resistances Rm_S, Rm_E, Rm_R and Rm_A have to be parameterized. These FEM results will be used in order to find the model parameters.

Stray flux resistance Rm_S. In order to keep the model structure well-arranged the four stray fluxes Φ_{S1}, Φ_{S2}, Φ_{S3} and Φ_{S4} will be merged into a global stray flux Φ_S:

$$\Phi_S = \Phi_{S1} + \Phi_{S2} + \Phi_{S3} + \Phi_{S4} \ . \tag{3}$$

Assuming that the flux is driven by the magnetomotive force Θ the stray flux resistance can be determined by:

$$Rm_S = \frac{\Theta}{\Phi_S} \ . \tag{4}$$

Figure 9 illustrates the resulting values as well as the approximation of the stray flux resistance Rm_S depending on the armature position x_A.
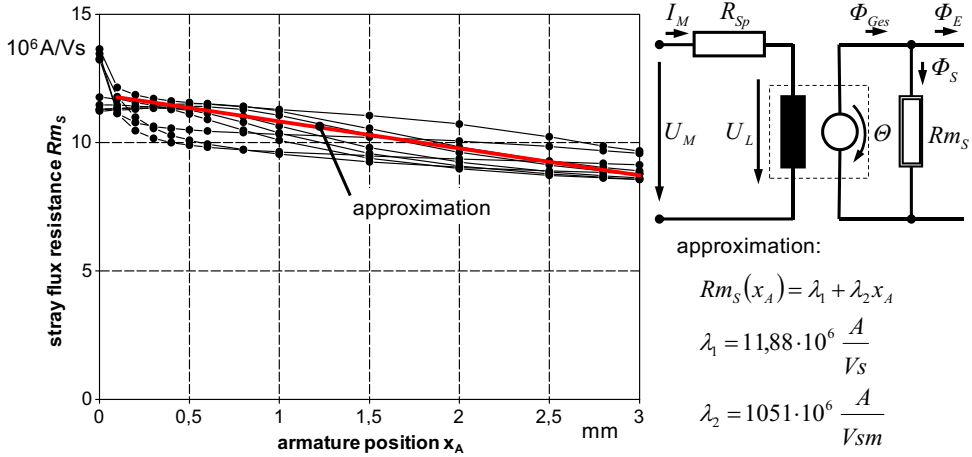
Figure 9   Approximation of the stray flux resistance Rm_S

Iron resistance Rm_E. That resistance is intended to describe the magnetic characteristic of the yoke, the pole pipe and the armature in one lumped parameter Rm_E. The cross section areas are relatively large and therewith the magnetic saturation is small. Rm_A and Rm_R are represent the more dominant resistances in the second loop of the network shown in figure 6. The nonlinear characteristic of the ferromagnetic material can be described by the *B(H)-*curve and is considered in the FEM-model. According to the definition of the iron resistance:

$$Rm_E = \frac{1}{B(H)A_E}Vm_E \tag{5}$$
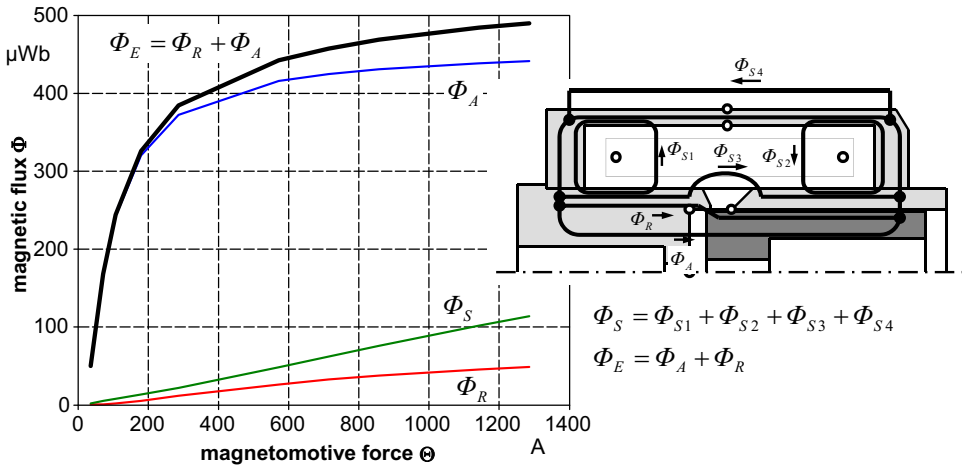
Figure 10   Determination of the iron resistance Rm_E

a cross section area A_E has to be defined. Due to the complex geometry this is impossible. Assuming that the resistances Rm_A and Rm_R are negligible at an armature position x_A=0mm only Rm_E and Rm_S are relevant. For that case the relation $\Phi_E = f(Vm_E)$ can be determined by FEM-simulation. The obtained characteristic is shown in figure 10 and implemented in the model.

Axial flux resistance Rm_A. The magnetic flux Φ_A pervading the axial face of the armature depends only on the air gap x_A. Here a geometrical approach can be used:

$$Rm_A(x_A) = \frac{x_A}{\mu_0 A_A} \ . \tag{6}$$

Radial flux resistance Rm_R. The radial flux resistance is intended to describe the effects around the cone. Figure 11 illustrates the flux distribution in that area in more detail. The radial flux Φ_R can be divided into two parts Φ_{RE} and Φ_{RL}. Three regions a, b and c are affecting the flux in the cone area. That is considered in the detailed model for Rm_R shown in figure 11. The three resistances are parameterized by the FEM results.
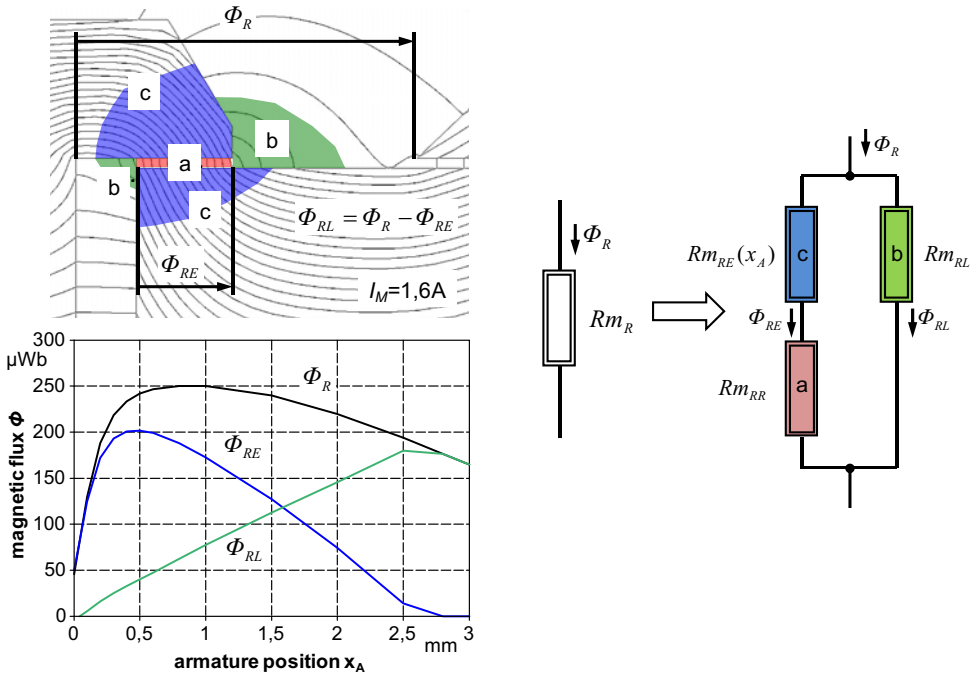
Figure 11   Flux distribution around the cone

Sticking all the resistances together the flux distribution determined by the FEM model can be simulated in a reluctance network as it is shown in figure 12. The comparison demonstrates that the chosen network structure as well as the parameterization is able to describe the flux distribution very well.
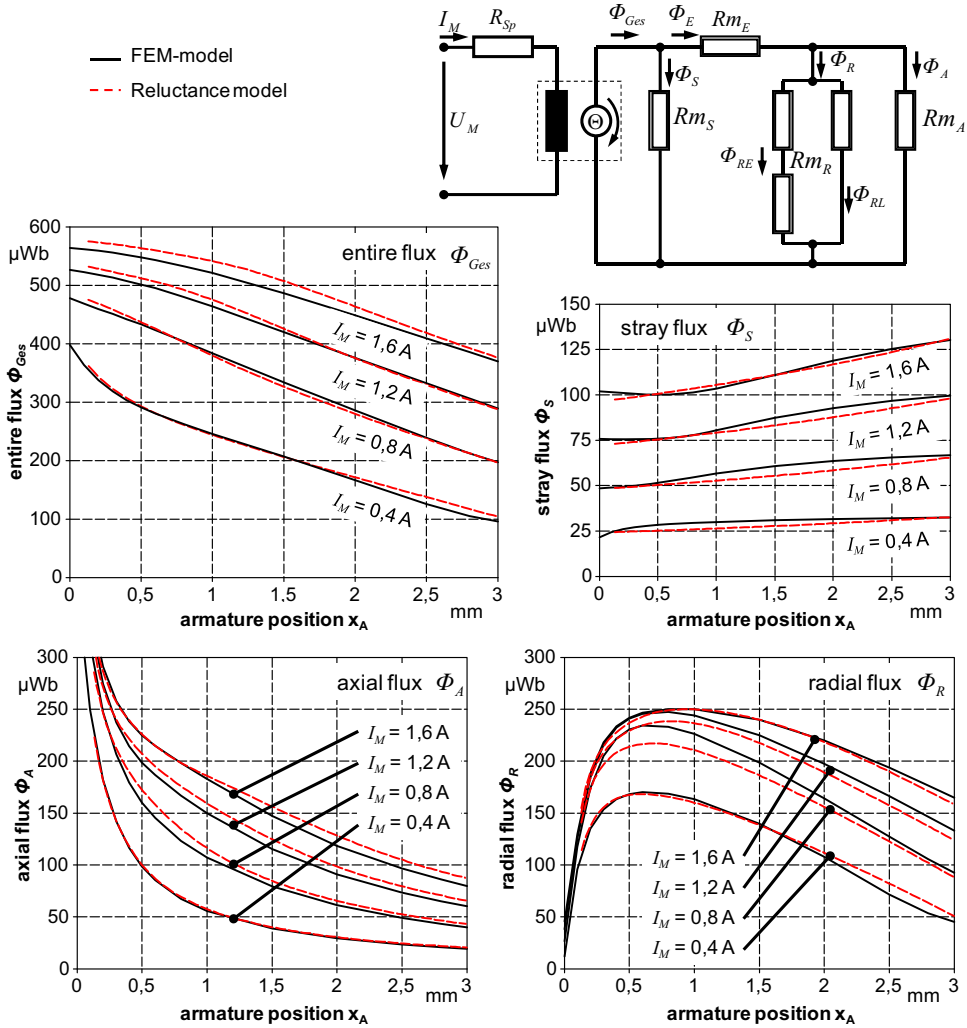
Figure 12   Comparison of the flux distribution between reluctance model and FEM model

5.3   Calculation of the armature force

Assuming that the armature force F_M is a function of the magnetic fluxes Φ_A and Φ_R two force components have to be determined:

$$F_M = F_{MA}(\Phi_A) + F_{MR}(\Phi_R).$$ (7)

FEM tools offer the opportunity to analyse force vectors acting on specified surfaces. Figure 13 illustrates such force vectors acting on the armature surface. According to the magnetic fluxes the resulting forces F_{MA} and F_{MR} are displayed over the armature position.
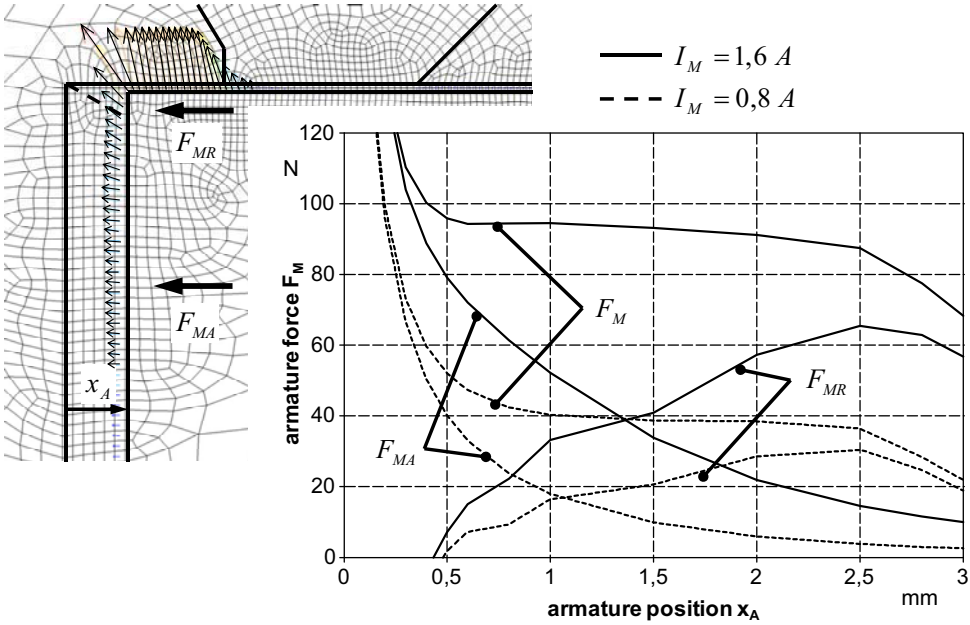
Figure 13   Force vector analysis by FEM results

In accordance with the force calculation for switching solenoids the axial armature force F_{MA} of a proportional solenoid can be determined by the analytical approach:

$$F_{MA} = \frac{\Phi_A{}^2}{2\mu_0 A_A}. \tag{8}$$

The radial armature force F_{MR} is due to the high nonlinearities in the cone area not that easy to describe. The characteristic $F_{MR} = f(\Phi_R)$ derived from the FEM model helps to overcome this challenge.

Finally the introduced reluctance network is able to determine the armature force F_M according to the current I_M and the armature position x_A. The model can determine the static and the dynamic performance with small computation efforts.

6   EXPERIMENTAL VALIDATION

In order to prove the model quality the simulation results have to be compared to experimental results. Figure 14 shows a comparison of the static force-stroke-characteristic. The force-current-dependency is quite acceptable. With high armature positions the the accordance of simulation and measurement results is getting less.

The reason for that characterstic can be found in the used approach for the calculation of the force $F_{MR} = f(\Phi_R)$. This approach is optimized to deliver optimal results in the working area of the solenoid ($x_A \leq 2,3mm$).
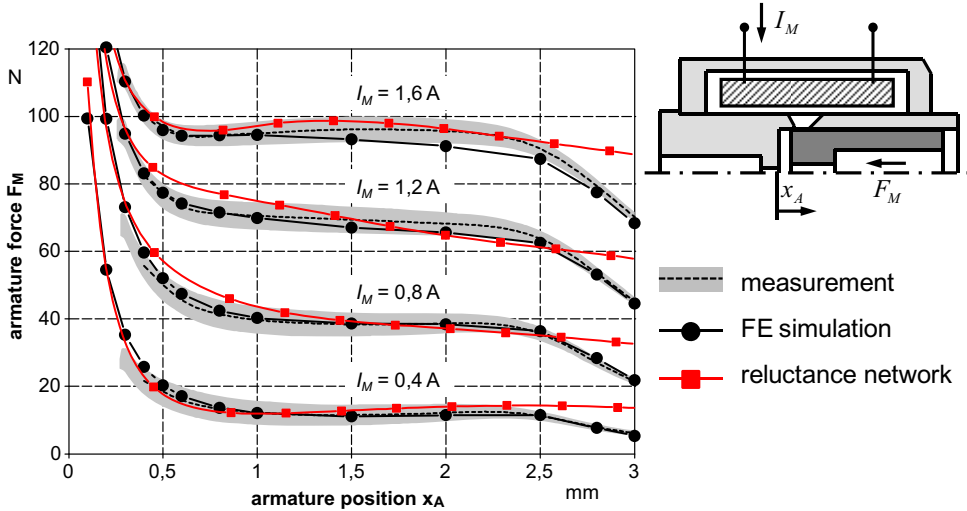
Figure 14   Measured and simulated force-stroke-relation

7   CONCLUSION

The paper presents a method to develop and to parameterize a relatively simple reluctance model for proportional solenoids. The elementary structure leads to marginal computation times and enables the model to be used in holistic valve models. The comprehensive use of the FE model and its results allows a parametrization were no experimental results are required. That enables the prediction of the expected valve performance in the very early design process. The validation of the dynamic performance with puls width modulation operation is ongoing.

Due to the very complex coherences the static behaviour does not match perfectly. In order to increase the precision two possibilities are imaginable. First the reluctance model has to be refined. That would definitely lead into a more complex model and into a time-consuming parametrization process. The second possibility could be a co-simulation between a FE-tool and lumped parameter simulation tool. The method and required effort needs to be investigated in more detail.

REFERENCES

(1) Geißler, G.   Optimierung und Einsatzgrenzen von Druckventilen
                         Dissertation, TU Dresden, 2002

(2) Schultz, A. W.   Simulationsgestützter Entwurf elektromagnetischer
                         Linearaktoren für fluidtechnische Ventile
                         Dissertation, RWTH Aachen, 2006

(3) Fetzer, J.   Numerische Berechnung elektromagnetischer Felder
     et al.   expert-Verlag, Renningen-Malmsheim, 2002

(4) Koch, W.   Zur Ermittlung des dynamischen Verhaltens von
                         Elektromagneten durch numerische Feldberechnung
                         Dissertation, TH Ilmenau, 1984

(5) N.N.   „ITI-SimulationX"-Referenzhandbuch
                         ITI GmbH, Dresden, 2006

(6) Wehner, D.   Virtual prototyping of pressure control valves
     Helduser, S.   5th International Fluid Power Conference, Aachen, 2006
     Lausch, H.   Proceedings, Vol. 3, S. 327-340

(7) Wehner, D.   Virtual Design of Electrohydraulic Valvesystems
     Helduser, S.   6th International Fluid Power Conference, Dresden, 2008
     et.al.   Proceedings, Vol. 2, S. 119-130

(8) Wehner, D.   Modellbasierter Systementwurf am Beispiel vorgesteuerter
                         Druckbegrenzungsventile, Dissertation, TU Dresden, 2009

(9) Hong, Y.-S.   Berechnung, Verbesserung und Weiterentwicklung von
                         Proportionalmagneten als elektromechanischer
                         Signalumformer für Proportionalventile
                         Dissertation, RWTH Aachen, 1986

(10) Tappe, P.-W.   Konzepte für schaltmagnetbetätigte Proportionalventile
                         Dissertation, RWTH Aachen, 1999

(11) Kallenbach, E.   Elektromagnete
     et al.   B.G. Teubner, Stuttgart, 2007

NOMENCLATURE

A	m^2	area
B	T	magnetic flux density
d	mm	diameter
F	N	force
H	A/m	magnetic field strength
I	A	current
J	A/m^2	current density
l	mm	length, distance
n	-	number of windings
R	Ω	ohmic resistance
U	V	voltage
Vm	A	magnetic potential
x	mm	Position
Θ	A	magnetomotive force
μ	Vs/(Am)	permeability
Φ	Wb	magnetic flux

INDIZES

A	axial
D	set value
el	electrical
E	iron
Ges	entire
J	joke
L	air
M	magnet, solenoid
$Mess$	measured
R	radial
S	stray
Sp	coil

Investigation of Separate Meter-In Separate Meter-Out Control Strategies for Systems with Over Centre Valves

Henrik C. Pedersen, Torben O. Andersen, Rico H. Hansen[1]**, Søren Stubkier**[2]
Department of Energy Technology, Aalborg University, 9220 Aalborg East, Denmark
[1]Wave Star, 2900 Hellerup, Denmark
[2]AVN Energy, 8600 Silkeborg, Denmark

ABSTRACT

Traditionally most mobile hydraulic systems are fitted with over centre valves for safety measures. However, it is a well known that over centre valves in combination with flow control valves may lead to oscillatory and unstable system behaviour if not designed correctly. There are several means to overcome this problem, but it typically implies higher energy consumption and/or decreased control performance. With the development of robust sensors and new valve types with separate meter-in, separate meter-out control it is, however, possible to overcome these stability problems in a much more intelligent way, also adding increased functionality to the system. The focus of the current paper is therefore on investigation of different control strategies for Separate Meter-In Separate Meter-Out (SMISMO) control of general single axis hydraulic system with a differential cylinder and an over-centre valve included.

The paper first presents a general model of the system considered, which is experimentally verified. This is followed by a discussion of different control strategies and their implications. For each of the control strategies controllers are described, taking into account the dynamics of the system and the coupling between the two cylinder chambers. Based on the described controllers the different control strategies are evaluated through via simulations and experimentally on a scale model of an excavator arm. Based on the findings, the performance of the different controllers are discussed and possibilities and limitations of the controllers are described.

1   INTRODUCTION

Within mobile hydraulic systems, over-centre valves (OCVs) or counterbalance valves are widely used for safety measures in load carrying applications as mobile cranes, telehandlers, winches etc. The purpose of the OCVs are multi-fold combining functions as leak tight load holding, shock absorption, cavitation protection at load lowering, pipe burst load holding and no drop before lift. It is however a well known fact that systems with load independent flow

control valves in combination with over-centre valves are prone to instability. As the latter is increasingly asked for by manufacturers, a major problem in present hydraulics is to design pressure compensated systems containing over centre valves that offer stable load lowering performance without unnecessarily compromising system efficiency and response. Naturally, this problem has attracted a lot of attention with emphasis on modelling and parameter variation [1,2,3,4,5,6,7] revealing a number of common mechanical stabilizing characteristics, such as lowering the pilot ratio, increasing the rod side (pilot line) volume or alternatively not using pressure compensated valves. It is however also possible to overcome the problem by using electrically controllable valves and using e.g. active damping. With the advancement of new valves, where it is possible to control the meter-in and meter-out side independently (separate meter-in, separate meter-out), new possibilities for controlling the system however become possible. This hence opens up for better performance and/or the energy consumption may be lowered, while still stabilising the system.

Separate Meter-In, Separate Meter-Out (SMISMO) has been the focus of several research activities, see e.g. [8,9,10,11,12], where focus primarily has been on decoupling states like for example actuator velocity and pressure. Lantto *et al.* [8] considered SMISMO in relation to decoupling of actuator velocity and pressure using a combined pump and valve control, whereas Jansson *et al.* [9] considered a scheme for decoupling of velocity and pressure in a hydraulic actuator, which however required velocity feedback to obtain static control of the actuator. Elfving *et al.* has considered different means for decoupled pressure control [10,11], whereas Nielsen [12] considered decentralised pressure/velocity control structures, with decoupling of velocity and pressure, also considering strategy switching. None of the research activities have however considered the problem in relation to systems which include an OCV.

The focus of this paper is therefore on control of OCV-systems using SMISMO-control strategies and utilising only pressure transducers. The paper first presents a model of a OCV-system with two proportional valves used as respectively meter-in and meter-out valve. Experimental results are presented showing the validity and limitations of the model, and a linear model is derived showing the coupling between the different states in the system. The model is the foundation for the presentation of different control strategies, which are all based on relatively simple open loop velocity control using only pressure transducers to determine the metering flow. Only direct strategies are considered, in which the meter-in side only controls either flow or pressure in the chamber in which the valve is connected to and similar for the meter-out side. Considerations regarding the couplings between the different states are however presented along with considerations regarding controllers. Based on the described controllers, both simulation and experimental results are presented, which constitute the basis for an evaluation of the possibilities of the different strategies.

2   SYSTEM MODELLING

As described in the introduction, the focus of this paper is to investigate different control strategies, when controlling SMISMO-systems with over-centre valves (OCVs). For this purpose the systems shown in Fig. 1 is considered, which is a standard cylinder mounted with an OCV, actuating a scale model of a simplified excavator arm. The experimental set-up may

be seen in Fig. 2. To control the system two directly actuated high bandwidth proportional valves are used.
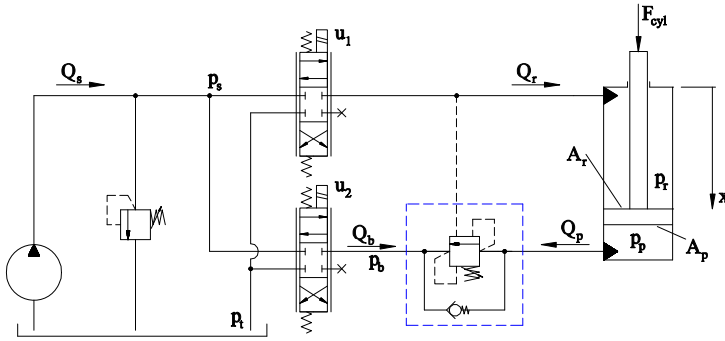
Figure 1: Illustration of the system, with the used notation. Notice the sign convention used to have positive correlation between Q_r and x.
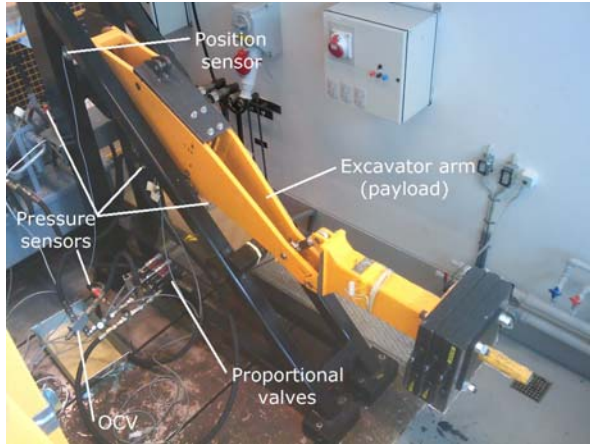
Figure 2: The experimental set-up with the excavator arm, valves and sensors.

As described in the introduction the systems is considered for the lowering situation, where it is well known that the inclusion of an OCV may lead to stability problems. The notation used may be seen in Fig. 1. Notice the sign convention for x, which is chosen to have positive correlation between Q_r and x. When referring to the cylinder being fully extended this hence means for $x = 0$. The pressure build up in respectively the rod side and piston side of the cylinder may be described by the continuity equation as:

$$\frac{dp_r}{dt} = \frac{\beta_e}{V_r} (Q_r - A_r \dot{x}) \tag{1}$$

$$\frac{dp_p}{dt} = \frac{\beta_e}{V_p} (A_p \dot{x} - Q_p) \tag{2}$$

Where $V_r = V_{r,0} + A_r x$ is the volume of the rod side chamber and $V_p = V_{p,0} - A_p x$ is the volume of the piston side chamber, with $V_{r,0}$ and $V_{p,0}$ being the default volumes in the cylinder and

connected hoses, with the cylinder in the top position. β_e is the effective oil bulk modulus and is modelled as:

$$\beta_e = \frac{1}{\frac{1}{\beta_{oil}} + \frac{V_{\%,air}}{\beta_{air}}} \tag{3}$$

With the volume content of air being determined as:

$$V_{\%,air} = \left(\frac{p_0 V_{\%,air,0}^{\kappa}}{p} \right)^{\frac{1}{\kappa}} \tag{4}$$

With p_0 being atmospheric pressure, $\kappa = 1.4$ (assuming an adiabatic process), $\beta_{oil} = 14.000$ bar (oil bulk modulus) and $\beta_{air} = 1.4p$. The effective oil bulk modulus is limited to 7000 $[Bar]$.

The force from the cylinder piston may be described as:

$$F_{cyl} = p_r A_r - p_p A_p - F_{fric} \tag{5}$$

With the friction force is modelled as:

$$F_{fric} = B_v \dot{x} + \left(F_c + F_s e^{-\alpha|\dot{x}|} \right) \tanh \left(\frac{\dot{x}}{\gamma} \right) \tag{6}$$

Where γ controls the slope of the friction curve around zero velocity to compensate for numerical switching problems. In the simulations this is set to $\gamma = 0.0001$ $[m/s]$. The friction in the mechanical system is included in the cylinder friction, whereby the model for the mechanical system may be written on standard closed form:

$$M(x)\ddot{x} + B(x,\dot{x})\dot{x} + G(x) = F_{cyl} \tag{7}$$

Where $M(x)$ is the equivalent inertia mass on the cylinder, $G(x)$ is the gravitational force and $B(x,\dot{x})$ contain the Coriolis and centripetal-terms, which for normal operating velocity is negligible, but is included for generality of the model.

Continuing with the model, the flow across the over-centre valve (for the lowering situation) may be written as:

$$Q_p = C_d A_o(x_o) \sqrt{\frac{2}{\rho}(p_p - p_b)} \tag{8}$$

Where ρ is the oil density, p_b is the back pressure given by Eq. (12), and $A_o(x_o)$ is the valve opening given by:

$$A_o(x_o) = \pi \left(d_o x_o \sin\theta + x_o^2 \sin^2\theta \cos\theta \right) \tag{9}$$

Where d_o is the spool diameter, θ is the cone angle and x_o is the spool position, which is determined from the force balance on the spool:

$$m_s \ddot{x}_o = p_r A_{pilot} + p_p A_{main} - p_b A_{back} - p_{cr} A_{main} - F_{flow} - B_{ocv} \dot{x}_o - F_{c,o} - k_s x_o \tag{10}$$

Where A_{pilot}, A_{main} and A_{back} are respectively the pilot area, main area and back pressure area of the valve. p_{cr} is the crack pressure of the valve, B_{ocv}, $F_{c,o}$ and k_s are respectively the

viscous friction coefficient, Coulomb friction in the valve and spring constant. Finally the flow forces are described by the stationary flow forces as:

$$F_{flow} = 2C_d A_o(x_o) \cos\theta \left| p_p - p_b \right| \tag{11}$$

The back pressure is found from the continuity equation as:

$$\frac{dp_b}{dt} = \frac{\beta_e}{V_b}(Q_p + Q_b) \tag{12}$$

Finally the proportional valves are modelled simply by the orifice equation and a critically damped second order system as:

$$Q_r = K_v u_1 \sqrt{p_s - p_r} \qquad , \quad u_1 \geq 0 \tag{13}$$

$$Q_b = K_v u_2 \sqrt{p_b - p_t} \qquad , \quad u_2 \leq 0 \tag{14}$$

$$u_i = \frac{\omega_n^2}{s^2 + 2\zeta\omega_n s + \omega_n^2} u_{ref.i} \tag{15}$$

Where K_v is the valve coefficient, and $u_{ref,i}$ is the reference voltage to the i'th valve. With the valves used the valve dynamics may generally be neglected compared to the dynamics of the systems. The model for the valve dynamics is however still included, whereby the influence of slower valve dynamics may be investigated in relation to the considered control strategies.

2.1 Model Verification

With the model described, the basis for the control strategies is available. In this section the model is compared with experimentally obtained data. The model contain several uncertain parameters being the air content in the oil $V_{\%,air,0}$, the viscous friction coefficient B_v, Coulomb friction F_c and stiction F_s in the cylinder along with coefficient controlling the decay of stiction α. These parameters are determined to have a reasonable fit of the model with the real system, with regard to both the different pressures levels and frequency. The friction coefficients of the OCV are also uncertain, but with limited influence on the overall system dynamics, why these are adjusted based on data for similar valves. The results of the validation with the adjusted parameters are shown in Fig. 3.

From the figures it may be seen that there are several deviations between the model and the measured data, especially in the first period for the rod side amplitudes. It may also be seen that in the measured data that there are downward bumps in at the rod side pressure peaks, which is not captured by the model. These deviations results from the parameter uncertainties and the simplifications made in the model. The main reason for the deviation is believed to be due to the friction in the system and the limitations in the model used. As both supply pressure and valve spool position is kept constant, the only thing which may yield this drop in the rod pressure peaks is the piston movement (and opening of the OCV), where stiction effects come into play. With the friction model used it is however not possible to capture this effect, without running into numerical problems. Despite these deviations the model do, however, capture the dynamics of the system sufficiently well in terms of frequency, pressure gradients and pressure levels. Although improvements could be made the model is sufficiently accurate for being able to test different control strategies and no further improvements are hence made.
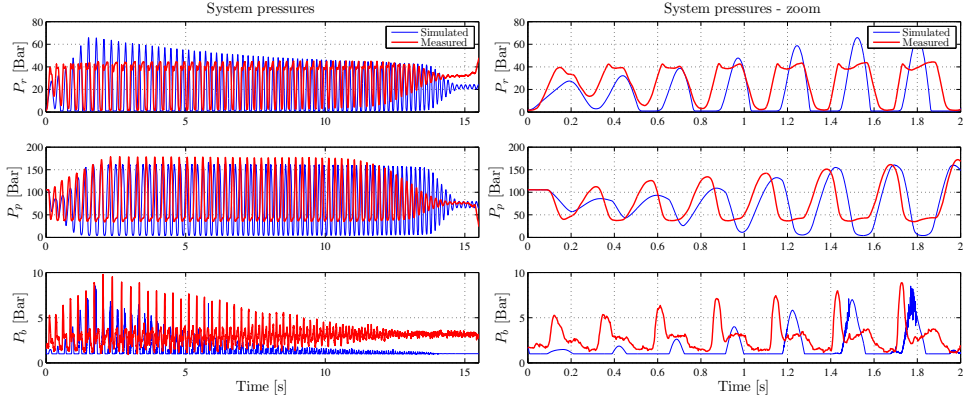
Figure 3: Experimentally and simulated pressures, when valve 1 is opened 10% and valve 2 is fully opened.

2.2   Linearised Model

To get an overview of the couplings between the different states in the system, the above model is slightly simplified and linearised. This not only gives an overview of the system, but also serves as basis for selecting suited controllers for the different control strategies. In the model the following simplifications are made: The volumes V_r and V_p are considered constant, as are the effective bulk modulus of the oil. The OCV spool dynamics is negligible compared to the dynamics of the system, whereby this may be neglected. Similar the dynamics of the proportional valves are disregarded in the diagram for simplicity reasons and the inputs to the system are the flows over the valves, as these are controlled based on the measured pressures. As changes in both gravitational, Coriolis and inertia forces are negligible for small movements, the mechanical system is simply represented by a constant inertia mass. Similarly both Coulomb friction and stiction are considered constant, and hence changes in these are neglected for both the cylinder and the OCV. Linearising and Laplace-transforming hereby yields the block diagram shown in Fig. 4.
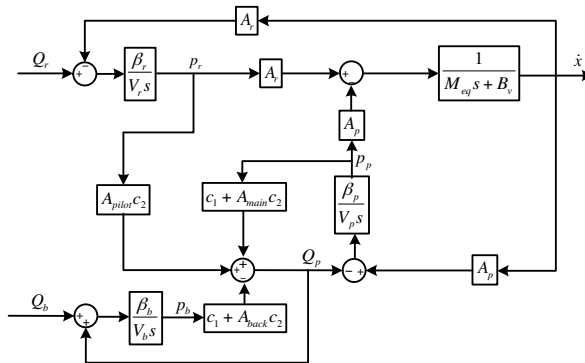
Figure 4: Block diagram for the linearised system.

The linearisation coefficients being given by:

Flow and flow-pressure coefficient OCV	
$K_q = C_d K_A \sqrt{\frac{2}{\rho} \left(p_{p,0} - p_{b,0} \right)}$	$K_{qp} = \dfrac{C_d K_A x_{o,0}}{\sqrt{2\rho \left(p_{p,0} - p_{b,0} \right)}}$
OCV area gradient	Flow force coefficients
$K_A = \pi \sin\theta \left(d_o + 2x_{o,0} \sin\theta \cos\theta \right)$	$K_{f,q} = 2C_d K_A \cos\theta \left(p_{p,0} - p_{b,0} \right) \qquad K_{f,qp} = 2C_d K_A x_{o,0} \cos\theta$

The subscript 0 denotes evaluation at the linearisation point. The two coefficients c_1 and c_2 are given by:

$$c_1 = K_{qp} - K_{f,qp} c_2 \qquad (16)$$

$$c_2 = \frac{K_q}{k_s + K_{f,q}} \qquad (17)$$

Dependent on primarily the piston, the parameters and hence stability of the system change quite significantly. When analyzing the system and designing controllers, choosing proper linearisation points is therefore important as discussed in the next section.

3   CONTROL STRATEGIES

As described in the introduction many different strategies for how to control a SMISMO-system may be developed dependent on the transducers allowed, the system considered and the requirements to this. In this paper four different strategies are considered for lowering a load in a system with an OCV. The strategies have the common feature that each strategy considers flow (velocity) control of the system on an open-loop basis, i.e. flow into or out of the cylinder is controlled in open loop, based on the inverse of the orifice formula. This is done, as these systems typically have an operator in the loop, why completely accurate flow control is not required, as long as the repeatability is approximately constant, hereby also removing the need for a flow transducer or alternatively a velocity transducer. The strategies considered may be divided into either meter-in strategies or meter-out strategies. The strategies considered are:

- Strategy 1: Meter-in strategy, where the flow into the rod side chamber is controlled via valve one (using pressure transducers to determine the flow) and using active damping, in form of a high pass filter, to stabilize the systems, see Fig. 5. The second valve is fully opened to minimize the back pressure of the OCV, hereby also minimizing the power consumption. This strategy requires two pressure transducers to measure supply pressure and rod side pressure respectively.

- Strategy 2: Meter-in strategy similar to strategy 1, but where the back pressure is raised using valve 2. The idea is here to keep the back pressure approximately constant to remove the influence of variations in the back pressure. A simpler strategy in this concern is simply to set the valve opening of the second valve to a small value, whereby the back pressure is also raised. The benefit of this may be a more stiff system, with higher effective bulk modulus values, compared to strategy 1, but at the expense of higher energy consumption.

- Strategy 3: Meter-out strategy where the flow out of the piston chamber is controlled by the second valve, based on measurement of back pressure. To accomplish this, the OCV-valve needs to be open, which require that the rod side pressure should be set so:

$$p_r \geq \frac{p_{cr}A_{main} + p_{back}A_{back} - p_pA_{main}}{A_{pilot}} \tag{18}$$

  The strategy hence requires at least two pressure transducers, to measure rod side pressure and back pressure, assuming the tank pressure may be considered known. One strategy in this concern could be to set the pilot pressure high enough to keep the OCV fully open when lowering. For back pressure compensated OCVs this strategy will hence practically remove the influence of the OCV, which is beneficial as hereby the OCV will simply work as a fixed orifice with a large opening and hence a small pressure drop. This will hence directly remove the stability related problems in the system. For the non-pressure compensated OCV considered here, it is however not possible to keep the OCV fully open by raising the pilot pressure as this will also just increase the back pressure, when utilising the meter-out strategy. The rod pressure should however be set high enough that it is the proportional valve and not the OCV which controls the flow out of the back volume.

- Strategy 4: Meter-out strategy similar to strategy 3. To dampen oscillations in the system pressures a high pressure filter (active damping) is again applied in the system, but this time measuring the piston pressure, see Fig. 6. Dampening piston pressure will also benefit the rod side pressure as the two are coupled through the piston, whereby system pressures in general may be dampened. It is in this regard not meaningful to apply the filter on the rod pressure[1], as the meter-in side is not a flow control and the rod pressure controller, dependent on tuning, compensate for the effect. Similarly applying the filter on the back pressure of the OCV, p_b, does not have a significant effect, as the back pressure and piston pressure is partly decoupled via the OCV, i.e. a steady back pressure, p_b, does not remove oscillations in the piston or rod pressure.

For both the two meter-out strategies, it should be noted that these do not compromise the hose-rupture feature of the OCV, as remove of the pilot pressure will still maintain the load holding feature. When lowering a hose rupture will hence "simply" mean the oil is exiting the system, but do not compromise safety of the system. An obvious fifth strategy could have been to control the meter-out flow via the OCV. However for this to work properly and be able to control the flow, it would require knowledge about the OCV opening area, which again requires knowledge of the spool position, which is not directly obtainable, and which may be difficult to estimate correctly due to the flow forces and friction in the valve. This strategy is hence not considered further, but future investigations may look into this. How the controllers are designed is described below.

Based on the block diagram shown in Fig. 4, different controllers are designed for the different strategies. The controllers considered here are limited to simple linear controllers to first investigate the properties of the different strategies. As stability of the system is of highest

---

[1]Doing so, do not increase the performance of the system. The integrator is instead replaced by an integrator-term and a lead-filter, where it is not possible to use the lead effect to increase performance.

importance, all controllers are adjusted with the primary objective to have a stable system, with a corresponding decrease in performance. For systems of this type it is known that the most critical operating point with regard to stability is for the cylinder in the top position, as here the volume ratio between the rod side and piston side is the smallest. This will hence be the point for which the controllers are adjusted. Due to the large parameters variations, which primarily results from the piston position, all of the above strategies may benefit from measurement of the piston position where a gain scheduling approach may be adopted, i.e. the controllers may be adjusted according to the operating point. However, this would require a position transducer, why not considered here, where focus is to investigate what is obtainable using only pressure transducers.

Strategy 1: In this strategy, only a active damping (high pass filter) is implemented on the rod side pressure, whereby high frequency oscillations are subtracted the input signal and hence dampened. The implementation is shown with red in Fig. 5. To dampen system oscillations the filter constant τ_r is set well below the lowest eigenfrequency in the system, whereas the feedback gain K_r is set to obtain reasonable stability margins in the top position.
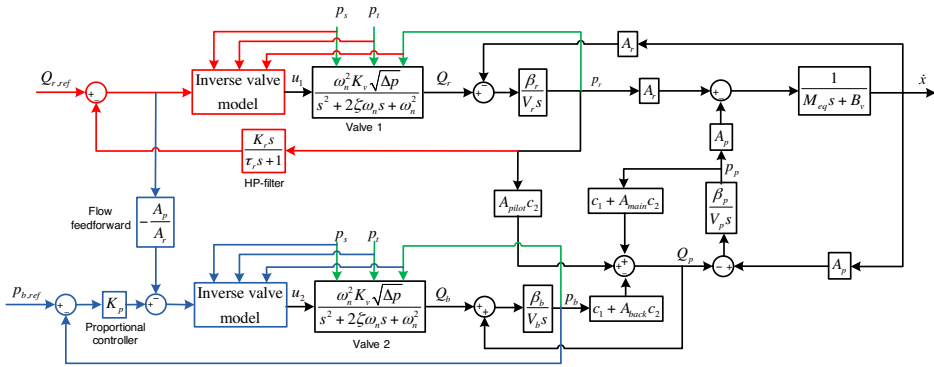
Figure 5: Strategy 1 (red) and 2 (red and blue).

Strategy 2: Utilizes the same high pass filter as strategy 1 on the rod side. The back pressure p_b is here controlled using a simple proportional controller, as the pressure build up is already a type one system, cf. Fig. 5. To compensate for the disturbance in form of the piston flow a flow feed-forward, based on the calculated rod flow is implemented. Care should be taken in adjusting the proportional controller, as pressure oscillations in the back pressure influence the opening of the OCV. Ideally the bandwidth of the back pressure control loop should hence be set significantly higher than the dynamics of the remainder of the system. In practice this may however prove difficult, as this require a high gain and even small disturbances in the measured pressure may therefore be influential. Similarly the flow feed forward only works, if this is known sufficiently accurate. In practice it may therefore be necessary to set the gain low and hence accept some back pressure oscillations. Increasing the back pressure also means that the delay in the system, before the systems begins to respond is increased, as the pressure in the rod side chamber has to increase to a higher level. For most systems this will not be a problem, although the high pass filter does slow down the pressure build up process.

Strategy 3: Here the meter-in side is not a flow control and there is hence no need to include the high pass filter on the rod side pressure control[2]. Similarly the flow feed forward term, is not included, as even small deviations in the estimated flow may lead to large deviations in pressure, due to the extremely small volume, especially in the top position. To control the pressure a simple PI-controller is utilized, to compensate for the disturbance from the displacement flow, see Fig. 6. The PI-controller is adjusted to have a break at approximately half of the eigenfrequency of the system, as it is not possible to obtain a higher bandwidth in the pressure loop, as the rod side pressure directly couples to the remaining dynamics in the system.

Strategy 4: Strategy 4 extends on strategy3 and hence used the same controller parameters, but with the high pass filter on the piston pressure, as shown in Fig. 6. The settings of the filter are chosen similar to what is done in strategy 1.
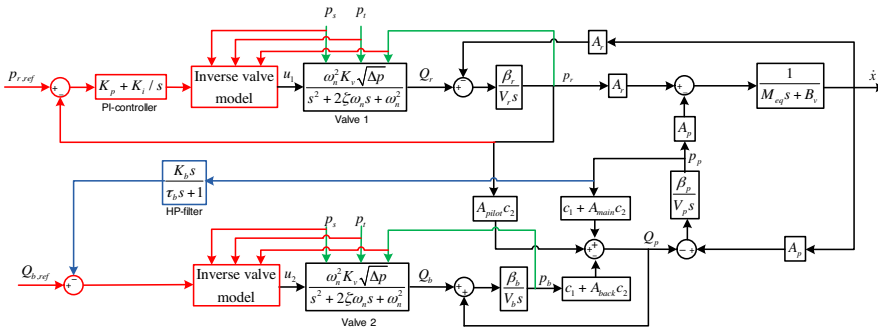
Figure 6: Strategy 3 (red) and 4 (red and blue).

Based on the above described controllers, the different strategies have been implemented and tested and the results of this are presented in the following.

4   CONTROLLER TESTING

The above described control strategies and corresponding controllers have all been implemented and tested in both simulation and experimentally. The results of these tests are shown in the following. In all cases the reference velocity is set to 0.1 $[m/s]$, although obtaining the correct steady state velocity is of secondary importance as the system typically is a HIL-system. The results for strategy 1 are shown in Fig. 7. The different pressures in the system are shown to the left and to the right the piston position. Similarly Fig. 8 shows the results for strategy 2, Fig. 9 for strategy 3 and Fig. 10 for strategy 4. For all the results the same controller parameters are used in the simulation model and for the experiment.

Considering first the meter-in strategies it is clear that strategy 1 not only stabilizes the system, but also gives a very smooth response, with very few pressure oscillations. The velocity

---

[2]Doing so, do not increase the performance of the system. The integrator is instead replaced by an integrator-term and a lead-filter, where it is not possible to use the lead effect to increase performance.
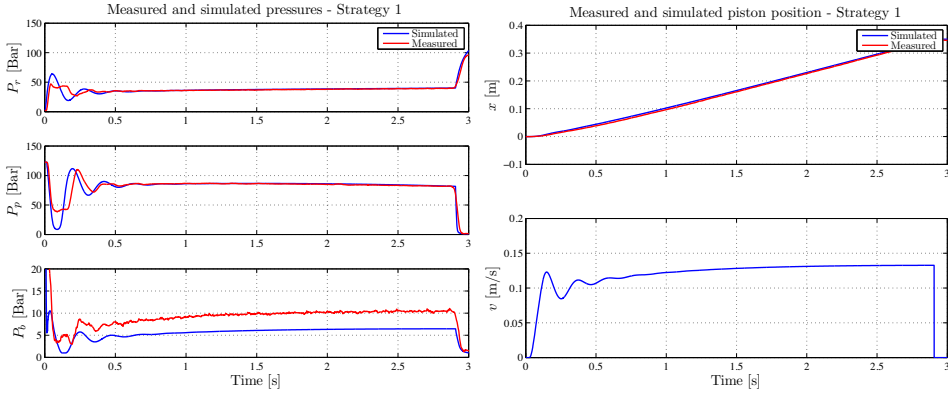
Figure 7: Simulation and experimental results using strategy 1. To the left the pressures in the system and to the right the piston position.
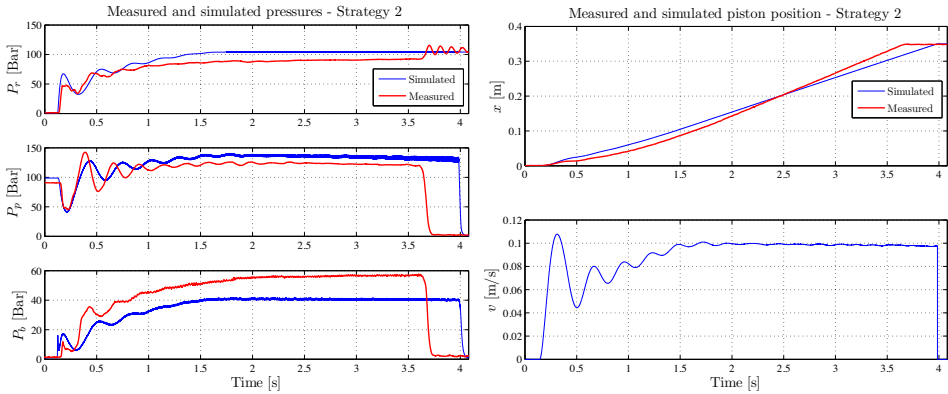
Figure 8: Simulation and experimental results using strategy 2. The back pressure reference is set to 50 bar.

is higher than required, but as described above this is not considered a problem as the system typically will be operated with a operator in the loop, why not a problem. The small deviations between the model and the experimental results again stem from the limitations in the model. The strategy furthermore has the advantage that it is very easy to adjust the filter gain, and the sensitivity of this gain is very low.

Considering strategy 2 it is seen that this is also capable of lowering the load, but with a more unsteady response with longer pressure pulsations and a more unsmooth velocity response. At the same time the pressure levels are also raised compared to strategy 1, hereby increasing energy consumption. Increasing or decreasing the pressure level (i.e. pressure reference) of the back pressure have practically no effect on the pressure oscillations, but only the pressure level. From the graphs it may also be seen that the proportional controller yields a steady state error in the back pressure, due to the flow disturbance from the piston flow, cf. Fig. 5. The problem with this strategy is, as described above, the pressure control of the back pressure,

where the gain has to be adjusted lower than desirable, due to disturbances and measurement noise in the system. The obtainable bandwidth of the pressure control is hence lower than desirable bandwidth and the pressure control cannot be considered completely decoupled from the remaining system dynamics. Adjusting the proportional gain is in this regard rather straightforward, although the gain is sensitive if set too high. The flow feed forward term does not help significantly in regard to dampening the pressure oscillations, as even small errors may lead to significant pressure gradients, due to the high gain (small volume) in the pressure loop. Removing the flow feed forward in this regard has little effect on the system. The latter may be attributed that even small offsets may result in wrongly estimated flows which may have a significant effect on the pressure response. Compared to strategy 1 there is hence no reason to consider strategy 2.
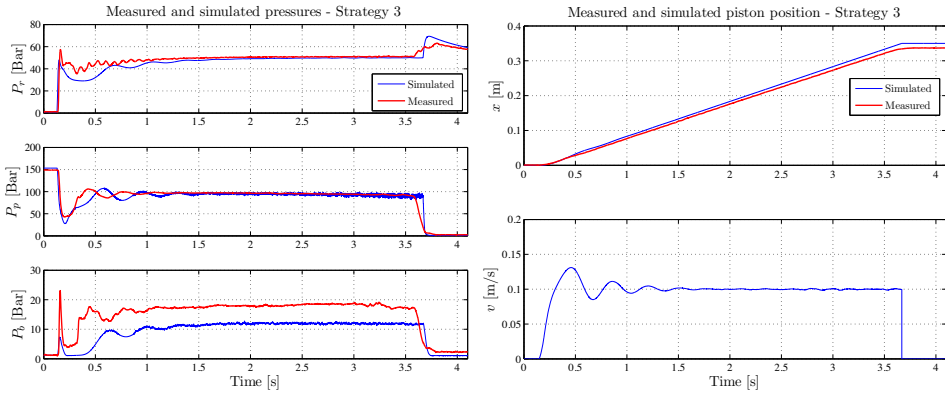
Figure 9: Simulation and experimental results using strategy 3. The rod pressure reference is set to 50 bar.
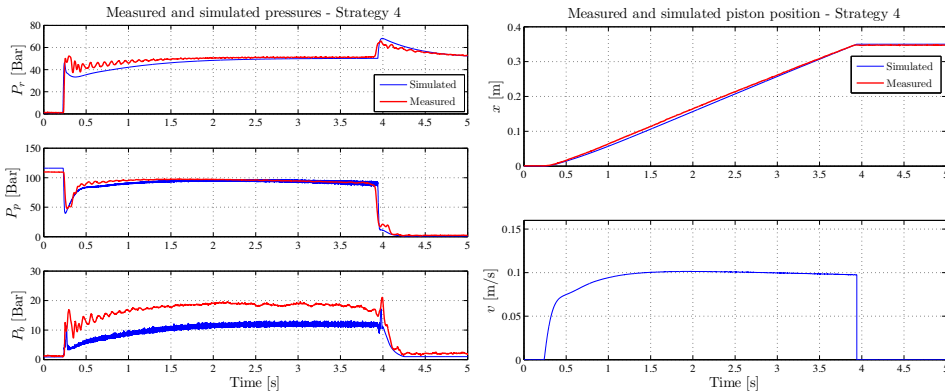
Figure 10: Simulation and experimental results using strategy 4. The rod pressure reference is again set to 50 bar.

Considering next the meter-out strategies it is seen that these are both capable of lowering the load, where the lowering velocity is very close to the reference velocity. Similarly it is seen that for both strategies there are small pressure oscillations in the measured response,

especially in the beginning, where the reference step is applied. This is primarily due to the controllers being adjusted rather aggressively, to be able to compensate for errors in the pressure when the cylinder is not in the top position, and where the gain in the system is lowered compared to the fully extended cylinder. The same oscillations are not seen in the simulations, where measurement errors and noise is not present and hence the controller output with be more smooth. The very high frequency oscillations in the piston and back pressure in the simulation results are due to the friction model used. In relation to the responses it should be noted that strategy 4 shows slightly better results with regard to the velocity and fewer large pressure oscillations, but at the expense of more small higher frequency oscillations also in the piston and back pressures (measured). The limited effect of the high pressure feedback should again be seen in relation to the OCV, which is continuously metering when pressure gradients arise, and hence influence the coupling between the piston chamber and the back pressure volume. It should in this regard be noted that the strategy shows acceptable results with the reference rod pressure set down below 40 bar, with only minor changes when setting the pressure reference to 50 bar. The rod pressure when the OCV opens is in this regard approximately 35 bar. Increasing the pressure reference above the 50 bar does not have a significant effect on the response, however, seen from an energy point of view increasing the reference pressure is undesirable. To reduce the pressure oscillations a small pre-filter on the pressure reference may however also aid. Apart from the first period where the pressures are settling, both the two strategies shows both steady velocity and pressures, and both strategies may hence be improved by better adjustment of controller parameters possibly based on piston position. None of the two strategies are however as robust towards incorrect controller parameters as strategy 1, due to the large gain variations, which require proper adjustment of the controller parameters for the strategies to work as desired.

Based on the above findings, strategy 1 is both the simplest to implement and adjust, the one which shows the best results with regard to energy consumption, and it only requires one pressure transducer, why being the obvious first choice if to be applied in a practical system. The three other strategies all consider pressure control on the non-metering side (for strategy 3 and 4 in a varying volume) which is not as straightforward to implement, due to the high gain and integrator effect, possibly combined with measurement noise and drift from sensors. Both strategy 3 and 4, however show reasonable results and may be better solutions than strategy 1 if more accurate velocity control is required. For each of the last three strategies it may however be possible to improve the results, by utilising more advanced controllers and adaption of controller parameters, to account for e.g. the varying volumes and reference pressures. Further work in this area will therefore consider more adaptive control and more advanced control strategies, where also cross coupling strategies may be considered.

5   CONCLUSION

The focus of this paper has been the possibilities arising from being able to control separately the meter-in and the meter-out flow in a system with an over centre valve to overcome stability problems and possibly improve performance. The paper first presented an experimentally verified model of a scaled excavator arm, being the foundation of the different control strategies. A linear model of the system was next presented, which was the basis for considering different control strategies. Four different control strategies were presented and controllers were described, suited for the different strategies. All the strategies are based on open loop

control of either meter-in flow or meter-out flow. Simulation and experimental results were presented for each of the controllers, from which it is found that the most robust controller is a simple meter-in strategy with a high-pass pressure filtered pressure feedback to stabilize the system. The meter-out strategies however also showed acceptable results, but require properly adjusted controllers and better results could probably be obtained with more advanced controllers not only adjusted for the fully extended position. Further work in this area will hence concentrate on more advanced controllers to account for parameter variations, possible switching between strategies under operation and more advanced control strategies, where cross-coupling control between the two chambers may also be considered.

REFERENCES

[1]   S. Miyakawa., *"Stability of a Hydraulic Circuit With a Counterbalance-Valve"*. Bulletin of the JSME, Vol. 21, No. 162, December 1978.

[2]   G. Overdiek, *"Dynamisches Verhalten von Senkbrems-Sperrventilen in Hydraulik-Hubwerk"*, Olhydraulik und Pneumatik, Vol. 24, No. 11, 1980 (in german).

[3]   G. Overdiek, *"Design and Characteristics of Hydraulic Winch Controls by Counterbalance Valves"*. European Conference on Hydrostatic Transmissions for Vehicle Applications, 29-30 September, 1981.

[4]   T. Persson, P. Krus and J.O. Palmberg, *"The Dynamic Properties of Over-Center Valves in Mobile Systems"*. 2nd International Conference on Fluid Power Transmission and Control, Hangzhou, China, November, 1989.

[5]   Y. Ramli, P.J. Chapple and D.G. Tilley, *"An Application of computer aided design (CAD) in Hydraulic Systems Using Counterbalance Valves"*,. 4th International Conference on CAD and CG, Wuhan, China, October, 1995.

[6]   B. Zähe., *"Stability of Load Holding Circuits with Counterbalance Valves"*. 8th International Bath Fluid Power Workshop, Bath, UK, September, 1995.

[7]   P.J. Chapple and D.G. Tilley, *"Evaluation Techniques For The Selection of Counterbalance Valves"*. The Expo and Technical Conference for Electro-hydraulic and Electropneumatic Motion Control Technology, Anaheim, USA, 23/24 March, 1994.

[8]   B. Lantto, A. Jansson and J.-O. Palmberg, *"A new concept of computer controlled electrohydraulic system the p-q pump and valve control"*. In Second Bath International Fluid Power Workshop, Bath, UK, September 21-22 1989.

[9]   A. Jansson, P. Krus and J.-O. Palmberg, *"Decoupling of response and pressure level in a hydraulic actuator"*. In The Fourth Bath International Fluid Power Workshop, Bath, UK, September 18-20 1991.

[10] M. Elfving, J.-O. Palmberg and A. Jansson, *"Distributed control of fluid power actuators - experimental verification of a decoupled chamber pressure controlled cylinder"*. In Fourth International Conference on Fluid Power Transmission and Control, Hangzhou China, September 9-11 1997.

[11] M. Elfving and J.-O. Palmberg, *"Distributed control of fluid power actuators - decoupled chamber pressure controlled cylinder"*. In Ninth Bath International Fluid Power Workshop, Bath, UK, September 9-11 1996.

[12] B.K. Nielsen, *"Controller Development for a Separate Meter-In Separate Meter-Out Fluid Power Valve for Mobile Applications"*, Ph.D. dissertation, Aalborg University Press, 2005, ISBN 87-89179-58-7.

Noise and Vibration

Condition Monitoring of Aircraft Fuel Pumps using Pressure Ripple Measurements

Nigel Johnston
University of Bath

Catherine Todd
Aero Engine Controls

ABSTRACT

Gear pumps are used for delivery of high-pressure fuel to aircraft engines. These pumps can suffer from erosion due to cavitation, which eventually causes an increase in leakage and reduced performance. An early warning of excessive wear is desirable, before the performance becomes unacceptable so that replacement can be scheduled conveniently without disrupting the operation of the aircraft.

Pressure ripple and flow ripple measurements were performed on a range of fuel pumps with bearing conditions ranging from good to badly worn. The flow ripple was determined indirectly by analysis of pressure ripple measurements. Results suggest that there is a clear and fairly consistent increase in the pressure ripple and flow ripple measured at the high-pressure outlet port when the bearing is in a worn condition. This increase seems to occur at a wear condition that is not sufficiently bad to worsen the pump performance significantly. This measurement could provide a clear and simple indication of pump wear, at an opportune point in the wear cycle. However whilst these results look promising they are not conclusive, as other differences between the pumps may have affected the results.

Keywords: Fuel pumps, gear pumps, condition monitoring, pressure ripple, flow ripple

1. INTRODUCTION

Pump flow ripple is a key feature of the operation of a hydraulic positive displacement pump, and is closely related to the pump's design and condition. If pump flow ripple can be measured, it can provide very useful information about the state of the pump which may be difficult to obtain by other means. However pump flow ripple cannot be measured directly as conventional flowmeters do not have sufficient bandwidth. Instead, indirect methods need to be used, in which the flow ripple is inferred from pressure ripple measurements.

Testing was performed on a selection of gear pumps used for high-pressure supply of fuel to aircraft engines. Cavitation is the main cause of wear in pumps of this type. In a gear pump, bearing blocks are pushed by fluid pressure against the end faces of the gears, forming a narrow clearance to minimise leakage. Wear mainly occurs on the thrust faces of the bearings, which may eventually cause a leakage path across the gear teeth from the high pressure side to the low pressure side. Wear may also occur on the faces of the gear teeth, though this wasn't considered in this work.

Pump components were interchanged between tests and a range of bearings of differing conditions of wear were included. Pressure ripple was recorded at the inlet and outlet of the gear pump.

The main aim of the investigation was to determine whether pressure ripple or flow ripple could be used as an indicator of pump condition for use in a pump health monitoring system. Secondary aims were to determine whether flow ripple could be determined from pressure ripple measurements, and to determine which quantity (flow ripple, pressure ripple) forms the best indicator.

1.1. The Secondary Source Technique

Pump flow ripple is a key feature of the operation of a pump and it is closely related to the pump's design, wear condition and operating conditions. If it can be measured it is a useful 'signature' of the pump which can be used by the pump designer and system designer, and can potentially be used as for health and condition monitoring [1]. The 'secondary source' method is a method for the indirect determination of pump flow ripple from pressure ripple measurements. It is described in detail by Edge and Johnston [2, 3, 4] and Johnston and Drew [5], and enables the flow ripple and the source impedance of a pump to be measured in terms of harmonic spectra.

The method is based on the measurement of harmonics of pressure ripple at various points along the length of the pipe connected to the port of the pump, and makes use in the analysis of the variations in pressure ripple which occur with distance. The pressure ripple in the pipe can be represented as two waves travelling in opposite directions. The waves add or cancel at different points along the pipe, resulting in different amplitudes, phases and waveforms. By measuring pressure ripple at several different points and by analysing the measurements mathematically, the waves in the two directions can be determined. It is then possible to calculate the pressure ripple and the flow ripple anywhere in that pipeline.
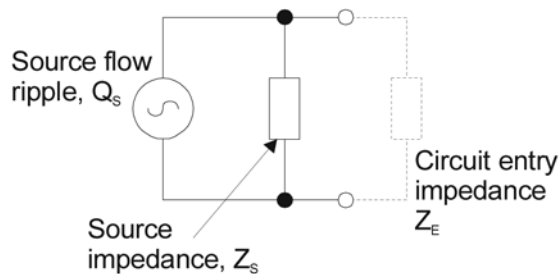
Figure 1 - Norton model of pump

Using the Norton model as shown in Figure 1, the flow ripple at the pump discharge port is defined by the equation:

$$Q_O = Q_S - \frac{P_O}{Z_S}$$ (1)

where Q_S is the flow ripple that would be produced by the pump discharging into a circuit of zero entry impedance, and Z_S is the pump source impedance. Q_S is the 'active' component, relating to the pumping action, and Z_S is the 'passive' component related to the resistance, leakage, compressibility and inertance (fluid mass effect) in the delivery passageway. Both of these are pump properties and are not dependent on the circuit.

In the `secondary source' method [2-6], the calculation of Z_S is separated from the calculation of Q_S. This is done by using a secondary source of pressure ripple, connected to the opposite end of the pipeline to the pump as shown in Figure 2. The secondary source is operated at a different speed to the test pump, and the harmonic components of the secondary source are measured. At these frequencies, provided that they do not coincide with harmonic frequencies of the test pump and that spectral leakage is negligible, Q_S can be assumed to be zero. The source impedance can be evaluated using equation (2).

$$Z_S = -\frac{P_O}{Q_O}$$ (2)
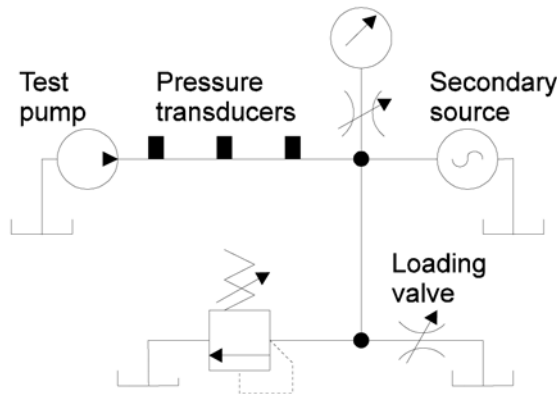
Figure 2 – Test rig for Secondary Source Technique

The pump flow ripple is determined by measuring the harmonic components of the test pump, with the secondary source not operational. The flow ripple Q_S can be determined from Equation (1), provided that Z_S is known at that frequency.

The 'secondary source' technique has been used extensively with oil hydraulic pumps and systems. Prior to this work little or no testing had been done using this method with fuel pumps.

2. TEST RIG DESCRIPTION

The test rig was set up as shown in simplified form in figure 3. The LP centrifugal pump was mounted in the same housing as the HP gear pump. The rig was instrumented to measure the pressure ripple and flow ripple at both low pressure (LP) and high pressure (HP) ports of the high pressure pump simultaneously. The ripple generator was a rotary valve designed to produce short, sharp flow pulses during its rotation [5, 6]. The test rig is shown in figure 4.
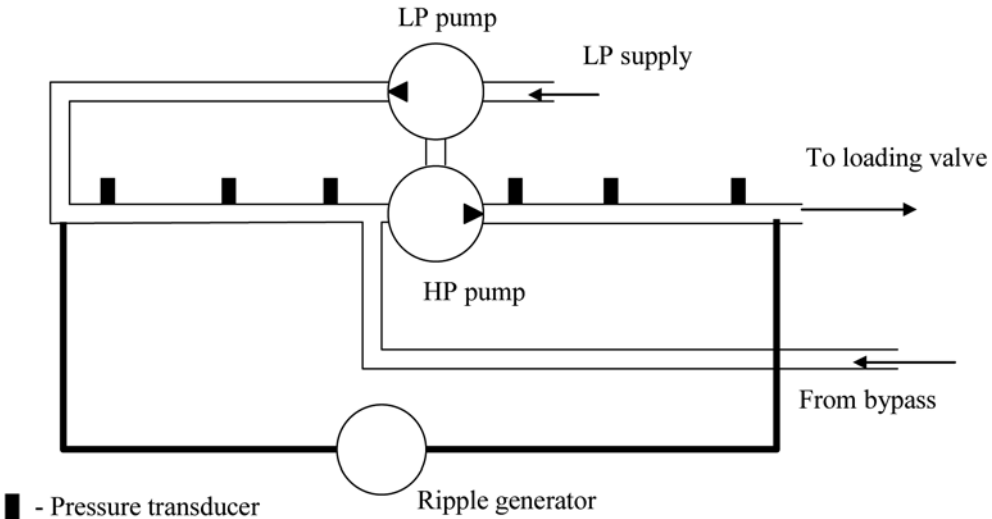
Figure 3 – simplified schematic of part of test rig

2.1 Test Conditions

Tests were performed at pump speeds of 2000 rev/min to 7000 rev/min at 1000 rev/min intervals, and pressures of 200, 600 and 1200 lbf/in^2 (14, 34 and 83 bar). The temperature was between 10°C and 15°C. Tests were repeated at some conditions for checking repeatability. Tests were performed on 12 pump builds; two different pump bodies were used and internal parts were interchanged giving a total of five 'good' condition pumps, three 'worn' (intermediate condition) pumps and four 'bad' (severely worn) pumps. In total over 240 tests were performed.

2.2 Steady Flow Results

Before each test a flow check was performed on each pump to provide a quantitative means of comparison. These tests were done at a range of speeds and pressures. Figure 5 shows the flowrate at 7000 rev/min plotted against nominal bearing condition. The flowrate is normalised relative to the average flowrate for 'good' condition. The flow rates for 'good' condition are very closely spaced. There is a small drop in flowrate (about 4%) and increased variation for the 'worn' condition, but a much larger drop in flowrate (15% to 30%) for the 'bad' condition.
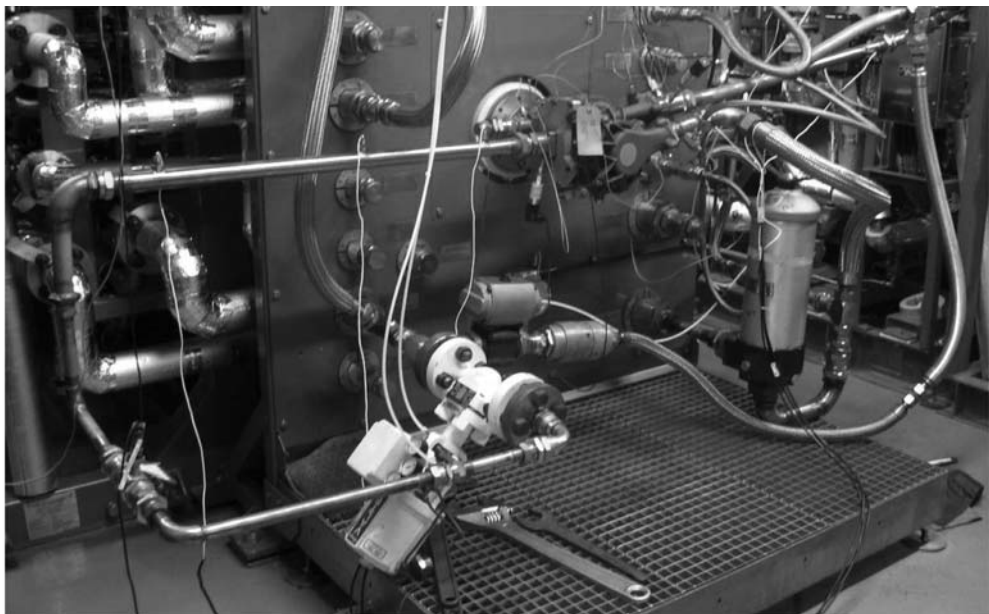
Figure 4 Photograph of test rig (ripple generator not included)
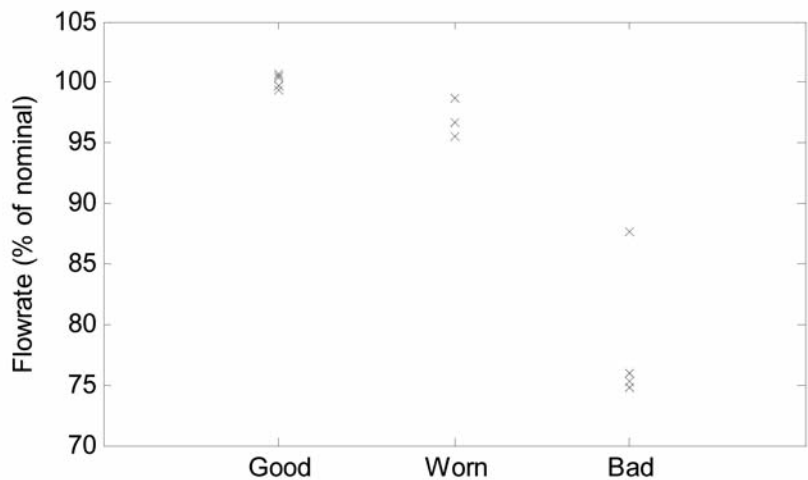
Figure 5 - Measured flowrate at 7000 rev/min vs. bearing condition

2.3 Ripple test procedure

Pressure ripple data were acquired from all six piezoresistive pressure transducers synchronously, along with a shaft reference pulse signal (one pulse per revolution) at 30 kHz per channel in a 1 second burst. The measurements were analysed using the FBN software [6] to obtain the harmonic amplitudes and phases at all multiples of shaft frequency up to 5000 Hz. These harmonic values were then processed using the FBN

software to determine the pump's outlet flow ripple. The speed of sound and bulk modulus of the fluid were also determined [7]. The flow ripple was evaluated in the form of 'anechoic flow ripple' [5, 6], representing the flow ripple that would be produced in an infinitely long tube. The flow ripple was evaluated as a harmonic spectrum, waveform and overall r.m.s. (root-mean-square) amplitude. The flow ripple analysis was only performed at the outlet port as it was found not to be possible to obtain reliable results from the inlet port data.

The flow ripple was determined using previously measured source impedance data in equation (1). Because of test rig limitations it was not possible to use the ripple generator for all of the pumps that were tested. For this reason the same impedance data were used for all pumps and it was assumed that the source impedance was the same for all pumps. This is an approximation as the impedance may change slightly as the fluid properties, pump compliance and leakage paths may change slightly with speed, pressure and temperature. However experience has shown that variations in impedance are usually small. The impedance that was used is shown in figure 6. This was obtained from a pump with 'good' bearings at 3000 rev/min and 600 lbf/in^2 (41 bar). This is It is a mainly capacitive characteristic with a negative phase and amplitude decreasing with frequency, but more complex effects are apparent at higher frequencies.
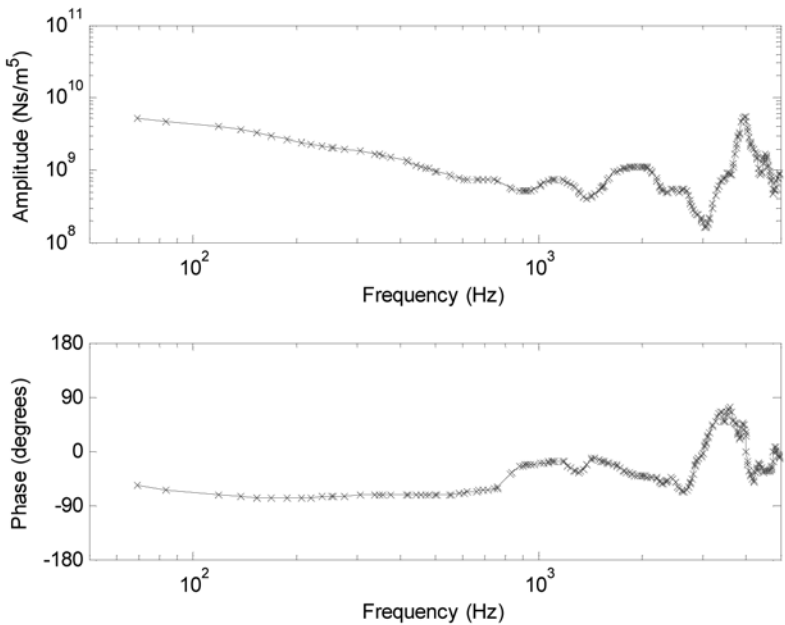
Figure 6 - Impedance data

3. RIPPLE TEST RESULTS AND DISCUSSION

Some representative flow ripple results for pumps with 'good', 'worn' and 'bad' bearings are shown in figures 7-9 (this is a small selection as about 240 tests were performed). Here

amplitude spectra and waveforms are plotted. The spectra show dominant peaks at multiples of 12 orders, these being the pumping harmonics as there are 12 gear teeth. The other harmonics are small and may be considered as background noise. The 12th order (first pumping harmonic) is the strongest in all cases.

Whilst there are differences for different conditions and different pump builds, the waveforms generally conform to the shape expected for a gear pump [8], somewhat similar to a rectified sine wave but with some pressure dependent 'spikiness'. The waveform amplitudes can be seen to be greater for the 'worn' and 'bad' bearings than for the 'good' bearings. In most cases the amplitude increases with pressure.
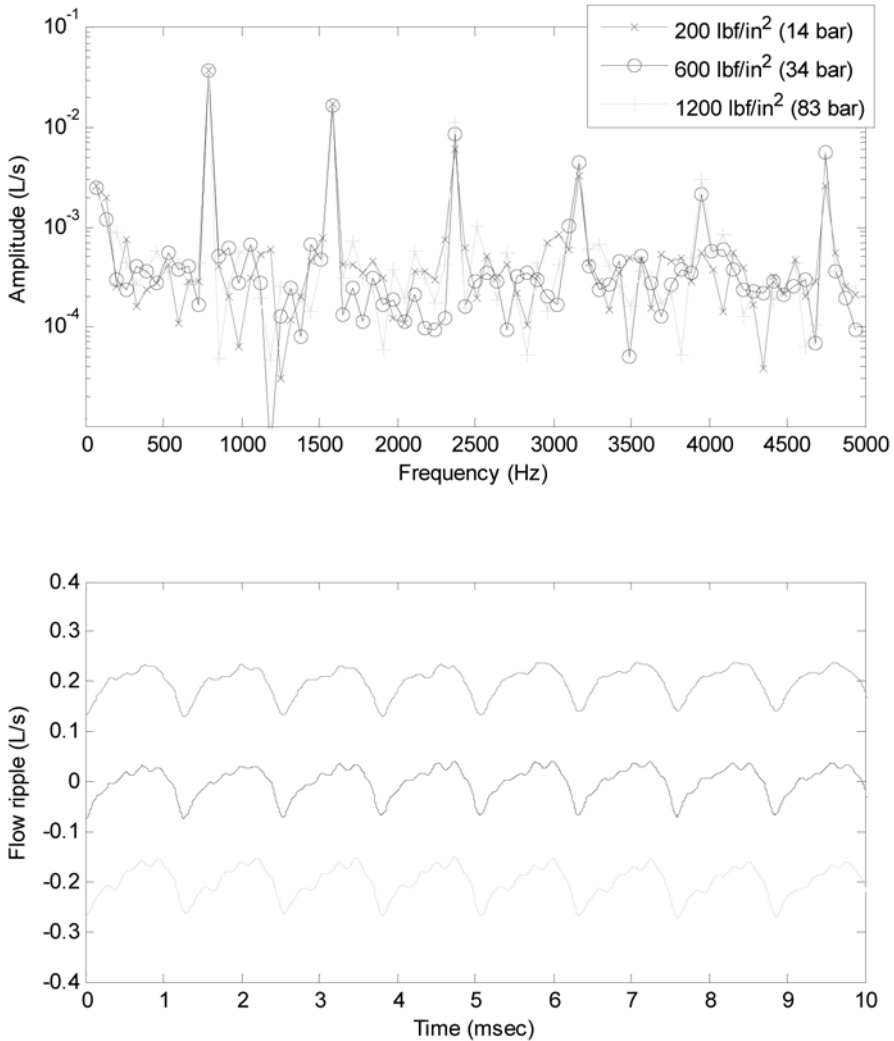
Figure 7 - Typical measured flow ripples, 'good' bearings, 4000 rev/min
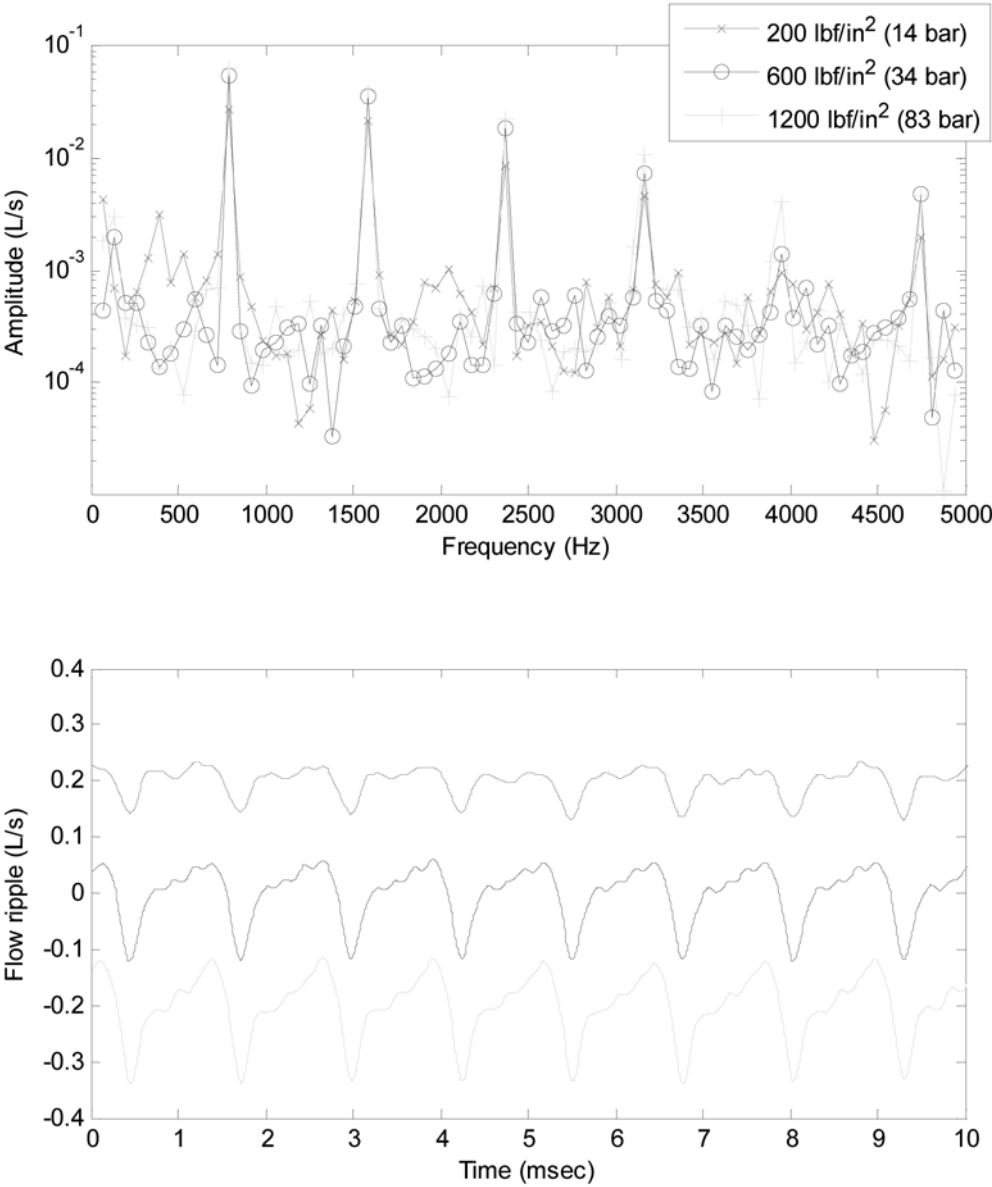
Figure 8 - Typical measured flow ripples, 'worn' bearings, 4000 rev/min
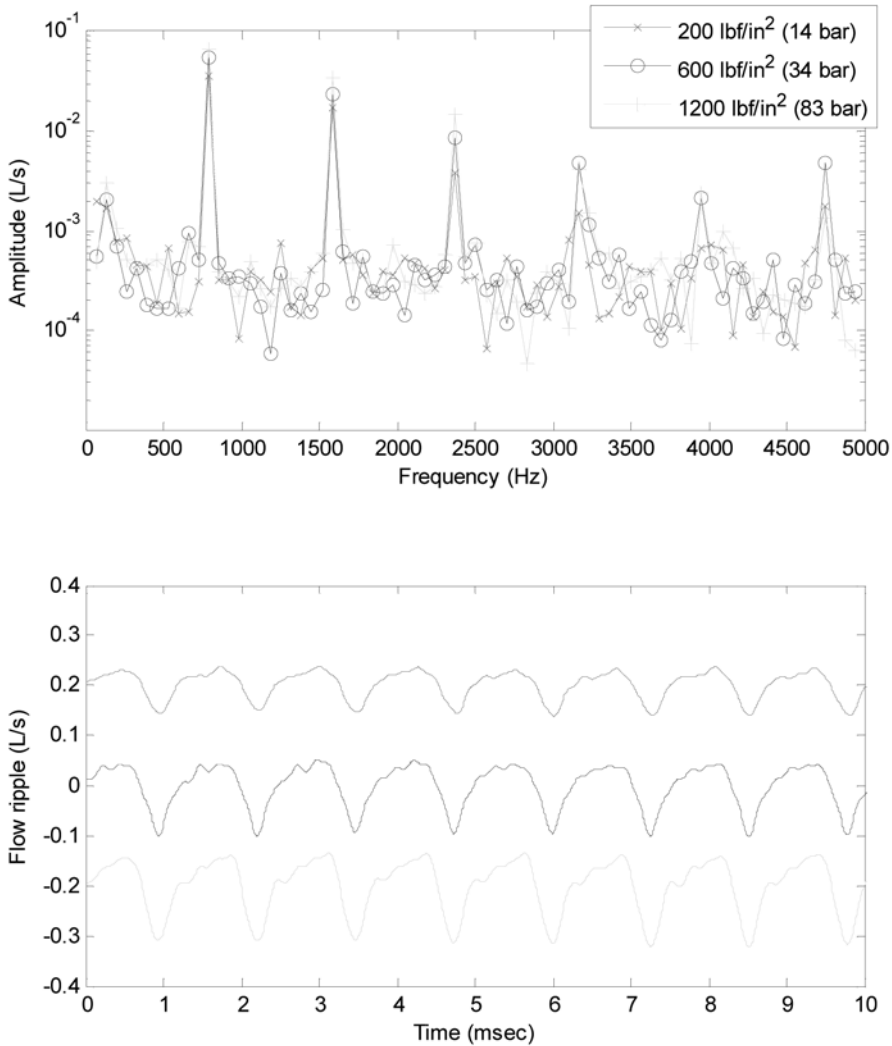
Figure 9 - Typical measured flow ripples, 'bad' bearings, 4000 rev/min

Repeatability was found to be good, as differences between the first and repeat tests at 3000rpm were negligible.

For pump health monitoring, a simple indicator of pump health is required, preferably a single-figure quantity. Various single-figure quantities were considered, including:

1. r.m.s. flow ripple, high pressure (delivery) port;
2. Peak-peak flow ripple, high pressure port;
3. r.m.s. pressure ripple at transducer nearest to pump, high pressure port;
4. First (pumping frequency) harmonic amplitude of flow ripple, high pressure port;

5. First (pumping frequency) harmonic amplitude of pressure ripple, high pressure port;

6. r.m.s. pressure ripple at transducer nearest to pump, low pressure (inlet) port;

7. First (pumping frequency) harmonic amplitude of pressure ripple, low pressure port.

The most consistent trends were found to occur with quantities 1, 3, 4 and 5 above. Similar trends occur for these four different quantities. This suggests that the extra complexity involved in measuring flow ripple may not be necessary as a simple pressure ripple measurement may be sufficient.

The r.m.s. pressure ripple at the high pressure port is plotted alone against bearing condition in figure 10. Only the cases that showed clear trends are shown here. There is a clear increase in amplitude from 'good' to 'worn' bearings, but there is also some variation between pumps with 'good' bearings in particular.
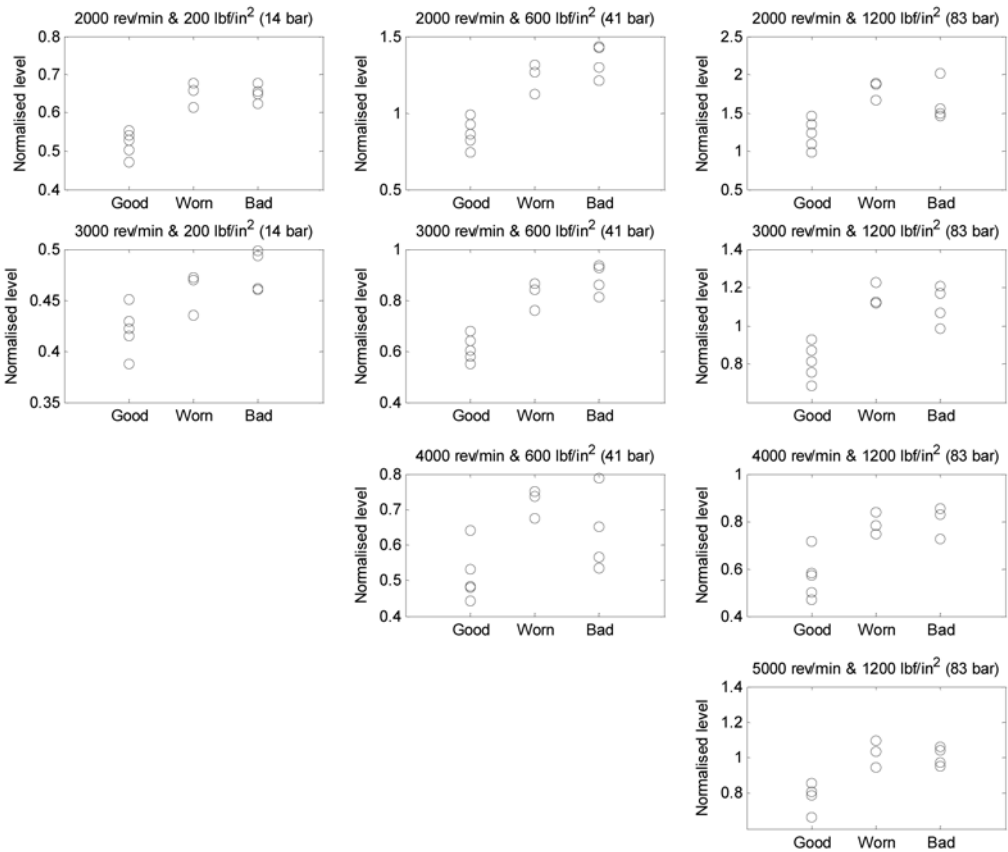
Figure 10 - HP r.m.s. pressure ripple vs. bearing condition

The pressure ripple is simple to measure, far more so than the flow ripple. Just one pressure transducer would be needed, situated near the pump HP port. This would need to be a

suitable high-frequency type such as a piezoelectric or piezoresistive type. Digital Fast-Fourier Transform (FFT) processing would be required if the amplitude of the first pumping harmonic was required; FFT processing might not be needed for the r.m.s. level.

The ripple level has been shown to increase significantly in the 'worn' condition, whilst figure 5 shows that the flowrate has reduced only very slightly at that condition. This suggests that the ripple level is very sensitive to wear in the bearings, and may be because wear in the bridging area near to the gear meshing point gives rise to a leakage path that opens and closes as the gear teeth pass. This may result in a small but cyclic leakage flow that increases the pump's flow ripple and hence the pressure ripple. Thus the ripple is likely to provide a good early warning of wear, before the pump performance itself starts to degrade.

The ripple levels depend strongly on speed and pressure, so it is important that comparisons are made at similar conditions. The trends appear to be clearest at relatively low speeds and high pressures.

It should be noted that the results here were obtained from different pump builds. Different pump bodies and gears were used for different runs, so the trends observed here may not be entirely due to the different bearings. In a real health monitoring situation, the degradation of one particular pump build over time would be monitored. This might give more consistent results as the arbitrary differences between individual components within each pump build would be eliminated.

4. HEALTH MONITORING

4.1 Requirements for Health Monitoring
The health monitoring system should provide an indication of pump wear and damage, at a time before the pump performance (flow and pressure) degrades below a satisfactory level, such that the pump can be scheduled for repair or replacement at a convenient time and place. It should require a minimum of additional components and instrumentation.

The flow test results (figure 5) suggest that the pumps with 'worn' bearings have a slight decrease in flowrate, but still operate satisfactorily. This level of wear might be a suitable point at which the health monitoring system identifies that maintenance is needed, whilst still allowing time to schedule the maintenance to occur at a convenient time and not requiring immediate emergency maintenance.

These results suggest that HP port pressure ripple amplitude would suit these requirements, as it requires a minimum of instrumentation (one transducer) and appears to provide a clear difference between 'good' condition bearings and 'worn' condition bearings. The results suggest that a large increase in the ripple level occurs before the pump performance degrades significantly.

The clearest indication of wear appears to occur at relatively low speeds and high pressures. Unfortunately these are conditions that do not occur during regular service. The lowest pump speed in service is generally over 4000 rev/min, which is the idle condition, at which

pressures are low. Consideration would have to be given to this constraint in developing a health monitoring system.

The 'secondary source' technique is too complex and intrusive to be used in-situ. However it could be used as a pre-installation test to determine the pump and system characteristics. From this the overall system transfer function relating system pressure ripple to pump flow ripple could be determined. The flow ripple could then be estimated from a single pressure ripple measurement during in-flight operation. However these results suggest that this may not be necessary in this case; the pressure ripple amplitude can be used directly as a diagnostic signal.

4.2 Possible Algorithm for Health Monitoring
The speed and pressure ranges should be divided into a number of 'bins' corresponding to conditions that occur during normal flight, and to conditions that give the clearest trends (from these tests, these conditions appear to be mainly at 2000-4000 rev/min). Each bin would be for a specific speed and pressure range (and possibly fuel temperature range and/or flight phase). The bins would not need to cover all possible conditions; if the engine was operating outside of the range of the bins then no monitoring would take place at that time; the monitoring would continue when the conditions returned to within one of the bins.

It would first be necessary to establish baseline levels for a pump in 'good' condition. From when the pump is first installed, the ripple should be measured continuously and the ripple level determined (by FFT or other processing) at regular intervals. The level should be stored in the relevant 'bin' using a low-pass filter or moving average to avoid sudden changes and anomalies. After a certain 'running-in' period the level in each 'bin' should settle to a roughly constant level. The level in each bin may then be taken as the reference level.

After the reference levels have been determined, health monitoring can then begin. The ripple level would be monitored at regular intervals. If the conditions fall into one of the range of one of the bins, the ratio X between the ripple level and the reference level for that bin would be calculated. A low-pass filter or moving average would then be applied to this ratio, to give a smoothed value and avoid anomalies, $\tilde{X}$ say. Ratios from all bins would feed into one $\tilde{X}$ value.

- If $\tilde{X} \approx 1$, this indicates that the pump is still in good condition.

- If $\tilde{X}$ exceeds a certain threshold (maybe 1.5) this indicates that the pump has worn.

The threshold would need to be set to a suitable value. If it was too low false alarms may occur, whilst if it was too high the monitoring may be too insensitive. The same applies to the time-constant for the low pass filtering or time-span of the moving averages.

Further work, and data for a pump through its life cycle from new to worn, are needed to develop and validate this algorithm.

5. CONCLUSIONS

The measured pressure ripple amplitude was found to be significantly greater for pumps with moderately worn bearings than with good bearings. At these moderately worn conditions there was found to be only a small reduction in delivery flowrate. This suggests that the pressure ripple amplitude might provide a simple and useful early warning of pump degradation, giving a clear indication at a time before the pump performance degrades significantly and allowing a suitable time window for maintenance to be scheduled after the indication occurs. Pressure ripple would be relatively simple to measure and process, and the monitoring would be automatic.

Flow ripple was measured successfully, and the measured flow ripple waveforms showed the expected characteristic shape, similar to a rectified sine wave. Similar trends were observed for the flow ripple and the pressure ripple in relation to pump wear. However the pressure ripple is much easier to determine and therefore preferable as an indicator.

However the results so far are not totally conclusive, as several components were changed between tests and some of the variations in ripple amplitude may have been due to other factors such as differences in pump bodies. To develop this method further, it would be beneficial to perform endurance testing on a pump instrumented with a pressure transducer, through the life of the pump from new through to a worn condition. Ideally the pump would be cycled through a representative range of conditions to simulate flight cycles.

REFERENCES

[1]   Yang, M, Modelling and analysis of pressure pulsations in hydraulic components and systems with particular reference to pump fault diagnosis, PhD Thesis, University of Bath, 2009

[2]   Edge, K.A., Johnston, D.N. The `secondary source' method for the measurement of pump pressure ripple characteristics, part 1: description of method, Proc. Inst. Mech. Engrs, part A, vol. 204, 1990, pp33-40

[3]   Edge, K.A., Johnston, D.N. The `secondary source' method for the measurement of pump pressure ripple characteristics, part 2: experimental results, Proc. Inst. Mech. Engrs, Part A, vol. 204, 1990, pp41-46

[4]   Johnston, D.N., Edge, K.A., A test method for measurement of pump fluid-borne noise characteristics, Trans. SAE, Section 2, Journal of Commercial Vehicles, #911761, 1991, pp148-157

[5]   Johnston, D N, Drew, J E, Measurement of Positive Displacement Pump Flow Ripple and Impedance, Proc. Inst. Mech. Engrs pt I, Vol 210, 1996, pp65-74

[6]   University of Bath, FBN Software Reference Manual Version 4.20, 2008

[7]   Johnston, D.N., Edge, K.A., In-situ measurement of the wavespeed and bulk modulus in hydraulic lines, Proc. Inst. Mech. Engrs, Part I, Vol. 205, 1991, pp191-197

[8]   Casoli P., Vacca A., Berta G.L., A Numerical Model for the Simulation of Flow in Hydraulic External Gear Machines, Bath Symposium on Power Transmission and Motion Control, 13-15 September 2006, University of Bath, UK.

Application of Hydraulic Sine Generator to Active Vibration Control

Jari Kostamo, Esa Kostamo, Jyrki Kajaste, Matti Pietola
Department of Engineering Design and Production
Aalto University School of Science and Technology

ABSTRACT

Vibration frequencies in rotating industrial machines may range up to several hundreds Hertz and in some specific applications the excitation forces can also be relatively high. These facts set demanding requirements for the devices which can be used to suppress the vibrations in most challenging cases. To overcome these problems a simple method for producing sinusoidal pressure fluctuations is presented in this paper and applied to active vibration control task. The method is based on a hydraulic sine generator designed especially for active vibration control solutions and it is suitable for high frequency and high power actuation. Different concepts for technical implementation are discussed and an experimental device based on a rotating gear plate is presented. The applicability of the device in active vibration control task is verified by experiments and it is shown the device is capable of outputting more than 1 kN force at 1 kHz frequency.

1. INTRODUCTION

The performance of many rotating machines is directly proportional to their speed of rotation. The common requirements to increase the productivity may set strain to increase the operating speed of rotating machines, but typically the resonance frequencies in heavier machine structures restrict the operating speed below the first poorly damped mode. Higher operating speeds can be achieved by improving the mechanical design and by using stiffer constructions but these approaches may lead to increased manufacturing costs. In some cases the resonances cannot be completely avoided as the machine structure may have several modes which are excited one after another when the rotating speed is slightly varied. It is also possible the mechanical design of a machine is complex and all possible resonance frequencies cannot be predicted in advance.

In the case of mechanical resonances the dynamic forces can easily increase to a level which is decade higher compared to force levels during normal operation. The increased dynamic stress reduces the life time of rotating machines and it may lead to severe failures.

To increase the operating speeds and performance of industrial machines and to overcome the resonance problems, active vibration control solutions have been increasingly proposed (1, 2). As active vibration control solutions are based on producing a counter force to the disturbance which causes the resonance, actuators capable of operating at the observed resonance frequencies are needed. Thus the frequencies required in some vibration control tasks reach up to several hundreds Hertz and the bandwidth of most common commercial actuators is not sufficient in all situations. If the force levels needed in vibration control task are measured in the range of several kN, the selection of commercial solutions is more limited.

Piezoelectric actuators have been proposed to many active vibration control tasks requiring good dynamical performance (3). The stroke of a piezoelectric actuator is typically rather small and mechanism to increase the stroke have been developed e.g. by (4) to facilitate the implementation to practical vibration control solutions and to optimize the size of the piezoelectric stack. Different configurations of electromagnetic actuators and active magnetic have also been widely applied in active vibration control of rotating parts (5, 6).

Even though electrical actuators provide many advantages over hydraulic solutions, hydraulic actuators maintain some important advantages over other technologies. The power density of a hydraulic actuator is still much higher than the power density compared to an actuator based on purely electromagnetic phenomena. Typically the hydraulic actuator can be made very small and the efficiency of the actuator part itself is high. This enables compact solutions which can output high force levels at high frequencies. (1). Hydraulic actuators can also be integrated to lubricated bearing to provide active damping capability (7-9).

The goal of this research was to develop a reliable actuator for high frequency active vibration control task and to validate the design by experiments. The targeted force levels were higher than 1 kN and the solution should be capable of operating up to 1 kHz frequency. The more common technologies based on high performance servo valves were considered too unreliable in log term industrial use and electromagnetic actuators would have yielded to too large constructions.

To overcome the problems related to generating high frequency actuation with hydraulic systems, an approach based on a rotating valve is discussed in this publication. The challenge with a rotating valve is that only certain frequencies can be simultaneously generated with a single device as the output frequency is related to the rotation speed of the shaft of the valve. However, this is often sufficient as the excitation frequencies in rotating machines occur at narrow band and there are simultaneously only one or few frequency components which need to be suppressed. Therefore actuators which are able to produce force at only one frequency can also be used in active vibration control if the frequency, phase and amplitude can be precisely adjusted.

2.   Concept and simulation model of the hydraulic sine generator

In this chapter the idea of a rotating valve is discussed and some concepts for implementing the functionality are presented. Based on the selected method a simulation model is derived

and the feasibility of the approach adopted in this publication is evaluated by analyzing the simulation results.

2.1 Concepts for hydraulic sine generators

During the development work of the HSG presented in this publication, different concepts and mechanical structures were considered to produce the needed pressure variations. As the functional principle of the HSG is based on a rotating spool or a gear plate which is used to open and close orifices, there are numerous variations to implement the necessary functionality.

One approach considered for producing the sinusoidal pressure fluctuations was based on an engraved rotating spool and a housing which had radial orifices. By rotating the spool inside the housing the orifices were supposed to be combined in sequences which would control the high pressure hydraulic oil to the actuator and from actuator to the low pressure tank line. A prototype of this construction was manufactured but the compensation of the hydrostatic forces was found to be problematic and the construction also yielded to fairly large valves. A variation of this concept included a hollow rotating which could have had orifice in the spool and in the housing.

The concept which was adopted for the final prototype was based on a rotating gear plate. By compensating the pressure forces inside the rotating valve the gear plate could be made easy to rotate. The concept based on a rotating gear plate can also be made very small and it is easy to design the valve for certain frequencies. A schematic diagram of the gear plate concept is show in Figure (1).
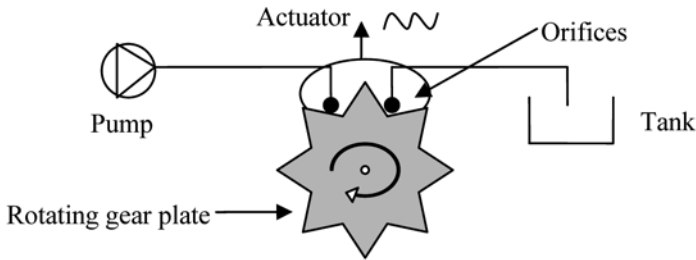
Figure 1: A schematic drawing of the rotating valve.

2.2 Model of the variable orifice

The feasibility of the concept was evaluated with a simulation model developed for the rotating valve. The model of the rotating valve consists of a variable sized orifice and of a model for the hydraulic actuator.

The model developed for the HSG relies on a well known model for the incompressible flow through an orifice. By assuming steady-state, incompressible, laminar flow in the valve the flow model assumed for the variable orifice can be described by Equation (1).

$$Q = CA\sqrt{2(P_1 - P_2)/\rho} \qquad (1)$$

where Q is volumetric flow rate, C_d is the metering coefficient, P_1 are the pressures on different sides of the orifice and ρ is the density of the fluid.

The flow model for the HSG assumes a circular orifice which is opened and closed by a tooth plate. Therefore the effective flow area of the orifice changes continuously from full circle to semicircle until it is fully closed. Then another orifice is opened which controls the fluid flow from the actuator to the low pressure tank line.

The flow area of the variable orifice can be defined by calculating the open area of the circle. The tooth gap of the rotating valve is square and the size of the gap is equal to the size of the circular orifice. The calculation of the area is demonstrated in Figure (2).
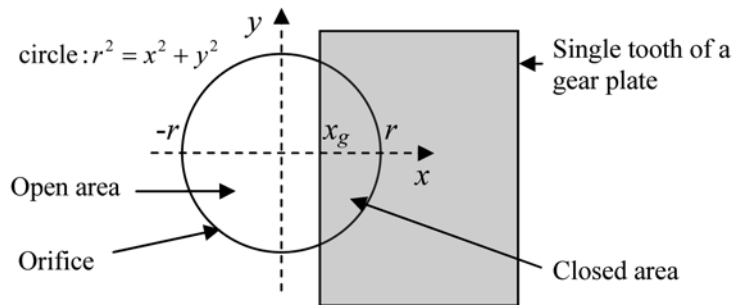
Figure 2: Functional principle of the variable orifice.

The open area for the orifice is given by the following definite integral:

$$A_{open} = 2 \int_{-r}^{x_g} \sqrt{x^2 - r^2}\, dx .$$ (2)

In Equation (2) A_{open} is the flow area of the orifice, r is the radius of the orifice and x_g denotes the boundary which is closed by the rotating gear plate. The function defined in Equation (2) is integrable and the integral can be calculated to give the following solution

$$A = x\sqrt{r^2 - x^2} + r^2 \tan^{-1}\left(\frac{x}{\sqrt{r^2 - x^2}}\right) .$$ (3)

The open area of the orifice can be obtained by substituting the integration limits to Equation (3). The substitution is done for different values of x_g and the result is shown in Figure (3). To avoid numerical problems and to facilitate an easy implementation of Equation (3) to a simulation model the equation is approximated with a 5th order polynomial which is also shown in Figure (3). It can be seen the polynomial can be used to approximate the original function with good precision.
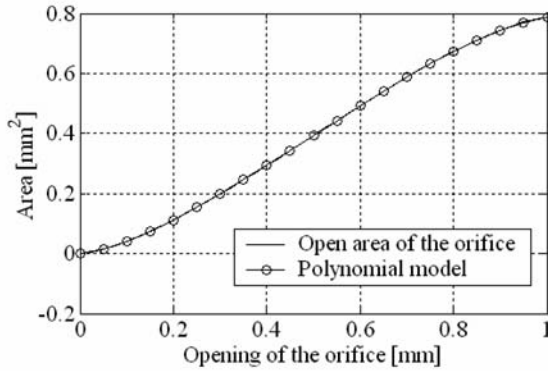
Figure 3: Open area of the variable orifice in the rotating valve.

2.3 Simulation model of the hydraulic sine generator

A model was developed in Matlab Simulink to simulate the performance of the proposed hydraulic sine generator system. The model was used to evaluate the feasibility the approach presented here and to gain insight into designing a HSG. Simulation model can also be used to numerically analyze the output waveform of the HSG and to evaluate the distortion frequency components which the HSG might generate in addition to the desired frequency.

The simulation model consists of two variable orifices described by Equation (3). The variable orifices are combined in opposite phases and the first orifice is used in supplying the pressurized hydraulic fluid to the actuator and the other orifice is used in controlling the fluid flow from the actuator to the tank line. The orifices are controlled by the same rotating gear plate.

The actuator in the simulated system was modeled with a small hydraulic volume of 10ml. The compliance of the hydraulic fluid in this volume simulates a small and stiff actuator which could be used to generate counter forces in vibration control tasks. From practical point of view it is important to keep the hydraulic volumes small in order to optimize the frequency bandwidth of the vibration control system.

The result of the simulated waveform at 500 Hz frequency is shown in Figure (4). It can be seen that the output waveform is not fully sinusoidal but the dominating frequency component is strongly related to the rotational frequency of the control valve.
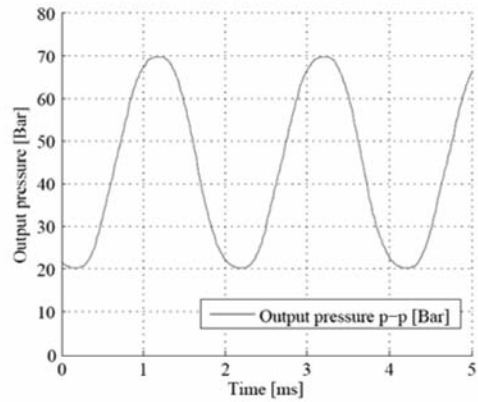
Figure 4: Simulated pressure waveform generated with HSG.

To analyze the waveform and frequency components more closely a Fast Fourier Transform was calculated for the signal presented in Figure (4). The frequency spectrum is shown in Figure (5) and the highest peak of the spectrum corresponds to the rotating frequency of the valve multiplied by the number of teeth in the gear plate. It can also be seen that there are no other significant frequency components and there is only a minor peak at the third harmonic frequency.
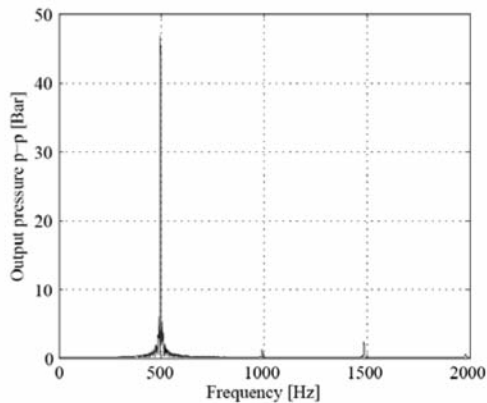
Figure 5: Frequency spectrum of 500 Hz sine wave generated with simulated HSG.

To analyze the behavior of the HSG over a wider operating range the simulations were carried out with frequencies ranging from 100 Hz to 1 kHz. The simulation results shown in Figure (6) to demonstrate that the behavior of the rotating valve is predictable and the dominating frequency component is always related to the rotational frequency of the valve.
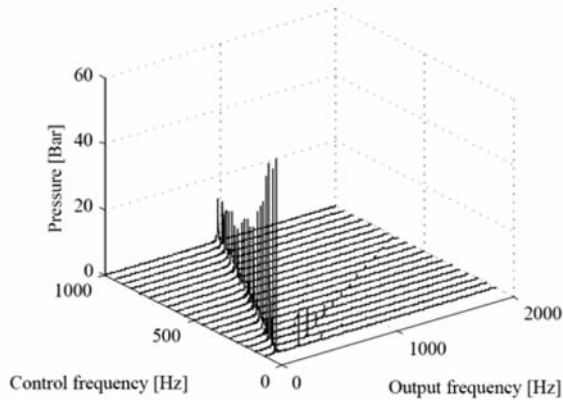
Figure 6: Frequency spectrum of the frequencies generated with HSG.

The result shown in Figure (6) also implies that several rotating valves could be combined with each other to produce more frequencies needed in some vibration control tasks. As the HSG generates only one major frequency component, several hydraulic sine generators can be combined if more resonance frequencies are required to be suppressed simultaneously.

3.   EXPERIMENTAL HYDRAULIC SINE GENERATOR

To evaluate the concept presented in this publication an experimental device was built. The HSG used for the experiments was set up by manufacturing a prototype of the rotating valve and by combining it with a digital servomotor to facilitate the control of frequency and phase. The amplitude of the sinusoidal signal was controlled with a proportional valve which could be used in controlling the fluid flow to the actuator.

3.1 Development of the HSG
The HSG presented in this paper was designed to operate with a commercial digital servo motor. By combining the rotating valve with a high quality servo drive, the problems related to precise control of rotating speed and adjustment of phase could be solved. The servo drive also adapts to the changes in reference signal rapidly and the settling time of the valve is therefore reduced.

The mechanical construction of the valve was designed so that frequencies in excess of 1 kHz can be generated while the maximum rotating speed of the servo drive is 3000 rpm. A design of a rotating valve with 24 teeth was chosen and thus the maximum output frequency of the valve is 1.2 kHz.

The rotating valve was designed so that the pressure differences inside the rotating parts were balanced. This yielded to a construction which could be rotated with a small torque and the friction losses did not produce unnecessary heat. The final construction of the valve was very easy to rotate and it turned out that the selected servo motor was heavily oversized for this application.

4.   EXPERIMENTAL SETUP

The experimental setup consisted of a membrane actuator combined with the hydraulic sine generator. To demonstrate the performance of the HSG in a vibration control task, a vibrating beam was designed and built. The vibrating beam could be exited with a voice coil actuator capable of producing a 120 N force.

4.1 The vibrating beam

To build a mechanical vibrating structure with a resonance frequency of 200 Hz, a vibrating beam was realized. By choosing a solid steel bar supported from both ends it was easy to manufacture a process that could be exited at its resonance frequency and it could be used in demonstrating a vibration problem which could occur in a machine structure. The vibrating beam can be exited with a voice coil to a resonance which has amplitude more than 200 times larger than the static deflection. Thus the dynamic forces in resonance are decades larger compared to non-resonating case. The functional diagram of the experimental setup is demonstrated in Figure (7)
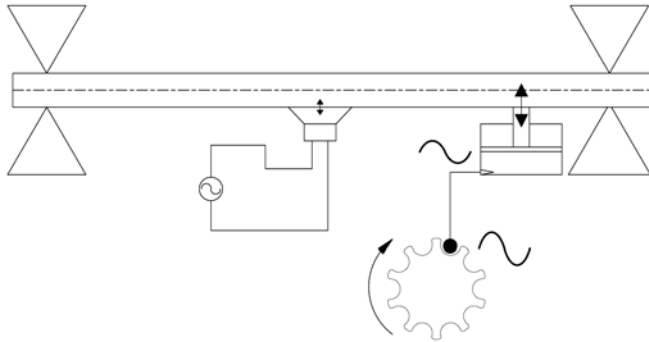
Figure 7: Test setup for the HSG.

The vibrating beam was supported from each end by two cylindrical bearings to minimize the damping the larger contact areas might induce. The vibrating beam used in experiments is shown in Figure (8).
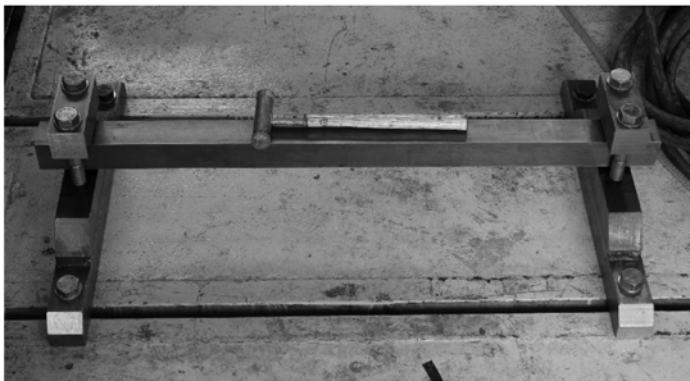
Figure 8: The vibrating beam demonstrating a machine structure with a resonance frequency at 200 Hz.

4.2 The vibration control system

The HSG was combined with a membrane actuator and the actuator was attached to the vibrating beam. As the hydraulic actuator was designed to be more powerful than the voice coil actuator used for simulating the disturbance force, the hydraulic actuator was mounted close to the end of the beam. In this location the potential of the HSG can be demonstrated as the location near the end of the beam is not optimal from the vibration control point of view. The figure of the experimental arrangement is shown in Figure (9)
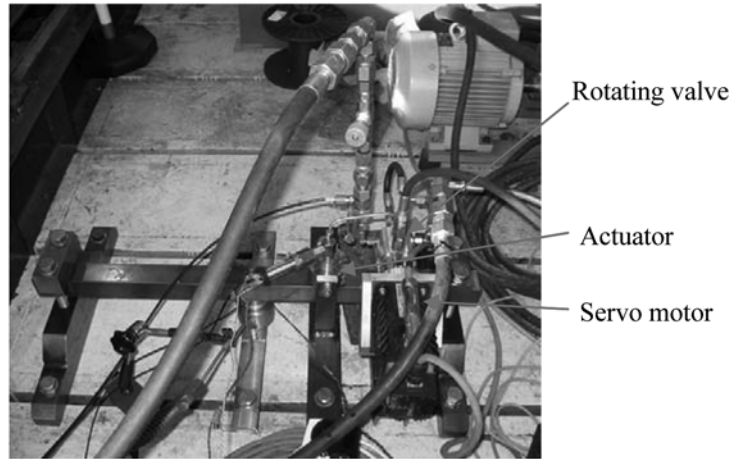
Figure 9: Test setup for evaluating the HSG in a vibration control task.

5.   MEASUREMENT RESULTS

The performance of the experimental HSG was first analyzed by measuring the pressure fluctuations the device could generate. Then a membrane actuator was attached to the HSG and the device was mounted to the vibrating beam. The vibrating beam was exited with the voice coil and the HSG was used to produce a counter force to excitation signal.

5.1 Measurements of the hydraulic sine generator

The waveforms of the HSG were analyzed to verify the functionality of the proposed device. The main goal of this first experiment was to be able to produce a significantly higher pressure fluctuation at the desired frequency and the other frequency components should remain at much lower levels. The pressure waveforms generated with HSG are shown in Figure (10).
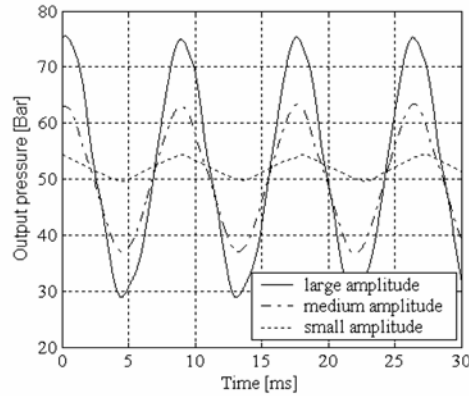
Figure 10: Demonstration of the amplitude control.

It can be seen from Figure (10) that the pressure variation is relatively close to sinusoidal and the amplitude of the pressure fluctuations can be controlled. To gain more insight in the performance of the HSG in a wider operating range, several tests were carried out between 100 Hz an 1100 Hz frequencies. To analyze the frequency content of the generated waveforms, an FFT was calculated for the signals and the results are plotted in Figure (11). It can be seen that the mode related to rotating frequency produces always the dominating frequency component and the performance of the HSG even improves at higher frequencies as the distortion components get smaller compared to the desired frequency.
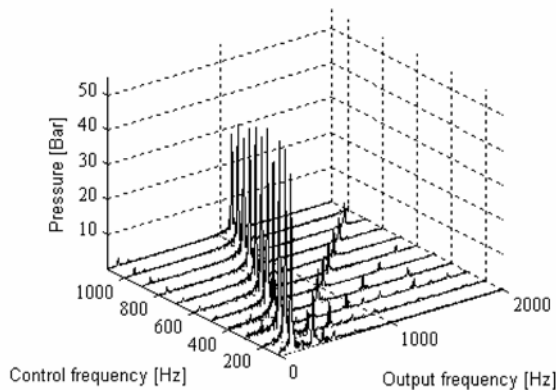
Figure 11: Frequency spectrum of the output pressure of the HSG.

5.2 Vibration control test

To verify the applicability of the HSG to an active vibration control task the vibrating beam was exited with the voice coil around the resonance frequency of the first mode. The undamped response of the beam was recorded and a resonance peak can be observed in Figure (12). Then the same experiment was repeated while the vibration control with HSG was applied to the beam. The result of active vibration control with HSG is also shown in Figure (12) and it can be seen the damped vibration amplitude is at its best nearly 200 times smaller than the undamped vibration amplitude.
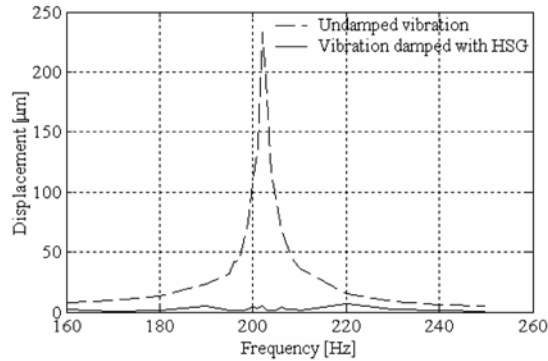
Figure 12: Vibration of the beam without and with HSG.

6.   Conclusions

A hydraulic sine generator was proposed for active vibration control task in this publication. A simulation model was developed for analyzing the performance of a rotating hydraulic valve for producing sinusoidal pressure fluctuations and it was shown the concept of rotating gear plate produces promising results. To verify the performance of the HSG in practice an experimental device was built and the pressure waveforms were analyzed. The measured results demonstrate the HSG can produce significant pressure fluctuations up to 1 kHz frequency and in combination with a small membrane actuator 1 kN force levels can be easily achieved.

To evaluate the performance of the HSG in an active vibration control task the HSG was combined with a membrane actuator and the device was mounted to a vibrating beam. The vibrating beam was excited with a voice coil actuator and the resonance of the first mode of the beam could be successfully suppressed by using HSG.

REFERENCES:

(1) H. Ulbrich, Comparison of Different Actuator Concepts for Applications in Rotating Machinery.*International Journal of Rotating Machinery,* vol. 1, pp. 61-71, 1994.

(2) L. SUN and J. M. Krodkiewski, Experimental Investigation of Dynamic Properties of an Active Journal Bearing.*J. Sound Vibrat.,* vol. 230, pp. 1103-1117, 3/9. 2000.

(3) A. B. Palazzolo, R. R. Lin, R. M. Alexander, A. F. Kascak and J. Montague, Test and Theory for Piezoelectric Actuator-Active Vibration Control of Rotating Machinery. *J. Vib. Acoust.,* vol. 113, pp. 167-175, April 1991. 1991.

(4) J Garcia-Bonito, e. a., A novel high-displacement piezoelectric actuator for active vibration control. *Smart Mater. Struct.,* vol. 7, pp. 31, 1998.

(5) C. R. Burrows, P. S. Keogh and M. N. Sahinkaya, Progress towards smart rotating machinery through the use of active bearings.*Proc. Inst. Mech. Eng. Part C,* vol. 223, pp. 2849-2859, 12/01. 2009.

(6) R. H. Christensen and I. F. Santos, Active Rotor-Blade Vibration Control Using Shaft-Based Electromagnetic Actuation.*J. Eng. Gas Turbines Power,* vol. 128, pp. 644-652, July 2006. 2006.

(7) R. Nicoletti and I. F. Santos, Frequency Response Analysis of an Actively Lubricated Rotor/Tilting-Pad Bearing System.*J. Eng. Gas Turbines Power,* vol. 127, pp. 638-645, July 2005. 2005.

(8) I. F. Santos and A. Scalabrin, Control System Design for Active Lubrication With Theoretical and Experimental Examples.*J. Eng. Gas Turbines Power,* vol. 125, pp. 75-80, January 2003. 2003.

(9) R. Nicoletti and I. F. Santos, Control System Design for Flexible Rotors Supported by Actively Lubricated Bearings.*Journal of Vibration and Control,* vol. 14, pp. 347-374, March 1. 2008.

Flow Ripple Reduction in Power Steering Hydraulic Pumps

Leonardo Zanetti Rocha*, Nigel Johnston** and Samir N.Y. Gerges*

* Federal University of Santa Catarina (UFSC)
** University of Bath

ABSTRACT

Noise in hydraulic power steering systems is mainly generated by the hydraulic pump due to the cyclic pumping mechanism that creates pulsating flow transmitted by the fluid. This flow ripple and pressure ripple, propagating through the hydraulic circuit, interacts in a complex way with the other parts of the vehicle, generating audible noise inside the vehicle. The present work shows two ways to reduce the flow ripple amplitude generated by a vane pump through the redesigning of the pump rotating group. First, a nine-vane rotor pump is proposed and, secondly, a pump with three discharge ports is proposed. To check their results, a MatLab/Simulink based pump model was created according to the new geometrical characteristics and the results are compared with the regular pump ones. Also, a flow ripple experimental test was run using the Secondary Source Method to validate the numerical model results of the regular pump. The new designs simulation results show large flow ripple amplitude reduction (from 6dB to 16dB per harmonic) as well as frequency displacement in the discharge flow ripple spectra in both designs. Also, the simulations show perpendicular force on the pump shaft generated by the non-balanced conditions created by the new designs.

1. INTRODUCTION

Noise produced by the hydraulic power steering pump during the car operation can, in some situations, be perceived inside the vehicle as an annoying sound. The flow variations (flow ripple) generated by the pump through its natural operating process, are transmitted along the power steering hydraulic circuit, interacting with the impedance of the hoses and tubes generating structural vibration and sound emission around the circuit.

In some vehicles, the hydraulic circuit is tuned in order to avoid perceived noise inside the cabin. Flexible hoses, sometimes with tuning cables, are usually used to increase circuit compliance in order to remove unwanted frequencies or reduce the flow ripple amplitude. In fact, there are several techniques and devices (like silencers, side branches, accumulators, etc) that can be used to reduce fluidborne-noise along the propagation circuit [1, 2].

However, if a pump can be produced with a lower noise profile, this may create a solution that is independent of the hydraulic circuit and that does not require costly and time-consuming tuning of the system to achieve the wanted perceived noise reduction.

The present work is aimed at vane pumps and proposes two new rotating group designs, aimed at flow ripple amplitude reduction.

In order to achieve those results, a MatLab/Simulink based numerical-model is created from a regular pump design and validated through the experimental Secondary Source Method, developed in the University of Bath [3-5]. The simulated results of each new design are compared with the regular pump ones. Comparison is made in terms of the flow ripple amplitudes, and also in terms of force fluctuations.

2. PUMP MODEL

The numerical model of the pump is based on the general continuity equation, choosing the chamber (between a leading vane and its trailing vane) as the control volume. Similar models were created by Dickinson et al [6], Chalu [7] and Yang [8].

All the dimensions (geometric data) were loaded into the model from the drawings of a regular ten-vane automotive hydraulic pump. The pressure variation is described by equation 1:

$$\frac{dp}{dt} = -\frac{B_e}{V}\frac{dV}{dt} - Q_{IN} - Q_{OUT} - Q_{LEAK} \tag{1}$$

where Q_{IN} is the flow in the inlet port, Q_{OUT} the flow in the discharge port, B_e the effective bulk modulus, V the chamber volume and Q_{LEAK} the flow resulting by the leakage path inside the pump.

The flows through the inlet and outlet ports are calculated using the orifice equation, which relates the pressure difference between the downstream and upstream sides of a restriction:

$$Q = C_d A \sqrt{\frac{2\Delta p}{\rho}} \tag{2}$$

where C_d is the orifice flow coefficient, A the orifice area, ρ the fluid density and Δp the pressure difference between the upstream and downstream sides.

The flow leakages are calculated using the equation for laminar leakage flow between two planes, with one of them moving:

$$Q_{LEAK} = \frac{Lh^3(p - p_a)}{12\mu t} \pm \frac{uLh}{2} \tag{3}$$

where h is the clearance, L the width of the gap, t length of the gap, ω the fluid viscosity and u the velocity. The first term of this equation describes the flow through the areas when both are fixed. The second term adds the effect of relative movement of the plates (Couette flow).

Analysing the pump operation and the way how the internal parts are assembled, several leakage paths can be identified where leakage flows can be calculated. So, equation 3 is used to calculate the following leakage paths into the pump rotating group.

Vane tip leakage:

$$Q_{vtl} = \frac{L_v h_1^{3}(p - p_a)}{12\mu t} \pm \frac{\omega r L_v h_1}{2}$$ (4)

Vane end leakage:

$$Q_{vll} = \frac{(r_c - r_r)h_2^3(p - p_a)}{12\mu t_v} \pm \frac{\omega(r_c + r_r)(r_c - r_r)h_2}{4}$$ (5)

Vane slot leakage:

$$Q_{vsl} = \frac{L_v h_3^3(p - p_{out})}{12\mu\left[h_v - (r_c - r_r)\right]}$$ (6)

where L_v is the vane length, h_1 vane tip clearance, h_2 the vane end clearance, h_3 vane slot clearance, ω the rotational speed of the vanes, p the fluid chamber pressure, p_a is the adjacent (leading or trailing) fluid chamber pressure, h_v the vane height, r_c the radius of the cam ring from the centre of the rotor, r_r the rotor radius.

Figure 1 shows a schematic of a fluid chamber showing the three leakage paths corresponding to equations (4), (5) and (6). The schematic also shows a leakage path across the end faces of the rotor, q_{rli}, which is not included in the current model as it is expected to be small.

The model also needs to include the 'under-vane' flow to the chambers at the inner radial faces of the vanes, caused by the vane movement:

$$Q_{uv_i} = v_i L_v t_v$$ (7)

where $v_i = - dr_i/dt$ is the radial speed of the vane. These chambers connect to the delivery port, and the pressure helps the vane with its radial movement to maintain contact against the ring wall, along with centrifugal forces. The sum of the under-vane flows results in the pump under-vane flow.

$$Q_{uv} = \sum_{i=1}^{N_v} Q_{uv_i}$$ (8)

where N_v is the number of pump vanes (in the standard pump, $N_v = 10$).
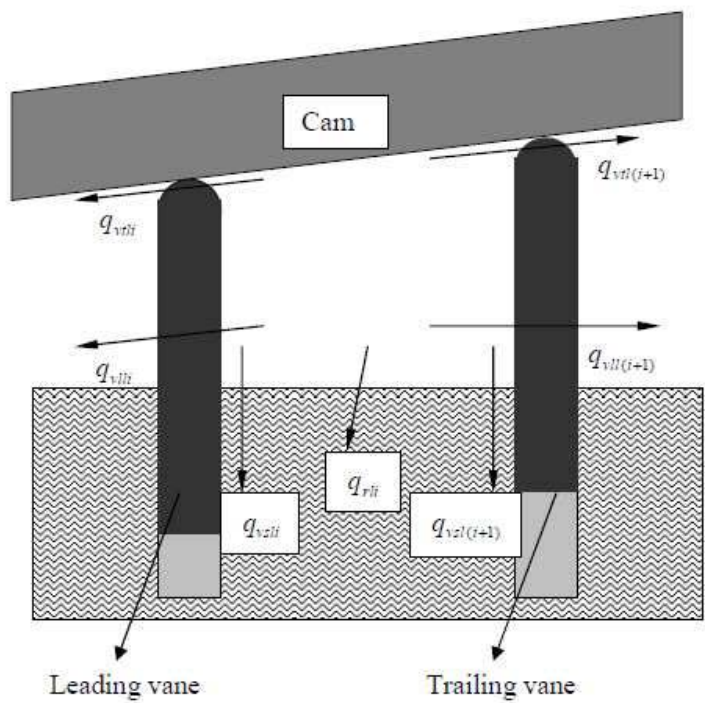
Figure 1 – Leakages flows into and out of the fluid chamber (from Chalu [7])

Some of the properties used in the simulation are listed in table 1. The fluid bulk modulus is reduced to allow for the effect of air bubbles and compliance of the rotor and vanes. The vane end clearance was estimated from the vane and rotor dimensions. The vane tip and vane slot clearances are simple estimates, and in practice these clearances would be expected to vary as the vanes move through their cycle.

Table 1 Properties used in simulation

Fluid viscosity	8.3 cP
Fluid density	870 kg/m^3
Effective bulk modulus	4×10^8 Pa
Flow coefficient for ports	0.6
Vane tip clearance	0.01 mm
Vane end clearance	0.019 mm
Vane slot clearance	0.01 mm
Rotor radius	20.7 mm
Rotor width	16 mm

3. SECONDARY SOURCE METHOD

The Secondary Source Method (SSM), developed at the University of Bath [3-5], was used to measure the pump flow ripple and the impedance.

The SSM is based on the measurements of the harmonics of pressure ripple at a series of points along the length of a rigid pipe connected either to the delivery and suction port of the test pump. The pressure ripple that occurs at two or three positions is analyzed to determine the pressure ripple.

From the Norton model shown in figure 2, is possible to find an equation to establish the pump flow at the discharge port:

$$Q_0 = Q_S - \frac{P_0}{Z_S} \tag{9}$$

where Q_s is the internal source flow, Q_0 the flow ripple at the pump discharge port, P_0 the pressure ripple at the discharge port and Z_s the source impedance.
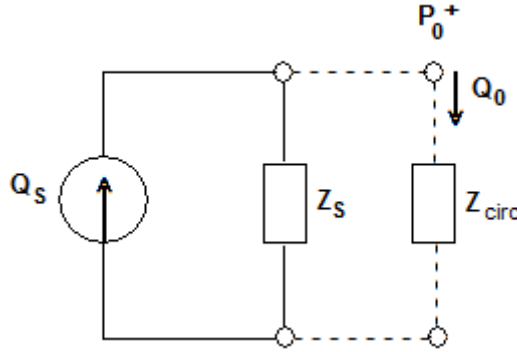
Figure 2 – Norton model of a pump.

In order to calculate the source impedance, a secondary source is situated downstream of the pump as shown in Figure 3. It can be shown that, if the second pump flow ripple frequencies do not coincide with the pump under test harmonic frequencies and the spectral leakages is negligible, Q_s can be assumed to be zero. So, equation 9 is simplified and the source impedance can be calculated as:

$$Z_S = -\frac{P_0}{Q_0} \tag{10}$$

Measurements of pressure ripple are then taken with the secondary source not operational, from which Q_s can be calculated easily through the Norton model given that Z_s, P_0 and Q_0 are known.

Even though the basic principles of SSM are presented, is not the aim of this paper to discuss it detail. More information and the detailed evaluation of the SSM can be found in [3] to [5].
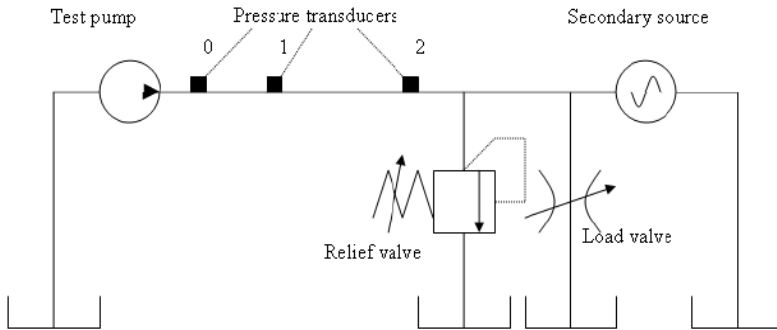
Figure 3 – Hydraulic Circuit for secondary source method [3].

The simulated results were compared with the experimental ones (measured using the SSM) and some results are shown in figure 4. These results show reasonably good agreement when the pump is run at low speed (1000 rpm in figure 4 (a) and (b)). However, for more extreme conditions (2000 rpm and 75 bar, figure 4 (c), for example), the shape of the flow does not match accurately with the simulated ones.

Whilst there are differences in the shapes of the waveforms, the peak-to-peak amplitudes are quite similar. Differences in the experimental and simulated results may be attributed to inaccuracies in the SSM as well as simplifications and assumptions in the simulation model. Uncertainties in the nature of the delivery passageway and integral flow control valve, which are not included in the model, may explain some of the differences. Nonetheless, the similarity in the amplitude and the trends of the results indicate that the results from the simulation model are reasonable and may be used to investigate the effect of changes in the design of the rotor, cam and ports.
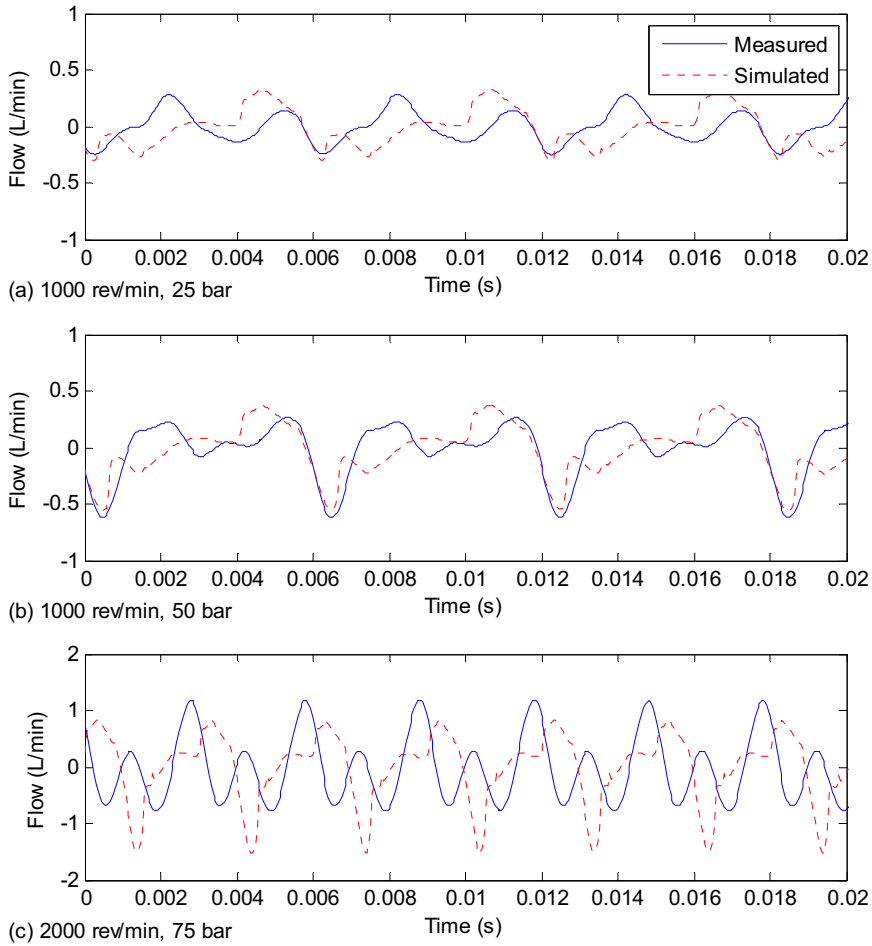
Figure 4 – Measured and simulated outlet flow ripple

4. NEW PUMP DESIGNS

4.1 Regular pump.

The regular automotive pump has two discharge ports located diametrically opposite each other, i.e., they are spaced by an angle of 180° regarding the centre of the thrust plate as the centre of the reference circumference. This kind of positive displacement pump is a so called *balanced pump* because these two opposite ports balance the force acting against the rotor (and all the walls of the chamber as well), reducing the shaft pump oscillations and overall vibrations. Figure 5 shows the inlet and outlet flow generated by just one fluid chamber. For this and all subsequent results the speed and pressure were 1000 rpm and 50 bar respectively, and all results were from simulation.
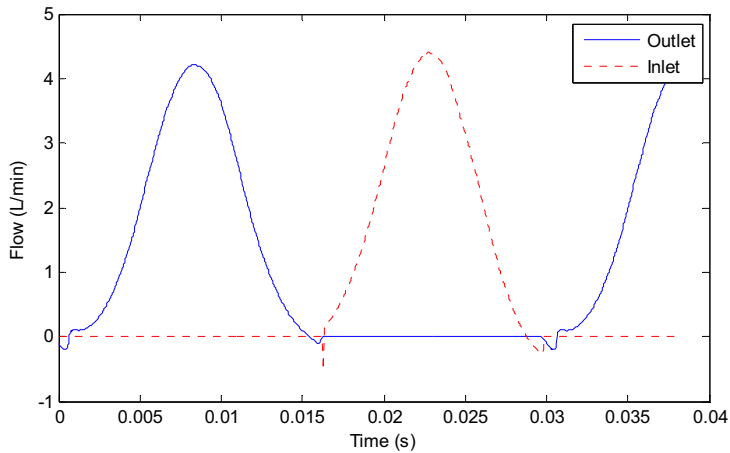
Figure 5 – Inlet and outlet flow for one fluid chamber.

As a result of this design, the discharge flow will be composed of the sum of the ten fluid chamber volumes per revolution.

The simulated waveform and amplitude spectrum of the flow at the discharge port are shown in Figure 6. The fundamental frequency f_0 is equal to the vane passing frequency f_V ($f_0 = f_V = \dfrac{N_V \Omega}{60} = 167$ Hz at 1000 rpm). This is the first and highest peak in the graph. Several smaller harmonics can also be seen.
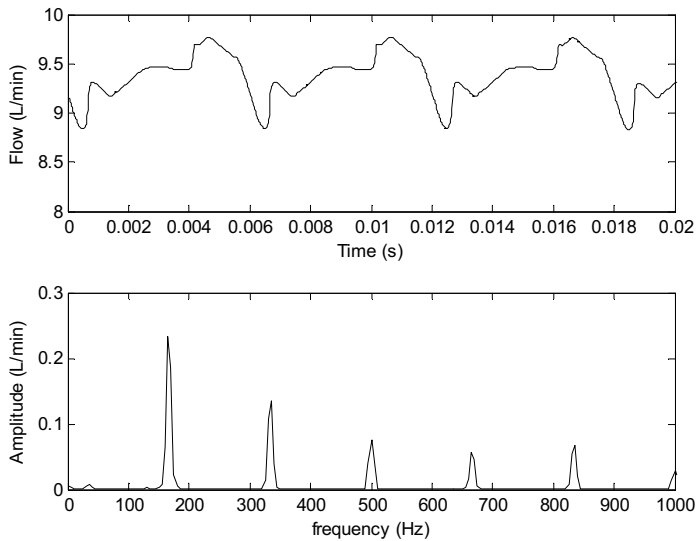
Figure 6 – Waveform and amplitude spectrum of total flow at outlet port.

4.2 Nine-vanes Pump.

In this design, the pump is modelled based on a rotating group containing a nine-slot rotor where the (nine) vanes are housed. The slots are equally spaced by an angle of 40° to each other while the other parts (ring and plates) remain the same. Figure 7 shows the rotor cross-section.
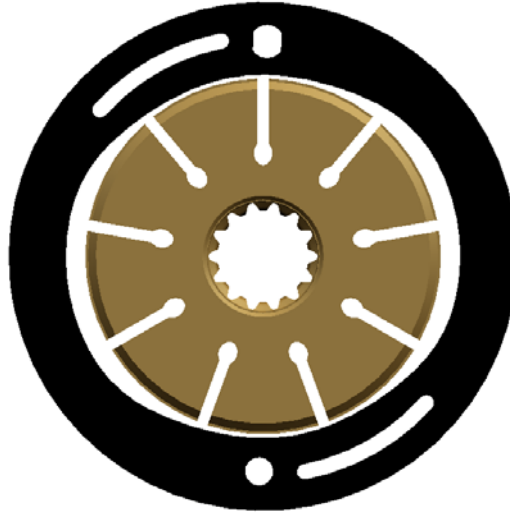
Figure 7 – Nine-vane rotor and cam.

Unlike what is found in the regular pump, where the diametrically opposite vanes (for example, the first and sixth vane) reach the discharge ports at the same time, in this nine-vanes design the opposite vanes will reach the respective discharge port in a different time, offset by a rotational angle of (40/2)°. The effect of this process is the destructive interference of the chambers' discharge flows at the outlet port, generating an increase in the flow ripple frequency and reduction in the amplitude. The predicted flow ripple waveform and amplitude spectrum are shown in Figure 8.

The mean flow level remains roughly the same in both regular and 9-vane pumps. This is because the cam profile is the same in both cases. The displacement in frequency and the amplitude reduction are clearly shown in Figure 8. Because the ports open alternately, the fundamental frequency f_0 is now given by $f_0 = 2 f_V = \dfrac{2 N_V \Omega}{60} = 300$ Hz. There is a great improvement moving the fundamental to higher frequency because the noise isolation of the hydraulic circuit tends to be better at high frequencies, further helping to reduce the noise. However the human ear is more sensitive to these higher frequencies. The tonal characteristic will be quite different, and the perception by the occupants of the car would need to be considered subjectively [9, 10].
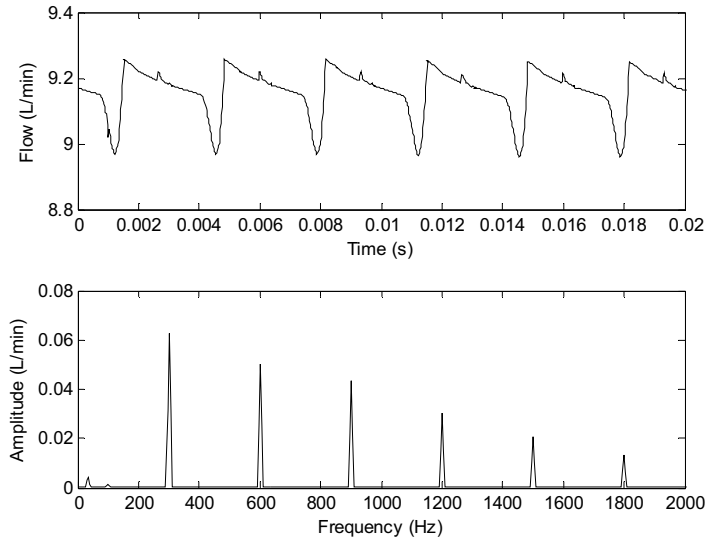
Figure 8 – Total flow at outlet port of the nine-vane design.

4.3 Three discharge port Pump.

In this design, the pump is modelled based on a rotating group composed of a standard ten-vane rotor but with three discharge and suction ports in the thrust and pressure plates. Also, the cam ring is redesigned to support the new plate's modifications as shown in Figure 9.

The 3 suction ports are spaced by an angle of 120° between themselves as well as the discharge ports. Each discharge and suction port has a radial length of 24° while the "pre-compression" zone (situated between the suction and discharge port) has a radial length of 36°, keeping the minimum angle between a leader and a trailing vane to avoid "short-circuit" between the ports. The cam profile was designed to give the same displacement as the other designs.

With this configuration, a fluid chamber reaches the beginning of a discharge port every 12° of rotation. For example, when a vane reaches the very beginning of the first discharge port, another vane will be in the middle of the second discharge port and another vane will be in the end of the third discharge port. This happens the same way in the suction port. The result of this three-phase fluid delivery is, again, the destructive interference of each delivered fluid *package*, achieving excellent outlet flow amplitude reduction. Figure 10 shows the flow ripple waveform and amplitude spectrum. The steady flow level is roughly the same as for the regular pump.
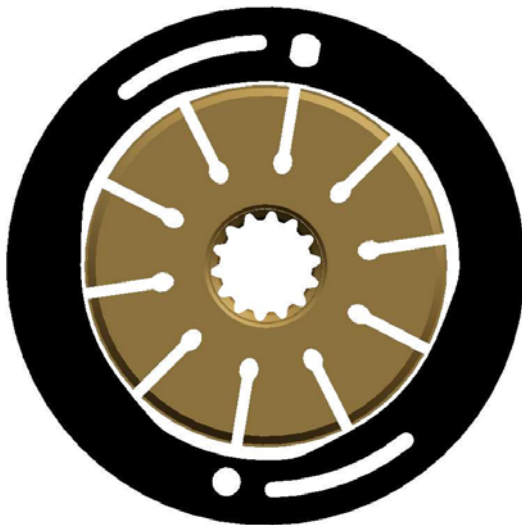
Figure 9 – Three-port cam ring internal profile.

As with the nine vanes design, in this three-port design there will be displacement in the frequency-domain. Now, the fundamental frequency f_0 changes from 167 Hz (regular pump) to $f_0 = 3f_V = 500$ Hz, changing the original tonal pump noise.
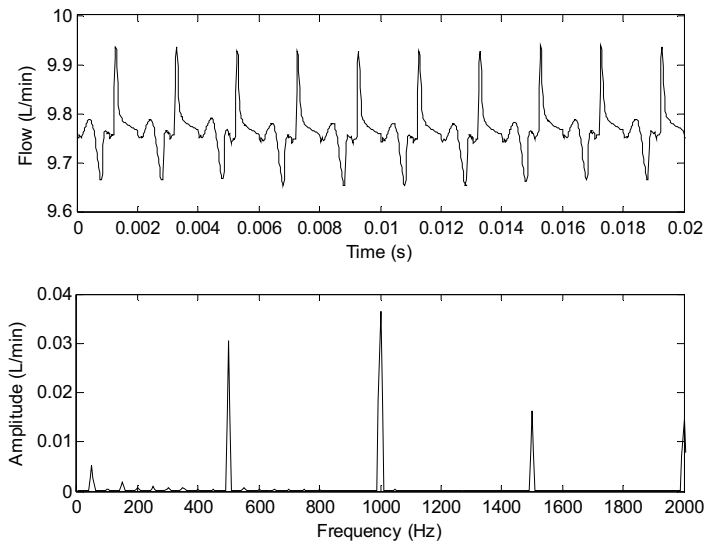
Figure 10 - Total flow at outlet port of the three discharge port design.

Figure 11 shows the reduction achieved per harmonic for each new design. This result shows a reduction around 12dB (9 vanes design) and 16dB (3 ports design) regarding the

first harmonic of the generated noise, and similar reductions for the higher harmonics. From the graph, it's possible to conclude that the 3 ports design gives the best flow ripple reduction. It should be noted that the timing of the ports and relief grooves, and the shape of the cam ring, may not be ideal for the new designs, and further improvement could be achieved by optimising the design.

Also, the frequency displacement will help the vehicle system to absorb the noise, as the high frequencies may be easier to reduce through the transmission path (fluid and air) than the low ones, and there are likely to be fewer significant harmonics.

Unfortunately the proposed designs result in instantaneous force imbalances because of the alternating port opening. The undesirable effect of these two new designs is shown in Figures 12 and 13. These graphs show the resulting perpendicular forces on the shaft and rotor during the pump operation. These were computed from the simulated pressures acting on the rotor and vanes. In the regular pump the theoretical forces would always be zero. For the modified designs there is a rapid and large force fluctuation.
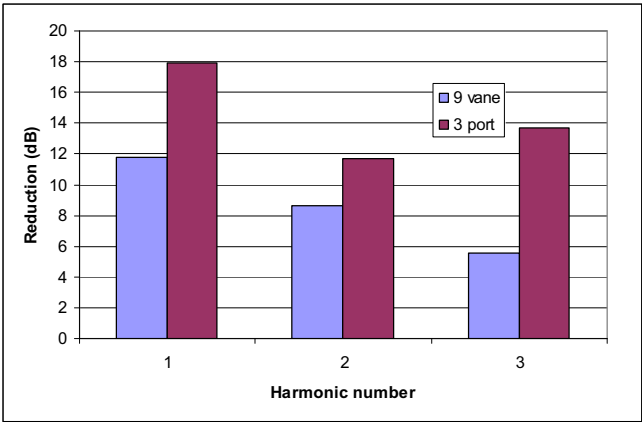
Figure 11 – Reduction in amplitude versus harmonic for the nine-vane and three-port pump designs, relative to the regular design.
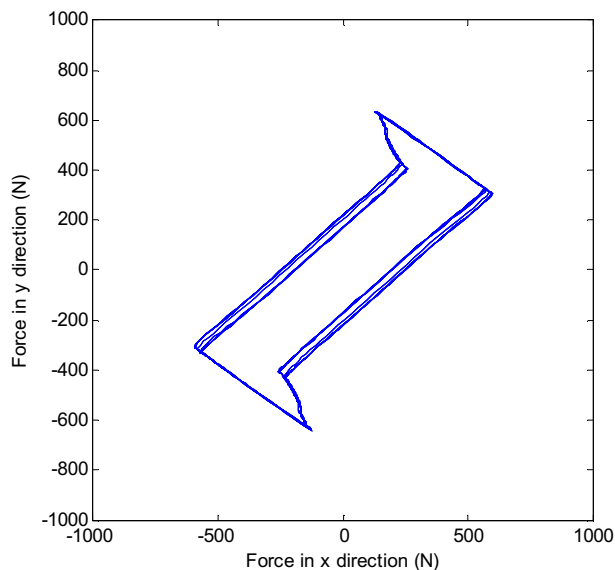
Figure 12 – Resulting lateral forces on rotor, nine-vane design.
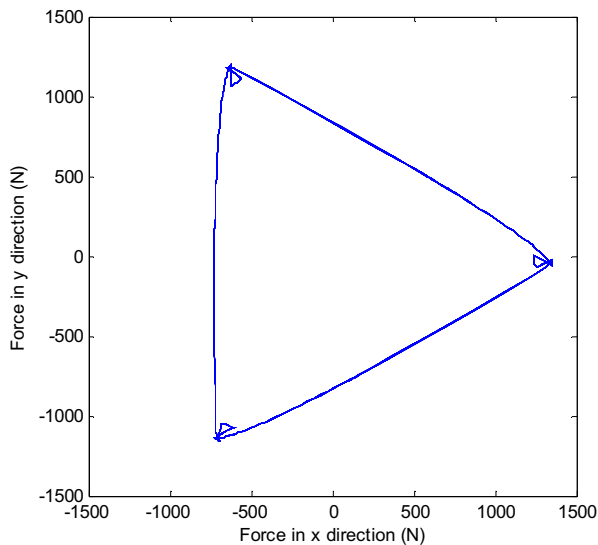
Figure 13– Resulting lateral forces on rotor, three-port design.

These resulting forces may generate excessive vibration on the shaft or housing, causing wear or even mechanical damage to the shaft bearing. Therefore, the practical use of these new rotating group designs in the regular automotive pump needs strategies to reinforce the shaft-bearing to avoid undesirable vibration and damage.

5. CONCLUSIONS

This work has shown a method to calculate and predict the outlet flow in an automotive positive displacement pump. Also, it presented an experimental method (Secondary Source Method) to rate the pump flow ripple that was used to validate the numerical results.

Two new rotating group designs were proposed; a nine-vane and a 3 port design, aiming for flow ripple amplitude reduction and frequency increase. Both designs have shown excellent flow ripple amplitude reduction (over 10dB for the first harmonic in both designs) and a displacement of the tonal noise frequency. Both effects, allied with the vehicle noise isolation capability, can improve the noise acoustical comfort and reduce the perceived noise inside the vehicle.

Nevertheless, these new designs showed an undesirable effect, presented by the non-compensated forces over the shaft-end. These resulting forces could generate extra shaft vibration and wear if the shaft and bearings are not properly designed to support those unbalanced forces.

REFERENCES

1   Gerges, S., Johnston, D.N., Rocha, L. Z. *Noise and Vibration in Fluid Power Systems*. Handbook of Hydraulic Fluid Technology, Taylor & Francis group, Florida, US, 2010.

2   Skaistis, S., *Noise control of hydraulic machinery*, Marcel Dekker, New York

3   Johnston, D.N. *Measurement and Prediction of the Fluid Borne Noise Characteristics of Hydraulic Components and Systems*. PhD Thesis, University of Bath, UK, 1987.

4   Edge, K.A., Johnston, D.N. *The `secondary source' method for the measurement of pump pressure ripple characteristics, part 1: description of method*, Proc IMechE, part A, vol. 204, 1990, pp33-40

5   Edge, K.A., Johnston, D.N. *The `secondary source' method for the measurement of pump pressure ripple characteristics, part 2: experimental results,* Proc IMechE, Part A, vol. 204, 1990, pp41-46

6   Dickinson A L, Edge K A, Johnston D N, *Measurement and prediction of power steering vane pump fluidborne noise*, SAE Transactions - Journal of Passenger Cars, vol 102, sect 6, 1993, #931294, pp1753-1761

7   Chalu, C. *Torque fluctuations and vibrations in a vane pump*. MPhil Thesis, University of Bath, UK, 2004

8   Yang, M. *Modelling and Analysis of pressure pulsations in hydraulic components and systems with particular reference to pump fault diagnosis*. PhD Thesis, University of Bath, UK, 2009

9   Rocha, L.Z., Paul, S., Jordan, R., Gerges, S. *Sound Quality Evaluations of Hydraulic Pumps*. SAE paper 2008-36-0583, São Paulo, 2008.

10   Leite, R.P., Paul., S. *Sound Quality: Basic concepts illustrated with an automotive field example.* Brazilian Acoustical Society magazine (SOBRAC), nº 37, Brazil, 2006.

Pumps and Motors

A Parameter Study of a Digital Pump

Miikka Jaurola, Kalevi Huhtala
Department of Intelligent Hydraulics and Automation, Tampere University of
Technology (TUT/IHA), Tampere, Finland

ABSTRACT

The studied digital pump differs from traditional hydraulic pumps in its flow control
method. Instead of using a valve plate or hydraulically operated check valves, the direction
of the flow in a reciprocating element of a pump or motor can be governed with
electronically controlled ON/OFF valves. Active ON/OFF valve control allows
programmability which in this case means that each reciprocating element can act as a
pumping, motoring or an idling element. Therefore hydraulic power can be transferred from
one outlet to another. Another benefit compared to a traditional valve plate is that the pre-
compression and decompression of the fluid during the work cycle can be adjusted
independent of the pressure at the outlet. This feature allows the optimization of the flow
ripple at the pump outlet.

A simulation model of a digital pump was built with a commercial software GT-Suite 7.0
and the model was verified with cylinder pressure measurements of a digital pump. Besides
concentrating on detailed modeling of the flow paths in cylinder head blocks, also the
characteristics of the active control valves are verified for the pump model. The model is
then used to study the pressure ripple behavior inside pump cylinder and in pump outlet
when active control valve parameters (e.g. nominal flow rate, response time) are varied.

In this paper the simulated results of the pressure ripple study are presented. Also the
verifying results comparing the measured and simulated results are included. The results of
the study will be used in the future studies of the digital pump-motor transformer (e.g.
controller studies and optimizing the components).

Keywords: digital pump-motor transformer, active valve control, mathematical model

1. **INTRODUCTION**

The delivery flow of a piston pump is cyclic due to the reciprocating motion of the working element. Loading the hydraulic circuit following the pump induces an oscillating pressure. Pressure oscillation induces structure and fluid born noise and excess wear in the components. Besides the circuit and the kinematics of the mechanism driving the piston, the pressure oscillation in the fluid circuit is also influenced by the device governing the direction of the delivery flow of the pump. Valve port plate and hydraulically controlled check valves are traditional examples of such devices used in piston pumps. These devices have typically fixed configuration: port plate being a disc with kidney shape holes and check valves having spring-mass-damper characteristics. Valve port plate design has been a keen interest in axial piston pump development and various methods for reducing the pressure ripple have been introduced. With port plate the main source for pressure ripple is improper pre-compression and de-compression. Nafz (1) and Harrison (2) summed up some of the solutions for improving the pre-compression in their own studies.

An alternative way to control the flow in a reciprocating pump element is utilizing electronically controlled valves. Each cylinder of the piston pump or motor has actively controlled 2/2 ON/OFF-valves acting as delivery and suction valves. Artemis Intelligent Power ltd has done pioneering research on development of pump-motor units with active valve control (3) and recently their applications have been noticed with awards. Linjama et al. presented potential improvements on system efficiency by providing bi-directional power flows between the prime mover and the hydraulic actuators with the concept of digital pump-motor unit with independent outlets (4).

Undercompression and overcompression of the fluid inside the pump cylinder must be minimized to minimize the flow ripple at pump outlet. This is not a problem if check valves are used to control the direction of the pump output flow since the hydraulic forces acting on the poppet open and close the valves. However if spool type valves are used there are no hydraulic forces to do the actuation "automatically" at the right moment. Therefore the actuation moments must be decided somehow. For example the pre-compression of the fluid inside the cylinder should be mathced with pump outlet pressure. Otherwise pressure overshoots or backflow from pump outlet back to cylinder chamber may occur. The actuation moment can be calculated with a model based controller or from a look-up table when the inlet and outlet pressures and the dimensions of the transformer unit are known. In other words, active valve control allows variable control of cylinder pre- and de-compression independent of system pressure levels. In addition to pre-compression and de-compression, also the delivery and suction valve characteristics affect the pressure ripple at pump outlet. This paper presents a simulation study where the influence of valve parameters on pressure ripple is studied as the digital pump-motor transformer is working as a pump.

2. **SIMULATION MODEL**

The pump-motor transformer studied in this paper, illustrated on left in figure 1, is modified from a six piston boxer pump. The boxer pump had check valves in the suction and delivery side to control the flow from cylinders. The main feature in the modification was

replacing the original valve blocks with custom made valve blocks featuring bi-directional 2/2 ON/OFF valves. The hydraulic diagram of the measurement installation is shown on right in figure 1. A more detailed description of the installation is presented in the experimental results by Heikkilä et al (5).
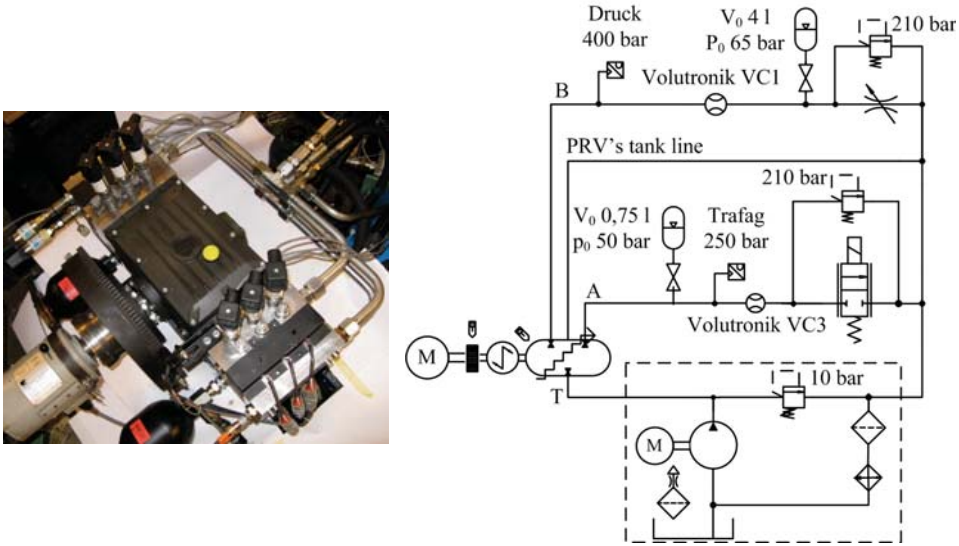
Figure 1. Test installation of a digital pump-motor transformer.

2.1 Simulation software and verification of the model

A simulation model of a digital pump-motor transformer was built with commercial software GT-Suite 7.0. The fluid flow modeling in GT-Suite involves solving the equations for conservation of continuity, momentum and energy (6):

Continuity:
$$\frac{dm}{dt} = \sum_{boundaries} \dot{m}$$

Energy:
$$\frac{d(me)}{dt} = -p\frac{dV}{dt} + \sum_{boundaries}(\dot{m}H) - hA_s(T_{fluid} - T_{wall})$$

Momentum:
$$\frac{d\dot{m}}{dt} = \frac{dpA + \sum_{boundaries}(\dot{m}u) - 4C_f\frac{\rho u|u|}{2}\frac{dxA}{D} - C_p\left(\frac{1}{2}\rho u|u|\right)A}{dx}$$

Model is split in pipe and flow split volumes that are connected to each other with orifice connections. The pipes are then discretized to subvolumes. The above mentioned equations are solved in 1D in the boundaries of each fluid volume of this so called staggered grid. This solving method gives good estimates of wave transients in high pressure (>100 bar) fluid systems but is rather time consuming. It is suitable for simulations with time intervals shorter than one second.
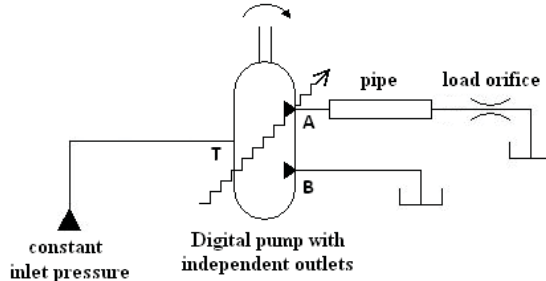
Figure 2. Schematic diagram of the simulation model.

The hydraulic circuit diagram of the simulation model is presented in figure 2. The digital pump has a 10 bar constant pressure source connected to the inlet side. The flow from pump outlet A is restricted with a load orifice. Outlet B is not used at all and is connected to tank.

The simulation model has six nearly identical submodels of each cylinder. The schematic diagram of the single cylinder model is shown in figure 3. A reciprocating motion of the piston is generated with a crank-slider mechanism object in GT-Suite with crankshaft running at 1000 rpm. Piston stroke is 16 mm and piston diameter is 20 mm which leads to a total geometrical displacement volume of 30 cm^3/rev with six cylinders.

Each cylinder has one inlet valve and two parallel outlet valves A and B. The inlet and outlet valves are modeled as simple round orifices with time dependant flow area. The diameter of the orifice is changed with a control logic which synchronizes the valve actuations with the piston displacement to realize the pumping work. Outlets A of each six cylinders are connected to each other to form port A. Likewise the outlets B and the inlets are connected to form port B and port T of the pump. This is described in more details by Heikkilä (5). As mentioned by Heikkilä, the valves used in the digital pump-motor transformer have rather large internal and external leaks. Internal valve leaks were modeled with annular leakage connections between valve upstream and downstream. External leaks were modeled in same way but from cylinder volume to tank. Laminar leakage through an annular groove is calculated from Poiseuille / Couette equation:

$$Q = \pi D_a \delta \left(\frac{\delta^2 \Delta p}{12 \mu L} - \frac{1}{2} U_{wall} \right)$$
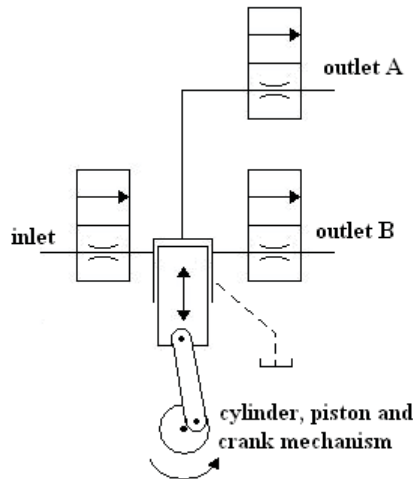
Figure 3. Schematic diagram of single cylinder submodel.

Verification was done with cylinder pressure measurements of the digital pump-motor transformer pumping fluid through an orifice connected to port A. The results show that the model is in fairly good agreement with the measurements shown in figure 4. The simulation model calculates greater pressure derivatives during the compression and decompression of the cylinder volume. Possible sources for this might be the inaccuracy in piston lift profile, different fluid properties. The piston lift profile of the pump was not measured. Instead common crank-slider kinematics was used in simulation model to calculate the piston position as the pump shaft rotates. In GT-Suite the fluid properties are governed by the state equation of the fluid and the continuity, momentum and energy equations mentioned above. For example the bulk modulus and the speed of sound are calculated as post-processing calculations instead of giving them as inputs in the model. (6).
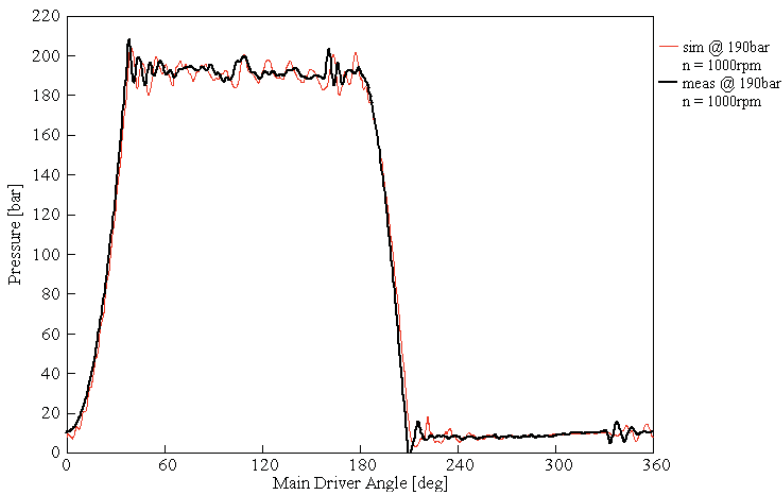
Figure 4. Measured and simulated cylinder pressure.

A number of model parameters were changed to see if a better match would be reached. Slight adjustments of the crank-slider mechanism, namely the length of connecting rod and the piston pin offset, did not result a seemingly better match. The amount of free air was also varied but this only delayed the start of pressure rise in the cylinder as the free air started to dissolve in the fluid. When free air was dissolved the pressure rate was very near to the case before adding the air as the dissolved air has very little effect on the bulk modulus of the fluid. The addition of sensible amount of internal and external leakages through the annular clearances did not soften pressure rise during compression. In this study the cylinder dead volumes were increased to get a closer correspondence between the simulated and measured pressure derivatives. Therefore simulated pressure ripple became longer in wave length compared to the measurements. The increased dead volume also increased the amplitude of pressure oscillation during the delivery stroke.

2.2 Valve parameter study

The inlet and outlet valves of each cylinder are modeled as simple orifices. The valves are actuated at certain moments of the pump work cycle. For outlet valve the opening takes place after the pre-compression of the fluid and closing is just before the top-dead-center is reached. Inlet valve is opened after the decompression and the valve is closed at bottom-dead-center.

At this point no controller is implemented in the simulation model to automatically decide the opening and closing moment. Instead the amount of pre-compression and decompression are set manually for each parameter setup by finding a proper advance or delay in relation to dead centers. A resolution of 0.25° pump shaft angle was used for this. Insufficient pre-compression and decompression causes loss of energy that is stored in the fluid under the previous compressions. In case of overcompression the energy stored in the compressed fluid inside the cylinder is lost as the fluid escapes through the outlet valve and to the pump outlet. Also if the inlet valve is held closed after the de-compression, the fluid starts cavitating. In this paper the principal rule for proper pre-compression is that flow direction through the outlet valve should be positive. This means that the fluid flows from pump cylinder to the pump output without changing direction during the delivery stroke. Same time the overcompression should be minimized.

Table 1. Different valve parameters

lift profile	pr 01, pr 02, pr 03
opening rate	0.5ms, 1ms, 5ms
nominal rate @ $\Delta p = 20$bar	20 lpm, 40 lpm

Three valve parameters are studied in this paper: valve lift profile, valve opening rate and valve nominal flow rate. The different settings for each parameter are summarized in table 1. To emphasize the effect of the above mentioned parameters, external and hydraulic forces, such as flow force, jet force or damping forces, are not acting on the spool in simulations.
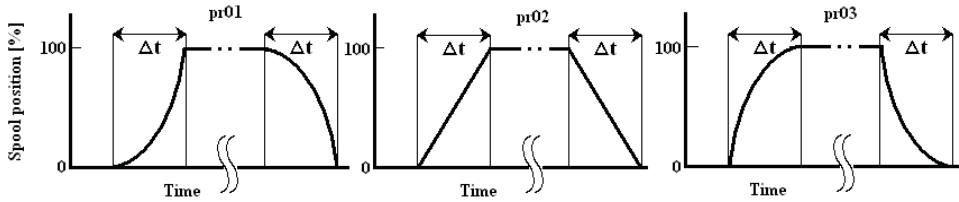
Figure 5. Valve lift profiles at with an opening rate Δt.

The opening and closing of the valve takes a certain time, Δt. In this study it is referred as the opening rate of the valve. During the opening rate the spool displacement follows a path which is referred as the valve lift profile. All sources of valve delays are excluded in this study as, up to certain point, they can be compensated with the valve control logic. The simplified shapes of the used profiles are presented in figure 5. The solver interpolates the spool position from a look-up table. Three different lift profiles were used in simulations: constant acceleration profile, linear profile and square root shaped profile using notation pr01, pr02 and pr03 with respect. Pr01 and pr02 are conventional lift profiles in hydraulic valves. Constant acceleration profile can be achieved with a solenoid and linear profile with a proportional magnet. The square root profile might be realized with proper spool overlaps and end cushioning. However the detailed discussion of how to realize the profiles in real world is not the focus of this paper. The nominal flow rate of the valve is set by changing the maximum diameter of the orifice acting as the valve. Values for diameters were 4.2mm for the bigger valve and 2.9mm for the smaller valve.

3. RESULTS

Simulations were run at pump speed of 1000 rpm with two pump outlet pressures: 100 bar and 200 bar. Figure 6 shows maximum cylinder pressures inside one cylinder chamber during a pumping cycle. The maximum value of chamber pressure may be a result of either a pressure overshoot or the pressure difference over the outlet valve depending on the boundary conditions of the compressed fluid volume; namely pre-compression and valve parameters. In most cases the maximum value was a consequence of pressure overshoot. The chamber pressure may overshoot at the beginning of the delivery as a result of too slowly opening outlet valve. Slow valve causes overdamping as the delivery flow is restricted longer before the valve is fully opened. If there is no excessive overshoot at the beginning of the delivery, the maximum chamber pressure is set by the maximum instantaneous displacement velocity of the pump piston during delivery stroke, the load orifice and the fully opened outlet valve.

As expected the maximum value for cylinder chamber pressure is bigger with the smaller outlet valve. Bigger valve releases the pressure peak faster and if no overshoot occurs, the bigger flow area generates less pressure loss over the valve. The elimination of backflow emphasizes the importance of valve lift speed in avoiding high pressure overshoots. Figure 6 shows that the acceleration of the fluid is affected by the combination of both opening rate and lift profile. The 5 ms valve with pr04 results roughly equal maximum pressure as the 0.5 ms valves. It points out that it is more important to get the spool to start moving quickly in the beginning than the actual time to reach the fully opened state. Figure 7 compares the spool displacement with different profiles and opening rates. It shows that a

5ms valve with pr03 has opened approximately 30% in the same time as the fastest valve has fully opened. Figure 6 also shows that with increasing pressure levels the valve profile becomes even more meaningful as the pressure derivative during compression increases due to the kinematics of the crank mechanism. Also valve timing and switching resolution becomes stricter as the piston velocity during pre-compression increases.
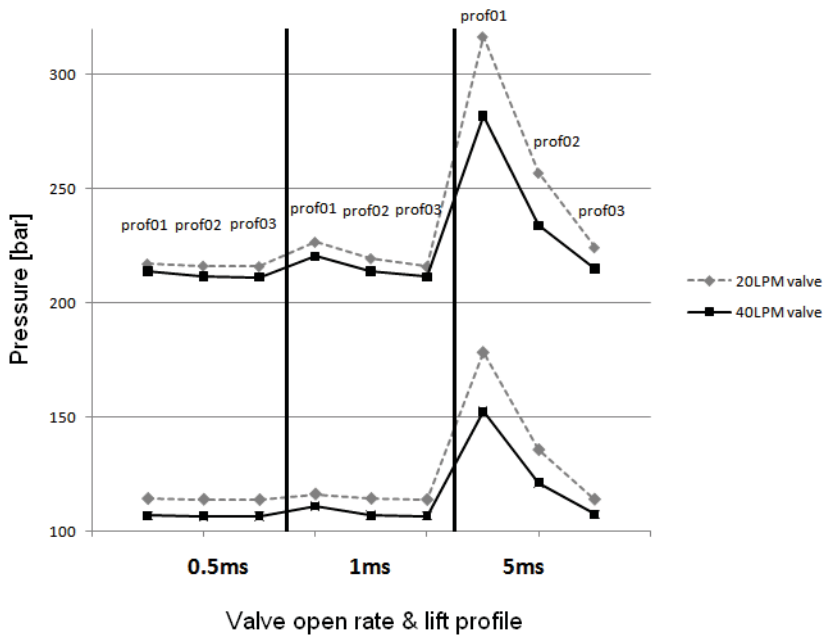
Figure 6. Maximum pressure values inside the pumping chamber with outlet pressures of 100bar (lower two) and 200bar.
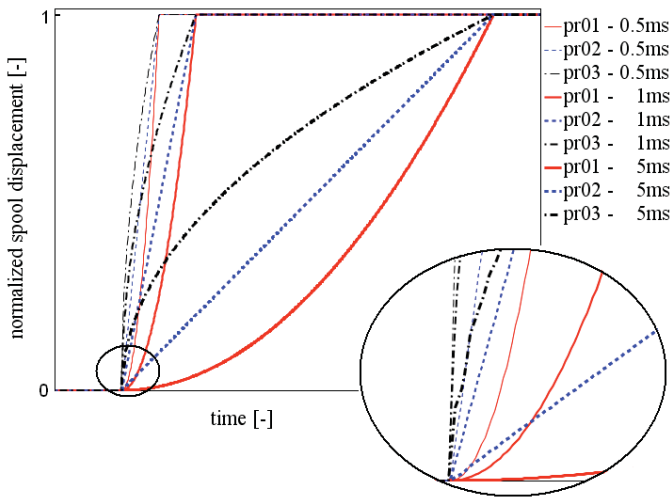
Figure 7. Spool displacement with different opening rates and opening profiles.
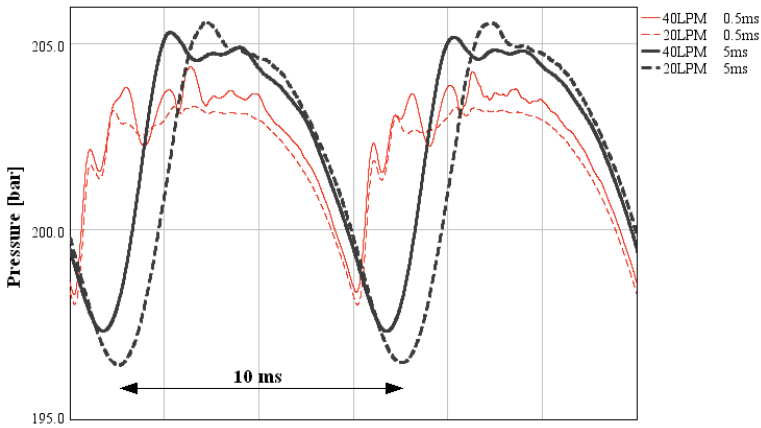
Figure 8. Simulated pump outlet pressure with valve profile 01.

The influence of valve parameters on pressure ripple at pump outlet was also studied from simulation results. An example plot of outlet pressure at port A is shown in figure 8. A six piston pump running at 1000 rpm has a base frequency of 100 Hz which dominates the power spectrum in frequency domain. Slower valves increase the amplitude of the base frequency because the delivery from each cylinder is delayed slightly due pressure overshoot inside the cylinder. A small valve increases the delay even more as the pressure peak is discharged slower. The discretization length (dx) of the outlet pipe connected to port A of the pump was increased to shorten the elapsed simulation time. With slow valves increasing the discretization length had only minor influence on the pressure amplitude. With fast valves the increase of *dx* damped the amplitude of frequencies between 800..1100 Hz.

Figure 9 shows the amplitude of the pressure ripple at the pump outlet with different valve parameters at pressure of 100bar and 200bar. The amplitude is calculated as a subtract of maximum and minimum values of outlet pressure ripple over one pump shaft revolution under steady state load condition. The amplitude is then normalized to mean outlet pressure over one shaft cycle. Amplitude of outlet pressure ripple shows similar behavior as the maximum pressure inside the cylinder. The increasing open rate again emphasizes the effect that lift profile has on the amplitude.

However, figure 9 suggests that greater valve flow capacity increases the amplitude with faster valves. High frequency oscillation is introduced as the fluid from the pump cylinder is accelerated suddenly. Smaller outlet valve damps these higher frequencies but since no excessive overshoot arise, there is no delay of delivery that would increase the base frequency. Thus the ripple amplitude is smaller. As the open rate increases the high frequency oscillation decays and the overcompression starts delaying the beginning of delivery from cylinder and the base frequency amplitude starts increasing. As overcompression occurs the increase in flow capacity starts to decrease the pressure ripple.
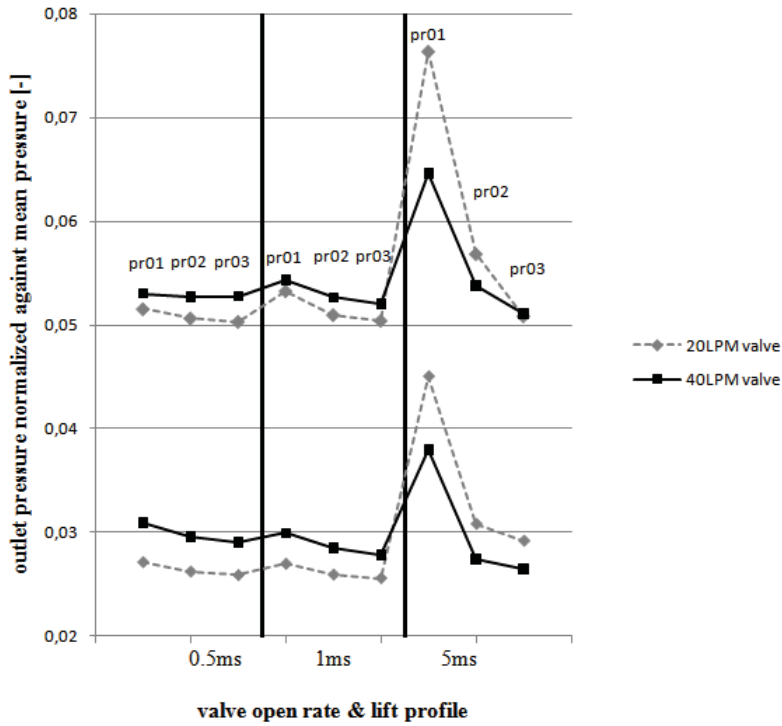
Figure 9. Normalized amplitude of the pressure ripple at pump outlet at 100bar (lower two plots) and 200bar.
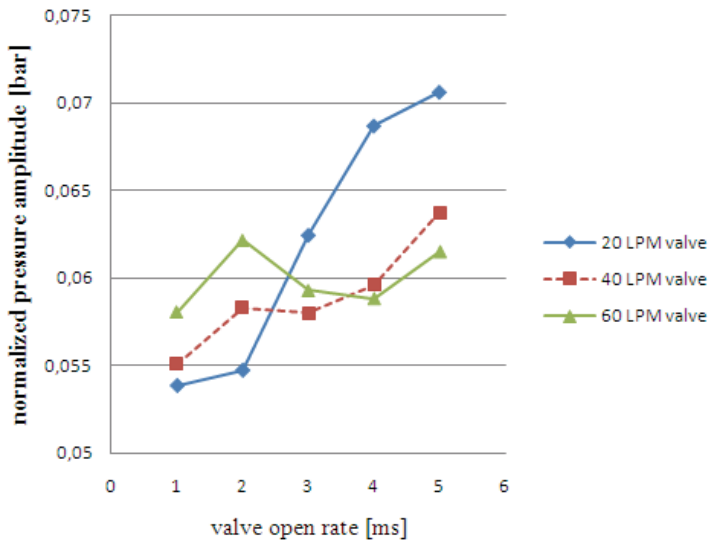
Figure 10. Influence open rate on pressure ripple amplitude at pump outlet with lift profile pr01 at 100 bar.

Additional simulations were run with extended parameter selection to get a better view of how the open rate and flow capacity act on the pressure ripple. Figure 10 shows the outlet pressure ripple amplitude at pressure of 100 bar using valve lift profile 01. Valves with nominal flow rates of 20, 40 and 60 liters per minute at Δp 20bar and opening rates of 1ms, 2ms, 3ms, 4ms and 5ms were studied. The results show somewhat linear increase of pressure amplitude for 20 LPM and 40 LPM valves. For the 60 LPM valve the amplitude is not as linear but the trend is slowly ascending as the open rate increases. As expected the rate of increase in amplitude is higher with smaller valves. Figure 11 shows the amplitude of 100 Hz base frequency with fast and slow valves at three nominal flow rates. With fast valves the nominal flow rate has only minor influence on the amplitude but as the flow rate increases a bigger valve starts to decrease the amplitude for the above mentioned reasons. Figure 12 shows how the higher order harmonics are damped with a slow valve. Most of the illustrated peaks show that bigger nominal flow rate generates bigger ripple amplitude in higher order oscillations.
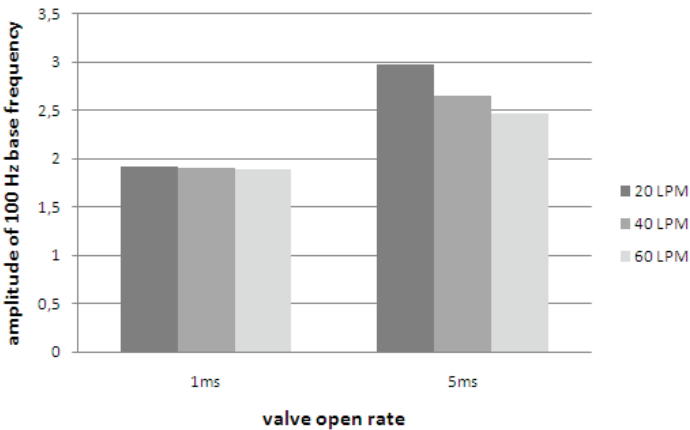
Figure 11. 100 Hz base frequency of Fast FourierTransformation taken from pressire ripple at pump outlet.
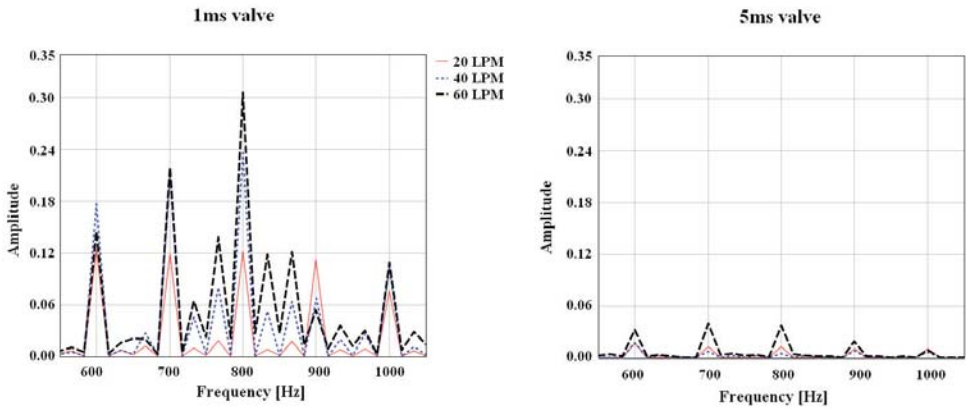
Figure 12. High frequencies amplitudes of Fast Fourier Transformation taken from pressure ripple at pump outlet..

In this study the valve parameters of both inlet and outlet valves were changed for each case and the parameters were equal. Some parameter setups resulted incomplete filling during suction stroke. In these cases the inlet pressure was not reached inside the cylinder and therefore a slightly longer precompression stroke was needed. Thus the piston velocity gets higher before the proper compression is gained and therefore boundary conditions are also different when the outlet valve is opened. As the focus of the study is in transients during the delivery phase it would have been more appropriate to keep the parameters of the inlet valve unchanged ensuring equal fillings for each case. Also a wider range of parameter values would have provided more information about the transitions in damping but due to the time consuming nature of the simulations, they could not be fitted in this study.

4. CONCLUSIONS

A simulation model of a digital piston pump with active valve control was build. Model was verified with measurement data and it was found to be in acceptable agreement with the measurements. The model was used to see how the parameters of the control valves influence the pressure transients both inside and outside the pump.

The studied valve parameters were valve lift profile, valve open rate and valve flow capacity. The maximum cylinder pressure depends on the combination of valve lift profile and open rate. Together they define the instantaneous valve spool displacement. For example a 5ms valve may cause near equal pressure peak inside the cylinder as a 0,5ms valve if a steeper lift profile is utilized at the beginning of the displacement. In other words, the faster the outlet valve starts to open, the less pressure overshoot is generated due to valve dynamics. In this study the boundary rule for comparing the valves was that no backflow at outlet valve was allowed. Therefore slower valves caused rather large overshoots in cylinder pressure.

The pressure ripple at pump outlet showed similar behavior as the cylinder pressure. However on closer look the outlet pressure ripple increased with bigger flow capacities when very fast valves were used..As the valve response time gets longer the high frequency oscillations decay and the increase in valve flow capacity starts to decrease the ripple as overshoot in cylinder pressure decreases.

NOMENCLATURE

$\dot{m}$ — boundary mass flux into volume, $\dot{m} = \rho A u$

m — mass of the volume

V — volume

p — pressure

ρ — density

A — flow area (cross-sectional)

A_s — heat transfer surface area

e — total internal energy (internal energy plus kinetic energy) per unit mass

H — total enthalpy, $H = e + \dfrac{p}{\rho}$

h — heat transfer coefficient

T_{fluid} — fluid temperature

T_{wall} — wall temperature

u — velocity at the boundary

C_f — skin friction coefficient

C_p — pressure loss coefficient

D — equivalent diameter

dx — length of mass element in the flow direction (discretization length)

dp — pressure differential acting across dx

Q — volume flow rate

D_a — diameter of the annulus

δ — thickness of annular passage

Δp — pressure differential

μ — dynamic viscosity

L — length of annular passage

U_{wall} — relative velocity between piston and bore

REFERENCES

[1] Nafz, T., Murrenhoff, H., Rudik, R., Active Systems for Noise Reduction and Efficiency Improvements of Axial Piston Pumps, Proceedings of Fluid Power and Motion Control 2008, Bath, UK.

[2] Harrison, A.M., Edge, K.A., Reduction of axial piston pump pressure ripple. Proceedings of the Institution of Mechanical Engineers, Part I: Journal of Systems and Control Engineering. Volume 214, Number 1 / 2000.

[3] Ehsan, Md., Rampen, W., Salter, S. Modeling of Digital-Displacement Pump-Motors and Their Application as Hydraulic Drives for Nonuniform Loads. ASME Journal of Dynamic Systems, Measurement, and Control, March 2000, Vol. 122, pp. 210 – 215.

[4] Linjama. M., Huhtala. K. Digital Pump-Motor Unit With Independent Outlets. 11 th Scandinavian International Conference on Fluid Power, June 2–4, 2009, Linköping, Sweden.

[5] Heikkilä. M., Tammisto. J., Huova. M., Huhtala. K., Linjama. M. Experimental Evaluation of Piston Type Digital Pump-Motor-Transformer with Two Independent Outlets. Accepted for publication in the Bath/ASME Symposium on Fluid Power and Motion Control, September. 15–17, 2010. Bath, England.

[6] Gamma Technologies, Inc. GT-SUITE Flow Theory Manual. Version 7.0. September 2009.

A Fully Coupled Thermo-Elastic Model for the Rotating Kit of Axial Piston Machines

Matteo Pelosi, Marco Zecchi and Dr. Monika Ivantysynova
Department of Agricultural and Biological Engineering & School of Mechanical Engineering, Purdue University, USA

ABSTRACT

The lubricating gaps of piston machines represent the main source of energy dissipation, fulfilling simultaneously a sealing and bearing function. The goal of the authors' research is to predict with a high level of confidence the fluid film thickness, the gap flow, the load carrying ability and the energy dissipation in those lubricating gaps. The paper presents a fully coupled fluid-structure and thermal model connecting the piston/cylinder and the cylinder block/valve plate gaps. The lubricating gaps numerical model considers the squeeze film effect due to the micro-motion of the moveable parts and simultaneously the change of fluid film thickness due to the pressure and thermal deformation of the solid parts. Heat transfer models allow obtaining the fully non-isothermal solution of the fluid flow, based on finite volume models of the mechanical bodies. The model is composed of two fully coupled modules. The first module integrates the energy equation in both cylinder block/valve plate and piston/cylinder gaps, calculating the heat fluxes generated by the viscous dissipation. These heat fluxes are then used by the second module for solving the entire temperature field in the cylinder block, bushings and pistons. A new set of surface temperature boundary conditions is thus generated for a further and more precise integration of the energy equation. Therefore, a complete thermal analysis and three dimensional temperature distribution of the entire rotating kit is obtained considering the simultaneous contribution to the heat transferred through the solid part from the cylinder block/valve plate gap and all the piston/cylinder gaps. The temperature distribution information is further used to calculate thermal stresses and the consequent thermal expansion of the bodies, predicting the impact on piston/cylinder and cylinder block/valve plate fluid film thickness.

Keywords: axial piton pump, piston/cylinder interface, cylinder block/valve plate interface, heat transfer, finite element method, lubricating gap

1. INTRODUCTION

The lubricating gaps of an axial piston machine represent a key design element. Fulfilling a sealing and bearing function, their optimization allows a significant reduction in energy dissipation and an improvement in pump and motor efficiency and power density. The goal of the authors' research is to discover the physical phenomena contributing to full film lubrication and the resulting energy dissipation in these critical machines interfaces, developing computational design and optimization methods. A better design of lubricating gaps geometry can avoid boundary friction and metal to metal contact, providing a sufficient load carrying capability in a fully developed hydrodynamic regime. Figure 1 shows the main

tribological interfaces of an axial piston machine, which unlike other lubricated contacts, represent a very complex physical system, since they guarantee simultaneously a bearing and sealing function under an oscillating load condition. Furthermore, piston, slipper and cylinder block motion are characterized by both a macro-motion derived from the kinematics of the machine and a micro scale movement resulting from oscillating pressure forces. The micro-motion is responsible for changing the fluid film thickness and for generating an additional pressure build-up due to the squeeze film effect. Fully laminar flow conditions are assumed in the lubricating gap, due to the very low Reynolds numbers defining the fluid behavior.
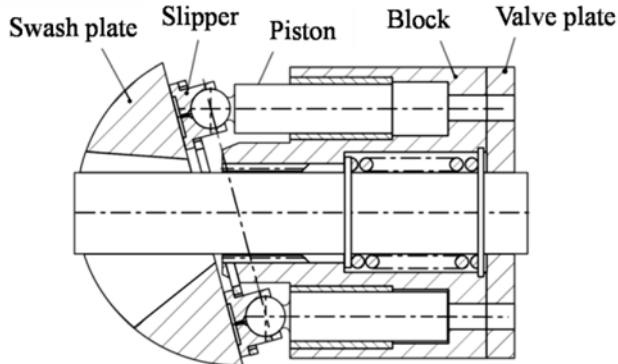
Figure 1: Lubricating gaps in an axial piston machine

The fluid film behavior is also affected by other physical phenomena happening at a micro scale level during machine operation. In particular, the impact of the heat transfer phenomena on fluid viscosity and therefore non-isothermal gap flow must be considered in order to accurately predict the gap flow. In addition, the temperature distribution in the solid bodies not only represents important information to define more accurate boundary conditions for the lubricating film, but also allows determining the thermal deflections of the surfaces forming the gap. Additional film thickness variations can be studied together with their impact on the hydrodynamic pressure build up. The content of this paper focuses on the extension of the fully coupled piston/cylinder interface model presented by Pelosi and Ivantysynova (1) to the entire rotating kit of an axial piston machine, taking advantage of the axial symmetry of the mechanical system. Moreover, the coupling of the rotating kit model with a fully coupled fluid structure model of the cylinder block/valve plate interface is necessary to obtain energy dissipation data generated in this lubricating gap. The impact of the cylinder block surface thermal deformation is also presented. The piston/cylinder interface model allows predicting the behavior of this purely hydrodynamic bearing and in particular the energy dissipated due to viscous friction which leads to a complex heat transfer problem, affecting the fluid film characteristics in different ways. On one side, the dissipated energy changes the oil viscosity and the gap load carrying ability. On the other side, the heat generated increases solid parts temperature forcing a temperature induced stress condition, which leads to bodies elastic deformation (expansion), directly affecting fluid film thickness. The surface of the solid parts is also loaded by the high operating pressures generated in the fluid film. A thermo-elastohydrodynamic lubrication condition (2-4) is therefore achieved and accurately modeled. Extensive research has been conducted in the past (5-8) in order to understand the behavior of the lubricating gaps in axial piston

machines. However, none of the developed models considered coupling of a fluid-structure non-isothermal model of the piston/cylinder interface with a fluid-structure non-isothermal model of the valve plate/cylinder block interface, in order to accurately predict the thermal and fluid film conditions in these interfaces. The authors have reached this step using in-house developed software, which allows the dynamic coupling of the various multi-domain models. In the following chapters a description of the fluid-structure non-isothermal model of the considered interfaces is followed by a detailed description of the models of the mechanical bodies, required to describe the heat transfer and surface deformation problem of the complete rotating kit. The developed fully-coupled model allows predicting the effect of material properties and surface shape of the typical tribological interfaces on the lubricating gaps overall performance and energy dissipation.

2. THE PISTON/CYLINDER FLUID-STRUCTURE NON-ISOTHERMAL GAP FLOW MODEL

The lubricating conditions taking place in the piston/cylinder interface can be modeled using two main differential equations which are then coupled with the solid domain. In particular, the Reynolds equation, Eq. 1, allows determining the pressure distribution within the lubricating gap due to hydrodynamic build up and squeeze motion.

$$\frac{\partial}{\partial \hat{x}}\left(\frac{h^3}{\mu}\frac{\partial p}{\partial \hat{x}}\right)+\frac{\partial}{\partial \hat{y}}\left(\frac{h^3}{\mu}\frac{\partial p}{\partial \hat{y}}\right)=6\left(v_{\hat{x}}\frac{\partial h}{\partial \hat{x}}+v_{\hat{y}}\frac{\partial h}{\partial \hat{y}}+2\frac{\partial h}{\partial t}\right) \tag{1}$$

The piston moves inside the cylinder following the kinematics dictated by the machine design, furthermore a relative rotation with respect to the cylinder bore occurs in most of the designs due to friction conditions in the piston/slipper interface, as stated in (10). The large oscillating external loads carried by the fluid film cause a continuous dynamic modification of the lubricating gap height, which self-adjusts its position in order to achieve a force balanced condition.
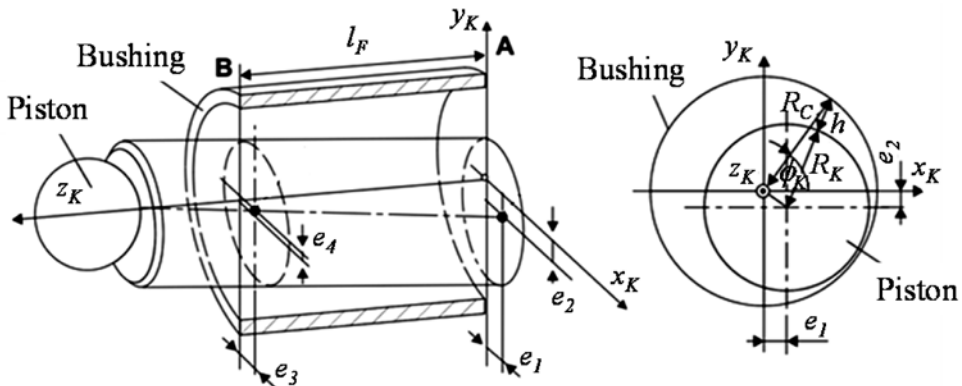
Figure 2: Piston/cylinder eccentricity and film thickness definition

This radial movement, which is in a range of only some microns, is defined as micro motion and contributes to the hydrodynamic pressure generation in the gap. Figure 2 shows the piston in its inclined position with respect to the cylinder axis z_K. The film thickness h is calculated using the distances e_1 and e_2 from C_A and the distances e_3 and e_4 from C_B, see Eq. (2) and Eq. (3). The micro-motion of the piston changes the position of the centers C_A and C_B periodically over one shaft revolution. The presented new model considers the change of fluid film thickness Δh resulting from the surface elastic deformation due to pressure and thermal loads.

$$h(z_K, \phi_K) = \sqrt{(R_Z \cos \phi_K - x_m(z_K))^2 + (R_Z \sin \phi_K - y_m(z_K))^2} - R_K + \Delta h \qquad (2)$$

The film thickness is calculated unwrapping the cylindrical gap on a Cartesian coordinate system $(\hat{x}, \hat{y})$, where:

$$x_m(z_K) = \frac{(e_3 - e_1)}{l_F} z_K + e_1 \quad \text{and} \quad y_m(z_K) = \frac{(e_4 - e_2)}{l_F} z_K + e_2 \qquad (3)$$

The Reynolds equation is solved numerically dividing the fluid film range into a structured computing grid. The iterative coupling between micro motion of the rigid parts and Reynolds equation is realized according to the method developed by Wieczorek, U. and Ivantysynova, M. (9), based on a Newton iterative algorithm which determined the film thickness from force balance calculations. The Reynolds equation is solved using a finite volume discretization, where special attention is paid to the equation source term, since the effect of the translation squeeze term due to the inclined and elastically deformed sliding surface, i.e. the piston surface, must be coupled with the effect of the elastically deformed stationary surface, i.e. the bushing and cylinder block surface. The solution of the Reynolds equation is not only affected by the surface elastic deformation of the gap surfaces but also by the values of local dynamic fluid viscosity, μ (10). Viscosity is strongly dependent on local fluid temperature, therefore to determine an accurate viscosity field, calculations on the energy transport phenomena occurring in the lubricating gap are necessary. The numerical solution of the energy equation, Eq. 4, based on a finite volume discretization allows determining the fluid film temperature distribution.

$$c_P \left(v_{\hat{x}} \frac{\partial T}{\partial \hat{x}} + v_{\hat{y}} \frac{\partial T}{\partial \hat{y}} \right) = \frac{1}{\rho} \left[\frac{\partial}{\partial \hat{x}} \left(\lambda \frac{\partial T}{\partial \hat{x}} \right) + \frac{\partial}{\partial \hat{y}} \left(\lambda \frac{\partial T}{\partial \hat{y}} \right) + \frac{\partial}{\partial \hat{z}} \left(\lambda \frac{\partial T}{\partial \hat{z}} \right) \right] + \frac{\mu}{\rho} \Phi_D \qquad (4)$$

The term on the left side of the equation correspond to the convective contributions to the energy transport, while the right side expresses the diffusive and source contributions. The source term is represented by the energy dissipation due to viscous fluid flow and is defined by Φ_D. The viscous dissipation is crucial information to solve the heat transfer problem and is a function of the fluid velocity gradients in axial and radial directions, as shown in Eq. 5.

$$\Phi_D = \left(\frac{\partial v_{\hat{x}}}{\partial \hat{z}} \right)^2 + \left(\frac{\partial v_{\hat{y}}}{\partial \hat{z}} \right)^2 \qquad (5)$$

The energy equation is solved following the method proposed by Ivantysynova, M. (11), where, for each integration step, the assumption of steady state condition is made and an unwrapped cylindrical gap on a Cartesian coordinates system $(\hat{x}, \hat{y}, \hat{z})$ is considered.

A precise determination of the pressure and temperature fields in the gap is achieved thanks to the iterative solution of the Reynolds and energy equations, considering the change in fluid properties and fluid film thickness due to the elastic deformation of the boundary surfaces. In addition, the calculation of the energy dissipated in the fluid film due to viscous flow is fundamental to determine the heat flux used as boundary condition for the rotating kit thermal model at the bushings and pistons surfaces. In particular, as discussed in the following sections, the axial symmetry of the machine is exploited. The generation of the heat transfer and surface deformation models of the cylinder block is obtained by mirroring the model of a single block section around the shaft axis.

3. THE CYLINDER BLOCK/VALVE PLATE FLUID-STRUCTURE NON-ISOTHERMAL GAP FLOW MODEL

The thermal analysis of the rotating kit of an axial piston machine involves the knowledge of the energy dissipated by the cylinder block/valve plate lubricating gap. In particular, the heat flux from the fluid interface to the cylinder block body must be determined to predict cylinder block temperature distribution. For this reason, the piston/cylinder interface model is coupled with a non-isothermal fluid-structure gap flow model of the cylinder block/valve plate interface. Similar to the piston/cylinder model, all time dependent external forces and moments are considered, which are required to be balanced by the hydrodynamic pressure field generated in the fluid film. The force balance is used to determine the gap height, $h_B(r,\varphi)$, at each volume centroid for each time step. The model considers the local change of gap height caused by the elastic surface deformation of the cylinder block and the impact that this has on the resulting hydrodynamic pressure field. The laminar fluid film model is based on the Reynolds equation expressed in polar coordinates and given below:

$$\frac{1}{r}\frac{\partial p}{\partial r}h_B^3 + \frac{\partial}{\partial r}\left(\frac{\partial p}{\partial r}h_B^3\right) + \frac{1}{r^2}\frac{\partial}{\partial \varphi}\left(\frac{\partial p}{\partial \varphi}h_B^3\right) = 6\mu\left(\omega\frac{\partial h_B}{\partial \varphi} + 2\frac{\partial h_B}{\partial t}\right) \quad (6)$$

Equation 1 demonstrates the high degree of dependence of the Reynolds Equation on the gap height, $h_B(r,\varphi)$. The model calculates the gap height between the cylinder block and valve plate at three points, h_{B1}, h_{B2} and h_{B3}, illustrated in Fig. 3. Based on these three points, the gap height for the entire fluid domain can be defined as:

$$h_B(r,\varphi) = r\sin\varphi\frac{\sqrt{\frac{1}{3}}}{R_{Ba}}(h_{B2}-h_{B3}) + r\cos\varphi\frac{1}{3R_{Ba}}(2h_{B1}-h_{B2}-h_{B3}) + \frac{1}{3}(h_{B1}-h_{B2}-h_{B3}) + \Delta h \quad (7)$$

A more accurate determination of the fluid film behavior is obtained by solving the energy equation in polar coordinates, Eq. 8. Using a finite volume discretization of the gap, the temperature distribution within the fluid is determined, considering the impact of viscous dissipation on the energy transport phenomena.

$$c_P\left(v_r\frac{\partial T}{\partial r}h_B^3+\frac{v_\varphi}{r}\frac{\partial T}{\partial \varphi}\right)=\frac{\lambda}{\rho}\left(\frac{\partial^2 T}{\partial r^2}+\frac{1}{r}\frac{\partial^2 T}{\partial \varphi^2}+\frac{\partial^2 T}{\partial z^2}\right)+\frac{\mu}{\rho}\Phi_D \tag{8}$$

The viscous dissipation term is also used to determine, analogously to the piston/cylinder interfaces, the heat flux generated in the cylinder block/valve plate lubricating gap and used as a boundary condition for the rotating kit thermal model rotating surface.

$$\Phi_D=\left(\frac{\partial v_r}{\partial z}\right)^2+\left(\frac{\partial v_\varphi}{\partial z}\right)^2+\frac{4}{3}\left(\frac{v_r}{r}\right)^2+\left(\frac{v_\varphi}{r}\right)^2 \tag{9}$$
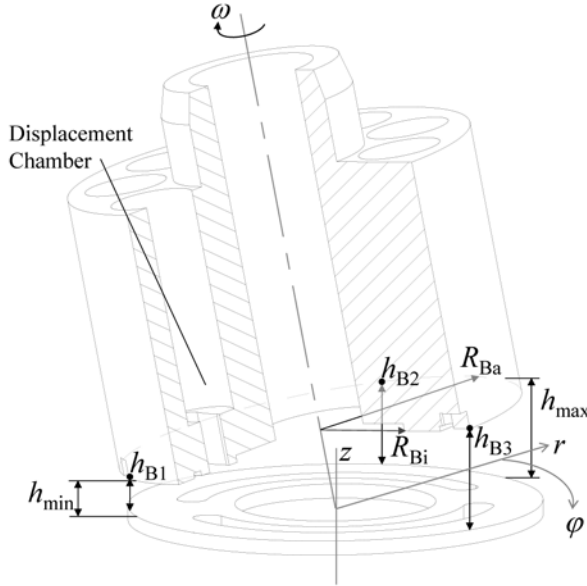
Figure 3: Cylinder block/valve plate film thickness definition

4.   THE PISTON AND CYLINDER BLOCK BODIES HEAT TRANSFER MODELS

The piston and cylinder block heat transfer models allow determining the solid parts temperature distributions based on the heat flux relative to the energy dissipated in the lubricating gap. The updated temperature information serves as new boundary condition for the gap flow non-isothermal model and to calculate the thermal stress condition of the solid parts. The heat transfer model is based on a finite volume discretization of the piston and cylinder block bodies. To describe heat conduction in the solid parts, the energy equation, Eq. 7, is significantly simplified. Since within the solid parts neither convection nor dissipation occurs, considering a Cartesian reference system, Eq. 8 becomes:

$$\left[\frac{\partial}{\partial \hat{x}}\left(\lambda\frac{\partial T}{\partial \hat{x}}\right)+\frac{\partial}{\partial \hat{y}}\left(\lambda\frac{\partial T}{\partial \hat{y}}\right)+\frac{\partial}{\partial \hat{z}}\left(\lambda\frac{\partial T}{\partial \hat{z}}\right)\right]=0 \tag{10}$$

where λ is the heat conductivity of the material.

4.1. Mesh Generation

The solid parts are discretized using a finite volume approach and a structured mesh. From the main dimensions of the solid parts the bodies are internally discretized and the main data for the finite volume solution are obtained. The piston mesh is based on the discretization of a cylindrical solid body, while the generation of the cylinder block mesh is more complex.

In particular, a single pump section is defined numerically. Subsequently, the section is rotated about the shaft axis a number of times equal to the number of pistons, until the cylinder block body is obtained. Figure 4 shows the numerical mesh generation process for the cylinder block.
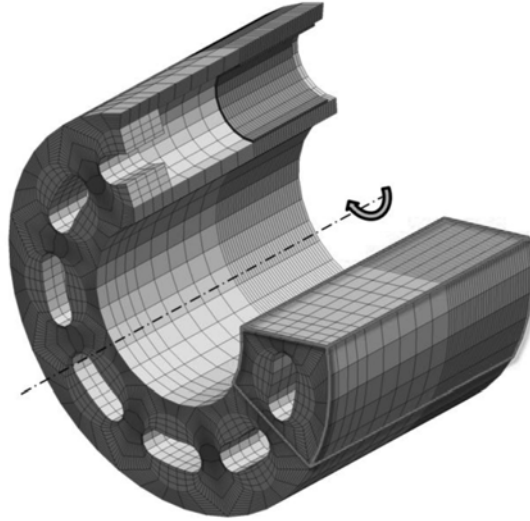
Figure 4: Cylinder block finite volume mesh generation scheme

The mesh obtained for the cylinder block is mainly unstructured because in certain regions the volume flux direction is non-orthogonal to the volume faces.

$$\Delta x = 0.5 \cdot \left(\overline{P_1 P_2} + \overline{P_3 P_4} \right)$$

$$\Delta y = 0.5 \cdot \left(\overline{P_2 P_3} + \overline{P_4 P_1} \right)$$

$$\overline{P_i P_j} = \sqrt{\left(x(P_i) - x(P_j) \right)^2 + \left(y(P_i) - y(P_j) \right)^2}$$
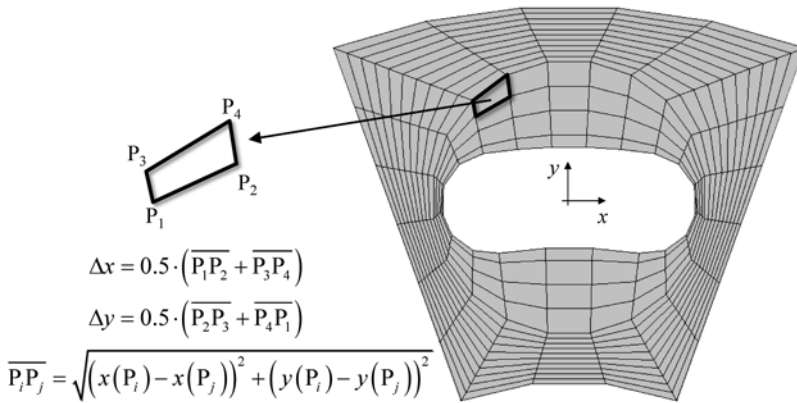
Figure 5: Cylinder block finite volume mesh simplification

However, in order to reduce the numerical complexity of the model; the unstructured mesh has been simplified to a structured mesh, neglecting the impact of the secondary gradients on the numerical solution. This approach is represented in Fig. 5.

4.2. Heat Flux Calculations

Since the temperature change in the fluid film is much faster than in the solid parts, the calculated energy dissipation is averaged over one revolution of the shaft and therefore the energy equation is considered as a quasi-steady-state problem for each time step. For each time step the fluxes of energy to the cylinder block and pistons from the lubricating interfaces are calculated based on the viscous energy dissipation, Eq. 11 and Eq. 12. . In particular, the lubricating gap is split in half and one half of the energy dissipated is transferred to one surface and the other half to the other surface, as shown in Fig. 6.
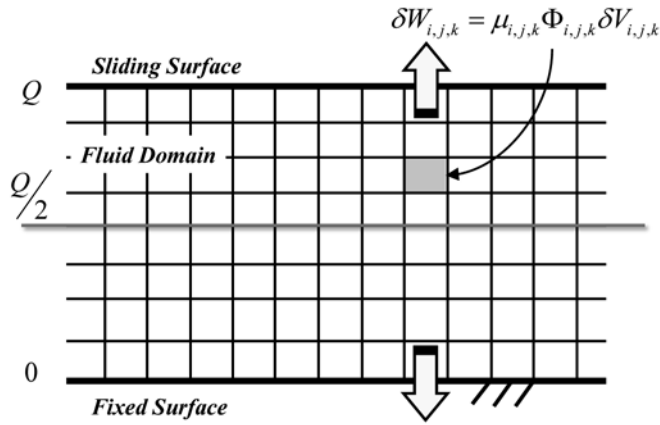
Figure 6: Instantaneous heat fluxes to surfaces from viscous energy dissipation

$$Q_{i,j}^{t \to t+\Delta t} = \sum_{k=0}^{k=Q/2} \left(\mu_{i,j,k} \Phi_{i,j,k} \delta V_{i,j,k} \right) \Delta t \tag{11}$$

$$Q_{i,j}^{t \to t+\Delta t} = \sum_{i,j,k=Q/2}^{i,j,k=Q} \left(\mu_{i,j,k} \Phi_{i,j,k} \delta V_{i,j,k} \right) \Delta t \tag{12}$$

At the end of one shaft revolution the total energy fluxes for each cell are averaged over the revolution time, Eq. 13, to obtain heat flux information used as Neumann boundary condition for the piston and cylinder block sliding surfaces.

$$\overline{W}_{i,j} = \frac{\sum_i Q_{t_i \to t_i + \Delta t_i}}{T} \tag{13}$$

4.3. Numerical Solution

The numerical solution of the temperature field in the solid parts requires the definition of precise boundary conditions. In particular, a Neumann boundary condition is used for the gap surface, where the normal gradient of temperature at the surface is known from the energy dissipation calculations carried out in the fluid model. A mixed boundary condition is assigned to the other boundary surfaces, where the value of the gradient of temperature at the surface is defined trough a specific convection coefficient. Separate convection coefficients have been estimated for the case and the displacement chamber regions. The boundary conditions are shown in Fig. 7.

Neumann Boundary
$Q_{i,j} = $ known from gap

Neumann Boundary
$Q_{i,j} = $ known from gap

Mixed Boundary
$Q_{i,j} = \alpha_{DC} \cdot (T_{i,j} - T_{DC}) \cdot \Delta t$

Mixed Boundary
$Q_{i,j} = \alpha_{CASE} \cdot (T_{i,j} - T_{CASE}) \cdot \Delta t$

Mixed Boundary
$Q_{i,j} = \alpha_{DC} \cdot (T_{i,j} - T_{DC}) \cdot \Delta t$

Mixed Boundary
$Q_{i,j} = \alpha_{CASE} \cdot (T_{i,j} - T_{CASE}) \cdot \Delta t$
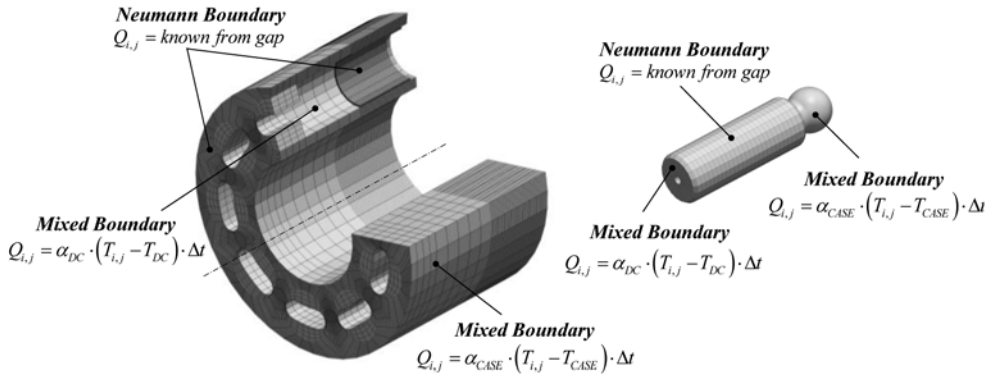
Figure 7: Cylinder block and pistons boundary conditions

The numerical solution of the equation is obtained by a discretization with a finite volume approach as described by Patankar, S. (12). The solution of the algebraic system of equations derived from the discretization is reached with a Gauss-Seidel over-relaxed iteration scheme, as shown by Jouini, N. and Ivantysynova, M. (13).
The full coupling of the heat transfer model with non-isothermal gap flow models of the piston/cylinders and cylinder/block valve plate interfaces considering parts sliding movement represent a novelty in this field of modelling axial piston machines tribological interfaces. In particular, a linear interpolation scheme, coupled with the multi-body dynamic part of the simulation code, assigns at each time step the correct flux boundary to the solid parts sliding surfaces and to the bushings of the cylinder block.

5. THE PISTON AND CYLINDER BLOCK BODIES ELASTIC DEFORMATION MODELS

A fully integrated finite element model for the fluid-structure interaction analysis represents a unique feature of this model. First studies conducted with this model have demonstrated that the micro deformations due to pressure and thermal loading that significantly influence the fluid film thickness. The finite element models of the solid parts overlay precisely their finite volume models for heat transfer calculation. The three dimensional analysis and

discretization is therefore realized using iso-parametric eight-node solids, commonly called hexahedrons in the finite element theory (14, 15).

5.1. Stress Analysis

The mesh generation discretizes the solid domain using a structured mesh for the piston and the bushing and a more complex unstructured mesh for the cylinder block. The finite element discretization and the stress-displacement analysis can be carried out with no simplifications of the mesh differently than the heat transfer analysis, which is based on finite volumes. As described by Pelosi, M.; Ivantysynova, M. (16) and Pelosi, M.; Ivantysynova, M. (17), the minimum potential energy principle is the basis of the finite element analysis. In particular, the total potential energy of an element can be defined by Eq. 14.

$$\boldsymbol{\Pi} = U_\varepsilon + V_{NF} = \frac{1}{2} \int_V \left(\mathbf{B}\,\boldsymbol{u} - \boldsymbol{\varepsilon}_T \right)^T \left(\mathbf{C} \left(\mathbf{B}\,\boldsymbol{u} - \boldsymbol{\varepsilon}_T \right) \right) dV - \boldsymbol{u}^T \begin{Bmatrix} F_{x1} \\ F_{y1} \\ F_{z1} \\ \vdots \\ F_{xn} \\ F_{yn} \\ F_{zn} \end{Bmatrix} \tag{14}$$

The total energy in the element $\boldsymbol{\Pi}$ is minimized relative to the nodal vector $\boldsymbol{u}$, differentiating the total energy with respect to each displacement and setting each resulting equation equal to zero.

$$\mathbf{k}\,\boldsymbol{u} = \int_V \mathbf{B}^T \mathbf{C}\,\mathbf{B}\,dV \begin{Bmatrix} u_{x1} \\ u_{y1} \\ u_{z1} \\ \vdots \\ u_{xn} \\ u_{yn} \\ u_{zn} \end{Bmatrix} = \begin{Bmatrix} F_{x1} \\ F_{y1} \\ F_{z1} \\ \vdots \\ F_{xn} \\ F_{yn} \\ F_{zn} \end{Bmatrix} + \int_V \mathbf{B}^T \mathbf{C}\,\boldsymbol{\varepsilon}_T\,dV = F_E + F_T \tag{15}$$

The resulting matrix equation, Eq. 15, is the working force deflection equation for the element and knowing the expression for the element stiffness matrix $\mathbf{k}$, the nodal forces vector due to external loads F_E and the nodal forces vector due to thermal induced stress F_T, the nodal displacements vector $\boldsymbol{u}$ is solved, upon imposing the constraints conditions. The solution of the system of equations is obtained using a conjugate gradient iterative approach. The thermal deformation of the solid parts is calculated at the end of each revolution, after the determination of the parts temperature distribution and thermal stresses. A new thermal deformation is calculated at the beginning of each revolution and kept constant until the next revolution is reached. On the other side, the pressure deformation must be recalculated at each of the Reynolds equation iterative steps being directly connected to the lubricating gaps dynamic pressure field. In order to reduce the simulation time, an influence matrix scheme has been implemented for the lubricating interfaces, as described by Pelosi and Ivantysynova (18), which avoids the full solution of the linear system of equations at each deformation calculation. An interpolation scheme, considering piston and cylinder block

sliding motions, assigns the correct surface elastic deformation to the fluid film. The pressure elastic deformation is therefore superimposed to the thermal elastic deformation.

5.2. Constraint Conditions

The constraints conditions on the solid parts represent a crucial aspect in the determination of surface elastic deformation. Proper constraint conditions must be therefore assigned to the pistons and the cylinder block models, according to their degrees of freedom. In particular, the constraint condition on the piston body is designed to obtain an axial constraint. In this way, the nodes of the solid part are free to move in radial direction, allowing focusing on the impact of the surface elastic deformation on the fluid film thickness. The cylinder block FEM model is constrained about its neck, to allow a complete freedom in the displacement of the mesh nodes in proximity of the sliding surfaces, being also in this case the determination of the surface elastic deformation affecting film thickness the final goal of the analysis.

6.   NUMERICAL SOLUTION ALGORITHM

The algorithm of the program can be explained referring to Fig. 8. The algorithm of calculation is the same for piston/cylinder and cylinder block/valve plate interfaces. The two interfaces are solved in sequence, communicating the exchanged external forces.
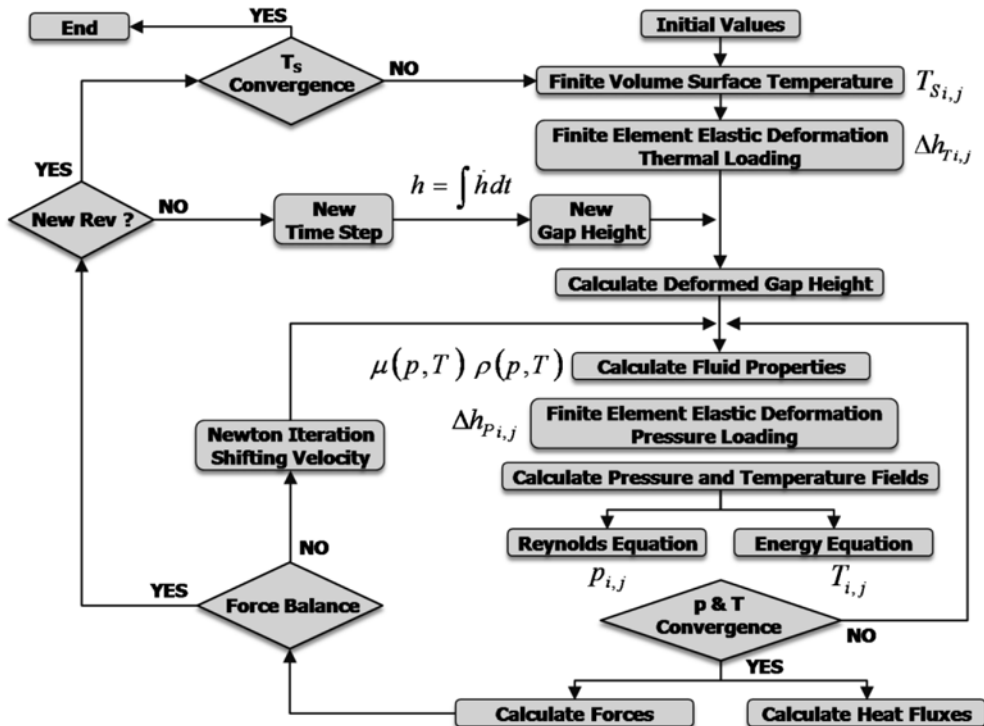
Figure 8: Numerical iterative algorithm scheme

The Reynolds and energy equations are solved iteratively for the lubricating interface updating the fluid properties (viscosity and density) and the surface elastic deformation due to the dynamic pressure field until convergence of pressure and temperature is reached. The load carrying capability of the gap is then determined together with the calculation of the external forces acting on the solid bodies. An outer loop based on a Newton iteration scheme, varies the shifting velocity of the part to achieve a load balanced condition. Furthermore, the heat fluxes due to the energy dissipated in the fluid film are determined at each time step. At the end of the revolution, the temperature distributions for piston and cylinder block are determined. These temperatures are used in the next revolution as a more accurate condition for non-isothermal gap flow calculations and to calculate based on finite element analysis the thermal expansions. The iteration continues until stable temperatures are reached.

7.   SIMULATION RESULTS

A simulation of an axial piston machine under the operating conditions shown in Table 1 has been carried out and is reported in this paper. Key parameters affecting the simulation results are represented of course by the material properties assumed for the mechanical bodies.

Differential Pressure	130	bar
Angular Speed	1000	rpm
Case Temperature	57.5	°C
Temperature at High Pressure Port	48.1	°C
Temperature at Low Pressure Port	43.3	°C

Table 1: Simulated operating conditions

In particular, a standard steel cylinder block with brass bushings has been adopted. Also the piston is assumed to be manufactured with the same type of steel. The material properties necessary for the heat transfer and elastic deformation calculations are shown in Table 2.

Material Properties	Pistons	Block	Bushings
Young Modulus[GPa]	210	210	130
Poisson Ratio [-]	0.27	0.27	0.31
Thermal Expansion Coeff. [E-6/°C]	12	12	19

Table 2: Mechanical parts material properties
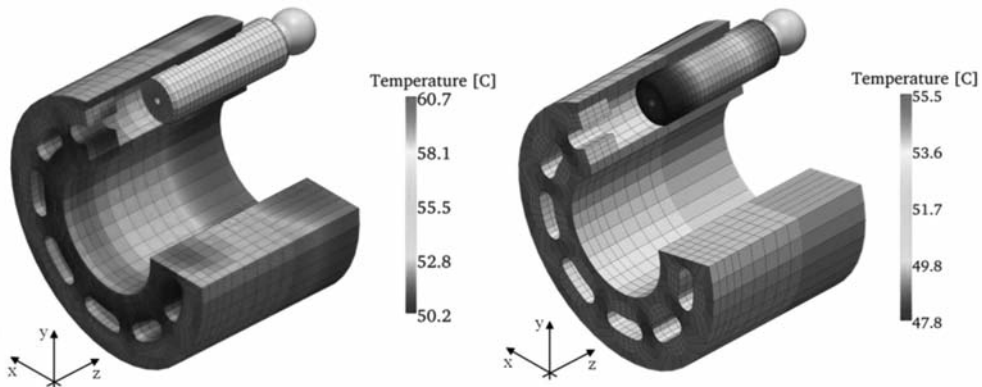
Figure 9: Temperature distributions in the piston and in the cylinder block

Figure 9 shows the temperature distribution calculated by the model for the solid parts. On the left the temperature distribution in the cylinder block is shown, while on the right the temperature distribution in the piston body is represented for the same operating and boundary conditions. The gradients of surface temperature are taken into account and used as more accurate boundary for the non-isothermal gap flow calculations. Other interesting information can be derived from the results given by the finite element analysis concerning thermal strain calculations. In particular, Fig. 10 shows the elastic deformation of the parts in the (x,y) plane, which represents for the piston/cylinder interface the radial direction defining fluid film thickness. On the left, the total thermal deformation of the cylinder block is shown; while on the right the thermal expansion of the piston is represented as well. The modification of fluid film thickness due to the expansion of the solid bodies is significant and affects hydrodynamic pressure build-up.
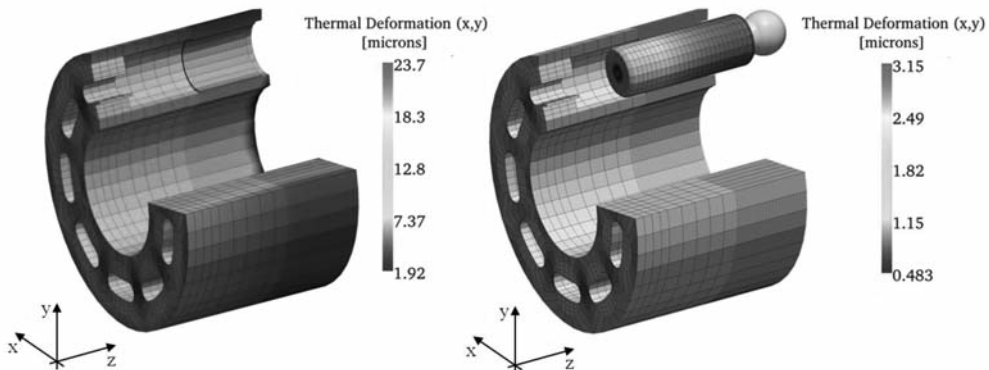
Figure 10: Thermal elastic deformation cylinder block and piston

The thermal elastic deformation happens also in cylinder block axial direction and this change in film thickness is directly affecting the cylinder block/valveplate lubricating gap hydrodynamic performance. In particular, Figure 11 shows the z-direction elastic deformation of the cylinder block sliding surface, the remaining portion of the block being neglected in the representation. The magnitude of this deformation is significant and cannot

be neglected during the study of this lubricating gap, since it introduces additional gradients of film thickness which directly affect the hydrodynamic performance of the interface.
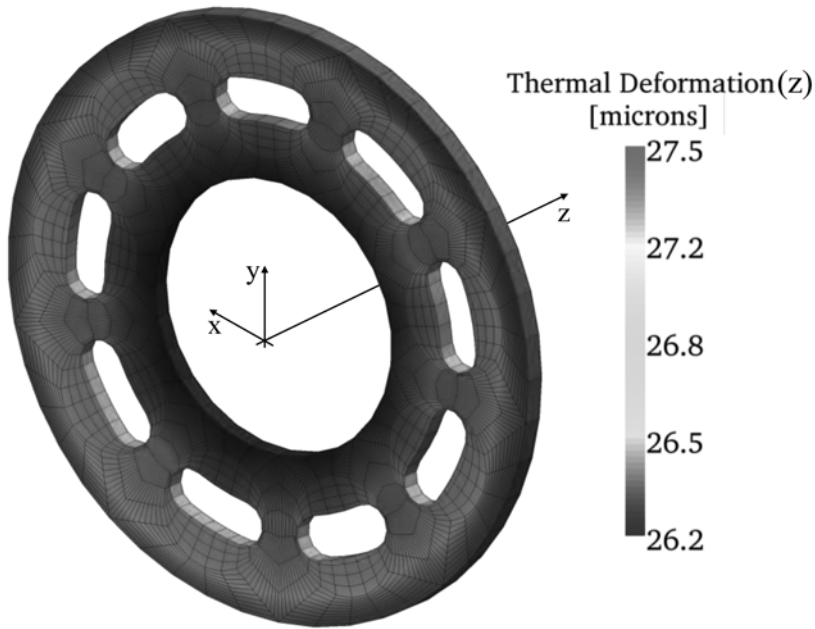
Figure 11: Thermal elastic deformation cylinder block surface in gap height direction

8.   CONCLUSIONS

A fully-coupled thermal model for the rotating kit of an axial piston machine has been presented in this paper. The model solves the heat transfer phenomena trough the piston and cylinder block solid parts considering the impact of different material properties and energy dissipation. The energy dissipated due to viscous friction in the lubricating gaps is calculated solving non-isothermal finite volume models for the piston/cylinders and cylinder block/valve plate interfaces. Furthermore, particular attention has been paid to the description of the coupling between the finite volume model responsible for the solution for the heat transfer problem trough the solid parts and the finite element model developed for the prediction of the surface elastic deformation of the rigid bodies. Numerical results are shown for cylinder block and pistons temperature distributions. The predicted temperature induced surface elastic deformation is shown for one operating condition and the corresponding variation of fluid film thickness for the sliding surfaces. As nest steps the authors will use the new model to compare simulation results with various measured parameters, like the dynamic pressure field between piston and cylinder, temperature fields and viscous friction. A large amount of measured results is available to the authors thanks to the previous research conducted by the authors' research group.

9. NOMENCLATURE

$\mathbf{B}$	Shape matrix	-
$\mathbf{C}$	Constitutive matrix	-
c_P	Fluid heat capacity	J/kg K
DC	Displacement chamber	-
dV	Element differential volume	
F_{xi}, F_{yi}, F_{zi}	Nodal external forces	
h	Gap height	m
$\Delta h_{i,j}$	Gap elastic deformation	m
h_{Bi}	Cylinder block/valve plate gap	
i, j, k	Index for the element nodes number	-
$\mathbf{k}$	Element stiffness matrix	-
p	Pressure	Pa
p_{ref}	Reference pressure	Pa
Δp	Differential pressure	Pa
t	Time	s
Δt	Differential time	s
v_x	Fluid velocity x direction	m/s
v_y	Fluid velocity y direction	m/s
v_r	Fluid velocity radial direction	m/s
v_φ	Fluid velocity circumferential direction	m/s
$\boldsymbol{u}$	Nodal displacements vector	m
$\mathbf{u}_{GAP}$	Influence matrix gap surface reference loading	m
$\mathbf{u}_{DC}$	Influence matrix DC loading	m
V_{NF}	Nodal forces loading energy potential	Nm
T	Total revolution time	s
ε	Strain vector	-
ε_T	Thermal strain vector	-
φ	Shaft angular rotation	rad
λ	Fluid thermal conductivity	W/mK
ρ	Fluid density	kg/m^3
μ	Fluid dynamic viscosity	Pa·s
r, φ	Polar coordinates cylinder block	
Π	Body total potential energy	Nm

10. REFERENCES

1. **Pelosi, M.; Ivantysynova, M.** 2009. A Novel Thermal Model for the Piston/Cylinder Interface of Piston Machines. *Bath ASME Symposium on Fluid Power and Motion Control (FPMC2009), [DSCC2009-2782],* Hollywood, USA.

2. **Kim, K.; Sadeghi, F.** 1992. Three-dimensional temperature distribution in EHD lubrication: Part I - circular contact. *ASME Journal of Tribology,* 114, pp. 32–41.

3. **Kim, K; Sadeghi, F.** 1993. Three-dimensional temperature distribution in EHD lubrication: Part II - point contact and numerical formulation. *ASME Journal of Tribology*, 115, pp. 36–45.

4. **Hamrock, B.; Schmid, S.; Jacobson, B.** 1994. *Fundamentals of Fluid Film Lubrication*. Marcel Dekker, New York, Chap. 18–23, pp. 451–678.

5. **Tanaka, K.; Kyogoku, K.; Nakahara, T.** 1999. Lubrication characteristics on sliding surfaces between piston and cylinder in a piston pump and motor (Effects of running-in, profile of piston top and stiffness). *JSME International Journal, Series C (Mechanical Systems, Machine Elements and Manufacturing)*, 42(4), pp. 1031–1040.

6. **Dowd, J. R.; Barwell, F. T.** 1974. Tribological interaction between piston and cylinder of a model high pressure pump. *Transactions ASLE*, 18, pp. 21–30.

7. **Fatemi, A.; Wohlers, A.; Murrenhoff, H.** 2008. Simulation of Elastohydrodynamic Contact between Piston and Cylinder in Axial Piston Pumps. *Proc. of the 6th International Fluid Power Conference*, Dresden, pp. 539–552.

8. **Huang C.; Ivantysynova M.** 2006. An advanced gap flow model considering piston micro motion and elastohydrodynamic effect. *4th FPNI Phd Symposium*, Sarasota, Florida.

9. **Wieczorek, U.; Ivantysynova, M.** 2002. Computer Aided Optimization of Bearing and Sealing Gaps in Hydrostatic Machines - The Simulation Tool CASPAR. *International Journal of Fluid Power*, Vol. 3, No.1, pp. 7-20.

10. **Ivantysyn J.; Ivantysynova M.** 2001. *Hydrostatic Pumps and Motor, Principles, Designs, Performance, Modeling, Analysis, Control and Testing*. New Delhi. Academic Books International.

11. **Ivantysynova, M.** 1985. Temperaturfeld im Schmierspalt zwischen Kolben und Zylinder einer Axialkolbenmaschine. *Maschinenbautechnik 34*, pp. 532–535.

12. **Patankar, S.** 1980. *Numerical heat Transfer and Fluid Flow*, Hemisphere Publishing Corporation, New York, Chap. 3–5, pp-25–109.

13. **Jouini, N.; Ivantysynova, M.** 2008. Valve Plate Temperature Prediction in Axial Piston Machines. *Proc. of the 5th FPNI PhD Symposium*, pp. 95–110.

14. **Hartley G.** 1986. *Fundamentals of The Finite Element Method*. Macmillan Publishing Company. New York.

15. **Felippa C.; Clough R.** 1969. The Finite Element Method in Solid Mechanics. *SIAM-AMS Proceedings II, American Mathematical Society, Providence, pp. 210-252*

16. **Pelosi, M.; Ivantysynova, M.** 2008. A New Fluid Structure Interaction Model for the Slipper-Swashplate Interface. *Proc. of the 5th FPNI PhD Symposium*, pp. 219–236.

17. **Pelosi, M.; Ivantysynova, M.** 2009. A Novel Fluid-Structure Interaction Model for Lubricating Gaps of Piston Machines. *Proc. of the 5th Fluid Structure Interaction Conference*, Crete, pp. 13-24.

18. **Pelosi, M.; Ivantysynova, M.** 2010. A Simulation Study on the Impact of Material Properties on Piston/Cylinder Lubricating Gap Performance. *Proc. of the 6th FPNI PhD Symposium*, pp. ...

19. **Lasaar, R.; Ivantysynova, M.** 2002. Advanced gap design – basis for innovative displacement machines. *Proc. of 3. IFK Internationales Fluidtechnisches Kolloquium*, pp. 215-230, ISBN 3-8265-9901-2, Aachen, Germany.

20. **Ivantysynova, M.; Huang, Ch.** 2002. Investigation of the gap flow in displacement machines considering the elastohydrodynamic effect. *5th JFPS International Symposium on Fluid Power*. Nara, Japan. pp. 219-229.

21. **Ivantysynova, M.; Huang, Ch.; Behr, R.** 2005. Measurements of elastohydrodynamic pressure field in the gap between piston and cylinder. *Bath Workshop on Power Transmission and Motion Control PTMC 2005,* Bath, UK, pp. 451 – 465.

22. **Ivantysynova, M.; Lasaar, R.** 2004. An investigation into Micro- and macro geometric design of piston/cylinder assembly of swash plate machines. *International Journal of Fluid Power*, Vol. 5 (2004), No.1 , pp. 23-36.

23. **Ivantysynova, M.; Huang, C.; Japing, A.** 2006. Determination of gap surface temperature distribution in axial piston machines. *Proc. of the 2006 ASME International Mechanical Engineering Congress*, IMECE2006-15249.

Analysis and optimisation of the pressure reversing process of external gear pumps

Martin Petzold; Walther Wustmann; Siegfried Helduser; Jürgen Weber
Institut für Fluidtechnik, TU Dresden, Germany

ABSTRACT

External gear pumps are widely used in Fluid Power applications. Despite their relatively simple design, their volumetric and hydro mechanical efficiency is rather high. On the other hand, the rates of pressure decrease during tooth engagement are very high, causing highly dynamic force alterations and increased pressure pulsations at the low- and high-pressure ports. During the enlarging of the displacement volumes the occurrence of cavitation on the low-pressure side is very likely. High noise emissions for this pump design are typical.

The paper presents investigations of the pressure changes in external gear pumps using Computational Fluid Dynamics (CFD). The CFD method can be used for the spatial resolution of fluid mechanical details without analytical assumptions to describe flow resistances. These benefits are outweighed by the time needed for the generation of dynamic flow grids. The commercial software *ANSYS FLUENT* is used to develop a 3D-CFD pump model. Comparisons are being made with experimental testing. Noise reduction potential is analysed by developing several variants of the pressure reversing geometry. As outstanding result of the investigation, the noise emission (acoustic power) of the pump could be reduced by 2 - 7 dB(A), whereas the pressure pulsations at the suction and delivery port of the pump were also decreased by up to 50 %. The investigations were funded by the German Research Foundation (Deutsche Forschungsgemeinschaft DFG).

1. INTRODUCTION

External gear pumps are characterised as compact displacement units with a constant displacement volume. With their relatively simple design they reach a high degree of reliability and robustness. However, this pump design is often characterised by an increased level of noise emission as a consequence of the rather high pressure decrease rates during the tooth engagement phase. Compared with (axial) piston pumps, external gear pumps exhibit the highest acoustic power levels for the same pump size. The highly dynamic force variations initiated by the pressure reversing processes cause the vibration of the pinions. These oscillations are transmitted by the tooth tips, the bearings and the fluid enclosed inside the intertooth volumes next to the housing, where it is emitted as airborne noise to the environment /F1/. Furthermore, the pressure pulsations of these pumps on the high and low pressure side are comparatively high. During the highly dynamic pressure decrease of the

enclosed oil volume, the occurrence of shear-layer cavitation is very likely. In combination with cavitation induced by a hydraulic undersupply and filling losses during the enlargement of the intertooth volumes on the suction side cavitation erosion and damages to parts of the pump can appear. These factors together lead to an increased noise emission and a limited durability of this pump type.

This paper continues previous investigations on this topic at the Institut für Fluidtechnik /W1, W2, W3/. An external gear pump with single flank sealing with a displacement volume of $V_1 = 19$ cm³ and a number of teeth of $z = 13$ is used as demonstrator. The CFD studies were performed for a delivery pressure of $p_1 = 120$ bar and a rotary speed of $n_1 = 1500$ min^{-1}. This operating point was taken as it lies in the middle of the admissible speed and pressure range of the analysed pump. Furthermore, cavitation is of minor importance for the operating behaviour. The pressure fluid is mineral oil ISO VG 46.

The CAD geometries were meshed using the program *GAMBIT*. The flow simulations were executed with the program *ANSYS FLUENT 12* on Opteron Dual Core Server machines. Each study has taken a calculation time of approximately six days.

2. THEORY OF THE REVERSING PROCESS OF EXTERNAL GEAR PUMPS

During pump operation, the pressure medium is absorbed by the opening tooth chambers on the suction side and transported along the housing circumference from the low-pressure (LP) to the high-pressure (HP) side. The displacement of the fluid occurs when the teeth roll off. The volume between the teeth is quickly reduced and thus the fluid amount enclosed therein. The pressure relief grooves, which are integrated in the axial bearings of the pumps, decisively influence the degree of pulsation, the degree of volumetric efficiency and the pressure decrease rate from the high pressure to the low pressure side. These grooves ensure that the pressure medium is squeezed out from the inter-tooth volumes on the high-pressure side and that it flows into the opening displacement volumes on the suction side. This process requires sufficient sealing between the HP and LP sections when the gear wheels roll off.

In external gear pumps the kinematic pulsation dominates, whereas the compression and the leakage induced pulsations have less importance /L1, L2/. According to **fig. 1**, the layout of the pressure relief grooves has great influence on the kinematic flow rate pulsation. The sealing web width (hydraulic mesh) has to correspond with the length of the path of contact $\overline{AE}$ to guarantee an optimal delivery with a minimum of pulsation. Therefore, the pressure relief grooves are symmetrical arranged to the centre distance line (fig. 1 left side). A translational displacement of the sealing edges of the grooves into the suction or delivery direction increases the pulsation and reduces the degree of volumetric efficiency. The original design of the investigated pump has pressure relief grooves, which are arranged symmetrical to the centre distance line.
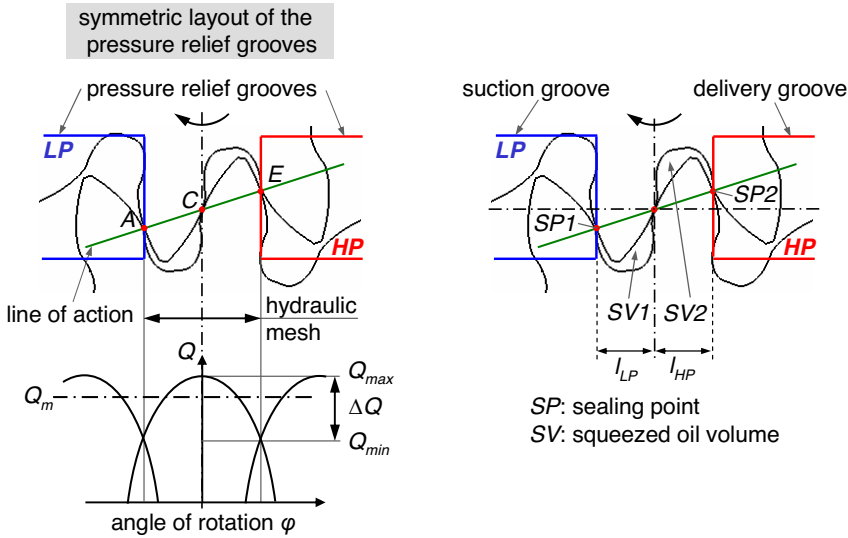
Figure 1   Kinematic flow rate pulsation for a symmetric layout of the pressure relief grooves with a rectangular profile

The dynamic processes in the squeezed oil volume *SV* are of decisive importance for the noise excitation. Fig. 1 shows the pressure relief grooves as rectangular grooves with zero overlap in the symmetrical alignment, where the squeezed oil volumes *SV1* and *SV2* are identical. In this position of the gear wheel´s oil is separated by the sealing points *SP1* and *SP2* of the touching tooth flanks between the high and low pressure side, as the sealing edges of the grooves align with these points. The squeezed oil volumes *SV1* and *SV2* are hydraulically connected via a tooth flank gap, which allows an oil transport.

Subsequently, a flow path opens between *SV1* and the suction groove as the rotation of the pinions continues. In the consequence, the pressurised oil in the squeezed oil volumes *SV1* and *SV2* expands abruptly in the low pressure side LP. This process is related with very high pressure change rates that initiate highly dynamic vibrations of the engaged teeth. For this kind of a pressure reversing geometry, the squeezed oil pressure peaks are rising with the increase of the rotary speed. For that reason pressure reversing geometries with underlap conditions have been established to avoid such pressure peaks. Furthermore, an increased cavitation intensity in the suction duct of the pump can occur, when the intertooth volume is not sufficiently supplied from the pressure relief geometry with oil during its enlargement. Then, filling losses effect a decrease of the static pressure in the intertooth volume below a critical value with the consequence of cavitation.

3. METHODS OF FLOW ANALYSIS

Numerical approach by CFD-simulation. Based on the 3D-CAD data of the solids of an external gear pump the inverse fluid volumes, consisting of the gearing, the pressure relief grooves and the suction and pressure pipe, were generated for the flow analysis. The

pressure relief grooves are integrated in the axial bearings on both end faces of the pinions. Due to the symmetrical design of the pumps a numerical half section model with a symmetry plane as boundary could be used. Previous investigations at the institute and research from other authors /C1, C2, E1, F1, L1, W1, W2, W3/ demonstrate the significance of the processes in the tooth engagement zone for the noise emission, the cavitation intensity and the pulsation characteristic, whereas the processes in the pressure build-up zone can often be neglected. In the studies presented here, exclusively the pressure decrease in the tooth engagement zone is taken into consideration. So, a reduced CFD-model of the external gear pump with only seven intertooth volumes was modelled, according to **fig. 2**. Comparative studies with a complete model are given in /W2, W3/.
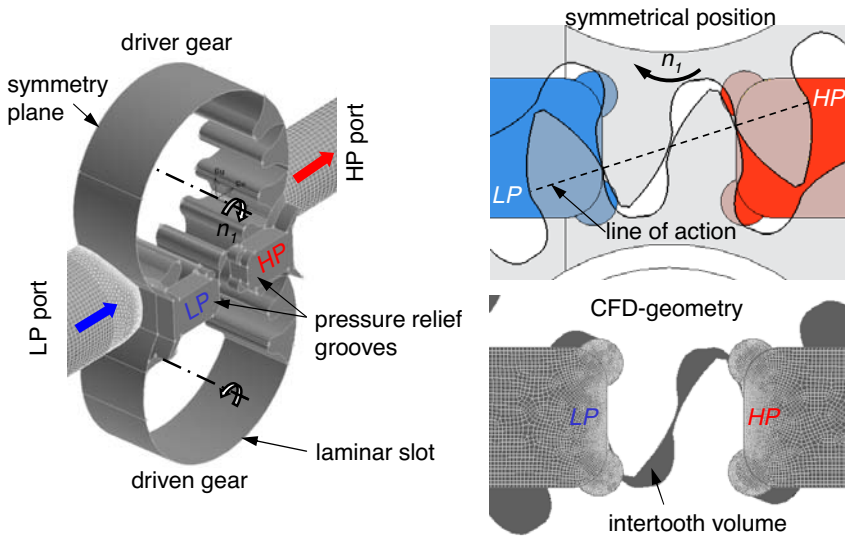
Figure 2   CFD-model of the external gear pump with the intertooth volumes, the reversing geometry within the axial bearings and the pipes

In analogy to the experimental investigations a low-reflection line termination (RALA) was modelled as outlet of a short pressure pipe with a length of approx. $l \approx 1$ m. The RALA operates on the basis of closing the straight pressure pipe with a finite length by a defined resistance, so that the total impedance of this configuration correspond to the frequency-independent characteristic wave impedance of a infinite long, straight pipe. In this way, reflections can largely be avoided /T1/. The modelled suction pipe is $l \approx 2$ m long. The field sizes, e.g. volume flow rate Q and static pressure p are detected in monitoring planes. The CFD-model requires an average of 1.9 million cells. The maximum time step size of $\Delta t = 3.3$ μs is limited by the dynamic mesh generation because the wall-bounded mesh cells can only be shifted by one element edge. Hence, nearly 1000 time steps are necessary to simulate the rotation around one tooth pitch of $\varphi = 360°/z \approx 27.7°$. To realise the dynamic mesh generation, the flow grid of the pump is separated into several fluid zones with interconnecting interfaces. In this way the continuously remeshed toothing area is connected with the pressure reversing grooves and the suction and pressure pipe. High grid resolutions are essential in the tooth engagement zone, where high flow gradients may occur. Using

analytical estimations of the Reynolds number *Re* for critical flow conditions, laminar behaviour was found for the selected operating point. So, no turbulence model had to be used. The laminar flow behaviour during the pressure reversing phase dominates because of the minimal clearances although the flow velocity rises up to approx. 100 m/s. In the suction and the delivery duct the local flow velocity is more than one magnitude smaller. More details concerning the simulation setup are given in /W3/.

To simulate the pressure pulsation as a consequence of the flow rate pulsation the compressibility of the pressure medium has to be modelled. As an approach, a fluid modelling based on the bulk modulus *K'* according to **fig. 3** was taken /H1/.

$$K' = K_{Fl} \cdot \frac{(1-\alpha_u)\left(1 - \frac{p}{K_{Fl}}\right) + \alpha_u \cdot \left(\frac{p_0}{p}\right)^{\frac{1}{\kappa}}}{(1-\alpha_u)\left(1 - \frac{p}{K_{Fl}}\right) + \frac{\alpha_u \cdot K_{Fl}}{\kappa \cdot p} \cdot \left(\frac{p_0}{p}\right)^{\frac{1}{\kappa}}} + K'_{min} \qquad \rho = \frac{\rho_0}{\left(1 - \frac{p - p_0}{K'}\right)} \qquad a = \sqrt{\frac{K'}{\rho}} = \sqrt{\left(1 - \frac{p - p_0}{K'}\right) \cdot \frac{K'}{\rho_0}}$$
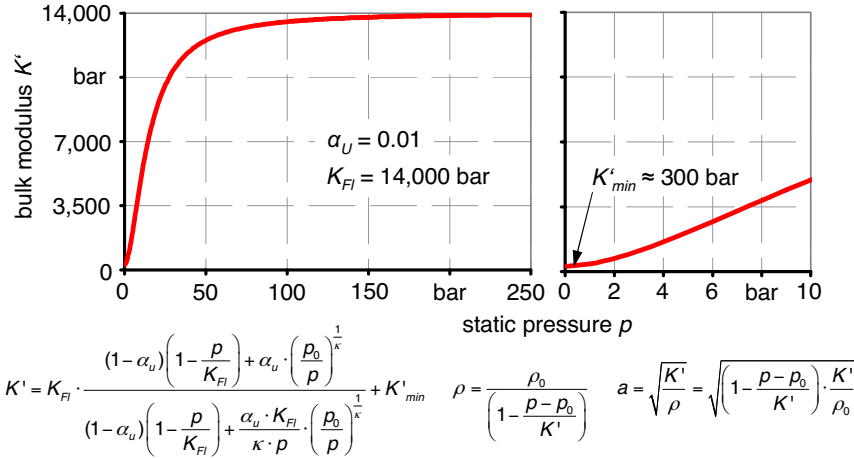
Figure 3   Bulk modulus *K'* of the fluid as function of the static pressure *p* and its relation to the density *ρ* and sonic speed *a*

The dependency of the bulk modulus *K'* on the static pressure *p* is the result of an isotropic change of state of a liquid-air mixture, where the liquid is assumed to be compressible with a constant fluid bulk modulus of $K_{Fl} = 14{,}000$ bar and an unsolved secondary phase with a volumetric fraction of air phase of $\alpha_U = 1$ %, which is described as ideal gas. This *K'*-model takes the pressure-dependent elasticity of the fluid into consideration and is validated in several cases. The pressure dependent speed of wave propagation *a* and the fluid density *ρ* arise from the given equations. To limit the numerical calculation effort no cavitation model is used.

Experimental investigations. Comparative experimental investigations were carried out in the anechoic chamber of the institute (accuracy class 1; ISO 3745). The acoustic power is determined according to the enveloping surface method (DIN 45635 part 26). Six microphones are arranged in a quarter-room between two reflecting walls aligned rectangular to each other covering the test pump within a cuboid with an edge length of 1 m. For the detection and analysis of the sound a program from *Bruel & Kjaer Pulse* was used. Furthermore, pulsation measurements in the suction and pressure pipe were performed. The positions of the pressure and flow rate sensors are identical with the monitor planes of the simulation model.

4. OPTIMISATION OF THE PRESSURE REVERSING PROCESS

The initial situation for the further development of the pressure reversing system constitutes a conventional pressure relief geometry with underlap condition in the symmetrical position between the relief grooves and the gearing according to fig. 2.

The relief grooves, which are overlapping into the intertooth volume to limit the squeezed oil pressure peaks, cause a short circuit flow from the delivery HP to the suction port LP with the consequence of distinct suction and high pressure pulsations, **fig. 4**.
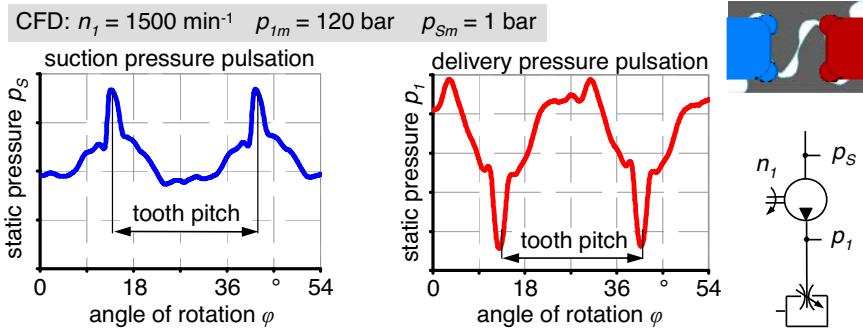
Figure 4   CFD-simulation of the suction and delivery pressure pulsation of the original reversing geometry with negative overlap

Moreover, the short circuit flow has a negative influence on the volumetric efficiency η_{vol}, as almost delivered oil flows back in the low pressure range. Finally, an increased cavitation tendency as a consequence of flow losses during the enlargement of the intertooth volumes was found for the original design by using CFD-simulation. On the other hand, the short circuit flow has a positive influence on the pressure decrease rate $\dot{p}$. Due to this leakage flow the pressure decrease takes more time and the force excitation of the pinions and consequently the noise emission decline. Analysing the original design the objectives for the modification of the control edges of the relief grooves are as follows:

- Reduction of the short circuit flow in the low pressure range,
    - minimisation of the suction and high pressure pulsation,
    - increase of the degree of volumetric efficiency,

- Decrease of the radiated acoustic power,

- Reduced pressure drop for the filling of the intertooth volume,
    - reduction of the cavitation tendency.

To achieve the objectives of noise reduction by the simultaneous increase of volumetric efficiency and reduction of pulsation, alternative pressure reversing concepts were worked out according to **fig. 5**. In contrast to the original design these concepts are only applicable for one direction of rotation. For both optimisations (B) and (C) the high pressure groove in form of a pocket was lengthened below the line of action towards the suction side to ensure a hydraulic short circuit between the intertooth volume and the high pressure port until the

symmetrical alignment, whereas the upper hole on the high pressure side was eliminated. This measure helps to reduce the short circuit flow. Moreover, the low pressure groove was extended to the intertooth volume above the line of action to facilitate the filling of the intertooth volume during its enlargement after the symmetrical alignment. The separation of the suction and pressure sided grooves below and above the line of interaction is necessary to prevent a hydraulic short circuit during the single contact phase. The new facet of our concept is the hydraulic short circuit between two intertooth volumes in the tooth engagement zone and the pressure build-up area along the housing circumference realised by a channel. Using internal pressure measurement in the driven pinion /W2, W3/, we found the pressure raise characteristic along the housing circumference. For the new pressure reversing concept, we chose an area along the housing where the pressure level is ¼ of the high pressure level to connect this area hydraulically with the intertooth volume in the tooth engagement zone.
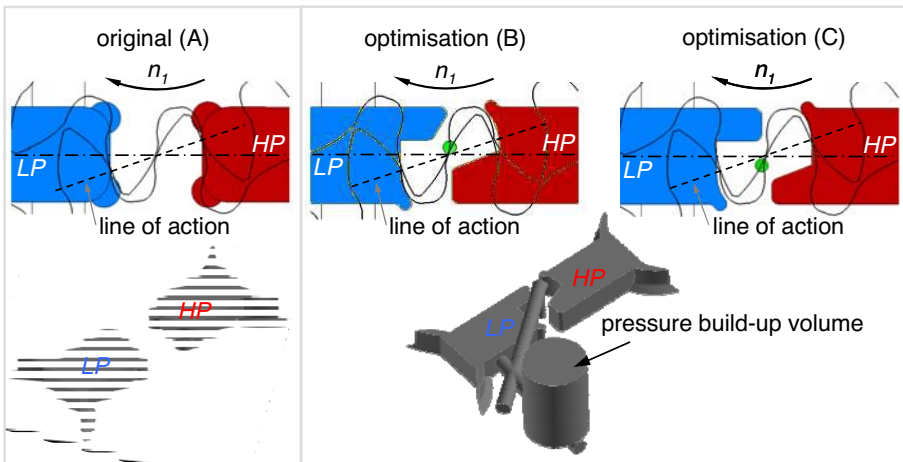
Figure 5   Optimisation of the original pressure relief grooves (A) - reversing concepts with pressure release holes connected with the pressure build-up area (B + C)

The hydraulic connection leads to the pressure decrease in the intertooth volume, whereas the pressure decrease rate is adjustable by means of the size and the position of the channel hole. The reduced pressure drop between the intertooth volume and the pressure build-up zone helps to reduce the pressure decrease rate $\dot{p}$ even in the first phase of the pressure decrease. During the second phase of the pressure reversing process the pressure relations in the intertooth volume and the pressure build-up zone are reversed. Then, the intertooth volume is hydraulically supplied by the pressure build-up zone, which prevents a pressure drop below a critical limit for the generation of cavitation as long as the flow bridge to the suction port is insufficiently dimensioned for cinematic reasons. Furthermore, the size and the position of the hole also determine the hydraulic short circuit during the single contact phase after the rotation by a half of a tooth pitch. Preliminary investigations /W3/ have shown, that the rise of the pressure increase rate is of subordinate influence on the noise emission compared to the pressure decrease rate. This aspect is particularly important with regard to the oil outlet from the pressure build-up to the low pressure zone for a short time.

For simulation the pressure build-up zone is simplified as a cylinder volume of equal size with a pressure boundary. The difference between both variants is on the one hand the position of the hole, which is situated above the line of action for the optimisation (B) and below this line for the optimisation (C). On the other hand, optimisation (C) is designed with an overlap condition, whereas optimisation (B) is dimensioned with a zero overlap condition. So, variant (C) has a larger rotational angle range for the pressure decrease, which helps to reduce the pressure decrease rate. Furthermore, both variants are characterised by large inflow areas at the sealing edges of the pressure relief grooves.

Fig. 6 shows the simulated pressure decrease rate $\dot{p}$ as an indicator for the noise emission in relation to the experimentally determined acoustic power level. With the new design of optimisation (C) a noise reduction could be achieved within the whole operational area. While the acoustic power declines by $\Delta L_{W,A} \approx 2 - 3$ dB(A) for the rotary speed of $n_1 = 1000$ min^{-1}, a reduction of the sound power of 5 dB(A) $\leq \Delta L_{W,A} \leq 7$ dB(A) was obtained for the rotational speed of $n_1 = 2000$ min^{-1}. The pressure decrease rate lies in the range of the original design. Without using pressurised fluid for a short circuit phase during the pressure reversing process, the degree of volumetric efficiency raises. In comparison to the original design, optimisation (B) is characterised by lower acoustic power levels for the rotary speed of $n_1 < 2000$ min^{-1}. For $p_1 \leq 100$ bar and $n_1 = 1000$ min^{-1} the acoustic power declines by nearly $\Delta L_{W,A} \approx 5$ dB(A). However, the effective period of the pressure release hole decreases for higher rotary speeds. The pressure drop does then no longer proceed gradually, so that an increased noise emission was detected for $n_1 = 2000$ min^{-1}. Therefore, the cross section of the hole of variant (B) should be modified in the next step.
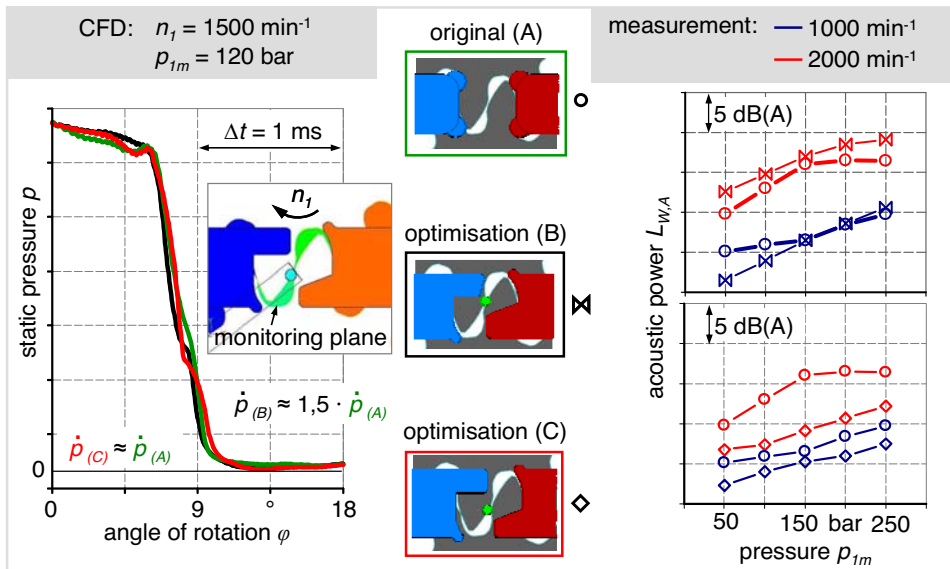
Figure 6   Simulated pressure decrease rate $\dot{p}$ of the variants A - C and the measured acoustic power $L_{W,A}$ of the variants (B) and (C) in comparison to the original (A)

Fig. 7 shows several approaches for the optimisation of variant (B). The overriding considerations are the increase of the effective flow area of the pressure release hole and its duration in combination with the gradual enlargement of the flow area during the tooth engagement phase.
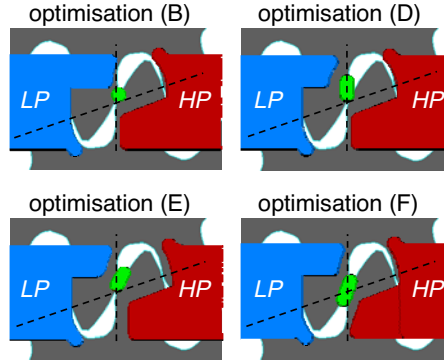
Figure 7   Optimisation studies of the pressure reversing geometry in the tooth engagement zone

While the pressure release hole was extended along the connecting line of the two pinion axes for optimisation (D), the variants (E) and (F) are designed with elongated pressure release holes along the tooth flanks to realise a gradual enlargement of the flow area. The modification of the pressure release holes is combined with the revision of the delivery grooves to prevent on the one hand squeezed oil pressure peaks and on the other hand short circuit flows. The combination of the elongated pressure release holes with the displacement of the delivery groove in the direction of the delivery port allows the extension of the pressure reversing process over a wider angular range. With the variant (E) the angular range for the reversing process could even be doubled in comparison to the original (A), **fig. 8**.
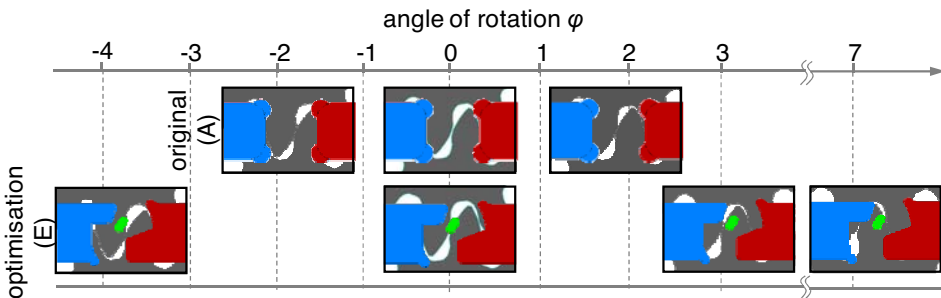
Figure 8   Comparison of the rotational angle range of the pressure reversing phase between the original (A) and the optimisation (E)

The lowest pulsations of the delivery pressure could be achieved with optimisation (B). In **fig. 9** the experimental results for the variant (B) in relation to the original (A) are given for different rotary speeds n_1 and static pressures p_1. Using CFD, a reduction of the delivery

pressure pulsation of approx. 35 % was predicted for the operating point of $n_1 = 1500$ min^{-1} and $p_1 = 120$ bar. The measured reductions of the pulsation of the delivery pressure were lower: For the rotary speed of $n_1 = 1000$ min^{-1} the high pressure pulsation could be lowered by 25 %, for $n_1 = 2000$ min^{-1} the amplitudes of pulsation could be reduced by an average of $\Delta p \approx 1$ bar.
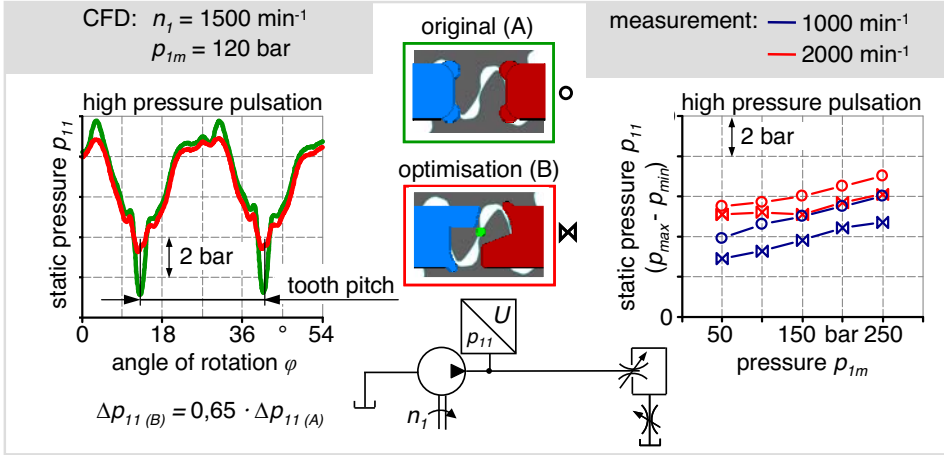
Figure 9   Comparison of the pulsation of the delivery pressure between the original (A) and the optimisation (B)

As we do not use the hydraulic underlap in the tooth engagement zone for all new pressure reversing systems, even the suction pressure pulsation could be reduced, **fig. 10**.
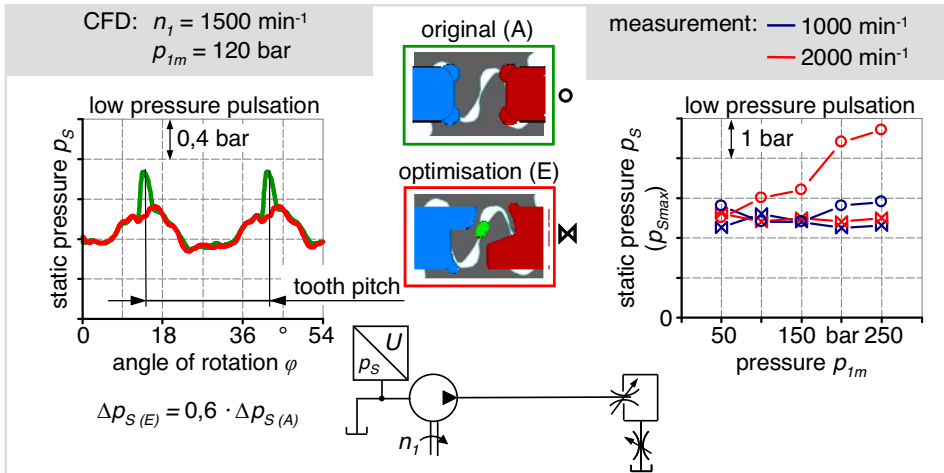
Figure 10   Comparison of the pulsation of the suction pressure between the original (A) and the optimisation (E)

Optimisation (E) can be taken as an optimum with a predicted pulsation to be 40 % lower than the original (A). The measured suction pressure pulsations remained almost without exception below the values of the original. Thereby the reduction of the suction pressure amplitudes is particularly high for great rotary speeds and high delivery pressures and reaches up to 50 %. Besides the reduction of the suction and delivery pressure pulsation, optimisation (E) is characterised by the lowest of all calculated pressure decrease rates during the tooth engagement phase, **fig. 11**. This simulated behaviour can be found in the noise emission of the pump, as expected. So, the emitted acoustic power $L_{W,A}$ could be decreased once more in comparison to the silent optimisation (C) by an average of $\Delta L_{W,A} \approx 1,5$ dB(A) for the low rotary speed of $n_1 = 1000$ min^{-1}. So, optimisation (E) is an average of $\Delta L_{W,A} \approx 3 - 4$ dB(A) quieter than the original (A). However, until now there is still optimisation potential for this geometry, as the pump shows increased noise emissions for high speeds with an average level of the original (A). For high rotary speeds optimisation (C) is much quieter than the original (A). The average acoustic power decreases by $\Delta L_{W,A} \approx 5 - 7$ dB(A). That implies a reduction of the acoustic power to ¼ of the original design. Especially for high speeds this design best fits the increased noise requirements.
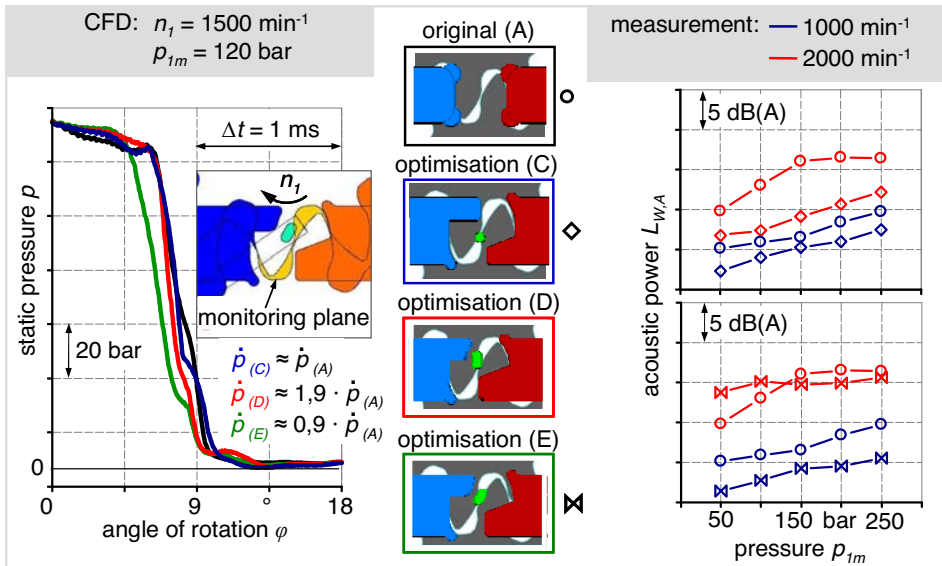
Figure 11 **Relation between the simulated pressure decrease rate $\dot{p}$ and the measured acoustic power $L_{W,A}$ of the variants (B) and (C) in comparison to the original (A)**

5. CONCLUSIONS AND OUTLOOK

This paper focuses the further development of the pressure reversing process of external gear pumps. Several approaches for the pressure reversing geometry were devised and analysed with the main objectives of reduced noise emissions, suction and delivery pressure pulsations combined with an increase of the degree of volumetric efficiency. Based on a

conventional pressure relief geometry with hydraulic underlap condition, the alternative reversing concepts for the groove and hole design were developed, only by using CFD. A distinct reduction of the sound emission of the pump could be achieved with a pressure release hole in the tooth engagement zone, which is connected with the pressure build-up area by a channel system. Furthermore, the objectives of a reduced pulsation in the suction and delivery pipe and the increase of the degree of volumetric efficiency could be proved. These studies show methods for the further optimisation of an established drive technology in fluid power. Using modern simulation techniques like CFD, improvements of the design with passive measures for noise reduction are still possible, even for apparently fully developed devices as external gear pumps.

ACKNOWLEDGEMENT

REFERENCES

/C1/ Casoli, P.; Vacca, A.; Berta, G.L.: Potentials of a numerical tool for the simulation of flow in external gear machines, 10th Scandinavian International Conference on Fluid Power, SICFP'07, 2007, Tampere

/C2/ Casoli, P.; Vacca, A.; Franzoni, G.; Guidetti, M.: Effects of some relevant design parameters on external gear pumps operating, 6. IFK, 2008

/E1/ Eaton, M.; Keogh, P.S.; Edge, K.A.: The modelling, prediction and experimental evaluation of gear pump meshing pressures, Proc. IMechE, 2006

/F1/ Fiebig, W.: Schwingungs- und Geräuschverhalten der Verdrängerpumpen und hydraulischen Systeme, Habilitation, Universität Stuttgart, 1998

/H1/ Helduser, S.: Fluidtechnische Antriebe und Steuerungen, Vorlesungsumdruck TU Dresden, 2009

/L1/ Link, B.: Förderstrompulsation von Außenzahnradpumpen, Ölhydraulik und Pneumatik, 1986, Nr.11

/L2/ Link, B.: Untersuchung der Förderstrom- und Druckpulsation von spaltkompensierten Außenzahnradpumpen, VDI Verlag, 1986

/T1/ Theissen, H.; Risken, W.: Messung der Volumenstrompulsation von Hydraulikpumpen, Ölhydraulik und Pneumatik, 1983, Nr. 5, S. 387-392

/W1/ Wustmann, W.; Helduser, S.; Wimmer, W.: CFD-Simulation of the Reversing Process in External Gear Pumps, 6. IFK, Dresden, 2008

/W2/ Wustmann, W.; Helduser, S.: CFD-Simulation of the Reversing Process in Hydrostatic Pumps, ANSYS Conference & 26. CADFEM User's Meeting, Darmstadt, 2008

/W3/ Wustmann, W.: Experimentelle und numerische Untersuchung der Strömungsvorgänge in hydrostatischen Verdrängereinheiten am Beispiel von Außenzahnrad- und Axialkolbenpumpe, Dissertation, TU Dresden, 2009

NOMENCLATURE

a	sonic speed, speed of wave propagation
K	bulk modulus
l	length
$L_{W,A}$	acoustic power, A-weighted
n	rotary speed
p	static pressure
$\dot{p}$	rate of pressure change
Q	flow rate
Re	Reynolds-number
t	time
V	displacement volume
z	number of teeth
α_U	fraction of air phase (volumetric)
η	degree of efficiency
κ	adiabatic exponent
ρ	density
φ	angle of rotation
ω	angular velocity
Δ	margin between two conditions

INDICES

0	environmental condition
1	delivery port
Fl	fluid, liquid phase
HP	high pressure
LP	low pressure
m	middle
max	maximum
min	minimum
S	suction port
SP	sealing point
SV	squeezed oil volume
vol	volumetric

Mathematical Modeling and Simulation of Sliding Contact Vane/Profiled Stator of Vane Pump

Radovan Petrović
Faculty of Mechanical Engineering,University of Kragujevac,
Dositejeva 19, 36000 Kraljevo, Serbia
Andrzej Banaszek
Technical University of Szczecin, Faculty of Maritime Technology
71-065 SZCZECIN, POLAND, Al. Piastów 41, tel. +48 91 4494850;
Maritime Academy of Szczecin, Faculty of Economics and Transport Engineering,
70-500 SZCZECIN, POLAND, Wały Chrobrego 1-2.
Ana Vasilev
Hydraulicc and pneumatics industry "Prva Petoletka"-Trstenik
PPT-namenska a.d. Cara Dušana 101, 37240 Trstenik, Serbia
Saša Batoćanin
Hydraulicc and pneumatics industry "Prva Petoletka"-Trstenik
PPT-namenska a.d. Cara Dušana 101, 37240 Trstenik, Serbia

ABSTRACT

Sliding contact vane/profiled stator in vane pump with double effect is described via its characteristic traits. The complete mathematical description of one such contact in the present paper was possible through the application of the following expressions and equations: continuity equation, clearance geometry, deformation equation, energy equation and expression for physical characteristics of working fluid. In the paper, a sufficiently accurate model has been carried out for elastohydrodynamic line contact [2] .

For forming the mathematical model, the following assumptions were introduced: only the two-dimensional case was observed, parameters don't depend on time, the working medium is newton fluid, inertia forces were disregarded in comparison to friction force, viscosity and thickness of working medium depend only on pressure and temperature, surfaces of parts in contact are ideally smooth, the working medium sticks to the surface, the surfaces of parts in contact become deformed elastically in semi-space, deformations caused by temperature change are disregarded and heat flux (flow) comes and is applied directly onto the surfaces of parts in contact [1].

By applying the mathematical model in original simulation program KRILP, developed for prototype of vane pump with double effect type 641- 4300, by PPT Trstenik company, Serbia, it is possible to analyze mutual influence of the following parameters on the pump's work: pressure, clearances, temperatures, viscosity in slide pair vane/profiled stator. Analysis may yield a completely new construction of prototype or entire family of vane pumps [3].

1. INTRODUCTION

Modern methods of designing and constructing the hydraulic pumps can not be applied without appropriate mathematical models of phenomena and processes occurring in real pump structures. Mathematical model of a process is an analytical interpretation with certain assumptions. A mathematical model requires a detailed theoretical research based on laws of fundamental sciences and branches in order to consider and interpret the process thoroughly, which is the basis for adopting the assumptions and for defining the equations.

Based on the experimental research results and the results of the mathematical modeling developing and application of the identification method of unknown parameters of the mathematical modeling of non stationary high dynamic processes and optimization technique. This way of solving the problem is only possible having the special computer program.

1.1 Vane pump with double effect made by Prva Petoletka Trstenik, Serbia

Vane pump with double effect is shown in Figure 1 and Figure 2.
Technical data:

- Speed : *1500 min^{-1}*

- Presssure: *210 $\cdot 10^5$ Pa*

- Flow: *62 l/min*

- Number of vanes: *10*

Figure 1. **Vane pump with double effect made by Prva Petoletka Trstenik, Serbia**
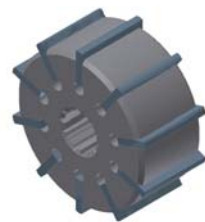
Figure 2. **Rotor with vanes**

2. SIMULATION OF SLIDE CONTACTS BETWEEN THE VANE AND PROFILED STATOR IN THE VANE PUMP

The complete mathematical model of such a contact can be presented by following equations [1]:

1. continuity equation

2. geometry of clearances and deformation equation

3. equation of energy

4. characteristics of working fluid

Almost complete mathematical model of elastohydrodynamic (EHD) line contact is derived in the following text. Within a few simplifications the mathematical model is developed which is then put into simulation program named KRILP giving the calculations of physical states of: pressure, clearance height, flows, velocity, temperature and viscosity in the slide contact of the vane and profiled stator in the vane pump.

2.1   Mathematical model

In order to form the mathematical model the following assumptions are adopted [4]:
-    only two-dimensional case is observed

-    all nominal quantities do not depend on time

-    working medium is newton fluid

-    inertia is disregarded in comparison to friction force

-    viscosity and density of working medium depend on pressure and temperature only

-    surfaces of the contacting parts are perfectly smooth

-    working medium sticks to the surface

-    surfaces of the contacting parts are deformed elastically in semi-space

-    deformation caused by temperature change are disregarded

-    heat flow comes and is applied directly onto the surfaces of contacting parts.

2.1.1 Equations of motion and continuity equations

Equations of motion are based on Navier–Stokes equations along with the stress/strain relation applied in impulse equations.

The changes of all quantities in z direction are disregarded so it follows that

$$\rho \cdot \frac{d_u}{d_1} = \rho \cdot g_x - \frac{\delta_p}{\delta_x} + \frac{2}{3} \cdot \frac{\delta}{\delta_x} \cdot \eta \left(\frac{\delta_u}{\delta_x} - \frac{\delta_v}{\delta_y} \right) + \frac{2}{3} \cdot \frac{\delta}{\delta_x} \cdot \eta \cdot \frac{\delta_u}{\delta_x} + \frac{\delta}{\delta_y} \cdot \eta \cdot \left(\frac{\delta_u}{\delta_y} + \frac{\delta_v}{\delta_x} \right) \quad (1)$$

$$\rho \cdot \frac{\delta_v}{\delta_t} = \rho \cdot g_y - \frac{\delta_p}{\delta_y} + \frac{2}{3} \cdot \frac{\delta}{\delta_y} \cdot \eta \left(\frac{\delta_v}{\delta_y} - \frac{\delta_u}{\delta_x} \right) + \frac{2}{3} \cdot \frac{\delta}{\delta_y} \cdot \eta \cdot \frac{\delta_v}{\delta_y} + \frac{\delta}{\delta_x} \cdot \eta \cdot \left(\frac{\delta_v}{\delta_x} + \frac{\delta_u}{\delta_y} \right) \quad (2)$$

These equations are derived according to the following coordinate system:
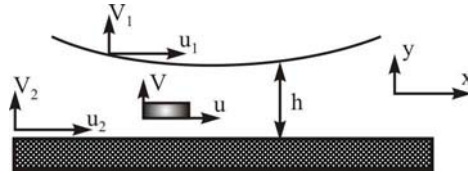
Figure 3. **Coordinate system**

In order to calculate the EHD contact, the influence of external force has the following expression: $\rho g_x ; \rho g_y$

whereas inertia forces $\rho \frac{\delta u}{\delta t} ; \rho \frac{\delta_v}{\delta t}$ are neglected.

Smooth body has a pure horizontal motion, so the clearance height h does not depend on time, which makes the vertical component of the speed in the clearance small in comparison to horizontal line. Therefore, it follows:

$$\frac{\delta_v}{\delta_z} = 0 ; \frac{\delta_v}{\delta_x} = 0 \quad (3)$$

The pressure in direction of clearance height is constant and it is variable only in x direction, which results in:

$$\frac{\delta_p}{\delta_y} = 0 \quad (4)$$

It is assumed that the change of velocity "u" in x direction is much smaller than in y direction which means that it can be disregarded:

$$\frac{\delta_u}{\delta_x} \ll \frac{\delta_u}{\delta_y} \tag{5}$$

By using all above mentioned simplifications the equation of motion is obtained as follows:

$$\frac{\delta_p}{\delta_x} = \frac{\delta}{\delta_y}\left(\eta \cdot \frac{\delta_u}{\delta_y}\right) = \frac{\delta_\eta}{\delta_y} \cdot \frac{\delta_u}{\delta_y} + \eta \cdot \frac{\delta^2 u}{\delta_y^{\,2}} \tag{6}$$

Continuity equation is derived in two-dimensional form.

$$\frac{\delta_\rho}{\delta_t} + \frac{\delta_{\rho u}}{\delta_x} + \frac{\delta_{\rho v}}{\delta_y} = 0 \tag{7}$$

Calculation should be made for stationary state only:

$$\frac{\delta_\rho}{\delta_t} = 0 \tag{8}$$

It follows that:

$$\frac{\delta_{\rho u}}{\delta_x} + \frac{\delta_{\rho v}}{\delta_y} = 0 \tag{9}$$

2.1.2 Energy equation

Lubricating layer in contact zone conducts total heat quantity dQ while the heat quantity dQ_L is conducted by thermal conduction and quantity of heat dQ_R is produced by inner friction [4].

$$\mathrm{d}Q = \mathrm{d}Q_L + \mathrm{d}Q_R \tag{10}$$

According to Fourier, the volume d_v in time d_t produces the following quantity of heat:

$$\mathrm{d}Q_L = \left[\frac{\delta}{\delta x}\left(\lambda \frac{\delta T}{\delta x}\right) + \frac{\delta}{\delta y}\left(\lambda \frac{\delta T}{\delta y}\right) + \frac{\delta}{\delta z}\left(\lambda \frac{\delta T}{\delta z}\right)\right] dV \cdot dt \tag{11}$$

where λ is heat conductivity of lubricating medium.

In the oil film the inner friction results in the following quantity of heat:

$$dQ_R = \left[\begin{array}{l} 2\left(\left(\dfrac{\delta u}{\delta x}\right)^2 + \left(\dfrac{\delta v}{\delta y}\right)^2 + \left(\dfrac{\delta w}{\delta z}\right)^2 \right) + \left(\dfrac{\delta v}{\delta x} + \dfrac{\delta u}{\delta y}\right)^2 + \left(\dfrac{\delta u}{\delta z} + \dfrac{\delta w}{\delta x}\right)^2 + \\ + \left(\dfrac{\delta w}{\delta y} + \dfrac{\delta v}{\delta z}\right)^2 - \dfrac{2}{3}\left(\dfrac{\delta u}{\delta x} + \dfrac{\delta v}{\delta y} + \dfrac{\delta w}{\delta z}\right)^2 \end{array} \right] \eta \cdot dV \cdot dt$$

$$dQ_R = \eta \cdot \Phi \cdot dV \cdot dt \tag{12}$$

Developed heat causes the increase of inner energy d and it is spent on the power :

$$dQ = \rho(di - Vdp)dV \tag{13}$$

By transforming the equations (10), (11) and (12) into equation (13) and dividing it by *(dVdt)* the following form is obtained:

$$\rho\left(\frac{di}{dt} - V\frac{dp}{dt}\right) = \frac{\delta}{\delta x}\left(\lambda\frac{\delta T}{\delta x}\right) + \frac{\delta}{\delta y}\left(\lambda\frac{\delta T}{\delta y}\right) + \left(\lambda\frac{\delta T}{\delta z}\right) + \eta \cdot \Phi \tag{14}$$

$$\frac{di}{dt} = c_p \frac{dT}{dt} - \left[T\left(\frac{\delta V}{\delta T}\right)p - V\right]\frac{dp}{dt} \tag{15}$$

By transforming the previous equation into dwo-dimensional case and by introducing the values c_p (specific heat capacity) and λ (thermal conductivity), it follows:

$$\frac{\delta T}{\delta x} \gg \frac{\delta T}{\delta y}, \ V = \frac{1}{\rho}; \frac{dT}{dt} = u\frac{\delta T}{\delta x}; \frac{dp}{dt} = u\frac{\delta p}{\delta x} = u\frac{dp}{dx} \tag{16}$$

i.e. the energy equations for compressible case are:

$$\rho c_p u \frac{\delta T}{\delta x} - \lambda\left(\frac{\delta^2 T}{\delta y^2}\right) = \eta\left(\frac{\delta u}{\delta y}\right)^2 + \rho\left[\frac{\delta(V\rho)}{\delta T}\right]_P uT\frac{dp}{dx} \tag{17}$$

$$\qquad\quad 1 \qquad\quad 2 \qquad\qquad 3 \qquad\qquad 4$$

1. eliminating heat by convection

2. eliminating heat by conducting it in normal direction to the clearance

3. producing heat due to viscous friction

4. producing heat due to compression

Velocities at the system boundaries correspond to velocities of smooth body.

Boundary temperatures are observed as variable and can be calculated according to Carslaw and Jaeger's formula :

$$T(x,h) = \frac{\lambda}{\sqrt{\pi \cdot \rho \cdot c \cdot u \cdot x^*}} \int_{xe}^{x} \frac{\delta T}{\delta y} / \xi, h \frac{d\xi}{\sqrt{x - \xi}}$$

(18)

3. PUMP DESCRIPTION AND SILENCING GROOVES CONFIGURATION

Figure 1. shows the general configuration of a vane pump. The pump consists of several vanes within a rotor. The vanes are nested in a circular array within the rotor at equal intervals. The vanes are held tightly against a ring using the force of fluid and the centrifugal force, and the bushing is held tightly against the rotor and ring. While the rotor is driven, a single chamber consists of neighboring vanes and rotor ring and bushings [7].
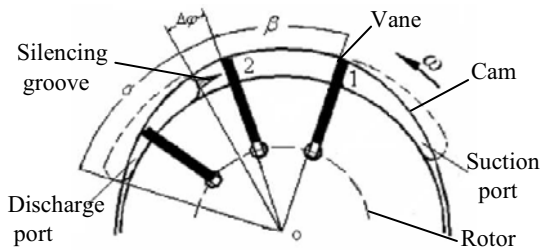
Figure 4.**Schematic diagram of vane pump**

Figure 5 shows the configuration of variable area silencing groove (I) and invariable area silencing groove (II) and complex silencing grooves (III) which are used on bushing. The section of variable area silencing groove and invariable area silencing groove are corresponding triangle and rectangle. The complex silencing grooves are parallel connection of triangle and rectangle. In this paper, the calculation of three type silencing grooves area follow the principle that the backfilling volume of oil through silencing grooves are same within the angle of transition regions($\Delta\varphi$). Figure 6 shows the area of three type silencing grooves as φ goes from 0 to $\Delta\varphi$.
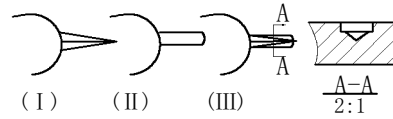
Figure 5. **Schematic diagram of silencing groove**
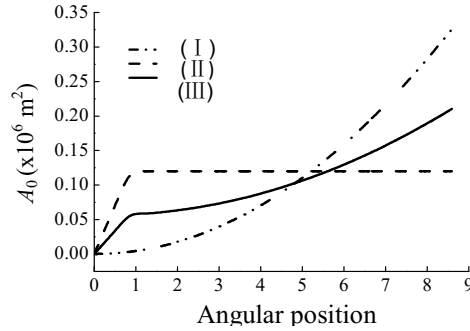
Figure 6. **Area of silencing grooves**

4. DIFFERENTIAL EQUATION OF FLUID PRESSURE WITHIN AN ENCLOSED CHAMBER

The instantaneous fluid pressure within an enclosed chamber is described by the standard pressure rise rate equation which is derived based upon the conservation of mass within the chamber and the definition of the fluid bulk modulus. This relationship is given by

$$\Delta P = -K\Delta V / V \tag{19}$$

Where V is the initial volume of an enclosed chamber, K is the bulk modulus of oil.
To simulate the pressure transients determined by Eq.(19), the differential equation was expressed in the following form

$$\frac{dP}{dt} = -(\frac{dK}{dt}\frac{\Delta V}{V} + \frac{K}{V}\frac{dV}{dt}) = \frac{dK}{dt}\frac{\Delta P}{K} - \frac{K}{V}\frac{dV}{dt} = \frac{dK}{dP}\frac{dP}{dt}\frac{\Delta P}{K} - \frac{K}{V}\frac{dV}{dt} \tag{20}$$

Then Eq.(20) can be rearranged by:

$$\frac{dP}{dt} = -\frac{1}{1 - \frac{\Delta P}{K}\frac{dK}{dP}}\frac{K}{V}\frac{dV}{dt} \tag{21}$$

5. INSTANTANEOUS FLUID PRESSURE AND PRESSURE GRADIENT IN THE CHAMBER WITHIN TRANSITION REGIONS

The volume variations dV of the chamber 1-2 (shown in Figure 4) in transition region were affected by the following two factors.

Firstly, when the chambers 1-2 located in transition region, the vane 2 advances into the rotor and fluid are encapsulated instead of being pushed into the discharge port. The volume variations for compression in the chamber is expressed by the equation

$$ dV_1 = \frac{-B}{2}(R^2 - \rho'^2_2)d\varphi + Bsd\rho'_2 \qquad (0 \le \varphi \le \Delta\varphi) \tag{22} $$

Where B is the width of vane, ρ' is the radius vector of ring, s is the thickness of vane.

Secondly, when the chamber located in transition regions the oil would backfill from discharge port to the chamber through silencing grooves. In the analysis that following, it will be assumed that the backfilling flow into the chamber is characterized by a high Reynolds number and that the classical orifice equation that is derived based upon the Bernoulli equation may be used to model the flow. The volume variations for backfilling into the chamber is expressed

$$ dV_2 = c_q A_0 \sqrt{\frac{2}{\rho}(p_s - p)} dt \tag{23} $$

Where c_q is the discharge coefficient, A_0 is the cross-sectional area of silencing groove, p_s is the discharge pressure of the pump. p is the instantaneous fluid pressure within the chamber in transition regions, the values of p vary between the intake pressure and the discharge pressure, ρ is the density of fluid.

The expression of volume variations dV within chamber 1-2 in transition region is given by

$$ dV = dV_1 + dV_2 $$

The differential was expressed in the following form

$$ \frac{dV}{dt} = \frac{dV_1 + dV_2}{dt} = \frac{-B\omega}{2}(R^2 - \rho'^2) + Bs\frac{d\rho'_2}{dt} + c_q A_0 (2\Delta p / \rho)^{\frac{1}{2}} \tag{24} $$

Where, ω is angular speed of the rotor.

Substituting Eq.(24) into Eq.(20) yield the expression of dp/dt in following form

$$ \frac{dp}{dt} = \frac{dp}{d\varphi}\frac{d\varphi}{dt} = -\frac{1}{1 - \frac{\Delta p}{K}\frac{dK}{dp}}\frac{K}{V}\frac{dV}{dt} = -\frac{1}{1 - \frac{\Delta p}{K}\frac{dK}{dp}}\frac{K}{V}(\frac{-B\omega}{2}(R^2 - \rho'^2) $$

$$ + Bs\frac{d\rho'_2}{dt} + c_q A_0 (2\Delta p / \rho)^{\frac{1}{2}}) $$

For simulation purposes, the above equation can be rearranged as

$$\frac{dp}{d\varphi} = -\frac{1}{1 - \frac{\Delta p}{K}\frac{dK}{dp}}\frac{K}{V}(\frac{-B\omega}{2}(R^2 - \rho'^2) + Bs\frac{d\rho'_2}{dt} + c_q A_0 (2\Delta p/\rho)^{\frac{1}{2}})\frac{1}{\omega} \tag{25}$$

Eq.(25) can be solved numerically for the instantaneous pressure of the chamber in transition regions . Example for one type high-pressure vane pump, Fig.4 shows p/p_s vary with the configuration of silencing groove under condition of p_s=17.5 MPa, n=1500 r/min and K=1200 MPa.It is shown in Fig.4 that the adoption of complex silencing grooves make the change of instantaneous pressure in the chamber more smoothly than the separateness adoption of variable area silencing groove or invariable area silencing groove in whole transition regions. Substituting the numerical results of P into Eq.(25) can yield the pressure gradient dp/dφ vary with the configuration of silencing groove as shown in Fig.5

6. ACTUAL FLOW OF PUMP

The idealized discharge-flow of the pump is determined by considering a pump that does not leak while displacing incompressible fluid. In this case, it may be shown that the discharge-flow is determined by the net flow q_{v1} generated from each chambers
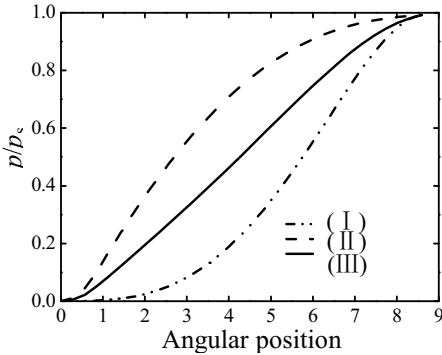
Figure 7. **Instantaneous pressure varying with the type of silencing grooves**
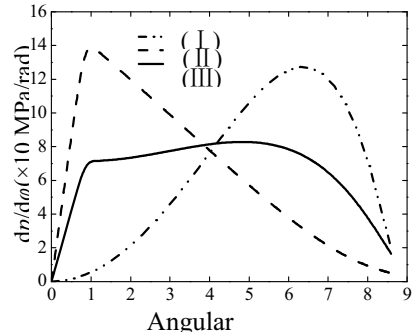
Figure8. **Pressure gradient varying with the type of silencing**

instantaneously positioned over the discharge port and negative flow q_{v2} that   occurs due to the thickness of vane [6].

6.1 Instantaneous flow generated by a single chamber

As shown in Figure 4, the flow rate generated by single chamber 1—2 is equal to the time   rate-of-change of the instantaneous volume of the chamber. Mathematically this is expressed

$$q_{V1} = -\frac{dV_{1-2}}{dt} = \frac{B}{2}(\rho_1^2 - \rho_2^2)\omega \tag{26}$$

6.2 Negative flow that occurs due to the thickness of vane

During the vane pass over the intake ports, the vane withdraws from the rotor by the oil pressure. Mathematically the negative flow q_{v2} that occurs due to the vane thickness is expressed

$$q_{V2} = -Bsd\rho / dt \tag{27}$$

6.3 Idealized flow of pump

Equations (26) and (27) describe the instantaneously flow of a single chamber. As the pump shaft rotates, Figure 6 illustrates the shape of instantaneously flow of a single chamber as it varies with φ.

Equations (26) and (27) may be used to express the instantaneous flow of pump as

$$q_{vsh} = 2\sum q_{v1} + 2\sum q_{v2} = B(R^2 - r^2)\omega - 2Bs\sum v \tag{28}$$

Figure 9 illustrates the shape of idealized pump flow as it varies with φ. From the results which are shown in Figure 9, it can be conclude that the vanes which pass over the intake ports withdrawing from the rotor is the only influential factors of idealized flow-ripple.
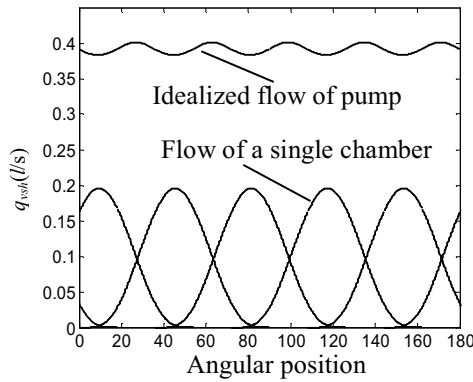
Figure 9. **Idealized flow of pump**

6.4 Negative flow that occurs due to the pre-loading process

When the chambers locate in transition region, for example chamber 1—2, the vane 2 advances into the rotor and fluid be compressed instead of be pushed into the discharge port. The instantaneous flow for compression of the chamber is expressed

$$q_{V3} = -\frac{B}{2}(R^2 - \rho_2^{\,2})\omega - Bs\frac{d\rho_2}{dt} \qquad (0 \le \varphi \le \Delta\varphi) \tag{29}$$

When the chamber located in transition regions the oil would backfill from discharge port to chamber through variable area silencing grooves and invariable area silencing grooves. In the analysis that following, it will be assumed that the backfilling flow into the chamber

is characterized by a high Reynolds number and that the classical orifice equation that is derived based upon the Bernoulli equation may be used to model the flow [3]. The backfilling flow is given by

$$q_{V4} = -C_q A_0 \sqrt{\frac{2}{\rho}(p_s - p)} \ \ (0 \leq \varphi \leq \Delta\varphi) \tag{30}$$

Substituting the result of Eq.(25) into Eq.(30) yield the result of the backfilling flow q_{v4} from discharge port to chamber through three type silencing grooves. At taking fluid bulk modulus K=1200Mpa, rotation n=1500 r/min, discharge pressure P_s=17.5MPa, and intake pressure P=0, the instantaneous flow $2q_{v3}+2q_{v4}$ when the chamber locate in transition regions are shown in Figure7.Figure 7 illustrates the shapes of backfilling flow under the adoption of three type silencing grooves as it varies with φ. From the results, one may generally conclude that the Max. Of negative flow is only half at the adoption of complex silencing grooves compare with the separateness adoption of variable area silencing groove or invariable area silencing groove.

6.5 Actual flow of pump

When taking into account the all factors above, the actual discharge flow of the pump is given by [3]

$$\begin{cases} q_v = q_{vsh} + 2q_{v3} + 2q_{v4} & (0 \leq \varphi \leq \Delta\varphi) \\ q_v = q_{v,sh} & (\Delta\varphi \leq \varphi \leq 2\pi/z) \end{cases} \tag{31}$$

Figure 10 shows the actual pump flow of Eq.(31) at the adoption of three type silencing grooves.By examining Figure 10, it can be conclude that the backfilling flow from
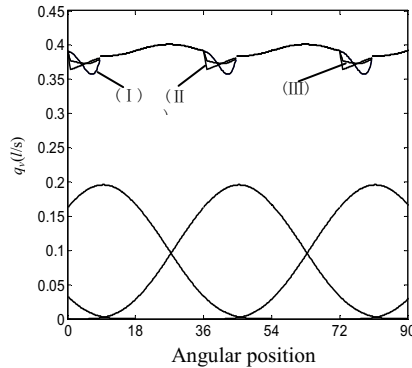
Figure 10: **Actual flow of pump**

discharge port to chamber through silencing grooves in transition region is the main influential factors of flow ripple in pump. The adoption of complex silencing grooves can diminish the maximum of backfilling flow and the amplitude of the flow ripple than the separateness adoption of variable area silencing groove or invariable area silencing groove. Multipurpose hydraulic test table is used for pumps testing, hydromotors (hydraulic engines), distributors, other hydraulic accessories (jacks, valves, etc) and assemblies and static tests of hydraulic components.

7. CONCLUSION

It is not possible to determine precisely enough the parameters of hydrodynamic process of the vane pump with double effect neither by experiments nor by mathematical modeling only. Accurate working parameters can be reached by combined application of experimental measuring, mathematical modeling of hydrodynamic process and nonlinear optimization but at the same time the system errors of measuring and unknown parameters can be determined.

The program KRILP developed for mathematical modeling, identification and optimization of vane pumps provides developing of a whole family of vane pumps in further research of hydrodynamic processes along with the analysis of advantages and disadvantages of vane pumps with double effect and developing different materials by components of pumps.

Nomenclature

ρ' - radius vector of ring;

s - vane thickness;

η - dynamic viscosity of working fluid;

ω - angular speed of rotor;

φ - angle of rotor rotation;

R, r - bigger and smaller radius of stator;

ρ - density of working fluid;

K - the fluid bulk modulus;

B - the width of big vane;

h - clearance height;

λ - heat conductivity of lubricating medium;

c_p - specific heat capacity;

V - initial volume of an enclosed chamber;

c_g - discharge coefficient;

A_o - cross-sectional area of silencing groove;

p_s - discharge pressure of the pump;

p - instantaneous fluid pressure .

References

1. Petrović,R. Mathematical Modeling and Experimental Research of Characteristic Parameters Hydrodinamic Processes of a Piston Axial Pump, *Strojniški vestnik - Journal of Mechanical Engineering 55(2009)4,* UDK 621.785.4

2.   Petrović,R. Mathematical Modeling and Experimental Verification of Operating Parameters   of Vane Pump With Double Effect *Strojniški vestnik - Journal of Mechanical   Engineering*   55(2009)1 UDC 621.9.04

3.   P. Milović, M. Gašić: Hydraulics in building machines, *International Scientific Conference "Source and Transmission of Power" - STP '88*, Faculty of Mechanical Engineering, Podgorica 1988.

4. R.Petrović, J.Pezdirnik, N.Todić: Optimization of oil-hydraulic cylinders of large measurements and high output power, *Ventil –Journal for fluid power, automation and mechanotronics* 15/2009/41 , ISSN 1318-7279,pp:330-338.

5.   C.L.Na, The distribution theory of axial piston pump in considering the compression of fluid, Beijing, *Weapons Industry Press*, (2003) 17. (in Chinese)

6.   Y.Q.Na, *Journal of Lanzhou University of Technology*, Vol.30, No.3 (2004)58. (in Chinese)

7.   Z.R.Wang, *Proc. 6th Int. Symp. on Fluid Power Transmission and Control*, Hangzhou, International Academic Publishers (2005)527.

Modelling and simulation

Next Generation Simulation Software using Transmission Line Elements

Mikael Axin[*], **Robert Braun**[*], **Alessandro Dell'Amico**[†], **Björn Eriksson**[†], **Peter Nordin**[†], **Karl Pettersson**[†], **Ingo Staack**[†], **Petter Krus**[‡]

Division of Fluid and Mechatronic Systems (FLUMES)
Department of Management and Engineering (IEI)
Linköping University, Sweden

[*] main authors
[†] contributors to the work
[‡] professor at the department

ABSTRACT

A suitable method for simulating large complex dynamic systems is represented by distributed modelling using transmission line elements. The method is applicable to all physical systems, such as mechanical, electrical and pneumatics, but is particularly well suited to simulate systems where wave propagation is an important issue, for instance hydraulic systems. By using this method, components can be numerically isolated from each other, which provide highly robust numerical properties. It also enables the use of multi-core architecture since a system model can be composed by distributed simulations of subsystems on different processor cores.

Technologies based on transmission lines has successfully been implemented in the HOPSAN simulation package, develop at Linköping University. Currently, the next generation of HOPSAN is developed using an object-oriented approach. The work is focused on compatibility, execution speed and real-time simulation in order to facilitate hardware-in-the-loop applications. This paper presents the work progress and some possible features in the new version of the HOPSAN simulation package.

1   INTRODUCTION

Fluid power systems are by no means simple to simulate and are characterized by difficulties such as strong nonlinearities, stiff differential equations and a high degree of complexity. By using conventional integration techniques it is necessary to use a small time step in order to deal with numerically stiff problems.

Another, more non-conventional, technique is represented by distributed modelling using transmission line elements. It is a suitable method for simulating large complex dynamic systems and is applicable to all physical systems, such as mechanical, electrical and pneumatics. However, the method is particularly well suited to simulate systems where wave propagation is an important issue, for instance hydraulic systems.

Previously, transmission line elements have successfully been implemented in the HOPSAN simulation package developed at Linköping University [1]. The first steps were taken in the late seventies, and the program was first used commercially in the early nineties. It is written in FORTRAN and provides a fast and stable simulation environment. However, over the years the complexity has grown to such an extent that maintenance, and further development, has become ineffective. Therefore, it was decided to make a fresh start, using modern programming languages and tools.

In this paper, the development of the next generation of the HOPSAN simulation package is presented and its future potential is discussed. The new version is implemented in C++, which provides good compatibility properties and enables an object-oriented approach. One of the most interesting features is however the possibility of taking advantage of multi-core processors, which is suitable with transmission lines and distributed solvers.

2   TRANSMISSION LINE ELEMENTS

In most commercial simulation packages, large differential equation systems are solved using a centralized solver. The basic idea with transmission line elements is to isolate different components from each other, allowing the differential equations in each component to be solved independently. This can be done by replacing pure volumes with line elements of a length corresponding to one time step between components and thus introducing a time delay between them. This method thus allows smaller equation systems to be solved independently using several distributed solvers.

The transmission line method originates from the method of characteristics as used in HYTRAN [2] and from Transmission Line Modelling [3]. Although the method has its roots back in the sixties [4], it has never been widely adopted. This could be because its advantages are not evident for small systems and that wave propagation is regarded as a minor phenomenon in most areas.
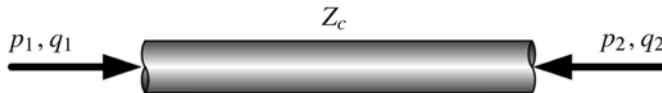
Figure 1: Transmission line element.

A transmission line, see figure 1, can be described by the four pole equation [5]. If friction is neglected and the equations are transformed into the time domain, the relation between flows and pressures can be described according to equation (1) and (2). For a more detailed

discussion, see for instance [6].

$$p_1(t) = p_2(t-T) + Z_c q_1(t) + Z_c q_2(t-T) \tag{1}$$
$$p_2(t) = p_1(t-T) + Z_c q_2(t) + Z_c q_1(t-T) \tag{2}$$

Note that the main property of these equations is the time delay they introduce in the communication between the ends. In order to collect all information that propagates from one end of the line to the other, the variables c_1 and c_2 are introduced.

$$c_1(t) = p_2(t-T) + Z_c q_2(t-T) \tag{3}$$
$$c_2(t) = p_1(t-T) + Z_c q_1(t-T) \tag{4}$$

Here c_1 and c_2 are called the characteristics and they represents the waves travelling in each direction through the line. With these, equation (5) and (6) is obtained.

$$p_1(t) = c_1(t) + Z_c q_1(t) \tag{5}$$
$$p_2(t) = c_2(t) + Z_c q_2(t) \tag{6}$$

The boundary conditions at the ends of the line are described by adjacent components. Typically, the flow is a function of the pressure and the pressure is calculated using equation (5). With equations (3) - (6), the block diagram in figure 2 is obtained.
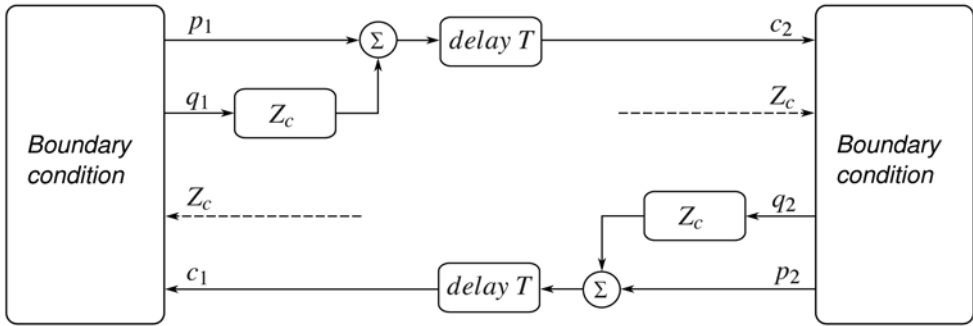
Figure 2: Block diagram of a lossless transmission line.

The separation in space between two components is thus modelled as a separation in time, due to the delay, which is equal to the simulation time step. With the speed of the wave propagation, the length of the transmission line can be calculated according to equation (7).

$$l = ha = h\sqrt{\frac{\beta}{\rho}} \tag{7}$$

With typical values for β and ρ, a time step in the range of 1-10 ms results in a line length in the order of 1-10 m. Using distributed solvers with transmission lines as connection elements thus gives a physically motivated partitioning of the system. In this way component

models can be numerically isolated from each other, which provide highly robust numerical properties [7]. It also enables the use of multi-core architecture since a system model can be composed by distributed simulations of subsystems on different processors, see section 5.1.

A drawback with the transmission line approach is that the line length introduces parasitic inductances in the system. This means that a pressure difference occurs between line ends when the flow changes. One way of dealing with the problem is to use a variable time step in order to limit the inductances to a desired level [8]. The main drawback with that approach is an increased simulation time. However, in most cases the inductance has a counterpart in the real world since most volumes in fact are distributed. Therefore, the parasitic inductances are not considered to be a major problem.

3   WORK PROGRESS OF THE NEW VERSION OF HOPSAN

HOPSAN is a simulation package for fluid power and hydro-mechanical systems developed at Linköping University. It provides a fast and robust platform for simulation, analysis and optimization of complex systems. The work on the new version is focused on several goals. One is to increase the compatibility with other software solutions. Another is investigating the possibility for simulation with multi-core, to utilize the full power of a modern computer. A third is to simulate large, dynamic and high-fidelity models in real-time. All these three will eventually enable and facilitate hardware-in-the-loop, power-in-the-loop or model-in-the-loop simulations. The software itself is an object-oriented C++ application, although the intention is to use a more user friendly high level script language, such as Python. This section is intended to provide an overview of the current status of the project.

3.1   Application Overview

The previous version of HOPSAN is written in FORTRAN, which is a fast but not very flexible programming language. For the new generation of HOPSAN, it was desirable to use an object-oriented language supporting dynamic memory allocation, while still sacrificing as little simulation speed as possible. As a consequence, the choice fell on C++, which in addition to these benefits also provides a good compatibility platform because many modern scientific software applications is written in C or C++.

Components are generated as object instances using dynamic memory allocation. This means that no compilation will be necessary before executing a simulation. This reduces the startup time of the simulation and eliminates the need for including a compiler in the installation package, as opposed to most other commercial simulation tools. Externally created components can be imported from DLL-files, where equations, ports and parameters are defined.

3.2   Graphical User Interface

The graphical part of the application is intended to provide a powerful yet user friendly interface. As seen in figure 3, the main window consists of a working area, component libraries, a toolbar and a message window. Each model or subsystem is represented by its own tab in the working area, and have unique simulation settings and model preferences. Components are added to a model by simply dragging them from the library area. So far there are three default libraries with hydraulic, mechanical and signal components. New libraries can also be added, and user defined components can be created. The graphical appearance of the components

can be displayed either with user defined symbols or according to ISO standard, see figure 4. Common editing features such as copy/paste, rotate, flip and undo history are also included, to facilitate model building.

When the model is finished, a simulation is executed by first selecting the simulation parameters (start time, time step and stop time) and then clicking the *simulate* button. Because of the transmission lines and the distributed solvers approach, no advanced solver settings are required prior to execution, and no compilation is necessary. The desired values can then be plotted and exported to vector graphics or gnuplot files. The graphical appearance of plot windows can be adjusted to desired line width and colors.

To facilitate the creation and maintenance of large systems, a model can be divided into groups or subsystems. The first of these is simply a graphical convenience, while subsystems can be saved to their own files and shared between different models and users. They can also be used to create a new user specified component.
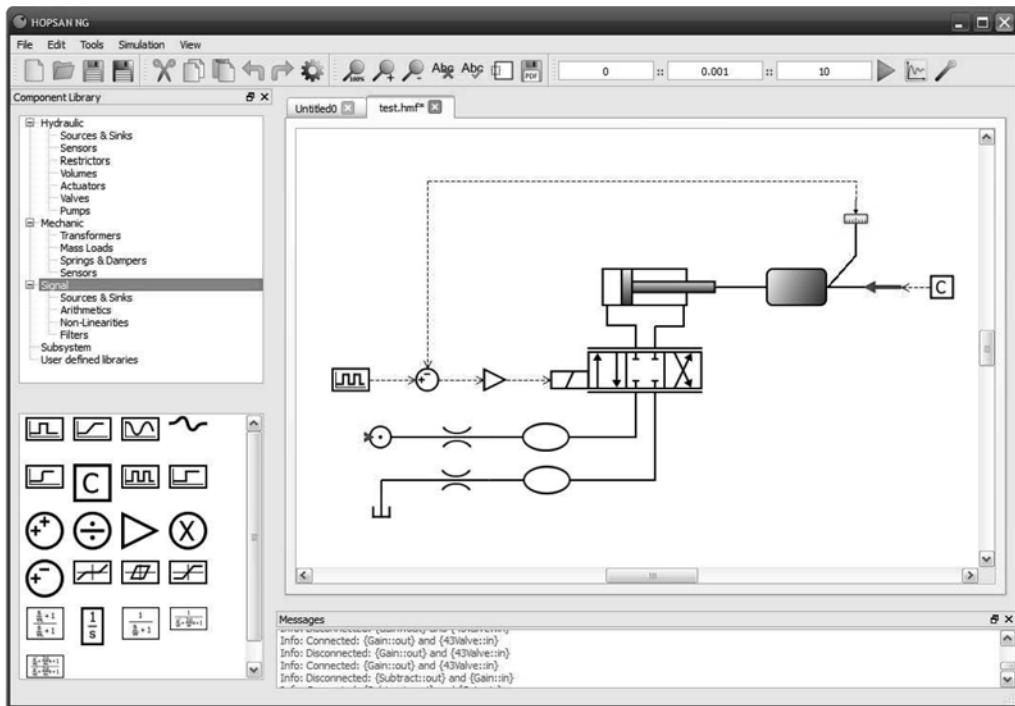
Figure 3: The main window consists of a working area, a component library, a toolbar and a message window.

(a) ISO 1219 Symbols   (b) User Defined Symbols
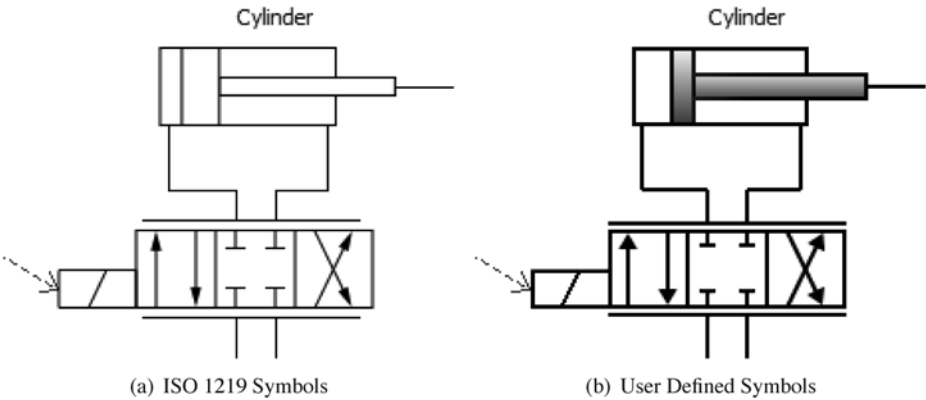
Figure 4: The user can choose between ISO graphics or a user defined graphical theme.

4   EXAMPLE

As an example, a valve controlled position servo has been modelled. In figure 5, the system is modelled in the new version of HOPSAN and figure 6 shows the same system, but modelled in the previous version. A constant pressure source, a reservoir and a fixed displacement hydraulic motor with an inertia load are attached to the servo valve. The position of the motor is read by a position sensor and fed back to the controller. A step from 0 to 3 m is used as input signal. Note also the two volumes between the valve and the hydraulic motor, representing the transmission line elements and thus the time delay between the valve and the motor.
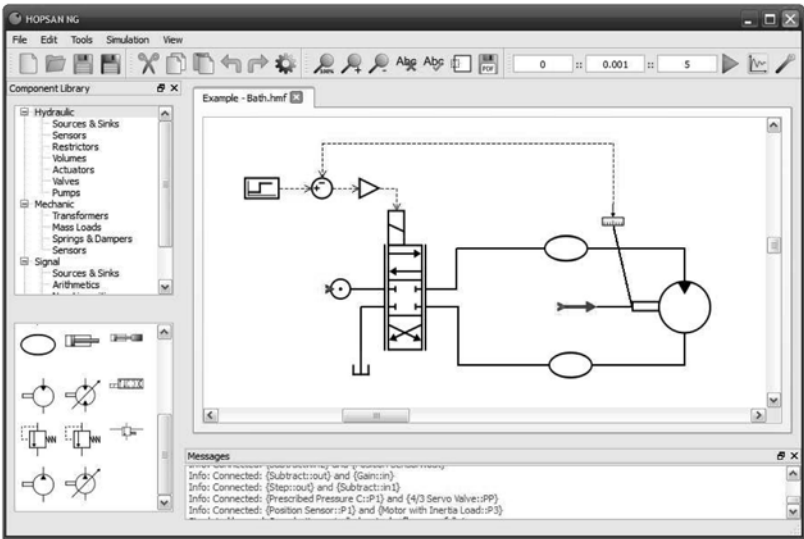
Figure 5: A valve controlled motor with position feedback is modelled in the new version of HOPSAN. Notice the volumes between the valve and the motor, representing transmission lines.
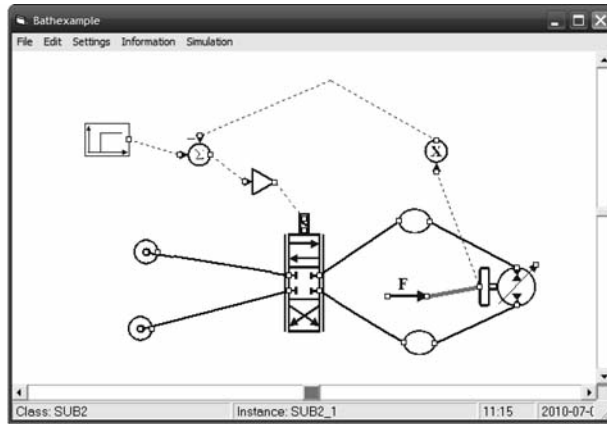
Figure 6: A valve controlled motor with position feedback is modelled in the old version of HOPSAN.

As can be seen in figure 7, the two systems show similar behaviour. It would be interesting to compare the execution speed between the two programs. Since the previous version of HOPSAN is written in FORTRAN, it should be slightly faster than the new one, written in C++. The object oriented approach is also likely to slow down the new version a bit. However, the reduction in execution speed is outweighed by increased compatibility and simplified component model generation, see section 5.2. There is also great opportunities for taking advantage of multi-core architecture, see section 5.1.

(a) New version of HOPSAN.   (b) Old version of HOPSAN.
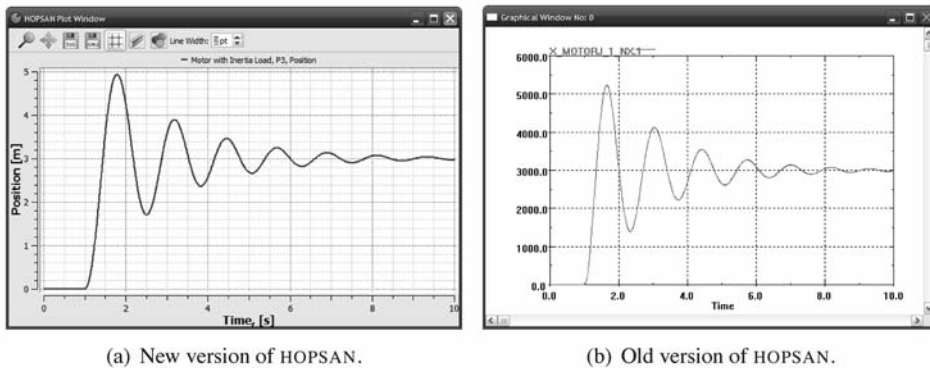
Figure 7: The step response of the position servo shows similar response in both HOPSAN versions, as was expected.

Because the new version of HOPSAN is not yet running in release mode, a fair comparison regarding the execution speed cannot be conducted. This is because the program is currently running in debug mode, which slows down the execution speed a lot. A comparison will however be published in the near future.

5   POSSIBLE FEATURES IN THE DEVELOPMENT OF HOPSAN

A more and more common field of use for simulation software is real-time simulation, especially with hardware-in-the-loop. This makes it possible to test certain physical or electrical components without having to build a full scale physical model, which can potentially reduce the cost of development and testing of new components, since it reduces the need for physical prototyping. It also makes the development process safer, since dangerous experiments can be examined in a safe environment before the physical test.

A strength with HOPSAN is its use of distributed solvers, in contrast to centralized solvers used by most commercial products. This is often a benefit in real-time simulations. It can for example make it easier to analyze systems with components from different vendors, and it increases the benefits from multi-core processing [9]. A related use is faster-than-real-time applications, where the behaviour of a system needs to be simulated prior to its physical use. This can for example be necessary in production equipment or in mission planning for autonomous vehicles. It does however put high demands on simulation speed and robustness.

5.1   Multi-Core, Real-Time and Hardware-in-the-Loop

As the increase of speed in processor cores have slowed down, the use of multi-core processors have increased rapidly. This makes it possible to execute several threads in one application, or several different applications, simultaneously without sacrificing execution speed, see figure 8. It is possible to take advantage of multiple processor cores with simulation software using centralized solvers, but the results are limited due to the fact that components are always depending on results from each other. For HOPSAN however, the advantages should be significantly larger because of the distributed solvers and transmission line approach. Components are either of capacitive or resistive type, and a component does never communicate with another component of the same type due to the time delay, as mentioned in section 2. It is then possible to execute each simulation step in two sequences, one for each component type, with communication between components only occuring between these sequences. By this separation it is possible to execute each component completely independently of other components.

Some aspects that must be considered is that the number of processor cores are limited, and that different components takes different amounts of time to simulate. Basically, the simulation speed is always limited by the component that requires the longest time to execute. It is however very unlikely that the number of processor cores will be greater than the number of components, which means that several components still must share the same processor core. The speed is then limited by the core with the largest total time requirement for the components. For this reason it is desirable to investigate the possibilities of measuring the execution speed for each component, either once at the first time step, or repeatedly during simulation with a certain time interval, to deal with non-linearities. This measurement data can then provide inputs for how to sort and distribute components to different processor cores, thus maximizing the total benefits. For example, a component that takes long time to simulate may require its own processor core, while several faster components can share the same one, as shown in figure 8. An early research regarding this is presented in [10] using separate computers, and subsequently in [11] using transputer technology, which was an early form of multi-core technology.
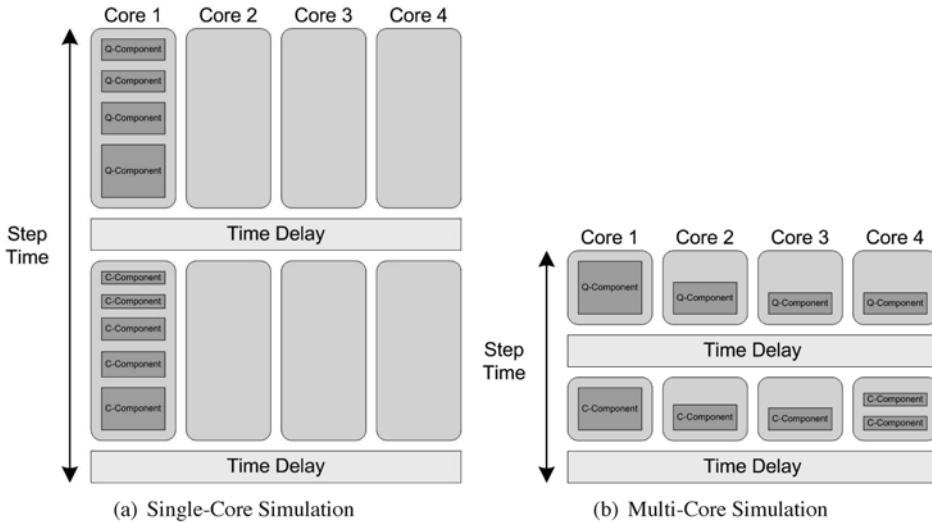
Figure 8: Distributing components equally over the processor cores can potentially increase simulation speed.

5.2 Compatibility and Model Generation

A decent property of a simulation software is compatibility with other applications and environments. This can for example be used for co-simulation, multi-domain simulations, data analysis, model generation or simply to take advantage of the strength from several environments. The compatibility features in HOPSAN will mostly be through automatically or manually exported shared libraries (DLL in Windows). These must be written according to a standard format that can be understood by the target environment. Examples of such standards are the "*Functional Mock-up Interface for Model Exchange*" (FMI) or the National Instruments' VeriStand interface. Some succesful experiments on this have already been conducted. Once imported in the target environment, it is crucial that the components are arranged and connected accordingly with the transmission line modelling system. Another possible target environment is Modelica, a multi-domain modelling language based on equations instead of assignments, enabling support for acausal modelling [12].

One of the significant strengths with the previous generation of HOPSAN is the extensive support for externally generated component models. Models can be created either from a Mathematica file using a script, or by writing the components directly in FORTRAN. It is also possible to save a model as a new component. This will be improved further in the new version, mainly as a result of the support for importing models from shared library files. This will make it easy for programmers to code their own components. Creating models using Mathematica and Modelica, and probably other environments, will also be supported. Another way of creating new components will be by building a subsystem model with system port blocks and then saving it as a new component.

5.3   Plotting and Data Analysis

Currently, data can be plotted by selecting a variable from a list or by simply right clicking on the desired port. In the future however, a more advanced plotting tool will be implemented. This will allow the user to for example plot several values in the same graph with shared or separate axes, and to make XY-plots.

Another interesting feature in the previous version of HOPSAN is the data analysis tools. It is for example possible to use transfer functions and fast Fourier transforms (FFT), and to plot bode diagrams and Nyquist diagrams to investigate the behaviour and stability properties of the system. These functions will be included in the new version as well.

5.4   Multi-Domain Simulation

The transmission line modelling method is by no means limited to fluid power systems. In fact, all physical systems that can be expressed with potentials and flows (or capacitances and resistances) can be modelled in this way. Transmission lines has been used for electrical networks [3], and the use of transmission lines for multi-body simulation has been demonstrated in [13] and in [14]. This makes HOPSAN a very suitable environment for multi-domain modelling. So far only hydraulic and some basic mechanical components are included, but in the future it is likely that extensive pneumatic, electric and advanced mechanical libraries will be included. For example, a heavy industrial robot could be modelled with electronics, hydraulics, electric motors and multi-body mechanics all in one model. Even though HOPSAN is created solely with technical applications in mind, the transmission line modelling method can in fact be used for many non-technical areas. Examples of other scientific fields that can be calculated using potentials and flows include biological systems, logistics and economics. Creating such non-technical libraries will however be up to the user.

6   CONCLUSIONS

Transmission line modelling using distributed solvers provides good numerical stability and is especially well suited for taking advantage of multi-core processors. This enables real-time simulation not only for small and simple systems, but for large and complex ones as well. The next generation of the HOPSAN simulation package has the potential of providing these features. A particularly interesting application is hardware-in-the-loop simulations, where robustness and execution speed plays an important role.

NOMENCLATURE

The quantities used in this paper are listed in table 1.

Table 1: Quantities

Quantity	Description	Unit
a	Speed of sound in oil	[m/s]
c	Wave variable	[Pa]
h	Simulation time step	[s]
l	Line length	[m]
p	Pressure	[Pa]
q	Flow	[m^3/s]
Z_c	Characteristic impedance	[sPa/m^3]
β	Bulk modulus	[Pa]
ρ	Density	[kg/m^3]

REFERENCES

[1] *The* HOPSAN *Simulation Program, User´s Manual*. Linköping University, 1985. LiTH-IKP-R-387.

[2] Air Force Aero Propulsion Laboratory. Aircraft hydraulic system dynamic analysis. Technical report, Air Force Aero Propulsion Laboratory, AFAPL-TR-76-43, Ohio, USA, 1977.

[3] P. B. Johns and M. A. O´Brien. Use of the transmission line modelling (t.l.m) method to solve nonlinear lumped networks. *The Radio and Electronic Engineer*, 50(1/2):59–70, 1980.

[4] D. M. Auslander. Distributed system simulation with bilateral delay-line models. *Journal of Basic Engineering*, Trans. ASME:195–200, 1968.

[5] T. J. Viersma. *Analysis, Synthesis and Design of Hydraulic Servosystems and Pipelines*. Elsevier Scientific Publishing Company, Amsterdam, The Netherlands, 1980.

[6] Petter Krus. *Distributed Techniques for Modelling and Simulation of Engineering Systems*. Linköping University. LIU-IEI-R-08/0020-SE.

[7] Petter Krus. Robust system modelling using bi-lateral deley lines. In *Simsafe*, Linköping, Sweden, 2005.

[8] Arne Jansson, Petter Krus, and Jan-Ove Palmberg. Variable time step size applied to simulation of fluid power systems using transmission line elements. In *The Fifth Bath International Fluid Power Workshop*, 1992.

[9] Petter Krus, Arne Jansson, Jan-Ove Palmberg, and Kenneth Weddfelt. Distributed simulation of hydromechanical systems. In *The Third Bath International Fluid Power Workshop*, 1990.

[10] Arne Jansson and Petter Krus. Real-time simulation using parallel processing. In *The 2nd Tampere International Conference on Fluid Power*, Tampere, Finland, 1991.

[11] J. D. Burton, K. A. Edge, and C. R. Burrows. Partitioned simulation of hydraulic systems using transmission-line modelling. In *ASME WAM*, New Orleans, LA, 1993.

[12] Peter Fritzson. *Principles of Object Oriented Modelling and Simulation with Modelica 2.1*. Wiley-IEEE Press, 2003.

[13] Petter Krus. Modeling of mechanical systems using rigid bodies and transmission line joints. *Journal of Dynamic Systems, Measurement, and Control*, 1999.

[14] D. Fritzson, J. Ståhl, and I. Nakhimov. Transmission line co-simulation of rolling bearing applications. In *The 48th Conference on Simulation and Modelling (SIMS'07)*, 2007.

CFX / Simulink Co-Simulation of a Wave Energy Converter

Andrew Roberts, Michael Schlotter, Andrew Plummer, Derek Tilley
Centre for Power Transmission and Motion Control
University of Bath

ABSTRACT

This paper describes a CFX/Simulink co-simulation strategy for wave energy converters, which comprise of a floating buoy and a hydraulic power take-off (PTO). ANSYS CFX computational fluid dynamics (CFD) code is used for the hydrodynamics model of a free-surface ocean wave, and the Matlab/Simulink SimHydraulics toolbox is used to simulate the hydraulic PTO system. Two indirectly coupled hydrodynamics-body-hydraulics interaction simulations are performed with this detailed model, and results are compared to an uncoupled simulation with an idealised representation of the PTO system. In the simplified model, the hydraulic system has a damper characteristic, so that the dynamics of the buoy can be treated as a forced mass-damper system with a constant damping coefficient. The forcing term comes from the fluids model, the damper appears in the hydraulics model, and the mass is included in the equation of motion for the system. It is found that this simplification works well for rough initial studies. However, certain PTO control methods are responsible for oscillations in the buoy velocity and hence in the power output of the system. If this effect is to be analysed, full co-simulation must be performed.

Keywords: Computational fluid dynamics, coupled simulation, wave energy converters, power take-off.

1. INTRODUCTION

Wave energy research has attracted considerable interest in recent years. Work in the area has mainly focused on the hydrodynamic modelling of devices with linear assumptions made for the power take-off unit. For a more detailed analysis, it is desirable to include realistic models of the power-take-off system in the simulation. The approach presented here is to couple a Simulink/SimHydraulics simulation for the hydraulics with ANSYS CFX code for the hydrodynamics.

Coupled simulations of simple problems involving hydraulics and fluids models have been used in previous research. A coupled simulation implies data transfer between two models at certain timesteps, whereas an uncoupled simulation runs independently based on initial conditions specified in the fluids or hydraulics model at the start of the simulation [1]. A coupled simulation allows the hydraulic processes to affect fluid behaviour and vice versa. An uncoupled simulation does not allow for this, but usually runs faster and is easier to implement. Whether uncoupled simulation is sufficient, or coupled simulation is necessary depends on the effects to be studied.

Coupled simulation approaches can be split into two main categories: directly coupled and indirectly coupled. Directly coupled implies that either the fluids or the hydraulics model operates as the master and calls the other model as slave. Numerical stability has been cited as a problem of directly coupled simulations [2]. Indirectly coupled implies that an external interface program exists between the fluids model and the hydraulics model. Indirectly coupled simulations have been used in the past on the basis that they allow the fluids and hydraulics models to operate at different timesteps [2], [3].

2. THE WAVE ENERGY CONVERTER

The wave energy converter considered here is a simplified point absorber as shown schematically in Figure 1. It consists of a toroidal buoy floating on the surface of the water connected with three hydraulic actuators to a quasi-static large mass. The hydraulic system converts the slow, linear relative motion between the two bodies to a fast rotational motion to drive a generator for electrical power production. The characteristics are tuned to extract the maximum amount of energy from the sea. The amplitude of the buoy is controlled by the resistive force of the actuators, which can be altered by switching individual actuators in and out of the system.
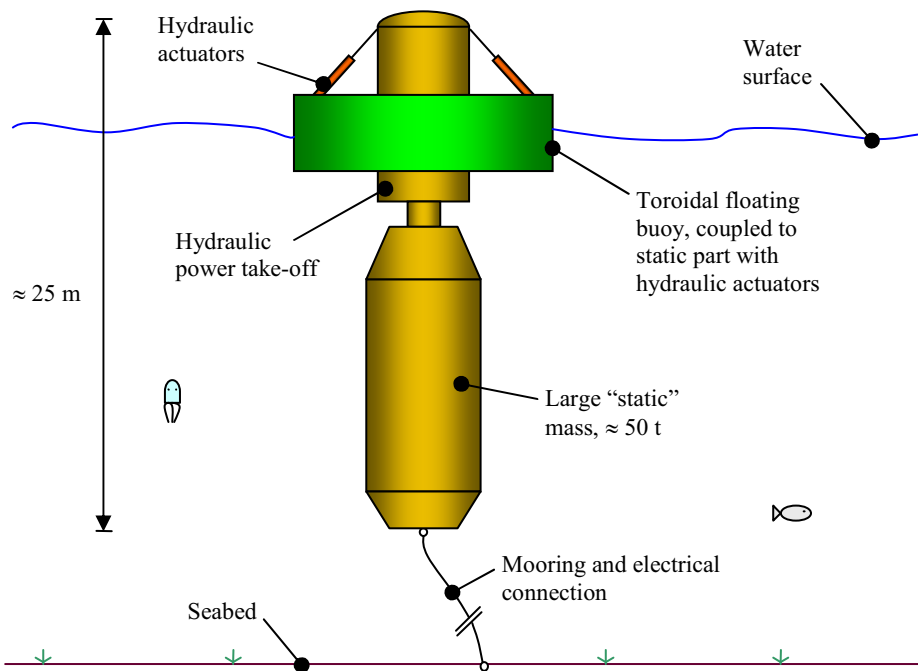
Figure 1: Schematic of a point absorber.

3. HYDRAULICS MODEL

Three cases were considered for the hydraulics model. In Case A it is assumed that the hydraulics model can be represented as a time invariant damping coefficient. Cases B and C contain a detailed simulation of hydraulic forces applied to the buoy. With the current control strategy, these forces have the characteristics of time-varying damping, which is dependent on the buoy motion. The differences between cases B and C are the input and output signals to the model, and the method of solving the equations of motion (EQM) of the buoy using Newton's 2nd law:

"Case A" is defined as:
  o   Hydraulics model idealized as a linear damper with constant damping coefficient.
  o   EQM for buoy solved by Matlab/Simulink.
  o   Damper model input is hydrodynamic force, output is buoy displacement.

"Case B" is defined as:
  o   Hydraulics model built in SimHydraulics with a detailed hydraulic force simulation.
  o   EQM for buoy solved by Matlab/Simulink.
  o   PTO model input is hydrodynamic force, output is buoy displacement.

"Case C" is defined as:
  o   Hydraulics model built in SimHydraulics with a detailed hydraulic force simulation.
  o   EQM for buoy solved by Fortran code.
  o   PTO model input is buoy velocity, output is hydraulic force.

Corresponding block diagrams are shown in Figure 2. Grey boxes indicate inputs and outputs of the Simulink model.

The model for cases B and C was built using SimHydraulics and consists of two main blocks for the controller and PTO. Fluid compressibility effects, nonlinear valve orifice equations, and adiabatic accumulator discharge characteristics are considered. The generator load is assumed to be proportional to the motor speed. The controller block implements a valve switching algorithm, which switches actuators in and out of the system and can be used for arbitrary switching sequences. Here, the switching sequence is based on the motion of the buoy. The full system comprises of three actuators. A schematic of a single unit is shown in Figure 3. The particular parameters used in the SimHydraulics model had an influence on the numerical stability of the integrator. It was found that the introduction of appropriate volume chambers and suitable component leakage was crucial. Future versions of SimHydraulics are likely to be more robust.

4. HYDRODYNAMICS MODEL

ANSYS CFX was used to implement the hydrodynamics model alongside custom Fortran code. Again, 3 different implementation cases are considered:

Case A

Case B

Case C
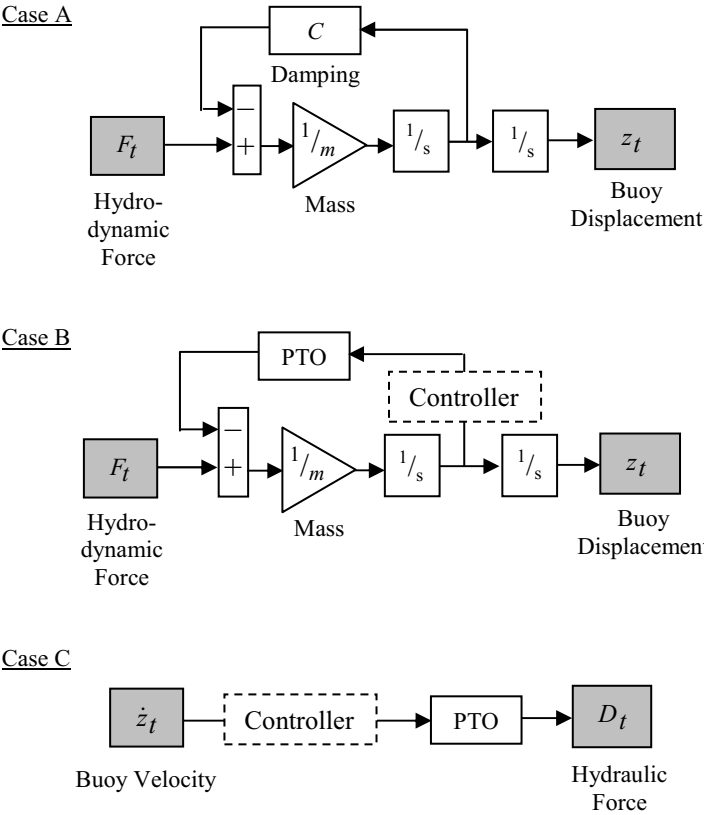
Figure 2: Implementations of the hydraulics model.
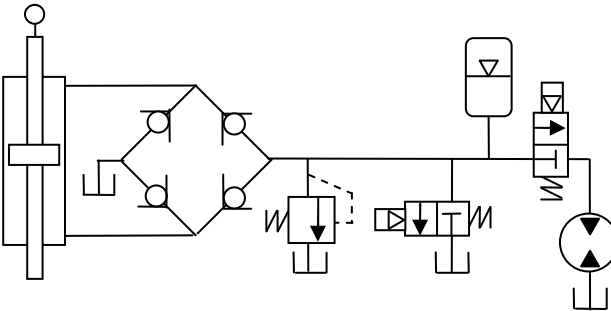
Figure 3: Hydraulic PTO system for a single actuator (cases B and C).

"Case 1" is defined as:
- o   EQM for buoy solved by Fortran code.
- o   No inputs or outputs.

"Case 2" is defined as:
- o   EQM for buoy solved by Matlab/Simulink.
- o   Input buoy displacement, output hydrodynamic force.

"Case 3" is defined as:
- o   EQM for buoy solved by Fortran code.
- o   Input hydraulic force, output buoy velocity.

The Fortran code was used to compute the EQM for the buoy using Newmark integration for cases 1 and 3. It was also used to input and output data from the model for cases 2 and 3. Block diagrams of all three implementations are shown schematically in Figure 4, where grey blocks indicate Matlab/Simulink or Fortran elements for input and output control.
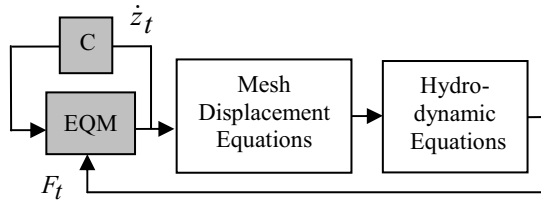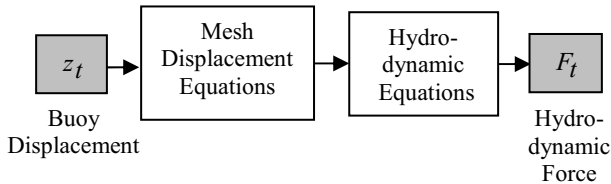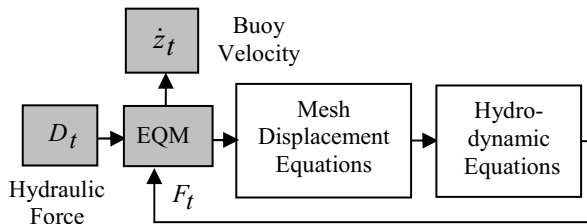
Figure 4: Implementations of the hydrodynamics model.

The boundary conditions of the CFD model are shown in Figure 5. In all cases simplicity and efficiency are preferred over complexity. In this model, only the absorber/buoy has been included, and only half of the buoy has been simulated due to symmetry. This means the computed force should be doubled to represent the full hydrodynamic force on the complete system.

4.1   Buoy Displacement

The displacement of the buoy is constrained such that it only has one degree of freedom in direction 3 (see Figure 5), i.e. a heave/vertical motion. The buoy displacement is measured relative to the initial displacement. The input buoy displacement, z_t is applied to the model as a mesh deformation to the subdomain and to the buoy surface (Equation 1), such that the subdomain and buoy surface move together. The subdomain is a region 1m around the buoy surface where the hydrodynamic force is computed. It moves with the buoy surface, thus avoiding unnecessary cell distortion and oscillations in the computed hydrodynamic force.

$$\delta_{3,buoy} = z_t \tag{1}$$

4.2   Mesh Displacement Equations

The applied mesh deformation at the buoy surface and subdomain must propagate through the rest of the domain in order to avoid cell distortion. The displacement applied to the wall and the subdomain is diffused to other mesh points by solving the following equation [5]:

$$\sum_{i=1}^{3} \frac{\partial}{\partial x_i} \left(\Gamma_{disp} \frac{\partial \delta_k}{\partial x_k} \right) = 0 \tag{2}$$

δ_k is the displacement relative to the previous mesh location and Γ_{disp} is the mesh stiffness, which determines the degree to which regions of nodes move together. We therefore have three equations from (2):

- o   Mesh displacement in direction 1 ($k = 1$).
- o   Mesh displacement in direction 2 ($k = 2$).
- o   Mesh displacement in direction 3 ($k = 3$).

These equations are solved for the three unknowns δ_1, δ_2 and δ_3 in the CFD model.

4.3   Hydrodynamic Equations

The computation of hydrodynamic force F_t requires the solution of the transport equations at every timestep. The CFD model applies the "Homogenous Model" for multi-phase flow. This means the two fluids (air and water) share the same flow field and a single phase momentum transport equation is applied, with variable density and viscosity. A "Free Surface Model" was also applied, such that the water and air are separated by a distinct resolvable interface, i.e. the surface of the wave (see Figure 5). The transport equations for incompressible flow are as follows:

$$\frac{\partial}{\partial t}(\rho u_k) + \sum_{i=1}^{3}\frac{\partial}{\partial x_i}(\rho u_i u_k - \tau_{ik}) = S_{Mk} - \frac{\partial p}{\partial x_k} \tag{3}$$

where

$$\tau_{ik} = \mu\left(\frac{\partial u_k}{\partial x_i} + \frac{\partial u_i}{\partial x_k}\right)$$

and

$$S_{M1} = S_{M2} = 0 \quad \text{and} \quad S_{M3} = -(\rho - \rho_a)g$$

also

$$\rho = r_w\rho_w + r_a\rho_a, \quad \mu = r_w\mu_w + r_a\rho_a$$

$$\sum_{i=1}^{3}\frac{\partial}{\partial x_i}(r_w u_i) = 0 \tag{4}$$

$$\sum_{i=1}^{3}\frac{\partial}{\partial x_i}(r_a u_i) = 0 \tag{5}$$

$$\sum_{i=1}^{3}\frac{\partial}{\partial x_i}(r_w u_i + r_a u_i) = 0 \tag{6}$$

The complete set of hydrodynamic equations represent 6 equations and 6 unknowns: u_1, u_2, u_3, r_w, r_a and p, i.e.

- o Momentum in direction 1 of homogenous fluid from Equation 3 (with $k = 1$) for u_1.
- o Momentum in direction 2 of homogenous fluid from Equation 3 (with $k = 2$) for u_2.
- o Momentum in direction 3 of homogenous fluid from Equation 3 (with $k = 3$) for u_3.
- o Mass conservation of water from Equation 4 for r_w.
- o Mass conservation of air from Equation 5 for r_a.
- o Volume conversation of homogenous fluid from Equation 6 for p, via pressure-velocity coupling, i.e. the Rhie-Chow interpolation $u_i = f(p)$ is substituted into Equation 6.

No turbulence model is used, since it was found that a laminar flow solution had around half the computing time of the turbulent flow solution.

For buoyancy calculations, the source term, S_{M3} appears in the momentum equation for direction 3 only (i.e. Equation 3 with $k = 3$, the direction of gravity). It represents a hydrostatic pressure variation with depth. The negative sign in front of the brackets for S_{M3} indicates that the pressure reduces as distance from the sea bed increases in direction 3. Subtraction of ρ_a for S_{M3} in Equation 3 is necessary since all pressures in the model are computed relative to an atmospheric pressure of 1 bar, which is set at a reference location (X_3).
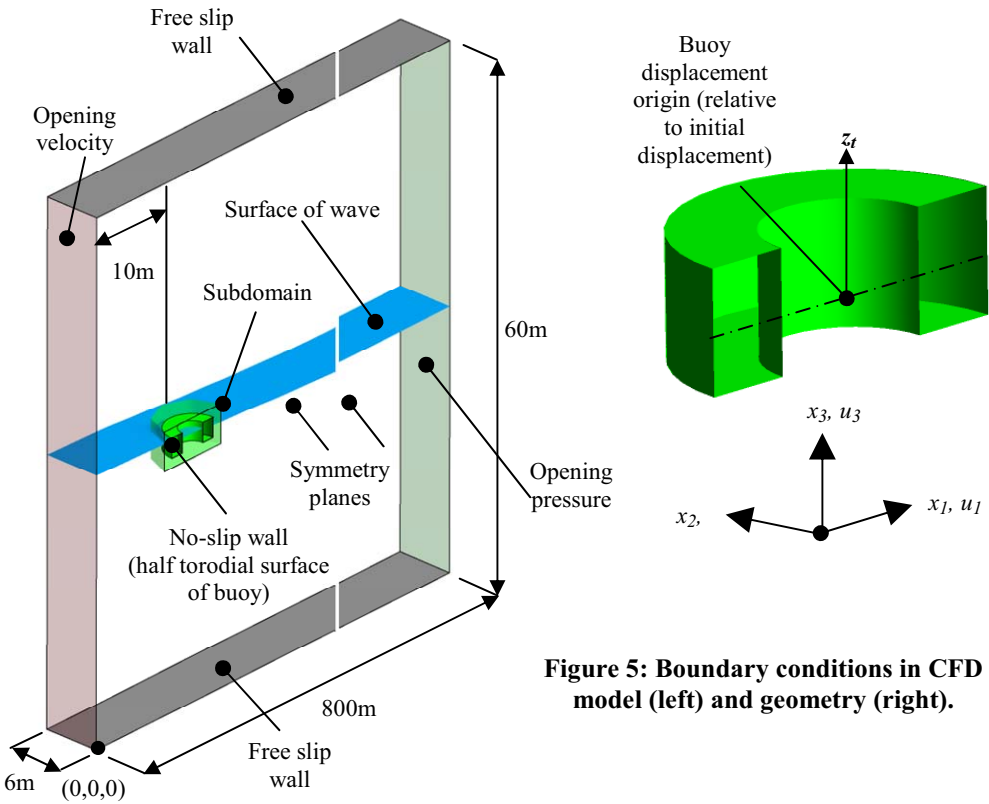
Figure 5: Boundary conditions in CFD model (left) and geometry (right).

Parameter	Value
Domain dimensions, X_1 x X_2 x X_3 [m]	800 x 6 x 60
Number of cells, NX_1 x NX_2 x NX_3 [-]	60 x 10 x 39
Simulation time, t_{TOTAL} [s]	30
Wave wavelength, L [m]	100
Wave amplitude, H [m]	1
Water depth, h [m]	30
Wave function, $h(t)$ [m]	$-H \sin(\omega t)$
Wave number, $k = 2\pi / L$ [rad/m]	0.06
Wave frequency, $\omega = \sqrt{gk \tanh(kh)}$ [rad/s]	0.75
Wave period, $T = 2\pi / \omega$ [s]	8.38
Wave linearity, kH [-]	0.06
Buoy area normal to x_3 direction, A [m^2]	17.8

Table 1: Domain size and wave input parameters.

Parameter	Value
$r_{w,t=0}$ [-]	1 for $x_3 < h$; 0.5 for $x_3 = h$; 0 elsewhere
$r_{a,t=0}$ [-]	$1 - r_{w,t=0}$
$u_{1,t=0}$ $u_{2,t=0}$ $u_{3,t=0}$ [m/s]	0
$p_{t=0}$ [Pa]	$(\rho_w - \rho_a)g(h - x_3)r_{w,t=0}$
$r_{w,x1=0}$ [-]	1 for $x_3 < h+h(t)$; 0.5 for $x_3 = h+h(t)$; 0 elsewhere
$r_{a,x1=0}$ [-]	$1 - r_{w,x1=0}$
$u_{1,x1=0}$ [m/s]	$-H\omega \dfrac{cosh(kx_3)}{sinh(kh(t))}\, sin(\omega t)r_{w,x1=0}$
$u_{2,x1=0}$ [m/s]	0
$u_{3,x1=0}$ [m/s]	$-H\omega \dfrac{sinh(kx_3)}{sinh(kh(t))}\, cos(\omega t)r_{w,x1=0}$
$p_{x=0}$ [Pa]	implicit
$r_{w,x1=800}$ $r_{a,x1=800}$ [-]	zero gradient
$u_{1,x1=800}$ $u_{2,x1=800}$ $u_{3,x1=800}$ [m/s]	implicit
$p_{x1=800}$ [Pa]	$\rho_w g(h - x_3)r_{w,t=0}$
ρ_w [kg/m^3]	997
ρ_a [kg/m^3]	1.18

Table 2: Initial and boundary conditions (subscript w = water, a = air).

4.4 Hydrodynamic Force

The absolute pressure and shear stress are used to evaluate the hydrodynamic wave force on the buoy, F_z. Pressures in Equation 3 are computed over time relative to a reference pressure of 1 atmosphere. The hydrodynamic wave force on the buoy can be computed as the integral of the pressure field and the viscous stresses on the instantaneous wetted surface of the buoy by the following expression:

$$F_z = \int_S \left(- p_{abs}n_3 + \tau_{wall,x3}\right) dS \tag{7}$$

where p_{abs} is the absolute pressure, n_3 is the face outward normal vector to each cell and $\tau_{wall,x3}$ is the tangential viscous shear stress on the cell face and S is the cell face area. The negative sign in front of p_{abs} indicates that the face outward normal vector is in the opposite direction to the pressure normal to the surface (i.e. the pressure must always act towards the surface). The hydrodynamic force is then defined as

$$F_t = 2F_z - mg \tag{8}$$

It is twice the force at the buoy surface (due to the use of a symmetry plane, see Figure 5) minus the weight of the buoy. The computed force F_t is returned to SimHydraulics in Case 2 of the coupled simulation.

5. DESCRIPTION OF UNCOUPLED AND COUPLED ALGORITHMS

The EQM for the buoy is:

$$m\ddot{z}_t = F_t - D_t \tag{9}$$

The buoy is moved by the forces acting on it, and it moves the fluid surrounding it:

  o The EQM for the buoy (Equation 9) is used to determine its displacement. The displacement is applied via the mesh displacement at the buoy surface.
  o The transient term in the fluid momentum equations (Equation 3) implies fluid advection is time dependent. The velocity of the fluid is affected by the velocity of the buoy because the buoy velocity is applied to the fluid via the no slip relative velocity boundary condition at the buoy surface (see Figure 5).

Four simulations were investigated and the terms used to denote them are defined as follows:

"Uncoupled simulation" is defined as:
  o Standalone hydrodynamics model with no data exchange, since there is no separate hydraulics model (Case 1 in Figure 4).
  o A constant damping coefficient represents the hydraulic system.
  o EQM for the buoy solved with hydrodynamics model (Fortran code).

"Simple coupled simulation" is defined as:
  o Hydrodynamic force is the output of hydrodynamics model (Case 2 in Figure 4) and buoy displacement is output of hydraulics model (Case A in Figure 2).
  o A constant damping coefficient represents the hydraulic system.
  o EQM for the buoy solved with hydraulics model (Simulink solver).

"Coupled simulation 1" is defined as:
  o Hydrodynamic force is output of hydrodynamics model (Case 2 in Figure 4) and buoy displacement is output of hydraulics model (Case B in Figure 2).
  o A full hydraulics model represents the hydraulics system.
  o EQM for the buoy solved with hydraulics model (Simulink solver).

"Coupled simulation 2" is defined as:
  o Buoy velocity is output of hydrodynamics model (Case 3 in Figure 4) and hydraulic force is output of hydraulics model (Case C in Figure 2).
  o A full hydraulics model represents the hydraulics system.
  o EQM for the buoy solved with hydrodynamics model (Fortran code).
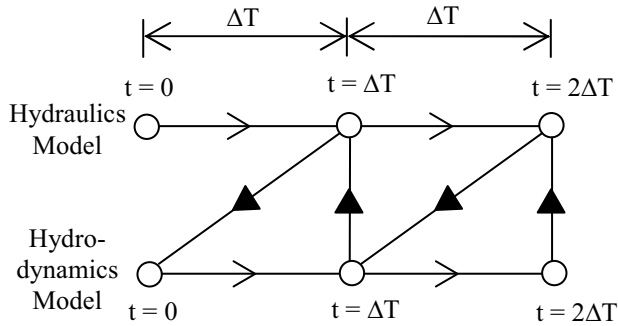
Figure 6: Coupling between hydraulics model and hydrodynamics model.

All the coupled simulations use sequential or explicit coupling between the hydrodynamics and hydraulics models (see Figure 6). The timestep used for all simulations was $\Delta T = 0.04$ s. Data exchange is achieved by reading and writing files to the hard disk. All files are deleted once read from the hard disk and each model is paused until a new file is written, thus generating the sequential coupling. The hydrodynamics model uses Fortran code to handle data exchange and the hydraulics model uses Matlab. Matlab also acts as the master controller, calling the hydrodynamics and hydraulics models at the beginning of the simulation. This is known as indirect coupling because an external master program exists between the hydraulics and hydrodynamics models.

The EQM for the buoy in all cases is treated implicitly with regard to either the hydrodynamic or the hydraulic force (the other force being held constant during the solution of the EQM). When the EQM is solved with the hydrodynamics model (Fortran), the hydraulic force is constant during the iterations of the solution. The mesh displacement equations and the EQM are solved every iteration of the hydrodynamic equations (i.e. more than once per timestep). When the EQM is solved with the hydraulics model, the hydrodynamic force is constant during the iterations of the solution. So the mesh displacement equations and the EQM are only solved once per timestep.

To check that the coupling strategy is stable, the uncoupled simulation was compared with the simple coupled simulation. In both simulations the damping coefficient was constant and set to $C = 200,000$ Ns/m. As expected, the results are indistinguishable. In particular there are no oscillations in the coupled result, indicating good robustness.

6. COMPARISON OF THE COUPLED SIMULATIONS

The purpose of this comparison is to establish whether there is a numerical difference between solving the EQM with the hydrodynamics model and solving it with the hydraulics model, and to check whether computing times of the two methods are similar. Figure 7 shows that the two coupled simulations both produce similar phase and amplitude in terms of buoy displacement, velocity and hydrodynamic force. The controller can activate or deactivate individual actuators. Activated actuators charge up the accumulators, whereas idle actuators have both chambers connected to tank. Whenever one of the three actuators is

switched on or off by the controller, the force applied from the hydraulics onto the buoy changes rapidly. Hence, both coupled simulations show oscillations in the velocity response.

Additionally, the buoy inertia term is small compared with the forces involved, leading to relatively large accelerations and hence changes in velocity. The slight difference in the nature of the oscillations between the coupled simulations could be due to the different solver implementations. In particular the definition of convergence for the EQM solution would be different. In the hydraulics model convergence of the EQM solution is based on the hydraulic force. However, in the hydrodynamics model, the convergence of the EQM solution is based on the hydrodynamic force. It is possible that reducing the timestep may minimise this effect. Alternatively, a staggered coupling strategy could be investigated, where data exchange occurs more frequently than once per timestep.
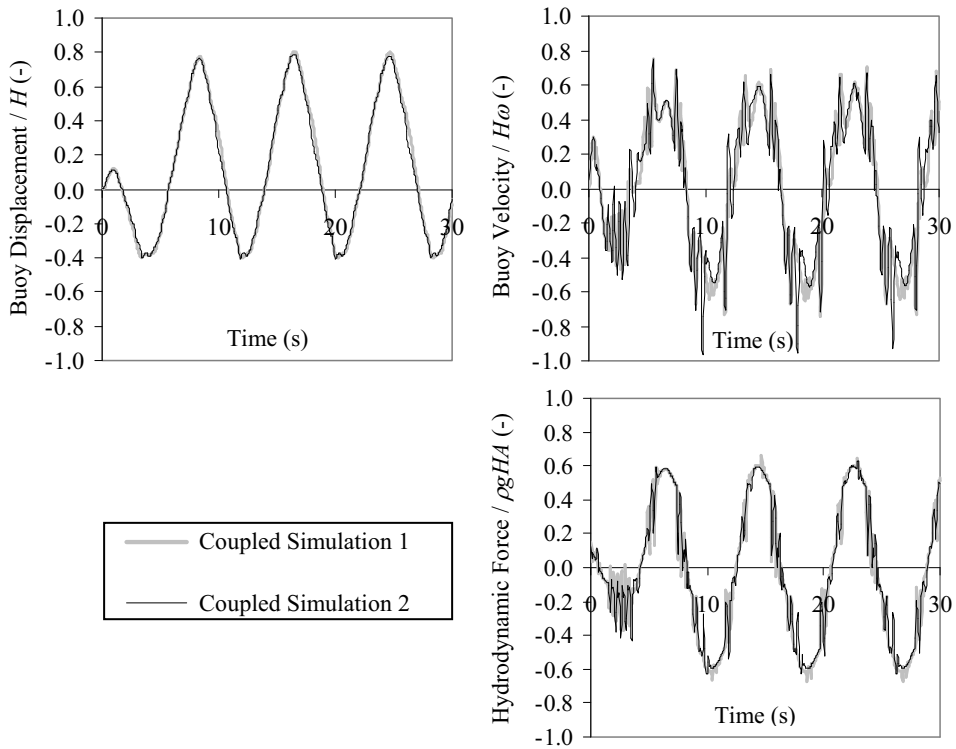
Figure 7: Comparison between coupled simulation 1 and coupled simulation 2.

The simulations were run on a 3.0GHz Pentium 4 Processor with 2GB RAM. The total computing time for coupled simulation 1 is around 12 hours, which is 30% more than that for coupled simulation 2. This is because the mesh displacement equations are being solved every iteration of the hydrodynamics equations for coupled simulation 1 and solving these equations takes high computational resources.

When the EQM is solved with the hydraulics model, the mesh displacement equations are solved only once per data exchange timestep. Just over half of the total computing time is due the CFD model. It may be possible to reduce it using a directional damping zone applied as a momentum source term in Equation 3 [5]. This would shorten the domain length of 800 m without generating detrimental reflections from the far opening.

7. COMPARISON BETWEEN COUPLED SIMULATION 1 AND THE UNCOUPLED SIMULATION

The purpose of this comparison is to see whether the coupled and uncoupled simulations exhibit similar characteristics. Figure 8 presents a comparison between the coupled simulation 1 and the uncoupled simulation.
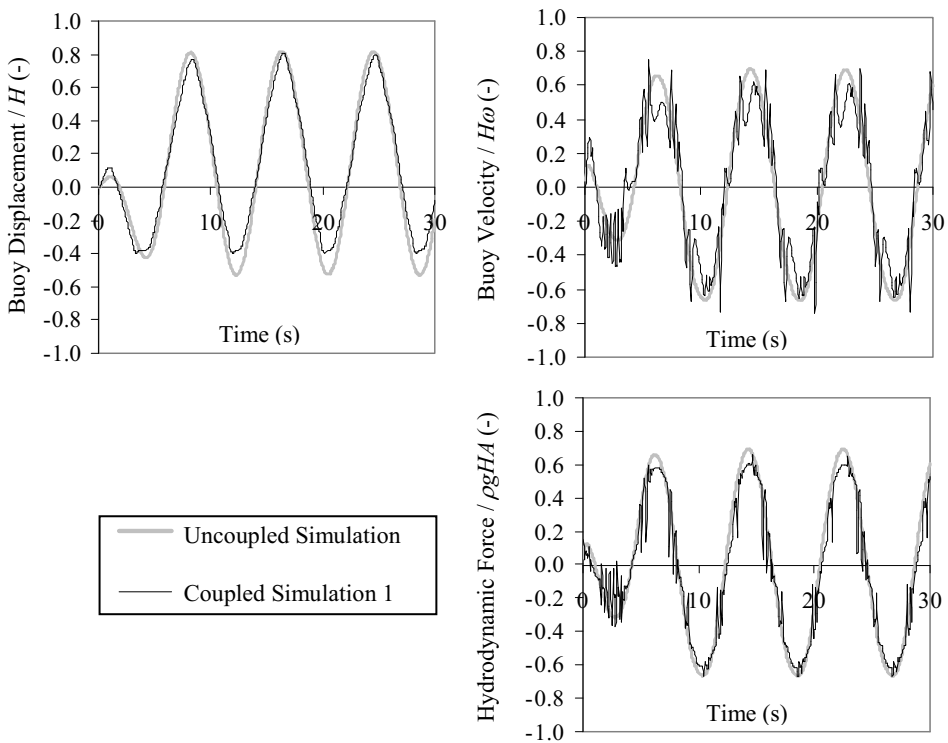
Figure 8: Comparison of uncoupled simulation with coupled simulation 1.

In this case, coupled simulation 1 solves the EQM for the buoy within the SimHydraulics model of the hydraulic system. The uncoupled case solves EQM within the hydrodynamics model, with a constant damping coefficient of 200,000 Ns/m. It is apparent that the displacement, velocity and hydrodynamic force are of similar order. Therefore, a simplified analysis with a fixed damping coefficient may be sufficient if the low-frequency buoy response is to be estimated [7].

8. CONCLUSIONS

Coupling between a hydrodynamics and hydraulics model was investigated. Two differently coupled simulations with the hydraulics represented as a constant damping coefficient produced identical results, indicating that the coupling method employed is inherently stable.

Two coupled simulations using a full hydraulics model were also compared. One solved the rigid body EQM with the hydraulics model in Simulink, and the other solved it with custom Fortran code, which is part of the hydrodynamics model. The latter solution requires more computational resources, because the mesh displacement equations are solved every iteration of the hydrodynamics equations. Comparing the two coupled simulations showed a slight difference, possibly due to the different numerical methods of solving the EQM.

It was shown that the full hydraulics model can be represented by a constant damping coefficient if higher frequency dynamics caused by the actuator switching control strategy, are not important for the particular analysis.

9. FUTURE WORK

Future work could include investigating a staggered coupling strategy, which may remove the dependence on the method of solving the EQM observed here. It may also improve the efficiency of the coupling strategy, since larger timesteps may be possible for the same accuracy. The efficiency of the CFD model could also be improved by using a damping zone in the fluid domain, thus removing the need for a long model to prevent reflections from the far opening. It is also necessary to assess the effect of inertia on the operation of the system. At the time of writing, the Fortran code used in this project is a proposed feature for the next version of ANSYS CFX.

ACKNOWLEDGEMENTS

REFERENCES

[1] E. Agamloh, A. Wallace, A. von Jouanne. *Application of fluid-structure interaction simulation of an ocean energy extraction device*. Journal of Renewable Energy, 33:748–757, 2008.

[2] Chen, Qing. *Numerical investigation of internal flow in hydraulic valves and dynamic interactions in hydraulic systems with CFD and simplified simulation methods*. PhD Thesis, Institute of Turbomachinery and Fluid Power at Darmstadt University of Technology, 2004.

[3] K. Habr. *Gekoppelte Simulation Hydraulischer Gesamtsysteme unter Einbeziehung von CFD*. PhD Thesis, Institute of Turbomachinery and Fluid Power at Darmstadt University of Technology, 2002.

[4] COPHIT Project. *Modelling Flow in the Airways*. Presentation at Mayneord Phillips Summer School, Oxford, 2003.

[5] J. Westphalen. *Extreme wave loading on offshore wave energy devices using CFD*. Transfer Report, Department of Architecture and Civil Engineering, University of Bath, 2007.

[6] M. Rahman. *Water Waves: Relating modern theory to advanced engineering practice*. Oxford University Press, ISBN 0-19-853478-7, 1995.

[7] J. da Costa, A. Sarmento, F. Gardner, P. Beirao, A. Brito-Melo. *Time domain model of the AWS wave energy converter*. 6th European Wave and Tidal Energy Conference, Glasgow, UK, 2005.

System Identification of Hydraulic Systems by the Self-Excited Oscillation Method

Takayoshi Ichiyanagi, Takao Nishiumi, Tetsuya Kuribayashi
National Defense Academy, Department of Mechanical Systems Engineering,
1-10-20 Hashirimizu, Yokosuka, Kanagawa, JAPAN

ABSTRACT

It has been well known that a hydraulic servo actuator system can be often dealt with a second order delay element when the controller for the system is designed. In the previous works, our research group developed a simple method utilizing the self-excited oscillation of the hydraulic servo actuator system to directly estimate the dynamic parameters such as the damping ratio and undamped natural frequency. The advantage of this method is a real-time identification ability that is able to identify these parameters instantaneously with changing the operating conditions. Although this method was confirmed to be very useful, it is available only when the spool valve is close to the neutral position, which corresponds to the operation of position control systems. In the practical situations, the spool valve sometimes operates at displaced position from the neutral center position such that a hydraulic motor speed is controlled. This paper proposes the revised self-excited oscillation method for this system. The experimental works are conducted by giving the various system pressures and angular velocities so as to validate the method. The resulting frequency characteristics of these identified transfer functions are then compared with those of the measured data by the frequency characteristics method.

Keywords: Hydraulic servo actuator system, System identification, Limit cycle

1. INTRODUCTION

Hydraulically driven actuators that are controlled by a servovalve have been used in various industry fields because they have several advantages such as high power density, compactness, and so on, over other type of actuator systems. For the development of these hydraulic servo actuator systems, it is required to know a precise knowledge of the system dynamic behavior and the corresponding mathematical descriptions. The hydraulic servo actuator system has non-linear characteristics in their dynamic behavior. However, it is often treated as simplified descriptions by linearized approximation for the design of a controller or analyzing the actuator dynamics. Their dynamic characteristics are generally dealt with as a second order delay element (1).

In order to design a controller of hydraulic servo actuator system adequately, an estimation of the dynamic parameters will be required. One of the practical ways to obtain these parameters is the use of an experimental identification method. Therefore various methods

have been proposed to estimate unknown parameters for each specific purpose until now. For the estimation of the dynamic parameters of second order delay element, which are the damping ratio ζ and the undamped natural frequency ω_n, the frequency response method or the step response method are known as a classic identification method and still often used as one of the practical methods. Identification method utilizing the limit cycle of identified system was other methods (2). In the process control fields, the automatic tuning technique of PID controller utilizing the limit cycle generated in the relay feedback system has been already applied to the industry (3). However, no report had been published for the application of hydraulic servo actuator system that has quick response dynamics and dealt with the second order delay element. Our research group developed a simple method utilizing the self-excited oscillation of the hydraulic servo actuator system to directly estimate the dynamic parameters of the second order delay element. The usefulness and the validity of the method were described in the previous reports. Firstly, this method was applied to a servovalve in the case where the output detector delay was negligible (4). Then, the effects of the output detector delay on the identified results were assessed by using an electric circuit, which simulated the detector delay as a first order delay element (5). Furthermore, this method was expanded to a real time identification system, which is realized by using a digital signal processor (6).

Even though the previous reports proved the usefulness of the proposed method, this method identifies the dynamic parameters only at the condition that the servovelve spool is close to the neutral position. In other words, the method was only available for the position controlled hydraulic servo actuator system. But in the practical operation conditions, if the actuator is hydraulic motor and when the motor rotational speed is controlled, the servovalve is operated as its spool valve is being displaced from the neutral position. The previous method is not able to apply to this velocity controlled hydraulic servo actuator systems. This paper addresses the revised self-excited oscillation method which can identify the dynamic parameters of velocity controlled hydraulic servo motor system. In this method the angular velocity self-excited oscillation around a constant rotational speed is utilized to identify the dynamic parameters. In addition, in order to evaluate the self-excited oscillation method, the dynamic parameters of an aircraft tail control surface simulator, are experimentally identified and examined.

The paper firstly describes the fundamental principle of the self-excited oscillation method for both the position control system and the proposed velocity control system. Then the experimental apparatus of identified hydraulic servo motor system are explained. The real time experimental identifications for the hydraulic servo motor system are carried out by providing the various system pressure and angular velocity. The identified results derived from the conventional frequency response method and the proposed self-excited oscillation method is compared to confirm the validity of the proposed method. Finally, in order to demonstrate the usefulness of this method, the dynamic parameters of the aircraft tail control surface simulator are identified.

2.   SELF-EXCITED OSCILLATION METHOD

2.1   Position control system

A schematic diagram of an identified hydraulic servo cylinder system is illustrated in Fig.1. It mainly consists of a hydraulic cylinder, a load mass, a servo amplifier and servovalve.

Firstly the position (and angular position) feedback control are considered to be an application of this hydraulic servo actuator system. It should be noted that a spool of the servo valve basically moves around the neutral position in this case. The linear transfer function from the servo amplifier input voltage V to the velocity of the cylinder position $\dot{y}$ can be described by Eq.(1) as the second order delay element, provided that the connecting pipes are treated as a lumped element characteristics and the dynamic characteristics of the servovalve is negligible, i.e. the servovalve dynamics is considerably faster than the hydraulic actuator response.

$$G_L(s) = \frac{\dot{y}(s)}{V(s)} = \frac{K_L \omega_n^2}{s^2 + 2\zeta\omega_n s + \omega_n^2} \tag{1}$$

where K_L, ω_n and ζ are the gain of the hydraulic servo actuator system, the undamped natural angular frequency and the damping ratio, respectively.

The self-excited oscillation method is able to directly identify the system dynamic parameters ω_n and ζ of the second order delay element by using the self-excited oscillation of the identified system. Figure 2 shows the block diagram of the position (angular position) self-excited oscillation system that was utilized to identify the linear transfer function G_L. This system is composed only by arranging a non-linear element K_N in forward side of the hydraulic servo actuator system G_L. Since the non-linear element, which is an ideal relay, has variable gain characteristics expressed by Eq.(2), the system causes the limit cycle at the point of stability limit.
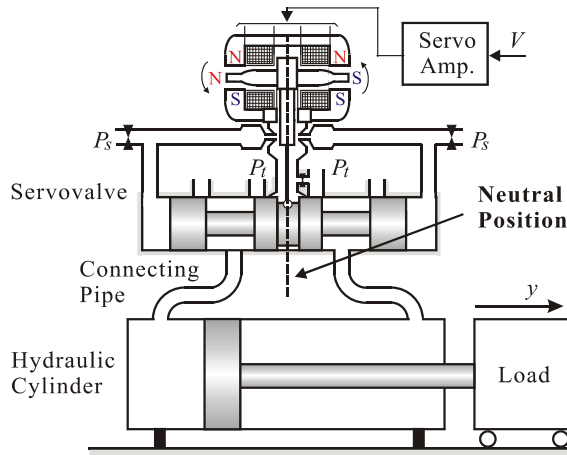
Fig.1 Hydraulic servo cylinder system
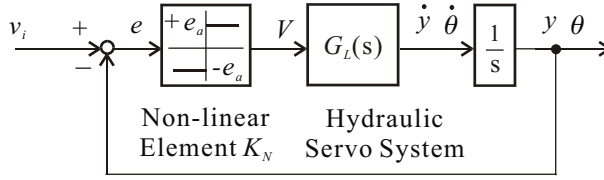
Fig.2 Position control self-excited oscillation system

$$K_x = \frac{e_a}{|e|} \qquad (2)$$

where e_a is the setting voltage of non-linear element. This non-linear element outputs the setting voltage $V = \pm\, e_a$ which is corresponding to plus or minus of the error signal e as shown in Fig.3. When the error signal becomes close to zero, the variable gain K_x is increasing and leads to an instability of the system. Then once the system enters the unstable region, the error signal becomes large in turn and the system goes to the stable region again. Finally this causes limit cycle. The wave shape of this limit cycle can be approximated to the sinusoidal wave in Eq.(3) with the amplitude V_s and the average angular frequency ω_s, however the real angular frequency is varying continuously.

$$y(t) \approx V_s \sin \omega_s t \qquad (3)$$

Since the non-linear element is variable gain characteristics, the gain at stability limit can be obtained in Eq.(4) by using Routh-Hurwitz stability criterion

$$K_{Nc} = \frac{e_a}{e_c} = \frac{2\varsigma\omega_n}{K_L} \qquad (4)$$
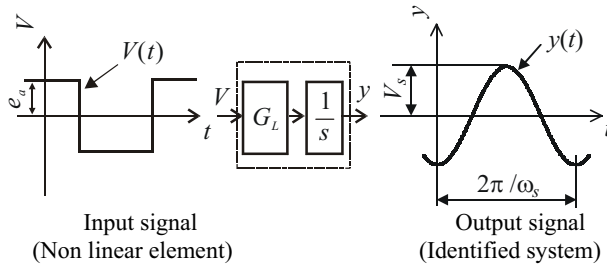
Fig.3 Input and output of identified system

The undamped natural angular frequency ω_n of the identified system can be defined as Eq.(5) by introducing the frequency correction factor ξ, because this value is equal to the angular frequency of the stability limit.

$$\omega_n = \frac{\omega_s}{\xi} \tag{5}$$

Then the damping coefficient of the identified system is derived from Eq.(4) and Eq.(5).

$$\zeta = \frac{\Gamma K_L e_a}{2V_s \omega_n} \tag{6}$$

where Γ is the amplitude correction factor defined as the ratio of the error signal e_c at the stability limit and the amplitude V_s of the limit cycle wave, i.e. self-excited oscillation wave.

$$\Gamma = \frac{V_s}{e_c} \tag{7}$$

Therefore in this identification method, two dynamic parameters can be easily obtained from Eq. (5) and Eq. (6) by measuring the amplitude V_s and the angular frequency ω_s of the measured self-excited oscillation wave. Two correction factors for the angular frequency and the amplitude are expressed by the following equations that were obtained and interpolated by simulation analysis.

$$\left. \begin{array}{l} \xi = 1.0 - 0.0315\zeta + 0.00415\zeta^2 - 0.000185\zeta^3 \\ \Gamma = 1.27 + 0.0647\zeta - 0.00762\zeta^2 + 0.000307\zeta^3 \end{array} \right\} \tag{8}$$

2.2 Velocity control system

Hydraulic motor is used for rotary acutuation mechanical systems. For the application of this rotary acutor system, the rotational speed (angular velocity) of the hydraulic motor is often controlled. Consider a condition where the hydraulic motor is driving at a constant rotational speed. In this case, the servovalve spool is displaced x from the neutral position as shown in Fig.4 and therefore the dynamic characteristics of the identified system are varied from the spool is around the neutral position, i.e., the position control system. In order to apply the self-excited oscillation method to this hydraulic motor angular velocity control system, the angular velocity ω is used for the feedback signal to make up the angular velocity self-excited oscillation system shown in Fig.5 (a). It is clear from Fig.2 and Fig.5 (a) that the open loop transfer functions of both the angular velocity self-excited oscillation system and the position self-excited oscillation system are the same. Therefore, all equations described above can be applied to obtain the dynamic parameters. However there is a problem in the measurement of angular velocity. The noise of high order harmonic frequency is often imposed in the measured angular velocity. This noise component generates the input signal, which is not based on the proper angular velocity self-excited oscillation, into the servo amplifier by passing through the non-linear element. Consequently it causes the inaccurate estimation of the dynamic parameters. Hence, in this

research, the integrator element is placed forward to the non-linear element to reduce the influence of this noise component. The self-excited oscillation system shown in Fig.5 (a) is transformed into the system shown in Fig.5 (b). It is the revised angular velocity self-excited oscillation system. The feed-forward signals are added into the input signal to the non-linear element v_e- (v_i/K_L) and to the servo amplifier $\pm e_a+(v_i/K_L)$. The former signal is oscillated around zero so that the non-linear element outputs $\pm e_a$ periodically. The later block diagram makes possible the self-excited oscillation at the controlled rotational speed.

2.3   Real time identification procedure

Hydraulic servo actuator systems have been utilized in the various industry motion fields. In the past decade, the control technology of these systems are rapidly developing due to the recent progress related to the electrical and electronic instruments including computers and sensors. Therefore the latest hydraulic servo actuator systems are sometimes equipped with the intelligent and advanced control strategy functions. The self-excited oscillation method can be also a suitable software application of these modern electro-hydraulic servo actuator systems, because this method is able to estimate the system dynamic parameters in real time. In this report, a digital signal processor is used to compute the algorithm of the self-excited oscillation method. The real time parameter estimation procedure is consist of next four process.
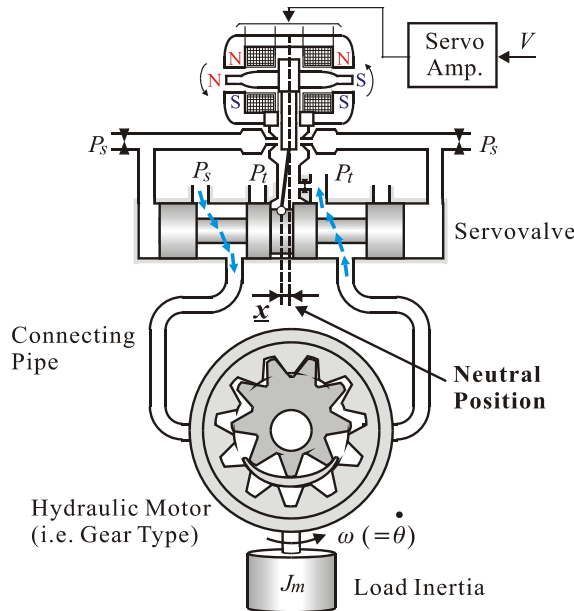
Fig.4 Hydraulic servo motor system
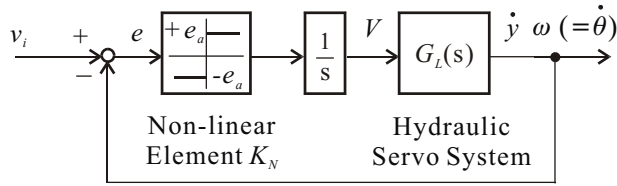
(a) **Velocity control self-excited oscillation system**
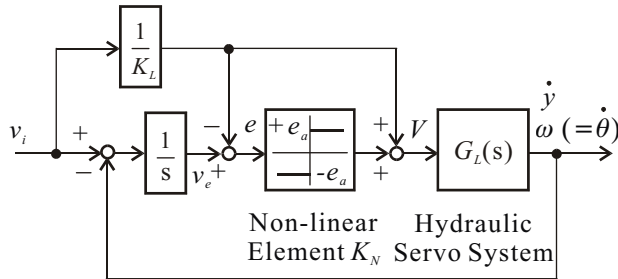
(b) **Revised velocity control self-excited oscillation system**

Fig.5 Velocity control self-excited oscillation system

(1) Measurement of self-excited oscillation wave

The position (angular position) or angular velocity signals are acquired from sensors through A/D converter.

(2) Low pass filter

For the position feedback systems, low pass filer will be required if the self-excited oscillation wave of identified systems contain some high frequency noise components. The design of filter is dependent on the noise frequency of the identified system.

(3) Analyze the measured wave

This is the process that finds the amplitude V_s and angular frequency ω_s of the self-excited oscillation wave. The wave signals of the self-excited oscillation are stored in the computer memory. Then the present wave data $y(i)$ is compared with the past data $y(i-1)$ and $y(i-2)$ where the i-1, i-2 are the time delay for one previous and two previous sampling time. The amplitude V_s can be derived from the difference between the positive peak data ($y(i-2) < y(i-1) > y(i)$) and the negative peak data ($y(i-2) > y(i-1) < y(i)$). The angular frequency ω_s is also obtained from the time data at the positive and negative peaks.

(4) Computation of dynamic parameters

From the amplitude V_s and angular frequency ω_s information obtained the previous process, the damping ratio ζ and undamped natural frequency ω_n are calculated from Eq.(5) to Eq.(8). Since these equations contain the amplitude and frequency correction factor that is

function of damping ratio ζ, the calculation must be done iteratively. In the iterative calculation, the first values of the correction factors are set to $\xi_1=0.95$ and $\Gamma_1=1.4$. Then the first value of the damping ratio ζ_1 can be estimated and is used for the second values of the correction factors ξ_2 and Γ_2. By iterating until the error becomes insignificant, the precise dynamic parameters ζ and ω_n are finally obtained. Since this iterating procedure usually takes only several iterations, the computing time is very short.

The DSP processes these procedures every sampling period. It should be noted that the least time of the parameter estimation in this method becomes the self-excited oscillation period, since the dynamic parameters can be obtained after analyzing the angular frequency of one self-excited oscillation wave.

3.   IDENTIFIED EXPERIMENTAL SYSTEMS

In order to verify the usefulness of the self-excited oscillation method, the dynamic characteristics of two different hydraulic servo actuator systems are identified. These are (a) a hydraulic motor system, (b) an aircraft tail control surface simulator. These applications are mainly used for the educational purpose of our academy to learn the mechanism of the hydraulic components and the integrated system of electronics and mechanics. They are also very useful applications to learn how the control theory is applied to a real system.

(a) Hydraulic motor system

Figure 6 shows the test hydraulic servo motor system used in this study. This is the laboratory test bed for the hydraulic rotary actuator applications. The hydraulic source unit consists of a pump, an electric motor, a relief valve and a main tank. The system supply pressure is adjusted by this relief valve. The identified hydraulic servo motor system
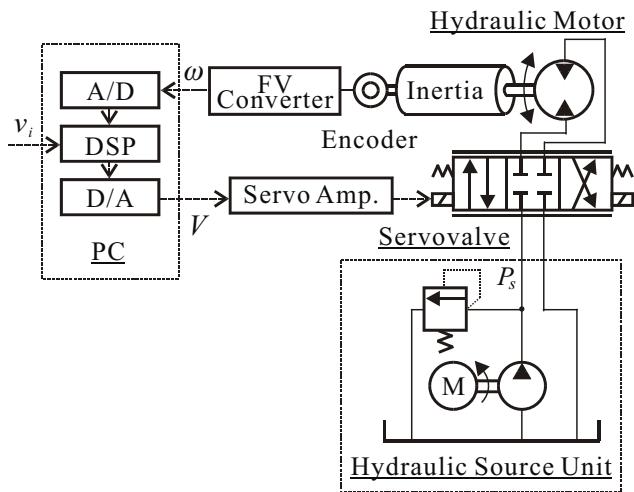
Fig.6 Experimental set up of hydraulic servo motor system

consists of the servovalve, the hydraulic motor and the load inertia. The gain of the hydraulic motor system K_L has been obtained in advance by measuring the static characteristics. This gain shows the dependency characteristics on the supply pressure P_s as expressed in Eq.(9).

$$K_L = 4.25 + 2.72 \times 10^{-6} P_s - 0.134 \times 10^{-12} P_s^2 \qquad (9)$$

where the supply pressure unit of this equation is [Pa]. The angular velocity ω is detected by the encoder and sent to the PC through a FV converter as a feed-back signal.

(b) Aircraft tail control surface simulator

Figure 7 shows the picture of the aircraft tail control surface simulator. This devise simulates the movements of the aircraft tail control surface by the inputs of a joystick and foot pedals. The tail control surface consists of the rudder and the stabilator which respectively control the yaw and pitch direction of the aircraft. The direction of rudder is manipulated with the movement of foot pedals and the stabilator's direction is controlled by the operators joystick. Both operators inputs are provided electrically to the servovalves through the DSP inserted computer. This is so called "fly by wire" system.
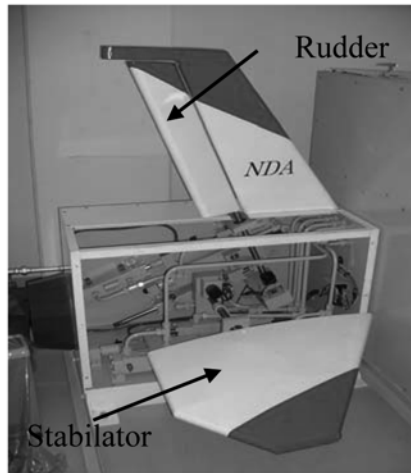
Fig.7 Aircraft tail control surface simulator

These applications of hydraulic servo actuator system are all combined with the computer. Hence for the real time identification of these systems, the digital signal processor embedded inside PC is used in this report to analyze the self-excited oscillation wave and calculate the dynamic parameters. The real time identification algorithm described in the previous chapter is written in MATLAB/Simulink® model code. Then the program is implemented in the single board type DSP (dSPACE DS1102:TI-TMS320C31 25MHz processor with 16bit AD/DA converter). The sampling time is chosen to 0.5 [ms]. Data

acquisition and editing parameter sets are managed by the virtual instrument panel on PC monitor (The software is "Control desk" by dSPACE). The identified parameters are also stored and displayed in this window as shown in Fig.8.

4.   EXPERIMENTAL RESULTS

Firstly the verification of the self-excited oscillation method for the angular velocity control system is discussed. This is the case that the self-excited oscillation method applies to the condition where the servovalve spool is constantly displaced from the neutral position. Figure 9 shows the example plot of the self-excited oscillation wave. The input and output signals of the non-linear element shown in Fig.5 (b) are examined. It can be seen from this figure that the noise component imposed on the angular velocity oscillation wave is completely attenuated and the non-linear element outputs the setting voltage e_a corresponding to the angular velocity self-excited oscillation period without suffering from the influence of the noise.

Figure 10 shows the results of the real time identification with changing the supply pressure P_s continuously from 5 MPa to 10 MPa at the reference rotational speed $K_L v_i$=32.5 rad/s and the setting voltage e_a=1.5 V. It is obvious that these dynamic parameters are estimated continuously by the proposed identification method. This indicates the realization of real time identification. The results also show the identified dynamic parameters are notably affected by the supply pressure. In particular, the undamped natural angular frequency ω_n increases almost in proportion to the supply pressure P_s. Concerning about the setting voltage e_a, if the amplitude of this voltage is too small, the self-excited oscillation does not occur properly because of the actuator's internal and external frictions. Therefore this voltage should be chosen large enough to generate the self-excited oscillation (the voltage is depend on the identified plant).
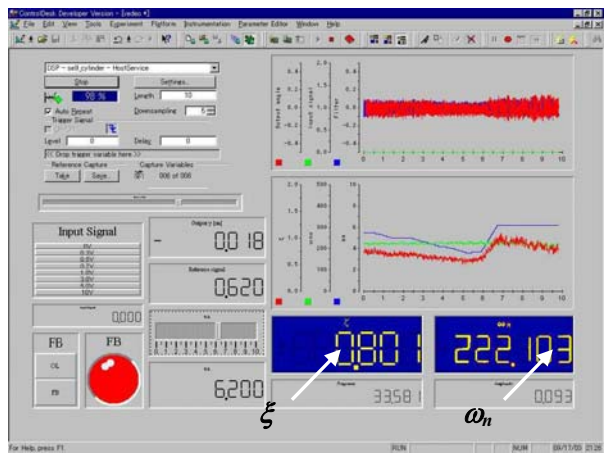
Fig.8 Control and measuring window of real-time identification system
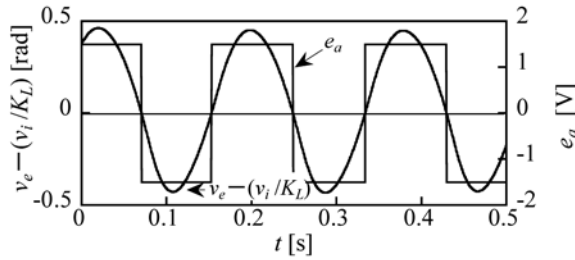
Fig.9 Example plots of self-excited oscillation waves

The identified dynamic parameters when the servovalve spool is displaced from the neutral position are shown in Fig.11. The rotational speed of the hydraulic motor $K_L v_i$ is varied from 0 rad/s to 120 rad/s continuously at the supply pressure P_s=8 MPa and at the setting voltage of the non-linear element e_a=1.5 V. This rotational speed range approximately corresponds to the displacement range of the servovalve spool. The maximum rotational speed in this identified hydraulic servo motor system is 140 rad/s at the maximum spool displacement. The result at $K_L v_i$=0 rad/s is the same condition as the angular position self-excited oscillation system. It is confirmed that the dynamic parameters at the servovalve spool is displaced are also identified continuously as well as the spool is in the neutral position.

In order to investigate the validity of the on-line identification results for the proposed method, comparison between the self-excited oscillation method and the frequency response method is carried out. Figure 12 shows the bode plot of the identified hydraulic motor system at the supply pressure P_s=8 MPa, the setting voltage of the non-linear element e_a=1.5 V and the rotational speed $K_L v_i$=0, 70, 133 rad/s. In this figure the line shows the
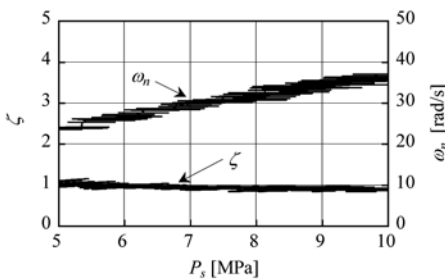
Fig.10 Identified dynamic parameters (hydraulic servo motor system, $K_L v_i$=32.5rad/s, e_a=1.5V)
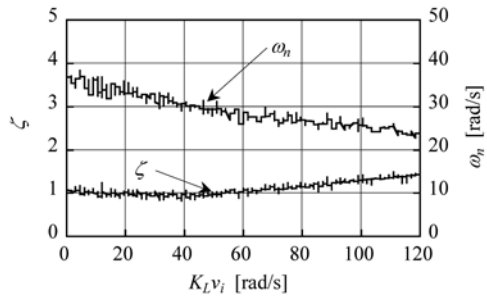
Fig.11 Identified dynamic parameters (hydraulic servo motor system, P_s =8MPa, e_a=1.5V)

self-excited oscillation method results obtained from Eq.(1) using the identified dynamic parameters ζ and ω_n, on the other hand, the plotted points show the experimental results from the frequency response. A good agreement is achieved between these two methods. This suggests the developed real time identification method for velocity control system is capable of practical usage.

Figure 13 shows the results of the real time parameter estimation for the rudder actuator part of aircraft tail control surface simulator with changing the supply pressure P_s at the setting voltage $e_a=0.1$ V. The two lines correspond to the dynamic parameters ζ and ω_n and data points and show the measured results from the frequency response method. It can be again seen that both results are matched well each other and the obtained dynamic parameters are dependent on the supply pressure P_s. As it is seen in the results until now, the present method enables a continuous identification of parameters in real time, while the frequency response method can only identify the system dynamic parameters at one supply pressure condition at one time. Hence, this method is able to identify the system characteristics without repeated tests, even if the characteristics are varied by certain effects such as oil temperature rise, external force disturbance, and so on. In addition, real-time identification results may be valuable information for the real time tuning of a controller, which optimizes the output of system, if an applied system allows a small oscillation of the present method.
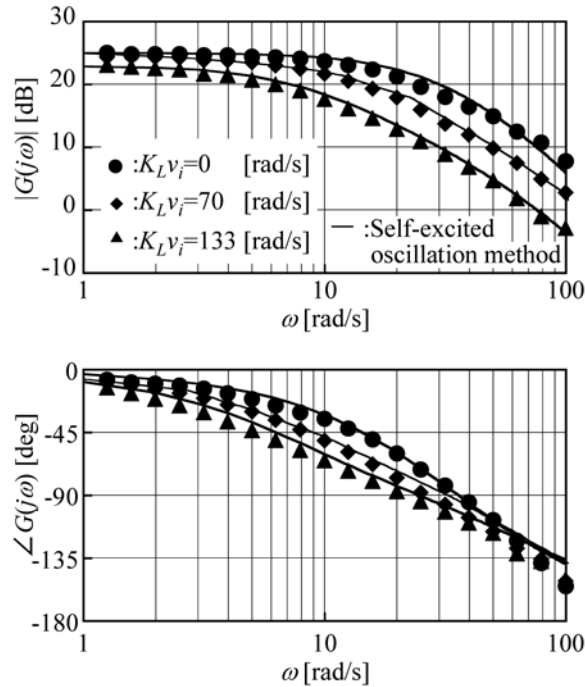
Fig.12 Comparison between self-excited oscillation method and frequency response (hydraulic servo motor system, P_s =8MPa, e_a=1.5V)
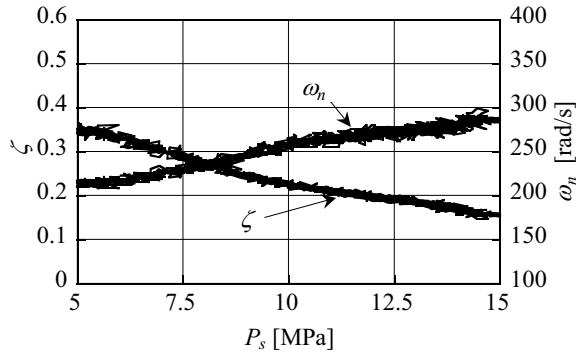
Fig.13 Identified dynamic parameters (rudder actuator part of aircraft tail control surface simulator, e_a=0.1V)

5.   CONCLUSIONS

The paper discussed about the applicableness of the self-excited oscillation method to the practical cases. Firstly, the method was revised for the hydraulic servo motor system which operates at a constant rotational speed. In this case, the sevovalve is always opened to delivery the flow and its spool is displaced from the neutral position. The angular velocity self-excited oscillation system was utilized for this system instead of the position self-excited oscillation system used in the previous reports. Then it was clarified that the present real time identification method was enable to identify the dynamic parameters of the hydraulic servo motor system, where the rotational speed are varied continuously. From the results examined for the revised method, it was verified that the proposed identification method also makes possible the real time parameter estimation of the hydraulic motor angular velocity system.

Secondary, the hydraulic applications such as an aircraft tail control surface simulator was chosen as the plant to be identified by the present method, so that the usefulness of this method in the practical situations was examined. The dynamic parameters were well acquired with the real time identification method for the position self-excited oscillation system. Then it was confirmed that the identified results for both applications coincided with the measured data obtained from the frequency response method.

NOMENCLATURE

e	deviation signal	V_s	amplitude of self-excited oscillation wave [V]
e_a	setting voltage of non-linear element [V]	y	cylinder position [m]
e_c	error signal at stability limit	v_i	reference input
G_L	transfer function of hydraulic servo motor system	x	spool displacement of servovalve [m]
G_N	transfer function of non-linear element	Γ	amplitude correction factor

J_m	load inertia [kgm^2]	θ	angular position [rad]
K_L	gain of hydraulic servo motor system [radV/s]	ζ	damping ratio
K_N	variable gain of non-linear element	ω	angular velocity [rad/s]
m	load mass[kg]	ω_n	undamped natural frequency [rad/s]
P_s	supply pressure [Pa]	ω_s	angular frequency of self-excited oscillation wave [rad/s]
P_t	tank pressure [Pa]	ξ	frequency correction factor
V	servo amplifier input voltage [V]		

REFERENCES

(1) Watton, J., 1989. Fluid power systems, Prentice Hall, ISBN 0-13-323197-6, pp299-301.

(2) Fujii, K., Ito, H. and Kita, T., 1968. Measurement method of dynamics for control system using limit cycle. *Journal of the society of instrument and control engineers*. Vol. 7, No.4, pp.248-257 (in Japanese)

(3) Astrom, K. J., Lee, T. H., Tan, K. K., and Johansson, K. H. 1995. Recent Advanced in Relay Feedback Method, *Proceedings of IEEE International Conference on systems*, pp.2616-2621.

(4) Konami, S., Nishiumi, T. and Hata, K., 1996, Identification of linearized electro-hydraulic servovalve dynamics by analyzing self-excited oscillations (First report, a case in which flow-rate detector delay is negligible), *Journal of Hydraulics & Pneumatics*, Vol. 27, No.4, pp. 143-149. (in Japanese)

(5) Konami, S., Nishiumi, T. and Hata, K., 1997, Identification of linearized electro-hydraulic servovalve dynamics by analyzing self-excited oscillations (Second report, a case in which flow-rate detector delay must be consider), *Journal of Hydraulics & Pneumatics*, Vol. 28, No.3, pp. 88-94. (in Japanese)

(6) Nishiumi, T., Ichiyanagi, T., Katoh, H. and Konami, S, 2005, Real-time parameter estimation of hydraulic servo actuator systems using self-excited oscillation method (Online identification of approximated transfer function composed of integral and second order lag elements), *Journal of Japan Fluid Power Systems Society*, Vol. 36, No.1, pp. 1-8. (in Japanese)

Use of Pipeline Wave Propagation Model for Measuring Unsteady Flowrate

Nigel Johnston, Min Pan
Department of Mechanical Engineering
University of Bath

ABSTRACT

A novel method for estimation of unsteady flowrate using pressure at two or three points along a pipeline is described in this paper. The pressure data are processed using a wave propagation model to determine the unsteady flow. Computer simulations show that the proposed method is effective for unsteady flowrate measurement to a high bandwidth. However, if the pressure values from two transducers are used, inaccuracies exist at certain frequencies when the transducer spacing coincides with multiples of half a wavelength. The accuracy can be improved by adding a third transducer with unequal spacing. The comparison and analysis of two-transducer and three-transducer techniques are investigated through simulation. This method may be applied to real time flowrate measurement, control systems or active noise cancellation systems.

1. INTRODUCTION

The estimation of unsteady flowrate is significant for the theoretical analysis of pipe system and practical applications. Many systems and methods have been proposed as the means to obtain the unsteady flowrate by determining the velocity of fluid. The techniques commonly applied in the past for measuring the velocity of fluids in unsteady flow consist essentially of Hot Wire Anemometer (HWA), Laser Doppler Velocimetry (LDV) or Particle Image Velocimetry (PIV) [1][2][3]. These methods are expensive and sophisticated, and they are particularly ill-suited to use on an industrial site [4]. Besides, the LDV and PIV cannot be used to determine the flowrate in real time. In fact, these techniques require post-processing of the acquired images in order to obtain the speed of the fluid. Furthermore the HWA and LDV methods measure the velocity at a point and not the volume flow rate; to determine the flow, assumptions have to be made about the velocity profile and corrections made.

On the other hand, many researchers presented measuring methods based on the mechanics of fluids in unsteady flow, estimating the flow from the pressure gradient, which is estimated from two pressure transducers a small distance apart [4][5][6]. These techniques make it possible to measure the flowrate in real time, combining low price, simplicity of implementation and reliability, as high bandwidth pressure transducers are readily available

and relatively easy to use. However, because of a simplified approximation to the wave behaviour, and the introduction of a pressure gradient calculation, it is necessary for the transducers to be closely spaced. This means that the pressure gradient is calculated from the difference between two similar measurements, magnifying the errors. Thus the flowrate measuring accuracy is degraded and the bandwidth is limited.

In this paper, methods are described for measuring the unsteady flowrate in a piping system, avoiding the limitations of previous two-transducer methods. The proposed methods are based on the wave propagation model to determine the flowrate using measured pressures as boundary conditions. This paper is organized as follows. Section 2 describes the mathematical model of pipeline using pipeline wave propagation model. The two-transducer and three-transducer techniques are presented in Section 3, together with simulated results. Conclusions are given in Section 4.

2. PIPELINE WAVE PROPAGATION MODEL

The motion equation in a pipeline and continuity equation are

$$\frac{\partial q}{\partial t}+\frac{q}{A}\frac{\partial q}{\partial x}+\frac{A}{\rho}\frac{\partial p}{\partial x}+f(q)=0 \tag{1}$$

$$\frac{\partial p}{\partial t}+\frac{q}{A}\frac{\partial p}{\partial x}+\frac{\rho c^2}{A}\frac{\partial q}{\partial x}=0 \tag{2}$$

On the assumption that $q/A \ll c$, the second terms in these equations can be neglected. So the equation (3) and (4) can be obtained as follows by using ordinary differential equations.

$$\frac{dq}{dt}+\frac{A}{\rho c}\frac{dp}{dt}+f=0 \ \ when \ \frac{dx}{dt}=c \tag{3}$$

$$\frac{dq}{dt}-\frac{A}{\rho c}\frac{dp}{dt}+f=0 \ \ when \ \frac{dx}{dt}=-c \tag{4}$$

These equations apply along the characteristic lines as shown in figure 1, which effectively represent waves travelling in the two directions. Assuming the pressure of point A and B are p_A and p_B, and the flows are q_A and q_B respectively. After a timestep Δt, the pressure and flow at point P can be calculated by using the value of p_A, p_B, q_A and q_B from the previous time step. The finite difference method is introduced to get the approximate equations along the pipe.

$$c^+: \ q_P-q_A+\frac{A}{\rho c}(p_P-p_A)+\Delta t f(q_A)=0 \tag{5}$$

$$c^-: \ q_P-q_B-\frac{A}{\rho c}(p_P-p_B)+\Delta t f(q_B)=0 \tag{6}$$

where $f(q_A)$ and $f(q_B)$ represent the friction at point A and B.
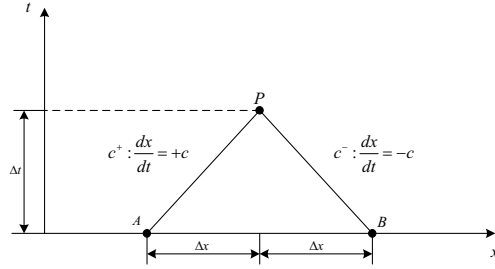
Figure 1   Characteristics line of pipe

This numerical method is known as the Method of Characteristics (MOC) and is a widely used, simple method which has very high accuracy (see, for example, [7, 8]).

For steady laminar flow $f(q)$ can be approximated as

$$f(q) = \frac{8v}{r^2} q \tag{7}$$

In practice, the friction term includes an unsteady or frequency dependent part except at steady state .The laminar flow with the sum of a steady term and a series of unsteady terms in the Fourier domain can be derived approximately as follows.

$$F_{APP}(Q) = \frac{v}{r^2}\left[8 + 4\sum_{i=1}^{k}\left(\frac{m_i j\omega}{\frac{vn_i}{r^2} + j\omega}\right)\right]Q \tag{8}$$

in which k indicates the number of terms, and n_i and m_i are weighting factors for the ith term. A method of determining values of n_i and m_i was proposed by Johnston [9]. Values of m_1, m_2 and n_1 were listed for a range of values of β, and other values were determined using the equations:

$$m_i = \beta m_{i-1} \text{ for } 3 \le i \le k \tag{9}$$

$$n_i = \beta^2 n_{i-1} \text{ for } 2 \le i \le k \tag{10}$$

The value of β can be chosen depending on the required accuracy, with small values of β giving the highest accuracy but requiring the highest number of terms k. The number of terms k can be determined by the expression $k = ceil\left(\frac{2\log r - \log(n_i v\Delta t)}{2\log\beta}\right) + 1$.

In order to use equation (8) as the friction model for simulation using the MOC in time domain, approximating equations can be represented by using inverse Fourier Transformation.

$$f(t+\Delta t) = \frac{8\nu}{r^2}q(t+\Delta t) + \frac{4\nu}{r^2}\sum_{i=1}^{k}y_i(t+\Delta t) \tag{11}$$

$$y_i(t+\Delta t) = y_i(t)e^{-\frac{n_i\nu\Delta t}{r^2}} + m_i[q(t+\Delta t) - q(t)]e^{-\frac{n_i\nu\Delta t}{2r^2}} \tag{12}$$

Substituting the equation for $f(t+\Delta t)$ into equation (5) and (6) yields the flowrate and pressure at any point along the pipe. The pressure and flowrate at the new timestep can be evaluated by rearrangement of equations (5) and (6) to give (13) and (14).

$$p_P = \frac{1}{2}\left[p_A + p_B + \frac{\rho c}{A}(q_A - q_B) + \Delta t \cdot \frac{\rho c}{A}(f_B - f_A)\right] \tag{13}$$

$$q_P = \frac{1}{2}\left[q_A + q_B + \frac{A}{\rho c}(p_A - p_B) - \Delta t(f_A + f_B)\right] \tag{14}$$

3. FLOWRATE MEASUREMENT METHOD

3.1 Two-transducer technique
The method was evaluated by simulation of a simple system as shown in Figure 2. Two transducers are arranged along the pipe to measure the pressure ripples p_1 and p_2.
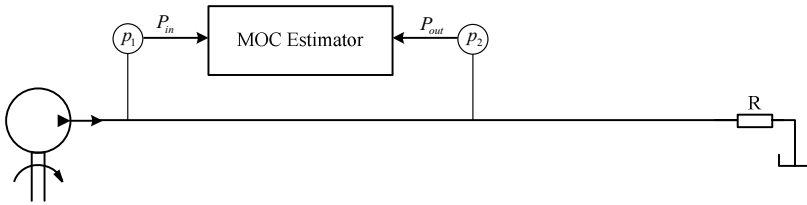
Figure 2 System schematic of two-transducer technique

The system was itself simulated using the MOC. Whilst this is clearly an idealised situation, it gives the opportunity to compare the estimated flow (determined by the MOC estimator) with the 'actual' flow (determined by the MOC system model). R represents the resistance of the load. The pressure ripples are generated by the pump at the upstream end. The pressure pulsations from (virtual) transducers 1 and 2 provide inputs P_{in} and P_{out} for the MOC estimator.

Figure 3 shows the results of flow measurement using the two-transducer technique. The simulation parameters used are presented in Table 1.

Table 1 Simulation parameters

Length	2.6 m
Diameter	0.01 m
Viscosity	30 cst
Density	870 kg/m^3
Speed of sound	1300 m/s
Number of nodes	21
Grid spacing	0.13 m
Friction terms k	4
Time step	0.1 ms
Simulation time	4 s
Upstream boundary	Flow chirp, 0-800 Hz over 4 seconds, 0.01 L/s amplitude
Pressure "transducer" locations	0.13m, 1.43m (nodes 2 and 12)
Downstream boundary resistance	2×10^9 Ns/m^5
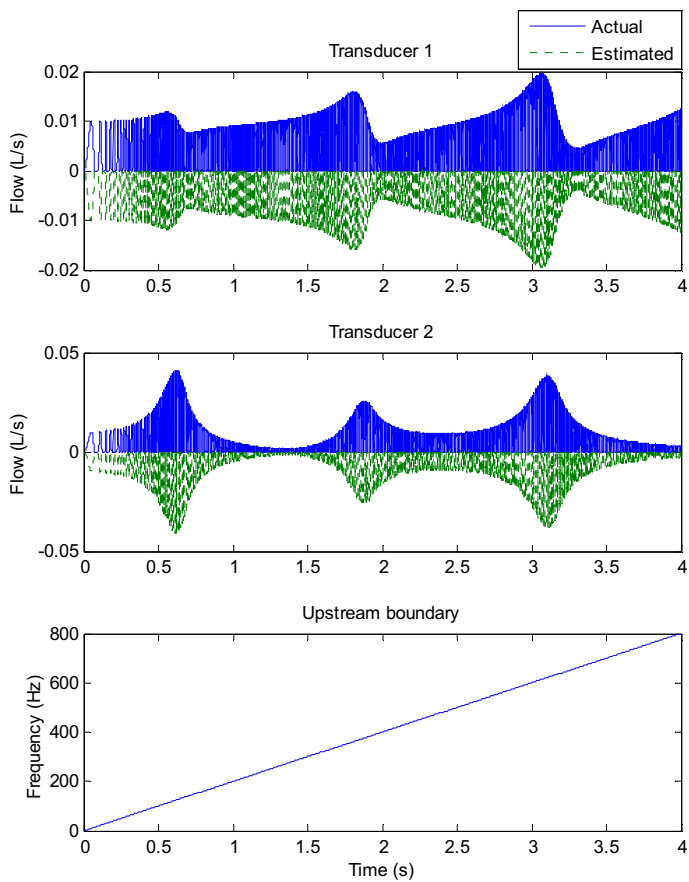
Figure 3 Comparison of actual and estimated flows at transducer 1 and 2 using two-transducer technique

For clarity only the positive half of the signal of actual value and the negative half of the signal of estimated value were shown. The bottom plot presented the upstream boundary with frequency variation with the sample time. It can be found that the estimated flowrate detected at the locations of two transducers by applying this method is identical to the actual theoretical values in the ideal conditions without disturbances. This would be expected as the MOC estimator is identical to the MOC system model.

However, the performance of the two-transducer technique can be degraded under imperfect conditions, particularly at the half-wavelength spacing (and integer multiples of half-wavelength). The spacing is defined as the distance between two (virtual) pressure transducers. In this case, the spacing is 1.3m from transducer 1 to transducer 2, and this is equal to a half wavelength at 500 Hz. In practice imperfections, errors and uncertainties might arise from transducer calibration factors and phase shifts, variations in fluid properties, and random noise. Figure 4 shows the effect of a 1% error in the calibration factor of (virtual) pressure transducer 2. This was estimated using Fast Fourier Transforms (FFT) of the actual and estimated flows at the two transducers. Large errors are apparent at about 500 Hz and 1000 Hz.
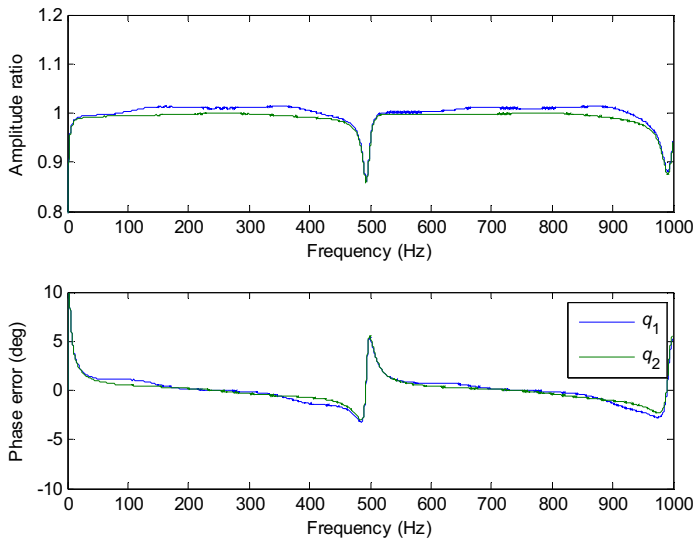
Figure 4 Errors at transducers 1 and 2 with a 1% error in calibration factor

The effect of a 1% difference between the speed of sound in the simulated pipeline and in the MOC estimator was also considered. This was done by changing the timescale of the data to the MOC estimator by 1%, remapping the predicted data to the new timestep by interpolation. Figure 5 shows the results of this. Large errors occur around 500 Hz and 1000 Hz. The noise on the data is a numerical artifact caused by changing the timestep and remapping the data, and can be ignored. In subsequent results presented in this paper, this noise has been removed by smoothing the data.
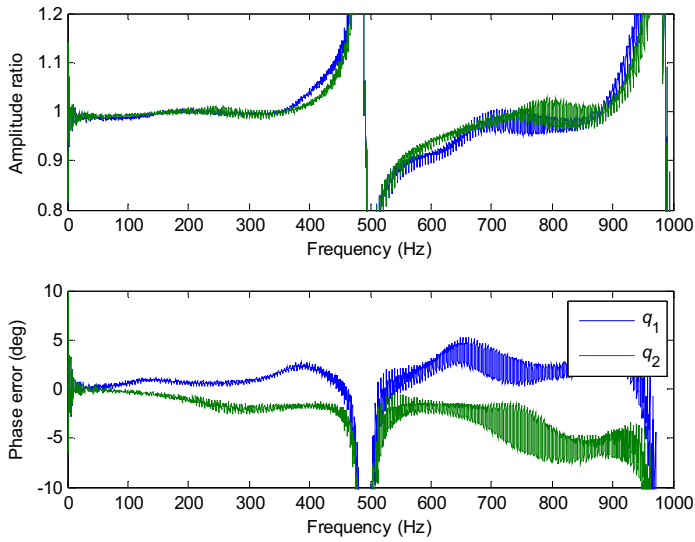
Figure 5 Errors at transducers 1 and 2 with a 1% error in speed of sound

Around the half-wavelength condition the errors in the predicted flows are much greater than the applied errors in the calibration factor and the speed of sound. The half-wavelength spacing problem can be shown easily if friction is neglected. From equation (15)

$$Q_1 = \left(P_1 \cos\frac{\omega\Delta x}{c} - P_2\right)\Big/ \sin\frac{\omega\Delta x}{c} \tag{15}$$

where P and Q are the Fourier transforms of pressure and flowrate, Δx is the spacing. When Δx equals to a multiple of a half-wavelength,

$$\Delta x = n \cdot (\lambda/2) \ \ (n = 1, 2, 3\ldots\ldots) \tag{16}$$

$$\frac{\omega\Delta x}{c} = \frac{\omega \cdot n \cdot \dfrac{\lambda}{2}}{c} = \frac{2\pi f \cdot n \cdot \dfrac{\lambda}{2}}{c} = n\pi \ (n = 1, 2, 3\ldots\ldots) \tag{17}$$

From equation (16) and (17), $\sin(w\Delta x/c) = 0$. So equation (15) for Q_1 is indeterminate and the pressure boundary conditions can be satisfied by an infinite range of flows. In practice, the friction in the system makes the denominator in equation (15) non-zero but very small, so that the equation becomes ill-conditioned around these frequencies. In order to eliminate this problem, an improved method is presented in the next section.

3.1 Three-transducer technique
The three-transducer technique uses two MOC estimators between three transducers as shown in figure 6. The spacing between transducers 1 and 2 and between 2 and 3 are different to avoid a half-wavelength condition arising in both estimators at any point within

a wide frequency range. This is a similar approach to that used in the 'Secondary Source method', which is a technique for measuring flow ripple in the frequency domain [10, 11].
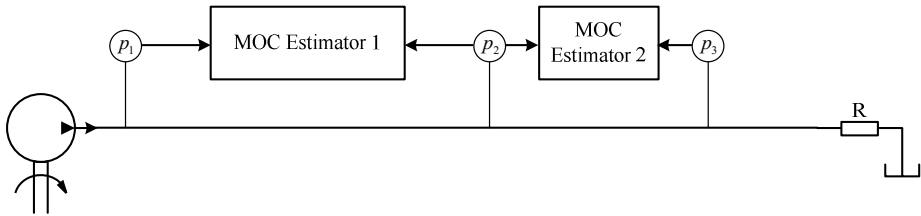
Figure 6 System schematic of three-transducer technique

The identical parameters were re-applied as used in two-transducer technique, and a third transducer was situated at the location of 2.21m. First, two MOC estimators were applied independently without the coupling resistance R. The amplitude ratios at the first transducer are shown in Figure 7, using two separate MOC estimators with a 1% error in the calibration factor of transducer 2. Figure 8 shows the same for 1% error in the speed of sound. In both cases it can be seen that large errors are apparent at about 500 Hz and 1000 Hz for the pair of transducers 1 and 2, and 800 Hz for the pair of transducers 2 and 3. Taking the average reduces the error by about half, but the errors are still large as the error from the ill-conditioned pair dominates. Therefore, a method of coupling the calculations is necessary in order to avoid the ill-conditioning.
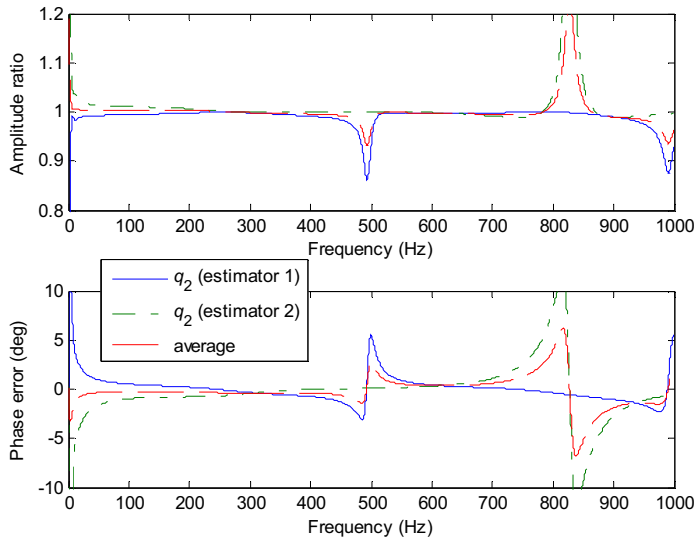
Figure 7 Errors at transducer 2 by using different transducer pairs, with a 1% error in calibration factor for transducer 2
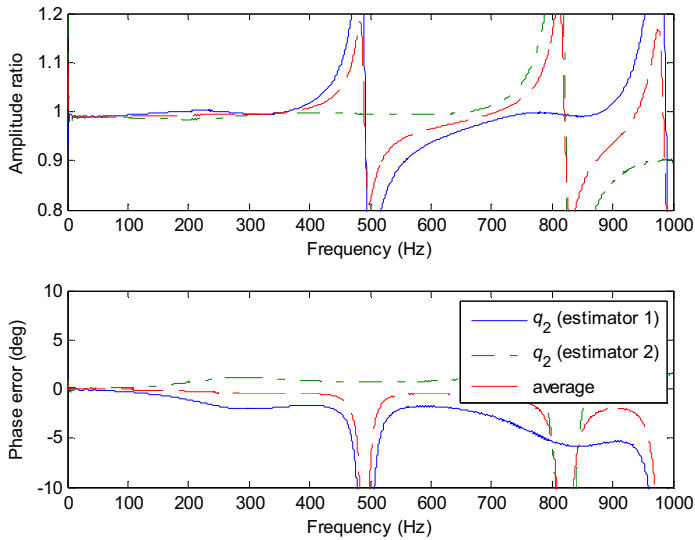
**Figure 8 Errors at transducer 2 by using different transducer pairs
with a 1% error in speed of sound**

However the two estimators and the second pressure transducer cannot be coupled directly as the difference in predicted flows has to be accounted for. A 'loose' coupling is proposed, where the two MOC estimators are coupled together directly, but are only indirectly coupled to the pressure transducer measurement via a (virtual) hydraulic resistance R. This is shown in Figure 9. Under perfect, idealised conditions the two flows q_2 and q_2' would be equal and the pressure p_{12} would be equal to the measured pressure p_2 from the second transducer. However under realistic, imperfect conditions, the two estimated flows q_2 and q_2' would not be equal, and the pressure p_{12} would be given by the equation

$$p_{12} = p_2 + (q_2 - q_2')R \tag{18}$$
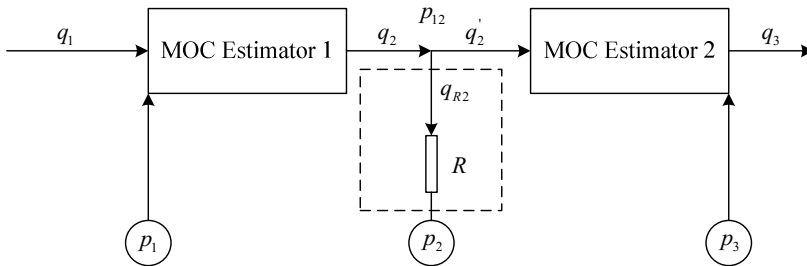
Figure 9 Coupling of MOC estimators

The flowrate q_1 and q_2 can be calculated by using the pressure p_1 and p_{12} with MOC estimator 1, whilst MOC estimator 2 is applied to predict the flowrate q_2' and q_3 from pressures p_{12} and p_3. A reasonable value of the resistance R needs to be chosen. A low

value of R results in the two MOC estimators being decoupled, and a high value of R results in pressure transducer 2 being decoupled and the two MOC estimators effectively behaving as a single one using the measured pressures at points 1 and 3. It has been found that reasonably good results are obtained if R is of a similar order to the magnitude of the characteristic impedance of pipe. In this case, best results were obtained with R equal to half the magnitude of the characteristic impedance, $R = 7.7 \times 10^9 \, \text{Ns/m}^5$, but the optimum value may depend on the system.

Figures 10 and 11 show the amplitude and phase errors of q_1, q_2, q_2' and q_3 relative to the actual flows at these points. The half-wavelength problem at the frequency 500Hz has almost been eliminated, though errors increase above about 800 Hz in figure 11. The errors resulting from the error in the calibration factor (figure 10) are smaller than those resulting from the speed of sound error (figure 11) (note the different scales).
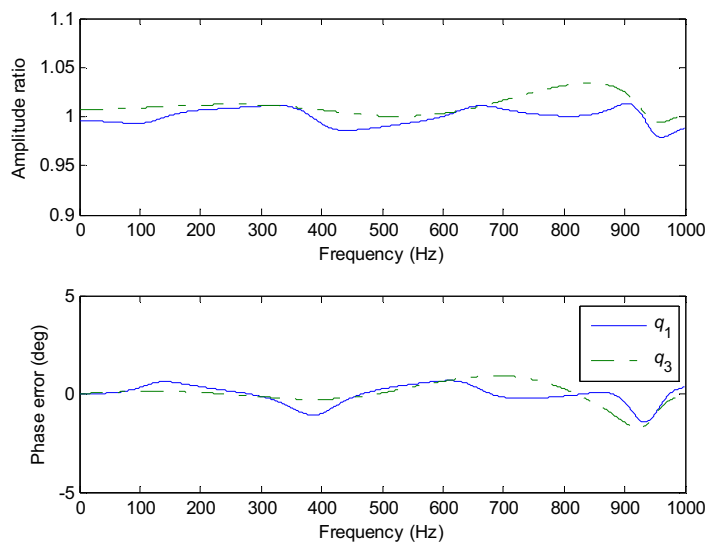
(a) Errors at transducers 1 and 3
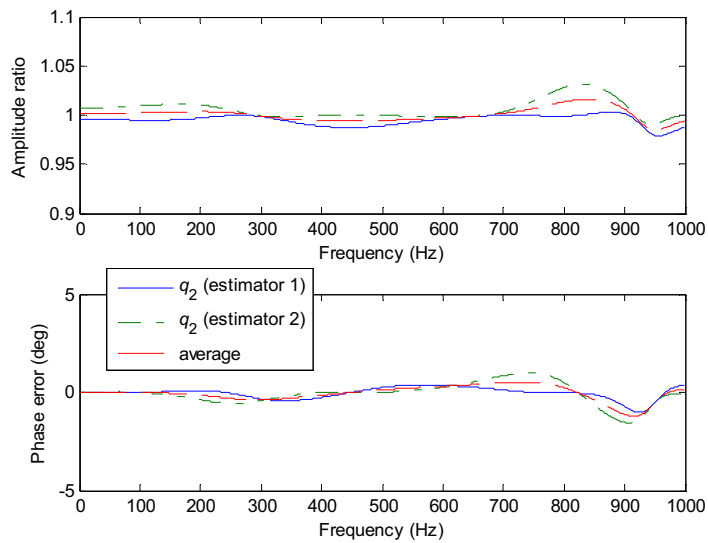
(b) Errors at transducer 2

**Figure 10 Errors using three-transducer technique
with a 1% error in calibration of transducer 2**
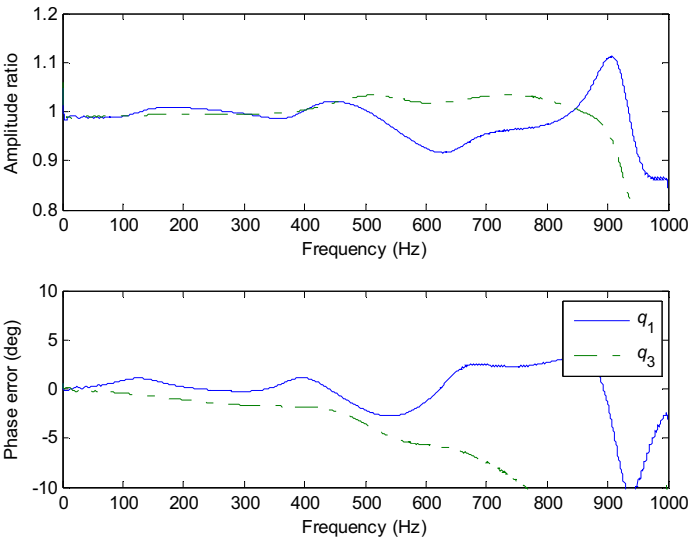
(a) Errors at transducers 1 and 3
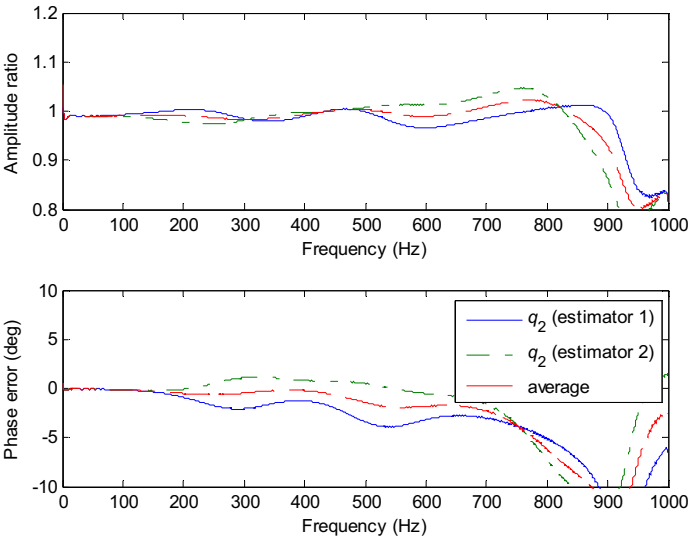
(b) Errors at transducer 2

**Figure 11 Errors using three-transducer technique
with a 1% error in speed of sound**

In practice there may be considerable uncertainty in the speed of sound. However, a technique exists for establishing the speed of sound using three pressure transducers [10-12], and the same three transducers can be used as for the flow measurement. It has previously been found to be possible to determine the speed of sound very accurately

using this method, provided that pressure ripple excitation is available with a high bandwidth.

This technique has only been found to work if the two MOC estimators are coupled to the second transducer via a resistance. If the two MOC estimators were coupled at the first or third transducer the estimators were found to be unstable.

The results presented here are purely through simulation. The next stage will be to implement the technique experimentally. However the accuracy of experimental results will be more difficult to evaluate, as it will be difficult to establish the unsteady flow by other means in order to obtain a meaningful comparison.

4. CONCLUSIONS

A two-transducer and a three-transducer method for measuring the unsteady flowrate in pipeline system have been investigated through simulation. The methods are based on wave propagation models to identify the unsteady flow from pressure measurements. Because the analysis is based on precise wave propagation models, there is no restriction on the transducer spacing. Previous methods have used finite difference approximations and consequently have required the transducers to be close together, limiting the bandwidth and the accuracy.

The methods were evaluated by applying known errors to simulated pressure data. The two transducer method was found to be inaccurate when the transducer spacing was close to a multiple of half the wavelength. This problem can be eliminated by using three unequally spaced transducers. Further work is needed to implement and evaluate the techniques experimentally, and this is planned to take place shortly.

NOMENCLATURE

A	pipe internal cross-sectional area
c	speed of sound
F	Fourier transform
f	friction term
k	number of terms in approximated friction series
L	length of pipe
m_i, n_i	weighting factors in approximated friction series
nx	divided element numbers
p	pressure
q	flow rate
Q	Fourier transform of flow rate
r	pipe internal radius
R	load resistance, virtual resistance coupling middle transducer
R_f	steady friction term
t	time
$\triangle t$	time step

x	distance along pipe
α	frequency
β	Frequency ratio for friction terms
ρ	Fluid density
v	Kinematic viscosity
ω	Angular frequency

REFERENCES

[1] Comte-Bellot, G., "Hot-wire anemometry". Annual review of fluid mechanics, Vol.8, pp.209-231.1976.

[2] Kato et al. "Laser Doppler velocimetry". US Patent No. 5 587 785. 1996.

[3] Prasad, A.K.. "Particle Image Velocimetry". Current science, Vol.79, (1), pp.51-60. 2000.

[4] Foucault et al. "Unsteady flow meter". US Patent No. 7 519 483 B2. 2009.

[5] Kojima, E., Shinada, M.. "Development of an active attenuator for pressure pulsation in liquid piping systems," JSME International Journal, SeriesⅡ, Vol.34, pp.466-473, 1991.

[6] Peube et al. "Method and apparatus for measuring unsteady flow velocity". US Patent No. 5 493 512. 1996.

[7] Wylie, E.B. and Streeter, V.L., "Fluid Transients in Systems", Prentice-Hall Inc., USA, 1993

[8] Vitkóvsky, J., Lambert, M., Simpson, A., and Bergant, A., "Advances in Unsteady Friction Modelling in Transient Pipe Flow," BHR Group Conference on Pressure Surges, Safe Design and Operation of Industrial Pipe Systems, BHR Group Conf. Series, Pub. No. 39, May, Wiley, 2000

[9] Johnston, D.N., "Efficient methods for numerical modelling of laminar friction in fluid lines," Transactions of ASME, Vol .128, pp. 629-634. 2006.

[10] Johnston, D.N. and Drew, J.E., "Measurement of Positive Displacement Pump Flow Ripple and Impedance", Proc. Inst. Mech. Engrs pt I, Vol 210, 1996, pp65-74

[11] ISO Standard 10767-1 (1996). "Hydraulic fluid power - determination of pressure ripple levels generated in systems and components. Part 1. Precision method for pumps."

[12] Johnston, D.N. and Edge, K.A., "In-situ measurement of the wavespeed and bulk modulus in hydraulic lines", Proc. Inst. Mech. Engrs, Part I, Vol. 205, 1991, pp191-197

Control

Simulation Study on Pressure Control using Nonlinear Input/Output Linearization Method and Classical PID Approach

Ufuk Bakirdogen*, Matthias Liermann**

*Institute for Fluid Power Drives and Controls (IFAS), RWTH Aachen, Germany
**American University of Beirut, Lebanon

ABSTRACT

This paper deals with the comparison of linear PID and a nonlinear control strategy to control pressure in a constant volume using a 4/3 way control valve. For the PID control at least three parameters have to be tuned. Rule sets for PID pressure control are very powerful if they derive directly from parameters which can be found in data sheets of the hydraulic components. Nonlinear control techniques are more complex. Their advantage, however, is that they take the nonlinearities of the plant into account and compensate them. The applied nonlinear approach in this paper is the input/output linearization in combination with full state feedback and state observer.

The pole placement problem is approached by analyzing a set of PID control rules which is widely accepted in industry and choosing the pole placement for the nonlinear controller accordingly. In addition, this paper presents another set of PID tuning rules which are derived using ITAE performance criterion. The closed loop poles of these two PID designs have been used to calculate the feedback controller gains of the nonlinear controller. The performance of these two linear PID and nonlinear controller designs is evaluated and compared in simulation based on overshoot, settling time, robustness and complexity.

1. INTRODUCTION

Hydraulic pressure control systems can be found in various industrial and vehicle applications such as in clutch actuation of automatic transmissions, anti-lock brake systems, presses and injection molding machines, paper machines and many more. These systems mainly consist of a proportional control valve, a hydraulic actuation cylinder and a pump system which supplies the pressurized hydraulic fluid for the system. The common point in the above mentioned applications is the dominance of pressure dynamics, which yields to neglect of motion dynamics of hydraulic actuation cylinder.

Different classical linear pressure control schemes have been proposed in the literature (1, 2). Especially the linear PID control scheme proposed by Boes in (1) offers an easy tuning of PID control parameters using known plant parameters. This approach is examined extensively in this work. This study mainly focuses on two different control strategies, the classical PID and input/output linearization based pressure control. In this context, the mathematical model of a pressure control application is derived in section 2. In section 3 PID pressure control and tuning methods are examined, namely the PID tuning rules proposed by Boes in (1) and an alternative way of PID parameter tuning method using an ITAE performance criterion. At the end of this section, pole/zero location analysis for both tuning rules is done. In section 4, input/output linearization based pressure control is introduced and derivation of input/output linearized system, state feedback controller and state observer designs are explained. Additionally, the problem of setting the state controller and state observer gains is discussed and a solution is proposed based on previously designed PID control poles. Finally, simulation results using hydraulic simulation environment DSH *plus* are presented in section 5 and controller performances are compared based on overshoot, settling time as well as complexity.

2. MATHEMATICAL MODEL OF PRESSURE CONTROL APPLICATION

The plant model for pressure control in this study shall be realized by a 4/3 way proportional control valve, a constant pressure supply and a fixed but adjustable hydraulic capacity such as a cylinder with a piston locked at a specific position in which pressure has to be controlled. This system is shown in **figure 1**.
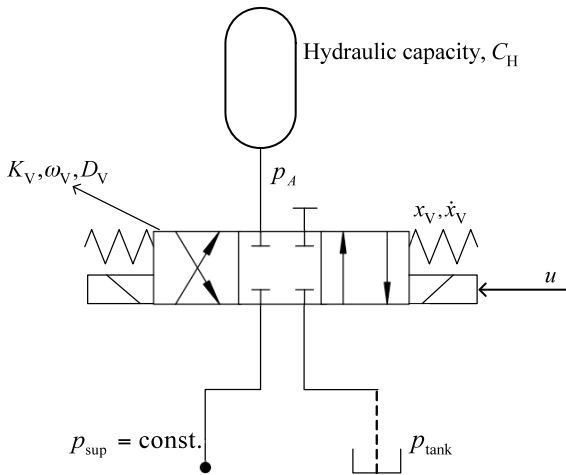
Figure 1: Plant model for pressure control

The dynamics of the 4/3 way proportional control valve can be modeled as a second order lag system (PT2 element) with gain K_V, natural angular frequency ω_V and damping ratio D_V (3, 4). The input is the control voltage u and the output is x_V valve displacement. The differential equation of the valve dynamics reads:

$$\frac{d^2}{dt^2}x_V\left(t\right) + 2 D_V \omega_V \frac{d}{dt}x_V\left(t\right) + \omega_V{}^2 x_V\left(t\right) = \omega_V{}^2 K_V u\left(t\right) \tag{2.1}$$

The capacity connected to the valve is modeled by the pressure equation which relates the balance of input/output flow to the pressure gradient. Two flows are considered, the valve flow Q_A and leakage $Q_{leakage}$. The pressure equation then is:

$$\frac{dp_A(t)}{dt} = \frac{E(p_A)}{V_A}[Q_A(t) + Q_{leakage}(t)] \tag{2.2}$$

with $E(p_A)$ being the pressure dependent bulk modulus and V_A the controlled fluid volume. According to (1), the bulk modulus which varies at different pressures can very well be assumed constant for the purpose of pressure control synthesis. Introducing hydraulic capacity C_H as a constant

$$C_H = \frac{V_A}{E} \tag{2.3}$$

and combining equations 2.2 and 2.3 gives

$$\frac{dp_A(t)}{dt} = \frac{1}{C_H}[Q_A(t) + Q_{leakage}(t)] \tag{2.4}$$

To complete the modeling the orifice flow equation should be described and added to the model. According to the stationary Bernoulli equation the flow through a sharp edged orifice is proportional to the square root of the pressure difference at its ports (4). For positive valve displacement, $x_V > 0$, flow is entering into the capacity:

$$Q_A\left(t\right) = B_V x_V\left(t\right)\sqrt{p_{sup} - p_A\left(t\right)} \tag{2.5}$$

and for negative valve displacement, $x_V < 0$, flow is going out of the capacity:

$$Q_A\left(t\right) = B_V x_V\left(t\right)\sqrt{p_A\left(t\right) - p_{tank}} \tag{2.6}$$

In these equations B_V is the valve discharge coefficient which is calculated using valve data-sheet parameters of maximum flow $Q_{Nominal}$ at rated pressure $P_{Nominal}$ (3):

$$B_V = \frac{Q_{Nominal}}{\sqrt{\Delta\left(P_{Nominal}\right)}x_{max}} \tag{2.7}$$

Combining equation 2.4 and 2.5 and also equation 2.4 and 2.6, the following equations can be reached. For positive valve displacement, $x_V > 0$:

$$\frac{d}{dt} p_A(t) = \frac{(B_V x_V(t) \sqrt{p_{sup} - p_A(t)} + Q_{leakage}(t))}{C_H} \tag{2.8}$$

and for negative valve displacement, $x_V < 0$:

$$\frac{d}{dt} p_A(t) = \frac{(B_V x_V(t) \sqrt{p_A(t) - p_{tank}} + Q_{leakage}(t))}{C_H} \tag{2.9}$$

Equations 2.1, 2.8 and 2.9 constitute the mathematical model of a plant for pressure control.

For the controller development, the nonlinearities in equations 2.8 and 2.9 should be eliminated. This can be done by linearizing the system around an operation point ($p_{tank} < p_{A0} < p_{sup}$) using taylor series expansion. After linearizing equations 2.8 and 2.9 around p_{A0} and x_{V0} as well as neglecting leakage flows which act as disturbances, transfer equations of the system for both positive and negative valve openings using equations 2.1, 2.8 and 2.9 can be written as:

$$\frac{\Delta p_A(s)}{\Delta u(s)} = \frac{V_{QU} \omega_V^2}{C_H s^3 + 2 C_H D_V \omega_V s^2 + C_H \omega_V^2 s} \tag{2.10}$$

where the flow gain parameter V_{QU} depends on the operating point, that means at which pressure level we observe the system and whether the valve is opened positively or negatively.

$$V_{QU} = B_V \sqrt{p_{sup} - p_{A0}} K_V \qquad \text{For positive valve opening} \tag{2.11}$$

$$V_{QU} = B_V \sqrt{p_{A0} - p_{tank}} K_V \qquad \text{For negative valve opening} \tag{2.12}$$

For the following analysis and synthesis, the choice of the flow gain value depends on which opening direction of the valve is more sensitive. Sensitivity depends on the square root of pressure difference in equations 2.11 and 2.12. If the pressure difference between supply pressure p_{sup} and operating pressure p_{A0} is greater than that of between tank pressure p_{tank} and p_{A0}, then equation 2.11 should be used because positive opening direction is more sensitive. If opposite is true, then equation 2.12 should be used, because negative opening direction is more sensitive now.

3. PID CONTROL AND TUNING METHODS

The PID control method which consists of proportional, integral and derivative feedback is a very powerful control method and is used in industrial processes today. The challenging part in this control method is the tuning of the control parameters for P, I and D parts which is done by trial-error method in practice. Therefore, it is valuable to have a good first guess for these parameters. In this section, a PID tuning method for pressure control application from the literature is examined, and then an alternative approach for a PID parameter tuning rule based on ITAE performance criterion is derived. The power of both methods lies on the easy tuning of parameters using simple formulas which consist of only known plant parameters. The block diagram of a PI-D pressure control system is shown in **figure 2**.
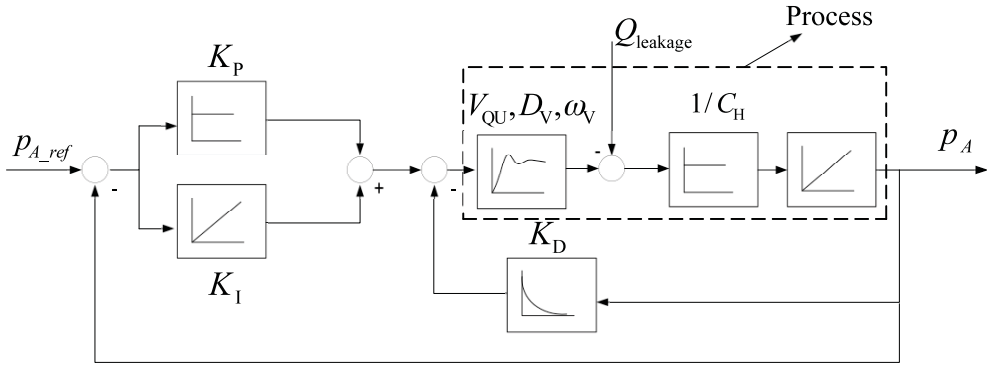
Figure 2: Block diagram of PID pressure control system

The PI-D controller has the derivative part only acting on the feedback rather than also on the input. The reason is to avoid peaks produced by the derivative part due to the step changes of the input signal. The transfer function of the closed loop system is:

$$\frac{\Delta p_A(s)}{\Delta p_{A\_ref}(s)} = \frac{V_{QU}\omega_V{}^2(K_P s + K_I)}{C_H s^4 + 2 C_H D_V \omega_V s^3 + (C_H + V_{QU} K_D)\omega_V{}^2 s^2 + V_{QU}\omega_V{}^2(K_P s + K_I)}$$

$$(3.1)$$

3.1 Method 1: PID tuning according to Boes (1)
The PID tuning method proposed by Boes described in (1) has been established in industry and therefore shall be used as a benchmark for the following control schemes. This method offers a powerful and easy tuning of PID parameters for pressure control applications. Depending only on the plant parameters, three simple formulas are given which are; (1)

$$K_P = \frac{C_H D_V \omega_V (\sqrt{2} - 1)}{V_{QU}} , K_I = -\frac{C_H \omega_V^2 (2\sqrt{2} - 3)}{4 V_{QU}} \qquad (3.2), (3.3)$$

$$K_D = \frac{C_H (2 + \sqrt{2}(2 D_V^2 - 1) - 2 D_V^2)}{V_{QU}} \qquad (3.4)$$

The derivation of these rules is not explained in (1) but it is stated that they are based on experiments and linear pole placement. If the closed loop transfer function in equation 3.1 is analyzed, it can be clearly seen that the system has 4 poles and one zero. The characteristic equation of the closed loop transfer function given in equation 3.1 divided by C_H is:

$$s^4 + 2 D_V \omega_V s^3 + (1 + \frac{\omega_V^2 V_{QU} K_D}{C_H}) s^2 + \frac{\omega_V^2 V_{QU} K_P}{C_H} s + \frac{\omega_V^2 V_{QU} K_I}{C_H} = 0 \qquad (3.5)$$

The analysis of equation 3.5 shows that the terms with proportional, integral and derivative gains include the flow gain and hydraulic capacity which are canceled when P, I and D gain formulas (equations 3.2 to 3.4) are employed. Thus the location of poles of the closed loop system becomes independent of the flow gain and hydraulic capacity. Another observation is that the damping ratio (cosine of the angle between secant from origin to pole and negative real axis) is always equal for both pole pairs of the closed loop transfer function. This can be easily seen on the zero-pole diagram in **figure 3** using the following typical numerical values.

$$\omega_V = 690.8 \ \frac{rad}{s}, \ D_V = 0.525, \ V_{QU} = 6.758 \cdot 10^{-5} \ \frac{m^3}{V \cdot s}$$

$$C_H = \frac{V_A}{E} = 1.442 \cdot 10^{-12} \ \frac{m^3}{Pa}$$

where $V_A = 2.148 \cdot 10^{-3} \ m^3$ and $E = 1.486 \cdot 10^9 \ \frac{N}{m^2}$

In figure 3, among the poles marked with asteriks, the pole pair which is closer to the imaginary axis clearly dominates the behaviour of the system. A third observation of our analysis is that as the angular frequency and damping of the valve increase, the pole pairs and the zero move to the left while keeping the trapezoidal shape.
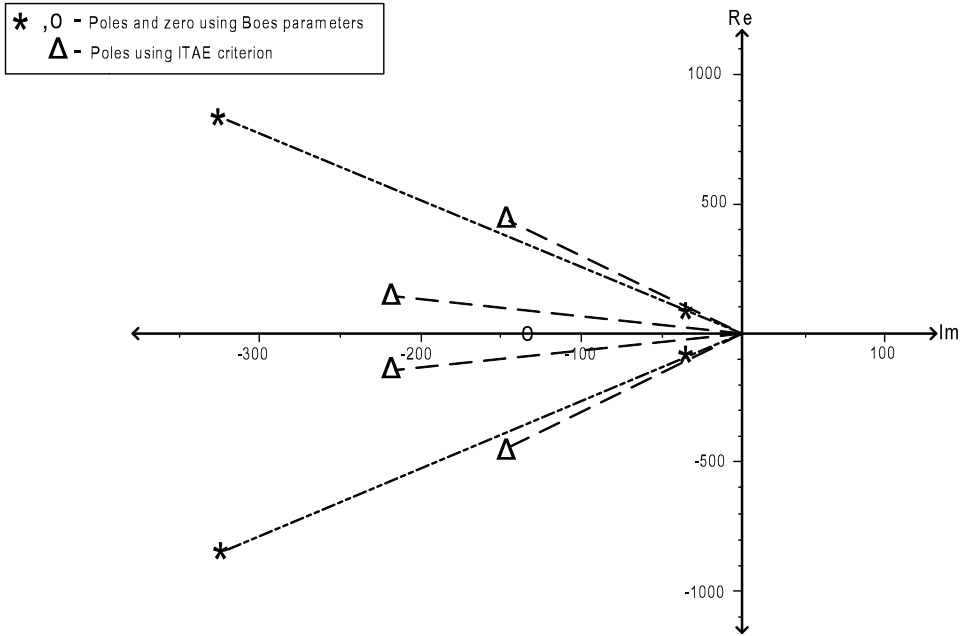
Figure 3: Pole/zero locations of closed loop system with PID tuning from Boes and ITAE

3.2 Method 2: PID tuning according to ITAE performance criterion

The PID tuning method for pressure control introduced in the preceding subsection is simple and powerful. However, the derivation of the controller parameter formulas is not clear. Also, as will be seen from simulation results, this approach can be well improved in performance. With the aim of finding a clearly derived and better set of parameters with good transient behaviour, an alternative approach using ITAE performance criterion has been derived, which, similarly to the previous method, only uses known plant parameters.

ITAE is an integral performance criterion which can be used to optimize control system performance. According to ITAE performance criterion, the best system is defined as the system that minimizes the ITAE index which is (5):

$$I_{ITAE} = \int_0^T t \left| e(t) \right| dt \tag{3.6}$$

Using this index, the characteristic polynomial coefficients of transfer functions of different orders which minimize the ITAE index can be found. According to (6), the transfer equation which minimizes the ITAE criterion for a 4th order all-pole system reads:

$$T(s) = \frac{\omega_n^4}{s^4 + a_1\omega_n s^3 + a_2\omega_n^2 s^2 + a_3\omega_n^3 s + \omega_n^4} \tag{3.7}$$

where $a_1 = 2.1$, $a_2 = 3.4$, $a_3 = 2.7$. It should be noted that these parameters minimize the ITAE index for a step input. This means that making parameters of the denominator of the closed loop transfer function of our PI-D pressure control problem in equation 3.1 equal to the parameters in equation 3.7, the tracking behaviour to a step input should be optimal.

Comparing the coefficients of s^3 gives:

$$2.1\omega_n = 2 D_V \omega_V$$

which leads to the conclusion that ω_n must be set to

$$\omega_n = 0.95 D_V \omega_V \tag{3.8}$$

The interpretation of this relationship is that the pressure control dynamics is limited by the valve dynamics and not by the pressure dynamics. Now using ω_n calculated in equation 3.8, the other coefficients are made equal and comparison of coefficients gives the following controller parameters:

$$K_P = 2.33 \frac{D_V^3 \omega_V C_H}{V_{QU}} \tag{3.9}$$

$$K_I = 0.82 \frac{D_V^4 \omega_V^2 C_H}{V_{QU}} \tag{3.10}$$

$$K_D = \frac{\left(3.08 D_V^2 - 1\right) C_H}{V_{QU}} \tag{3.11}$$

Since the ITAE minimized functions in (6) are based on systems that have only poles, the resulting closed loop transfer function of the pressure control system (Eq. 3.1) has to be modified slightly to be also an all pole system, that is, no zeros should appear in the system. The zero in the system described by equation 3.1 can be canceled using a prefilter which satisfies the following equation:

$$\frac{G_C G_P G_{pref\,ilter}}{1 + G_C G_P} = \frac{\omega_n^4}{s^4 + 2.1\omega_n^3 s + 3.4\omega_n^2 s^2 + 2.7\omega_n^3 s + \omega_n^4}$$

where G_C is the controller, G_P is the plant to be controlled and $G_{pref\,ilter}$ is the prefilter, that should be placed behind the reference signal generator. So the transfer function of the prefilter reads:

$$G_{pref\,ilter} = \frac{C_H \omega_n^4}{\omega_V^2 V_{QU}(K_P s + K_I)} = \frac{D_V \omega_V}{2.84 s + D_V \omega_V} \tag{3.12}$$

Considering equation 3.5 and equations 3.9 to 3.11, it can be stated that poles of the closed loop system with ITAE PID tuning do not depend on flow gain and hydraulic capacity, similar as in the case for the system with Boes PID tuning. For a comparison with the pole-zero locations of the controller proposed by Boes, the same parameters in subsection 3.1 are used and results are presented in figure 3.

Unlike the poles from the system proposed by Boes, the pole pairs are so close to each other that it cannot be said which one is dominant. In addition, there is no zero in this system. A comparison of step response in time domain will be given in section 5.

4. INPUT/OUTPUT LINEARIZATION BASED PRESSURE CONTROL

The general idea of input/output linearization is to transform the nonlinear system dynamics algebraically into a (fully or partly) linear one, so that linear control techniques can be applied (3). This is a powerful control technique and applications on hydraulic drives can be found in the literature (8, 9). In order to achieve this, a nonlinear transformation of the control signal should be derived (linearizing control law) and the complete model should be expressed in new coordinates z as a linear model after applying a coordinate transformation. A general nonlinear system is defined as:

$$\frac{d\mathbf{x}}{dt} = \mathbf{f}(\mathbf{x}) + \mathbf{g}(\mathbf{x})u(t) \, , \, y(t) = h(\mathbf{x}) \tag{4.1}$$

To find such a nonlinear transformation for the control signal, first the output signal must be differentiated so many times until an explicit relationship between input u and output y is obtained. The number of successive differentiations until obtaining an explicit relationship between input and output signals is called the relative degree. And when the relative degree is equal to the system order, then input/output linearization takes a special form and is called exact input/output linearization. When the pressure plant model in 2.8 and 2.9 (neglecting leakage flows) are expressed in state space form together with equation 2.1 for positive valve displacement, $x_V > 0$, we have:

$$f(\mathbf{x}) = \begin{pmatrix} \dfrac{B_V x_2 \sqrt{p_{\text{sup}} - x_1}}{C_H} \\ x_3 \\ -2 D_V \omega_V x_3 - \omega_V{}^2 x_2 \end{pmatrix}, g(\mathbf{x}) = \begin{pmatrix} 0 \\ 0 \\ \omega_V{}^2 K_V \end{pmatrix}, y = x_1 \qquad (4.2)$$

and for negative valve displacement, $x_V < 0$:

$$f(\mathbf{x}) = \begin{pmatrix} \dfrac{B_V x_2 \sqrt{x_1 - p_{\text{tank}}}}{C_H} \\ x_3 \\ -2 D_V \omega_V x_3 - \omega_V{}^2 x_2 \end{pmatrix}, g(\mathbf{x}) = \begin{pmatrix} 0 \\ 0 \\ \omega_V{}^2 K_V \end{pmatrix}, y = x_1 \qquad (4.3)$$

where $x_1 = p_A$, $x_2 = x_V$, $x_3 = \dot{x}_V$ and the output $y = h(\mathbf{x})$ is defined as the chamber pressure p_A.

The first derivative of the output function yields:

$$y^{(1)} = \frac{\partial h(\mathbf{x})}{\partial \mathbf{x}} \frac{d\mathbf{x}}{dt} = \frac{\partial h(\mathbf{x})}{\partial \mathbf{x}} (f(\mathbf{x}) + g(\mathbf{x})u) = L_f h(\mathbf{x}) + L_g h(\mathbf{x})u \qquad (4.4)$$

where $L_g h(\mathbf{x}) = 0$ for all operation points in the control range for both positive and negative valve openings. So the first derivative of the chamber pressure is not influenced by the valve input voltage. If differentiation is continued, at third step we can get a nonzero input u in the expression as following:

$$y^{(3)} = \frac{\partial L_f{}^2 h(\mathbf{x})}{\partial \mathbf{x}} \frac{d\mathbf{x}}{dt} = \frac{\partial L_f{}^2 h(\mathbf{x})}{\partial \mathbf{x}} (f(\mathbf{x}) + g(\mathbf{x})u) = L_f{}^3 h(\mathbf{x}) + L_f{}^2 L_g h(\mathbf{x})u \qquad (4.5)$$

where $L_f{}^2 L_g h(\mathbf{x}) \neq 0$ for all operating points in the control range for both negative and positive openings. This means that the valve input voltage has a direct influence on the third derivative of the chamber pressure. It also means that the pressure plant model has a relative degree of 3 and we can perform an exact input/output linearization. For positive valve displacement, $x_V > 0$, the input function is:

$$L_f{}^2 L_g h(\mathbf{x}) = \frac{B_V \sqrt{p_{\text{sup}} - x_1}\, \omega_V{}^2 K_V}{C_H} \tag{4.6}$$

and for negative valve displacement, $x_V < 0$, the input function is:

$$L_f{}^2 L_g h(\mathbf{x}) = \frac{B_V \sqrt{x_1 - p_{\text{tank}}}\, \omega_V{}^2 K_V}{C_H} \tag{4.7}$$

In order to define an input/output linearized system, new z coordinates can be defined for positive valve displacement, $x_V > 0$, as:

$$\dot{\mathbf{z}} = \begin{pmatrix} \dot{z}_1 \\ \dot{z}_2 \\ \dot{z}_3 \end{pmatrix} = \begin{pmatrix} y \\ \dot{y} \\ \ddot{y} \end{pmatrix} = \begin{pmatrix} h(\mathbf{x}) \\ L_f h(\mathbf{x}) \\ L_f{}^2 h(\mathbf{x}) \end{pmatrix} = \begin{pmatrix} p_A \\[2mm] \dfrac{B_V x_V \sqrt{p_{\text{sup}} - p_A}}{C_H} \\[4mm] -\dfrac{1}{2}\dfrac{B_V{}^2 x_V{}^2}{C_H} + \dfrac{B_V \dot{x}_V \sqrt{p_{\text{sup}} - p_A}}{C_H} \end{pmatrix} \tag{4.8}$$

and for negative valve displacement, $x_V < 0$:

$$\dot{\mathbf{z}} = \begin{pmatrix} \dot{z}_1 \\ \dot{z}_2 \\ \dot{z}_3 \end{pmatrix} = \begin{pmatrix} y \\ \dot{y} \\ \ddot{y} \end{pmatrix} = \begin{pmatrix} h(\mathbf{x}) \\ L_f h(\mathbf{x}) \\ L_f{}^2 h(\mathbf{x}) \end{pmatrix} = \begin{pmatrix} p_A \\[2mm] \dfrac{B_V x_V \sqrt{p_A - p_{\text{tank}}}}{C_H} \\[4mm] \dfrac{1}{2}\dfrac{B_V{}^2 x_V{}^2}{C_H} + \dfrac{B_V \dot{x}_V \sqrt{p_A - p_{\text{tank}}}}{C_H} \end{pmatrix} \tag{4.9}$$

With these new state definitions, we write the derivatives of $\mathbf{z}$ in state space form as:

$$\dot{\mathbf{z}} = \begin{pmatrix} \dot{z}_1 \\ \dot{z}_2 \\ \dot{z}_3 \end{pmatrix} = \begin{pmatrix} 0 & 1 & 0 \\ 0 & 0 & 1 \\ 0 & 0 & 0 \end{pmatrix} \begin{pmatrix} z_1 \\ z_2 \\ z_3 \end{pmatrix} + \begin{pmatrix} 0 \\ 0 \\ L_f{}^3 h(\mathbf{x}) + L_f{}^2 L_g h(\mathbf{x}) \end{pmatrix} u \, , \; y = z_1 = p_A$$

$$\tag{4.10}$$

Now, we have reached a state space system which has a linear dynamics with a nonlinear input function. Defining an appropriate nonlinear feedback and a new input variable υ :

$$u = \frac{\upsilon - L_f^{3} h(\mathbf{x})}{L_f^{2} L_g h(\mathbf{x})} \, , \tag{4.11}$$

we can linearize the system as:

$$\dot{\mathbf{z}} = \begin{pmatrix} \dot{z}_1 \\ \dot{z}_2 \\ \dot{z}_3 \end{pmatrix} = \begin{pmatrix} 0 & 1 & 0 \\ 0 & 0 & 1 \\ 0 & 0 & 0 \end{pmatrix} \begin{pmatrix} z_1 \\ z_2 \\ z_3 \end{pmatrix} + \begin{pmatrix} 0 \\ 0 \\ 1 \end{pmatrix} \upsilon \tag{4.12}$$

The linearization is also illustrated in **figure 4** below:
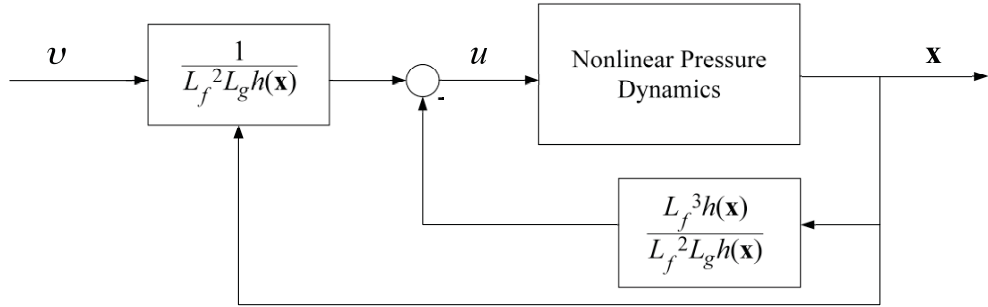
Figure 4: Input/Output linearization depicted by a block diagram

Equation 4.11 is called the linearizing control law and by introducing this expression to the nonlinear system, the nonlinear system turns into a linear one as defined in 4.12. The derived linearizing control law for the pressure plant model is a long expression which is not printed here due to the space limitation.

4.1 Pole placement problem

In the previous subsection, the derivation of input/output linearization for the pressure plant model has been completed. To control such a system, full state feedback controller can be used and the motivation of the full state feedback control is to provide the new virtual input υ as a function of all three states and the reference value. If the states are fed back to the system, multiplied with a state gain matrix and supplied to the system as input, the input function becomes:

$$\upsilon = -\mathbf{k}_{state}\mathbf{z} \tag{4.13}$$

Using the state space representation in 4.12 and equation 4.13, a closed loop system forms and reads as:

$$\frac{d\mathbf{z}}{dt} = (\mathbf{A} - \mathbf{bk}_{state})\mathbf{z} \tag{4.14}$$

where;

$$\mathbf{A} - \mathbf{bk}_{state} = \begin{pmatrix} 0 & 1 & 0 \\ 0 & 0 & 1 \\ -k_{state1} & -k_{state2} & -k_{state3} \end{pmatrix} \tag{4.15}$$

The problem of choosing the state controller gains k_{state1}, k_{state2} and k_{state3} is called pole placement problem. Depending on the values of these parameters, the roots of the characteristic polynomial change, so the places of the poles in the Re-Im plane. To guarantee the stability, these poles have to be in the left side of the Re-Im plane, however being stable is not sufficient since the design also has to meet desired transient response characteristics of the closed loop system, such as settling time and overshoot. There are overall 3 poles to placed in case of input/output linearized pressure control system, so the pole patterns of previously designed PID pressure control systems can be used, because of the proved performance of these poles. However, there are 4 poles in the PID control system described in (1). For the state controller, only dominant pole pair and the real part of the other pole pair from the PID system in (1) will be used in simulations, which results in the following state controller gains:

$$k_{state1\text{-}Boes} = 3.93 \cdot 10^6 \ \frac{V}{Pa}, \ k_{state2\text{-}Boes} = 3.79 \cdot 10^4 \ \frac{V}{s \cdot Pa}, \ k_{state3\text{-}Boes} = 400 \ \frac{V \cdot s}{Pa}$$

In case of the ITAE PID system, instead of taking directly the pole pattern from the PID system, the 3rd order ITAE function is used to calculate state controller gains, which are according to (5):

$$k_{state1\text{-}ITAE} = 4.12 \cdot 10^7 \ \frac{V}{Pa}, \ k_{state2\text{-}ITAE} = 2.75 \cdot 10^5 \ \frac{V}{s \cdot Pa}, \ k_{state3\text{-}ITAE} = 604 \ \frac{V \cdot s}{Pa}$$

4.2 Observer design

To be able to use a full state feedback controller, all the states of the system have to be known or measured. Since measurement of valve spool displacement and valve spool acceleration is impractical, estimation of these states via a Luenberger's state observer is a reasonable solution. Together with the state observer, closed loop system can be defined as:

$$\frac{d\mathbf{z}_{est}}{dt} = \mathbf{A}\mathbf{z}_{est} + (\mathbf{b}\mathbf{k}_{State})\mathbf{e} + \mathbf{k}_{Obs}(y - \mathbf{c}^T\mathbf{z}_{est}) \qquad (4.16)$$

where $\mathbf{k}_{Obs}$ is the observer gain vector, $\mathbf{e}$ being the error vector, $\mathbf{z}_{est}$ being the estimated state vector and $\mathbf{c}^T = \begin{pmatrix} 1 & 0 & 0 \end{pmatrix}$. With the addition of the state observer, another pole placement problem arises. The observer gain vector has to be determined so that matrix $(\mathbf{A} - \mathbf{k}_{Obs}\mathbf{c}^T)$ has its all eigenvalues (or poles) in the left side of Re-Im plane. In case of input/output linearized pressure control system, there are 3 observer gains to be set. However, when the observer is combined with a state feedback controller, having a stable observer will not be a sufficient criterion. In this case the observer should operate 2 to 5 times faster than the controller (7). This means that the poles of the observer should be 2 to 5 times of the left of the dominant poles of the system with state controller. But in terms of experimentation, the farther the poles of the observer go to the left, the more sensitive the observer becomes to measurement noises (7). In simulations with nonlinear controller, 3 observer poles are placed at -800 on real axis when ITAE pole pattern used. In case of pole pattern from (1), the 3 observer poles are placed at -90 on the real axis.

5. SIMULATION RESULTS AND COMPARISON OF CONTROLLER PERFORMANCES
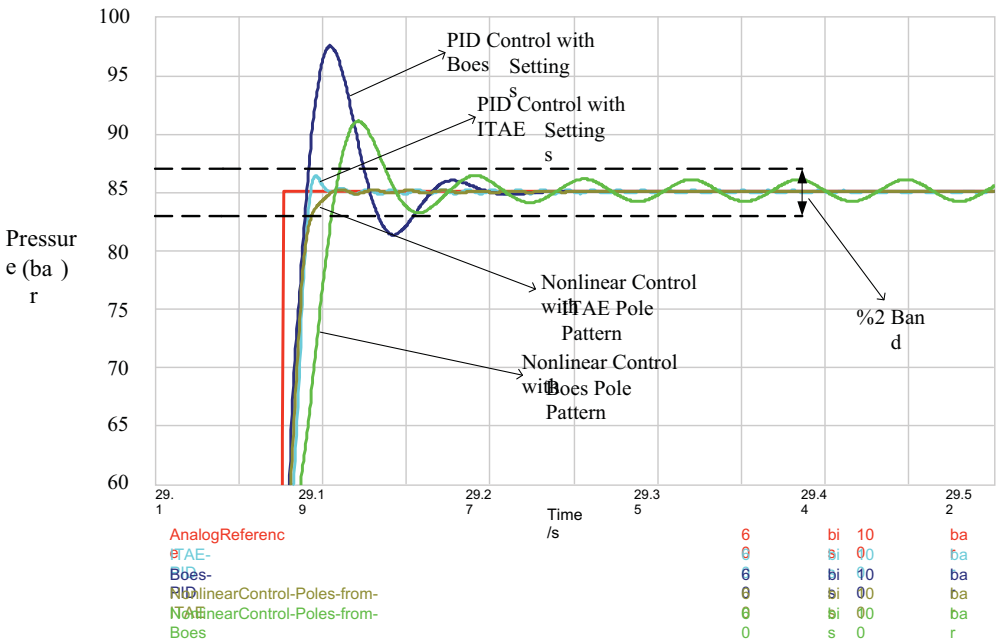
Figure 5: Simulation results

In order to see the performances of the controllers, the system has been modeled and simulated using hydraulic simulation environment DSH® *plus*. The reference pressure

signal used in simulations is a rectangular signal with upper value of 85 bar and lower value of 55 bar. The plant parameters are already given in subsection 3.1 and PID controller parameters can be calculated using corresponding formulas. For the PID controllers, a time constant of 0.5 ms has been used for the derivative parts. In **figure 5** pressure signals after a step signal from 55 bar to 85 bar can be seen. In terms of transient behaviour, the PID controller with Boes settings shows the most overshoot among others. Least overshoot exhibits the nonlinear controller with ITAE pole pattern. If settling time is defined for the %2 percentage band, it can be seen from figure 5 that the PID controller with Boes settings as well as the nonlinear controller with pole pattern from Boes have longer settling times compared to the others. In terms of steady state behaviour, the nonlinear controller with pole pattern from Boes shows undamped oscillations, which indicates that the choice of the pole pattern which were derived from PID controller poles with Boes settings is not the best choice. Among the PID controllers, PID controller with ITAE settings shows better damping and settling characteristics. When the complexity is taken into consideration, it can be seen that nonlinear controllers are more complex compared to the PID controllers.

6. CONCLUSIONS

In this paper, two different control schemes for pressure control, namely PID and nonlinear control have been analyzed. A well-known PID scheme for pressure control has been examined and an alternative PID scheme has been derived using ITAE performance criterion. In addition, a nonlinear controller which is based on input/output linearization has been designed. To analyze the performances of the controllers, a pressure control system has been modeled and simulated using DSH *plus*. Results show that nonlinear controller with pole pattern from ITAE has the best steady state and transient behaviour. Also, the PID controller with ITAE settings has a smaller overshoot and better settling behaviour compared to the PID control scheme proposed in (1). Robustness of the controllers has not been analyzed here, and could be a subject for further research. In terms of complexity, nonlinear controllers need more effort for design and implementation compared to PID controllers and don't show significant better performance.

LIST OF SYMBOLS

B_V	Valve discharge coefficient
C_H	Hydraulic capacity
D_V	Valve damping coefficient
E	Bulk modulus of hydraulic fluid
K_D	Derivative gain
K_I	Integral gain
K_P	Proportional gain
$\mathbf{k}_{Obs}$	Observer gain vector
K_V	Valve input gain
$\mathbf{k}_{state}$	State feedback controller gain
p_A	Pressure in the controlled volume
p_{A0}	Operation pressure in the controlled volume

$\Delta P_{Nominal}$	Nominal pressure difference of valve
p_{sup}	Supply pressure from the pump
p_{tank}	Reservoir pressure
Q_A	The flow rate in- and out from controlled volume
$Q_{Nominal}$	Nominal flow rate of the valve
u	Valve input signal
V_A	Volume of the hydraulic capacity
V_{QU}	Valve flow gain
x_V	Valve stroke
$\dot{x}_V$	Valve spool velocity
x_{V0}	Operation stroke of the valve spool
x_{max}	Maximum valve spool stroke
ω_V	Valve eigenfrequency

REFERENCES

(1) Boes, C., Lenz, W., Müller, J., Digital Servo Valves with Fieldbus Interface in Closed Loop Applications, The 8th Scandinavian International Conference on Fluid Power, May 2003, Tampere, Finland

(2) Yang, K., Oh , I., Lee, I. Pressure control of hydraulic servo system using proportional control valve, Journal of Mechanical Science and Technology, Vol. 13, Nr. 3, Pg. 229-239, March 1999, Korea

(3) Jelali, M., Kroll, A. Hydraulic Servo-systems, 1. Edition, Springer, 2003, London

(4) Murrenhof, H. Servohydraulik-geregelte hydraulische Antriebe, 3. Edition, Shaker, 2008, Aachen

(5) Dorf, R., Bishop R. Modern Control Systems, 11. Edition, Prentice Hall, 2008, New Jersey

(6) Graham, D., Lathrop R. C. The Synthesis of Optimum Response: Criteria and Standard Forms, Part 2, Trans. of the AIEE 72, November 1953

(7) Ogata, K. Modern Control Engineering, 3. Edition, Prentice Hall, 1997, New Jersey

(8) Hahn, H., Piepenbrink, A., Leimbach, K. Input/Output Linearization Control of an Electro Servo-Hydraulic Actuator, Proceedings of the Third IEEE Conference, Pg. 995-1000, August 1994, Glasgow

(9) Donath, M., Vossoughi, R. Dynamic Feedback Linearization for Electrohydraulically Actuated Servosystems, Proceedings of the 1992 Japan/USA Symposium on Flexible Automation, Pg. 595-606, July 1992, San Francisco, CA

Control Strategy for Water Hydraulic Driven Hybrid Parallel Robot

H Wu, H Handroos
Faculty of Technology, Lappeenranta University of technology
P.O. Box 20, FIN-53851 Lappeenranta, Finland
huapeng.wu@lut.fi

ABSTRACT

This paper presents a novel mobile parallel robot, which is able to carry out the welding and machining processes from inside the international thermonuclear experimental reactor (ITER) vacuum vessel. The kinematic design of the robot has been optimized for the ITER access. To improve the performance of the robot, a hybrid control system is designed and an advanced controller has been developed, master-slave control for tracking motion is used to avoid un-synchronous motion of two drive motors, and the pressure feedback together with a high-pass filter is applied to reduce vibration in the machining process.

1. INTRODUCTION

The sectors of the international thermonuclear experimental reactor (ITER) require tolerances of 10 mm which are more stringent than normally expected for the size of the structure involved. The walls of ITER sectors are made of 60 mm thick stainless steel and are joined together by high efficiency structural and leak tight welds. In addition to the initial vacuum vessel (VV) assembly, sectors may have to be replaced for repair. Since commercially available machines are too heavy for the required machining operations and the lifting of a possible e-beam gun column system, a new flexible, lightweight and mobile robotic machine is being considered.

Traditional industrial robots that have been used as general-purpose positioning devices are open chain mechanisms that generally have the links actuated in series. This kind of manipulators usually has long reach and large workspace, but inherently not very rigid and has poor dynamic performance at high speed and high dynamic loading under the operating condition. Compared with open chain manipulators, parallel mechanisms generally have high stiffness, high accuracy and high force/torque capacity in the reduced workspace and have found many applications in manufacturing systems [1, 2, 3, 4]. The development of full remote welding and cutting tools, contributed by the US Home Team, was completed in June 1998 [5], of which the robot was built in the serial link arm on a rail-mounted vehicle and moving on guide rail, however it is not able to carry out the machining process inside the ITER due to its low stiffness. Since there are no commercial solutions applicable to the

ITER assembly, a hybrid parallel robot machine, using water hydraulic drives to achieve the required force density and clean environment, has been developed.

2. STRUCTURE OF VV AND MACHINING PROCESS

The inner and outer walls of the VV are made of 60 mm thick stainless steel, 316L, and are welded together indirectly, i.e., through an intermediate, called "splice plate", inserted between the sectors to be joined. This splice plate has two important functions: (*i*) to allow access to bolt together the thermal shield between the VV and coils; and (*ii*) to compensate for the mismatch between adjacent sectors to obtain a good fit-up of the sector-sector butt weld. The robot end-effector passes through the inner wall splice plate opening to reach the outer wall. The assembly process has to be carried out from inside the VV (Fig. 1) [6].
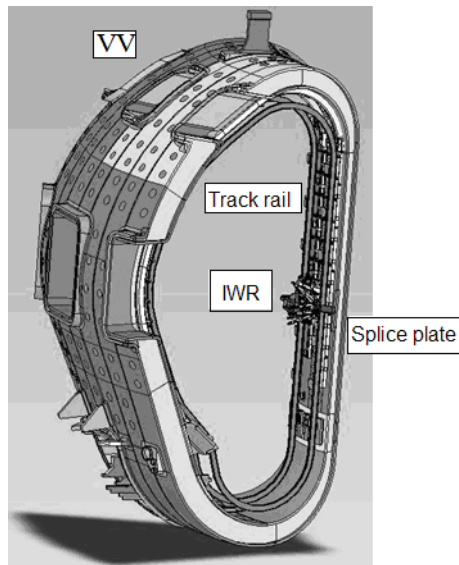
Figure 1 Structure of VV sector and robot

The assembly or repair will be performed according to four phases: cutting, edge machining and smoothing, welding, and the NDT control. The robot functions as a transportation device for welding, machining, and inspecting the end-effector.

The welding force is small and only comes from the weight of the welding device, which may be up to 200 kg for an e-beam welder. The maximum robot force arises from cutting, and the dynamic force can be up to 3 kN.

3. KINEMATIC MODEL OF ROBOT

The new parallel robot has ten degrees of freedom (Fig. 2), and it consists of two relatively independent sub-structures: (*i*) the Hexa-WH — a Stewart platform-based parallel

mechanism driven by six water hydraulic cylinders, which contributes full six degrees of freedom for the end-effectors; and (*ii*) the carriage offering the other four degrees of freedom for the Hexa-WH, namely the tip motion, the rotation, the linear motion and the tracking motion are the four degrees to enlarge the workspace and to offer the high mobility of the robot. Thus robot IWR is a hybrid redundant manipulator for having four extra degrees of freedom provided by the carriage.
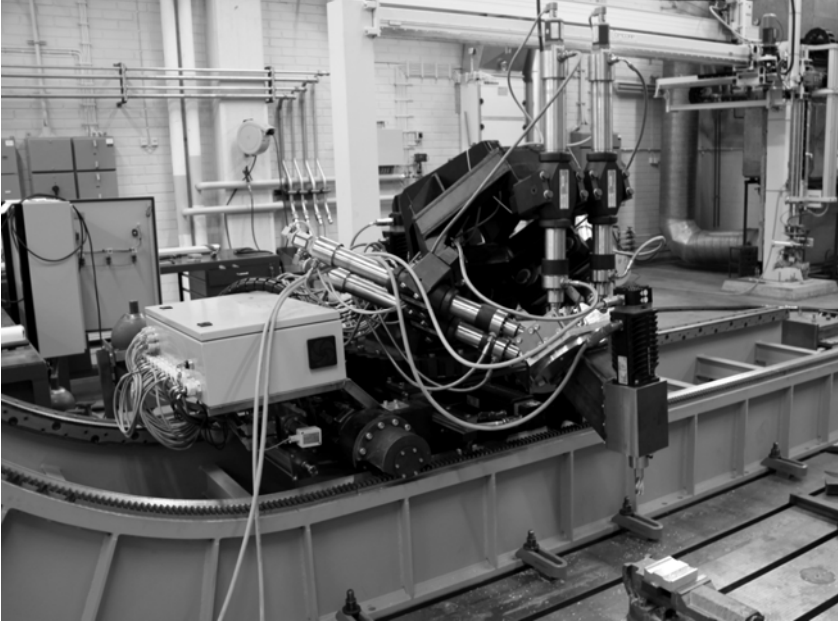
Figure 2 Parallel robot IWR

4. KINEMATIC ANALYSIS

The kinematics of the robot is very complicated because of its redundant structure; the kinematics analysis can first be given in two individual parts, exactly the carriage part and the Hexa-WH part, and then the combination of these two parts.

The coordinate system (Fig. 3) is set up as the following: frame O is fixed on the tracking rail, frame O_0 to the corner of the carriage frame, frame O_1 to the corner of the linear table, frame O_2 above the centre of the rotation plate, frame O_3 at the rotation joint, frame O_4 in the centre of the Hexa-WH frame, and frame O_5 at the centre of the end-effector.

4.1 Forward kinematics
The carriage offers four degrees of freedom to the robot — two linear motions and two rotations, and the Hexa-WH offers full 6 degrees of freedom. The transformation matrix can be defined as:

$$T_c = T_0 \cdot T_1 \cdot T_2 \cdot T_3 \cdot T_4 \cdot T_5, \tag{1}$$
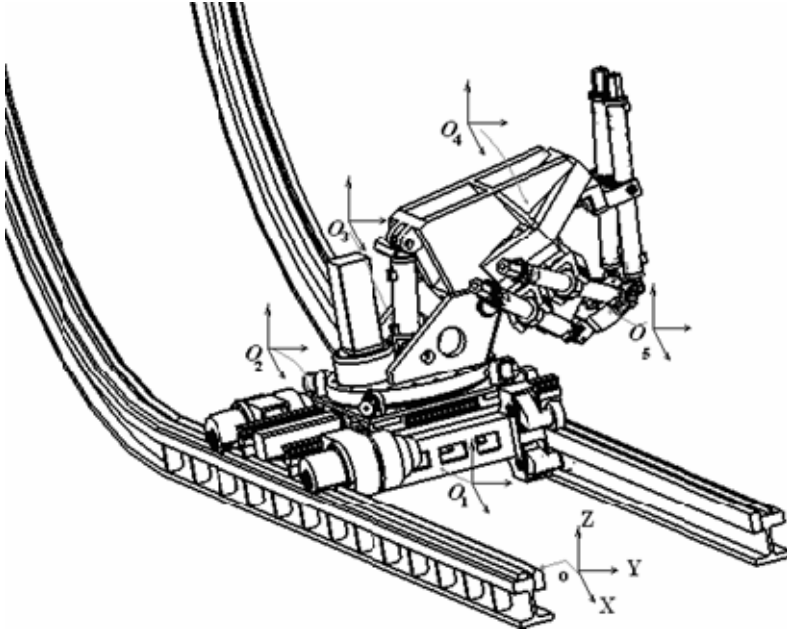
Figure 3 Coordinate system

where:

$$T_0 = \begin{bmatrix} 1 & 0 & 0 & X_0 \\ 0 & 1 & 0 & Y_0 \\ 0 & 0 & 1 & Z_0 \\ 0 & 0 & 0 & 1 \end{bmatrix}, T_1 = \begin{bmatrix} 1 & 0 & 0 & X_1 \\ 0 & 1 & 0 & Y_1 \\ 0 & 0 & 1 & Z_1 \\ 0 & 0 & 0 & 1 \end{bmatrix}, T_2 = \begin{bmatrix} c\phi & -s\phi & 0 & X_2 \\ s\phi & c\phi & 0 & Y_2 \\ 0 & 0 & 1 & Z_2 \\ 0 & 0 & 0 & 1 \end{bmatrix}, T_3 = \begin{bmatrix} 1 & 0 & 0 & X_3 \\ 0 & 1 & 0 & Y_3 \\ 0 & 0 & 1 & Z_3 \\ 0 & 0 & 0 & 1 \end{bmatrix},$$

$$T_4 = \begin{bmatrix} c\varphi & 0 & s\varphi & X_4 \\ 0 & 1 & 0 & Y_4 \\ -s\varphi & 0 & c\varphi & Z_4 \\ 0 & 0 & 0 & 1 \end{bmatrix}, \text{ and } T_5 = \begin{bmatrix} c\alpha c\beta & c\alpha s\beta s\gamma - s\alpha c\gamma & c\alpha s\beta c\gamma + s\alpha s\gamma & X_5 \\ s\alpha c\beta & s\alpha s\beta s\gamma + c\alpha c\gamma & s\alpha s\beta c\gamma - c\alpha s\gamma & Y_5 \\ -s\beta & c\beta s\gamma & c\beta c\gamma & Z_5 \\ 0 & 0 & 0 & 1 \end{bmatrix}. \text{ Here } s$$

is short for *sine* and *c* for *cosine*.

Given the parameters of joints, the forward kinematics of the robot can be formed as

$$\vec{P} = T \bullet \vec{P}_0 = T_1 \cdot T_2 \cdot T_3 \cdot T_4 \cdot T_5 \cdot \vec{P}_0. \qquad (2)$$

The numeric iterative method is employed to solve the forward kinematics of the Hexa-WH.

4.2 Inverse kinematics of robot
As the robot has four redundant degrees of freedom, the inverse kinematics model of the carriage is given before that of the Hexa-WH.

4.2.1 Inverse kinematics of carriage

The inverse kinematics of the carriage is defined as to find the values of the four actuators with respect to the frame O, given the position and an orientation of P_4 on the Hexa-frame. The principle of the carriage mechanism is shown in Fig. 4.
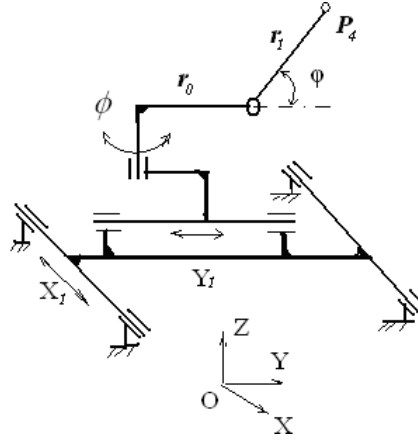
Figure 4 Mechanism of carriage

In real applications, the rotation angle ϕ is only fixed at a few values, which are $0°$, $\pm 90°$, and $180°$; the values of other actuators are calculated by fixing ϕ, i.e., for a given position $P_4(x,y,z)$, the center of Hexa-frame, the following relations exist:

$$
\begin{aligned}
X_1 + (r_0 + r_1 \cos\varphi)\cos\phi &= x, \\
Y_1 + (r_0 + r_1 \cos\varphi)\sin\phi &= y, \\
r_1 \sin\varphi &= z.
\end{aligned}
\tag{3}
$$

From Eq. (3), the following results come out:

$$
\begin{aligned}
\varphi &= \arcsin(z / r_1), \\
X_1 &= x - (r_0 + r_1 \cos\varphi)\cos\phi, \\
Y_1 &= y - (r_0 + r_1 \cos\varphi)\sin\phi.
\end{aligned}
\tag{4}
$$

4.2.2 Inverse kinematics of Hexa-WH

O_4 is coinciding with P_4 at the carriage side. Fig. 5 defines the coordinates of the Hexa-WH. The inverse kinematics for the Hexa-WH is defined as finding values for cylinders, given the position and the orientation of the end-effector with respect to the Hexa-frame:

$$
\vec{L}_i = \overrightarrow{O_4 O_5} + R \cdot \vec{r}_i' - \vec{r}_i, \quad (i = 1, 2, 3, 4, 5, 6),
$$

$$
\text{being } R = \begin{bmatrix} c\alpha c\beta & c\alpha s\beta s\gamma - s\alpha c\gamma & c\alpha s\beta c\gamma + s\alpha s\gamma \\ s\alpha c\beta & s\alpha s\beta s\gamma + c\alpha c\gamma & s\alpha s\beta c\gamma - c\alpha s\gamma \\ -s\beta & c\beta s\gamma & c\beta c\gamma \end{bmatrix}.
\tag{5}
$$
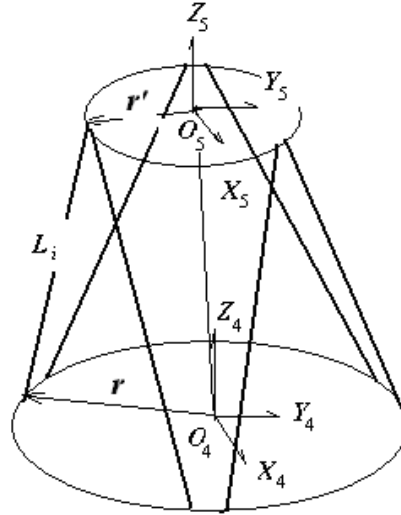
Figure 5 Hexa-WH

When (x,y,z,γ,β,α) is defined with respect to frame O_4, the length of each cylinder is:

$$l_i = \left|\vec{L}_i\right| = \sqrt{(\overrightarrow{O_4O_5} + R \cdot \vec{r}_i' - \vec{r}_i) \bullet (\overrightarrow{O_4O_5} + R \cdot \vec{r}_i' - \vec{r}_i)} \qquad (6)$$

5. CONTROL ALGORITHM

An open architecture of hardware and the programmable software are developed. Fig. 6 shows the structure of the hardware control system. The controller is an industrial-PC-based motion controller. It provides a reliable and easy-at-use environment for controlling the robot because Earthnet bus is used in the connection of iPC and I/O interfaces.

The software (Fig. 7) includes the graphical interface, the trajectory planning, the forward and inverse kinematics models, the interpolator, the controller, and the I/O interface functions. All those functions should be integrated with the program offered by iPC and run absolutely in real time.

Graphical interface is a high level program, it includes the functions for parameter setting, condition monitoring, and graphical visualization. User can easily exchange information with this program.

Trajectory planning is also a high level program. As the robot has redundant actuators, the trajectory planning is much more difficult than usual, so an optimization algorithm, which is subjected to minimize the deflection of the robot during motion, has been employed.

Forward and inverse kinematics models and interpolator are real time functions, which generate data for the motion controller.

Controller is a real time function including the water hydraulic controller and the motor controller. As the robot has two tracking motors and the speed of the motors are not always the same at some positions, a master–slave control algorithm has been used.

I/O interface functions are real time functions, which enable transferring data from sensors to controllers and from controllers to drivers.
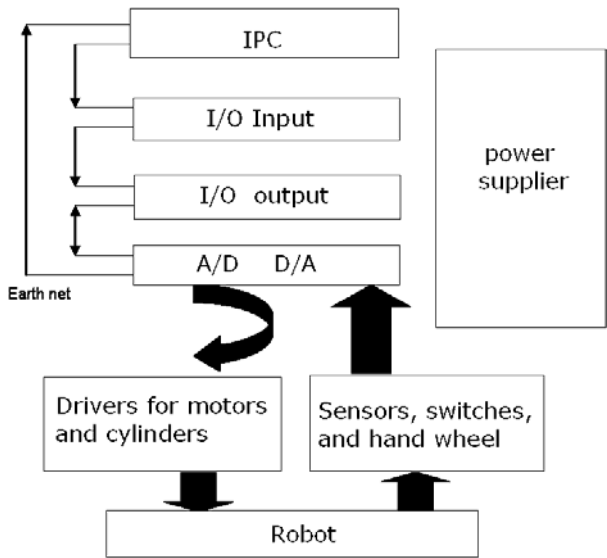
Figure 6 Structure of robot controller
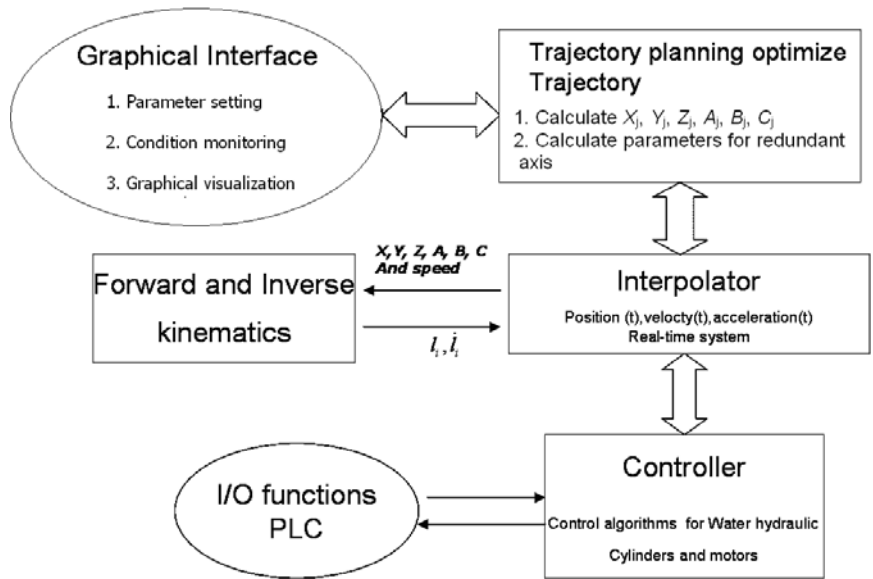
Figure 7 Structure of software

5.1 Control of drive motor

Two drive motors are used for carriage motion. As the tracking rails are not always straight and they have different radius of curvature at different regions, the speeds of two motors can not be the same when the robot crosses two different curves, thus the torque control together with the position feedback algorithm is implemented. Fig. 8 shows the control principle.
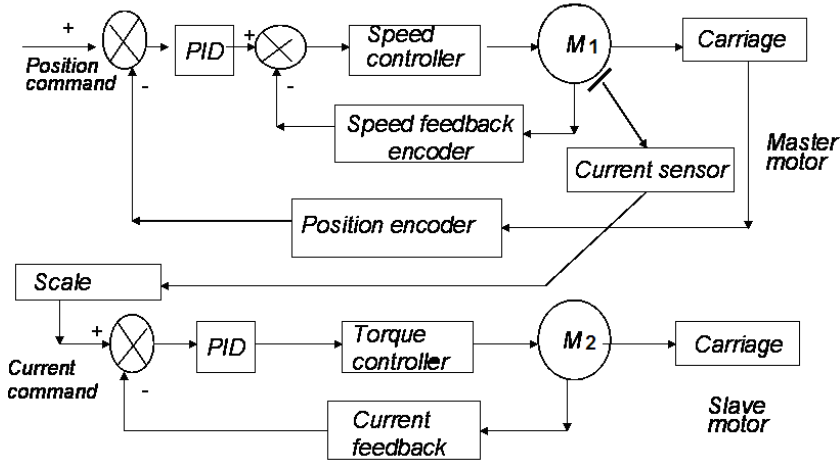
Figure 8 Motor control

In this method one motor works as master and the other one as slave. For the master motor, the position control with the speed feedback algorithm is used to guarantee the required speed and the position of the carriage. For the slave motor, the torque control is used to contribute the driving torque for the carriage.

5.2 Control of water hydraulic cylinder

In the machining process, the robot vibrates due to the dynamic machining force, and this vibration will cause two problems, which are the bad machined surface and the damage to machine tools like miller and also the robot itself. To reduce the vibration, the position control plus the payload pressure feedback control is applied in hydraulic position servo.

Figure 9 shows the control scheme. The output commands of the upper level include the position and the speed references for the servo cylinder controllers. The servo control consists of position loop and speed loop that provide accurate and fast trajectory tracking. The load pressure feedback is used for damping the self-excited oscillations normally occurring at natural frequency. The speed loop can eliminate the speed error, while the pressure feedback damps the vibration of the hydraulic actuator. The hydraulic cylinders normally lack damping which makes their control difficult by using conventional PID-controllers. The damping can effectively be increased by means of the load pressure feedback. But the major drawback in using the pressure feedback is the negative effect on the static stiffness of the actuator. So the high pass filters are used to remove the negative effect of the pressure feedback at low frequency.

Figure 9 Control scheme

6. EXPERIMENTAL SYSTEM

The tests for welding and machining have been carried out.

6.1 Welding test

To guarantee the welding quality, a seam tracker, which guides the robot motions along the centre of the welding seam, is employed. The seam tracker offers 6 DOF local coordinates of the sensor related to the welding seam. In the robot controller, a trajectory planning program has been designed to handle the data from Scout and to correct the welding trajectory, and an on-line teaching algorithm has been developed (Fig. 10).

The laser welding test was curried out with the first prototype of robot driven by oil hydraulic power. The work piece was randomly placed along Y and Z directions with angle of about 1 degree to Y- and X-axes, which were unknown to the robot before the seam finding. The YAG laser used in testing has the maximum output power 3 kW, and 200 mm focal length which results in a $\phi 0.6$ *mm* focal spot on the work piece. The beam parameter product is 25 mm-mrad. The work piece is stainless steel, AISI 316LN, with 7 mm thick, 600 mm long, and 0.2 mm root gap for welding. Fig. 11 shows the results of laser welding with seam tracker; as shown in the micrograph, the welding did not go through the plate at cross section 3; the failure is caused by the mechanical problem in one cylinder.

Figure 10 Configuration of laser welding

6.2 Speed tracking

The performance of tracking motion of robot is given in Fig. 12. In the speed tracking testing, the speed command, 538 mm/min, was given to the tracking motor 1 (short as Motor 1), while the tracking motor 2 (short as Motor 2) acting as a slave driver, one extra encoder is mounted at the center of the carriage between these two motors to measure the speed and the position of the carriage. Before the time point of 27 second, the robot had been running on the flat rack. After this point, Motor1 went into the circle area and Motor 2 was still running on the flat rack. As the speed command was sent to Motor 1, the speed of Motor 1 kept almost constant while Motor 2 was slower due to the running position in the flat area. As the assembly error exists at the joining point between the flat rack and the circle rack, the speed of each motor has slightly jumps around this point.

6.3 Machining test

The machine milling was carried out. The high speed steel miller was used in machining. The milling tool has the diameter of 25 mm. The spindle speed was set 1200 r/min and the feeding speed about 100 mm/min. The accuracy of the milled surface can reach 0.1 mm. However the backlash exists in joints and between cylinder rods and cylinders, the vibration can not totally be eliminated, further improvement of the mechanism is required. Fig. 13 shows the working environment and the milling results. The machined surface quality can reach the requirements. The carbide tools are much more capable for cutting the stainless steel and they will be used in the cutting operations to be performed in the ITER.
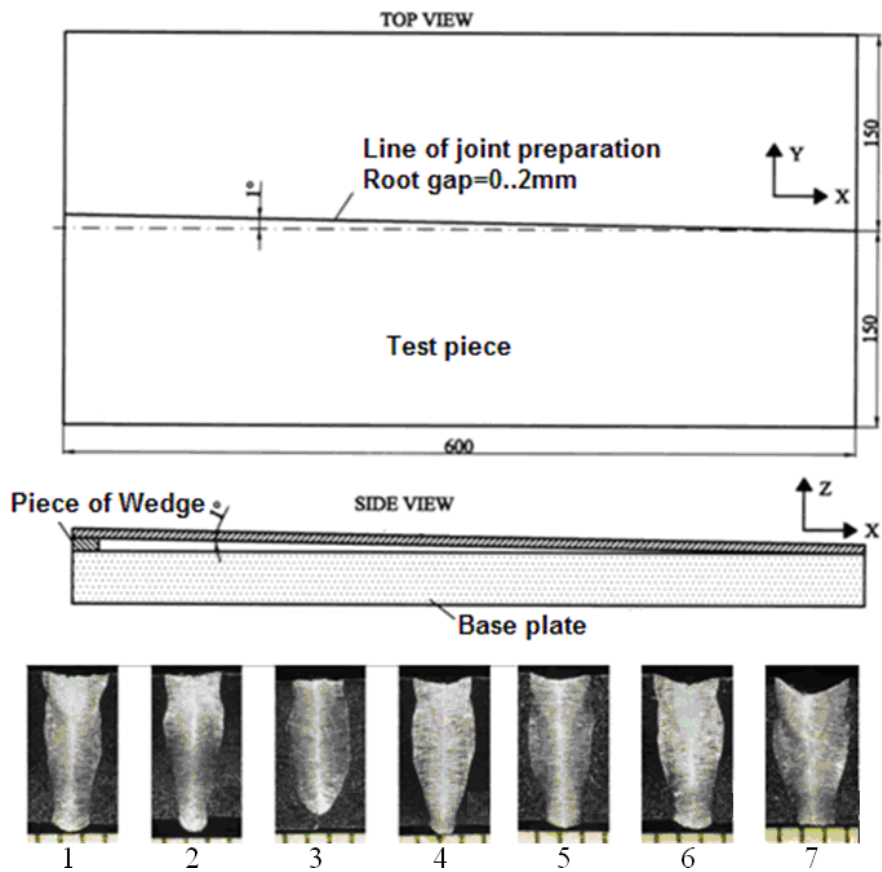
Figure 11 Laser welding test piece and micrographs of results
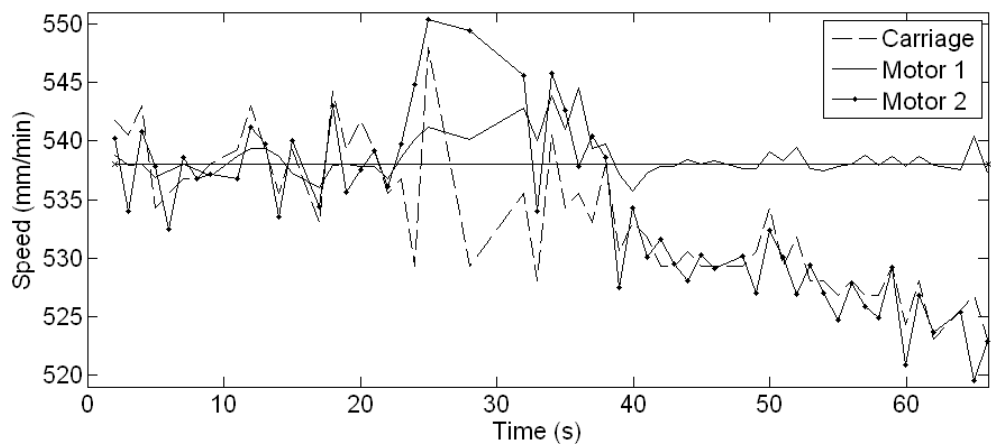
Figure 12 Speed tracking test (the horizontal line between two crosses "×" is the command speed)

<div align="center">(a)   (b)</div>
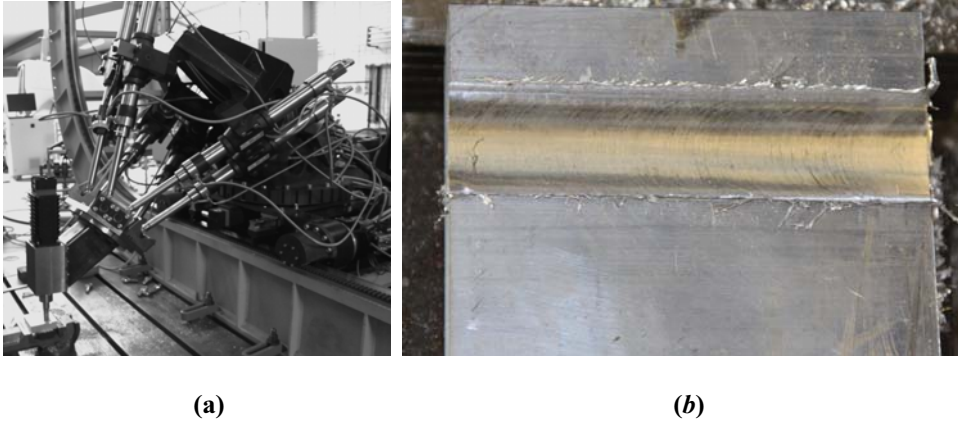
<div align="center">Figure 13 Milling test. (<i>a</i>) Test environment; (<i>b</i>) results</div>

7. CONCLUSIONS

A parallel robot, driven by hydraulic cylinders, has been developed to assemble and to repair the Vacuum Vessel of ITER. It can accurately and stably hold all necessary machining end-effector and welding end-effector in all positions. Kinematics models are very complicated because of the redundant structure; they have to be formed separately for the Hexa-WH and the carriage. The hybrid control system and the controllers have been designed; and the experimental results of the laser welding tests with seam tracker are shown. It can be seen from micrographs of the selected welded cross-sections that in most of the welded cross-sections the welding goes thought the narrow gap, except in one section; the failure is caused by the mechanical problem of one cylinder in certain region. In the machine milling test, the surface accuracy is smaller than 0.1 mm; however the vibration still exists during the machining because of the backlash of the joint and big tolerance between the cylinder rod and the guide. Further improvements need to be done for the mechanical parts.

Acknowledgement

Notation

l_i	*length of the ith cylinder*
r_1	*tilt beam length*
r_0	*rotation radius*
φ	*tilt angle*
ϕ	*rotation angle*
γ, β, α	*orientation of end-effector*
O_i	*frame i*
$\vec{r}_i$	*joint vector of the ith cylinder on the Hexa-frame concerning frame O_4*
$\vec{r}_i^{\,'}$	*joint vector of the ith cylinder on the end-effector regarding frame O_5*
x,y,z	*coordinates of the centre of the Hexa-frame*
X_1	*linear motion along X-axis*
Y_1	*linear motion along Y-axis*

References

[1] http://www.parallemic.org/Patents.html.

[2] M Honegger, A Codourey, E Burdet. "Adaptive control of the Hexaglide, a 6 dof parallel manipulator", in Proc. IEEE Int'l Conf. on Robotics and Automation, Albuquerque, New Mexico, Apr 1997.

[3] K H Häfele, H Haffner, P Spencer. "Automatic fettling cell — an example for applying computer- aided robotics", Industrial Robot, 1992; **19**(5):31-34.

[4] Zhe Wang, Zhixing Wang, W Liu, Y Lei. "A study on workspace, boundary workspace analysis and workpiece positioning for parallel machine tools", Mechanism and Machine Theory, 2001; **36**:605-622.

[5]K Koizumi, L Jones, V Krylov, D E Nelson, M Onozuka. "ITER R&D: vacuum vessel and in-vessel components: vacuum vessel" Fusion Engineering and Design, 2001; **55**:193-203.

[6] H Wu, H Handroos, J Kovanen, A Rouvinen, P Hannukainen, T Saira, L Jones. "Design of parallel intersector weld/cut robot for machining processes in ITER vacuum vessel", International Journal of Fusion Engineering and Design, 2003, **69**:327-331.

[7] L Jones. "Study to optimise intersector welding robot design and machining characteristics", Final report, Jan 2002.

[8] H Wu, H Handroos. "Parallel mechanisms based on telescopic structure and applications", in Proc. 32nd Int'l Symposium on Robotics, Seoul, Apr 2001.

[9] H Handroos, H Wu, P Pessi, Y Liu, H Yousefi, E Tenkanen, J Hopea. "Dynamic test rig for intersector welding robot (IWR) for VV sector field joining", Final report, 2003.

Multiple Sliding Mode Control for an Electrohydraulic Actuator System

Mohammed A. El Sayed, Saeid Habibi
Department of Mechanical Engineering, McMaster University, Hamilton, On, Canada

ABSTRACT

This article presents the development of a multiple loop sliding mode control strategy for improving the performance of hydrostatic actuation systems. In these actuators, the presence of nonlinearities associated with pump/motor static friction and backlash, pressure drop in the piping system, and nonlinear friction at the load have a significant effect on the performance and positional accuracy of the system. Earlier studies have indicated that the friction characteristics of the hydrostatic actuation systems are very nonlinear, displaying stick-slip (static-coulomb) type behavior. In trajectory tracking applications, this results in oscillations near the zero velocity zone.

Sliding mode control was reported to reduce these oscillations by providing a soft adaptive scheme that would compensate for the nonlinear friction. In this article, the concept of sliding control will be extended, by incorporating a secondary inner-loop controller. to enhance the accuracy of tracking in the position and velocity trajectories. Simulation results supported by theoretical analysis indicate that a considerable improvement in performance can be achieved by the implementation of this control strategy.

Keywords:
Sliding Mode Control, Electrohydraulic Actuator, Multiple Sliding Mode control

1. NOMENCLATURE

A	Hydraulic cylinder piston area
B; B_2; B_0	Coefficients of the quadratic friction model
D_p	Pump volumetric displacement
F	Actuator induced force
F_f	Load friction force
J_{pm}	Motor/pump inertia
L	Leakage coefficient
M	Sliding mass of the mechanical load

$P_1; P_2$	Actuator chamber pressures
$P_a; P_b$	Pump port pressures
P_{case}	Pressure at the case drain
P_{pipe}	Minimum system pressure in the outer circuit
$Q_1; Q_2$	actuator flows
$Q_a; Q_b$	Pump flows
V_o	Mean actuator chamber volume
$x_o; x$	The mean position, and displacement from the mean position
β_e	Hydraulic bulk modulus
ξ	Pump cross-port leakage coefficient
ω_p	Pump angular velocity

2. INTRODUCTION

Hydraulic systems are commonly used for actuation and manipulation of heavy loads. They are found in a variety of different industries, such as in automotive, manufacturing, robotics, construction, and aerospace. Conventional hydraulic systems use a centralized constant pressure supply system. Pressurized fluid is then channelled to actuators using servo-valves. The advantages of these systems are their high torque to mass ratio, and the ability to control speed and direction with relative accuracy (1). However, according to (2-4), there are also disadvantages such as the requirement of a bulky centralized supply, leakage, noise, and reduced energy efficiency due to orifice flow and the requirement for maintaining a constant supply pressure.

Electro-Hydrostatic Actuation systems (EHA) alleviate many of the above mentioned shortcomings of servo-valve controlled hydraulic systems. In the EHA position control is achieved by regulating the pumping action. Here, a fixed or a variable displacement pump can be used to move oil from one chamber of the actuator to the other. Fixed displacement gear pumps have been successfully used for precision control of inertial loads. Load manipulation is achieved by changing the speed and the direction of the pump with an electrical servomotor. A high precision EHA was prototyped in (2, 5, and 6) and has achieved sub-micron resolution.

In this EHA, two control loops were used. These consisted of an outer-loop proportional controller and a high gain inner-loop pump velocity controller. The latter was reported to desensitize the system to dead-band caused by friction at the pump motor interface. In (8), a gain scheduled proportional controller, and a fuzzy controller were applied to the outer position control loop to improve the positional accuracy. A further study involved re-tuning of the gain scheduled proportional controller to improve its performance in trajectory tracking applications in (7), and reported that chatter is observed in both load velocity and acceleration, which is linked to the nonlinear behavior of friction at the load. It was stated that using sliding mode control suppresses the chattering effect, thus resulting in improved velocity and acceleration profiles.

In (7), sliding mode control was proven as a very effective tool in suppressing the friction induced limit cycle oscillations. The effectiveness of this strategy is dependent on adjusting

the smoothing boundary layer thickness for the switching component of the control signal. However, it should be noted that the role of the smoothing boundary layer has been to date targeted to eliminating chatter caused by the switching action and uncertainties in sliding mode control. Larger system uncertainties; require a larger boundary layer thickness in order to effectively eliminate the chatter. Because of the decoupling effect that the boundary layer thickness has with the amount of error in all the trajectories, a larger boundary layer thickness would increase the amount of error present in the positional accuracy, a tighter boundary layer thickness on the other hand, will improve the positional accuracy at the expense of inducing chatter noticeably in the velocity and the acceleration profiles.

In this paper, a new form of sliding mode control with a secondary inner-loop is introduced. This inner-loop will result in the addition of a secondary boundary layer thickness that adds an additional degree of freedom.

3.   ELECTRO-HYDRAULIC ACTUATOR (EHA) SYSTEM

In this paper the EHA system of Fig. 1 will be used with its design details given in (5). This system consists of an electric motor, a gear pump, a symmetrical actuator, pressure and position sensors, an accumulator, pressure relief sub-circuit, and an optional filtering sub-circuit. The pump only operates when control action is needed, and thus the system has the advantage of an overall better energy efficiency in comparison to swash plate controlled hydrostatic or valve controlled hydraulic systems, (6). However, volumetric efficiency is compromised at very low pump speeds, and a dead-band is present, resulting in an effect similar to backlash (9). In this section, the mathematical model of the EHA is reviewed and refined.
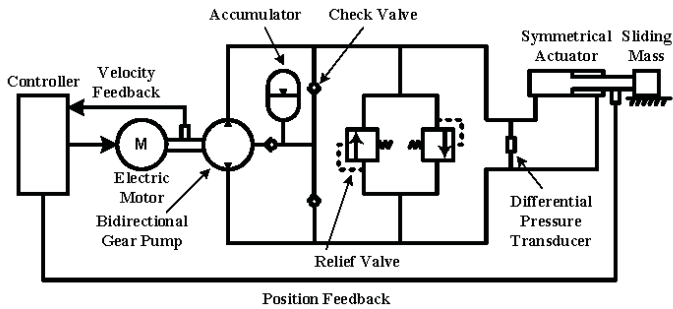
Figure 1   The EHA circuit diagram, (8)

A simplified pump/actuator model was developed in (10) and is given as:

$$D_P \omega_p = A\dot{x} + \frac{V_o}{\beta_e}\left(\frac{dP_1}{dt} - \frac{dP_2}{dt}\right) + \zeta(P_1 - P_2) + 2\zeta P_{pipe} + \frac{L}{2}(P_1 - P_2) \qquad (1)$$

The EHA system is connected to a horizontal sliding mass and the equation of motion for the actuator is obtained as follows:

$$(P_1 - P_2)A = M\ddot{x} + F_f \tag{2}$$

Where F_f is the friction force, in a study performed by Chinniah in (11) on the EHA prototype, the nonlinear behavior of friction in EHA was experimentally measured. A "quadratic" model was proposed, which was used in conjunction with the Extended Kalman Filter for online estimation of friction parameters. The friction force was assumed to be a second order equation in load velocity, given by Eq. (3)

$$F_f = B\dot{x} + (B_2\dot{x}^2 + B_0)sign(\dot{x}) \tag{3}$$

$$(P_1 - P_2)A = M\ddot{x} + B\dot{x} + (B_2\dot{x}^2 + B_0)sign(\dot{x}) \tag{4}$$

Taking the derivative of both sides of Eq. (4)

$$\left(\frac{dP_1}{dt} - \frac{dP_2}{dt}\right) = \frac{M}{A}\dddot{x} + \frac{B}{A}\ddot{x} + \frac{2B_2\dot{x}\ddot{x}}{A}sign(\dot{x}) \tag{5}$$

The pump/actuator pipe connection is modeled as a pressure drop P_{pipe}, which is a function of flow in the EHA system, P_{pipe} is approximately modeled by using Darcy's pipe flow equation as:

$$P_{pipe} \approx K_{pipe}Q_L^2 \approx K_{pipe}D_p^2\omega_p^2 \tag{6}$$

Linearizing this equation leads to

$$\Delta P_{pipe} \approx 2K_{pipe}D_p^2\omega_{p_o}\Delta\omega_p \tag{7}$$

Substituting Eqs. (4), (5), and (7) into Eq. (1) yields,

$$
\begin{aligned}
D_p\left(1 - 4K_{pipe}\zeta D_p\omega_{p_o}\right)\Delta\omega_p \\
= \frac{MV_o}{A\beta_e}\Delta\dddot{x} + \left(\frac{BV_o + M\beta_e\left(\zeta + \frac{L}{2}\right)}{2A\beta_e}\right)\Delta\ddot{x} + \left(\frac{A^2 + B\left(\zeta + \frac{L}{2}\right)}{A}\right)\Delta\dot{x} \\
+ \frac{2B_2V_o\dot{x}\ddot{x} + \beta_e\left(\zeta + \frac{L}{2}\right)(B_2\dot{x}^2 + B_3)}{A\beta_e}sign(\dot{x})
\end{aligned}
\tag{8}
$$

In practice $4K_{pipe}\zeta D_p\omega_{p_o} \ll 1$ and this allows the development of a linear model. Choosing the state variables x_i, as shown in Eq. (9), assuming the presence of system noise, and using the sampling period T_s, replacing the input term ω_p as u, the state space discrete equations may be approximated (using the "forward difference" approach to discretization) as :

$$x_1(k+1) = x_1(k) + T_s x_2(k) + T_s w_1(k)$$
$$x_2(k+1) = x_2(k) + T_s x_3(k) + T_s w_2(k)$$
$$x_3(k+1)$$

$$= \left[1 - T_s\left(\frac{BV_o + MB_e\left(\zeta + \frac{L}{2}\right)}{MV_o}\right)\right] x_3(k) - T_s \frac{\left(A^2 + B\left(\zeta + \frac{L}{2}\right)\right)\beta_e}{MV_o} x_2(k) \tag{9}$$

$$- T_s \frac{2B_2 V_o x_2(k) x_3(k) + \beta_e\left(\zeta + \frac{L}{2}\right)(B_2(x_2(k))^2 + B_3)}{MV_o} sign(\dot{x}) + \frac{T_s A D_p \beta_e}{MV_o} u(k)$$

$$+ T_s w_3(k)$$

For the control design in this paper, the friction will be linearized. However, all simulation results will be performed on the nonlinear plant model, this will provide a realistic situation, where actual friction dynamics are not known and a highly uncertain simple friction model is used for the control design. As such the system model used for control design is written as:

$$x_1(k+1) = x_1(k) + T_s x_2(k) + T_s w_1(k)$$
$$x_2(k+1) = x_2(k) + T_s x_3(k) + T_s w_2(k)$$

$$x_3(k+1) = \left[1 - T_s\left(\frac{BV_o + MB_e\left(\zeta + \frac{L}{2}\right)}{MV_o}\right)\right] x_3(k)$$

$$- T_s \frac{\left(A^2 + B\left(\zeta + \frac{L}{2}\right)\right)\beta_e}{MV_o} x_2(k) + \frac{T_s A D_p \beta_e}{MV_o} u(k) + T_s w_3(k) \tag{10}$$

The discrete equation can now be represented by the more generic form

$$X(k+1) = \Phi X(k) + Gu(k) + W(k) \tag{11}$$

Where

$$\Phi = \begin{pmatrix} 1 & T_s & 0 \\ 0 & 1 & T_s \\ 0 & -T_s \dfrac{\left(A^2 + B\left(\zeta + \frac{L}{2}\right)\right)\beta_e}{MV_o} & \left[1 - T_s \dfrac{\left(BV_o + M\beta_e\left(\zeta + \frac{L}{2}\right)\right)}{MV_o}\right] \end{pmatrix} \tag{12}$$

And

$$G = \begin{pmatrix} 0 \\ 0 \\ T_s \dfrac{A D_p \beta_e}{MV_o} \end{pmatrix} \tag{13}$$

4.   SLIDING MODE CONTROL

Sliding mode control is known for its ability to provide robustness and stability in controlling dynamic systems in the presence of uncertainties. In (12) Misawa developed a discrete sliding mode control to provide stability for nonlinear systems with uncertainties that do not satisfy the matching condition. Later in (13) this design was extended for linear systems and was reported to provide good results. In (7) Wang adopted Misawa's control technique to design a controller for the EHA system for trajectory tracking applications. Using an accurate model of nonlinear friction in the controller design, simulation results indicated the ability of the controller to provide accurate tracking while suppressing the chatter in acceleration and velocity profiles. In this section, this control design will be reviewed along with simulation results of its application to the EHA system.

4.1 Application of SMC to EHA system

Consider a linear dynamical system of the form shown in in Eq. (11), in trajectory tracking applications it is desired to design a controller to force the system state vector to follow a desired trajectory X_d. In terms of tracking error $e(k) = X_d(k) - X(k)$, the objective could be restated as driving the error as close as possible to zero. As such, a sliding manifold is defined as:

$$\Sigma = (e(k)|s(k) = Ce(k) = 0) \tag{14}$$

A smoothing boundary layer is defined as:

$$\Psi = (e(k)||s(k)| = |Ce(k)| \leq \psi) \tag{15}$$

Assuming that uncertainties (w) are bounded such that:

$$|Cw| \leq \gamma \tag{16}$$

The control input is defined as:

$$u(k) = u_{eq}(k) - (CG)^{-1}s(k) + (CG)^{-1}K_c sat\left(\frac{s(k)}{\psi}\right) \tag{17}$$

$$u_{eq}(k) = (CG)^{-1}C(X_d(k+1) - \Phi X(k)) \tag{18}$$

$$K_c = \gamma + 2\Delta t\epsilon, \psi \geq \gamma + \Delta t\epsilon \tag{19}$$

$$sat\left(\frac{s}{\psi}\right) = \begin{cases} +1 & if \quad s > \psi \\ \dfrac{s}{\psi} & if \quad |s| \leq \psi \\ -1 & if \quad s < \psi \end{cases} \tag{20}$$

Where, ϵ is an arbitrary positive constant.

Table 1 EHA parameters

Parameter	Value	Units
M	20	kg
A	5.05×10^{-4}	m^2
B	760	Ns/m
V_o	6.85×10^{-5}	m^3
L	5×10^{-13}	m^3/sPa
ζ	2.5×10^{-13}	m^3/sPa
β_e	2.1×10^{8}	Pa
D_p	1.7×10^{-7}	m^3/rad

The EHA model is given in equation Eq.(10), with parameters value provided in table. 1. Figure 3 shows the simulation results from the application of the control strategy of Eq. (17), where it is evident that because of the inaccuracy in the friction model, the computed control signal is not accurate enough to impart enough acceleration to the system, such that the acceleration error would lie within the boundary layer. Accordingly the switching term in the SMC controller will cause chattering around the desired trajectory. Expanding the boundary layer thickness can eliminate chattering at the expense of positional accuracy as shown in Fig. 4.
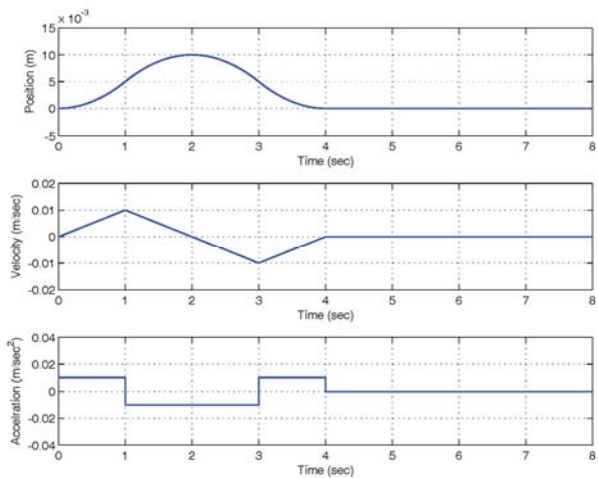
Figure 2   Desired trajectory
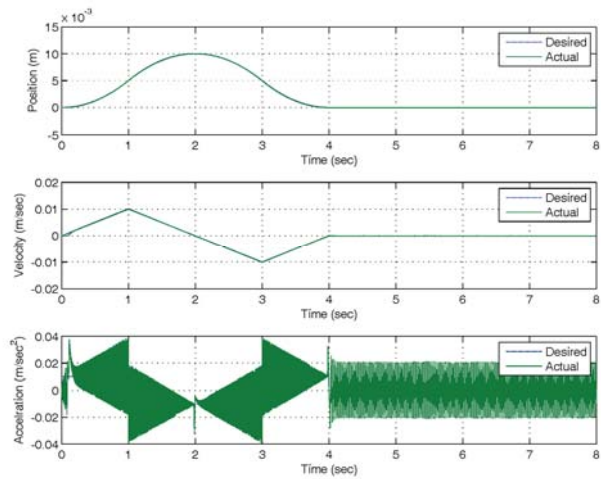
Figure 3   EHA simulation results, inaccurate friction model, and small boundary layer thickness
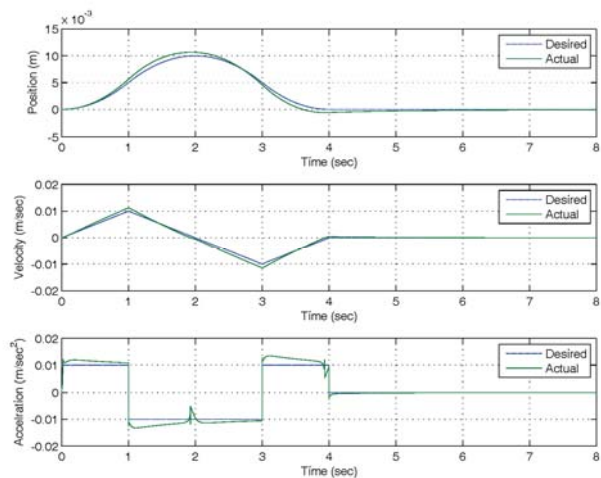
Figure 4   EHA simulation results, inaccurate friction model, and large boundary layer thickness

5.   MULTIPLE SLIDING MODE CONTROL (MSMC)

The simulation results discussed in the previous section indicates that while sliding mode control has the ability to provide a mechanism for chatter suppression, there exists a tradeoff between chattering and positional accuracy. To provide greater flexibility in dealing with

this effect a secondary inner-loop SMC controller can be used to improve positional accuracy while suppressing chattering in acceleration trajectory following. The secondary controller is a reduced order controller, such that it uses the error in position and velocity to derive a secondary sliding surface with a secondary boundary layer. The output of this controller is then used to apply a correction to the desired acceleration trajectory to compensate for the inaccuracy in the friction model, and hence eliminate the chatter without compromising the positional accuracy. In this section, the mathematical representation of this strategy will be presented along with simulations results from its application to the EHA system.

5.1 MSMC mathematical formulation

Consider a linear dynamical system of the form shown in Eq. (11). Let:

$$C = (C_1, C_2) \tag{21}$$

$$\boldsymbol{X} = (\boldsymbol{X}_1^T, \boldsymbol{X}_2^T) \tag{22}$$

$$\Phi = \begin{pmatrix} \Phi_{11} & \Phi_{12} \\ \Phi_{21} & \Phi_{22} \end{pmatrix} \tag{23}$$

$$G = \begin{pmatrix} 0_{n-1} \\ G_2 \end{pmatrix} \tag{24}$$

The system of Eq. (11), could be rewritten as

$$X_{1,k+1} = \Phi_{11} X_{1,k} + \Phi_{12} X_{2,k} \tag{25}$$

$$X_{2,k+1} = \Phi_{21} X_{1,k} + \Phi_{22} X_{2,k} + G_2 u_k \tag{26}$$

The multiple sliding mode control strategy is composed of two control elements in an additive form, consisting of a main control element and a secondary control element. The main control element uses the system model of Eq. (11) to derive a control action that would drive the states to follow the specified state trajectory associated with position and acceleration. The secondary control element works in two stages. In the first stage the upper partition of the state vector $X_{1,k+1}$ of Eq. (25) is used to derive a desired corrective input for the lower partition of the state vector $\widehat{X}_{2d,k}$. This input is then used in the second stage to provide additional control action. The additional control action will reduce the error in the X_1 state vector by introducing a secondary switching element with a tighter boundary layer thickness for the X_1 state vector, as follows.

For the main outer-loop controller, the same strategy as in the previous section is followed, with:

$$u_{eq} = (CG)^{-1} C\left(\boldsymbol{X}_{d_{k+1}} - \Phi \boldsymbol{X}_k\right) \tag{27}$$

$$u_m = u_{eq} - (CG)^{-1} s_k + (CG)^{-1} K_c sat\left(\frac{s_k}{\psi_c}\right) \tag{28}$$

For the secondary controller, the first stage derives a corrective acceleration term as follows:

$$\hat{X}_{2d,k} = u_1 = -(C_1\Phi_{12})^{-1}S_{1_k} + (C_1\Phi_{12})^{-1}K_{1_c}Sat\left(\frac{S_{1_k}}{\psi_{1_c}}\right) \tag{29}$$

In the second stage the acceleration corrective action is mapped to the output space using the following equation

$$u_s = (C_2G_2)^{-1}K_{2_c}Sat\left(\frac{C_2\hat{X}_{2d,k}}{\psi_{2_c}}\right) \tag{30}$$

Finally the full control action is established using the main control element and the secondary control element, according to the following equation

$$u_k = u_m + u_s = u_{eq} - (CG)^{-1}S_k + (CG)^{-1}K_cSat\left(\frac{S_k}{\psi_c}\right)$$
$$+ (C_2G_2)^{-1}K_{2_c}Sat\left(\frac{C_2\hat{X}_{2d,k}}{\psi_{2_c}}\right) \tag{31}$$

5.2 Simulation results

Simulation results have been obtained using the Multiple Sliding Mode Control (MSMC). As in the previous case the controller is applied to a simulation model with nonlinear friction as given in Eq. (9). Figure 5 shows the system output using the proposed MSMC strategy; it is clear that the strategy is successful in improving the tracking accuracy with no chatter in the acceleration profile.
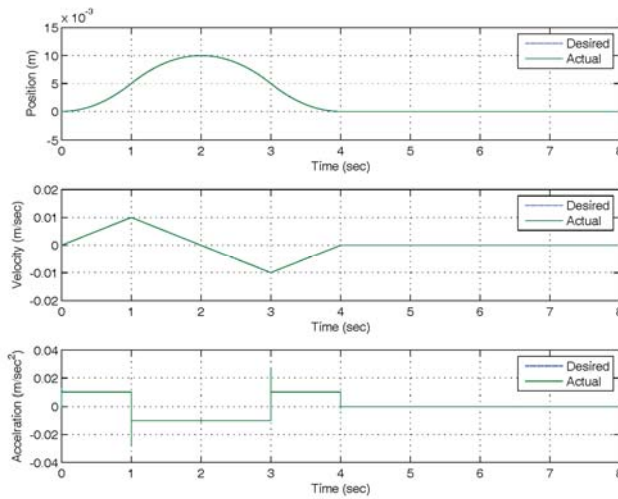
Figure 5   EHA simulation results, MSMC strategy

6.   CONCLUSIONS

In this paper, a Multiple Sliding Mode Control strategy is proposed to improve the tracking accuracy in Electrohydraulic Actuation systems (EHAs). The controller is implemented on a validated model of an EHA prototype. Simulation results indicate a considerable improvement in the tracking accuracy while suppressing the previously reported chatter in acceleration due to non-linear friction. The MSMC strategy presents a useful adaptive mechanism for compensating non-linear friction.

REFERENCES

(1)   J. Watton, "Fluid Power Systems", Prentice-Hall Int. (UK), Hemel Hempstead, 1989.

(2)   S. Habibi and A. A. Goldenberg, "Design and analysis of a new symmetrical linear actuator for hydraulic and pneumatic systems", Transactions of the Canadian Society for Mechanical Engineering, vol. 23, pp. 377-396, 1999.

(3)   W. Qian, "Neural Network Control of Nonlinear Hydraulic systems", 1999.

(4)   H. D. Tran and D. B. DeBra, "Design of a fast short-stroke hydraulic actuator", CIRP Annals, vol. 43, pp. 469-472, 1994.

(5)   S. Habibi and A. Goldenberg, "Design of a new high-performance electrohydraulic actuator", IEEE/ASME Transactions on Mechatronics, vol. 5, pp. 158-164, 2000.

(6)   S. Habibi, R. Burton, and E. Sampson, "High Precision Hydrostatic Actuation Systems for Micro and Nano Manipulation of Heavy Loads", Journal of Dynamic Systems, Measurement, and Control, vol. 128, pp. 778-787, Dec.2006.

(7)   S. Wang, S. Habibi, R. Burton, and E. Sampson, "Sliding mode control for a model of an electrohydraulic actuator system with discontinuous nonlinear friction", Minneapolis, MN, USA," 2006, pp. 8-38.

(8)   E. B. Sampson, "Fuzzy Control of the ElectroHydraulic Actuator", M.Sc. Thesis, University of Saskatshawan, 2005.

(9)   S. Habibi, J. Roach, and G. Luecke, "Inner-loop control for electromechanical (EMA) flight surface actuation systems", New York, NY 10016-5990, United States, Journal of Dynamic Systems, Measurement and Control, Transactions of the ASME, vol. 130, pp. 051002-1, 2008.

(10) S. R. Habibi and G. Singh, "Derivation of Design Requirements for Optimization of a High Performance Hydrostatic Actuation System", International Journal of Fluid Power, vol. 1, pp. 11-29, 2000.

(11) Y. A. Chinniah, "Fault Detection in the ElectroHaydraulic Actuator using Extended Kalman Filter", Ph.D. Thesis, University of Saskatchewan, 2004.

(12) E. A. Misawa, "Discrete time sliding mode control for nonlinear systems with unmatched uncertainties and uncertain control vector", Transactions of the ASME. Journal of Dynamic Systems, Measurement and Control, vol. 119, pp. 503-512, 1997.

(13) E. A. Misawa, "Discrete time sliding mode control: The Linear Case", Transactions of the ASME. Journal of Dynamic Systems, Measurement and Control, vol. 119, pp. 819-821, 1997.

Sealing, friction and leakage

Investigation of the Acceleration Effect on Dynamic Friction of EHA System

Wei Li †, Richard Burton †, Saeid Habibi ‡, Greg Schoenau † and FangXiang Wu †
† Department of Mechanical Engineering, University of Saskatchewan
‡ Department of Mechanical Engineering, McMaster University

ABSTRACT

In some early modeling studies on a high precision Electro-Hydrostatic Actuator (EHA) by the authors, it was observed that under certain conditions, limit cycles were predicted in the output actuator displacement but were not observed physically even though the parameters used in the modeling were based on experimental measurements. It was suspected that the measured (and subsequently modeled) friction characteristics of the actuator were part of the reason for this discrepancy.

In this paper, dynamic friction modeling of the EHA is experimentally investigated. It was found that the traditional steady-state friction characteristic – the so-called Stribeck effect obtained by measuring the friction forces at different constant velocities - is a poor representation of the true dynamic friction when the EHA experiences various accelerations during the control process, such as the step response.

In this paper, a new term "unsteady state friction" is defined and subsequently measured, examined, and analyzed. Experimental results reveal that this unsteady state friction is a more general form of the dynamic friction. In addition steady state friction is just a special case of the unsteady state friction, which is highly acceleration dependent. When the acceleration increases, the Stribeck effect decreases, indeed, can reach conditions where it no longer exists within the operating velocity range. A novel experiment to measure the friction of the EHA system is presented. A new nonlinear friction model (a 3D surface model) including the acceleration factor is proposed, which indicates that the Stribeck curve is just a special case of the dynamic friction model when the system acceleration is approaching zero. This result can be applied to any actuator (linear and rotary) and provides a new way in which the dynamic friction can be viewed and modeled.

NOMENCLATURE AND PARAMETER VALUES

Variables	Definitions	Values
$A_1 = A_2$ $= A$	Actuator pressure area	$5.05 \times 10^{-4}\,\mathrm{m}^2$ *
D_p	Pump volumetric displacement	1.6925×10^{-7} $\mathrm{m}^3/\mathrm{rad}$ *
M	The mass of load	20 kg
$F_\mathrm{f}(t)$	The friction force	N
P_1, P_2	The chamber pressures of two ends of the actuator	Pa
ΔP	The differential pressure	Pa
Q_{pMax}	Max flow rate of the pump	m^3/s
X	Displacement of actuator	m
L_{Max}	Max travel range	~0.12 m *
β_e	Effective bulk modulus of hydraulic oil	2.1×10^8 Pa *
ω_p	Pump angular velocity	rad/s
$\mathrm{Acc} = \ddot{X}$	Acceleration of piston	$\mathrm{m/s}^2$
X_{Max}	Max displacement	m
ω_{pMax}	Max pump angular velocity	rad/s
$v = \dot{X}$	The velocity of piston	m/s

V_{Max}	Max velocity of the piston	~0.13 m/s
f	The frequency of velocity	Hz
t	Time	sec
F_C	Coulomb friction	N
F_b	Breakaway friction	N
v_S	Pseudo-Stribeck velocity	m/s
B	Viscous friction coefficient	N/m/s
$F_\mathrm{C}(a)$	Unsteady Coulomb friction	N
$F_\mathrm{b}(a)$	Unsteady breakaway friction	N
$k_v(a)$	Velocity coefficient	No Dimension
$k_a(a)$	Acceleration coefficient	No Dimension
$v_b(a)$	Breakaway offset velocity	m/s
$v_\mathrm{S}(a)$	Unsteady pseudo-Stribeck velocity	m/s
$B(a)$	Unsteady viscous friction coefficient	N/m/s
n	Exponent number for Stribeck curve	1 or 2
* Values obtained from [1]		

1.   INTRODUCTION

An Electro-hydrostatic actuator (herein referred to as the EHA system) [2] as a hydraulic system can exhibit many nonlinear behaviors, the source of which can be attributed to such things as nonlinear bulk modulus, nonlinear viscosity, and nonlinear friction, amongst others [3, 4]. Of these properties, nonlinear friction is perhaps the most dominant and is a primary source of disturbance for motion control systems and may largely contribute to steady state errors, limit cycles, and poor performance. Many controller designs are highly dependent on the accuracy of the friction model used in the friction compensation loop. For this reason, friction identification and modeling has been one of the most important issues in the design of high-performance motion control systems [5].

Even though the topic of friction is a relatively old one, and has played an important role in many practical and engineering applications, surprisingly it is not as well understood as one might expect it to be [6, 7]. "Dynamic" friction has been traditionally referred to as the friction force which results once motion occurs between sliding surfaces. Literature pertaining to dynamic friction identification, measurement and modeling is vast [8, 9]. Due to its highly non-linear nature, friction is very difficult to model. Most available friction models are, in essence, empirical, that is, they are based on limited observations and interpretations. In this sense, the resulting models are valid only for the specific scope of test conditions, such as the level and type of excitation used to obtain the data [10]. Indeed, the list of frictional effects one may wish to describe varies widely from application to application. In most cases, the selection of a particular friction law is made heuristically without any explanation [11]. In some cases, the friction is simplified by a linearized model; as a result, application of this linearized model can often lead to erroneous results [12].
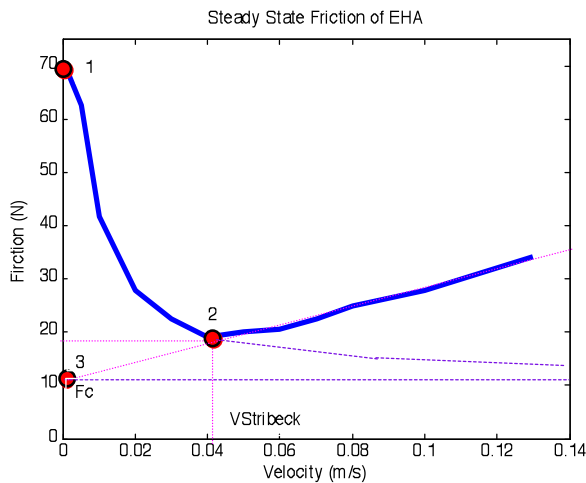
Figure 1 Typical Stribeck curve for the EHA system

Stribeck published his work on the dynamic friction between lubricated surfaces over 100 years ago, which resulted in the well-known Stribeck curve showing the correlation between friction force and velocity [13, 14]. Such a curve measured in the EHA system is illustrated in Figure 1. It is a friction phenomenon which gives rise to decreasing friction with increasing velocity at low velocity (essentially a negative viscous friction slope). In other

words, it was indicated that friction decreases after "breakaway" by overcoming the "breakaway friction" and increases after the velocity passes the Stribeck velocity. This increase was attributed to fact that the thickness of the lubricant film presented between the sliding surfaces increases with the sliding velocity [15]. It has been shown that the Stribeck effect is valid from application to application as long as lubrication between surfaces exists in the "steady state" velocity (with no acceleration) condition. It is necessary to clearly define friction terms since a new definition will be introduced. "Breakaway friction" is the friction which is generated before movement of the sliding surfaces. The static friction force will always be equal to the force applied until it reaches the "breakaway" point. With reference to Figure 1, the "peak friction" (F_b indicated by point 1 in Figure 1) value is defined as the breakaway friction (commonly labeled as the static friction). As discussed earlier, the dynamic friction is the friction under motion conditions. At this point it is necessary to clarify that usually the curve shown in Figure 1 is obtained by measuring the friction at discrete velocity points; that is, the curve is not measured in a continuous fashion. This is a very important consideration because it is not known what the acceleration is at each point; indeed, it most cases, the acceleration is zero. This will be discussed at great length in a later section. If the dynamic friction has been obtained where the acceleration at the discrete measurement velocity points is zero, the dynamic friction curve is defined as being a "steady state" friction characteristic. If acceleration at each point is not zero, this dynamic friction is defined as the "unsteady state" friction. The region where the friction decreases is called the Stribeck region and the point where the velocity again increases is the Stribeck velocity ($V_{Stribeck}$ indicated by point 2 in Figure 1).

The form of the curve in Figure 1 is the Stribeck characteristic and is defined mathematically by equation (1) as follows:

$$F_{Steadystate\_friction}(v) = F_c + (F_b - F_c)e^{-\left(\frac{v}{v_s}\right)^n} + Bv \qquad (1)$$

where the parameters F_c, F_b, v_s and B are constant and defined graphically in Figure 1. The Coulomb friction (F_c) can be obtained by extending the viscous friction line (indicated by point 3 in Figure 1). Coulomb friction can be defined as a dynamic friction that would exist if the system is in motion and no or little lubrication between two sliding surfaces exists, which is almost independent from the motion velocity [12].

Chinniah [1] used an experimental procedure to measure friction in the particular EHA system of interest in this study. His approach was to keep the piston moving at various constant (discrete) velocities (at zero acceleration) within the velocity range and then measure the differential pressures across the actuator to obtain the steady state nonlinear friction model. A typical result was shown in Figure 1 which displays a form consistent with the classical Stribeck curve. Because this is a discrete approach, the more velocity points used, the more continuous the friction curve becomes. However, accurate measurement of the breakaway friction could not be achieved but had to be estimated using numerical extrapolation methods. This is a problem with using discrete experimental measurement approaches. If a technique which uses a continuous measurement of force with velocity can be implemented, this problem does not exist.

From the literature, the Stribeck friction model has been verified experimentally and is quite widely used in the simulation and control of the practical systems [16]. It is apparent that

most dynamic friction models reflect the Stribeck effect illustrated in Figure 1, but with some modifications such as those found in the Bristle model, the Karnopp model, the Reset Integrator model, and the LuGre model amongst others [5, 6, 16-18]. (Out of interest the name LuGre is not based on a person but a combination of a model produced at Lund and Grenoble laboratories. [19]). These models basically reflect a combination or transition between Coulomb friction, viscous friction, and the Stribeck effect. However, the Stribeck fiction model has a major limitation in that it is only applicable to what the authors have labeled steady state conditions at the measurement points (i.e., constant or very slow changing sliding velocity under constant normal force). In other words, the Stribeck fiction model, as one of classical friction models, does not reflect the rate of change of the velocity at the measured points.

In many applications, machines can operate under what the authors have defined as "unsteady" state conditions (i.e., very rapid changes in slip velocity) where the velocities of the actuators or motors are not constant over time. It is extremely important from a modeling and control point of view to study unsteady state friction and to develop accurate nonlinear models which reflect these specific operating conditions. Furthermore, from an experimental point of view, friction is quite difficult to measure reliably even under steady state conditions, let alone unsteady state conditions. This could account for the fact that very few publications exist which consider the Stribeck characteristic under unsteady or non zero acceleration conditions.

In 1943, Sampson et al. [20] first started to question the Stribeck friction model based on his limited experimental observations in that the friction may not be solely be a function of the velocity, but rather a function of the "past history" of the motion; however, since the "past history" of the motion was not well defined in this paper, improvement to the Stribeck model was not made. In 1990, Hess et al [21] first introduced a novel approach to explore the dynamic friction in the lubricated contact surfaces by measuring the friction under the oscillating sliding velocities at various frequencies. It was observed that the frequency of velocity variation had a significant effect on the shape and size of the friction vs. velocity curve. This study put dynamic friction in a new light by recognizing that there was a frequency effect which needed to be accounted for. This frequency effect could be considered as the history of the velocity measurement. Harnoy et al [22-27] continued this approach by developing an unique apparatus to measure friction in the presence of sinusoidally-varying velocity at various frequencies. The preliminary finding of Harnoy et al. was the effect of the reduction in the magnitude of the friction near zero velocity as the frequency of oscillation increased [27]. This echoed Sampson et al's observation that the friction was not only a function of the instantaneous velocity, but was also a function of previous velocities. Harnoy et. al also attempted to explain the dynamic friction under unsteady state conditions by the physical principles of hydrodynamic lubrication.

On the other hand, the research of Owen et al. [28] showed that the Stribeck effect can be reduced or eliminated by rotating the piston, which clearly indicated that the Stribeck effect might not apply in some motion conditions. Further, Chatterjee et al [29] found that the breakaway friction force uniformly decreases with the increasing frequency of velocity variation which matched the conclusion from Canudas de Wit. [5], that is, the varying break-away force depends on the rate of change of the applied force. Most recently, Yanada et al. [30] modeled the unsteady state friction by a modified LuGre model which took the lubrication film thickness into account as an extra parameter. Unfortunately, any extra parameter added to the LuGre model makes the model parameters' identification too

difficult to accomplish, because the parameter-estimating task of LuGre model itself was already very tough due to the some unmeasurable states in the model .

A commonality (and perhaps a limitation) in the experimental procedures used by above researchers was that the friction force – velocity relationships were established by changing the frequencies of the velocity waveforms. It is proposed in the authors' (this) paper that the history of the velocity is more appropriately represented by the acceleration as opposed to the frequency of the velocity. In the aforementioned studies, assuming that the frequency is constant, the acceleration of the system could vary from $-X_{Max}(2\pi f)^2$ to $X_{Max}(2\pi f)^2$ over just one cycle, as is illustrated in equation (2). Thus acceleration is not constant during the measurement process; Changing the frequency of velocity only changes the amplitude of the acceleration.

$$Acc = -X_{Max}(2\pi f)^2 \sin(2\pi f) \qquad (2)$$

It was believed that the experimental approach could be improved upon significantly by keeping the acceleration constant over the measurement of friction force. This paper presents a probing study of friction behavior in unsteady state conditions where velocity varies with time by changing acceleration from low to high. Consequently, the main focus of this paper is to introduce a new way to measure and model the unsteady state friction at the actuator. The system studied was of a particular type of high precision hydrostatic system (EHA) in which an understanding of the nature of friction was critical for precision control. It must be noted that although this paper refers to this particular system, the concept is believed to be valid for all actuators which display the Stribeck effect. A particular aspect of friction, which explores the relationship between acceleration and friction forces, is examined and a novel 3D friction model is proposed. The potential for capturing friction forces in a predictive model is also explored .

This paper initially introduces research that has been conducted in the area of friction modeling and has introduced the definitions of steady and unsteady state friction. Section 2 briefly outlines the motivation for the work. Section 3 presents the experimental setup. Sections 4 and 5 will consider the dynamic friction measurement and the experimental results and section 6 will discuss the results and provide conclusions and future works. It must be made clear that the results shown are applicable to the particular EHA systems studied. At the time of paper preparation, extension to a more generalized actuator – friction model has not been completed.

2.   RESEARCH MOTIVATION

Although not central to the overall friction study, it is interesting to understand the motivation for this work. In early studies of step responses of a model of the EHA which employed the traditional Stribeck curve, it was found that in the open-loop mode, a highly under-damped response was observed (indeed, under certain conditions, severe limit cycles were exhibited). The problem was that this was not observed experimentally even though the friction model was experimentally obtained from the same system. It was therefore postulated that either the model was wrong or the parameters (noticeably the nonlinear friction) was not correct. This prompted an intense examination of the literature and subsequent preliminary experiment tests which then led to the conclusion that acceleration effect played an important role in the behavior of unsteady state dynamic friction.

3.   EXPERIMENT SETUP

In this section, the experimental setup used for friction measurement is described. The Electro-Hydraulic Actuation system (EHA) considered in this study is shown Figure 2 [31] .
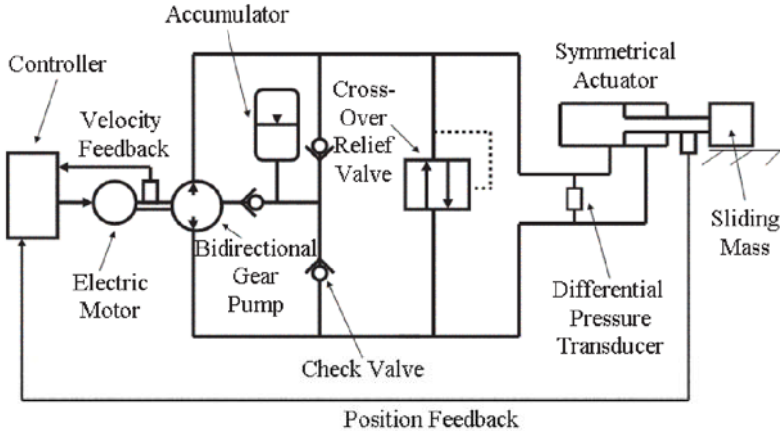
Figure 2 Schematic of Electro-Hydraulic Actuator (EHA) system [31]

The EHA is a closed hydrostatic system in which the actuator output flow is ported back into the inlet of the pump (as opposed to the fluid passing through a reservoir first in the open-circuit systems). Movement of the actuator is controlled by varying the amount of flow that comes from the pump which in turn is controlled by changing the direction and the angular speed of the pump driving motor. Because the system is closed, the actuator must be symmetric and thus for linear actuation special actuators have to be designed. A closed system of this form is highly desirable because it does not require any valve to modulate the flow which increases the system efficiency.

Studying time-varying systems requires fast and accurate measurement techniques with both storage and analyzing systems that can handle large data. An encoder with 50 nm resolution was used to measure the displacement of the mass, while a differential pressure transducer - Validyne DP15 was used to measure the differential pressure between the two ends of the actuator. The calibrations of the encoder and pressure transducer were performed before all experiments. Data acquisition was done by using a multifunction analog & digital I/O board PCI-DAS1602/16. This card with a sampling frequency of 500 Hz digitizes the analog input signals fed into the computer, and also converts the computer's digital output signal into analog form to drive the AC motor. The card features a 16-bit analog input and output resolution. It is designed to operate in computers with PCI bus accessory slots. Each test was repeated three times and the average of these tests are shown. The experimental scatter was found to be very small. Details of the EHA system used in the study can be found in [2].

4.   FRICTION MEASUREMENTS

As mentioned in the introduction, earlier work on the EHA system produced a friction velocity relationship which followed the Stribeck curve [1]. Acceleration was kept zero and as such the friction was considered to be a steady state friction. In this paper, it was proposed to create constant acceleration conditions and as such, a novel method for the

friction measurement was developed. The following assumptions were made during the friction measurement experiment, for system modeling and finally for simulation:

• The relative sliding velocities and the operation time was small enough such that thermal effects could be neglected;
• The dynamics effect of the pressure transducer could be neglected due to the fast response feature of the model Validyne DP15.

The EHA friction is the sum of the mass sliding friction and piston cylinder friction. A mass in sliding contact with a surface is a common situation and can represent a highly nonlinear system due to the slip-stick friction at the contact surface. Since hydraulic actuators operate under certain supply pressures, tight sealing is required to prevent them from any leakage [32, 33]. As a result, it has been shown that the piston friction can be substantial. Let the overall friction of the EHA be represented by $F_f(t)$. Because of the inertial term, friction cannot be directly measured because the inertial force must be subtracted. This can be observed from equation (3) :

$$F_f(t) = (P_1 - P_2)A - M\ddot{X} = \Delta PA - M\ddot{X} \qquad (3)$$

In order to measure the friction , it is necessary to measure the differential pressure of the actuator and the acceleration of the EHA system. However, measuring differential pressure and acceleration posed substantial challenges in constructing the experimental setup.

The first challenge was getting an accurate differential pressure between the two ends of the actuator. Because the available pressure transducer was very susceptible to outside noise associated with the AC motor driving the EHA, a low pass third order Butterworth filter with a cut off frequency of 20 Hz was used to "clean up" the differential pressure signal. The second challenge was to measure the velocity. Several methods of measuring or estimating velocity were examined. It was decided that the "cleanest" signals could be obtained by differentiating the position signal from the high precision encoder and then filtering the signal using digital filters. The acceleration was estimated from the desired position data differentiated twice with filtering being done only on the velocity signal.

By controlling the position of the actuator to follow a desired parabolic waveform, the velocity increased in a linear fashion and the acceleration became constant for the desired velocity range. Thus by changing the magnitude of the position waveform, friction forces (via pressure differential across the actuator) could be measured (and plotted) as a function of velocity at a constant acceleration. Acceleration became the family parameter in the resulting plots. It is important to note that the resulting friction curves are continuous with velocity.   The EHA system has a limitation both in position (due to the stroke limitation) and in the maximum actuator velocity (due to the maximum speed of the electric motor and the pump displacement). Therefore, for the particular EHA application chosen, the limit on stroke was 0.12 (m) and velocity range was constrained to be between 0 – 0.13 (m/s) .

5.   EXPERIMENTAL RESULTS

As was previously stated, under conditions of low acceleration, friction could only be estimated at discrete points by inputting the EHA with triangular positional (step velocity) waveforms. This resulted in a "discrete friction - velocity" plot and as such breakaway friction had to be estimated using extrapolation techniques (Figure 1), However, by keeping

acceleration constant, the velocity can increase continuously from 0 to maximum velocity; as a result, friction could be calculated from the pressure differential across the actuator and from the acceleration (see equation (3)) continuously and interpolation and extrapolation were not necessary.
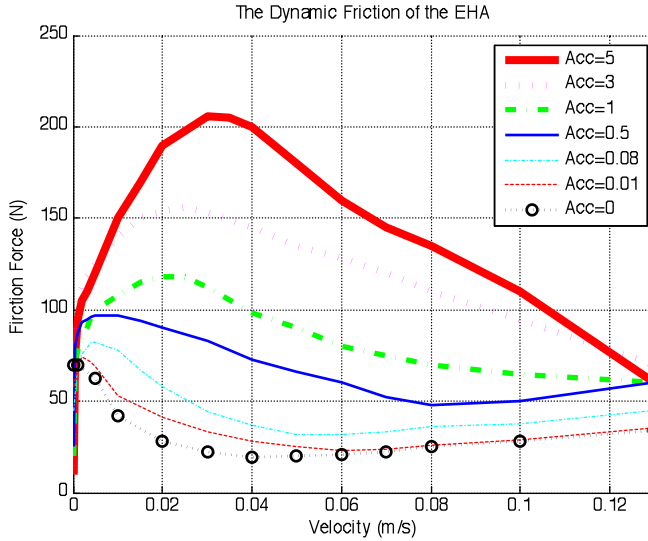
Figure 3 Unsteady state friction vs. velocity curves for various accelerations (selected for display)

Figure 3 shows experimental friction forces that were obtained for various accelerations. The friction - velocity characteristic which was acquired continuously was obtained for sliding accelerations of 0.01 to 5 (m/s/s). NUTO H32 Oil was used. All experimental tests were repeated three times and it was very evident that for the same temperature, the results were repeatable (essentially undistinguishable differences if the plots were superimposed).

It is evident that the breakaway frictions at zero velocity and the peak frictions are no longer the same as illustrated in Figure 1. In addition, the magnitude of the peak friction forces and the Stribeck velocities increase in magnitude with the increasing acceleration. It is noteworthy that the traditional Stribeck friction characteristic is evident at zero acceleration. The unsteady state friction characteristic can be expressed in a functional form by equation (4) below:

$$F_{Unsteadystate\_friction}(v,a) =$$

$$F_c(a) + (F_b(a) - F_c(a))(k_v(a)v + v_b(a))^{k_a(a)a} e^{-\left(\frac{v}{v_s(a)}\right)^n} + B(a)v \qquad (4)$$

where parameters $F_c(a)$, $F_b(a)$, $k_v(a)$, $v_b(a)$, $k_a(a)$, $v_s(a)$ and $B(a)$ are not constant and instead are functions of the acceleration. It remains a challenge to fully describe these parameters and is the topic of future research by the authors. At this point a brief explanation of the parameters of equation (4) is warranted. Compared with equation (1), when the motion of the EHA system changes from unsteady state to steady state, $F_c(a)$ will

approach F_c. $F_s(a) - F_c(a)$ will approach $(F_s - F_c)$;and unsteady item $(k_v(a)v + v_b(a))^{k_a(a)a}$ will disappear by approaching 1. Further, $v_s(a)$ will approach v_s and $B(a)$ will approach B. Therefore, the unsteady state friction will transform to the Stribeck friction. In other words, the equation (1) is just a special form of equation (4).

Based on the physical meaning of the general friction model – unsteady-state dynamic friction (see equation (4)), the Coulomb friction stays constant as F_c which can be viewed from two different perspectives. From Figure 1, the extension of the linear segment will have an intersection with the friction axis at Coulomb friction. From **Error! Reference source not found.**, it is observed that the breakaway friction decreases but tends to converges to a constant value - Coulomb friction when the acceleration increases.
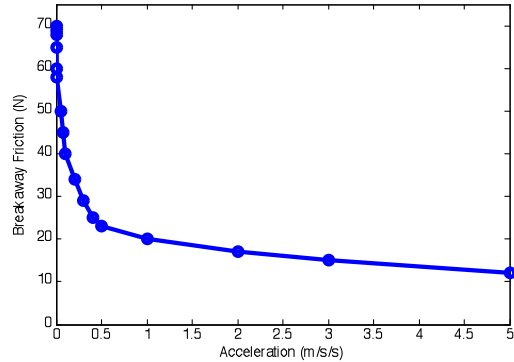
Figure 4 Breakaway Friction Curve of the EHA System

The breakaway frictions for the results of Figure 3, are shown in **Error! Reference source not found.**. These results can be compared to the results from Olsson, H. et al. [8], in which their experimental trends paralleled those shown in **Error! Reference source not found.**., that is, the breakaway forces did depend on the accelerations. With reference to equation (4), $F_b(a)$ and $v_b(a)$ are the breakaway friction and the breakaway offset velocity respectively, which are functions of accelerations. And, which help to build the curve of breakaway frictions over accelerations (**Error! Reference source not found.**). At low accelerations, $F_b(a)$ and $v_b(a)$ are larger, the breakaway frictions have larger values, At high accelerations, $F_b(a)$ and $v_b(a)$ are smaller, the breakaway frictions have smaller values and approaches the Coulomb friction F_c.

$k_v(a)$ and $k_a(a)$ are the velocity coefficient and the acceleration coefficient of the unsteady state friction respectively, which can significantly affect the positive slopes of the friction – velocity curves. At low accelerations, $k_v(a)$ is small, $k_a(a)$ is large, the friction – velocity curves (shown in Figure 3) have little negative or little positive slope after breakaway. At high accelerations, $k_v(a)$ is large, $k_a(a)$ is small, the friction - velocity curves will have a strong positive slope after breakaway occurs.

$k_S(a) = \dfrac{1}{v_s(a)}$ is defined as the Stribeck effect coefficient which can determine the negative slope of the unsteady state friction – velocity curves after the peak frictions. A smaller $k_S(a)$ translates to a smaller negative slope of the unsteady state friction, Vice-versa. Based on the hydrodynamic lubrication theory, the viscous friction coefficient $B(a)$ stays nearly constant, and will be very close to the value of B. The last parameter is the exponent number of the Stribeck curve n, the default value being 1. In some cases, it can be 2 or greater; however, it could make the friction model too complex for practical applications.

Similar plots could be developed for peak frictions (blue line with circle markers) and Stribeck velocities (green line with cross markers); however, a more meaningful representation can be developed using a 3-D plot of the results as shown in Figure 5. In this plot, acceleration is the third parameter and hence the data shown in Figure 3 appears as the 3-D plot of Figure 5. A map such as this can be very important in simulations since the map can be represented as a 2D lookup table. If the velocity and acceleration are known, then the friction force can readily be estimated. Furthermore, for constant acceleration, the coefficients of the Stribeck equation can be estimated. In Figure 5, when the velocity = 0, the intersection curve (red dot line with star markers) represents the breakaway friction curve (shown in **Error! Reference source not found.**), whereas, when the acceleration = 0, the intersection curve (black line with triangle markers) is the steady state friction curve or Stribeck curve (shown in Figure 1).
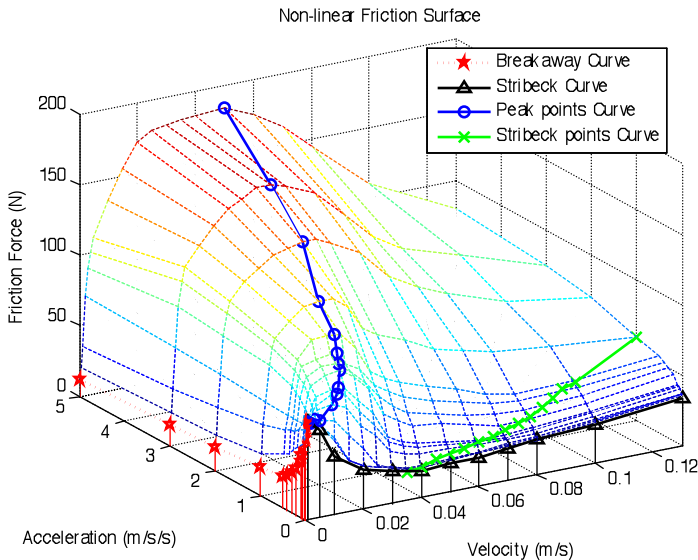

Figure 5 3D nonlinear friction surface (2D lookup table)

One observation that is worth noting is the change in the slope of the friction velocity curve at low velocities as the acceleration is increased. At low acceleration, the slope is negative

and could be destabilizing. However for the same velocity range at high accelerations, the slope is positive and hence can stabilize the system.

6.   DISCUSSION AND CONCLUSIONS

For most mechanical systems, the friction in motion condition is usually defined as a dynamic friction. However, the definitions of the dynamic friction in most literature are either vague or inadequate. As previously stated, two types of dynamic friction conditions were defined: unsteady state friction and steady state friction. Steady state dynamic friction is defined as the dynamic friction under steady velocity conditions, (i.e., zero or very small acceleration condition). On the other hand, unsteady state dynamic friction is defined as the dynamic friction under unsteady velocities, where the actuator motion occurs under significant acceleration conditions.

In this paper, unsteady state friction behavior in EHA system was experimentally examined by varying velocities under various constant acceleration conditions.   A 3D friction model (Figure 5) reflecting this acceleration factor has been developed. In the steady state, the peak friction point overlaps the maximum breakaway point, and the system displays negative damping during the low velocities range. As the acceleration of the system increases, the breakaway point magnitude decreases, the magnitude of the peak friction increases, and the velocity at which the peak friction increases (introducing a positive friction velocity curves at low velocities). Physical explanation of this novel 3D friction model is not immediately clear, but it is believed that this is closely associated with film thickness during the accelerating period [35].

In conclusion, just like the steady state friction is a special case of the unsteady state friction, the Stribeck effect is a special case of the more general unsteady state friction model (Figure 5 and equation (4)). This paper provides an insight on how to model the dynamic friction, particularly for the unsteady state motion. Based on this work, the authors are working toward an united friction model which can cover all the static and dynamic friction situations into a so-called rate dependent friction model (including hysteresis). In addition, the authors are working to determine the functional forms of equation (4) by system identification and parameter estimation techniques, which would then replace the 2D lookup table in simulations and controller designs. As stated in the introduction, the authors are examining other applications to establish that the friction characteristics observed in this study can be universally applied to more generalized applications.

REFERENCES

[1]   Chinniah, Y. A., 2004, "Fault Detection in the Electrohydraulic Actuator using Extended Kalman Filter," PhD Thesis, University of Saskatchewan.

[2]   Habibi, S., Burton, R., and Sampson, E., 2006, "High Precision Hydrostatic Actuation Systems for Micro-and Nanomanipulation of Heavy Loads," Journal of Dynamic Systems, Measurement and Control, Transactions of the ASME, **128**(4) pp. 778.

[3]   Li, W., Burton, R., and Habibi, S., 2007, "Investigation of a High Precision Hydrostatic Actuation System - How Nonlinearities Affect its Performance," 2007 ASME International Mechanical Engineering Congress and Exposition.

[4]   Merritt, H.E., 1967, "Hydraulic control systems," Wiley, New York.

[5]   Canudas de Wit, C., Olsson, H., Astrom, K. J., 1995, "A New Model for Control of Systems with Friction," Automatic Control, IEEE Transactions on, **40**(3), pp. 419.

[6]   Feeny, B. et. al., 1998, "A Historical Review on Dry Friction and Stick-Slip Phenomena," Applied Mechanics Reviews, **51**(5), pp. 321.

[7]   Wikiel, B., 2000, "Stick-Slip Motion for Two Coupled Masses with Side Friction," International Journal of Non-Linear Mechanics, **35**(6), pp. 953.

[8]   Olsson, H., Astrom, K. J., Canudas de Wit, C., 1998, "Friction Models and Friction Compensation," European Journal of Control, **4**(3), pp. 176.

[9]   Armstrong-Helouvry, B., Dupont, P., and Canudas De Wit, C., 1994, "A Survey of Models, Analysis Tools and Compensation Methods for the Control of Machines with Friction," Automatica, **30**(7), pp. 1083.

[10] Al-Bender, F., 2008, "Characterization of Friction Force Dynamics," IEEE Control Systems Magazine, **28**(6), pp. 64.

[11] Vielsack, P., 2001, "Stick-Slip Instability of Decelerative Sliding," International Journal of Non-Linear Mechanics, **36**(2), pp. 237.

[12] Berger, E. J., 2002, "Friction Modeling for Dynamic System Simulation," Applied Mechanics Reviews, **55**(6), pp. 535.

[13] Stribeck, R., 1902, "Die Wesentlichen Eigenschaften Der Gleit- Und Rollenlager" VDI-Zeitschrift Des Vereines Deutscher Ingenieure, **36**, pp. 1342–48.

[14] Jacobson, B., 2003, "The Stribeck Memorial Lecture," Tribology International, **36**(11), pp. 781.

[15] Popovic, M. R., 1996, "Friction Modeling and Control", PhD Thesis, University of Toronto.

[16] Armstrong-HÃlouvry, B., 1991, "Control of machines with friction," Kluwer Academic Publishers, Boston :, pp. xi, 173 p. :.

[17] Karnopp, D., 1985, "Computer Simulation of Stick-Slip Friction in Mechanical Dynamic Systems," Journal of Dynamic Systems, Measurement and Control, Transactions of the ASME, **107**(1), pp. 100.

[18] Haessig Jr, D. A., and Friedland, B., 1991, "On the Modeling and Simulation of Friction," Journal of Dynamic Systems, Measurement and Control, Transactions of the ASME, **113**(3), pp. 354.

[19] Johanastrom, K., 2008, "Revisiting the LuGre Friction Model," IEEE Control Systems Magazine, **28**(6), pp. 101.

[20] Sampson, J. B., Morgan, F., Reed, D. W., 1943, "Friction Behaviour during the Slip Portion of the Stick-Slip Process," J. Appl. Phys., **Vol.14**, pp.689-700.

[21] Hess, D. P., and Soom, A., 1990, "Friction at a Lubricated Line Contact Operating at Oscillating Sliding Velocities," Journal of Tribology, **112**(1), pp. 147.

[22] Harnoy, A., 2008, "Modeling and Measuring Friction Effects," IEEE Control Systems Magazine, **28**(6), pp. 82.

[23] Harnoy, A., 1997, "Simulation of Stick-Slip Friction in Control Systems," ASLE Transactions, **40**(2), pp. 360.

[24] Rachoor, H., and Harnoy, A., 1996, "Modeling of Dynamic Friction in Lubricated Line Contacts for Precise Motion Control," Tribology Transactions, **39**(2), pp. 476.

[25] Harnoy, A., and Friedland, B., 1994, "Dynamic Friction Model of Lubricated Surfaces for Precise Motion Control," S T L E Tribology Transactions, **37**(3), pp. 608.

[26] Harnoy, A., Friedland, B., and Rachoor, H., 1994, "Modeling and Simulation of Elastic and Friction Forces in Lubricated Bearings for Precise Motion Control," Wear, **172**(2), pp. 155.

[27] Harnoy, A., Friedland, B., Semenock, R., 1994, "Apparatus for empirical determination of dynamic friction," Anonymous American Automatic Control Council, **1,** pp. 546.

[28] Owen, W. S., and Croft, E. A., 2003, "The Reduction of Stick-Slip Friction in Hydraulic Actuators," Mechatronics, IEEE/ASME Transactions on, **8**(3) pp. 362.

[29] Chatterjee, S., 2004, "Effect of High-Frequency Excitation on a Class of Mechanical Systems with Dynamic Friction," Journal of Sound and Vibration, **269**(1), pp. 61.

[30] Yanada, H., 2008, "Modeling of Dynamic Behaviours of Friction," Mechatronics, **18**(7), pp. 330.

[31] Sampson, E. B., 2005, "Fuzzy Control of the ElectroHydraulic Actuator," pp. 1- 151, Master Thesis, University of Saskatchewan.

[32] Sekhavat, P., 2006, "Impact Stabilizing Controller for Hydraulic Actuators with Friction: Theory and Experiments," Control Engineering Practice, **14**(12), pp. 1423.

[33] Amin, J., 1996, "Implementation of a friction estimation and compensation technique Control Applications, 1996., Proceedings of the 1996 IEEE International Conference on", pp. 804.

[34] Armstrong, B. S. R., 1988, "Dynamics for Robot Control- Friction Modeling and Ensuring Excitation," **Ph.D.** pp.198.

[35] Sugimura, J., 1998, "EHD Film Thickness in Non-Steady State Contacts," Journal of Tribology, **120**(3), pp. 442.

Application of the Fourier transform for actuator leakage diagnosis

Amin Yazdanpanah Goharrizi[1] and Nariman Sepehri[2]
 Fluid Power and Tele-Robotics Research Laboratory
Department of Mechanical and Manufacturing Engineering
University of Manitoba, Winnipeg, MB, Canada R3T-5V6

ABSTRACT

Application of the Fourier transform, to detect internal leakage in hydraulic actuators is examined. By analyzing the dynamics of the actuator, it is shown that the internal leakage increases the damping characteristic of the system and decreases the Bode magnitude of pressure signal over valve displacement, around the hydraulic natural frequency. This is further confirmed, by decomposing the original pressure signal, using this method, and identifying the frequency component sensitive to the internal leakage. The root mean square of the processed pressure signal is used as a fault indicator. The effectiveness of the proposed approach is shown through experimental results.

Keywords: fault detection, hydraulic actuators, internal leakage, Fourier transform.

1.   INTRODUCTION

Hydraulic systems play an important role in a wide variety of industrial applications: robotics (hydraulic manipulators used in mining and underwater exploration), manufacturing (precision machine tools), aerospace (actuation of aircraft control surfaces), and training (flight simulators). Reliability and safety are important issues in most of the above applications. Thus, condition monitoring of fluid power systems is earning more consideration to reduce the cost of maintenance and prevent the system from further deteriorating. Faults in fluid power systems, and methods for detecting them have been documented by Watton [1]. This paper focuses on the internal (cross-port) leakage in hydraulic actuators. Internal leakage is caused by the wear of piston seal that closes the gap

---

[1] Graduate Research Fellow
[2] Professor and corresponding author. Email: nariman@cc.umanitoba.ca

between the moveable piston and the cylinder wall. As a result, the hydraulic fluid is displaced between the two chambers of the actuator. Internal leakage affects the dynamic performance of the system since the entire flow is not available to move the piston against the load. It cannot be detected until the actuator seal is completely damaged and the actuator fails to respond to a control signal.

Research on actuator internal leakage fault identification, in spite of its importance, is limited. Tan and Sepehri [2] applied the Volterra nonlinear modeling concept to implement an on-line fault diagnosis scheme in hydraulic systems. By constructing a parametric space, actuator leakage faults were detected. The techniques is similar to the work by Le et al. [3], who employed neural networks and dynamic feature extraction technique to classify leakage type and level in hydraulic actuators. In both studies, systems with various fault types (including internal leakage fault) must be emulated (through simulations or via experiments) and Volterra/neural network models were developed beforehand. An and Sepehri [4] studied the feasibility of using extended Kalman filter (EKF) to detect actuator internal leakage fault. They further extended this work to include both friction and loading as unknown external disturbances [5]. Although the requirement of using a model for internal leakage was removed by An and Sepehri [4,5], the need for knowing the model of hydraulic actuator still remains a challenge. In order to overcome the difficulties associated with modeling nonlinear hydraulic systems, a linearized model with an adaptive threshold (to compensate for the error due to linearization) was used by Shi et al. [6] to detect internal leakage faults.

Motivated by developing methods that do not rely on a model of the system or fault, the authors initiated research directed at employing a signal processing method for internal leakage detection in hydraulic actuators. The method is based on Fourier transform that breaks down a signal into constituent sinusoids of different frequencies and amplitudes. With this decomposition, one can identify the most prevalent frequency components of a signal. Therefore, this technique has recently drawn widespread attention as promising tools to deal with fault detection. Al-Ammar et al. [7] used the fast Fourier transform (FFT) for fault detection in transformer impulse test. Lim et al. [8] used FFT residuals of the vibration signals for the purpose of fault detection in induction motors. In this paper, we investigate how the FFT transform can be used to detect hydraulic internal leakage fault. By studying the dynamics of the system, it is shown that, the net effect of internal leakage is to increase the damping characteristic, which in turn, decreases the Bode magnitude around the hydraulic natural frequency. Therefore, by processing pressure signal at one side of the hydraulic actuator, the frequency band that is sensitive to the effect of internal leakage can be captured. It is then verified that under normal operating conditions, the amplitudes of the processed pressure signal, at the chosen frequency band, are higher than those under faulty operating condition caused by internal leakage. Therefore, the root mean square (RMS) of the processed pressure signal is calculated as a fault indicator.

2.   EXPRIMENTAL TEST RIG

A photograph of the test-rig, on which all the experiments are carried out, is shown in Fig. 1. The actuator is a double rod type having a 610 mm (24 in) stroke, 38.1 mm (1.5 in) bore diameter, and 25.4 mm (1 in) rod diameter. It is controlled by a high performance Moog

D765 servovalve. The actuator is powered by a pump operating at a nominal pressure of 17.2 MPa (2500 psi). The position of the actuator is measured using a cable-driven optical rotary encoder and is monitored by a PC via a Keithley M5312 quadrature incremental encoder card. The PC is also equipped with a DAS-16F input/output board that is used to send the input signal generated by the software to the valve. The DAS-16F is also used to monitor the outputs of all other instruments, which includes a number of pressure transducers and several flowmeters. As illustrated in Fig. 1, the piston seal leakage is emulated by opening a ball valve that connects the two chambers of the actuator. This allows hydraulic fluid to be bypassed across the piston. The severity of leakage is controlled by adjusting a needle valve. A positive displacement flowmeter, is used to measure the leakage flow rate.
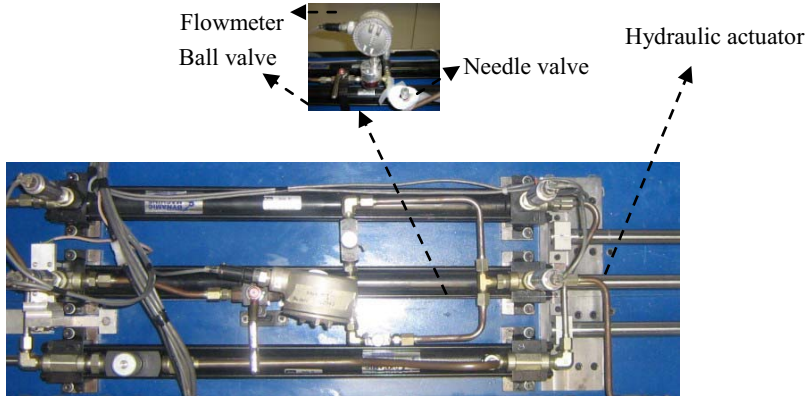
Figure 1   Test rig upon which all experiments were carried out.

3.   MODELLING AND ANALYSIS

The equations that describe the dynamics between the valve displacement x_v and the piston position x_p can be formed as [9]:

$$\dot{x}_p = v_p$$

$$\dot{v}_p = \frac{1}{m}(AP_1 - AP_2 - dv_p)$$

$$\dot{P}_1 = \frac{\beta}{V + Ax_{P_1}}(C_v\sqrt{\frac{2}{\rho}}wx_v\sqrt{\frac{P_s}{2} + \frac{x_v}{|x_v|}(\frac{P_s}{2} - P_1)} - q_l - Av_p)$$

$$\dot{P}_2 = \frac{\beta}{V - Ax_p}(-C_v\sqrt{\frac{2}{\rho}}wx_v\sqrt{\frac{P_s}{2} + \frac{x_v}{|x_v|}(P_2 - \frac{P_s}{2})} + q_l + Av_p)$$

(1)

Referring to (1), the system states are actuator position x_p, actuator velocity v_p, and line pressures P_1 and P_2. Parameters m and d are the mass of the load and the effective viscous

damping of the actuator, respectively. Parameter A refers to the annulus area of the piston, β is the effective bulk modulus of the hydraulic fluid, V is the volume of fluid contained on either side of the actuator when it is centered. C_v is the valve orifice coefficient of discharge, and ρ is the density of hydraulic fluid. The parameter w is the area gradient, and supply pressure is denoted by P_s.

Leakage is difficult to model exactly [10]. Here, the actuator internal leakage is assumed to be turbulent, and thus follows the following relationship:

$$q_l = K_i \sqrt{|P_1 - P_2|} \, \mathrm{sgn}(P_1 - P_2) \tag{2}$$

K_i is the turbulent leakage coefficients whose values depend on the severity of leakage fault.

By linearizing the nonlinear dynamics of the actuator about an operating point, o, and using the assumption that $V \gg A|x_p|$ [9], the linearized equations are obtained:

$$\Delta \dot{x}_p = \Delta v_p$$

$$\Delta \dot{v}_p = \frac{1}{m}(A\Delta P_1 - A\Delta P_2 - d\Delta v_p)$$

$$\Delta \dot{P}_1 = \frac{\beta}{V}[K_{1f}\Delta x_v - K_{1p}\Delta P_1 - \frac{K_i}{2\sqrt{|P_{10} - P_{20}|}}\Delta(P_1 - P_2) - A\Delta v_p] \tag{3}$$

$$\Delta \dot{P}_2 = \frac{\beta}{V}[-K_{2f}\Delta x_v - K_{2p}\Delta P_2 + \frac{K_i}{2\sqrt{|P_{10} - P_{20}|}}\Delta(P_1 - P_2) + A\Delta v_p]$$

In (3), Δ, denotes a perturbation from the operating, e.g., $\Delta x_p = x_p - x_{po}$. K_{1f} and K_{2f} are flow gains:

$$K_{1f} = K_v w \sqrt{\frac{P_s}{2} + \frac{x_{v0}}{|x_{v0}|}(\frac{P_s}{2} - P_{10})}$$

$$K_{2f} = K_v w \sqrt{\frac{P_s}{2} + \frac{x_{v0}}{|x_{v0}|}(P_{20} - \frac{P_s}{2})} \tag{4}$$

K_{1p} and K_{2p} are called flow-pressure coefficients:

$$K_{1p} = \frac{K_v w |x_{v0}|}{2\sqrt{\frac{P_s}{2} + \frac{x_{v0}}{|x_{v0}|}(\frac{P_s}{2} - P_{10})}}$$

$$K_{2p} = \frac{K_v w |x_{v0}|}{2\sqrt{\frac{P_s}{2} + \frac{x_{v0}}{|x_{v0}|}(P_{20} - \frac{P_s}{2})}} \tag{5}$$

Note that, for an equal area actuator driven by a matched and symmetrical valve, the pressure in one cylinder half rises above $P_s/2$ while the pressure in other cylinder half decreases below $P_s/2$ by roughly the same amount. Thus, for an extending stroke, the individual cylinder pressures are $P_1 \approx 1/2(P_s + P_L)$ and $P_2 \approx 1/2(P_s - P_L)$. where, $P_L = P_1 - P_2$ is the

load pressure. Due to the relationship between P_1 and P_2, it is quite often the case that $K_{1f} \approx K_{2f} = K_f$ and $K_{1p} \approx K_{2p} = K_p$ [9]. The transfer functions relating pressures ΔP_1 and ΔP_2 to spool valve displacement, Δx_v, can now be found as:

$$\frac{\Delta P_1(s)}{\Delta X_v(s)} = \frac{0.5K_f(ms+d)\omega_h^2 / A^2}{s^2 + 2\zeta_h \omega_h s + \omega_h^2} \qquad (6)$$

$$\frac{\Delta P_2(s)}{\Delta X_v(s)} = \frac{-0.5K_f(ms+d)\omega_h^2 / A^2}{s^2 + 2\zeta_h \omega_h s + \omega_h^2} \qquad (7)$$

In (6) and (7), $\omega_h = \sqrt{\dfrac{2\beta A^2}{mV}}$ is the hydraulic natural frequency,

$\zeta_h = \dfrac{dV\omega_h}{4\beta A^2} + \dfrac{m(K_l + 0.5K_p)\omega_h}{2A^2}$ is the hydraulic damping and $K_l = \dfrac{K_i}{\sqrt{|P_{10} - P_{20}|}}$.

By studying the characteristic equation of transfer functions (6) and (7), it is seen that the internal leakage adds damping to the dynamics of the actuator and this effect intensifies as the leakage severity increases. Given the purpose of this paper, it is important to also capture the frequency range within which the pressure signal is sensitive to the internal leakage. The Bode plot of the transfer function (6) is therefore, plotted in Fig. 2, given the parameters that resemble the experimental test rig in Fig. 1. Note that for the normal operating condition $K_i = 0$. For the actuator with internal leakage about 0.7 L/min, $K_i = 5.83 \times 10^{-8} \, \mathrm{m^3}/\sqrt{\mathrm{Pa}}.\mathrm{sec}$ is chosen. As one can see, internal leakage changes the Bode magnitude around the hydraulic natural frequency, ω_h, which is found to be 70 Hz for the system under investigation. The Bode plot of transfer function (7) displays the same results.
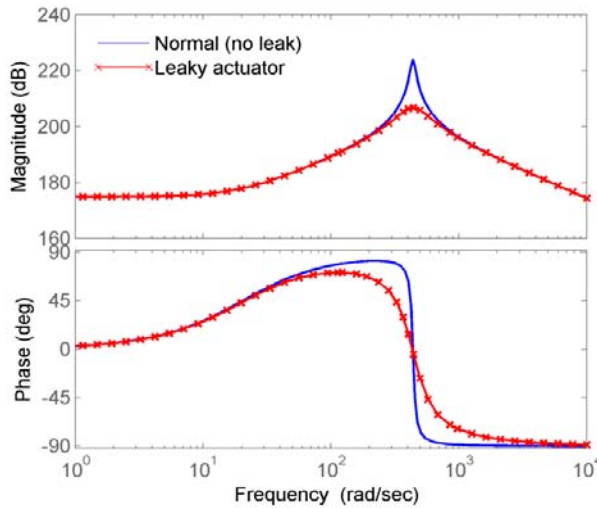
Figure 2 Bode plot of transfer function relating chamber pressure to valve spool displacement for normal and leaky actuator.

4.   DATA PROCESSING BASED ON SPECTRUM ANALYSIS

Fourier analysis breaks down a signal into constituent sinusoids of different frequencies. It can be categorized as a continuous Fourier transform (CFT) and a discrete Fourier transform (DFT). The Fourier transform of a continuous time signal, $x(t)$, is defined as:

$$X(w) = \int_{-\infty}^{+\infty} e^{-jwt} x(t) dt \tag{8}$$

$X(w)$, is a complex decomposition of the original signal $x(t)$, into constituent exponential functions at each frequency w. The discrete Fourier transform, on the other hand, converts a sampled time representation of a signal into a sampled frequency representation. It results in a frequency versus amplitude relationship. The discrete Fourier transform is given as follows:

$$X[n] = \sum_{k=0}^{N-1} x[k] e^{-2\pi i n k / N} \qquad n = 0,1,\ldots,N-1 \tag{9}$$

where $x[k]$ is the original signal and N is the length of the sampled original signal vector. The DFT can be computed efficiently in practice using a fast Fourier transform algorithm [11].

5.   RESULTS AND DISCUSSION

As was mentioned earlier, internal leakage introduces damping to the dynamics of the hydraulic actuation system and alters the transient response of the chamber pressures. Here, the sub-band informative signals sensitive to the effect of internal leakage, are obtained by decomposing the original pressure signal at one side of the hydraulic actuator using the fast Fourier transform. The effectiveness of this approach is investigated through both simulation and experimental studies.

5.1. Simulation Results

A periodic square wave signal with 3V (peak-to-peak) amplitude is applied to the servovalve as the input. This structured input signal was shown to be suitable for off-line applications as it is simple and includes low and high frequency components allowing rich excitation of the pressure signals from which, one can observe the effect of internal leakage. The resulting actuator displacement for a healthy actuator is shown in Fig. 3. The pressures at the actuator chambers are shown in Fig. 4.
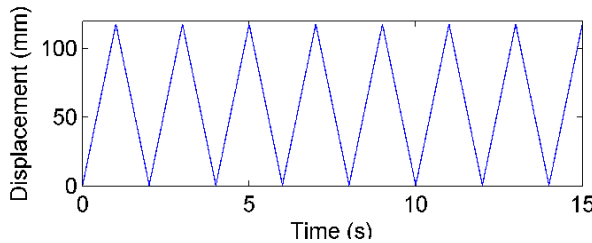
Figure 3 Displacement response of hydraulic actuator under normal operating condition (simulation).
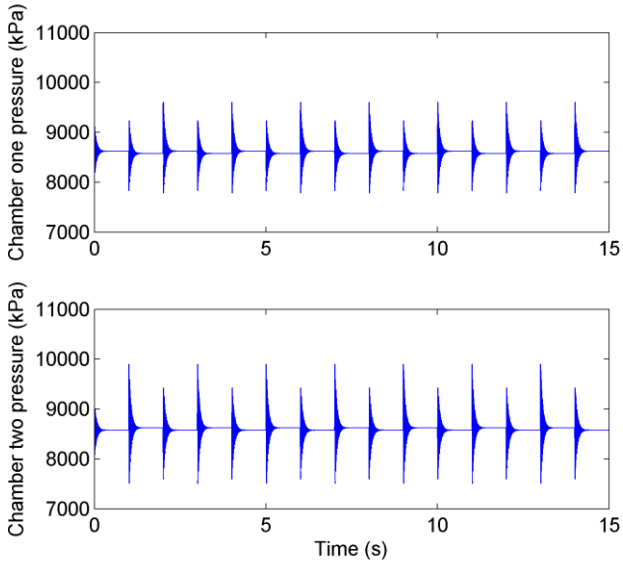
Figure 4 Pressure signals in chambers one and two under normal operating condition (simulation).

With the same input, an internal leakage of about 0.7 L/min with $K_i = 5.83 \times 10^{-8}$ m^3/$\sqrt{\text{Pa}}$.s is introduced to the system. The resulting pressures in chamber one and two are plotted in Fig. 5.
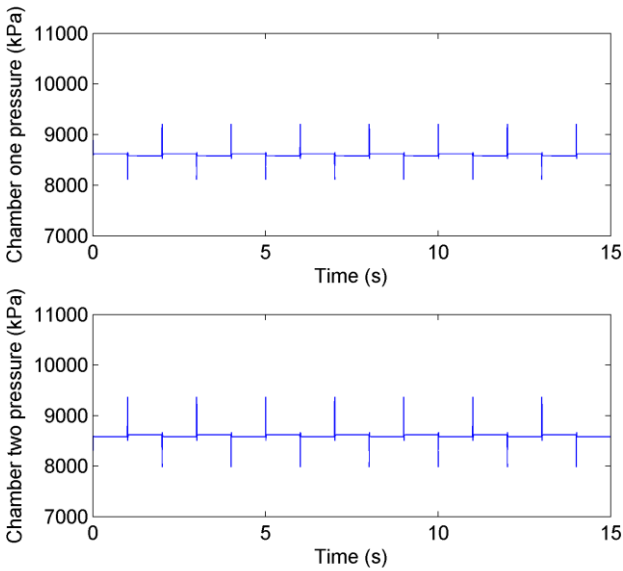
Figure 5 Pressures in chambers one and two of hydraulic actuator with internal leakage (simulation).

Note that internal leakage alters the transient responses in the line pressures, which can be detected by carefully comparing Figs 4 and 5. As the internal leakage value becomes smaller, however, the difference between healthy and faulty original pressure signals is less noticeable. Therefore, the original pressure signals cannot provide sufficient information to easily support the actuator health diagnosis when the size of leakage is small; they must be decomposed into more informative sub-band signals.

The results of applying the FFT to chamber one pressure signal under normal and faulty operating conditions are shown in Figs 6 and 7, respectively. From these plots, the feature frequency band is identified to be in the range of around 60 to 80 Hz. This is consistent with the frequency band determined by Bode plot in Section 3.
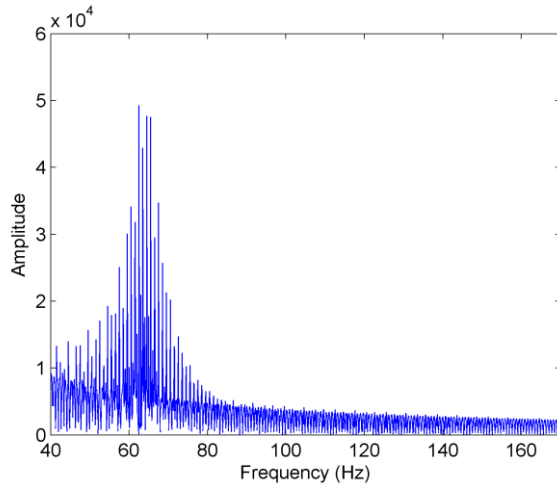
Figure 6 Fast Fourier transform of chamber one pressure signal for actuator under normal operating condition (simulation).
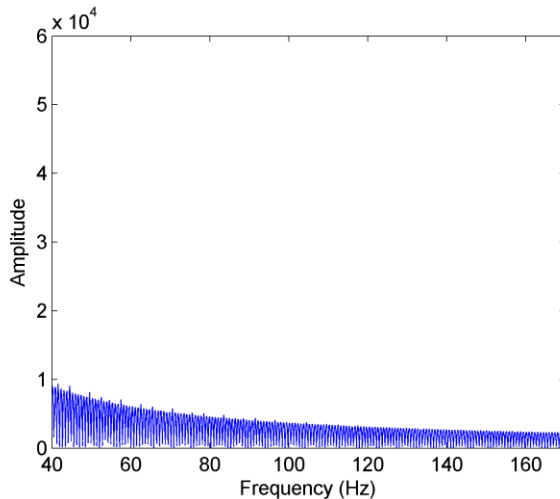
Figure 7   Fast Fourier transform of chamber one pressure signal for actuator with internal leakage (simulation).

The issue of robustness of fault detection techniques to the changes of system parameters, for example the bulk modulus in hydraulic actuators, is very important and needs to be addressed [12,13]. In this paper, we study the effect of changes in bulk modulus value on frequency response of the system which is important for diagnosis when using FFT (see Eqs.6, 7). Consistent with the discussion by Yu [14], we consider a 10% increase and decrease in effective bulk modulus. The results are shown in Fig. 8. As one can see the interesting frequency range is changed without affecting the amplitude of the processed pressure signal.
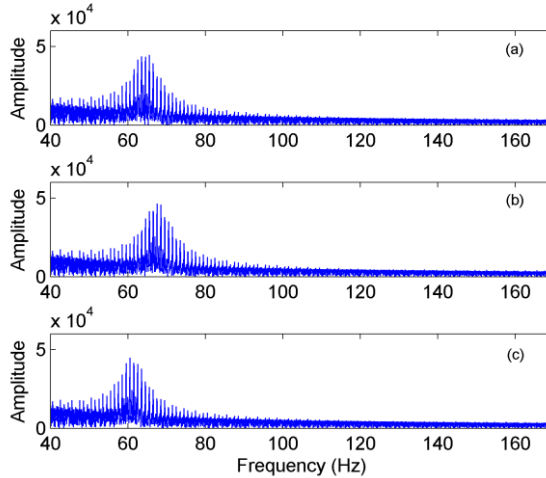
Figure 8 Fast Fourier transform of chamber one pressure signal for actuator under normal operating condition: (a) healthy actuator; (b) 10% increase in bulk modulus; (c) 10% decrease in bulk modulus.

5.2. Experimental Results

For all experiments, the same input as the simulation is applied. The pressures at the actuator chambers are the same as the one obtained by simulation results. Hence, they are not plotted here to avoid duplication. The results of applying FFT to chamber one pressure signal under normal and faulty operating condition (internal leakage, with mean value of 1.54 L/min) are shown in Figs 9 and 10, respectively. From these plots, the feature frequency band is identified to be in the range of around 65 to 85 Hz. This is almost consistent with the frequency band determined with simulation result. However, a small shift is believed to be due to changes in effective bulk modulus and other parameters of actuator during experiments. Again internal leakage results in a decrease in amplitude and energy of the FFT spectra of the pressure signal around the interesting frequency band.
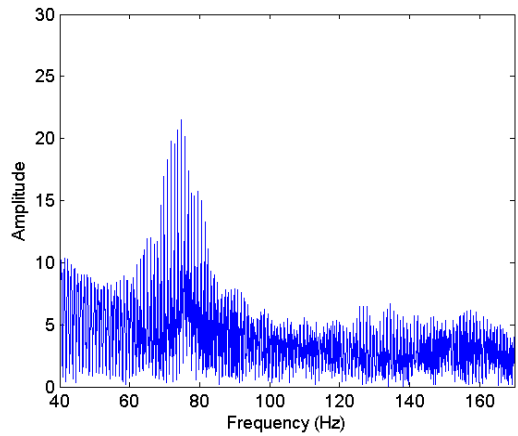
Figure 9 Fast Fourier transform of chamber one pressure signal for actuator under normal operating condition (experimental).
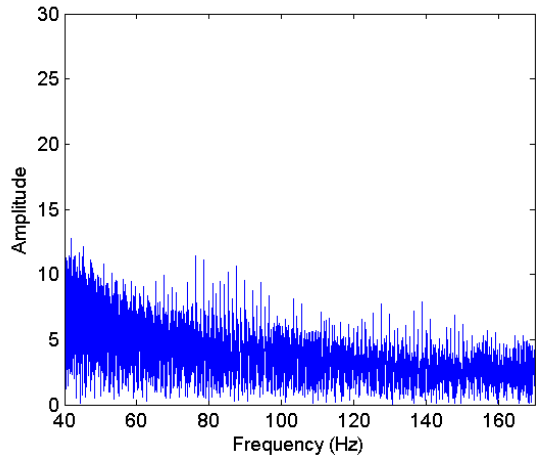
Figure 10 Fast Fourier transform of chamber one pressure signal for actuator with internal leakage (experimental).

To facilitate comparison, the root mean square (RMS) values of the processed pressure signal by FFT for frequency band of (65-85 HZ), are calculated. The results are shown in Table 1. From the results, one can conclude that the index calculated by the FFT method is useful for internal leakage detection.

Table 1 RMS values of FFT from the measurement of chamber one pressure for normal actuator and actuator with internal leakage of 1.54 L/min in average.

RMS index	Healthy Actuator	Faulty Actuator	Percentage of changes
FFT Method (65-85Hz)	7.01	5.08	**27.5**

The final set of tests is to demonstrate the consistency of the results presented so far. In this set of experiments, the test rig was run 18 times under normal operating condition as well as small and medium leakage situations at various times. The small leakage (of average 0.124 L/min) that was introduced in this test caused a reduction of ≈2.6% of the available flow rate to the actuator. The medium leakage was of average 0.808 L/min and caused an average reduction of ≈17% of the available flow rate. The average values, reported here, were taken over the entire 18 tests.

The scaled RMS values using FFT spectrum in the frequency range of 65-85Hz are shown in Fig. 11. Note that scaling is done by dividing the RMS values by the maximum one to facilitate the comparison. The results firstly show that the RMS values of the FFT spectra of the pressure signal, in the frequency band of interest, reduce with the severity of internal leakage. Secondly, the variation of the RMS values over the entire tests is less, as the leakage level increases from no leak to medium leak.
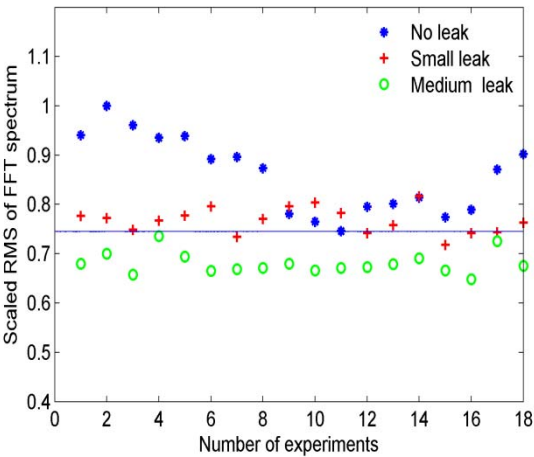
Figure 11 Scaled RMS values of FFT spectrum obtained from healthy actuator and actuator experiencing small and medium leakages with mean values of 0.124 L/min and 0.808 L/min, respectively (experimental).

Also, we chose a baseline as minimum RMS values obtained from the FFT under normal operating condition (refer to Fig 11). Given these baselines, small leakage type is identifiable 30% of the times and the medium ones are detectable almost all the times with FFT.

6.   CONCLUSION

Internal leakage fault diagnosis using the fast Fourier transform (FFT) implemented in this paper. Using a model of hydraulic functions, it was shown that the internal leakage adds damping to the hydraulic actuator dynamics and decreases the Bode magnitude of pressure signal over the valve spool displacement around the hydraulic natural frequency. Thus, informative sub-band signals, sensitive to the effect of internal leakage, can be extracted from the original pressure signal at one side of the actuator. In this paper, the fast Fourier transform was employed and the RMS of the FFT spectrum within the feature frequency band was shown to be an appropriate leakage fault indicator. Results from simulations and experiments were used to show how the FFT detects internal leakages without the need to include models of the actuator and/or the leakage fault.

REFERENCES

[1] J. Watton, Modeling, monitoring and diagnostic techniques for fluid power systems, Springer, 2007.

[2] H. Tan, and N. Sepehri, "Parametric fault diagnosis for electrohydraulic cylinder drive units," IEEE Trans. Industrial Electronics, 49, pp. 96-106, 2002.

[3] T. T. Le, J. Watton, and D. T. Pham, "Fault classification of fluid power system using a dynamic feature extraction technique and neural networks," J. of Sys. and Cont. Eng., 211, pp.307-317, 1998.

[4] L. An and N. Sepehri, "Hydraulic actuator leakage fault detection using extended Kalman Filter," Int. Journal of Fluid Power, 6, pp. 41-51, 2005.

[5] L. An and N. Sepehri, "Leakage fault detection in hydraulic actuators subjected to unknown external loading," Int. Journal of Fluid Power, 9, pp.15-25, 2008.

[6] Z. Shi, F. Gu, B. Lennox, and A. D. Ball, "The development of an adaptive threshold for model-based fault detection of a nonlinear electro-hydraulic system," Control Eng. Practice, vol. 13, pp. 1357-1367, 2005.

[7] E. Al-Ammar, G. G. Karady, and H. Jin Sim, "Novel technique to improve the fault detection sensitivity in transformer impulse test," IEEE Trans. on Power Delivery, 23, pp.717-725, 2008.

[8] H. S. Lim, K. T. Chong and H. Su, "Motor fault detection method for vibration signal using FFT residuals," Int. J. of Applied Elec. and Mech., 24, pp.209-223, 2006.

[9] H. E. Merritt, Hydraulic control systems. John Wiley & Sons, New York, 1967.

[10] P. Garimella, and B. Yao, "Model based fault detection of an electro-hydraulic cylinder," American Control Conference, pp. 484-489, 2005.

[11] J. G. Proakis, and D. G. Manolakis, Digital signal processing, 4th ed. Prentice Hall, 2007.

[12] J. Stoustrup, and K. Zhou, "Robustness issue in fault diagnosis and fault tolerant control," Journal of Control Science and Engineering, Editorial, 2 pages, 2008.

[13] M. Benini, M. Bonfe, P. Castaldi, W. Geri and S. Simani, "Design and analysis of robust fault diagnosis schemes for simulated aircraft model," Journal of Control Science and Engineering, Editorial, 2 pages, 2008.

[14] D. Yu, "Fault diagnosis for a hydraulic drive system using a parameter-estimation method," Control Engineering Practice, vol. 5, pp. 1283-1291, 1997.

Numerical analysis of the lubricating gap between bushes and gears in external spur gear machines

Marco Zecchi[*]**, Andrea Vacca**[*]**, Paolo Casoli**[**]
[*] Maha Fluid Power Research Center, Purdue University, West Lafayette (IN), United States
[**] Industrial Engineering Department, University of Parma (Italy)

This paper presents a numerical model for the description of the flow field in the lubricating gaps between gears and sliding bushings (or bearing blocks) in external spur gear machines. These lubricating gaps strongly affect the unit (pump or motor) performance: the leakage flow influences its volumetric efficiency, while the friction losses can lead to poor hydromechanical efficiencies. Moreover, the balance of the forces acting on the sliding elements necessary to achieve high durability and reliability of the unit is based on the pressure field established in the lubricating gap. In this work the lubricating gap is solved considering the Reynolds eq., including all terms related to a possible tilt between the elements and to the squeeze effect (due to the micromotions of the parts), in order to achieve a detailed description of the flow field and of the carrying ability of the interface. A relevant effort was directed towards the development of an automatic procedure able to define the computational mesh and solve the flow field in the lubricating gap for each angular position of the gears starting directly from the CAD drawings of the machine. The developed code considers also the effects of the recesses usually machined on the sliding elements. Starting from the knowledge of the pressure in each tooth space volume (calculated using an external tool) the model not only permits a deep description of the flow field into the lubricating gap, but it also allows the calculation of the overall reaction forces exerted on the sliding elements. On the basis of these forces, considerations about the correct balance of these elements can be done. Besides the details concerning the model implementation, the paper presents its potentials assuming some simplifications about the motion of the sliding elements.

NOMENCLATURE

$\boldsymbol{V}$	oil velocity	[m/s]
u, v, w	oil velocity, cartesian components	[m/s]
$\boldsymbol{V_g}$	gear's tangential velocity	[m/s]
p	oil pressure	[Pa]
p_{LP}, p_{HP}	suction and delivery mean pressure	[Pa]

μ	oil dynamic viscosity	[Pas]
ρ	oil density	[kg/m³]
h	gap height	[m]
h_{min}, h_{max}	min and max gap height	[m]
h_0	mean value of the gap height	[m]
ω	pump angular speed	[1/s]
d	pump wheel base	[m]
R	gear's outer diameter	[m]
T_0, T_1, T_2	datum points for gap height calculation	[]
Q_{leak}	pump leakage flow	[m³/s]
F	total force on the bushing, from the gears side	[N]
F_{gap}	fraction of F relative to the gap contribution	[N]
F_{TS}	fraction of F due to the TSVs contribution	[N]
$\mathscr{A}_{TS}$	sum of the area TSs area	[m²]
$\mathscr{A}_{LP}$	area of the low pressure groove	[m²]
$\mathscr{A}_{HP}$	area of the high pressure groove	[m²]
$\mathscr{A}_i$	area of a mesh face	[m²]
$\boldsymbol{n}_i$	normal vector of a mesh face	[m]
L	length	[m]
M	mass	[kg]
T	time	[s]
t_x, t_y	relative bushing tilt in x and y direction	[]
$\Gamma_{F_{gap}}$	$(\mu\omega R^2)/(p_{HP}h_0^2)$ operative conditions parameter for pressure force on the gap side of the bushing	[]
Γ_Q	$(p_{HP}h_0^3)/(\mu\omega R^3)$ operative conditions parameter for drain leakage	[]
Λ	$(F_{gap} - (F_{gap})_{t=0})/(p_{HP}R^2)$ widening thrust increase	[]

Operators

$\nabla\cdot$	divergence operator
∇	gradient operator
∇^2	gradient operator

Abbreviations

GU	gear unit
TS	tooth space
TSV	tooth space volume

1 INTRODUCTION

Reliability, low cost and manufacturing simplicity are the main reasons for the success of external gear machines as energy conversion units in many fluid power applications. These features come from the simple principle of operation of the unit and from its limited number of mechanical elements (Fig. 1).

Basically, the principle of operation of external gear units (GUs) is very easy to understand: with the gears' rotation the fluid is transferred from the inlet to the outlet through the peripheral, and the displacing action is realized by the meshing process. The sliding elements (bushings or bearing blocks, in common solutions) are then necessary to seal the fluid during the transfer process, but also they permit to obtain a
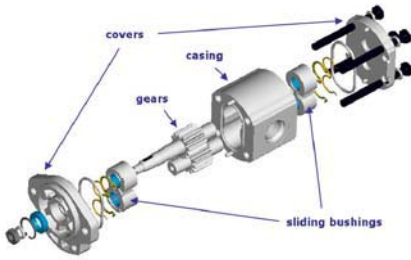
Figure 1: Exploded view of an external gear pump
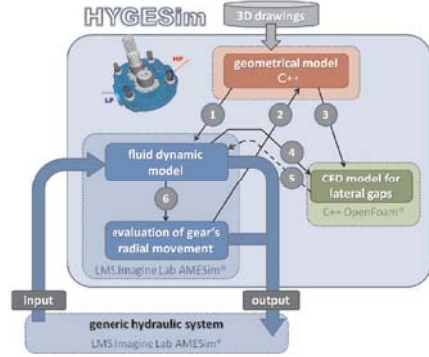
Figure 2: The HYGESim modules and flux of data between them

proper timing of the commutations between the internal tooth space volumes and the inlet/outlet port, thank to recesses always machined in correspondence of the meshing zone.

Despite the limited number of internal elements, their multi-functionality (i.e. mechanic to fluid potential energy conversion, motion transmission and displacing action for the gears; sealing and timing for the lateral sliding elements) strongly complicates the design of each part of the machine.

These features have been captivating the interest of scientists in the field of fluid power for decades: first studies about the modelling of the displacing features typical of the meshing process date back to 1946 [1]. The graphical or analytical methods proposed by the first studies have been overcame by more recent works, especially thanks to the advances of all disciplines of engineering and computer science: several lumped parameter approaches were proposed (most significant model are those proposed in [2, 3, 5, 6, 7, 8]) as well as CFD models (like [9, 10]), with the aim of understanding all the peculiar phenomena involved in the operation of the machine and to develop tools capable to support the design process.

The mentioned CFD based approaches permit to evaluate the features of the internal flow though the machine with high level of detail, however many simplifications are usually required (as concerns the pressure boundary conditions, the constancy of the axes of rotation and of the position of the sliding elements). Instead, the lumped parameter approach, typically suitable to describe the flow through positive displacement machines, can be utilized to develop numerical models able to limit the assumptions required by the more complex CFD models.

The simulation model taken as reference in this work, named HYGESim (HYdraulic GEar machines Simulator), is developed following this idea (details concerning the HYGESim modeling approach can be found in [6, 8]). Essentially, the structure of the code can be represented in Fig 2: a lumped parameter fluid dynamic model solves the internal flow calculating the pressure inside each TSV; a mechanical model evaluates the instantaneous position of the axes of rotation of both gears. Geometrical data re-

quired by those models are precisely calculated by a dedicated tool that uses directly the CAD 3D drawings of the unit as input.

In the model presented in [6, 8], the leakages at gears lateral sides are evaluated with a simple 1D approach (Fig 3). As shown in the mentioned work, this assumption permits to well estimate the volumetric efficiency of the unit. However, as presented in [11], the flow in this zone can highlight significant 2D features. This strongly motivate the introduction of a further, CFD 2D module coupled with HYGESim (Fig 2), able to describe the flow in this lubricating gap.

Basically, the module is based on the integration of the Reynolds equation in the lubricating gap bounded by the gears and the sliding element during the operation of the GU (pump/motor), considering the instantaneous pressures evaluated by the HYGESim fluid dynamic model as boundary conditions. Similar approaches are utilized to describe the lubricating gaps in GUs [4] or in other other positive displacement units, like in the model presented in [12]. However, as represented in Fig 4, in typical designs of GUs the domain of calculation of this lubricating gap is characterized by unique geometric peculiarities due to the features of the meshing zone.

Moreover, for hydraulically balanced GUs, the sliding elements can reach the equilibrium (achieved by the balance of forces and torques acting on the element) with a proper tilt, as a function of the operating conditions of the units. This has been experimentally proved in [13, 14], where proper capacitive sensors were used to measure the variability of the gap height of the gap of Fig 4.
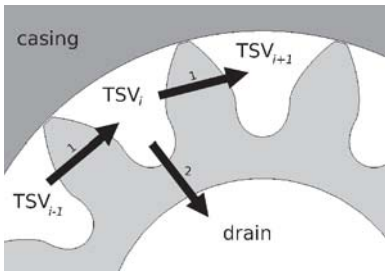
Figure 3: Leakages between adjacent TSVs at gears lateral surface: between adjacent TSVs (1) or to the drain (2)
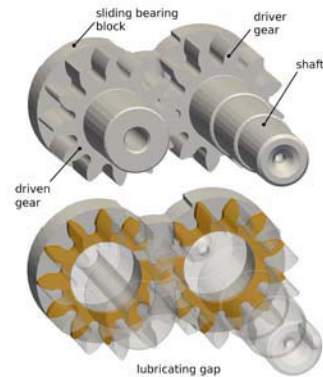
Figure 4: Lubricating gap at gears' lateral side

In this work, the description of the pressure field into the gap of Fig 4 is achieved considering a detailed geometry description of the GU and all physical terms of Reynolds equation that can play a significant role during the operation of the unit. In this way, the forces due to fluid pressure acting on the sliding elements can be calculated with precision, permitting the designer to use the results of the simulation for designing purposes: the proper areas of compensation in the sliding elements can be calculated (according to the GU designs described in [15]) having in the same time also accurate informations about the corresponding leakage flow and energy consumption.

Beyond the numerical approach utilized to solve the lubricating gap flow, this paper focused also on the proper formulation of the dependent/independent variables that should be utilized to express a generic global result of the calculation (in particular as regards the resultant force and its point of application), following the principles of the Dimensional Analysis. Respect to previous researches on the same topic [16], the approached presented in this work is based on an analytical formulation characterized by a less number of simplified hypothesis (as concern the tilt of the bushes or the effects due to squeeze lubrication) and on a different methodology of the integration of the flow equations in the computational domain. Furthermore, the possibility of using the developed code starting from the HYGESim results through an automatic procedure, permits to investigate results without simplifying hypothesis as concerns the pressure boundary conditions (i.e. TSV pressure, pressure at outlet/inlet ports).

2 MODELLING APPROACH

The implemented model solves the flow in in the clearance between the gears end-faces and the bearing blocks. The domain of calculation is depicted in Fig 4. Following paragraphs describe how the flow is calculated for each angular position of the gears.

2.1 Reynolds equation

At each angular displacement, the analysis of the flow inside the clearance bounded by the bearing blocks and the lateral side of the gears can be performed following the classical approach of the lubricating theory. The particular features of the lubricating gap (highlighted in in Fig. 5) allow to make several simplifications for the description of the flow field:

- the fluid inertial forces are negligible respect the viscous ones;

- the pressure field is 2D - thus $p = p(x, y)$ - therefore the pressure is assumed to be not variable in the coordinate z, along the gap height;

- the component of the velocity in the direction normal to the gap plane can be neglected, and the velocity can be expressed as $\boldsymbol{V} = (u(x, y, z), v(x, y, z))$, where u and v are still functions of the three spatial directions;

- the gradient of velocity in the gap plane (x, y) is negligible respect the component in the direction of the gap height so that $\partial \boldsymbol{V} / \partial z \gg \partial \boldsymbol{V} / \partial x$ and $\partial \boldsymbol{V} / \partial z \gg \partial \boldsymbol{V} / \partial y$

In these conditions, the fluid pressure in the clearance is independent from the fluid velocity, and can be described by the well known Reynolds equation:

$$\boldsymbol{\nabla} \cdot \left(-\frac{h^3}{12\mu} \boldsymbol{\nabla} p \right) + \left(\frac{\boldsymbol{V}_b + \boldsymbol{V}_t}{2} \right) \cdot \boldsymbol{\nabla} h - \boldsymbol{V}_t \cdot \boldsymbol{\nabla} h_t + \boldsymbol{V}_b \cdot \boldsymbol{\nabla} h_b + \frac{\partial h}{\partial t} = 0 \qquad (1)$$

Equation (1) is derived under following hypotheses:
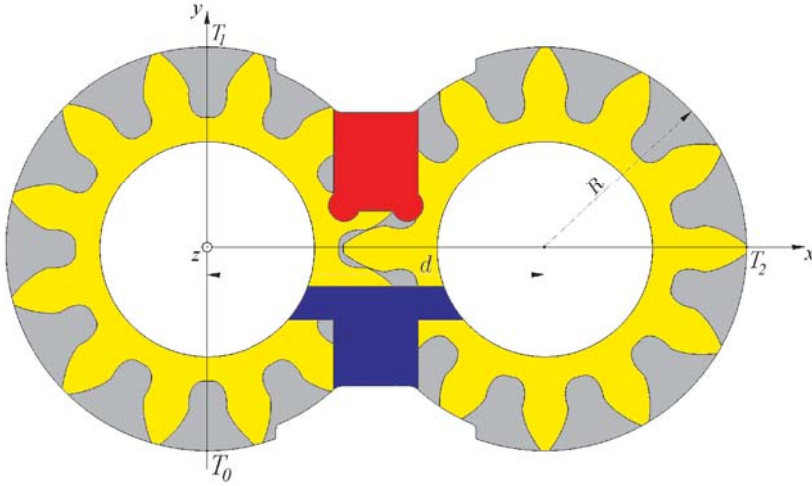
Figure 5: Sketch of areas of interest on the sliding element surface relative to the gear side. The yellow area represents the lubricating gap, the grey area highlights the teeth spaces and the red and blue areas are refereed to respectively HP and LP grooves.

- both surfaces defining the gap domain are supposed to be in motion, being $\boldsymbol{V_t}$ the velocity of the top surface and $\boldsymbol{V_b}$ the velocity of the bottom one;

- the gap height h is given by the difference $h_t - h_t$. h_t is the "top" gap height defined by the distance from an ideal $x - y$ plane (described by the gear's lateral surface in the case it imagined to be perfectly flat) and the bushing surface. h_b is the "bottom" gap height, defined by the distance from the same plane and the actual position of the gear's lateral surface (that might have an arbitrary shape).

In the case considered in this study (Fig. 4) Eq. (1) can be further simplified by the following consideration:

- gear's lateral surface might present non-flatness due to the polishing process generally incorporated in the manufacturing, as described in [13], but in this work these details are not considered, therefore $h_b = 0$ and $h_t = h$. However the model developed allows to deal with any kind of gear's lateral surface shape, and a detailed description of this research will be presented in future works.

- the only surface with motion is the bottom one, defined by the gears lateral side, therefore $\boldsymbol{V}_t = 0$ and $\boldsymbol{V}_b = \boldsymbol{V}_g$

Thanks to these observations the problem can be described with the equation:

$$\boldsymbol{\nabla} \cdot \left(-\frac{\rho h^3}{12\mu} \boldsymbol{\nabla} p \right) + \frac{\boldsymbol{V}_g}{2} \cdot \boldsymbol{\nabla} h + \frac{\partial h}{\partial t} = 0 \qquad (2)$$

From Eq. (2), it is evident how an hydrodynamic effect on the sliding elements can be achieved only with the Couette term, related to the gears velocity and with the

normal squeeze term related to the micro-motion of the floating elements at gears' lateral sides.

2.2 Definition of the computational domain

In order to realize a flexible simulation tool, able to dial with all possible GU design, a lot of effort was put in realizing a code able to define automatically the computation domain starting from the CAD drawings of the GU. In particular the STL (STereo Lithography) file format of the gears and of the profile of the recesses machined on the sliding elements are the input required by the developed tool to solve the flow field within the lubricating gap.

2.2.1 Generation of the mesh

A C++ application was developed to accomplish the goal of creating a mesh domain - in which Eq. (2) can be solved - from the STL geometry definition of the different elements through an automatic procedure.

Mesh for driver and driven gear are created starting from the STL definition file of a slice of gear (represented in Fig. 6(a)); because for the sake of symmetry this slice is sufficient to define both gears.

From the STL definition a proper lists of point (ordered along the profile) are defined. Each list is then interpolated using straight lines, arcs or splines. This allows to process the resultant profile with almost any 2D mesh library; in this research `gmsh` [17] was integrated in the developed code to create a discretized domain with 6-node prism elements. During this process, portions belonging to the driver gear are separated (by means of different attributes) from the ones appertaining to the driven gear, since different boundary conditions have to be considered to solve Eq. (2), like the dragging velocity, TSV pressure, etc.

The tool developed is very flexible and allows to generate mesh for any type of gear, with different number of teeth, and different shape of tooth profile.

(a) Representation of the STL solid model of the gear slice required by the mesh generator

(b) Example of an automatic generated mesh with $50k$ six nodes prism elements
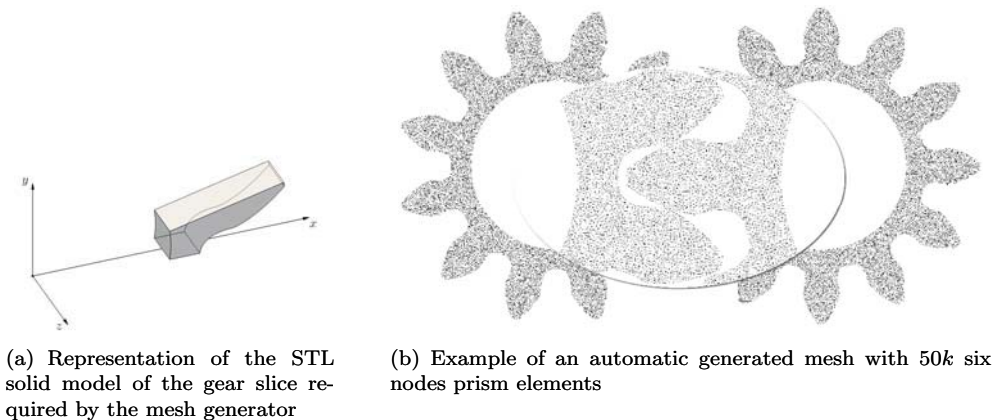
Figure 6: Automatic gear mesh generation

2.2.2 Dynamic mesh modification

To simulate the operation of a generic GU, it is necessary to consider a dynamic mesh, capable to follow the rotation of both gears. To accomplish this process, it is not sufficient to rotate the mesh generated with the passages above described. Indeed the raw mesh of the two gears (Fig. 7) must be modified during the simulation, accordingly with the angular position of the gears.

As a matter of fact, the presence of the grooves machined on the sliding elements strongly affects the domain of calculation with an high influence of the angular position of both gears. As clearly represented by Fig. 4, gears side area inside the grooves boundaries doesn't have to be considered in the integration of Eq. (2), because in that region there is no leakage flow, the pressure is uniform and equal respectively to the port (outlet or inlet) connected with the (outlet or inlet) groove. This modification

(a) before mesh modification   (b) after mesh modification
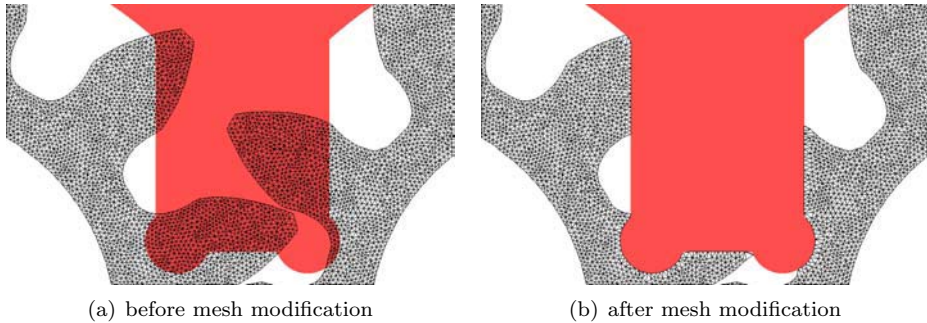
Figure 7: Example of modification of the mesh of Fig. 7 through the intersection with high pressure groove boundary

is accomplished by means of an automatic procedure. Starting from the STL files representative of the solid models of the grooves, at at each angular position of the gears

1. the cells of the mesh that are inside the groove profile (Fig. 7(a)) are eliminated;

2. the resulting mesh is corrected, by reshaping the elements at the boundaries to strictly preserve the geometric details. This step is required because the projection of boundary nodes on the grooves profiles can lead to the generation of elements with inconsistent topology. For this purpose proper control checks of mesh consistency are implemented in the model. Fig 7(b) shows a detail of the final result of this process, for a particular angular position.

2.3 Definition of pressure boundary conditions

Once the computational domain is defined, to solve Eq. (2) the implemented procedure needs to properly set all pressure boundary conditions. As above mentioned, these values come from the calculations performed by the HYGESim fluid dynamic model, which provides as output the instantaneous pressure inside each TSV of both gears (Fig 2). Therefore, at each angular position, the developed code generates the mesh following the steps described at the previous paragraphs, and then apply the

TSV pressure to proper patches of the calculation domain.

Fig 8 illustrates all the boundary patches used in the model for a 12 teeth gear unit. TSV sides are labelled with the gear type (DR for DriveR gear and DN for DriveN gear) and a progressive number in accordance to HYGESim notations to distinguish each TSV. Pressure on this boundaries is assumed to be uniform and only time (angular) dependent. For the tooth tips the labelling follows the same convention used for the TSVs; in this case pressure is assumed to vary linearly along each boundary, according with the hypothesis of laminar flow in the gap between the tooth tip and pump casing. On the gear drains the pressure is assumed to be uniform and equal to the drain pressure, in case of pump. On the boundaries defined by the intersections between gears and relief grooves the pressure is set to the values of the high and low pressure ports (also this value is taken as a result of the HYGESim simulation and can be time dependent).
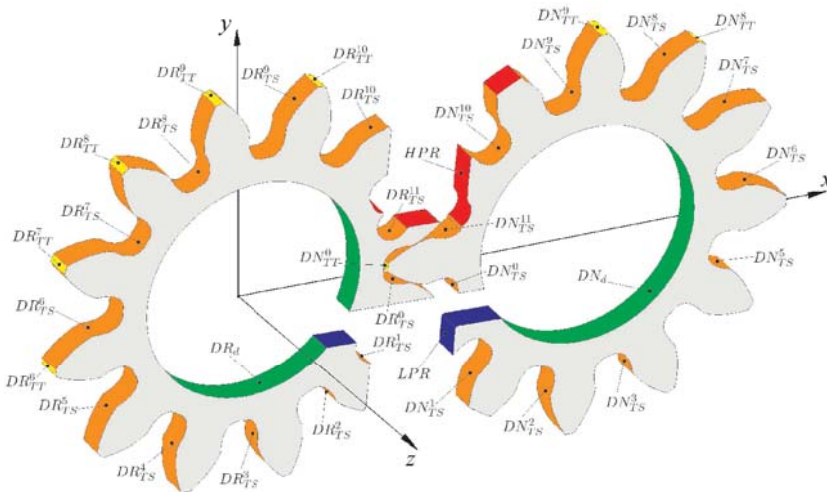
Figure 8: Different types of boundary patches. Orange is referred to teeth spaces, yellow to teeth tips and green to the gears drains. The intersection region is in red for high pressure port and in blue for low pressure port.

With reference to Fig. 8, for all patches outside the meshing zone the automatic setting of the pressure boundary conditions is a process easily solved by means of the output provided by HYGESim. Instead, a more sophisticated process is implemented in the meshing region. This because the portions of the tooth profiles that have to be considered as patches at constant pressure change shape, as a function of the angular position of the gears. Fig 9 shows a detail about the pressure field resulting from Eq. (2) and better clarify the methodology utilized to assign the boundary conditions in the meshing zone. The definition of the patches corresponding to the TSVs is automatically carried out considering the points of minimum distance between the two gears. For example, in Fig. 9 six regions are defined by means of two points on each gear; by combining these regions three TSV can be defined in the meshing zone.
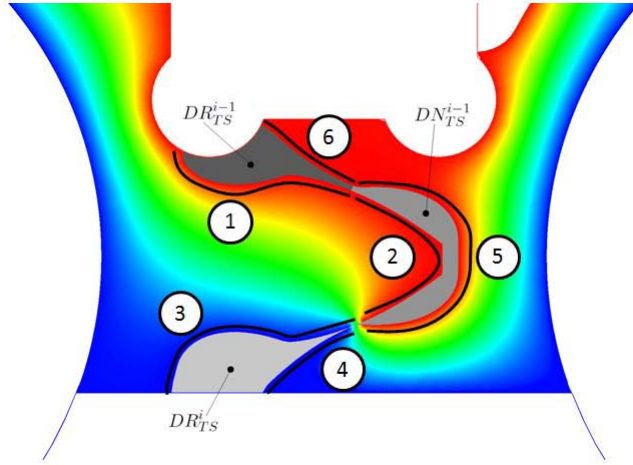
Figure 9: Detail about a pressure field resulting from Eq. (2) in the meshing zone. Result obtained assuming $h(x,y) = cost$. Portions of tooth profile at constant pressure (assumed as bounday counditions) are in evidence.

Thanks to the way in which the mesh is managed, this kind of geometrical computation can be done inside the model, ensuring an high level of precision. The pressure values to assign on these patches are still read from HYGESim: this allows to take into account al the complex phenomena involved in the meshing process, like pressure picks, or cavitation.

2.4 Calculation of the gap height and sliding element shifting velocity
The height of the gap is defined considering the three datum points sketched in Fig. 5. Using the gap height information on that points is easy to demonstrate that for an arbitrary point in the computational domain:

$$h(x,y) = x\frac{2h_{T_2} - h_{T_1} - h_{T_0}}{2(d+R)} + y\frac{h_{T_1} - h_{T_0}}{2R} + \frac{h_{T_0} + h_{T_1}}{2} \tag{3}$$

Furthermore, the velocity of the sliding element can be expressed as the time derivative respect of Eq. (3)

$$\frac{\partial h}{\partial t}(x,y) = x\frac{2\frac{\partial h_{T_2}}{\partial t} - \frac{\partial h_{T_1}}{\partial t} - \frac{\partial h_{T_0}}{\partial t}}{2(d+R)} + y\frac{\frac{\partial h_{T_1}}{\partial t} - \frac{\partial h_{T_0}}{\partial t}}{2R} + \frac{\frac{\partial h_{T_0}}{\partial t} + \frac{\partial h_{T_1}}{\partial t}}{2} \tag{4}$$

To show the potentials of the developed procedure, the values of shifting velocities at the reference points (Fig. 5) in this work are assumed as input of the simulation. However, similarly to the methodology described in [12], these values can be found out assuming the sliding velocities as unknowns from the equilibrium of forces acting on the sliding elements (assuming that the sliding element force balance can be obtained by changing the hydrodynamic reaction in the gap able to balance all the other external forces). An implementation of such a procedure, which would also permit to evaluate

the correct design of the hydraulically balanced GU, within the HYGESim simulation environment represents a future step of this research.

2.5 Numerical solution of Reynolds equation

Solution of Reynolds equation is carried out taking advantage of the powerful Open-FOAM libraries. In particular, a new solver has been developed to solve Eq. (2), discretized over the domain previously described using finite volume method. The code solves the resulting linear system of equations with a efficient implementation of the Preconditioned Conjugate Gradient method.

A lot of effort has been spent to make the solution of Reynolds equation very quick, in order to obtain a fast simulation model and make it suitable for future developments, like the introduction of the above described calculation of the dh/dt terms to solve the micro motion of the sliding elements. In that case the law of motion will be calculated by means of the forces balance at each instant of time, that is achieved by changing the micro-motion of the sliding element through an iterative procedure in which Reynolds equation might need to be solved several times.

2.6 Calculation of leakages

The calculation of pressure field in the lubricating area of Fig. 4 can be utilized to calculate the leakages to the drain or between adjacent TSVs (figure 3). This information can be used to improve the 1D formulation used within HYGESim [7, 8]; in this work is considered the overall flow toward the drain.

This flow can be evaluated by the summation of the integral of the fluid velocity over each face of the boundary discretization

$$Q_{leak} = \sum_i \iint_{\mathscr{A}_i} \boldsymbol{V}_i \cdot \boldsymbol{n}_i \, da_i \tag{5}$$

where $\boldsymbol{n}$ is the normal vector of the face (pointing always outside the domain) and $\boldsymbol{V}$ is the fluid velocity. Under the assumptions described in §2.1 the fluid velocity can be expressed in cartesian coordinates by the following relations

$$u = \frac{1}{2\mu} \frac{\partial p}{\partial x} z(z-h) + \frac{h-z}{h} u_g \tag{6}$$

$$u = \frac{1}{2\mu} \frac{\partial p}{\partial y} z(z-h) + \frac{h-z}{h} v_g \tag{7}$$

Integration of equation (8) can be carried out for each boundary element considering Fig.10, whit a multiple integral.

$$Q_{leak_i} = \int_{s_0}^{s_1} ds \int_{\alpha(s)}^{\beta(s)} (un_x + vn_y) \, dz = \int_{s_0}^{s_1} ds \int_{0}^{h_0 + \frac{h_1 - h_0}{s_1 - s_0} s} (un_x + vn_y) \, dz \tag{8}$$
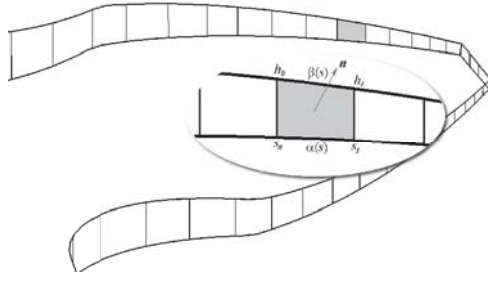
Figure 10: Zoom representing a boundary face, on which equation (8) **is integrated**

Using $s_0 = 0$ and $s_1 = \delta$ the leakage over a selected boundary of N faces can be expressed with summation over all the faces

$$
Q_{leak} = \sum_i^N \left[-\frac{\delta_i}{48\mu} \left(n_{x_i} \left. \frac{\partial p}{\partial x} \right|_i + n_{y_i} \left. \frac{\partial p}{\partial y} \right|_i \right) \left(h_{0_i}^3 + h_{1_i}^3 + h_{0_i} h_{1_i}^2 + h_{0_i}^2 h_{1_i} \right) \right.
$$
$$
\left. + \frac{\delta_i \left(h_{0_i} + h_{1_i} \right)}{4} \left(n_{x_i} u_{g_i} + n_{y_i} v_{g_i} \right) \right] \tag{9}
$$

2.7 Calculation axial thrust on the bearing block

One of the main goal of this work is the evaluation of the axial thrust acting on the sliding elements of the GU. The accurate evaluation of the thrust and of the coordinates of its point of application is useful for design purposes: form the knowledge of these parameters the designer is facilitated in the definition of the sliding elements features that permit to obtain a proper hydraulic balance of the GU. Moreover, as above mentioned, it can be considered as the first step for the development of a numerical tool able to calculate the features of the balance of the sliding elements. The pressure forces F acting in the z direction (Fig. 5) on the sliding element is given by two contributions:

$$
F = F_{gap} + F_{TS} \tag{10}
$$

The first is the overall hydrostatic-hydrodynamic effect in the lubricating gap, and it can be calculated as:

$$
F_{gap} = \sum_i p_i \, \delta\mathscr{A}_i \tag{11}
$$

where the summation term includes all the cells of the computational domain used to discretize the area of Figure 5, $\delta\mathscr{A}_i$ is the area of the i-th cell and p_i the corresponding pressure resulting from the solution of Reynolds equation.

Instead, the F_{TS} term in Eq. (10) is purely hydrostatic: it considers the contribution of all portions pertinent to the TSVs and to the inlet/outlet relief grooves (Fig. 5)

$$
F_{TS} = \left[\sum_{i=1}^z \mathscr{A}_{TS_i} p_{TS_i} \right]_{DR} + \left[\sum_{i=1}^z \mathscr{A}_{TS_i} p_{TS_i} \right]_{DN} + \mathscr{A}_{HP} p_{HP} + \mathscr{A}_{LP} p_{LP} \tag{12}
$$

the two summation terms in Eq. (12) pertain to driver gear and driven gear respectively; the last two terms at second member represent the contribution of the recesses. All pressure terms in Eq. (12) are dependent on time (or angular position of the gears) and results from the HYGEsim fluid dynamic model.

2.7.1 Teeth spaces area and center of mass calculation

As highlighted at section 3, the meshing process strongly affects the shape of the TSVs. Therefore, a precise evaluation of the axial thrust and of its point of application requires an accurate evaluation of all $\mathscr{A}_{TS}$ terms in Eq. (12). To accomplish this result, the geometrical module of HYGESim has been extended with an additional C++ application that permit the calculation of all $\mathscr{A}_{TS}$ terms and of their center of mass.

Figure 11 represents an example of area evolution for one particular TSV (i.e. DR^0_{TS} in Figure 8) of the 12 teeth pump taken as reference in this work. $\mathscr{A}_{TS}$ is represented by the thicker line, while the finer line describes the variation of the tooth space due only to the meshing process, to highlight the effect of the intersection with grooves.
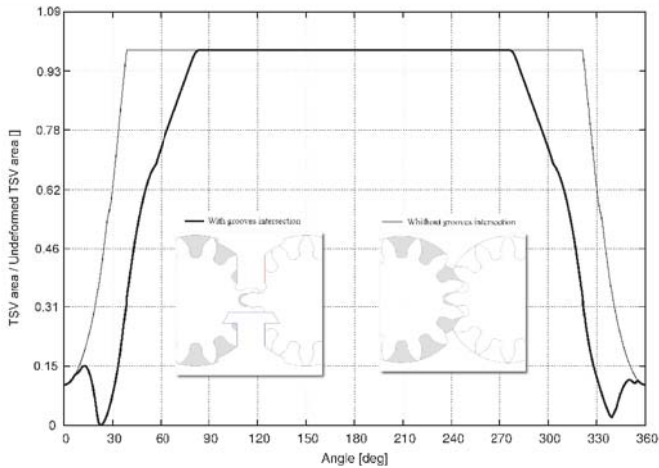
Figure 11: Evolution of the tooth space area $\mathscr{A}_{TS}$, for the drive gear's reference tooth space

3 RESULTS

The results of the developed tool are presented in two different forms. First a qualitative interpretation of the resulting flow field into the lubricating gap is presented, highlighting the importance of different terms in the Reynolds equation. Then integral results in terms of axial thrust and leakage flow are provided. For this purpose a dimensional analysis is briefly presented to individuate the most effective non dimensional parameters that can be utilized to represent the results. Finally, other potentials of the developed procedure that comes from the integration with HYGESim are presented.

All the results pertain to the geometry of the CASAPPA PLP20 11.2 Standard, 12 teeth pump.

3.1 Qualitative results of the flow field

In Fig. 12 it is represented an example of result (for a particular angular position of the shaft) for the unit working with a Δp of 150bar and a speed of 950r/min. The pressure field displayed in the Fig. 12(a) is obtained setting a constant gap height and preventing any squeeze effect. In these conditions Eq. (2) reduces to the Laplace equation (i.e. $\nabla^2 p = 0$); therefore the resulting pressure field derives from the diffusion of the boundary values. This condition is intended to be the term of comparison to understand the effects of the bearing block inclination and micro-motion on the pressure field in the lubricating gap.

(a) Effect of *Poiseuille term*

(b) Effect of *Couette term* (physical wedge)

(c) Effect of *normal squeeze* term

Figure 12: Analysis of the physical meaning of terms in Reynolds equation.12 teeth GU working at 1000r/min **with** $\Delta p = 150$bar

Figure 12(b) highlights the effect of the Couette term in Eq. (2). The map on the left represents to gap height, and can be seen that the bearing block is now inclined,
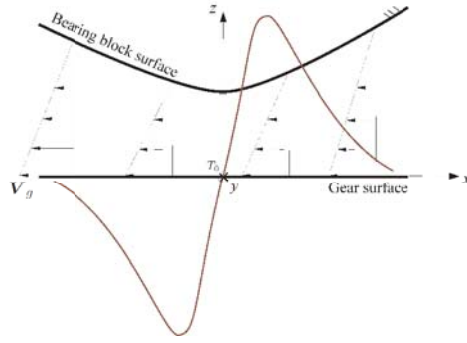
Figure 13: Effect of the Couette term

being closest to the driver gear over the datum point T_0. The main effect of this configuration is a pressure drop on the left of T_0 and a pressure build-up on the right, respect to the case of Fig. 12(a). The explanation of this behaviour can be understood by noticing that each term in Eq. (2) represents a net flow rate, and that the mass in the lubricating area must be conserved. Looking at the gap from the exterior, and focusing on point T_0 the unwrapped boundary surface looks like the sketch of Fig. 13. Considering any pair of the four sections represented, it can be observed that the net flow rate exiting the corresponding referen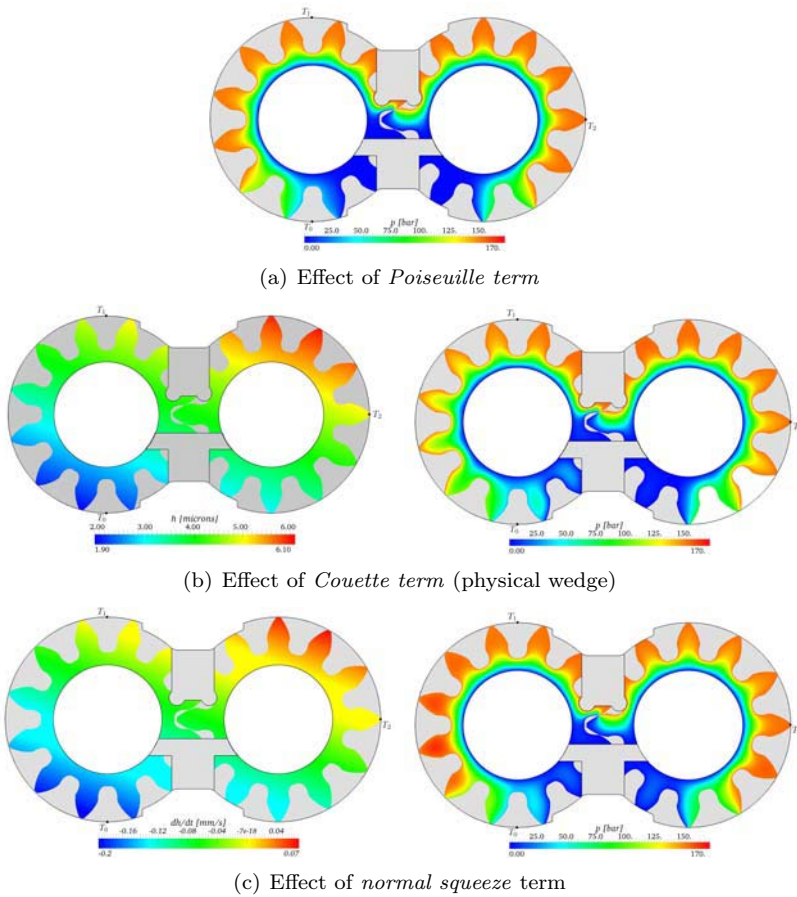ce volume is different respect to the one that is entering. This because the net flow rate is proportional to area of the triangles that have as base the vector V_g (equal everywhere on the gear surface) but different height. The contribution on the pressure field given by the Couette term is qualitatively sketched by the line: the pressure-reaction tends to restore the mass balance, creating a flow opposite to the one generated by the dragging effect of the gears rotation.

Figure 12(c) focuses on the normal squeeze effect - last term in Eq. (2). As the map on the left shows, the simulation assumes the bearing block to move towards the gears over the reference point T_0, and the opposite movement on the opposite side. The pressure-reaction in this case is a built-up around T_0, because in this region the thickness of the gap is decreasing; at the opposite side the increasing gap hight generates a pressure drop effect. The explanation of this behaviour is based on considerations analogues to the ones done to explain the Couette effect.

3.2 Representation of global results
According to the hypothesis made in the developed model (isothermal flow, absence of deformation) the resultant fluid force on the bearing block can be expressed mainly as function of the following parameters

$$F_{gap} = f(R, p_{HP}, p_{LP}, \omega, h_0, t_x, t_y, \mu) \tag{13}$$

Being 3 the dimensions of the problem (L, M, T) the group of linearly independent repeating variables R, ω, p_{HP} can be chosen to express the dimensionless form of the Eq. (13). Following the Buckingham theorem, after some manipulation can be found

that Eq. (13) may be expressed in terms of dimensionless groups as:

$$\frac{F_{gap}}{p_{HP}R^2} = g'\left(\frac{p_{LP}}{p_{HP}}, \frac{h_0}{R}, t_x, t_y, \frac{\mu\omega}{p_{HP}}\right) \tag{14}$$

Similar forms can be found also for others global results related to the lubricating gap, like point of application of the axial thrust, or the leakages to the drain:

$$\frac{Q}{\omega R^3} = g''\left(\frac{p_{LP}}{p_{HP}}, \frac{h_0}{R}, t_x, t_y, \frac{\mu\omega}{p_{HP}}\right) \tag{15}$$

In past works [13, 16] the effect of the operating conditions were grouped in only one independent dimensionless variable. The validity of this assumption should be proved showing that

$$\frac{F_{gap}}{p_{HP}R^2} = g'\left(\frac{p_{LP}}{p_{HP}}, t_x, t_y, k_1\left(\frac{\mu\omega}{p_{HP}}\right)^a\left(\frac{R}{h}\right)^b + k_2\right) \tag{16}$$

and

$$\frac{Q}{\omega R^3} = g''\left(\frac{p_{LP}}{p_{HP}}, t_x, t_y, k_1\left(\frac{\mu\omega}{p_{HP}}\right)^a\left(\frac{R}{h}\right)^b + k_2\right) \tag{17}$$

for some value of the constants k_1, k_2 and the exponents a and b.

In this work the non-dimensional axial thrust and non dimensional drain leakage were calculated for given Δp and μ and different values of the relative tilts, over a wide range of variation of the two parameters R/h and $\mu\omega/p_{HP}$.
The simulation data were fit with a function like

$$f\left(\frac{\mu\omega}{p_{HP}}, \frac{R}{h}\right) = k_1\left(\frac{\mu\omega}{p_{HP}}\right)^a\left(\frac{R}{h}\right)^b + k_2 \tag{18}$$

The results (one example is in Fig. 14) shown that the simulation data fit best using the parameters shown in Tab. 1. Therefore two different operative parameters can be

	F_{gap}	Q
k_1	$7.78 \cdot 10^{-4}$	0.3288
a	1.091	-0.997
b	2.253	-2.996
k_2	1.175	$7.79 \cdot 10^{-8}$

Table 1: Best fit parameters for equations (16) and (17)

defined:

$$\Gamma_{F_{gap}} = \frac{\mu\omega}{p_{HP}}\frac{R^2}{h_0^2} \qquad \Gamma_Q = \frac{p_{HP}}{\mu\omega}\frac{h_0^3}{R^3} \tag{19}$$

The operative parameter $\Gamma_{F_{gap}}$ is consistent with the representation of the results used in [13, 16], while Γ_Q is proposed in this work for the first time.

(a) Non dimensional axial thrust

(b) Non dimensional drain leakages
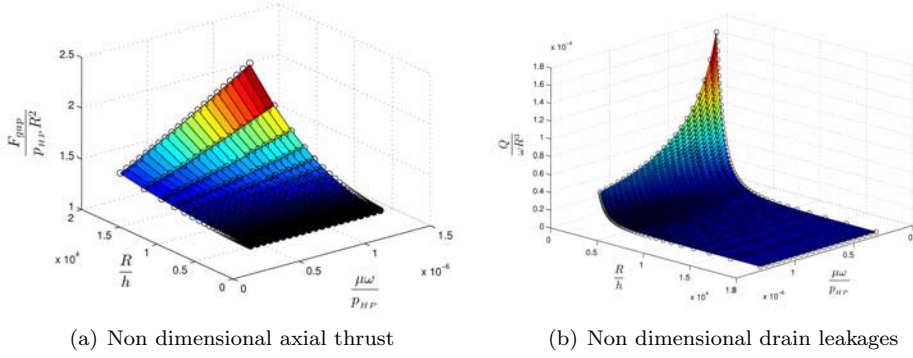
Figure 14: Validation of the parameters $\Gamma_{F_{gap}}$ and Γ_Q for $t_x = 0.5$, $t_y = 0$ and $\Delta p = 150$bar. The circles represent the simulated values, while the surfaces are obtained using equations (16) and (17) and values in Tab. 1

3.3 Effect of the bushing inclination

As observed in previous works [13, 16] the non-flatness of the gap due to the bushing tilt significantly influences the widening thrust. The numerical procedure described in this work permit a similar analysis, but comprising also the effect of bushing tilt angle on the drain leakage. The effect of widening thrust can be analysed through the parameter

$$\Lambda = \frac{F_{gap} - (F_{gap})_{t=0}}{p_{HP} R^2} \tag{20}$$

where Λ is the non-dimensional difference between the axial thrust relative to a particular tilt and the axial thrust referred to the flat condition (with no hydrodynamic effect). Similarly, the effect of the drain leakage can be studied defining the parameter

$$\Omega = \frac{Q_{leak} - (Q_{leak})_{t=0}}{\omega R^3} \tag{21}$$

with analogue definition. Dimensional analysis shown that Λ and Ω are not only function of the relative tilt, but also of the operative condition parameters $\Gamma_{F_{gap}}$ and Γ_Q.

In Fig. 3.3 are represented the widening thrust and the drain leakage for the pump considered in this work. In typical design of GU the tilt along the y axis, t_y, can be neglected respect to the one along the x axis, t_x (Fig 5), therefore $t_x = t = h_{max} - h_{min}/2h_0$, hence positive tilt in figure corresponds to the minimum clearance lying adjacent to the delivery port while negative tilts corresponds to the minimum clearance lying adjacent to the suction port.

As concerns the dependence of the widening thrust with parameters t, $\Gamma_{F_{gap}}$. (Fig. 15(a)), the results are in very good agreement with what found in [13, 16].
The behaviour of drain leakage as a function of t, Γ_Q is represented in Fig. 15(b). In general drain leakage increases with the operative parameter Γ_Q, this can be easily justified whit the increment of h_0. In Fig. 15(b) opposite behaviours are noticeable for the positive values of t and the negative ones. In particular the inclination of the

(a) Axial thrust   (b) Drain leakage
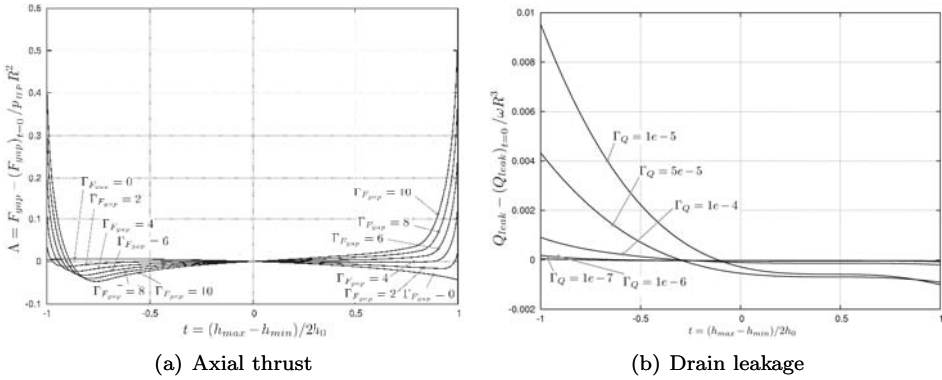
Figure 15: Widening thrust and the drain leakage as a function of t and operative parameters $\Gamma_{F_{gap}}$ and Γ_Q
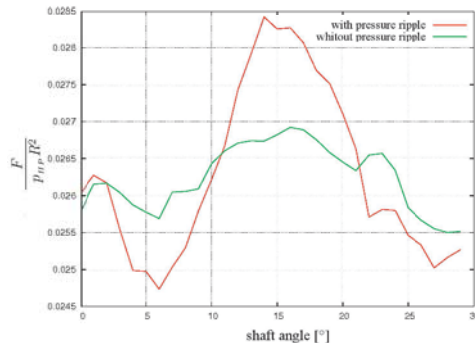
Figure 16: Effect of the pressure ripple on the dimensionless axial thrust

bushing towards the suction port promotes the drain leakage. In this condition in fact the main part of the overall drain surfaces is on the high pressure side, where there are the biggest pressure gradients and hence high velocities of fluid directed towards the drain. In the opposite case the main drain surface is located on the low pressure side, where the pressure gradients are smaller.

3.4 Potentials given by the integration with HYGESim

The last result exemplifies the potentials given by the integration of the developed model with the existing HYGESim model. As a matter of fact, beyond the possibility of performing fast and automatic simulations this integration permits to highly adhere to the real operating conditions of the unit during the simulation. For example, the effect due to the non-constancy of the pressure at delivery ports can be considered. As shown in Fig. 16 (where an extreme condition for the pressure pulsation is used for the comparison), this effect, typical in positive displacement machines, can significantly affect the parameters related to the flow in the considered lubricating gap.

4 CONCLUSIONS

In this paper a numerical approach for the evaluation of the features of the lubricating gap between the gears lateral side and the sliding bushings is presented. The developed model is based on the solution of all terms of the Reynolds that can play a significant role in during the operation of external gear machines. The model implementation is made in C++, taking advantages of OFoam libraries, and pursues the goal of simulation swiftness, versatility and automation: simulations can be performed starting directly from the CAD drawings of the unit, while the required boundary conditions are given as output of the existing tool HYGESim, developed to solve the overall flow through the machine. Results presented in the paper describe in details the flow features in the considered gap, describing the different terms of the basic equation utilized. Moreover, it is shown how the model can be used to derive gross features of the gap, such as the leakages and the axial thrust acting on the sliding elements. A future development of the code will consist the implementation of a fully dynamic model, where the micromotion of the sliding elements will be solved allowing the definition the instantaneous geometric configuration of the lubricating gap.

REFERENCES

[1] Beecham T.E.,Shewchuk J.R., 1946, *High Pressure Gear Pumps, Proc. I.Mech.E.*, vol. 154, pp. 417-429.

[2] Mancò S., Nervegna N., 1989, *Simulation of an External Gear Pump and Experimental Verification*, JHPS Int. Symposium on Fluid Power, Tokio, Japan.

[3] Falfari S., Pelloni P., 2007, *Setup of a 1D Model for Simulating Dynamic Behaviour of External Gear Pumps*, Commercial Vehicle Engineering Congress & Exhibition, October 2007, Rosemont, IL, USA.

[4] Itou T., Shimamura T., Imamura W. 2010, *Study on a theoretical design method for external gears pump*, 7th IFK 2010 Int. Fluid Power Conference, 22-24 March 2010, Achen, Germany.

[5] Zardin B., Borghi M., 2008, *Modelling and Simulation of External Gear Pumps and Motors*, 5th FPNI PhD Symposyum, 1-5 July 2008, Kracow, Poland.

[6] Casoli P., Vacca A., Berta G.L., 2007, *Potentials of a Numerical Tool for the Simulation of Flow in External Gear Machines*, SICFP07, The Tenth Scandinavian Int. Conference on Fluid Power, May 21-23, 2007, Tampere, Finland.

[7] Eaton M., Edge K., 2001, *Modelling and Simulation of Pressures within the Meshing Teeth of Gear Pumps*, Int. Conf. on Recent Advantages in Aerospace Actuation Systems and Components, June 13-15, 2001, Toulouse, France.

[8] Vacca A., Guidetti M., 2010, *HYGESIM: a simulation model for external gears machines. Part 1: numerical approach*, submitted to International Journal of Fluid Power

[9] Wustmann W., Helduser S., Wimmer W., 2008, *CFDSimulation of the Reversing Process in External Gear Pumps*, 6th Int. Fluid Power Conference, 31/03-02/04 2008, Dresden, Germany

[10] Simerics Inc, Pumplinx software `http://www.simerics.com/pumplinx_software.html`

[11] Casoli P., Vacca A., Berta G.L., Zecchi M., 2009, *A CFD Analysis of the Flow Field in the Lateral Clearance of External Gear Pumps*, The 11th Scandinavian Int. Conference on Fluid Power, SICFP09, June 2-4, 2009, Linkping, Sweden.

[12] Wieczorek, U., Ivantysynova, M., 2002, *Computer Aided Optimization of Bearing and Sealing Gaps in Hydrostatic Machines The Simulation Tool Caspar*, International Journal of Fluid Power 3 (2002), No. 1, pp. 7-20.

[13] Ko E., Kurban O., Hooke, C.J., 1997, *An Analysis of the Lubrication Mechanisms of the Bush-Type Bearing in High Pressure Pumps*, Tribology International, Vol. 30, No. 8 pp. 553-560, 1997 Elsevier Science Ltd.

[14] Ko E., Hooke, C.J., 1997, *An Experimental Investigation into the Design and Performance of Hydrostatically Loaded Floating Wear Plates in Gear Pumps*, Wear Vol. 209 pp. 184-192, 1997 Elsevier Science Ltd.

[15] Ivantysyn J.,Ivantysynova M., 2003, *Hydrostatic Pumps and Motors*, Tech Books Int., New Delhi, India.

[16] M. Borghi, M. Milani, F. Paltrinieri and B. Zardin *Studying the Axial Balance of External Gear Pumps* SAE 2005 Commercial Vehicle Engineering Congress and Exhibition Rosemont, Chicago Illinois (U.S.A.), 1-3 Novembre 2005.

[17] Christophe Geuzaine and Jean-Franois Remacle *Gmsh: a three-dimensional finite element mesh generator with built-in pre- and post-processing facilities* `http://www.geuz.org/gmsh/`

[18] OpenCFD Ltd, OpenFOAM®: open source CFD, `http://www.openfoam.com/`

A Simple Model of Piston-Cylinder Gap Efficiency in Positive-Displacement Hydraulic Pumps and Motors

Kim A. Stelson, Professor and Director
Feng Wang, Postdoctoral Fellow*
Center for Compact and Efficient Fluid Power
University of Minnesota
Minneapolis, MN 55455
U.S.A.

*Permanent affiliation: The State Key Laboratory of Fluid Power Transmission and Control, Zhejiang University, Hangzhou 310027, China.

ABSTRACT

This paper describes a simple model of the piston-cylinder gap in positive-displacement hydraulic pumps and motors. Fundamental equations and dimensionless scaling are used to describe flow and mechanical losses and relate these losses to overall pump and motor efficiency. The equations are cast in dimensionless form where it is shown that efficiency depends on three dimensionless groups; the dimensionless viscosity, dimensionless gap height and the fractional displacement. To achieve this simplification, an unconventional definition of dimensionless viscosity is shown to be required. Finally, the dimensionless viscosity that results in the maximum piston-cylinder gap efficiency is derived for both pumping and motoring. Because of the simplicity of the approach it is hoped that it would provide a useful example of one aspect affecting efficiency of hydraulic pumps and motors for both for practicing engineers and students in university fluid power courses.

KEYWORDS: hydraulics, hydraulic pumps, hydraulic motors, positive-displacement pumps, positive-displacement motors, cylinder, piston, lubrication, gap, efficiency, volumetric efficiency, mechanical efficiency, optimization, viscosity, similitude, dimensional analysis, dimensionless groups.

1. INTRODUCTION

In fluid power transmission, efficiency is of upmost importance, and efficiency depends on fluid viscosity. If the viscosity is too high, the viscous mechanical losses will reduce efficiency. If the viscosity is too low, leakage will reduce efficiency. The optimal viscosity represents a balance of these two effects. This tradeoff would exist in all of the lubricating gaps in a pump or motor. In this paper we concentrate on optimizing the efficiency of the piston-cylinder gap. The piston-cylinder gap serves three functions, to seal the fluid, to provide lubrication and to support loads. To be practical, any solution must satisfy these three functions.

A hydraulic piston pump or motor is a complex device with multiple cylinders in cyclic operation. Detailed descriptions and analyses of these affects can be found in recent monographs by Ivantysyn and Ivantysynova (2003) and Watton (2009). Volumetric losses are caused by leakage through multiple flow paths including gaps in the valve plate, slipper and between the piston and cylinder. Mechanical losses occur due to relative motion across these gaps. Compressibilty and the valve timing also affect efficiency.

Parametric models of pumps and motors that predict performance have been developed and subsequently refined by Wilson (1946), Reethof (1960), Schlosser (1961), Thoma (1969), McCandlish and Dorey (1984), and others. The model parameters are generally measured from tests. Volumetric, mechanical and energy

efficiency are conventionally plotted versus dimensionless viscosity, $\hat{\mu} = \mu\omega/p$, and fractional displacement, f, as discussed by Wilson (1946) and He (1981).

When comparing experimental measurements with model predictions of pump and motor efficiency from parametric models, significant scatter and systematic deviation from experiments have been observed. Pourmovahed (1992) compared Wilson's model with experiments, and Manring (2005) has shown that experimental error can have a considerable influence on the results. Recently there is less activity in developing parametric models, the general opinion being that further refinement would not yield better results accept in limited circumstances. For systems studies, lookup tables based on experimental data are often more accurate than parametric models. Instead, more recent research can concentrated on detailed numerical modeling of pumps and motors. An exception ot this trend is the recent work of Jeong (2007) and Jeong and Kim (2007) on parametric models of axial piston motors. Watton (2007) has shown the importance of including the load characteristics in opimizing the efficiency of axial piston motor drives.

In this paper we concentrate on the influence of viscosity on losses in the piston-cylinder gap and its effect on overall pump and motor performance. The approach is unlikely to apply to other classes of positive displacement pumps and motors such as the vane or gear type. Other important effects in piston pumps and motors have been neglected and would have to be considered separately. Nevertheless, if the pump or motor parameters are measured rather than predicted from first priniciples, the model could also mimic the effects of other gaps in the pump since they have the same tradeoff between volumetric and mechanical losses. The resulting parametric model can be shown to be of the same form as that of Reethof (1960). The optimization follows the same approach as Reethof, with the key difference being that the approach used here relies entirely on fundamental variables and parameters and avoids the use of empirically measured coefficients. This fundamental approach enables simplifications and insights that were not available previously. Further, the approach used here can be shown to be consistent with the gap power minimization approach presented in Lu (2002) and in Ivantysyn and Ivantysynova (2003).

2. BASIC EQUATIONS

Consider a cylindrical bore with a piston inside of it of diameter, D, and length, L. The gap between the piston and the bore is d. In the gap, assume incompressible laminar flow of a Newtonian fluid of viscosity, μ . It is reasonable to assume laminar flow since the Reynolds would be in the laminar range. Since $d<<D$, the flow between the piston and cylinder can be approximated as flow between two flat plates (Wilson, 1950). A schematic of the situation for both pumping and motoring is shown in Figure 1.

An external force, F, is exerted on the piston and is opposed by the pressure, p. The piston moves with a velocity, U, and flow exits the cylinder with volumetric flow rate, Q.
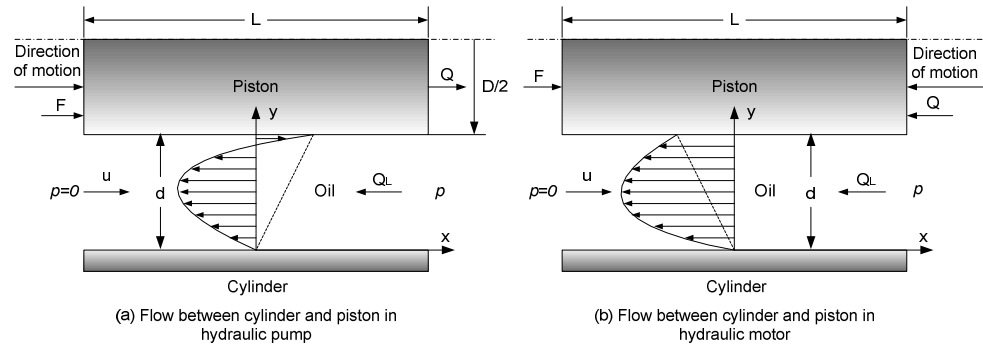

Fig. 1 Flow between cylindrical bore and piston in hydraulic pump and motor

The model works equally well for pumping and motoring where the sign convention is that Q and U are positive for pumping and negative for motoring.

The velocity, u, in the gap is given in many textbooks (see, for example, Wilson, 1950):

$$u = \frac{Uy}{d} + \frac{1}{2\mu}\frac{dp}{dx}(y^2 - yd)$$
(1)

y is the coordinate within the gap, with $y=0$ located at the stationary cylinder, and $y=d$ located at the piston moving with velocity U. The pressure gradient is

$$\frac{dp}{dx} = -\frac{p}{L}$$
(2)

The leakage flow is given by:

$$Q_L = -\pi D \int_0^d u\, dy = -\frac{\pi Dd}{2}U + \frac{\pi Dd^3}{12\mu L}p$$
(3)

The flow exiting the cylinder is the ideal flow minus the leakage flow. Thus,

$$Q = \frac{\pi D^2}{4}U - Q_L = \frac{\pi D(D+2d)}{4}U - \frac{\pi Dd^3}{12\mu L}p$$
(4)

The shear stress, τ, exerted by the fluid on the piston is:

$$\tau = \mu\frac{du}{dy} = \frac{\mu}{d}U + \frac{d}{2L}p$$
(5)

A force balance on the piston gives:

$$F = \frac{\pi D^2}{4}p + \tau\pi DL = \frac{\pi D(D+2d)}{4}p + \frac{\mu\pi DL}{d}U$$
(6)

Since $d<<D$, $D+2d$ can be replaced with D in equations 4 and 6 with negligible error giving:

$$Q = \frac{\pi D^2}{4}U - \frac{\pi Dd^3}{12\mu L}p$$
(7)

$$F = \frac{\pi D^2}{4}p + \frac{\mu\pi DL}{d}U$$
(8)

In equation 7, the first term on the right-hand side is the ideal flow, and the second term is the leakage flow. In equation 8, the first term on the right-hand side is the ideal force, and the second term is the viscous drag force.

Note that the viscosity is in the denominator of the leakage flow term in (7), but in the numerator of the drag force term in (8). Thus, eliminating the leakage requires that the viscosity be infinite, but eliminating the drag force requires that the viscosity be zero. Thus, increasing the viscosity increases the volumetric efficiency, but decreases the mechanical efficiency. There exists an optimal viscosity for energy efficiency that balances the competing leakage and drag force effects.

Most hydraulic pumps and motors are rotary, but our analysis to this point has been for translation. In a rotating system, the force is applied at an effective radius, R, from the center of the shaft. The torque, T, and angular velocity, ω, of the shaft are given by:

$$T = FR \tag{9}$$

$$\omega = U / R \tag{10}$$

Using these relations, equations (7) and (8) can be recast in rotary form as:

$$Q = \frac{\pi D^2 R}{4}\omega - \frac{\pi D d^3}{12\mu L}p \tag{11}$$

$$T = \frac{\pi D^2 R}{4}p + \frac{\mu \pi D L R^2}{d}\omega \tag{12}$$

The ideal flow rate, Q^*, can be found be eliminating the leakage in equation (11), and the ideal torque, T^*, can be found from eliminated the viscous drag torque from equation (12) resulting in:

$$Q^* = \frac{\pi D^2 R}{4}\omega \tag{13}$$

$$T^* = \frac{\pi D^2 R}{4}p \tag{14}$$

These can be compared to the standard form of the ideal pump equations:

$$Q^* = \frac{V}{2\pi}\omega \tag{15}$$

$$T^* = \frac{V}{2\pi}p \tag{16}$$

V is the pump displacement, that is, the volume of fluid pumped by rotating the shaft one revolution.

Comparing (13) to (14) or (15) to (16) shows that the pump displacement is related to R by

$$V = \frac{\pi^2}{2}D^2 R \tag{17}$$

R is not a physically measurable quantity, but rather is calculated from the displacement using (17).

The generic approach of equations 9 and 10 may seem at first to be inadequate for a machine as complex as a hydraulic pump and motor where the total flow is the sum of flows from individual cylinders and the total torque is resultant combination of many forces with all of the complexities of kinematic nonlinearites and discontiuous operation controlled by valve plate timing. Nevertheless, the approach is adequate for our purposes here. R is best thought of in functional rather than physical terms. The mechanism of the pump or motor is a mechanical linear-rotational transfomer, and the approximation assumes a lossless, constant modulus, transformation. The approximation is that pumps and motors are steady-state machines, and they are in fact intensionally designed to be as steady as possible. In real machines the parameter, R, is not constant but is cyclically varying resulting in ripple of torque, pressure, flow and rotation speed. The

approximation of constant R amounts to neglecting the ripple. For variable displacement pumps or motors the effective radius is reduced by the fractional displacement as discussed in the next paragraph.

The equations can be modified for variable displacement pumps by multiplying the displacement by a factor, f. As the displacement varies from zero to the maximum, f varies from zero to one. In making this change we are assuming that the loss terms are not a function of displacement, a reasonable assumption. With this modification, (11) and (12) become:

$$Q = \frac{\pi D^2 Rf}{4}\omega - \frac{\pi D d^3}{12\mu L}p \tag{18}$$

$$T = \frac{\pi D^2 Rf}{4}p + \frac{\mu\pi DLR^2}{d}\omega \tag{19}$$

3. LOSS FACTORS AND EFFICIENCY

It is convenient to define loss factors for flow and torque. The loss factor for flow, l_Q, is the leakage flow divided by the ideal flow.

$$l_Q = \frac{d^3}{3LDRf}\left(\frac{p}{\mu\omega}\right) \tag{20}$$

The loss factor for torque, l_T, is the drag torque divided by the ideal torque.

$$l_T = \frac{4LR}{dDf}\left(\frac{\mu\omega}{p}\right) \tag{21}$$

The loss factors are related to efficiencies. For pumps, the actual flow is less than the ideal flow because of leakage. The volumetric efficiency, η_Q, is the ratio of the actual flow to the ideal flow. It is related to l_Q by:

$$\eta_Q = 1 - l_Q \tag{22}$$

For pumps, the actual torque is greater than the ideal torque because of mechanical drag. The mechanical efficiency, η_T, is the ratio of the ideal torque to the actual torque. It is related to l_T by:

$$\eta_T = \frac{1}{1 + l_T} \tag{23}$$

The overall energy efficiency for pumps, η_P, is the product of the volumetric and mechanical efficiencies. It is related to the loss factors by:

$$\eta_P = \eta_Q \eta_T = \frac{1 - l_Q}{1 + l_T} \tag{24}$$

For motors, the actual flow is greater than the ideal flow because of leakage. The volumetric efficiency, η_Q, is the ratio of the ideal flow to the actual flow. It is related to l_Q by:

$$\eta_Q = \frac{1}{1+l_Q} \tag{25}$$

For motors, the actual torque is less than the ideal torque because of mechanical drag. The mechanical efficiency, η_T, is the ratio of the actual torque to the ideal torque. It is related to l_T by:

$$\eta_T = 1 - l_T \tag{26}$$

The overall energy efficiency for motors, η_M, is the product of the volumetric and mechanical efficiencies. It is related to the loss factors by:

$$\eta_M = \eta_Q \eta_T = \frac{1-l_T}{1+l_Q} \tag{27}$$

4. DIMENSIONLESS GROUPS

Fundamental insight can be gained by expressing the loss factors and efficiencies in dimensionless groups (Kline, 1965). Looking at the loss factors, note that the viscosity always appears combined with pressure and angular velocity in the same way. This is the dimensionless viscosity conventionally defined as:

$$\hat{\mu} = \frac{\mu\omega}{p} \tag{28}$$

For optimum performance, the dimensionless viscosity should be kept constant. For example, for high-pressure, low-speed operation, the viscosity should be high. For low-pressure, high-speed operation, the viscosity should be low.

The loss factors also contain dimensionless groups of physical dimensions. These are the dimensionless diameter, $\hat{D}$, and the dimensionless gap height, $\hat{d}$. These are defined as:

$$\hat{D} = \frac{D}{\sqrt{LR}} \tag{29}$$

$$\hat{d} = \frac{d}{D} \tag{30}$$

With these definitions, the loss factors become:

$$l_Q = \frac{1}{3}\hat{d}^3\hat{D}^2 \frac{1}{f}\frac{1}{\hat{\mu}} \tag{31}$$

$$l_T = 4\frac{1}{\hat{d}}\frac{1}{\hat{D}^2}\frac{1}{f}\hat{\mu} \tag{32}$$

Equations (31) and (32) express the loss factors as four dimensionless groups: $\hat{d}$, $\hat{D}$, f and $\hat{\mu}$. But, $\hat{D}$ and $\hat{\mu}$ can be combined into a single group, $\hat{\mu}/\hat{D}^2$, lowering the number of dimensionless groups from four to three. The new definition of dimensionless viscosity is:

$$\hat{\mu} = \frac{\mu \omega L R}{p D^2} \tag{33}$$

With this new definition the loss factors become:

$$l_Q = \frac{1}{3} \hat{d}^3 \frac{1}{f} \frac{1}{\hat{\mu}} \tag{34}$$

$$l_T = 4 \frac{1}{\hat{d}} \frac{1}{f} \hat{\mu} \tag{35}$$

The efficiency for pumps can be expressed in terms of dimensionless groups by substituting loss factors from (34) and (35) into (24). This gives

$$\eta_P = \frac{1 - l_Q}{1 + l_T} = \frac{1 - \frac{1}{3} \hat{d}^3 \frac{1}{f} \frac{1}{\hat{\mu}}}{1 + 4 \frac{1}{\hat{d}} \frac{1}{f} \hat{\mu}} \tag{36}$$

The efficiency for motors can be expressed in terms of dimensionless groups by substituting loss factors from (34) and (35) into (27). This gives

$$\eta_M = \frac{1 - l_T}{1 + l_Q} = \frac{1 - 4 \frac{1}{\hat{d}} \frac{1}{f} \hat{\mu}}{1 + \frac{1}{3} \hat{d}^3 \frac{1}{f} \frac{1}{\hat{\mu}}} \tag{37}$$

5. OPTIMIZATION

We now consider the optimization of the model for the three independent dimensionless variables, $\hat{\mu}$, $\hat{d}$ and f. If the optimization is unconstrained, it can be shown from equations 36 and 37 that the optimal value of efficiency of pumps and motors is 100% in a limiting process where $\hat{\mu}$ and $\hat{d}$ approach zero and f approaches one. This limit is of theoretical interest only, and has little practical meeting. In practice, the value of f is required by the operating condition, but for most efficient operation, it should always be made as close to unity as possible. It then remains to optimize μ or $\hat{d}$ with the other variable held constant.

First consider finding the opimum dimensionless gap size with the dimensionless viscosity held fixed. To find the optimal dimensionless gap giving the maximum efficiency for pumps, we set $\partial \eta_P / \partial \hat{d} = 0$ in (36). After some manipulation the following quadratic equation results:

$$\hat{\mu}^2 - \frac{4}{3} \frac{\hat{d}^3}{f} \hat{\mu} - \frac{\hat{d}^4}{4} = 0 \tag{38}$$

The equation has two roots, one positive and one negative. Taking the positive root as the only physically meaningful result,

$$\hat{\mu} = \frac{2}{3}\frac{\hat{d}^3}{f}\left(\sqrt{\left(\frac{9}{16}\frac{f^2}{\hat{d}^2}+1\right)}+1\right) \tag{39}$$

Since $\hat{d} \ll 1$ in all practical cases, the expression, $\sqrt{\left(\frac{9}{16}\frac{f^2}{\hat{d}^2}+1\right)}+1$, in equation 39 can be replaced with

$\frac{3f}{4\hat{d}}$ causing little error and simplifying equation 39 to:

$$\hat{\mu} = \frac{\hat{d}^2}{2} \tag{40}$$

Equation 40 can be inverted to find the optimum dimensionless gap size.

$$\hat{d} = \sqrt{2\hat{\mu}} \tag{41}$$

In dimensioned terms, the optimum gap size is:

$$d = \sqrt{\frac{2\mu L\omega R}{p}} = \sqrt{\frac{2\mu LU}{p}} \tag{42}$$

in agreement with the minimum power dissipation analysis presented in Lu (2002) and Ivantysyn and Ivantysynova (2003).

Substituting (41) into (36), the maximum efficiency of a pump with optimum dimensionless gap size is

$$\eta_P = \frac{1 - \frac{2}{3}\frac{\sqrt{2\hat{\mu}}}{f}}{1 + \frac{2\sqrt{2\hat{\mu}}}{f}} \tag{43}$$

Next consider finding the opimum dimensionless viscosity with the dimensionless gap size held fixed. To find the optimum dimensionless viscosity leading the maximum efficiency for pumps, we set $\partial\eta_P/\partial\hat{\mu} = 0$ in (36). After some manipulation the following quadratic equation results:

$$\hat{\mu}^2 - \frac{2}{3}\frac{\hat{d}^3}{f}\hat{\mu} - \frac{1}{12}\hat{d}^4 = 0 \tag{44}$$

The equation has two roots, one positive and one negative. Taking the positive root as the only physically meaningful result,

$$\hat{\mu} = \frac{1}{3}\frac{\hat{d}^3}{f}\left(\sqrt{\left(\frac{3}{4}\frac{f^2}{\hat{d}^2}+1\right)}+1\right) \tag{45}$$

Since $\hat{d} \ll 1$ in all practical cases, the expression, $\sqrt{\left(\dfrac{3}{4}\dfrac{f^2}{\hat{d}^2}+1\right)}+1$, in equation 45 can be replaced with

$\dfrac{\sqrt{3}f}{2\hat{d}}$ causing little error and simplifying equation 45 to:

$$\hat{\mu} = \frac{\hat{d}^2}{2\sqrt{3}}$$

(46)

In dimensioned terms, the optimum viscosity for pumping is

$$\mu = \frac{pd^2}{2\sqrt{3}\omega LR} = \frac{\pi^2 pd^2 D^2}{4\sqrt{3}\omega LV}$$

(47)

Substituting (40) into (36), the maximum efficiency of the pump is

$$\eta_P = \frac{1 - \dfrac{2}{\sqrt{3}}\dfrac{\hat{d}}{f}}{1 + \dfrac{2}{\sqrt{3}}\dfrac{\hat{d}}{f}}$$

(48)

To find the optimum dimensionless gap size or viscosity for motors, the exact same procedure as was applied for pumps can be used using equation 27 instead of 24. The exact same optimal conditions obtain. The optimal dimensionless gap size for motors is given by equation 41 with the resulting maximum efficiency given by equation 43 and the optimal dimensionless viscosity for motors is given by equation 46 with the resulting maximum efficiency given by equation 48. Remarkably, the efficiency curves for motors are almost identical to those of pumps in spite of the difference in the efficiency expressions for pumps and motors given in equations 24 and 27.

6. RESULTS

Figure 2 shows the predictied efficiency of a pump as a function of dimensionless gap ratios, $\hat{d}$, for dimensionless viscosities, $\hat{\mu}$, of 0.5 x 10^{-6}, 1.0 x 10^{-6} and 2.0 x 10^{-6} with displacement fraction f=1. The figure for a motor would be indistinguishable.
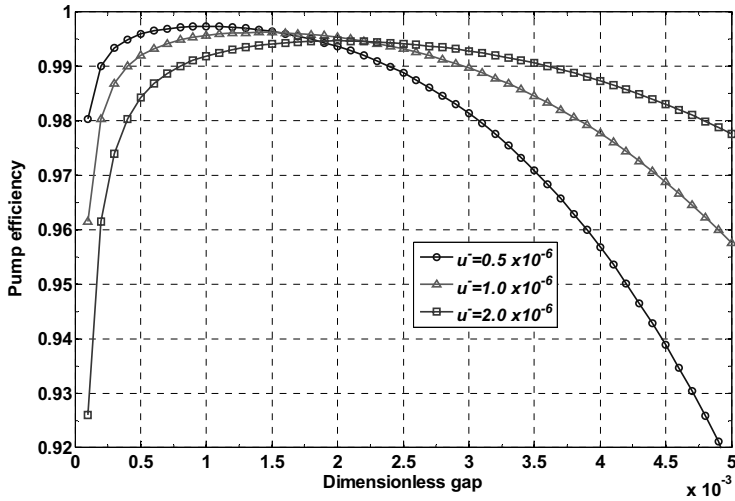
Fig. 2 Pump efficiency as a function of dimensionless gap for different dimensionless viscosities (displacement fraction *f*=1)

Figure 3 shows the predicted efficiency of a pump as a function of dimensionless viscosity, $\hat{\mu}$, for dimensionless gap ratios, $\hat{d}$, of 0.001, 0.002 and 0.005 with displacement fraction *f*=1. Again, the figure for a motor would be indistinguishable.

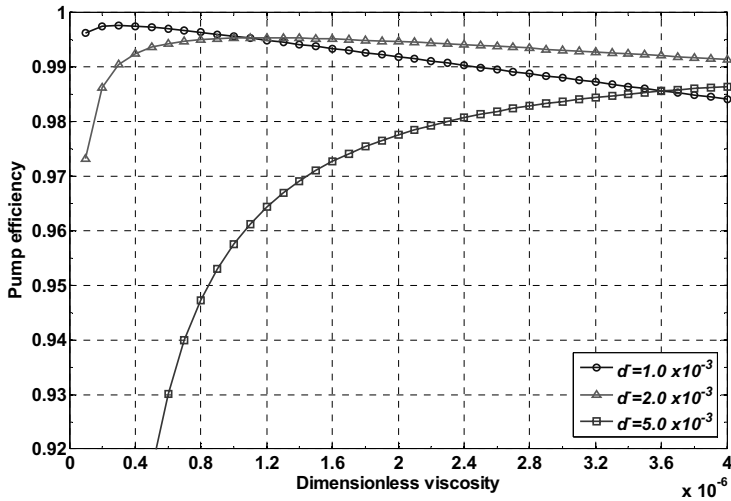**Fig. 3 Pump efficiency as a function of dimensionless viscosity for different dimensionless gap ratios (displacement fraction *f*=1)**

Figure 4 shows the predicted efficiency of a pump as a funtion of dimensionless viscosity, $\hat{\mu}$, for displacement fraction, *f*, of 0.2, 0.5 and 1.0 with dimensionless gap, $\hat{d}$ = 2.0 x 10^{-3}. As with the previous two figures, the figure for a motor would be indistinguishable.
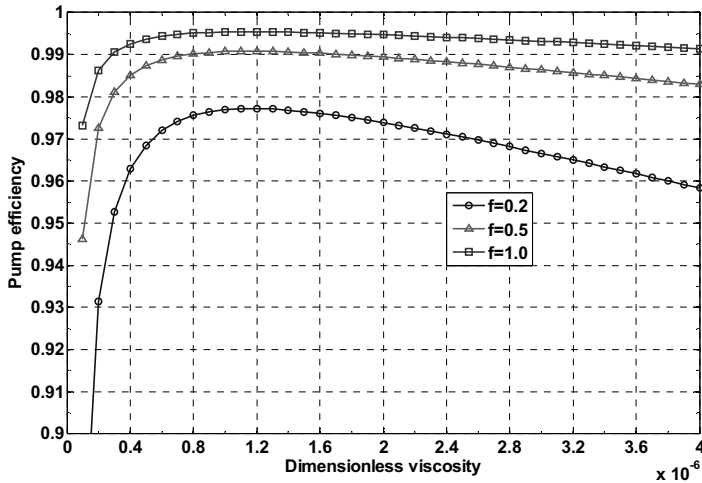
Fig. 4 Pump efficiency as a function of dimensionless viscosity for fractional displacements of 0.2, 0.5 and 1.0 with a dimensionless gap height of 2.0 x 10^{-3}

Some of the most important aspects of pump and motor efficiency can be seen from Figures 2, 3 and 4. As predicted, when the optimum dimensionless viscosity is used, pumps and motors with smaller dimensionless gaps are more efficient than those with larger dimensionless gaps. The optimum dimensionless viscosity depends on the dimensionless gap height, with larger dimensionless gaps requiring larger dimensionless viscosities. Also, higher fractional displacements are more efficient than lower fractional displacements. For each fractional displacement and gap height, a maximum efficiency can be seen to occur at an optimum viscosity. Also, the optimum viscosity and maximum achievable efficiency is the same for pumping and motoring.

7. OBSERVATIONS

In the equations for pumps or motors, deviations from ideal behavior are caused by viscous drag and leakage, both of which depend on dimensionless viscosity. As the dimensionless viscosity increases, the leakage decreases but the viscous drag increases. Thus, an optimum dimensionless viscosity is desired that balances the two effects. Equation 46 provides an equation for the optimum dimensionless viscosity and equation 48 gives the maximum achievable efficiency for pumping or motoring.

It is also worth considering the effects of the other dimensionless groups, $\hat{d}$ and f . It can be seen from equation 36 and 37 that f should be kept as large as possible to maximize efficiency. This is consistent with experience since it is well known that variable displacement pumps and motors should be operated near maximum displacement to maximize efficiency. Equation 40 gives the optimum value of $\hat{d}$ with the $\hat{\mu}$ held constant. Optimum pairs of $\hat{d}$ and $\hat{\mu}$ should be kept as small as practical to maximize efficiency. This is true, but there are real practical limits to how small viscosity and gaps can be. Manufacturing accuracy, surface roughness and thermal and mechanical deformation all limit how small the gaps can actually be made. Further, the gap must be large enough to support the side loads in operation.

8. CONCLUSIONS

The fundamental equations describing the losses in the piston-cylinder gap and their influence on the performance of pumps and motors have been summarized in this paper. The model includes ideal behavior, viscous drag and leakage. The equations have been cast in dimensionless form. With an unconventional definition of dimensionless viscosity of equation 33, the efficiency becomes a function of three

dimensionless groups; the dimensionless viscosity, $\hat{\mu}$, the fractional displacement, f , and the dimensionless gap height, $\hat{d}$.

It is important to understand the limitations of the model. Emphasis is put on the leakage and mechanical drag effects in the cylinder, but other leakage paths and sources of drag exist in the pump. These will generally mimic the mathematical form of the losses in the cylinder. To the extent that these additional factors mimic the losses in the cylinder, the model can capture these effects by modifying parameters to increase both the leakage and mechanical drag resulting in the model of Reethof (1960). Further, there are loss effects that are quite different form leakage and mechanical drag. The model assumes continuous operation while real machines operate discontinuously with cyclical motion of the pistons and the beginnings and ends of the discontinuous events controlled by the valve plate. Inefficiencies from the discontinuous nature of pump and motor operation are not captured by the model. Further, the fluid is assumed to be incompressible, but compressibility has an influence on efficiency.

Models can be judged on their simplicity, generality and accuracy. The model presented here is simple and general, but likely not very accurate. Concentrating on the losses in the piston-cylinder gap provides a useful archetype for fluid power instruction that clearly explains the how pressure, speed, viscosity and physical dimensions affect pump and motor efficiency.

ACKNOWLEDGEMENTS

REFERENCES

C. He, *Hydraulic Components (in Chinese),* China Machine Press, Beijing, 1981, pp. 16-22.

J. Ivantysyn and and M. Ivantysynova, *Hydrostatic Pumps and Motors,* Tech Books International, New Delhi, 2003.

H. S. Jeong, "A Novel Performance Model Given by the Physical Dimensions of Hydraulic Axial Piston Motors: Model Derivation*," J. of Mech. Sci. and Tech.,* Vol. 28, 2007, pp. 83-97.

H. S. Jeong and H. E. Kim, "A Novel Performance Model Given by the Physical Dimensions of Hydraulic Axial Piston Motors: Experimental Analysis*," J. of Mech. Sci. and Tech.,* Vol. 28, 2007, pp. 630-641.

S. J. Kline, *Similitude and Approximation Theory,* McGraw-Hill, New York, 1965.

Y. Lu, *Technical Manual of Hydraulics and Pneumatics (in Chinese),* China Machine Press, Beijing, 2002, pp. 34-36

N. D. Manring, "Measuring Pump Efficiency: Uncertainty Considerations," *Trans. of ASME, J. of Eng. Res. Tech.,* Vol. 127, 2005, pp. 280-284.

D. McCandlish and R. E. Dorey, "The Mathematical Modelling of Hydrostatic Pumps and Motors," *Proc. Inst. of Mech. Eng.,* Vol. 198B, no. 10, 1984, pp. 165-174.

A. Pourmovahed, "Uncertainty in the Efficiencies of a Hydrostatic Pump/Motor," *ASME paper 92-WA/FPST-9,* 1992, pp. 1-11.

G. Reethof, "Characteristics of Positive-Displacement Pumps and Motors" in J. F. Blackburn, G. Reethof and J. L. Shearer, eds., *Fluid Power Control,* M.I.T. Press, Cambridge, MA, 1960, pp. 90-129.

W. M. J. Schlosser, "Mathematical Model for Displacement Pumps and Motors," *Hydraulic Power Transmission,* 1961, pp. 252-257, 269 and 324-328.

J. Thoma, "Mathematical Models for Displacement Pumps and Motors," *Hydraulic Pneumatic Power*, 1969, pp. 642-651.

J. Watton, "An Explicit Design Approach to Determine the Optimum Steady State Performance of Axial Piston Motor Drives," *Proc. Inst. of Mech. Eng., J. of Systems and Control Engineering,* Vol. 220, Part I, 2006, pp. 131-143.

J. Watton, *Fundamentals of Fluid Power Control,* Cambridge Univ. Press, 2009.

W. E. Wilson, "Rotary-Pump Theory," *Trans of ASME.,* Vol. 68, 1946, pp. 371-384.

W. E. Wilson, *Positive-Displacement Pumps and Fluid Motors,* Sir Issac Pittman and Sons, London, 1950, pp. 100-106.

IC engines and automotive applications

Optimization and energy consumption of Electro-Hydraulic Valve Actuation system through valve event timing range

Mika Herranen, Kalevi Huhtala, Matti Vilenius
Tampere University of Technology, Department of Intelligent Hydraulics and Automation (TUT/IHA).

ABSTRACT

Flexible gas exchange valve actuating systems are developed in order to improve the fuel efficiency and lower emissions of the combustion engines.

The aim of this research is to find out power consumption at different performance values of the flexible electro-hydraulic valvetrain system (EHVA). The dynamic demands are high for the electro-hydraulics in this application. That is why it's challenging task both power consumption and performance of the system point of view. The EHVA system is needed to design according to the highest load and speed situation. Therefore energy consumption and efficiency under normal running conditions may be relatively poor. In this study the energy consumption of certain EHVA system is investigated by means of simulations. Among others, effect of the cylinder pressure load when exhaust valve is opened, return spring rates, and pressure level control are investigated. Then, actuators of the intake and exhaust valves are optimized in order to find out real energy consumption of the hydraulic system.

This research proved that flexibility of the gas exchange valve actuation has costs at energy consumption side. Also other hydraulic solutions should be applied in order to keep the efficiency higher and the energy consumption at lower level.

Keywords: Variable, Electro-Hydraulic, valve, actuation, energy, consumption

1. INTRODUCTION

Different variable valvetrain systems have been developed in order to improve the efficiency and reduce the emissions of the internal combustion engines. Electro-Hydraulic Valve Actuation (EHVA) has certain benefits compared to other electro-mechanical or mechanical variable valve actuation systems, but it also has some demerits. One of them is overall efficiency. Throttled control is wasting plenty of energy, and energy saving systems are complex and expensive (1), (2). EHVA system has to be dimensioned according the highest load condition. When normal working point requires less power, the adaptation of the hydraulic system defines the total efficiency of the system. With proper selection of the hydraulic system and optimization, the power consumption of electro-hydraulic valve actuation can be near or even better than power consumption of conventional, mechanical cam driven system (1), (3), (4), (5). This study concentrates on the power consumption of the electro-hydraulic valvetrain in different working points, and efficiency of the current hydraulic system.

2. STUDIED EHVA SYSTEM

The simplified hydraulic circuit of the studied EHVA system is presented in Figure 1. Both intake and exhaust gas exchange valves have actuator of their own, and they are controlled by individual hydraulic valves. System is position feedback controlled. Actuators are single-acting, only the upper chamber is directed either to pressurized line or to tank line. Lower chamber is connected to constant pressure, which slightly helps pushing the oil out from upper chamber and thus getting the actuator piston away from gas exchange valve mechanism. There is only surface contact between the actuator and gas exchange valves, so the actuator cannot draw gas exchange valves to close direction.
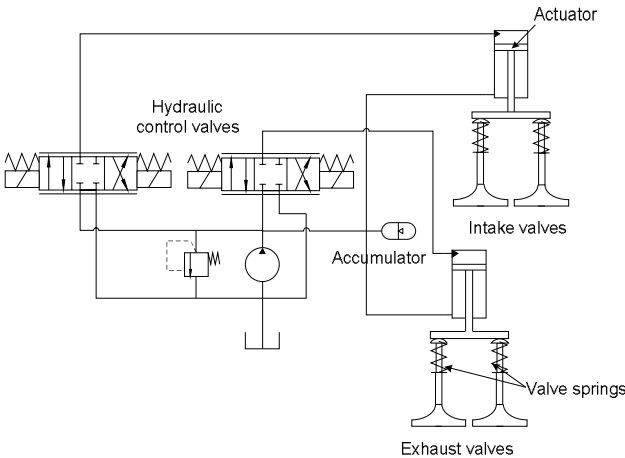
Figure 1 Schematic hydraulic diagram of the EHVA

3. SIMULATION MODEL

Simulation model was made by AMESim simulation program, where the mechanical valvetrain and hydraulic system both were modelled (Figure 2). Cylinder pressure was also modelled into the system in order to get realistic amount of load affecting to the gas exchange valve during the diesel engine run. Cylinder load was fed into simulation model only as a function of crank angle, and therefore the gradient of pressure difference over the gas exchange valves was not driven by the actual gas exchange valve opening. Simple p-control was used as a valve actuation controller, and realistic valve lift curves were fed into the controller.

In simulations, hydraulic efficiency was determined by calculating the relation between hydraulic energy consumption and energy required to open the gas exchange valves. Opening energy was calculated by integrated product of velocity of the actuator and force produced by upper hydraulic chamber, during the opening sequence. Hydraulic energy was calculated by product of hydraulic flow from the pump and corresponding pressure, and integrating that over the opening time. Contrary to previous hydraulic diagram, hydraulic pump used in simulation was constant pressure regulated pump. Closing sequence was not investigated, because closing is assumed generated only by return springs. Energy needed to close the valvetrain is stored to the spring during the opening sequence.
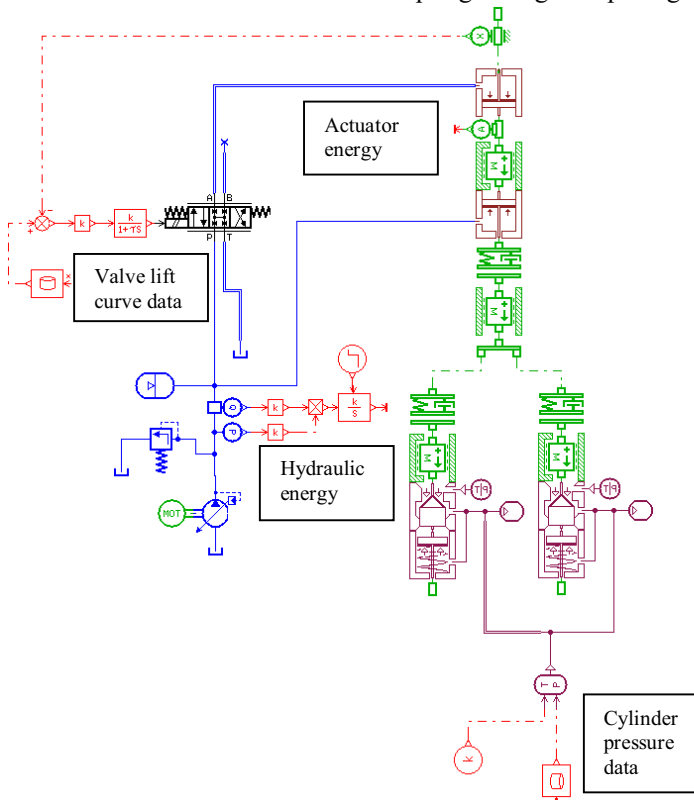
Figure 2 Schematic presentation of the used AMESim simulation model

Cylinder pressure and valve lift data was measured from real engine. Initial simulation main parameters are shown in table 1.

Table 1 Initial simulation parameters

Working pressure	Pipes length	Pipes diameter	Moving mass	Spring constant	Spring pre-tension	Accumul. size	Pump respond time
250 bar	0.2 m	0.01 m	2.9 kg	110 N/mm	3000 N	1 Litre	0.02 s

Investigated parameters were RPM, return spring load rate, and cylinder pressure at the moment of the exhaust valve opening. Difference between feedback-controlled follow the curve-type and rectangular control signal was investigated.

4. SIMULATION RESULTS

4.1 Engine RPM effect to the efficiency
First, effect of the rotational speed of the diesel engine was investigated. Working pressure was kept constant 250 bars, used return springs were k=110N/mm @ pre-tension of 3kN. Cylinder pressure at the opening moment was at maximum investigated level, 14 bars. Even the opening was made faster when higher rotational speed was applied; the efficiency was at the same level (Figure 3). Only exhaust actuator was investigated here.
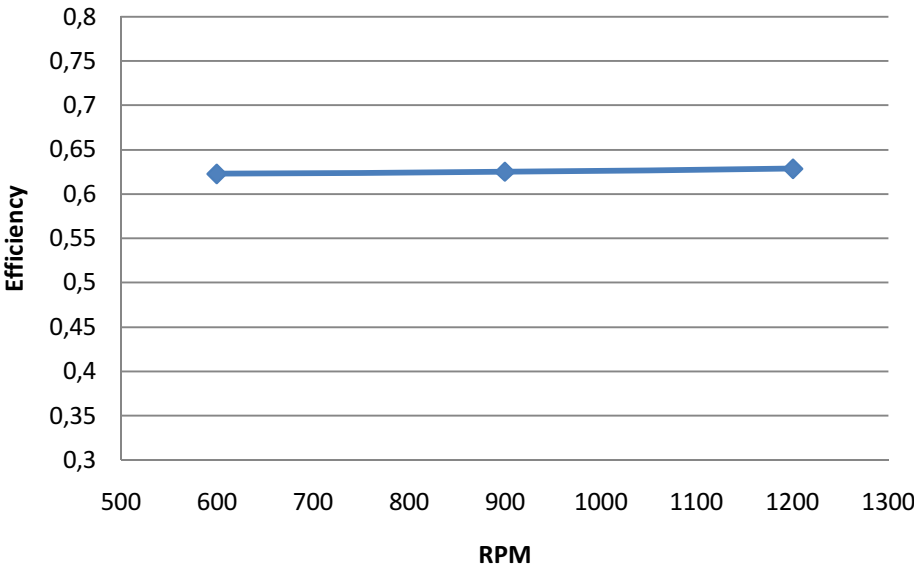
Figure 3 Hydraulic efficiency at different RPM

4.2 Return spring effect to the efficiency and energy consumption

Next, different return springs of the gas exchange valve, were modelled. Investigated spring rates/pre-tensions were 100N/mm @ 3kN pre-tension, 60N/mm @ 1kN pre-tension, and 35N/mm @ 0,5kN pre-tension (which is smallest spring still capable to close the valves within the required time range). Working pressure and opening cylinder pressure were kept constant. With stiffer springs the efficiency is clearly better (Figure 4).
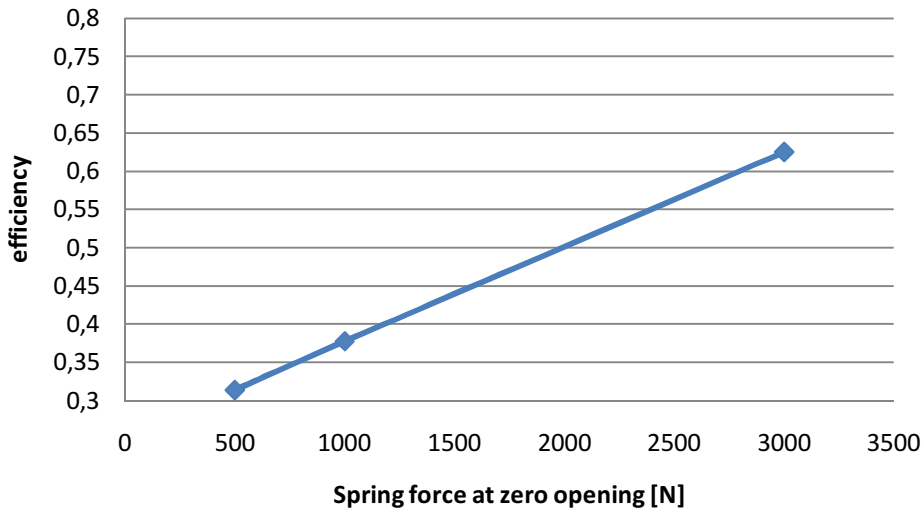
Figure 4 Return spring load effect to the hydraulic efficiency of the actuator

Effect of spring to the energy needed to open the actuator is shown next in Figure 5. With weaker spring, the total energy consumption is clearly lower, if only efficiency has proved to be less too.
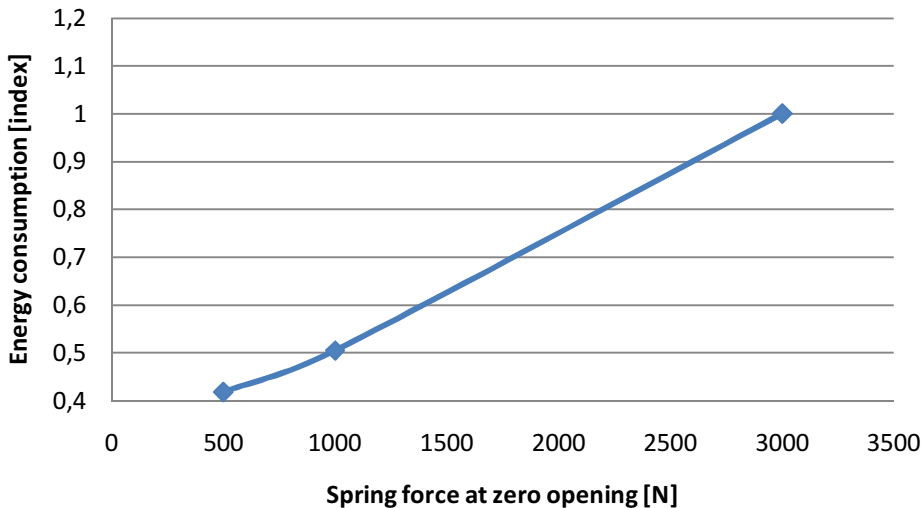
Figure 5 Relative energy consumption of one actuator with different return springs

4.3 Cylinder pressure load effect to the efficiency

Next, the effect of the cylinder pressure at the opening moment of the gas exchange valve was investigated. This corresponded different load conditions of the diesel engine. Investigated opening cylinder pressures were 14 bars, 6 bars, and 1 bar. Working pressure and return springs were constant. Efficiency of this initial condition is shown in Figure 6. Efficiency of the exhaust gas opening rises, when higher cylinder load is applied.

Cylinder load is used as a function of all further investigated parameters, because engine load is the main altering parameter in real environment. Because the EHVA system is needed to design according to highest loading situation, possible controlling parameter would be the working pressure, if the maximum load is not applied. Pressure control is rather easy to apply in normal hydraulic systems. When the working pressure was dropped to lowest possible value where the system can perform the adequate curve tracking, the efficiency can be raised slightly (Figure 6).
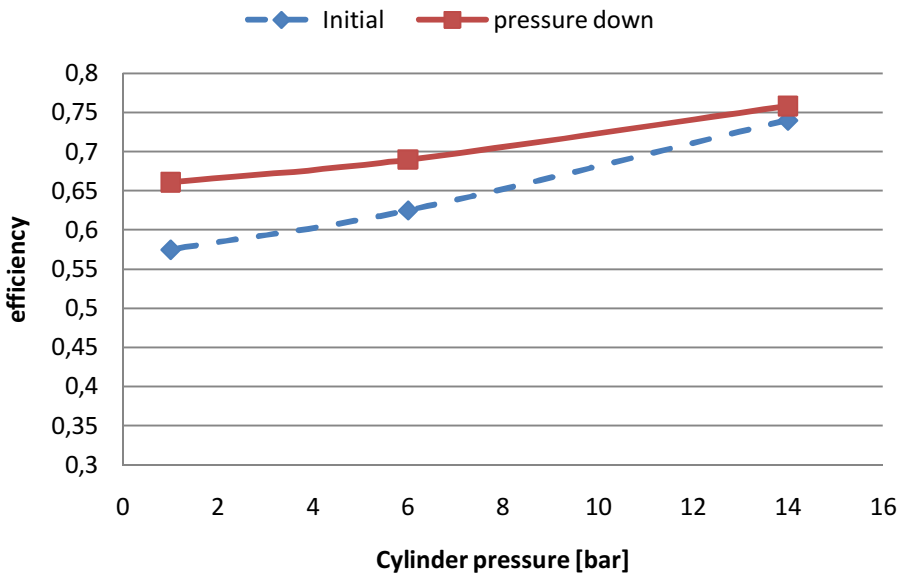
Figure 6 Effect of the working pressure drop to the hydraulic efficiency of the exhaust actuator

4.4 Effect of the raised working pressure and decreased actuator area to the efficiency

When the working pressure is raised to the 350 bars and further to 420 bars, effect of the flow changes was then investigated by changing the effective hydraulic area of the actuator, when the load condition allowed that (in each investigated cylinder pressure point). This is just theoretical point of view, because building of such system could be complex and difficult. With higher 420 bars working pressure, the diameter wasn't able to decrease more when going under 6 bar cylinder pressures. This was due to force required to compress the return spring. The Cylinder gas force is present only at the beginning of the opening, but the effect of the spring force is increasing in the end of the opening.

Efficiency of the hydraulics is at same level than which could be achieved with pressure dropping. More significant difference is found only at highest load case, where about 5% difference is found between highest and lowest working pressure (Figure 7).
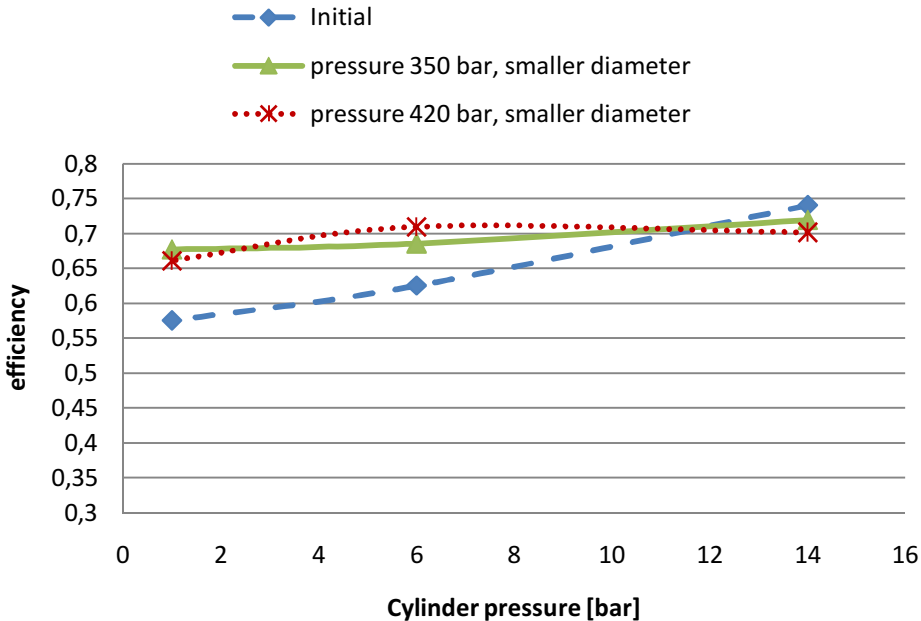
Figure 7 Hydraulic efficiencies of the different working pressures and optimized exhaust actuator areas

4.5 Effect of the opening control to the efficiency and energy consumption
In previous cases opening was controlled by the feedback loop, and the opening curve was purposed to keep close to original opening curve shape. When more freely opening was allowed by giving the controller only rectangular reference command (still with p-control), situation slightly changes. The efficiency of the exhaust actuator is increasing (Figure 8), but at the same time, the total energy consumption also increases (Figure 9). Both has clear reasons; due to throttled control, losses in follow the curve method are higher that rectangular reference method, where throttling is only present in the very beginning and end of the stroke. In rectangular reference method opening is also slightly faster, which means that force is higher due to higher acceleration but also higher cylinder pressure during the opening. Like said earlier, the cylinder pressure was not acting fully realistic, because in the simulations it was not driven by actual opening area of the gas exchange valve, and therefore rectangular opening was done against higher load than in follow the curve case. In Figure 9 is shown the energy requirement of the exhaust actuator, as an index. Actuator energy consumption with initial parameters against highest cylinder load was marked as value "1", and other values were compared to that.
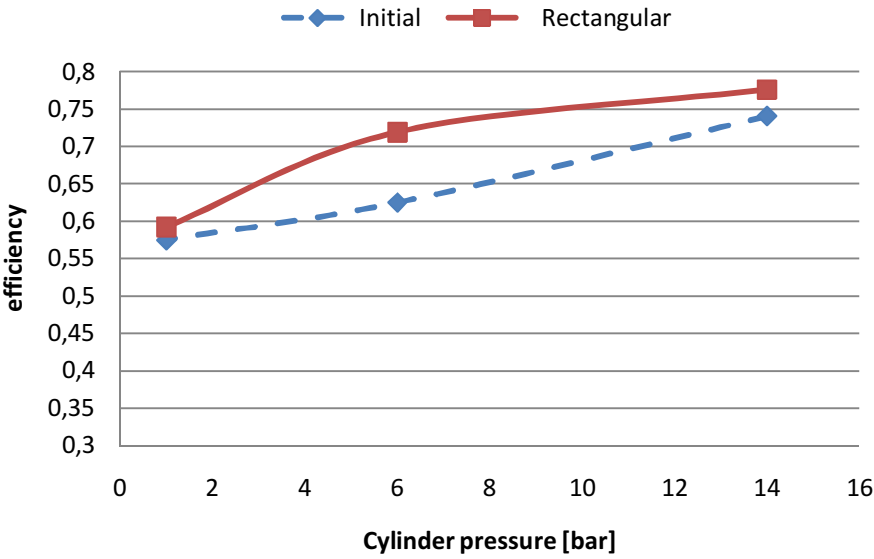
Figure 8 Exhaust actuator hydraulic efficiencies of the different controlling methods
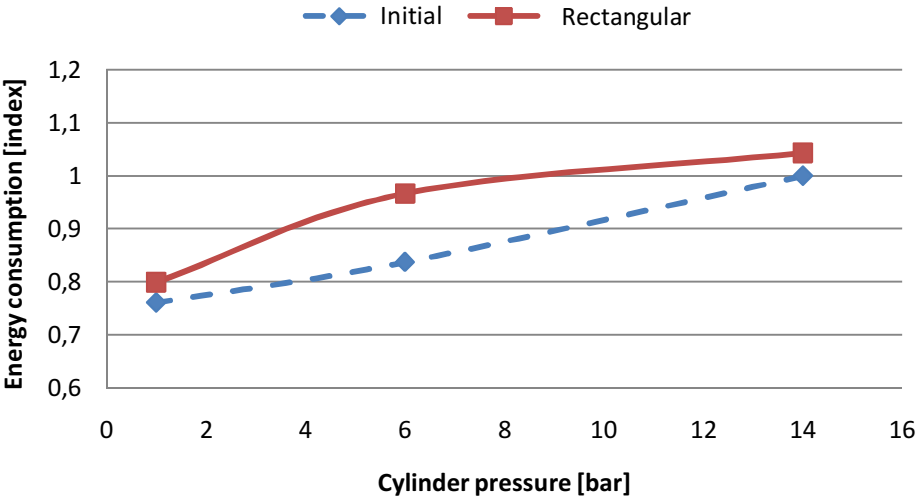
Figure 9 Relative exhaust actuator energy consumption

4.5 Energy consumption

Efficiency of the hydraulic system is important issue, but like shown before, efficiency and energy consumption are not necessarily acting same way. An interesting information is also total the energy consumption of the different working points, and corresponding energy outtake of the hydraulic pump. This defines the energy consumption of the whole valve valvetrain system in engine level (i.e. how much energy is needed to use from engine output to actuate the gas exchange valves). Hydraulic circuit has big influence to the energy consumption (2), (6), but also effect of the environment variables and design parameters were explored here. In Figure 10 is shown relative energy consumption of the exhaust valve only, when previously presented parameters are investigated as a function of opening cylinder pressure. In addition, effect of dropping the working pressure with about 15% larger diameter of the both actuators is also included. The results show that there is no big difference which kind of "optimization" method is used; energy needs from the pump (and from the engine) are close each other in each load conditions.
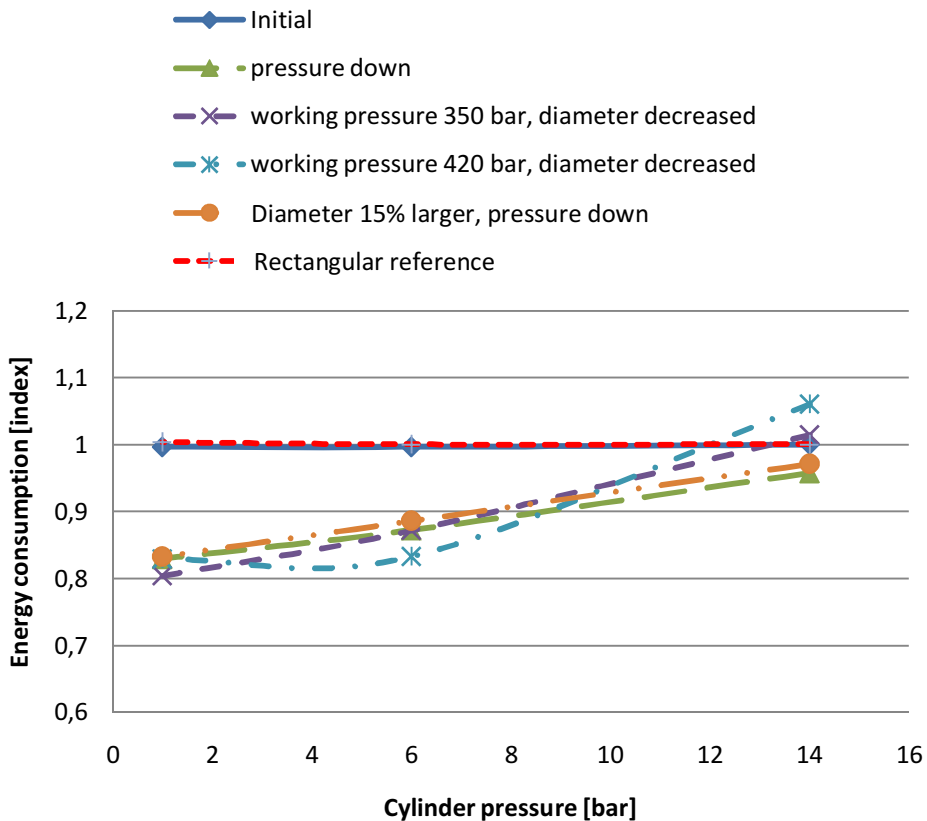
Figure 10 Relative hydraulic energy required to actuate the gas exchange valve

4.6 Optimized valvetrain

In optimized valvetrain, first the diameters of the actuators were decreased as small as possible. Because the exhaust actuator had to overtake largest the force, was the actuator area already optimized in initialization design process when the working pressure was set to 240 bars. The intake actuator diameter could be decreased about 10 %, due to lack of the cylinder pressure in the moment of the intake valve opening. This will lead to some decrease of the energy requirement from the hydraulic pump. Relative energy consumption when both actuators were included in simulation model is shown in Figure 11. Index value 1 was same working point as before. Second, by dropping the working pressure, some improvement in efficiency was achieved. Results of the dropped pressure are shown in same graph. Third, the rectangular reference is applied.
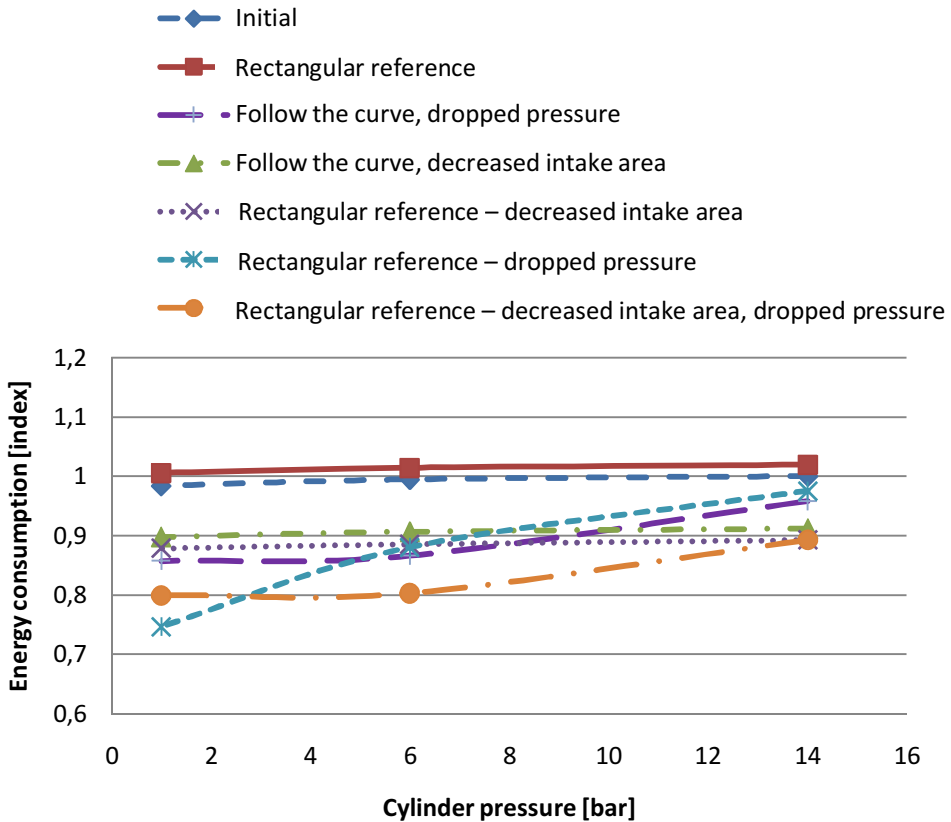
Figure 11 Relative total hydraulic energy consumption, different control and optimization methods

Optimized intake area is giving about 10% dropping of the energy consumption, but with pressure dropping and rectangular reference, decrease could be up to 20% in lower load cases. The rectangular reference with dropped pressure gave better results, because only thing that matters was getting the valves open during certain time range. Follow the curve method needed more pressure reserves due the extra throttling during the movement. Rectangular reference with dropped working pressure reached its limits in middle of the

cylinder pressure range; because pressure couldn't be dropped lower due to high spring loads. In follow the curve method, if both pressure and intake area were decreased, required curve tracking was not possible.

Due the nature of the cylinder pressure force, highest force was needed in the beginning of the opening. When the exhaust valve opens, the pressure difference over the gas exchange valve rapidly drops, and the required force will be smaller. This leaded to use the idea where the actuator would have two-staged pressurized area (7). After the cylinder pressure was dropped, only smaller actuator area was activated, and flow to the actuator was thus decreased during the end of the stroke. 2-staged area could be utilized only to the exhaust actuator, because the force variation during the stroke is more or less opposite (due to spring force) with intake valve. The 2-stage method gives approximately 20% decrease of the energy consumption, and gives overall best results through the cylinder load range (Figure 12). The rectangular reference with the 2-stage area gives no improvement.
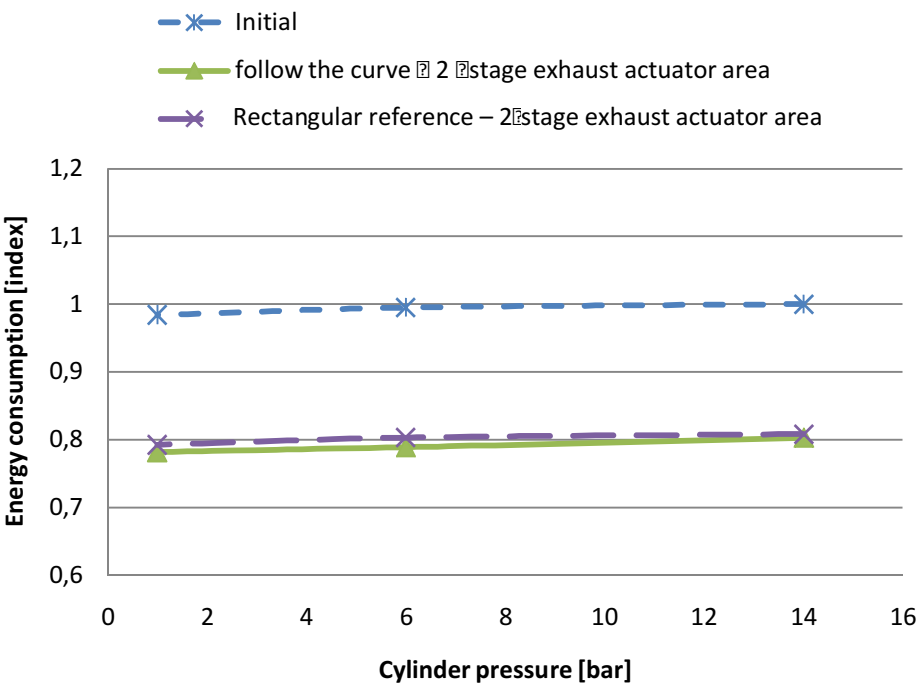
Figure 12 Relative total energy consumption, 2-stage exhaust actuator area

5. DISCUSSION

Better hydraulic efficiency levels in case where the higher load was present (either due to return spring or cylinder load) was probably achieved because the pump was taking nearly constant energy in every case, but in higher loads, actuator opening needed more pressure and thus more energy. Hydraulic efficiency was thus relatively better with higher loads because less throttling was needed.

With pressure adjustment, the hydraulic efficiency was improved. This was also due to constant pressure pump, which worked this way closer to actual pressure level required by the actuator in lower load conditions. Efficiency was still dropped when going to the lower loads, for same reason than explained above. The pressure control is easy and commonly used technique in hydraulics, and would be recommended to use in future applications. If the working pressure was raised and diameter of the actuator was correspondingly decreased, nearly similar efficiency of the system was achieved, independent on what the pressure level was. Thus required flow was smaller with higher pressures (and flow resistances lower), but evidently effect of the pumping losses and the fluid compressibility countered that. At highest working pressure point, some difference was found, probably due to fluid compressibility and leakages. Also larger constant actuator area was tested with working pressure droppings, and results in energy consumption were similar.

The rectangular reference control, when higher pressure was required in the actuator (highest cylinder load), had better efficiency than the throttle control method. Reason for this was, like judged before, smaller losses over the control valve. If total energy consumption was taken as a main goal, things were slightly changed. Even the rectangular reference control had better efficiency; it also consumed more energy than the follow the curve based control. This was directly due to faster movement of the actuator against higher pressure load. In real life the difference could be slightly smaller, now the cylinder pressure was not totally realistic in every working point.

In energy consumption point of view was almost just the same, what kind of parameter modification was used; was the only working pressure dropped, or was working pressure raised and actuator diameter (flow) at the same time dropped. Energy saving could be achieved with all methods, if only the effect would be better when load conditions were lower, which comes directly from better efficiencies compared to unmodified situation.

The rectangular reference method could drop the overall energy consumption only when used with other methods, otherwise the energy consumption was worse than trajectory control. One reason for this could be that now both actuators were opened very closely, and therefore pressure in the pump dropped more than acting single actuator. Pressure behaviour is dependent on the hydraulic system, and when the energy consumption was calculated from the pressure and flow values, this working point gave better efficiency.

The return spring had remarkable effect to energy consumption. With stiffer springs more energy is stored in the spring compression, but closing required only part of that energy. Any additional energy was thus wasted in closing, which was not seen in efficiency when only opening was investigated. The effect was seen in total energy consumption. This would be worth to investigate closer in future, if the spring could be replaced by hydraulic return for instance.

In optimization, the total energy consumption was investigated. Because smaller forces were affecting to the intake valve, was the actuator area possible to be decreased. This reduced of course the flow demand from the hydraulic pump. Also the working pressure dropping had clear effect, like showed earlier with the exhaust actuator. Variable effective area of the exhaust actuator was giving also good results, but this kind of system didn't allow decreasing the working pressure any more.

6. CONCLUSIONS

The efficiency of the EHVA hydraulic system is not most important issue, if the matter is considered in engine total efficiency point of view. Certain modification can improve the hydraulic efficiency, but increase of the overall power consumption may counter the benefit. In that case the total power consumption of EHVA has significance. Simulations showed that up to 20% energy decrease could be achieved by hydro-mechanical and control solutions. The working pressure can be adjusted according the load conditions, or the active pressurized area can be changed. The rectangular reference control may give better efficiency, but the total energy consumption had no big difference to the trajectory curve control. With re-design of whole hydraulic circuit and method to control actuators, even better results would be able to achieve.

References

(1) Zheng (David) Lou, Camless Variable Valve Actuation Designs with Two-Spring Pendulum and Electrohydraulic Latching. SAE 2007-01-1295. Warrendale, U.S.A.

(2) Mika Herranen, Kalevi Huhtala, Matti Vilenius. The Energy Balance of Electro-hydraulic Linear Actuation System. Proceedings of the International Conference on Power Engineering-09 (ICOPE-09). 2000. Kobe, Japan.

(3) Christopher W. Turner, Guy R. Babbitt, Christopher S. Balton, Miguel A. Raimao, Daniel D. Giordano. Design and Control of a Two-stage Electro-hydraulic Valve Actuation System. SAE 2004-01-1265. Warrendale, U.S.A.

(4) J.H.Lumkes Jr, W.van Doorn IV, J.Donaldson. The Design and simulation of high force low power actuation system for camless engine. Proceedings of IMECE2005. Orlando, Florida USA.

(5) William de Ojeda, Jorge Fernández. Hydraulic Needle Valve Actuator and its Application to a Camless Engine. Proceedings of IMECE'03. Washington, D.C. USA.

(6) Mika Herranen, Kalevi Huhtala, Matti Vilenius. The Electro-Hydraulic Valve Actuation (EHVA) for Medium Speed Diesel Engines – Development Steps with Simulations and Measurements. SAE 2007-01-1289. Warrendale, USA.

(7) Pat. US 5595148A, Hydraulic Valve Control Device. Daimler Benz AG, Stuttgart, Germany. Appl. 588768, 19.1.1996 (21.1.1997).

Design, virtual prototyping and test of a regenerative shock absorber for race cars

J-Charles MARE* and Paul-Etienne BERTHE**
* Université de Toulouse; INSA, UPS; Institut Clément Ader
135, avenue de Rangueil, F-31077 Toulouse, France
jean-charles.mare@insa-toulouse.fr
** PKM Consulting, Parc d'activités de Signes, 22 av. de Madrid, F-83870 Signes, France
paul.etienne.berthe@pkm-consulting.com

ABSTRACT

This communication deals with energy regenerative damping. A two quadrants electro-hydrostatic damper is designed, simulated, manufactured and tested. The proposed damper involves a single rod linear jack, a charging accumulator, a manifold block with four check valves mounted as a full hydraulic rectifier and a hydraulic motor connected to an electrical generator. The proposed top level modelling is performed in order to point out in a simple and efficient way the contribution of both functional and parasitic effects such as inertia, friction, valves cracking pressure and flow rate pressure gradient. On basis these results, the initial design is modified to reduce the motor flow and to admit more conventional components for the demonstrator. A design exploration is run for the components sizing with special consideration to off-the-shelf references. Then, a virtual prototype is built within the LMS-AMESim simulation environment to verify the preliminary design and to assess the damper transient behaviour. Finally, the experimental results measured from the individual test of the first prototype are displayed and analyzed.

Keywords: damper, energy, race cars, regenerative, shock absorber

1. INTRODUCTION

Towards the quest for increased performance, car racing competitors often respond by introducing significant concepts or technological step changes that generally propagate to the public market after a few years of maturation and cost reduction. Although it is not directly driven by more environment-friendly considerations, energy saving appears in car racing as a key driver for performance improvement. Energy saving concepts for road applications are generally based on hybrid power transmissions that allow regenerative braking, e.g. (1)(2). Even if the idea of recovering energy from the road excitation at the suspension level is not new (3), no significant track of practical developments and testing has been found in the scientific literature. The present communication deals with the

design, the simulation and the testing of a new concept of regenerative suspension. The so-called Powershock-SG2E technology associates a hydraulic cylinder, a hydraulic manifold and a hydraulic motor that drives in a constant direction of rotation an electrical generator. This project has been introduced by the PKM consulting company with support of Institut Clément Ader – INSA Toulouse for modelling and simulation. It has been partly funded in 2009 by the French Research Agency (ANR) and awarded as the best technological innovation of year 2010 at the Birmingham Autosport show.

The first part of the communication is dedicated to the description of the regenerative shock absorber as well as the top level modelling, in order to point out in an analytical way the key parameters and the influence of the major parasitic effects. The second part deals with the system level simulation of the regenerative shock absorber that has been used to support and improve the design. In the last part, experimental results are presented and discussed. The parasitic effects are quantified and identified to update the regenerative suspension model, to steer the development of specifically designed components and to allow future car level simulation before real testing.

2. REGENERATIVE SHOCK ABSORBER

The potential interest of an energy regenerative suspension can be illustrated by Figure 1. It displays the time history of the instant power dissipated in a shock absorber that has been calculated form data collected during a 4 minutes off-road run. The dissipated energy is really not negligible as it represents 105 % of the energy spent for engine ignition and injection or 83 % of the energy spent for lights. It must be kept in mind that a demand of 100 W electrical power increases the consumption of a conventional car by typically 0.15 litre per 100 kilometres.
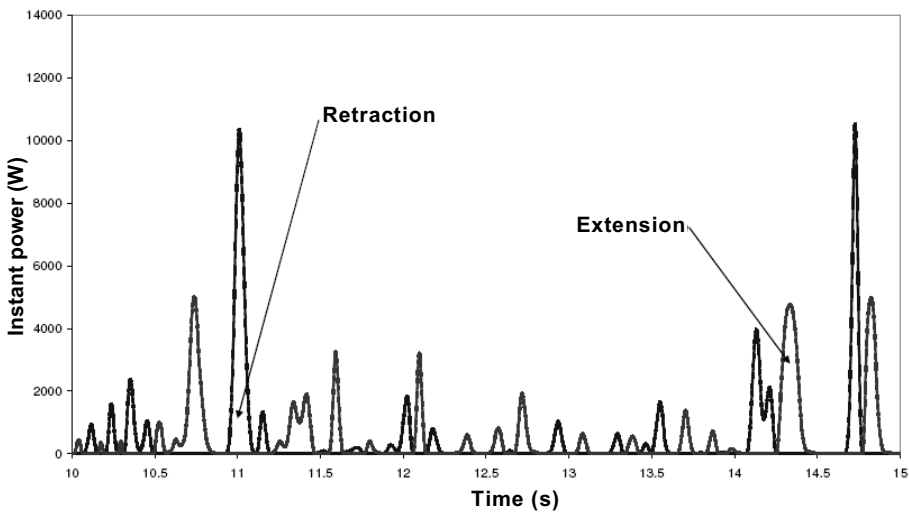
Figure 1. Instant power dissipated in a shock absorber

2.1. Principle of operation

The development of the Powershock regenerative suspension is based on the architecture depicted by Figure 2.
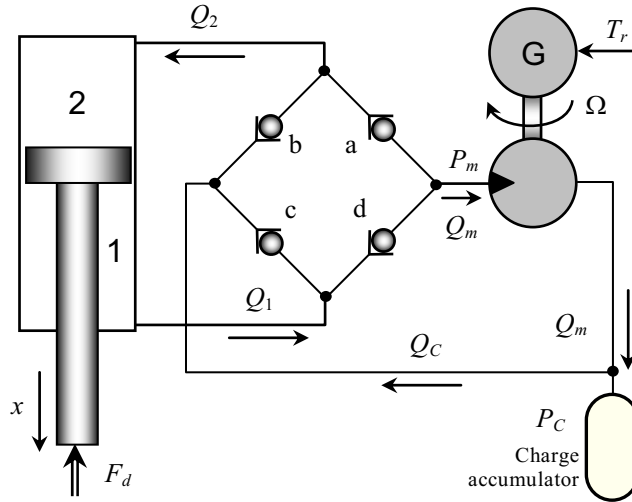
Figure 2. Principle of the regenerative Powershock damper

The regenerative suspension design involves a single rod hydraulic cylinder and a charge accumulator that are quite identical to those used in conventional passive dampers. The accumulator fulfils four important functions such as

-   charging the cylinder chambers to avoid air release or cavitation,
-   allowing the fluid volume to change versus temperature,
-   compensating for small external leakages,
-   compensating for the change of the geometrical volume offered by the cylinder to the fluid versus the rod retraction.

In the regenerative design, the hydraulic cylinder is used ideally as a hydro-mechanical power transformer from the road excitation to a constant displacement hydraulic motor that drives an electrical generator. Four check valves are associated as a full bridge to make a rectifier function, forcing the fluid to flow in the same direction through the motor-generator, whatever the alternating displacement of the cylinder rod. In such a way, there is neither speed reversal nor associated unacceptable inertia torques introduced by the motor-generator. In the retraction phase, the extended chamber 1 is re-fed by the charge accumulator through the valve c while the compressed chamber 2 feeds the hydraulic motor through valve a. Valves b and d remain closed. In the extension phase, the extended chamber 2 is re-fed by the accumulator through the valve b while the compressed chamber 1 feeds the hydraulic motor through valve d. Valves a and c remain closed. The damping function is achieved by controlling the load created by the electrical generator onto the cylinder through a dedicated power electronics that is out of scope of the present study. The resistant electromagnetic torque demanded by the electrical generator is considered as the regenerative damping signal.

2.2. Modelling

The potential parasitic effects are identified to be the check valves cracking pressure and flow rate pressure gradient, the friction and the inertia of the rotating assembly and the hydraulic motor internal leakage. The top level modelling and analysis is conducted in order to point out the contribution of the design parameters and the potential parasitic effects on the damping characteristic. The hydro-mechanical part of the regenerative shock absorber is modelled accordingly by the following set of equations. As oil compressibility only introduces high dynamics effects, it is not considered for the top level analytical modelling. The bandwidth to be reproduced by simulation is limited to a few hertz.

- Continuity applied to chambers 1 and 2

$$Q_1 = S_1 \frac{dx}{dt} \tag{1}$$

$$Q_2 = S_2 \frac{dx}{dt} \tag{2}$$

- Continuity applied to hydraulic motor

$$Q_m - Q_l = D\Omega \tag{3}$$

- Hydraulic motor internal leakage (laminar flow assumed)

$$Q_l = a(P_m - P_C) \tag{4}$$

- Charge accumulator (polytrophic evolution of the gas)

$$P_C V_g^k = \text{constant} \quad \text{with} \quad V_g = V_{g0} - \int (Q_m - Q_C) dt \tag{5}$$

- Newton second law applied to the rotating assembly

$$J \frac{d\Omega}{dt} = \Delta P_m D - T_f - T_r \quad \text{with} \quad \Delta P_m = P_m - P_C \tag{6}$$

- If only stiction and viscous friction are considered, then

$$T_f = T_C + f\Omega \tag{7}$$

- Flow rectifier

$$Q_a = G_a (P_2 - P_m) \tag{8}$$

$$Q_b = G_b (P_C - P_2) \tag{9}$$

$$Q_c = G_c (P_C - P_1) \tag{10}$$

$$Q_d = G_d (P_1 - P_m) \tag{11}$$

- Damper force (rod and piston masses neglected)

$$F_d = S_2 P_2 - S_1 P_1 - F_{fd} \tag{12}$$

2.3. Top level analysis

The following developments will be conducted in the <u>particular case of extension</u> (however, they can be easily modified to apply to the retraction case).

In order to get analytical results as far as possible, it is proposed to study the damper force in static then in constant extension rate conditions (4). In this attempt, it is interesting to re-write equation (12) as

$$F_d = (S_2 - S_1)P_2 - S_1(P_1 - P_2) - F_{fd} \tag{13}$$

and to remark that perfect check valves would lead to:

$$P_2 = P_C \quad Q_m = Q_1 \quad \text{and} \quad Q_C = Q_2 \tag{14}$$

making

$$V_g = V_{g0} + (S_2 - S_1)x \tag{15}$$

After combination with equation (5), the first term of the right hand side in equation (13) becomes

$$(S_2 - S_1)P_2 = \frac{(S_2 - S_1)P_{C0}}{\left[1 + \dfrac{(S_2 - S_1)}{V_{g0}} x\right]^k} \tag{16}$$

This first term represents the parasitic elastic effect introduced by the charging function. This effect already exists in conventional mono-tube or bi-tube passive dampers.

The check valves of the flow rectifier can be modelled in a more realistic and simple way combining their cracking pressure P_o and their flow rate pressure gradient K_{QP} as follows. When the check valves are fully opened, they operate as fixed orifices. In this case, equation 17 is to be considered as a quasi linearized model of the valve allowing formal calculations:

$$\text{For } i = a...d \quad Q_{vi} = K_{QP}(\Delta P_{vi} - P_o).(\Delta P_{vi} > P_o) \tag{17}$$

Under these considerations, equation (16) should be modified replacing equation (14) by equation (17) for valve b. This would point out a parasitic coupling with the rod velocity.

Considering the check valves model equation (17), the second term of the right hand side in equation (13) can be expressed as

$$S_1(P_1 - P_2) = \frac{K}{(1+\tau s)}T_r + \left[\frac{M's+f'}{(1+\tau s)} + f''\right]\dot{x} + \left[\frac{K}{(1+\tau s)}T_C + 2S_1 P_o\right] \tag{18}$$

This clearly points out the functional and parasitic effects influencing the damping function:

$$- \quad K = \frac{S_1}{D(1 + af/S_1^2)} \approx S_1/D \tag{19}$$

is the functional torque/force gain for the control of regenerative damping. This functional effect is clearly made by this first term of the right hand side of equation (18): controlling the resistant electromagnetic torque of the electrical generator as a proper function of extension speed creates the required damping effect. The high bandwidth of electromagnetic torque control should not introduce any phase lag between the demanded and the current value of the resistant electromagnetic torque that could alter the damping/regenerative function.

$$- \quad \tau = \frac{aJ}{D^2 + af} \approx \frac{aJ}{D^2} \tag{20}$$

is the parasitic time constant due to the coupling between the rotating inertia and viscous friction.

$$- \quad M' = \frac{JS_1^2}{D^2 + af} \approx \frac{JS_1^2}{D^2} \tag{21}$$

is the parasitic mass reflected by the rotor inertia J at the damper rod level.

$$- \quad f' = \frac{fS_1^2}{D^2 + af} \approx \frac{fS_1^2}{D^2} \tag{22}$$

is the parasitic viscous friction coefficient reflected by the rotor viscous friction f at the damper rod level.

$$- \quad f'' = \frac{2S_1(S_1 + S_2)}{K_{QP}} \tag{23}$$

is the parasitic viscous friction coefficient reflected by the check valve flow rate pressure gradient K_{QP} at the rod level.

The last factor of the right hand side of equation (18) models the parasitic damper forces that are introduced by the Coulomb friction torque T_C of the rotating assembly and the valves cracking pressure P_o. If the time constant effect is forgotten, these terms produce the same effect as a pure Coulomb friction force acting between the damper cylinder and rod, introducing apparent stiction.

From these results, the proposed formal analysis indicates clearly (quantitatively and physically) the contribution of the different parasitic effects induced by the regenerative components. As it could have been predicted, Coulomb and reference torque at the rotating assembly level are reflected at the damper rod level with a factor equal to the transformation ratio S_1/D. In the same manner the inertia and viscous effects (J and f) are reflected with a factor equal to the squared transformation ratio. It is reminded that the same development can be applied to the retraction case without any difficulty.

2.4. Assessment of parasitic effects and design improvement

The typical application of the regenerative damper concerns race and all terrain cars. The analysis of the data collected as for Figure 1 clearly indicates that the mean retraction/extension rate is typically 200 mm/s although the instantaneous rate reaches 4 m/s very occasionally. For this reason, it is not necessary to design the regenerative system for rates greater than 1 m/s that would oversize the design and magnify the parasitic effects due to inertia or friction. For these high velocities, the damping function will be ensured by passive pressure relief valves connecting the cylinder chambers as in conventional dampers. So, the cylinder rod and piston diameters have been kept identical to current shock absorbers. As an order of magnitude, the typical damping effect to be produced below 1 m/s is 3100 Ns/m in the retraction mode and 3900 Ns/m in the extension mode. The asymmetry of the damping characteristic is moderate.

The motor/generator assembly has to be selected in order to minimize the reflected mass, viscous and Coulomb effects while admitting the range of angular velocity in response to the flow delivered by the cylinder. These two constraints are opposed: lowering velocity requires higher displacements that lead to increased size. This is certainly one of the main issues for the industrial development of such a regenerative damper.

From the steady state model, it has been shown that the large hydrostatic area of the piston generates high flows in the compression mode under high compression rates. This forces the motor-generator rotor to operate under overspeed conditions. For this reason, it has been proposed to modify the design, allowing the large chamber to re-fed the rod side chamber in compression mode, as illustrated by Figure 3. In such a way the flow passing through the hydraulic motor is reduced to the same range for both extension and retraction phases.
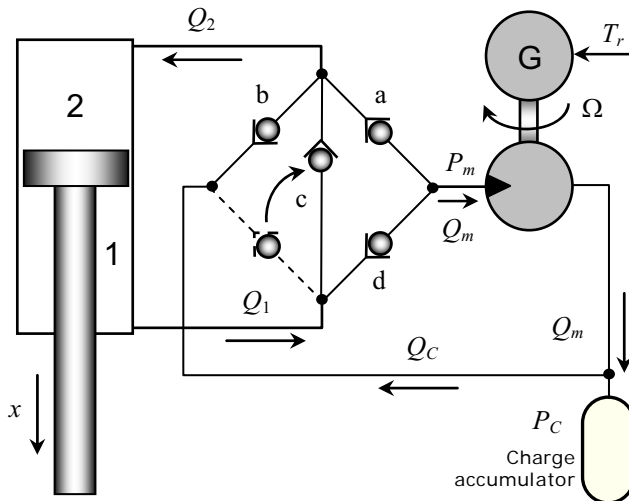

Figure 3. Modified hydraulic layout of the regenerative damper

A simple design exploration has been implemented for the steady state model, varying:
- the maximal service pressure of the cylinder and the hydraulic motor (175 bar for conventional components or 350 bar for high performance components with reference to aerospace products),
- the hydraulic motor displacement (standard 3.5 cm³/rev or 6.6 cm³ rev, aerospace 2 cm³/rev),
- the maximal operating extension / retraction rate in regenerative mode (1, 2 or 4 m/s)

to make 12 candidate designs as the standard motors can not operate over 175 bar. These choices allow making a demonstrator from industrial components as a first step.

The cylinder rod and piston diameters have been determined from the maximal service pressure (175 or 350 bar) and the maximal damping force to be generated under the maximal velocity. The motor/generator maximal speeds in retraction and extension modes have been calculated accordingly in order to verify that they were lying within the admitted operating domain. Only 5 designs were found to be acceptable. No design coped with the 4 m/s maximal rate of extension/retraction.

The parasitic effects due to motor inertia, viscous friction and Coulomb friction have been estimated, as summarized on Table 1.

Table 1. Reflected effects from design choices
(values are given for retraction then for extension)

Design \ Reflected effect	Mass (kg)	Viscous friction (Ns/m)	Coulomb friction (N)
175 bar, 3.5 cm³/rev, 1 m/s	7.9/12	242/366	33/41
<u>175 bar, 6.6 cm³/rev, 1 m/s</u>	<u>2.2/3.2</u>	128/194	35/43
175 bar, 2 cm³/rev, 1 m/s	24/36	237/359	116/142
350 bar*, 3.5 cm³/rev, 1 m/s	5.9/8.9	58/87	57/70
350 bar*, 6.6 cm³/rev, 1 m/s	29/34	288/331	127/137

* the common service pressure of shock absorbers is about 200 bar.

The more attractive combination comes from line 2. The reflected mass is reduced (the motor inertia is identical for 3.5 cm³/rev and the 6.6 cm³/rev references) while the motor is quite a standard one. The design of line 4 presents a reduced reflected viscous friction but the motor should be derived from aerospace products and the cylinder rod diameter is not consistent with buckling issues. For the selected design of line 2, the equivalent viscous effect is to be compared with the damping effect to be produced that is typically in the range 3000 / 5500 Ns/m: the parasitic effect represents less than 6% of the desired effect to be produced by energy regeneration.

3. VIRTUAL PROTOTYPE

The virtual prototype of the regenerative damper has been developed within the LMS-AMESim® simulation environment.

To start with, a fully passive damper has been modelled as a reference. The static hydraulic characteristic of the extension and retraction damping valves have been identified from the measured damping force. This latest, got from a dedicated test-bench, has been represented as a specific third order polynomial of the rod speed, eq (24), for each retraction and extension phases:

$$F_{se} = c_1 \dot{x}_e + c_2 \dot{x}_e^2 + c_3 \dot{x}_e^3 \tag{24}$$

The corresponding static hydraulic characteristics of the extension and retraction damping valves have been identified through a curve fitting process to get a simple but realistic model in the general form of equation (25). When a null flow is forced at null pressure drop, the mean modelling error remains as low as 0.3 % of the full flow range.

$$Q_v = c_3 |\Delta P_v|^{c_4} \operatorname{sgn}(\Delta P_v) \tag{25}$$

The regenerative damper model is displayed on Figure 4 (shown for the initial design). The regenerative damping control law establishes the electromagnetic torque setpoint as a function of the measured extension rate, according to the identified damping force F_{de} of the reference damper.
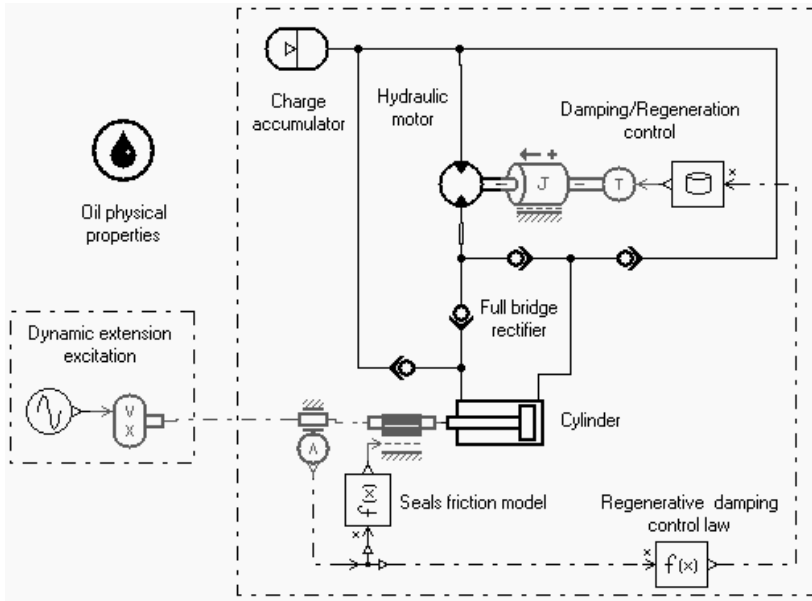

Figure 4. Virtual test bench of the regenerative shock absorber

The model parameters are taken as far as possible form the components datasheets of the first prototype. The pump used for the prototype has a displacement of 3.5 cm^3/rev. Even if both pump and electrical generator are not closely adapted to the need, using such off-the-shelf components provides a rapid concept proof and experimental data for model and component improvements.

The virtual prototype of the regenerative damper has been used to assess the parasitic effects that were introduced individually from the perfect regenerative components. The model has been build as far as possible form standard components of the AMESim software library where the hydraulic capacitance of the cylinder is taken into consideration but not the motor one. In order to avoid any algebraic loop, it was then necessary to introduce a compressible line model between the hydraulic rectifier and the motor inlet. However, when the additional hydraulic capacitance is set to realistic values, it does not influence the shock absorber behaviour in the usual frequency range. The main results obtained form the virtual testing can be summarized as follows:

- Real check valves. As predicted by the top level steady state model, the valves cracking pressure has a very little influence on the damping characteristic. It is also confirmed that the flow rate pressure gradient produces an equivalent viscous friction effect as predicted by the analytical model. Even for very large flows coming from high retraction/extension rates, the parasitic viscous force due to K_{QP} can be easily kept below 10% of the damping force to be produced with a reasonable and realistic rated valve area.

- Friction of the rotating assembly. It was confirmed that viscous friction of the rotating assembly is a main contributor for parasitic effects. As predicted by the analytical model, viscous friction is directly reflected at rod level through the squared value of the transformation ratio. Realistic values of equivalent viscous friction at rotating assembly can induce significant parasitic effects. The hydraulic motor used for the demonstrator was modified in order to cope with the charge pressure level. Low friction shaft seals were mounted, showing a significant reduction in the friction level.

- Inertia of the rotating assembly. The inertia effects have been introduced in three steps (a - without inertia, b - with the motor inertia but without the alternator inertia, c – with all inertia considered) while the value of the assembly friction was kept at the realistic value of 0.002 Nm/rpm. The reflected inertia effect is perceptible (phase lag effects in the force/velocity plot) only when the alternator inertia is considered. It appears that the reflected inertia effect is really an issue that must be addressed by developing a specific hydraulic motor / electric generator with a design to inertia and design to integration view.

4. DEMONSTRATOR AND TESTS

A first prototype, based on the architecture of Figure 2 has been manufactured, integrated and tested. The prototype has a piston diameter of 44 mm, a rod diameter of 22 mm and a total stroke of 200 mm. Two views are given on Figure 5. The hydraulic motor and the

electrical generator are located on the left of the right image while the charge accumulator is visible on the right. In order to clearly identify the individual contribution of all component parasitic effects, the tests were run in a step-by-step way.
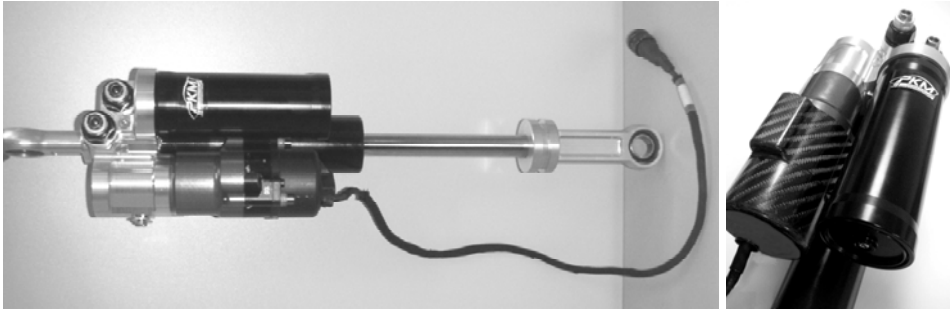

Figure 5. Images of the first prototype of the regenerative damper

The step 1 aims at measuring the behaviour of the reference damper with a proper setting of the damping valves.

The step 2 aims at characterising the regenerative damper without alternator and with the final setting of the damping valves creating a motor bypass at high pressure differences. This allows identifying the effects of the check valves, the motor inertia, internal leakage and friction.

In the step 3, the alternator is mounted but not connected electrically. Only the alternator inertia and friction are added from step 2.

In the last step 4, the alternator is loaded by one or two lights that produce a nominal resistive load of 55 and 110 W respectively. Even if the load power is only 17% of the maximal power that can be generated by the alternator, this way was found as efficient to start with the demonstration without needing depth studies of the controller and the associated power electronics.

The main results are summarised on Figure 6. The experiments are run for a sine wave type retraction with 35 mm mean and 60 mm peak to peak magnitude, up to 0.56 m/s. The reference damping characteristic is measured setting all the original damping orifices as fully opened and without alternator (label "fully opened – no alternator"). Then the damper variable orifices are set closed in order to activate the regenerative operation without alternator (label "no alternator"). Finally, the damping characteristics are plotted with a connected alternator for null, 55W and 110 W resistive loads.

For this first prototype assembled with off-the-shelf components, the parasitic damping of the regenerative assembly is not negligible, up to twice the fully opened damping factor. However, when passing from a null load to a 55W load, the change of the damping characteristic is clear and very significant (up to + 80%). There is no significant change in the damping characteristic when the load goes from 55 to 110 W. A Stribeck like effect can be observed around 100 mm/s, being probably representative of the breakaway point of the rotating assembly (no changes below 100 mm/s).

These first experimental results have been obtained in a short time to demonstrate the energy regenerative concept. It is obvious that further development will require special design of hydraulic motors and electrical generators in order to lower the contribution of the parasitic effects. Combining the modified architecture of Figure 3 and high pressure operation is also an attractive way of improvement.
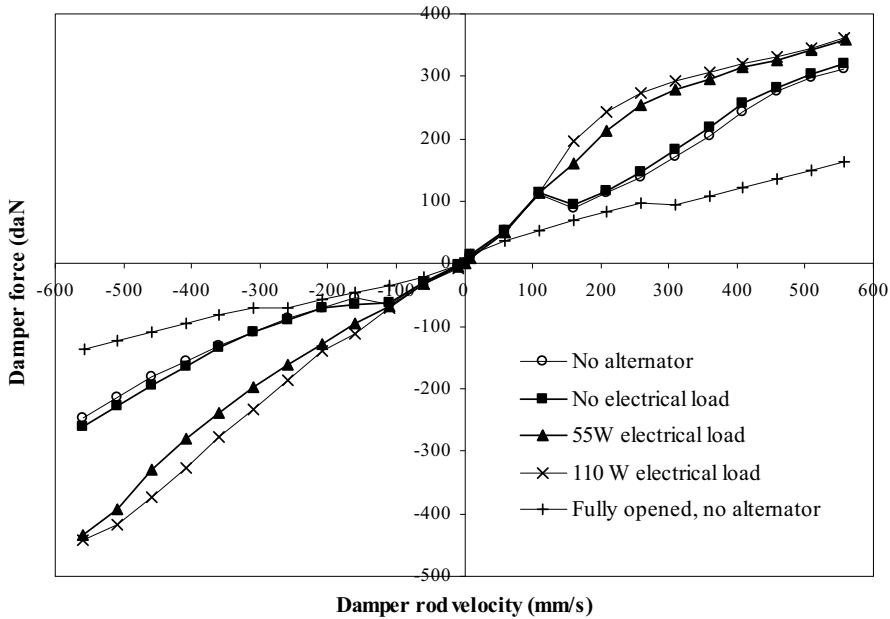
Figure 6. Damping characteristics

5. CONCLUSION

The present communication aimed at presenting the latest results in the development of a regenerative damper for race cars. The top level modelling and formal analysis have shown the qualitative and quantitative contribution of the components design and parasitic parameters on the regenerative damper performance. In particular, it has been clearly pointed out that parasitic effects appears as alias Coulomb and viscous friction plus reflected mass that add to the controlled damping effect. During the selection of off-the-shelf components for the development of a first demonstrator, only a few candidate components were found. Especially for very low displacement, high speed and high pressure hydraulic motors. A design exploration allowed selecting the best industrial component to demonstrate the interest of such regenerative dampers in a short time. In parallel, a design modification has been proposed in order to reduce the maximal flow passing through the motor for future prototypes. A preliminary design verification has been conducted on basis the time domain simulation of a virtual prototype that allowed assessing the steady state as well as the transient behaviours of the regenerative damper. The analysis of the first real experiments has proven the interest of the regenerative concept and the importance of specifically developing an integrated hydraulic motor / electric generator to reduce the contribution of the parasitic effects.

NOMENCLATURE

a	Hydraulic motor leakage coefficient (m^3/sPa)
$c_1 \ldots c_4$	Parameters for representation model
D	Motor displacement (m^3/rd)
f	Viscous friction factor (Nms/rd)
f'	First viscous friction factor (N/m)
f''	Second viscous friction factor (N/m)
F	Force (N)
$\mathcal{G}$	Hydraulic conductance function
J	Rotating assembly inertia (kgm^2)
k	Polytropic index (-)
K	Gain factor for regeneration (rd/m)
K_{QP}	Flow rate pressure gradient (m^3/sPa)
M'	Reflected mass (kg)
P	Pressure (Pa)
Q	Flow (m^3/s)
s	Laplace variable equivalent to d/dt (1/s)
S	Hydrostatic area (m^2)
t	Time (s)
T	Torque (Nm)
V	Effective volume under pressure (m^3)
x	Rod to cylinder extension (m)
Δ	Difference
Ω	Motor/generator angular velocity (rd/s)
τ	Time constant (s)

Subscripts

a, b, c, d	Index for check valves
C	Charge
C	Coulomb
d	Damper
e	Experimental
f	Friction
g	Gas
l	Leakage
i	Check valve index
m	Hydraulic motor
o	Opening
r	Regenerative
v	check valve
0	Value at $x = 0$ (full extension)
1, 2	Rod side or piston side

REFERENCES

(1) **Kepner R. P.,** Hydraulic Power Assist - A Demonstration of Hydraulic Hybrid Vehicle Regenerative Braking in a Road Vehicle Application, Sae paper: 2002-01-3128, November 2002

(2) Hydraulic hybrids from Rexroth: hydrostatic regenerative braking system HRB, brochure from Rextoth Group, reference RA 98 310/08.08, from http://www.boschrexroth-us.com

(3) **Wendel G.R., Stecklein G.L.,** A regenerative active suspension system, SAE Publication SP-861, Paper No. 910659, 1991, pp. 129–135

(4) **Berthe P-E., Maré J-C,** Consideration to the design of free surface oleopneumatic spring dampers, Proceedings of the Fifth Scandinavian International Conference on Fluid Power, Vol. 3, pp 67-80, Linköping, Sweden, 28-30 May **1997**, ISBN 91-7871-975-5

Optimization of Liquid Piston Dynamics for Efficiency and Power Density in a Free Liquid Piston Engine Compressor

Joel A. Willhite and Eric J. Barth
Laboratory for the Design and Control of Energetic Systems
Mechanical Engineering, Vanderbilt University
Nashville, TN, USA

ABSTRACT

An optimization of piston dynamics to achieve performance goals of a High Inertance Free Liquid Piston engine Compressor (HI-FLPC) is presented in this work. The proposed HI-FLPC is a compact device that utilizes combustion of hydrocarbon fuel to provide a supply of pressurized air for use in untethered pneumatic systems. The liquid piston of this device is configured such that its geometry is exploited to produce a high inertance, which produces an advantageous (slower) dynamic response as compared to a rigid piston of equal mass. The slower dynamics achieved by the liquid piston allow for reduced valve sizes for the compressor, a direct inject-and-fire engine with no compression stroke, and the capability of more balanced operation for a single-piston device. These attributes create a more energy-dense device than developed in prior work. A review of the dynamic model of the HI-FLPC is presented along with experimental model validation of the liquid piston. Simulation studies were conducted to optimize liquid piston dynamic characteristics for overall system performance of an experimental prototype.

Keywords: Free-piston engine, compressor, inertance, liquid piston, compact, efficient, power supply, untethered pneumatic system.

1. INTRODUCTION

The first free piston machine designed by Pescara [1] in 1928 was used as an air compressor. Free piston engines were most commonly commercially used as air compressors up to the mid-twentieth century. Other applications for the technology were investigated, such as gas generators for use in automobiles and small power plants. However, the lack of adequate sensing and control technology led to the free piston engine being largely abandoned after 1960 [2]. Modern electronic controls available today have led to a second generation of free piston engine research, particularly for use as hydraulic pumps. Mikalsen [3] provides an extensive review of both early free-piston engine compressor and gas generator applications as well as the recent research in free piston hydraulic pumps and linear alternators.

Interest in free piston air compressors has also recently resumed for the purpose of providing a compact, energy-dense, untethered power source for pneumatically actuated autonomous human-scale robotic systems. The goal is to achieve a higher overall system-

level energy and power density than current autonomous systems utilizing batteries and servomotors. Riofrio, et al [4] designed a device that incorporated a liquid trapped between elastomeric diaphragms as a piston. This free liquid-piston compressor (FLPC) addressed efficiency problems for engines of its size range (sub 1 kW) by eliminating the blow-by and friction losses of standard piston configurations. Willhite, et al [5], took advantage of the liquid piston idea by exploiting the geometry of the liquid piston of the FLPC to create a high inertance. This configuration allowed for desired (i.e., slower) piston dynamics to be achieved without the necessity of adding piston mass, thereby increasing the energy and power density of the system. This paper continues with the investigation of this High Inertance Free Liquid Piston Compressor (HI-FLPC). An experimental validation of the liquid piston dynamic model is discussed, and simulation studies of the HI-FLPC are performed to tune the dynamic characteristics of the liquid piston to optimize performance for an experimental prototype of the HI-FLPC.

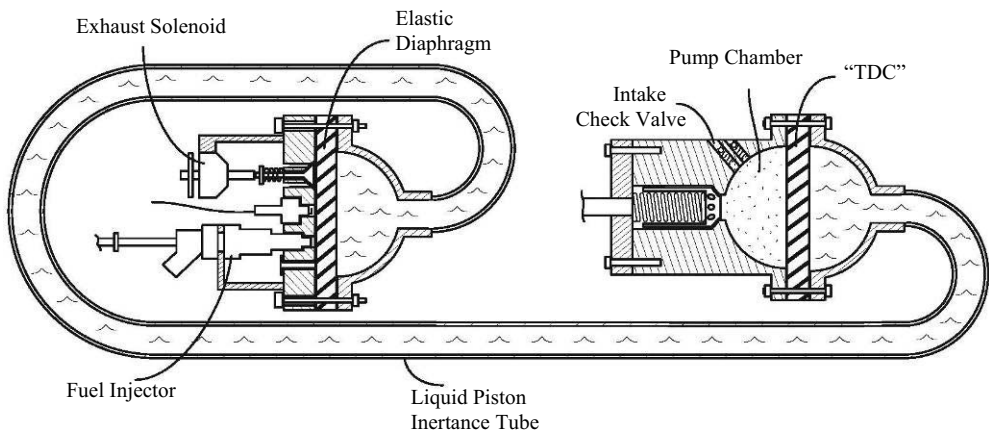## 1.1 Basic Operation of the HI-FLPC

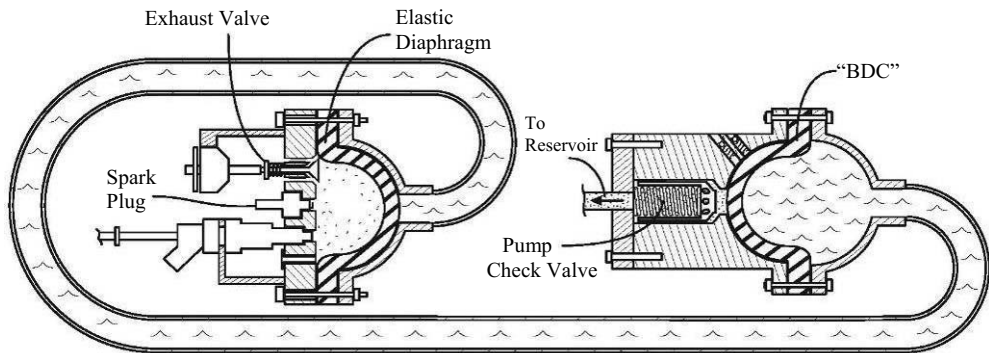**Figure 1   Schematic of HI-FLPC at TDC**

Figure 2   Schematic of HI-FLPC at BDC

Figure 1 is a representation of the HI-FLPC just before the power stroke of the engine, when the liquid piston diaphragms are relaxed. This is analogous to Top Dead Center (TDC) in conventional engines. The power stroke begins with injection of pressurized air from the system reservoir that is mixed with a hydrocarbon fuel, causing the elastic diaphragm to begin to stretch and the combustion chamber volume to increase. The dynamic inertial load of the liquid piston limits the expansion so that injection and ignition can occur without an appreciable drop in air/fuel pre-combustion pressure. This dynamic process eliminates the need for a compression stroke. The mixture then combusts, rapidly increasing the pump chamber volume and converting the combustion energy into kinetic energy of the liquid piston. On the compressor side of the piston, this kinetic energy is used to compress and pump the air from the pump chamber. Once the pump chamber air pressure exceeds the reservoir pressure, the pump check valve opens and mass flow into the reservoir occurs. Figure 2 illustrates the configuration of the device at the moment pumping is completed, similar to conventional Bottom Dead Center (BDC). At this point, the combustion exhaust valve is opened and the piston diaphragms begin to relax, reversing the flow direction of the liquid piston. During this return stroke, exhaust is expelled from the combustion chamber and fresh air enters the pump chamber through a check valve. Note that diaphragm stiffness is the only driver of the return stroke. Once the piston has returned to its original TDC position, the cycle can be repeated.

The lack of a compression stroke allows the engine compressor to "fire on demand"- that is, there is no need to have a starting routing or maintain an idle cycle. This allows the HI-FLPC to operate at varying frequencies by controlling the delay between TDC and the command for air/fuel injection.

2. DYNAMIC MODEL

Unlike conventional IC engines, free piston engines (including the HI-FLPC) are more heavily influenced by the dynamic responses and interactions of their components. For example, the stroke length of a conventional IC engine is kinematically defined by mechanical linkage to a crankshaft; a free piston engine's stroke length and even TDC and BDC positions are determined by the dynamic response of the piston and the dynamics of the load on each side of the piston, which includes combustion, compression/pumping and valve response rates. For this reason, a dynamic model is necessary for determination of performance and design optimization of the HI-FLPC.
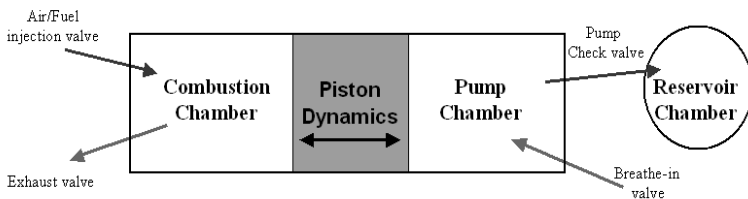

Figure 3. Control volumes, mass flows, and piston dynamics of the HI-FLPC model.

The model developed for the HI-FLPC in sections 2.1 – 2.3 consists of three control volumes: the combustion chamber, the pump chamber, and the reservoir. The combustion and pump chamber control volumes are coupled by the liquid piston dynamics. Mass flows and valve response dynamics are modeled for the injection and exhaust valves of the combustion chamber, as well as the pump and intake check valves of the pump chamber.

2.1 Control Volume Pressure and Temperature Dynamics

The following is an overview of the derivation of the pressure and temperature dynamics of the gas in each of the model control volumes. For a more detailed treatment of this derivation, see [4] and [6]. Equation (1) represents the power balance for each jth control volume (specifically, the combustion chamber, the pump chamber, and the reservoir):

$$\dot{U}_j = \dot{H}_j + \dot{Q}_j - \dot{W}_j \tag{1}$$

where $\dot{U}$ is the rate of change of internal energy, $\dot{H}$ is the net enthalpy flowing into the control volume, $\dot{Q}$ is the rate of heat transfer into the control volume and $\dot{W}$ is the work rate of the gas. Each term in Eq. (1) can be expanded as follows:

$$\dot{H}_j = \sum_k \dot{m}_{j,k} \left(c_{p_{in/out}}\right)_{j,k} \left(T_{in/out}\right)_{j,k} \tag{2}$$

$$\dot{W}_j = P_j \dot{V}_j \tag{3}$$

$$\dot{U}_j = \dot{m}_j \left(c_v\right)_j T_j + m_j \left(c_v\right)_j \dot{T}_j = \frac{1}{\gamma_j - 1}\left(\dot{P}_j V_j + P_j \dot{V}_j\right) \tag{4}$$

where $\dot{m}$ is the kth mass flow rate entering or leaving each jth control volume, with constant-pressure specific heat $c_{p_{in/out}}$ and temperature $T_{in/out}$. P and V are the pressure and volume in the control volume, c_v is the constant volume specific heat and γ is the ratio of specific heats of the gas in the control volume. Equations (2-4) can be used to form the differential Equations (5) and (6), which describe the pressure and temperature dynamics of the gas in each control volume.

$$\dot{P}_j = \frac{\left(\gamma_j - 1\right)\sum \dot{m}_j \left(c_{p_{in/out}}\right)_j \left(T_{in/out}\right)_j + \left(\gamma_j - 1\right)\dot{Q}_j - \gamma_j P_j \dot{V}_j}{V_j} \tag{5}$$

$$\dot{T}_j = \frac{\sum \dot{m}_j [\left(c_{p_{in/out}}\right)_j \left(T_{in/out}\right)_j - \left(c_v\right)_j T_j] - P_j \dot{V}_j + \dot{Q}_j}{m_j \left(c_v\right)_j} \tag{6}$$

The dynamics of the combustion process of the engine are treated as a $\dot{Q}$ term of the combustion chamber control volume. A detailed description of this combustion model, is in Yong. [6].

2.2 Mass Flows

The mass flow terms $\dot{m}_j$ in Equations (5) and (6) are determined by the following equation describing isentropic flow through an orifice, from Richer and Hurmuzlu [7]:

$$\dot{m}_j = \psi_j\left(P_u, P_d\right)$$

$$= \begin{cases} C_d a_j C_1 \dfrac{P_u}{\sqrt{T_u}} & \text{if} \quad \dfrac{P_d}{P_u} \leq P_{cr} \\[4mm] C_d a_j C_2 \dfrac{P_u}{\sqrt{T_u}}\left(\dfrac{P_d}{P_u}\right)^{1/\gamma_u}\sqrt{1-\left(\dfrac{P_d}{P_u}\right)^{\gamma_u-1/\gamma_u}} & \text{if} \quad \dfrac{P_d}{P_u} > P_{cr} \end{cases}$$

(7)

where C_d is a non-dimensional discharge coefficient of the valve, a_j is the area of the valve orifice, P_u and P_d are the upstream and downstream pressures, T_u is the upstream temperature, γ_u is the ratio of specific heats of the upstream gas. The constants C_1, C_2, and the critical pressure for choked flow, P_{cr}, are determined by:

$$C_1 = \sqrt{\frac{\gamma_u}{R_u}\left(\frac{2}{\gamma_u+1}\right)^{\gamma_u+1/\gamma_u-1}} \quad , \quad C_2 = \sqrt{\frac{2\gamma_u}{R_u\left(\gamma_u-1\right)}} \quad , \text{ and}$$

$$P_{cr} = \left(\frac{2}{\gamma_u+1}\right)^{\gamma_u/\gamma_u-1}$$

(8)

where R_u is the gas constant of the upstream substance. The dynamic responses of valves can then be modeled as dynamically determining the orifice area. In the case of electronically actuated valves, the lift of the valve and the subsequent revealing of a_j can be modeled as a second order response to a current. In the case of a check valve, the orifice area is the dynamic response to a differential driving pressure lifting the valve off the seat.

2.3 High-Inertance Piston Dynamics

The dynamic model of the high inertance liquid piston summarized here was developed in [5]. Consider a configuration consisting of three sections of a liquid, as shown in Figure 4. A power balance based on fluid flow due to the movement of the piston boundaries (in our case, diaphragms stretching and relaxing) is given by Equation 9, where P is the pressure difference across the left and right moving boundaries, and Q is the volumetric flow rate of the piston fluid.

$$PQ = \frac{d}{dt}\left[\frac{1}{2}m_1\left(\frac{Q}{A_1}\right)^2 + \frac{1}{2}m_2\left(\frac{Q}{A_2}\right)^2 + \frac{1}{2}m_3\left(\frac{Q}{A_3}\right)^2\right]$$
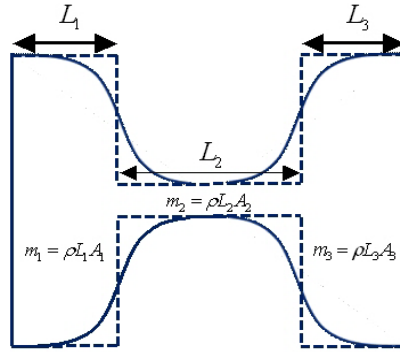
(9)

Figure 4. Three sections of the high inertance liquid piston.

Substituting $m_i = \rho L_i A_i$ for the masses of liquid in each flow region, differentiating, substituting $\dot{L}_1 = -Q/A_1$, $\dot{L}_2 = 0$ and $\dot{L}_3 = Q/A_3$, and solving for pressure, we obtain Equation 10:

$$P = \left[\frac{\rho L_1}{A_1} + \frac{\rho L_2}{A_2} + \frac{\rho L_3}{A_3} \right] \dot{Q} + \frac{\rho}{2} \left[\frac{1}{A_3^2} - \frac{1}{A_1^2} \right] Q^2$$

(10)

which consists of a dynamic term relating P and $\dot{Q}$ through the inertance of the fluid slug and a steady-state term due to the area changes between regions. For our model, A_1 and A_3 are equal, thereby eliminating the steady state term. We can now describe the inertance as:

$$I = \left[\frac{\rho L_1}{A_1} + \frac{\rho L_2}{A_2} + \frac{\rho L_3}{A_3} \right]$$

(11)

Viscous losses of the liquid are modeled by a resistive term relating pressure and volumetric flow, taken from the Darcy-Weisbach equation:

$$R = \frac{8\rho}{\pi^2 d_2^4} Q \cdot f \frac{L_2}{d_2}$$

(12)

where ρ is the density of the fluid (water), and d_2 is the diameter of the high inertance tube. The friction factor f was (conservatively) taken from the Moody Chart to be 0.025.

A stiffness term is also developed, relating pressure P to the change in volume of the outer sections of the liquid piston due to the expansion of the diaphragms. Willhite [8] describes the experimental technique used to measure this relationship for a sample diaphragm, which is almost linear. For our optimization model, we will assume a linear relationship, such that:

$$P = K\Delta V \quad \text{, noting that } \Delta V = \int Q$$

(13)

Combining the relationships in Equations (11) through (13), the total dynamics of the piston are given by:

$$\Delta P = I\dot{Q} + RQ + K\Delta V \tag{14}$$

2.3.1 Experimental Piston Dynamics Model Validation

An experimental setup of the liquid piston was used to validate the dynamic model of the high inertance liquid piston (shown in Figure 5). The liquid piston is housed by two hemispherical sections on each end, connected by the high inertance tube with a 7.9 mm inner diameter and a length of 1680 mm. The piston liquid is captured by two diaphragms with diameters of 25.4 mm. On the opposite side of each diaphragm is a sealed chamber of air. Testing consisted of supplying step-like driving pressures of varying amplitudes to one of the air chambers via a three-way valve. The response of the piston was measured by observing the pressure rise in the sealed chamber on the other end of the liquid piston (response chamber). Simulations of these experiments were then conducted, using the piston model in the same configuration as the test. Stiffness of the diaphragms was experimentally determined beforehand. The responses of the piston were plotted against model responses to the same pressure driving functions. One example of these responses to a maximum driving pressure of 750 kPa is shown in Figure 6. Note that two different modeled responses are present; one model assumes isothermal behavior of the response chamber and the other assumes an adiabatic process. Since the piston response in this test is on the same order of magnitude time scale as the pump stroke of the HI-FLPC, it is assumed that the piston model developed captures all significant dynamics of the liquid.
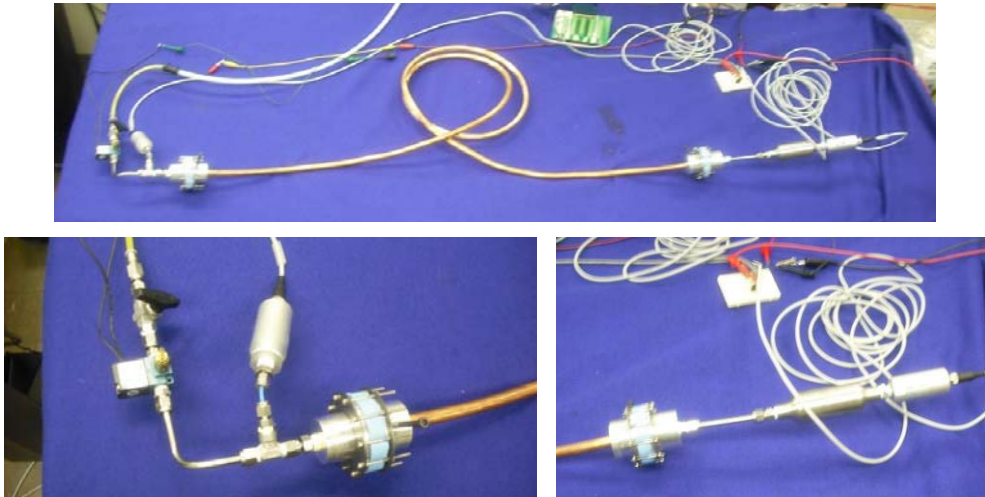

Figure 5. Experimental setup used to validate the liquid piston model. Shown on the left is a three-way valve used to provide a driving pressure, along with a pressure sensor. The tube shown on top contains the liquid piston trapped by two diaphragms. Shown on the right is a sealed air chamber and pressure sensor used to (indirectly) measure the piston response.
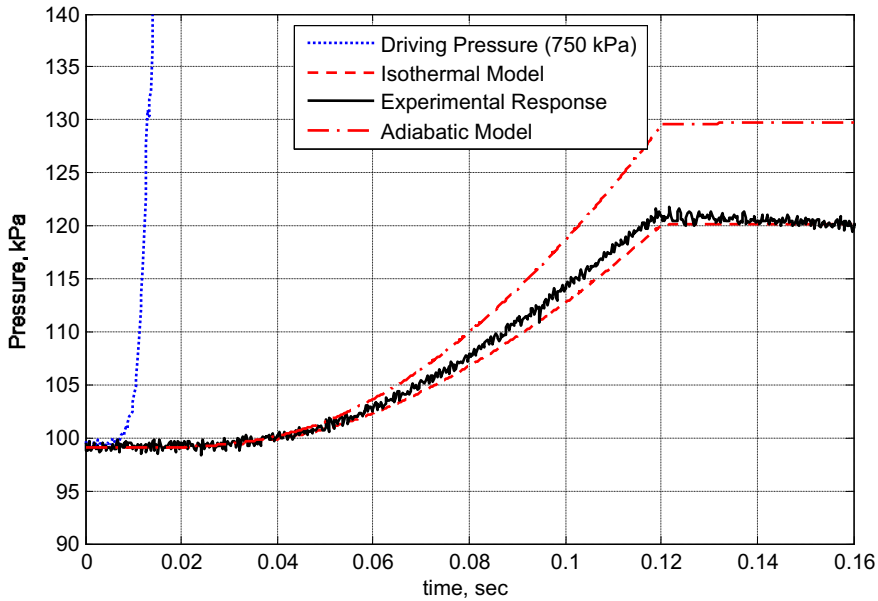
Figure 6. Experimental piston response compared to the liquid piston dynamic model (for adiabatic and isothermal models of the response chamber).

3. MODEL-BASED OPTIMIZATION STUDIES

An experimental prototype of the HI-FLPC is currently being developed. Performance targets for the device are centered around the need for a compact, efficient untethered power source for small-scale pneumatic power applications. These targets include overall system mass of under 2kg and an output of 75W, and an overall system efficiency of at least 10% from chemical potential of the fuel to cool pneumatic potential in the reservoir.

To develop the HI-FLPC prototype, a complete model of the device was implemented in MATLAB, using the control volume dynamics of Equations (5) and (6), the liquid piston dynamics as modeled with equation (14), and the combustion process as modeled in [6]. All valve opening and closing dynamics affecting each valve orifice area a_j were modeled as second order and fitted to experimental data for the valves chosen for the HI-FLPC (see Willhite, et al, [8] for examples).

3.1 Simulation Results for Proposed Experimental Prototype

Simulations were performed to tune the liquid piston dynamics for optimum performance of an experimental prototype of the HI-FLPC. Device parameters that were not adjusted during the simulations were: all valve parameters, piston diaphragm radius (25.4 mm) and pump chamber volume ($3.43 \times 10^4 \, \text{mm}^3$). A design point for the prototype was chosen from these simulations, with liquid piston parameters A_2 and L_2 set at 324 mm^2 and at 1778 mm. Figure 7 shows the pressure profiles of the control volumes at this design point for the pump

stroke of the HI-FLPC model. The output power for the simulation is 136.8W, at a cycle frequency of 18 Hz and a total projected system mass of 2.07 kg. Efficiency of the cycle is calculated to be 27.4%.
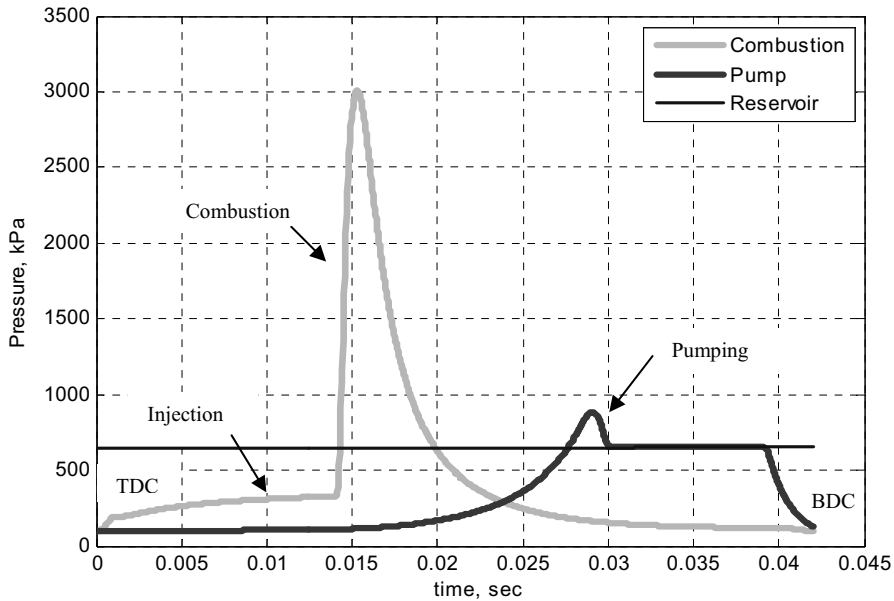

Figure 7 Control volume pressures for power stroke of HI-FLPC at the design point.

3.2 Effects on Performance of Liquid Piston Characteristics

Simulation studies were performed to investigate how changes in the dynamic characteristics of the piston from the design point of Section 3.1 would affect overall performance of the HI-FLPC. These simulations separately varied the L_2 and A_2 geometry of the liquid piston, and the stiffness of the piston diaphragm in order to investigate their individual effects on efficiency and power density of the device. The following sections discuss the simulation results for the variation of these three parameters.

3.2.1 Varying Inertance Tube Cross-Sectional Area

Figure 8 shows simulation results for the maximum power density and system efficiency versus piston inertance, where the inertance is varied by adjusting the liquid piston cross-sectional area. Maximum power density is calculated from the amount of energy pumped into the reservoir per stroke, the stroke duration and the mass of the device. Each of these values vary for the different cross sectional areas simulated. A dry system mass of the HI-FLPC is assumed (fuel mass not included) that includes the mass of: the structure, all components, and the liquid piston. The frequency of operation assumes no pause between cycles of the engine. Efficiency is defined as the amount of pneumatic potential added to the reservoir divided by the chemical potential (lower heating value) of the hydrocarbon

fuel. The performance of the device at the design point of Section 3.1 is shown for reference. To ensure a proper comparison, the air/fuel input was adjusted for each simulation to fully pump the air charge in the compressor chamber into the reservoir. This results in the same amount of output energy for each cycle.
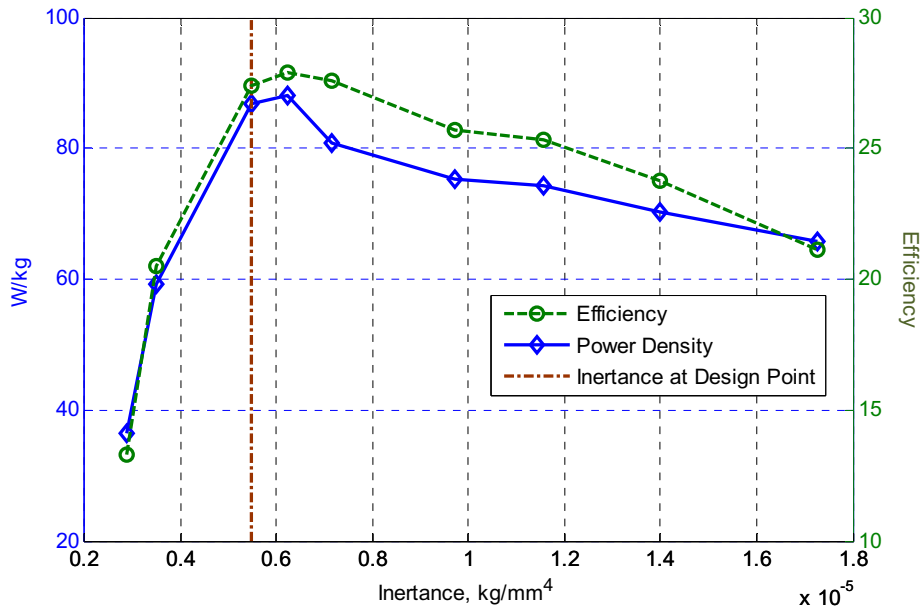
Figure 8. Power density and efficiency versus inertance by varying liquid piston cross-sectional area, A_2

While it is normally expected to see a trade-off between power and efficiency, certain characteristics of the HI-FLPC cause the coinciding power density and efficiency peaks. As inertance increases from the design point (5.46×10^{-6} kg/mm^4), the power density decline is due to a slower piston dynamics lengthening the pump stroke. The drop in efficiency is primarily a result of an increase in viscous losses of the piston due to the decrease of A_2. These dominant viscous losses for smaller cross-sectional piston areas (larger inertance) are the main reason for the chosen value of A_2.

For inertance below the design point, the steep drop-off in efficiency is predominantly caused by two factors. The first and most dominant factor is on the pump side: the piston dynamics are now too fast for the pump check valve to close in time, allowing for some backflow of reservoir air into the pump chamber. The second and more minor factor is that the lower inertance provides less dynamic load on the air/fuel injection, resulting in a lower pressure of the air/fuel mass input just before combustion. This is similar to a smaller compression ratio in a traditional four stroke engine.

3.3.2 Varying Inertance Tube Length

Next, the inertance of the piston was varied by changing the length L_2 of the liquid piston while holding A_2 constant at the current design point. Once again, the dropoff in efficiency and power density for lower inertances is due to the inability of the pump check valve to react fast enough to the piston dynamics. As inertance gets higher, power density decreases due to longer pump stroke durations. Efficiency increases up to and beyond the design point due to better pump check valve performance and the higher pressure of the air/fuel mass input just before combustion. However, as inertance increases further this effect is dominated by viscous losses of the piston, and efficiency peaks.
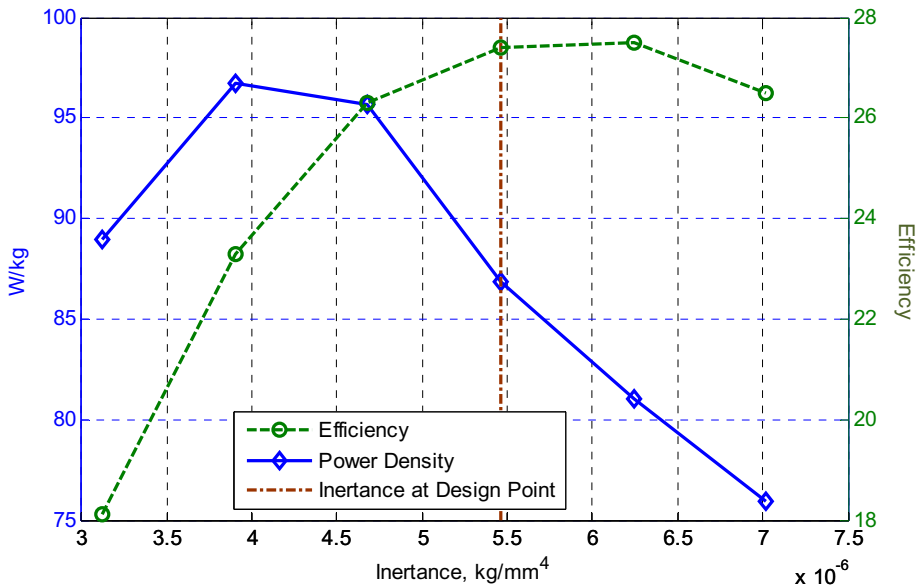
Figure 9   Maximum Power Density and Efficiency Versus Inertance by Varying Liquid Piston Inertance Tube Length

3.3.3 Varying Diaphragm Stiffness

Variations of diaphragm stiffness yields a fairly straight-forward trade-off between power and efficiency. Increasing the diaphragm stiffness stores more combustion energy during the pump stroke, thereby speeding up the return stroke which reduces the overall system cycle time. The extra energy needed from combustion to fully expand the diaphragms decreases overall efficiency, while the higher operating frequency increases output power. Note that for the current design point, some efficiency is being sacrificed for better power density. Less stiff diaphragms may be experimented with once the prototype is complete to maximize efficiency while still maintaining the output power targets.
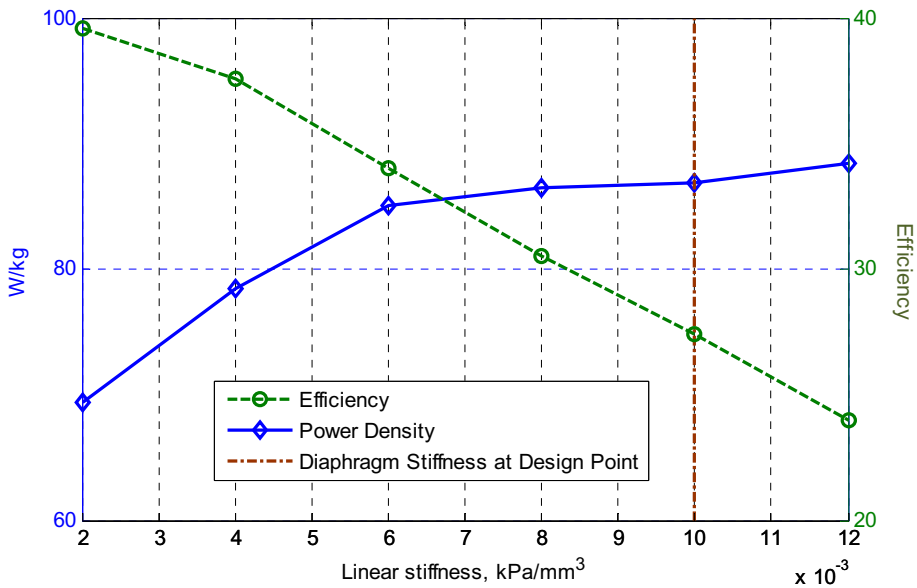
Figure 10   Maximum power density and efficiency versus diaphragm stiffness

5. CONCLUSIONS

This paper presented the operation of a high inertance free liquid piston compressor (HI-FLPC). A review of the development of a dynamic model for the HI-FLPC was presented. Experimental validation of the liquid piston dynamics was performed. Simulation studies were performed to optimize the piston dynamics for best overall performance of the engine and pump subsystems of the HI-FLPC.   Now that all components of the proposed experimental prototype are specified, fabrication of the HI-FLPC device has begun. The engine section, complete with injection and exhaust valve, is shown in Figure 11. Testing of engine-side performance (only loaded by the liquid piston) has begun, and will be followed by compressor section fabrication and a complete experimental characterization of the performance of the complete HI-FLPC engine compressor.
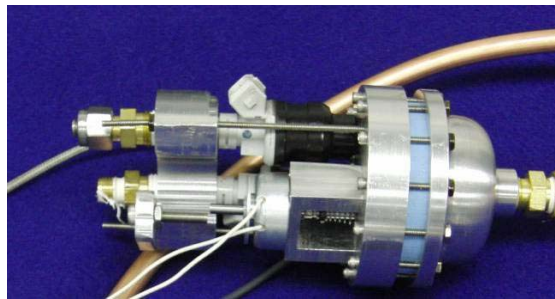
Figure 11. Experimental prototype combustion head mounted to liquid piston

ACKNOWLEDGEMENTS

REFERENCES

[1]   Pescara, R. P., "Motor Compressor Apparatus," U.S. Patent No. 1,657,641, Jan. 31, 1928.

[2]   Johansen, T. A.; Egeland, O.; Johannessen, E. A.; Kvamsdal, R, "Free-Piston Diesel Engine Timing and Control – Toward Electronic Cam- and Crankshaft," *IEEE Transactions on Control Systems Technology*, vol. 10, no. 2, March 2002, pp. 177 – 190.

[3]   Mikalsen, R. and Roskilly, A. P., "A Review of Free-Piston Engine History and Applications," *Applied Thermal Engineering*, vol. 27, 2007, pp. 2339 – 2352.

[4]   Riofrio, J and Barth, E. J., "Design and Analysis of a Resonating Free Liquid-Piston Engine Compressor," *2007 ASME International Mechanical Engineering Congress and Exposition (IMECE),* IMECE2007-42369, November 11-15, 2007, Seattle, WA.

[5]   Willhite, J. A. and Barth, E. J., "Reducing Piston Mass in a Free Piston Engine Compressor by Exploiting the Inertance of a Liquid Piston". *2009 ASME Dynamic Systems and Control Conference & Bath/ASME Symposium on Fluid Power and Motion Control.* DSCC2009-2730, pp. 1-6, October 12-14, 2009, Hollywood, CA.

[6]   C. Yong, C.; Riofrio J. A.; and Barth, E. J., "Modeling and Control of a Free-Liquid-Piston Engine Compressor," *Bath/ASME Symposium on Fluid Power and Motion Control (FPMC 2008)*, pp. 245-257, September 2008.

[7]   Richer, E., and Hurmuzlu, Y., "A High Performance Pneumatic Force Actuator System: Part 1 – Nonlinear Mathematical Model". *ASME Journal of Dynamic Systems, Measurement and Control*, 122, September, 2000, pp. 416-425.

[8]   Willhite, J. A. and Barth, E. J., "Experimental Characterization of Critical Dynamic Model Parameters for a Free Liquid Piston Engine Compressor," *6th FPNI Ph.D. Symposium*, Purdue University, June 2010, to appear.

Modeling and Simulation for Requirement Generation of Heavy Vehicles Steering Gears

Alessandro Dell'Amico, Jochen Pohl, Petter Krus
Div. of Fluid and Mechatronic Systems (FLUMES),
Dep. of Management and Engineering (IEI)
Linköping University, Sweden

ABSTRACT

Today's passenger vehicles are becoming more and more safe as more steering related active safety functions are being introduced. As an example, lane keeping assist functions or even electronic vehicle stability with steering intervention can be mentioned. However, the same trend can yet not be witnessed for heavy vehicles, which is, among others, due to a lesser degree of controllability of the steering system. While electric power assisted steering has been introduced in passenger cars in recent years on a broader basis, electric power assisted steering is yet not suitable for heavy vehicles due to heavier loads on the steering rack. Heavy vehicles thus lack a freely programmable steering system. The purpose of this paper is to generate and evaluate the requirements of future hydraulic actuation concepts for heavy vehicles, where emphasis is put on the required steering actuator linearity and bandwidth. Both actuator response and linearity are decisive for transmitting a proper steering feel to the driver. In this study we provide a structured approach to derive the required bandwidth as a function of the system sizing and provide a simulation supported method for deriving the requirements of linearity and accuracy.

1   INTRODUCTION

The requirements on power steering systems in road vehicles have been steadily increasing, where even the need for freely controlling the steering wheel torque have become apparent. The latter is due to the steady introduction of active safety and comfort functions. Active safety functions, which have been proven to have a positive effect on overall vehicle safety, refer to systems that provide assistance to the driver in more or less critical situations in order to avoid accidents. Active safety functions play an increasingly important roll in future safety strategies and it is therefore essential that sub systems in road vehicles, such as power steering systems, are adjusted to meet new demands. While this statement is primarily true for passenger cars, this trend is now also starting to enter the truck industry.

Traditional Hydraulic Power Assisted Steering (HPAS) systems cannot meet these new demands due to the control units pure hydro-mechanical solution. Many passenger car models, that previously have been equipped with hydraulic support, have been equipped with electrically driven steering gears, so called Electric Power Assisted Steering (EPAS). These systems must not be confused with so called Electro Hydraulic Power Assisted Steering (EHPAS), where the pump in the conventional HPAS systems is driven by an electric motor. The aforementioned requirements are fulfilled by EPAS systems to a great extent, which solves the problem for passenger cars. For trucks, however, pure EPAS systems are not available today, mainly due to high power requirement during low speed maneuvering.

The purpose of this paper is to derive and evaluate requirements for a future hydraulic power assisted steering emphasizing variable assist torque and reduced energy consumption. The requirements are based on both a linear analysis of the system as well as simulation based analysis of a complete tractor- semitrailer combination and will be presented both at a concept level and a component level.

2   REQUIREMENTS ON FUTURE POWER ASSISTED STEERING TECHNOLO-GIES

There are a number of essential requirements for future power- steering systems. The German passenger car manufacturer BMW summarizes these as follows(see [1]):

1. Enabling full steer-by-wire functionality and preserving or optimizing the present steering feel.

2. Significant reduction of the fuel consumption portion compared to present hydraulic power-steering systems.

3. Sufficient power capacity for all vehicle classes.

We have to note that these statements represent the point of view of a passenger car manufacturer. These requirements have most likely to be rephrased in order to suit the truck industry. An attempt to rephrase the requirements for commercial vehicles could result in the list below:

1. Possibility to realize steering related active safety and comfort functions.

2. Enabling the possibility to design the change of steering feel with load and predictable steering feel for a large range of vehicle configurations[1].

3. Increased directional stability.

4. Significant reduction of fuel consumption compared to present hydraulic power-steering systems.

5. Sufficient power capacity for all vehicle classes.

6. Providing means for safe operation during failure modes of the system and fulfilling legal requirements for steering wheel torques for a wide range of vehicle configurations.

---

[1]The term steering feel summarizes a number of characteristics such as on-center torque built up, steering wheel return ability as well as torque levels during off center handling and low speed maneuvering/shunting.

3   VEHICLE AND STEERING SYSTEM MODELING

This sections describes the fundamental equations behind the modeling of the complete vehicle. The vehicle used here is a tractor with semitrailer. The tractor has two axles (4x2) and the semitrailer has three axles. Relevant data for the vehicle is shown in table 1. The modeling is divided into studying the vehicle and the steering system separately and both models are validated against measured data. The main use of the vehicle model is to derive requirements for a future hydraulic power assisted steering system, both for heaviest load scenario and on center handling.

Tractor only			Tractor + Semitrailer		
Tractor mass	8009	kg	Total mass	36540	kg
Front axle mass	6008	kg	Front axle mass	7860	kg
Rear axle mass	2001	kg	Rear axle mass	9900	kg
Wheelbase	3.7	m	Semitrailer axle mass	3x6260	kg

Table 1: Vehicle data.

3.1   Tractor-semitrailer model
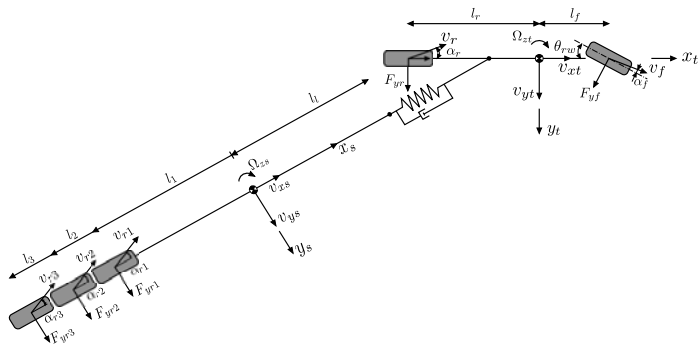
Figure 1: The bicycle model of the tractor semitrailer.

The vehicle model is based on the well known bicycle model [2]. Even though the bicycle model inherits several limitations, it is suitable for the purpose of this work, as the driving scenarios chosen are limited to lateral accelerations below $2 m/s^2$. The vehicle can be divided into two separate bodies with individual local frames, see figure 1. The connection between the tractor and the semitrailer is represented by a spring and damper. The benefit from this is that the two bodies can be kept separately in their local frames and additional bodies can easily be connected. The spring and damper is also seen to represent the (stiff) compliance in the connection between the tractor and semitrailer. The governing equations are based on Newton's second law and the moment law, stated below for the tractor.

$$\dot{v}_x = \frac{\sum F_t - F_{yf}\sin(\delta_{rw}) - F_{lx}}{m} + v_y\Omega \tag{1}$$

$$\dot{v}_y = \frac{F_{yf}\cos(\delta_{rw}) + F_{yr} - F_{ly}}{m} - v_x\Omega \tag{2}$$

$$\dot{\Omega} = \frac{\sum M}{I_z} \tag{3}$$

The acceleration in the longitudinal direction depends on the sum of the tractive forces, the sine component of the lateral force for the front tires and the force from the connection between the tractor and semitrailer. The lateral direction is similar, where the acceleration depends on the lateral forces from each tyre and the lateral force from the connection point. The second term in both equations are a consequence of the fact that all states are expressed in their local coordinate systems. The angular acceleration is the sum of all moments from each lateral force divided by the inertia of the vehicle. Similar equations can be set up for the semitrailer in its own local coordinate system. The difference is that there are no tractive forces. Instead the semitrailer is driven by the connection force. The definition of all forces can be seen in figure 1. The lateral forces are pure linear models. This limitation is adequate within the working range for the model. The lateral forces are a function of the so called cornering stiffness C_α and the slip angle.

$$F_y = C_\alpha\alpha \tag{4}$$

The slip angles can be defined in terms of vehicle states.

$$\alpha_f = \theta_{rw} - atan\left(\frac{v_f}{v_x}\right) = \theta_{rw} - atan\left(\frac{v_y + l_f\Omega}{v_x}\right) \tag{5}$$

$$\alpha_{ri} = atan\left(\frac{v_{ri}}{v_x}\right) = atan\left(\frac{-v_y + l_{ri}\Omega}{v_x}\right) \tag{6}$$

where the cornering stiffness is a linear function of the normal load, and depends also of the tire properties and the contact between the tire and ground.

$$C_\alpha = f(F_z) \tag{7}$$

3.2 Steering system model
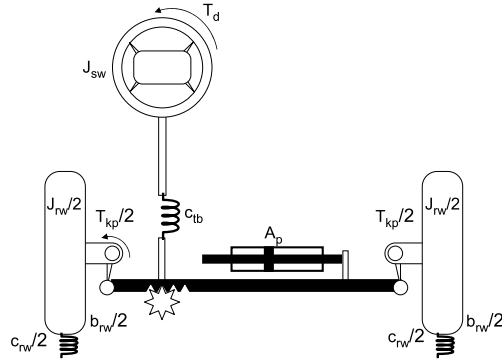
Figure 2: Simple model of a vehicle steering system.

In its simplest form, the steering system can be seen as a two mass system connected by a spring representing the torsion bar, figure 2, see also [3] The upper mass is connected to the steering wheel where the driver applies the input torque to the system and the lower mass is connected to the wheels. The following equations define the behavior of the steering system.

$$J_{sw}\ddot{\delta}_{sw} = T_d - C_{tb}\left(\delta_{sw} - \theta_{rw}i_{sw2rw}\right) - b_{sw}\dot{\delta}_{sw} \tag{8}$$

$$J_{rw}\ddot{\delta}_{rw} = T_{ha} - T_{kp} + C_{tb}\left(\delta_{sw} - \theta_{rw}i_{sw2rw}\right)i_{sw2rw} - b_{rw}\dot{\delta}_{rw} - T_f^{max} \tag{9}$$

The amount of assistance torque, T_{ha}, is defined by a so called boost curve, where the input to the boost curve is the torsion bar torque and output is the hydraulic pressure drop over the piston. A typical boost curve is shown in figure 3. There is both coulomb friction from the steering column and a pressure dependent friction within the cylinder. The friction within the cylinder is the dominant one and is therefore the only friction considered here.

Figure 3: A typical boost curve

A deeper analysis of the hydraulic power assisted steering is performed in a later section. The forces generated by the tires are divided into studying dry park and high speed maneuvers

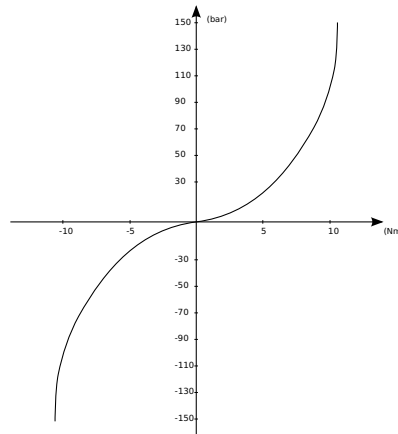separately. At dry park there are no lateral forces acting on the tires. The kingpin torque can therefore be seen as a spring with hysteresis. The spring effect of the tires are becoming very small at higher vehicle speeds due to the immediate relaxation of the tire. Here the dominant kingpin torque is the aligning torque due to the deformation of the tire when subjected to cornering forces. This means that the lateral force is not acting at the center of the tire, but rather a distance behind the center called the pneumatic trail, p_t. The kingpin torque can therefore be defined as

$$T_{kp_{drypark}} = \begin{cases} C_{rw}\delta_{rw} & ,T_{kp} < T_{kp}^{max} \\ T_{kp}^{max} & ,else \end{cases} \tag{10}$$

$$T_{kp_{highspeed}} = p_t F_y \tag{11}$$

Measurements were performed in order to validate the model and establish values for model parameters.

4   VEHICLE MEASUREMENTS AND VALIDATION

Both a sine sweep and a step input were applied to the steering wheel. The following states were measured:

- Steering wheel angle

- Steering wheel torque

- Hydraulic pressure

- Longitudinal speed

- Yaw rate

The validation was divided into validating the vehicle and the steering system separately

4.1   Optimization based model evaluation and validation of the vehicle model

In order to find unknown parameters, an optimization routine was used to match simulation data against measured data. The optimization routine used in this work is the Complex-RF method [4], which is a further development of the original Complex method [5]. The optimization routine was fed with measurements from both the tractor only and the tractor with trailer, in order to use as much information as possible. The longitudinal velocity is used as input to the model. The optimization problem can be formulated as follows:

$$min \quad f(\mathbf{x}) = \sum_{j=1}^{12} \int_{t_{start}}^{t_{end}} \left| \Omega(\mathbf{x}, v_{x,j}) - \Omega_{measured} \right| dt$$

$$\mathbf{x}^{lower} \le \mathbf{x} \le \mathbf{x}^{upper} \tag{12}$$

where $\mathbf{x}$ is defined as:

$$\mathbf{x} = \begin{bmatrix} I_{z,t} & C_{\alpha_f} & C_{\alpha_{r,t}} & I_{z,s} & C_{\alpha_{r,s}} \end{bmatrix}$$

The parameter $j = 1..12$, represents the velocities $v_x = [50\ 70\ 90]\ kph$ for each of the four cases; tractor with sine sweep, tractor with step input, tractor + trailer with sine sweep, tractor + trailer with step input. Figure 4 shows the result of the optimization for the sine sweep at 90 kph for the tractor with semitrailer.
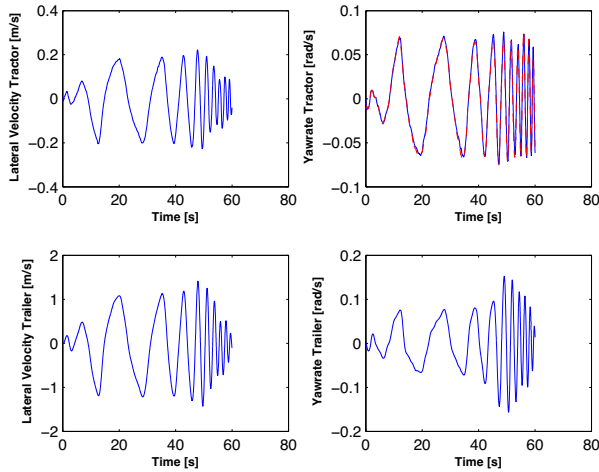
Figure 4: Simulated (solid) and measured (dotted) states for sine sweep.

4.2   Steering system evaluation

Measurement was also performed for dry park to find the heaviest rack loads. The measurements were made for different steering wheel angles and with the measured driver torque and hydraulic pressure, the kingpin torque could be calculated. Figure 5 shows the kingpin torque over road wheel angle for the dry park maneuvers. It clearly shows the behavior of the tire as a hysteresis curve. It can also be seen that at small deviations the tire acts like a spring.
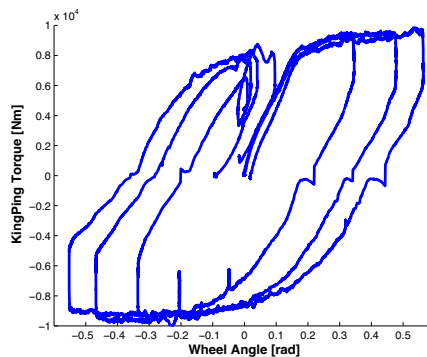
Figure 5: Tire hysteresis curve at dry park.

For high speed maneuvers another optimization was performed to find the pneumatic trail

and friction level. The steering system model was used together with the vehicle model that calculated the lateral force on the front axle for the given steering wheel angle cycle. The optimization routine was set to minimize both steering wheel angle error and pressure error. The result is shown in figure 6 for a vehicle speed of 90 *kph*. Since the simulated pressure matches the measured pressure well the result indicates that the load on the steering system, aligning torque and friction, are identified correctly. However, one can not tell whether the friction or pneumatic trail corresponds to the actual values, it can only be stated that the total load is correct. However, this setup is used for the derivation of the actuator requirements.
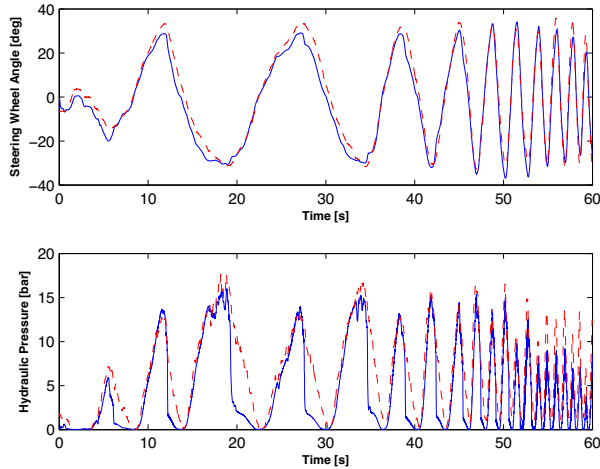
**Figure 6: Simulated (solid) and measured (dashed) steering wheel angle and hydraulic pressure at 90 *kph*.**

5   LINEAR ANALYSIS

A short linear analysis of a so called boost curve controlled steering system is performed. The boost curve concept is today still the predominant means of controlling a power assisted steering system. Here the driver supplied torque is measured and amplified by the assistance system, that is the drivers torque is "boosted". The relation between drivers torque and assistance torque or force is often nonlinear, such as due to the turbulent flow regimes in open center hydraulic assistance systems.

The purpose of this analysis is to provide insight for deriving requirements for required actuator bandwidth for the subsequent sections.

Figure 2 shows a mechanical model intended as a practical illustration for the derivation of the block diagram in figure 7, where the important dynamics of a boost curve controlled steering system are shown. We obtain the following system of equations if Newtons 2nd law is applied on this system, as well a relation for the generation of hydraulic assistance as underlying equations for the block diagram.

$$
\begin{aligned}
J_{sw}\delta_{sw}s^2 &= T_d - C_{tb}\left(\delta_{sw} - \delta_{rw}i_{sw2rw}\right) - \delta_{sw}sb_{sw} \\
J_{rw}\delta_{rw}s^2 &= T_{ha} - T_{kp} + C_{tb}\left(\delta_{sw} - \delta_{rw}i_{sw2rw}\right)i_{sw2rw} - C_{rw}\delta_{rw} - s\delta_{rw}b_{rw} \\
T_{tb} &= C_{tb}(\delta_{sw} - \delta_{rw}i_{sw2rw}) \\
T_{ha} &= T_{tb}A_pK_{bc}/i_{pp2rw}
\end{aligned}
\tag{13}
$$

Figure 7: Block diagram for steering system with boost curve control.

From the above equations we can derive the transfer function G from steering wheel angle δ_{sw} to road wheel angle δ_{rw}:
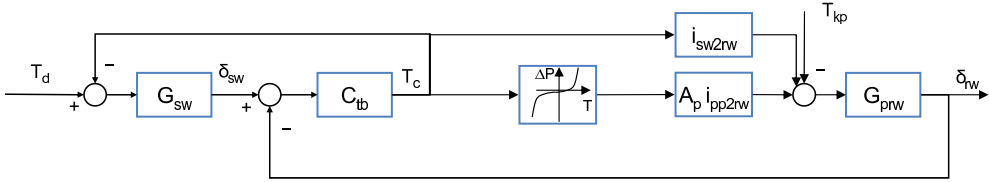
$$
G = \frac{\delta_{rw}i_{sw2rw}}{\delta_{sw}} = \frac{K_g}{\frac{s^2}{\omega_{ss}^2} + 2\frac{\delta_{ss}}{\omega_{ss}} + 1}
\tag{14}
$$

where the eigenfrequency ω_{ss} and damping δ_{ss} as well as steady state gain are given by:

$$
\omega_{ss} = \sqrt{\frac{\frac{i_{sw2rw}}{i_{pp2rw}}A_pK_{bc}C_{tb} + C_{tb}i_{sw2rw}^2 + C_{rw}}{J_{rw}}}
\tag{15}
$$

$$
\delta_{ss} = \frac{1}{2}b_{rw}\sqrt{\frac{i_{pp2rw}}{J_{rw}}}\sqrt{\frac{1}{A_pK_{bc}C_{tb}i_{sw2rw} + i_{pp2rw}i_{sw2rw}^2C_{tb} + i_{pp2rw}C_{rw}}}
\tag{16}
$$

$$
K_g = \frac{1}{1 + \frac{C_{rw}}{A_pK_{bc}\frac{i_{sw2rw}}{i_{pp2rw}} + i_{sw2rw}^2C_{tb}}}
\tag{17}
$$

Here G_{sw} is the transfer function from total steering wheel torque to steering wheel angle δ_{sw}, where the entering torque difference consists of the driver supplied hand torque T_d and the torsion bar reaction torque T_c. The torsion bar twist angle is calculated as a difference between the steering wheel angle and the pinion angle δ_p. We assume for this analysis that the steering column is significantly stiffer than the torsion bar, so that the steering column stiffness can be neglected. The torsion bar torque is measured and a so called boost curve or assistance map is used in order to generate the desired assistance torque. The boost curve gain is here denoted as K_{bc} and the hydraulic assist torque is summed to the torsion bar torque in order to form the total actuation torque on the steering rack. The steering rack transfer function G_{prw} calculates the pinion angle given the input torque. A disturbance torque due to for instance outer road disturbances enters the control loop at the sum of torques, and the loops ability to suppress disturbances can be studied.

The transfer function is plotted in figure 8 using data from a conventional steering system in heavy vehicles. The system bandwidth increases with an increasing amount of supplied driver's torque, while at the same time the dimensionless damping ratio is decreased. However, the model oversimplifies the hydraulic circuit, as the amount of damping is operating point dependent as well. The true amount of dimensionless damping is therefore underestimated in this example.
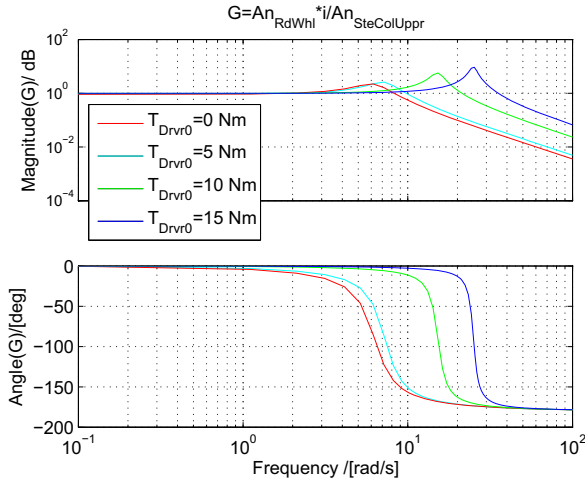
Figure 8: Bode plot for closed loop transfer function from steering wheel angle to road wheel angle for different operating points in terms of supplied drivers torque.

In this section it has been shown that a boost curve essentially is a proportional controller, where the reference value for the desired steering wheel torque is lacking, i.e. the desired steering wheel torque is "zero". If we increase the boost gain K_{bc}, two things happen. For the first, the systems ability to suppress disturbances increases which is very much wanted, and for the second, the control error between the steering wheel torque and its reference value decreases. This is very much unwanted, as the reference torque is set to zero, and a vehicle with such a reference torque is not drivable.

The steering system exhibits a varying bandwidth through the introduction of a driver torque dependent "boost"- amplification, as shown in this section. The bandwidth increases with increasing operating point in the driver's torque. The positive side of the coin is thus that an underlying actuator, as mentioned in the introduction, can have an operating point dependent bandwidth as well, as long as the actuator bandwidth is significantly higher than the steering system.
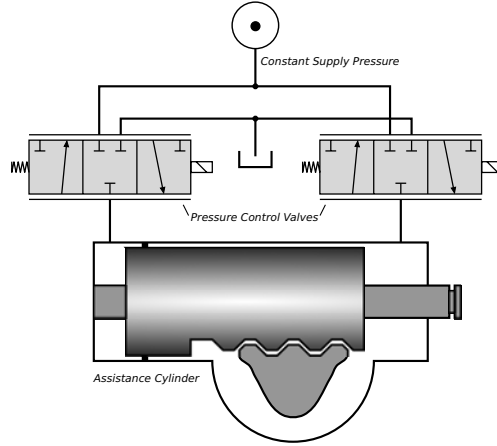
Figure 9: Pressure control of the cylinder chambers in the steering gear.

For a future hydraulic power assisted steering, some kind of pressure control is needed. The analysis is valid for any type of valve, but is made with an emphasis on the valve configuration in figure 9. The left and right chambers are identical and the following equations are therefore specified for one chamber. The equations are already linearized and transformed to the Laplace domain and capital letters are used for linearized variables. See [6] for a more detailed approach. The pressure change in the volume is described by the continuity equation for that volume.

$$Q_v = A_p X_p s + \frac{V}{\beta} P_l s \tag{18}$$

where $A_p X_p s = Q_p$ is the required flow due to the movement of the piston. The continuity equation can therefore instead be written as:

$$Q_v - Q_p = \frac{V}{\beta} P_l s \tag{19}$$

The flow through the valve depends both on the spool position and pressure drop.

$$Q_v = K_q X_v + K_c (P_s - P_l) \tag{20}$$

where the flow gain and pressure-flow coefficient respectively are defined as:

$$K_q = \frac{\partial q_v}{\partial x_v} = C_q w \sqrt{\frac{2}{\rho} (P_s - P_{l0})} \qquad K_c = \frac{\partial q_v}{\partial (p_s - p_l)} = \frac{C_q w x_{v0}}{\sqrt{2\rho} (P_s - P_{l0})}$$

The movement of the spool gives an opening of the valve. Here is assumed that the movement of the spool can be described by a second order lag with gain K_A, resonance ω_v and damping δ_v.

$$X_v = \frac{K_A}{\frac{s^2}{\omega_v^2} + \frac{2\delta_v}{\omega_v} s + 1} u \tag{21}$$

The controller signal u depends on the difference between the reference pressure and the actual pressure.

$$u = \left(P_{ref} - P_l\right) G_{cntrl}(s) \tag{22}$$

The above equations can now be formed into the block diagram in figure 10.
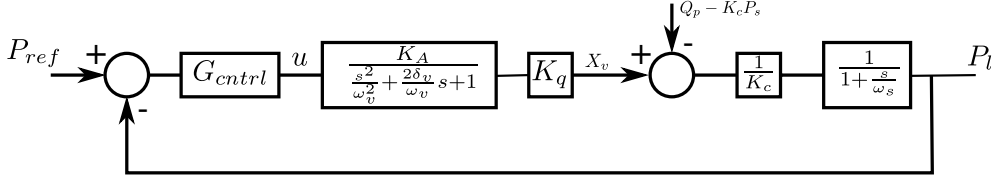
Figure 10: Block diagram of a pressure control loop.

From the block diagram the open loop gain can be defined, with the assumption of a proportional controller gain K_{reg}.

$$A_u(s) = K_{reg} \frac{K_A K_q}{K_c} \frac{1}{\frac{s^2}{\omega_v^2} + \frac{2\delta_v}{\omega_v}s+1} \frac{1}{1 + \frac{s}{\omega_s}} \tag{23}$$

This also defines the gain margin of the pressure loop.

$$G_m = \frac{2\delta_v \omega_v}{K_v \omega_s} \tag{24}$$

where $K_v = \frac{K_{reg} K_A K_q}{K_c}$. The demand for stability requires $G_m > 1$. The closed loop defines the bandwidth for the pressure loop.

$$G_c(s) = \frac{K_v}{\left(1 + \frac{s}{\omega_s}\right)\left(\frac{s^2}{\omega_v^2} + \frac{2\delta_v}{\omega_v}s+1\right) + K_v} \tag{25}$$

For a good valve design, $\omega_v >> \omega_s$ and it is common that $K_v >> 1$. This means that the bandwidth of the pressure loop can be defined as:

$$\omega_b = K_v \omega_s \tag{26}$$

With a desired gain margin, the bandwidth can instead be defined in terms of the valve response and the gain margin.

$$\omega_b = \frac{2\delta_v \omega_v}{G_m} \tag{27}$$

Given the above equation, we are now able to calculate the required bandwidth of the valve, given the overall bandwidth of the steering system as such, as it has been derived above. Furthermore, the pressure loops bandwidth may be operating point dependent, as the steering systems bandwidth is dependent on the supplied drivers torque. The bandwidth of the valve can now be expressed as

$$\omega_b \approx 3\omega_{ss}$$

$$\omega_v = \frac{3\omega_{ss} G_m}{2\delta_v} \tag{28}$$

6 NONLINEAR ANALYSIS

Figure 11: A closed loop of the complete system with driver, steering system and vehicle.

The purpose of a nonlinear analysis is to derive the requirements of linearity and accuracy of a future hydraulic power assisted steering. This analysis is done with the help of simulation. The complete sy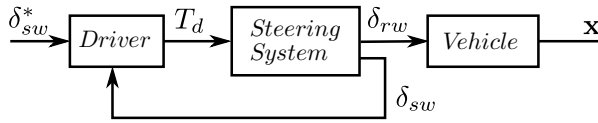stem is shown in figure 11, where a driver model is added to the previously described steering system model and vehicle model. No attempt has been made in order to find the driver dynamics. The driver is therefore seen as a pure controller that takes a desired steering wheel angle and actual steering wheel angle and applies a steering wheel torque. The torque is therefore a consequence of the steering system. By introducing nonlinearities in the pressure loop of the steering system model, the outcome in driver torque can be checked against preset requirements in driver torque. To set the requirements is a field of research itself and should be made with the help of professional drivers. This has not been within the scope of this paper and the level of requirement are based purely on experience, and is defined as

$$\Delta T_d \leq max(0.2, 0.1 \cdot T_d) \quad [Nm] \tag{29}$$

where ΔT_d is the difference between driver torque in the original system and the driver torque in the modified system. The nonlinearities in the pressure loop are supposed to reflect the nonlinearities that could be present in the hydraulic valve used for the future HPAS. These are mainly friction and overlap, and can be expressed as a hysteresis in the pressure loop. The requirements have also been derived for different level of friction in the system. This is interesting since different steering system configurations have different amount of friction. A batch run was performed for different level of friction where the hysteresis width was increased with 0.01 bar until the torque error reached the maximum allowed error.

The result of the run is shown in figure 12. The left plot shows the maximum allowed hysteresis for different amount of friction, defined as mean amount of friction of the total load over one cycle. The right plot shows one run with ∼40 % of friction and a hysteresis width of 0.14 bar.
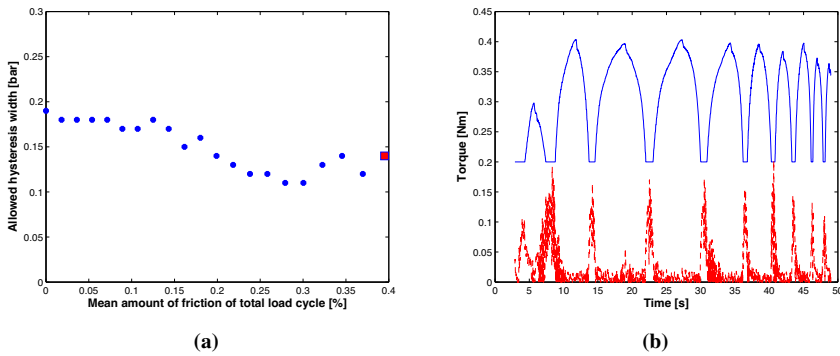
Figure 12: (a) Allowed hysteresis for different friction levels. (b) A run corresponding to marker in (a).

What can be seen is that the steering system is basically as much sensitive for variations in the boost curve regardless the amount of friction in the system, which seems reasonable since the two compared systems have the same amount of friction.

7   DISCUSSION AND FUTURE WORK

It has been shown that with modeling and simulation of a tractor semitrailer, requirements for a future HPAS can be derived. This was done by both a linear and nonlinear analysis of the system and for different driving scenarios. Dry park maneuvers generates the highest rack loads on the vehicle. It was shown how the steering system can be seen as a closed loop system, from a linear point of view, from steering wheel angle to road wheel angle (or total steering wheel torque to road wheel angle). This means that any inner loop bandwidth of the system must be significantly higher than the total bandwidth in order to guarantee similar performance. The purpose of a future actuator concept is to replace the open center valve. From a fuel consumption point of view, the most attractive solution would be to use a closed center valve, and hence an inner loop that controls the pressure, that takes a reference pressure from, for example, an underlying boost curve. For a general pressure loop, the required bandwidth can be expressed in terms of dynamic valve parameters and loop gain margin. The other driving scenario has been to study the steering system on-center at high speed, for instance when driving straight on a high way. Here, nonlinearities in the system become much more evident and are of importance. A complete model of the vehicle with driver was developed for this purpose. For a given driving cycle the driver torque can be studied with this model. By alternating the accuracy of the pressure, the change in driver torque was checked against a preset maximum level. The accuracy of the pressure loop reflects both nonlinearities in the valve of a future concept and how well the controller must perform. Even though there are uncertainties of the level of friction in the system, by alternating the amount of friction, it was seen that the requirement on pressure accuracy is basically unchanged. A low friction level is beneficial for fuel consumption while being an important parameter regarding the steering feel.

The next step in the process is to generate and evaluate a suite of hydraulic actuation concepts, based on the requirements defined in this paper. In addition to these requirement, an important objective is to keep the required bandwidth as low as possible as high bandwidth is associated with high cost. A similar statement can be made for linearity.

8   CONCLUSIONS

When designing a future hydraulic power assisted steering for heavy vehicles, it is important to preserve the characteristics of the present system. In this way the present system is used as the basis for defining the requirements for a future hydraulic power assisted steering. This work has presented a way to derive the requirements for such a system. It was shown that for any actuator concept, it is sufficient to study the pressure loop of the actuator. Requirements of the actuator were defined, expressed in valve response and stability margins. Requirements of actuator linearity and accuracy were also defined, based on simulations of a complete tractor semitrailer model.

9   NOMENCLATURE

Parameter	Description	Unit
β_e	effective compression module	$[Pa]$
ρ	fluid density	$[kg/m^3]$
A_p	piston area	$[m^2]$
b_{sw}	steering shaft damping	$[Nms/rad]$
b_{rw}	road wheel damping	$[Nms/rad]$
c_{tb}	torsion bar stiffness	$[Nm/rad]$
c_{rw}	lumped road wheel stiffness	$[Nm/rad]$
i_{sw2rw}	gear ratio: steering wheel to road wheel angle	$[-]$
i_{pp2rw}	gear ratio: piston position to road wheel angle	$[rad/m]$
J_{sw}	steering wheel inertia	$[kgm^2]$
J_{rw}	road wheel inertia	$[kgm^2]$
T_{kp}	kingpin torque due to front axle side force	$[Nm]$
T_{hp}	hydraulic assist torque	$[Nm]$
T_d	driver torque	$[Nm]$
V	total volume (piston and pipe) volume	$[m^3]$
K_C	valve pressure-flow coefficient	$[m^3/(sPa)]$
K_q	valve flow gain	$[m^2/s]$
K_{reg}	proportional controller gain	$[-]$
K_{bc}	boost curve gain	$[Pa/Nm]$
K_g	steering system steady state gain	$[Pa/Nm]$
w	area gradient	$[m]$
c_q	contraction coefficient	$[-]$
x_v	spool position	$[m]$
x_p	piston position	$[m]$
x_i	reference piston position	$[m]$
p	pressure	$[Pa]$
Q_v	valve flow	$[m^3/s]$

Parameter	Description	Unit
F_y	lateral force on axles	$[N]$
α	slip angle	$[rad]$
l_f	front axle distance	$[m]$
l_r	rear axle distance	$[m]$
Ω	yawrate	$[rad/s]$
v_y	lateral velocity	$[m/s]$
v_x	longitudinal velocity	$[m/s]$
l_l	distance to connection point	$[m]$
M	mass	$[kg]$
C_α	cornering stiffness	$[N/rad]$
F_z	normal load	$[N]$
θ_{rw}	road wheel angle	$[rad]$
θ_{sw}	steering wheel angle	$[rad]$
T_f	pressure dependent friction	$[Nm]$
p_t	pneumatic trail	$[m]$
I_z	vehicle inertia	$[kgm^2]$
ω_{ss}	steering system resonance	$[rad/s]$
δ_{ss}	steering system damping	$[-]$
δ_p	pinion angle	$[rad]$
P_l	load pressure	$[Pa]$
P_s	supply pressuret	$[Pa]$
ω_v	valve response	$[rad/s]$
ω_s	volume breakfrequency	$[rad/s]$
δ_v	valve damping	$[-]$
u	actuator controlsignal	$[-]$
K_a	valve gain	$[-]$
G_m	gain margin	$[-]$
s	laplace operator $(i \cdot \omega)$	$[1/s]$

REFERENCES

[1] Steffen Müller. Zukünftige verbrauchsarme Servolenkungen für volle Steer-by-Wire-Funktionalität. *ATZ*, 2004.

[2] J.Y. Wong. *Theory of Ground Vehicles*. John Wiley & Sons, Inc., third edition edition, 2001.

[3] Marcus Rösth. *Hydraulic Power Steering System Design in Road Vehicles*. PhD thesis, Linköping Studies in Science and Technology, Linköping University, 2007.

[4] P. Krus and J. Andersson. Optimizing optimization for design optimization. In *Proceedings of DETC'2003, ASME Design Automation Conference*, Chicago, 2003.

[5] M.J. Box. A new method of constrained optimization and a comparison with other methods. *The Computer Journal*, 8:42 – 52, 1965.

[6] Herbert E. Merritt. *Hydraulic Control Systems*. John Wiley & Sons, USA, 1967.

Valves, orifices and stability

An experimental, numerical and theoretical study on valve chatter

Csaba BAZSÓ, Csaba HŐS, PhD
Department of Hydrodynamic Systems, Budapest University of Technology and Economics, Budapest, Hungary

ABSTRACT

Pressure relief valves tend to become unstable even under steady-state system conditions. The amplitude of the oscillation is usually so large that the valve body hits the seat, which results not only in high noise level but also in severe damage of the elements. This paper presents a theoretical, numerical and experimental study on relief valve chatter. Experiments were performed with an especially simple direct-operated relief valve. The acceleration of the valve body and pressure time histories at the two ends of the transmission line were recorded and it was found that in the range of low flow rates a relatively constant frequency is present due to the oscillations of the valve body. Several series of measurements were performed with different set pressures, the results are interpreted in terms of waterfall diagrams, with flow rate as the parameter being varied. In the mathematical modeling, the valve body was considered as a one-degree-of-freedom oscillating system. The fluid model was linearly compressible, its inertia, the friction and the unsteady wave effects were neglected. The discharge coefficient was considered as constant. Linear stability analysis was performed on the model yielding an analytical estimation of the onset of self-excited oscillations. Numerical simulations were also performed on this model, with a measurement-based discharge coefficient model. The stability limit was also located numerically. A reasonable agreement was found between the numerical, theoretical and analytical stability borders.

Keywords: hydraulic relief valve, valve chatter, fluid-structure interaction, impacting oscillation

1 INTRODUCTION

Hydraulic systems are widely used in such industrial applications where large forces or torques are to be exerted with high stiffness and small response time. An essential component of such systems is the relief valve, which protects other system elements from overpressure peaks reducing the excess pressure in a safe manner. However, it is known that relief valves tend to oscillate under certain conditions, e.g. if the valve is oversized. Due to the complex fluid-structure interactions it is challenging to describe relief valve instability (called valve chatter), for examples of such studies, see (4)-(11), (15), (16).

Several researches are concerned with the analysis of the flow rate through conical valves. Geometry of the valve, valve body position and turbulence level are among the influencing factors. Stone (1) in 1960 studied experimentally the discharge coefficients and steady flow forces on the poppet valve. Takenaka (2) in 1964 studied the performance of several hydraulic control valves. He established dynamic equations for unsteady behaviour predictions, but unfortunately no experimental validation was given. He determined formulae for the discharge coefficient for several ranges of the Reynolds number based on his experiments. Urata (3) in 1969 performed experiments to study the static characteristics of the thrust of poppet valves under different conditions. The experimental results revealed his estimation for the thrust using the momentum theory and boundary layer theory.

Many studies deal with the smooth and non-smooth self-excited nonlinear vibration that occurs under certain circumstances neglecting the wave effects in the pipeline ((4), (5), (6), (7), (8), (9), (10)), and several works focus on the acoustic oscillations in the pipe which will react back on the valve. Thomann (11) in 1976 investigated analytical expressions for the frequency and the amplification close to the stability limits as well as for long and short pipes. The theoretical predictions were compared with experiments and good agreement was found.

This study aims to collect measurement data for valve chatter analysis. On one hand, static performance curves (fluid forces and discharge coefficients) are reported under steady-state operation. On the other hand, spectra of acceleration signals are presented and compared to analytical and numerical predictions.

2   MATHEMATICAL MODELLING

2.1   Governing equations

Figure 1 depicts the hydro-mechanical model of a direct-operated pressure relief valve. The conical valve body of mass m is connected to a spring with spring constant s and viscous damping k. The pre-compression of the spring will be denoted by x_0 while x stands for the displacement of the body. Only the capacity of the pressure transmission line will be modeled by its bulk modulus E and volume V. The spatially averaged pressure in the transmission line is denoted by p, the constant flow rate entering the transmission line is Q_p, while the outflow is Q_{out}, the latter depends both on the valve body displacement x and pressure p.
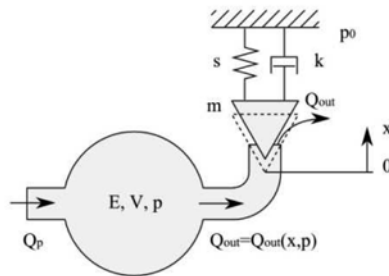
Figure 1 Mechanical model of the hydraulic system

In what follows, we assume that the force on the valve body due to the change of momentum can be neglected compared to the pressure term. The estimation of the viscous damping k is highly nontrivial, we will return to this issue later. The inertia, friction and internal (wave) dynamics of the fluid in the transmission line are also neglected. By applying Newton's second law of motion on the valve body and considering the mass balance of the transmission line the governing equations are

$$\dot{x} = v$$
$$\dot{v} = \frac{A_v}{m} p - \frac{k}{m} v - \frac{s}{m}(x + x_0)$$
$$\dot{p} = \frac{E}{V}\left(Q_p - Q_{out}(x, p)\right)$$

(1)

The flow rate through the poppet valve is given by

$$Q_{out}(x, p) = c_1 x \, C_d \sqrt{\frac{2}{\rho} p} = \gamma \, x\sqrt{p}, \qquad \gamma = c_1 C_d \sqrt{\frac{2}{\rho}} \qquad (2)$$

where $A(x)=c_1 x$ is the flow-through area and the discharge coefficient C_d also depends on the valve lift and system pressure. Several researchers (e.g. (12), (13)) suggest that the discharge coefficient can be described by the Reynolds number as a single parameter. As it will be shown in section 3.3, in this case this cannot be done. However, in the following theoretical calculations the discharge coefficient will be assumed to be constant. In the case of numerical simulations measured values of C_d will be used for interpolation.

Impingement of the valve body on the seat might occur, for which the following collision condition is applied

$$x(t^+) = 0, \quad v(t^+) = -r\, v(t^-), \qquad (3)$$

where r is the restitution coefficient, t^+ and t^- denote the time before and after the collision, respectively.

2.2   Linear stability analysis
In what follows, for the sake of simplicity, we assume that the discharge coefficient is constant. The equilibrium of system (1) is given by $v_e = 0$ and $x_e = A_v p_e / s - x_0$, where p_e is the solution of

$$Q_p = c_1 C_d \left(\frac{A_v p_e}{s} - x_0\right)\sqrt{\frac{2}{\rho} p_e} \; . \qquad (4)$$

If the spring precompression is set to zero the equilibrium pressure is easy to calculate, however, for the general $x_e \neq 0$ case it is cumbersome to obtain. In what follows, the

notation of p_e will be used, however, it is not a free parameter but for a given set of system parameters (e.g. pump flow rate and precompression) determine p_e uniquely.

Close to the equilibrium, the dynamics is governed by the eigenvalues of the linear coefficient matrix $\underline{\underline{J}}$ given by

$$\underline{\underline{J}} = \begin{pmatrix} 0 & 1 & 0 \\ -s/m & -k/m & A_v/m \\ \alpha(p_e) & 0 & \beta(p_e) \end{pmatrix}, \tag{5}$$

where

$$\alpha(p_e) = -\frac{E}{V}\gamma\sqrt{p_e} \quad \text{and} \quad \beta(p_e) = -\frac{E}{V}\gamma\frac{x_e}{\sqrt{p_e}}. \tag{6}$$

The eigenvalues are the roots of the characteristic polynomial

$$\det(\underline{\underline{J}} - \lambda\underline{\underline{I}}) = \lambda^3 + a_2\lambda^2 + a_1\lambda + a_0 = 0 \tag{7}$$

with

$$a_0 = \frac{A_V E\gamma\sqrt{p_e}}{mV} + \frac{s}{m}\frac{E\gamma\ x_e}{2V\sqrt{p_e}}, \quad a_1 = \frac{s}{m} + \frac{k}{m}\frac{E\gamma\ x_e}{2V\sqrt{p_e}}$$

$$\text{and} \quad a_2 = \frac{k}{m} + \frac{E\gamma\ x_e}{2V\sqrt{p_e}}. \tag{8}$$

We are interested in computing those critical parameter values at which oscillations are born in the system. This happens if we have purely imaginary eigenvalues (Hopf bifurcation) as explained e.g. in (14). Inserting $\lambda = i\omega$ into (7) and forcing both the real and imaginary parts to vanish, we find that the necessary condition for stability loss and the frequency of the appearing oscillation is

$$a_0 = a_1 a_2 \quad \text{and} \quad \omega = \sqrt{a_1}. \tag{9}$$

Let us describe a simple and iteration-free way of computing the above stability border. For a given equilibrium pressure p_e, the critical valve displacement x_e is computed by using (9). Then, spring precompression $x_{0,crit}$ is calculated from $x_e = A_v p_e / s - x_0$ and finally the corresponding critical flow rate $Q_{p,crit}$ is computed by virtue of (4).

2.3   Numerical simulations

Let us briefly describe the details of numerical simulations. System (1) was implemented in Matlab environment and the built-in fifth-order Runge-Kutta solver was used, including automatic error estimation and step-size control. For locating the collision points where the valve body hits the seat, the event handling function was activated and the impact law (3) was applied. The tolerances of integration and event location were left at their default values.

During the integration process, the discharge coefficient was interpolated over measured values (see the next section for details) as a function of valve lift (x) and inlet pressure (p).

The computations started with an initial integration of *0.2* seconds, which was found to be long enough for the influence of initial conditions to vanish. Then, another *1* seconds of integration was performed, whose spectra was compared to the measurements.

3   MEASUREMENTS

3.1   Test rig

The sketch of the test rig and the test valve are shown in Figure 2. The test valve (5) and the gear pump (1) driven by a DC electric motor were connected by a hydraulic hose (2). The test valve was a spring-loaded single-stage pressure relief valve pre-compressed by the adjusting wheel (9) with conical valve body of *60°* cone angle and spring constant *15* kN/m.

Pressure transducers (type HBM P11) (3, 4) were mounted at the two ends of the hose (i.e. one close to the relief valve and another one at the pressure side of the gear pump). The displacement was not measured directly under dynamic conditions. When it was needed (e.g. when setting the spring precompression or while the discharge coefficient measurements), it was measured manually with a displacement indicator. To record the acceleration of the valve body (7) a piezoelectric accelerometer (type Brüel&Kjaer) (6) was fastened onto its shaft (8). The fluid force measurements were performed with the help of a load cell type Kraftaufnehmer KM300. Finally, the flow rate was measured with a metering tank mounted at the exhaust port of the relief valve.
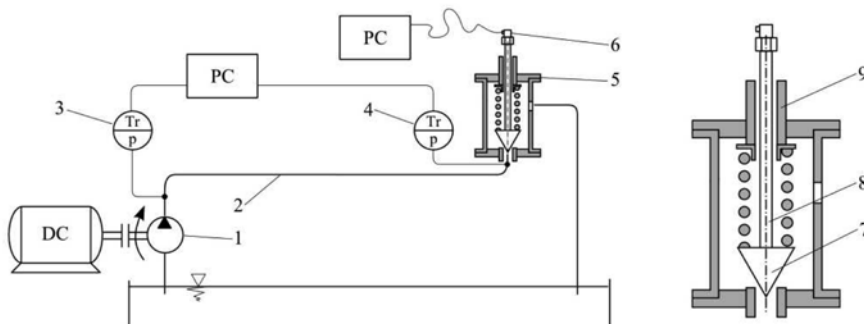

Figure 2 Sketch of the test rig and the test valve

The presence of the two pressure transducers allowed the direct measurement of the sonic velocity and the reduced bulk modulus. With the sudden opening and closing of a by-pass valve pressure transients were generated and by correlating the two pressure signals the sonic velocity could be computed. Its value was found to be between *966-1290* m/s. In what follows the average value of *1210* m/s was used.

3.2   Thrust on the poppet valve

Experiments were performed in which the spring was removed and a load cell was used to measure the fluid force acting on the valve. The theoretical force is given by

$$F = \Delta p A_v - \rho Q v \cos \alpha , \qquad (10)$$

where α is the half-cone angle (*30°* in our case). We employ the usual assumption that the flow angle through the gap equals the half cone angle, see (3). As the second term describing the force due to the momentum change is not included in the mathematical model, an emphasis was put on the influence of this term. Figure 3 depicts the measurement results together with the theoretical values. As it can be seen, equation (10) over predicts the fluid force, especially without the momentum term. It is also clearly seen that the larger the flow rate is, the more important it becomes to include the force due to the momentum change across the poppet valve. However, even with the simpler form of (10) employed in the stability analysis the error between the theoretical and measured values is less than 10%.
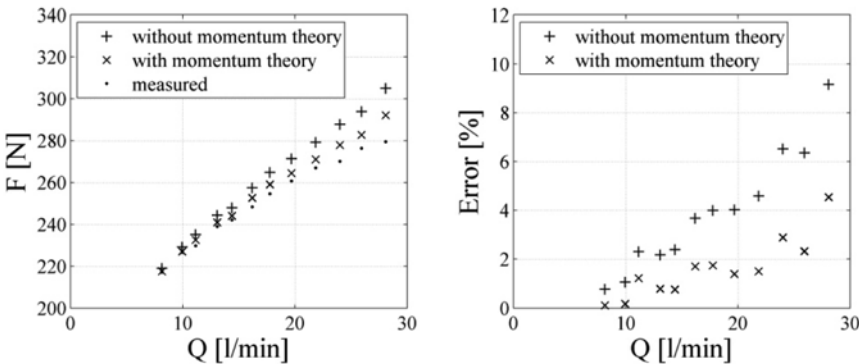
Figure 3 Left: Theoretical and measured force acting on the valve body. Right: discrepancy between the theoretical and measured values.

3.3   Discharge coefficient

Another important issue was the proper modelling of the discharge coefficient. Hence measurements were performed in which the flow rate, the inlet pressure and the valve displacement were measured simultaneously (under steady-state conditions). Thus the discharge coefficient was computed by virtue of (2). The result is shown in Figure 4. It has to be noted that by plotting the discharge coefficient as a function of the Reynolds number (as described e.g. in (12), (13)), we experienced a single consistent curve. The Reynolds number is computed as follows

$$\text{Re} = \frac{\dfrac{Q}{A(x)} \cdot D_{seat}}{\upsilon}, \tag{11}$$

where D_{seat} is the diameter of the inlet, υ is the kinematic viscosity of the medium.
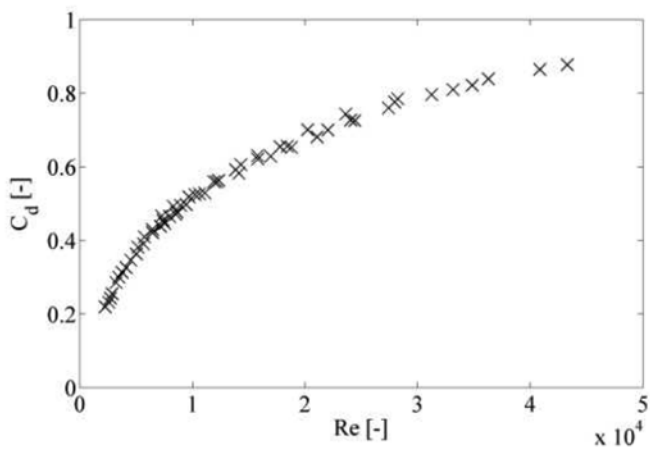

Figure 4: Discharge coefficient as a function of the Reynolds number.

4   RESULTS

Several series of measurements were performed with different set pressures (i.e. spring precompression values). For a given set pressure, the flow rate was systematically increased up to approx. 30 l/min, while the pressure signals and the acceleration signal were recorded. Then, the spectra of the acceleration signals were plotted as a function of the flow rate resulting in the left-hand side column of Figure 5. The frequency of the pressure excitation from the gear pump (revolution number times teeth number) is clearly seen in all Figures, being linearly proportional to the flow rate. The other series of peaks correspond to the chatter frequency and it is clearly seen that this one is present only for low flow rates and its frequency is fairly constant. Plotting the spectra of the pressure signal gives the same results both qualitatively and quantitatively.

The parameter values of the numerical simulations are listed in Table 1.

Table 1 System parameters used in the simulations

Parameter	Value	Parameter	Value
m	0.4 kg	ρ	870 kg/m^3
s	15 kN	V	2.963×10^{-4} m^3
k	300 Ns/m	c_l	0.0236 m
A_v	1.767×10^{-4} m^2	E	1.274×10^9 Pa

There were two parameters which could not be measured, namely the restitution coefficient *r* and the viscous damping coefficient *k*. Several numerical computations were performed with a wide range of the restitution coefficient (from 0.1 to 1) and it was found that the value of *r* hardly changes the dominant frequency or the critical flow rates. Concerning the viscous damping it was found to influence the stability limit significantly. The results presented is Figure 5 and 6 were obtained with *k*=300 Ns/m. This large value was set
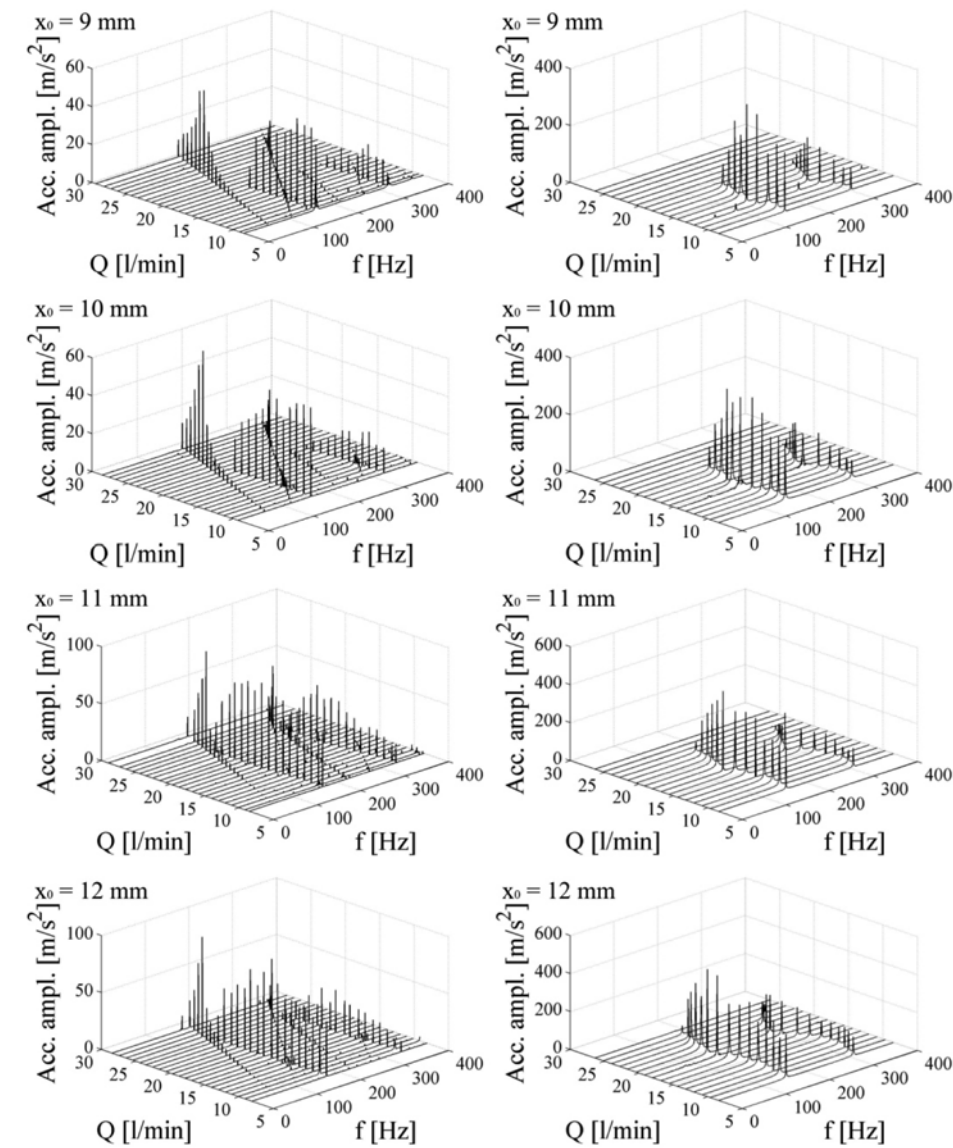

Figure 5 Left column: spectra of the measured acceleration signals of the poppet valve body. Right column: spectra of the acceleration of the poppet valve body in the case of numerical simulations, for several parameter values.

artificially at $x_0=8$ mm to match the numerical and experimental results but was not modified in the rest of the simulation. Note that this is the only damping in the numerical simulations while in the real system there are several origins of energy dissipation; e.g. friction and viscoelastic behavior of the hydraulic hoses, the inertia of the oil driven by the oscillating valve body, etc. The pump flow rate was assumed to be constant.

The right-hand side of Figure 5 depicts the spectra of the acceleration resulting from the numerical simulations at the same parameter values. It can be clearly seen that there is a quantitative coincidence between the measurements and the simulations. Although there are small "wiggles" in the case of the simulations, the frequency of the oscillation and the critical flow rate corresponding to the onset of chatter are very close.
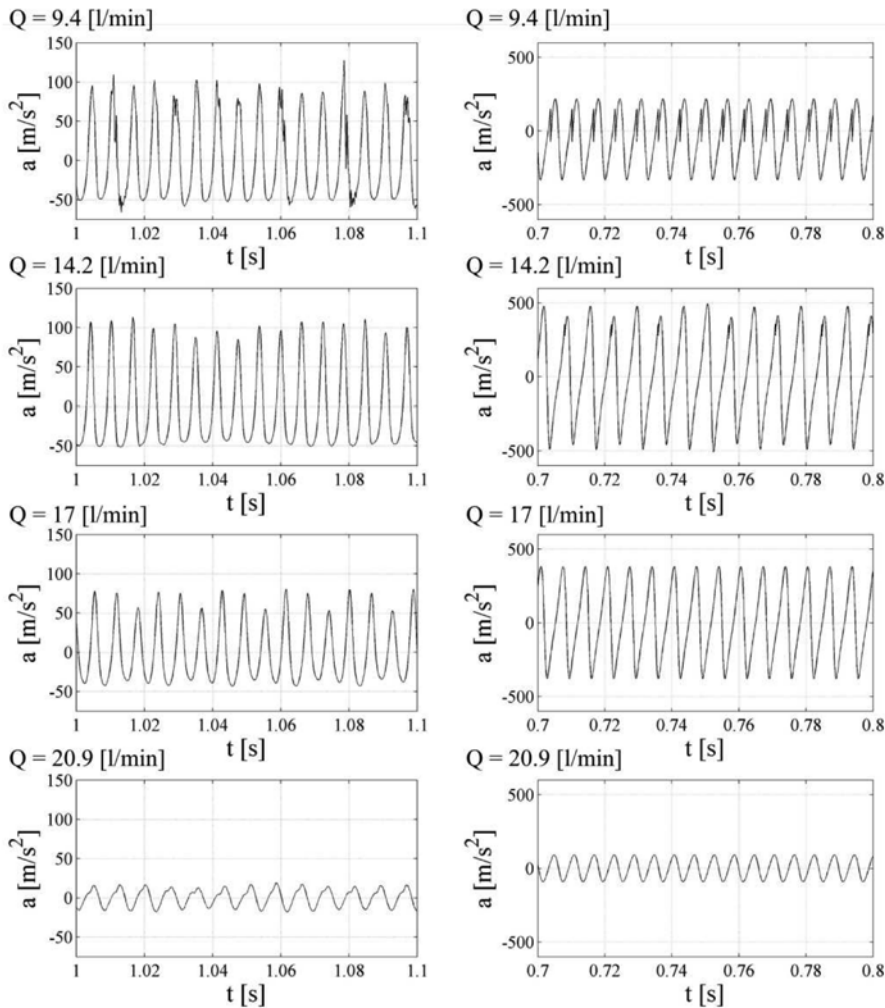

Figure 6 Left column: measured acceleration time history of the poppet valve body. Right column: time history of the acceleration of the poppet valve body obtained by numerical simulations.

Figure 6 shows examples of measured and simulated acceleration time histories in the case of x_0 = 10 mm. Note that although the shape of the oscillation is poorly described by the simulation, the frequencies are close to each other.

Figure 7 presents the essence of our study in a compact way: the critical flow rate and the frequency of the appearing oscillation are shown as a function of the set pressure. As it can be seen on the left-hand side, for a given set pressure, there is a critical flow rate above which the equilibrium is stable. The higher the set pressure is, the higher the critical flow rate becomes. The theoretical curve and the measured and simulated boundaries are close to each other.

On the right-hand side the frequency of the appearing oscillation is shown. Note that the simulation and the experiment are close to each other; however, the analytical estimation under predicts the frequency. The reason of this discrepancy is that equation (9) does not take into account the impact dynamics, which – roughly speaking – cuts out a portion of the periodic motion predicted by the Hopf bifurcation. Hence the analytical calculation predicts higher periods and lower frequencies.
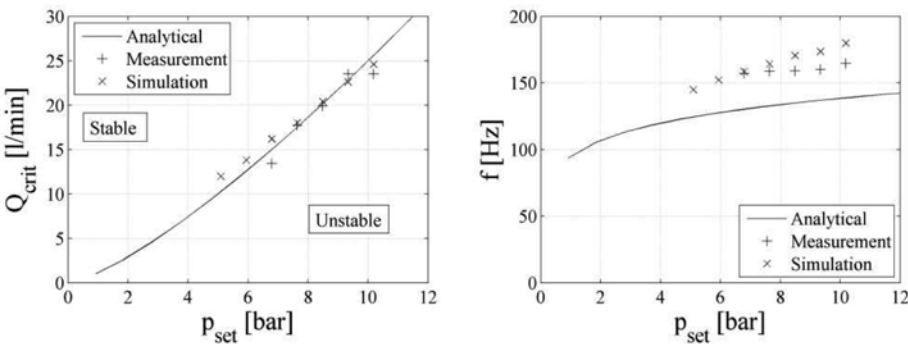
Figure 7 Left: Critical flow rate (left) and the frequency of the oscillation (right) as a function of the set pressure.

The left-hand side of Figure 8 depicts the effect of pipe length on the critical flow rate for a d = 12 mm diameter hydraulic hose with reduced bulk modulus of $E = 1.274 \times 10^9$ Pa. Note that in our model, the volume of the fluid is the parameter, hence the same Figure can be used to describe the effect of pipe diameter. The right-hand side Figure compares the critical flow rate for different values of reduced bulk modulus of the fluid and the transmission line. It is clearly seen from both figures that decreasing the pipe length or increasing the reduced bulk modulus (using hydraulic hoses instead of rigid pipes) results in poorer performance an earlier onset of instabilities.

Figure 8 Left: Critical flow rate for (left) different pipe lengths and for (right) different values of reduced bulk modulus of the transmission line.
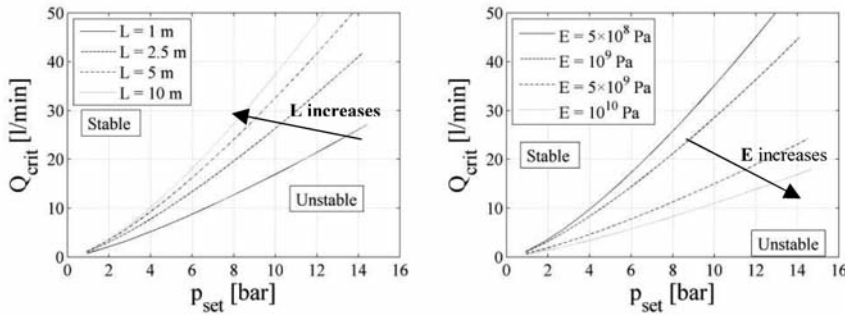
5   Conclusions

Theoretical and experimental analysis of relief valve chatter was reported in this paper. A simple mathematical model was presented consisting of three nonlinear ordinary differential equations. Linear stability analysis was performed with constant discharge coefficient resulting in an analytical estimation of the critical flow rate. It was found and confirmed experimentally that for low flow rates the equilibrium is unstable and the stable oscillation appears. Numerical simulations were also performed with measured discharge coefficient. A relatively large damping coefficient had to be chosen to match the theoretical, numerical and experimental stability boundaries. However, this damping coefficient is not necessarily unphysical because there were several unmodelled energy dissipating phenomena e.g. friction and viscoelastic behavior of the hydraulic hoses, the inertia of the oil driven by the oscillating valve body. It was found that the restitution coefficient has hardly any influence on the dynamical behavior of the system. It was also experienced that increasing the transmission line length or decreasing the reduced bulk modulus stabilizes the system.

References

(1) J. A. Stone. Discharge coefficients and steady state flow forces for hydraulic poppet valves. ASME Journal of Basic Engineering, 1960:82:144-152, 1960.

(2) T. Takenaka. Performances of oil hydraulic control valves. Bulletin of the JSME, 1964:7(27):566-576.

(3) E. Urata. Thrust of Poppet Valve. Bulletin of the JSME, 1969:12(53):1099-1109.

(4) J.E.Funk. Poppet Valve Stability. Journal of Basic Engineering, 1964:207–212.

(5) K.Foster, M.M.Kulkarni. Steady-amplitude, Self-excited Oscillations of Hydraulic Spool Valves. Journal of Mechanical Engineering Sci. 1968:10:306–318.

(6) Gábor Licskó, Alan Champneys, Csaba Hős. Nonlinear Analysis of a Single Stage Pressure Relief Valve. IAENG International Journal of Applied Mathematics, 39:4, 2009

(7) K.Kasai. On the Stability of a Poppet Valve with an Elastic Support. Bulletin of JSME 1968:11:1068-1083.

(8) S. Hayashi, T. Hayase, T. Kurahashi. Chaos in a Hydraulic Control Valve. Journal of fluids and structures, 1997:11:693–716.

(9) Hayashi, S. Instability of Poppet Valve Circuit. JSME International Journal, 1995:C38(3):357-366.

(10) Wang W., Hayashi S., Hayase T., Shirai A. Local Stability of a Direct-Acting Poppet Valve Circuit with a Long Pipeine. Nihon Yukuatsu Gakkai Ronbunshu. 1999:30(3):67:74

(11) Hans Thomann. Oscillations of a simple valve connected to a pipe. Journal Zeitschrift für Angewandte Mathematik und Physik. 1976:1:27

(12) H. E. Merritt. Hydraulic Control Systems. John Wiley and Sons, 1967.

(13) W. Borutzky, B. Barnard, and J. Thoma. An orifice model for laminar and turbulent conditions. Simulation Practice and Theory, 10:141-152, 2002

(14) Y. A. Kuznetsov. Elements of Applied Bifurcation Theory. Springer, 1998.

(15) D.N. Johnston, K.A. Edge, M. Brunelli. Impedance and stability characteristics of a relief valve. Proceedings of the Institution of Mechanical Engineers, Part I: Journal of Systems and Control Engineering, 2002:216 (5):371-382

(16) G. MacLeod. Safety Valve Dynamic Instability: An Analysis of Chatter. J. Pressure Vessel Technol. 1985:107(2):172-178

Determining the Probability of Performance and Stability for a Metering Poppet Valve

Richard Carpenter (racf8f@mail.missouri.edu)
Roger Fales (falser@missouri.edu)
Mechanical and Aerospace Engineering Department
University of Missouri
Columbia, Missouri

ABSTRACT

A method is developed for determining the probability of achieving stability and achieving a performance objective of a metering poppet valve. The work is an application of a probability stability/performance analysis technique being developed by the authors. Using statistical information such as the probability density function of the system parameters, the goal is to determine the probability of a metering poppet valve system achieving or not achieving a frequency domain performance specification. An H-infinity control system is applied to the valve. A performance specification is given for the valve and converted into a performance weight transfer function for the analysis. The metering poppet valve is an example of realistic higher order system with uncertain parameters. The valve has spring feedback integrated into a pilot control system. The spring rate, valve component masses, and viscous friction are considered to be random variables with normal distributions. In this work, a prediction is made of the percentage of valve systems that would not achieve the given frequency domain performance requirement. The prediction applies if the valve were manufactured in a series production with component parameters that have known statistical qualities.

1. INTRODUCTION AND BACKGROUND

In this work, uncertainty modeling and valve performance analysis are considered for a metering poppet valve (MPV) with an H-infinity control system. The MPV was designed and built at the University of Missouri. The valve design was based largely on linearized model root locus techniques and the use of nonlinear simulations (Muller, 2008). The design techniques used were similar to those used by Li for a spool valve application (Li, 2002). The prototype was completed in 2008 with initial test results appearing for the first time in a paper by Fales and Li (2008).

In recent years, there has been an interest in developing poppet valves for flow metering applications in place of the typically used spool valves (Ardema, 1997), (Schexnayder, 1995), and (Yang, 2005). The poppet valve offers certain advantages over the spool valve. Mainly, poppet valves have extremely low leakage when closed, they require less precise machining, they are capable of adjusting themselves with wear, and they are self-flushing and therefore less sensitive to contamination (Manring, 2005). Key disadvantages to using the poppet valve for flow metering are centered on dynamic stability

---

issues of poppets which have been studied by Hayashi (1995) and Funk (1964) for example. The performance of metering poppet valves in feedback control systems have been found to be limited by various factors such as the location of an open loop pole in a valve studied by Zhang et al (2002) and model uncertainty studied by Fales (2006).

The following paragraph gives a brief description of the operation of the metering poppet valve design presented in this work. With respect to Figure 1, the valve is in the closed position with high pressure connected to the inlet port while low pressure is connected to the outlet port. The only two pathways from high to low pressure are sealed by poppet seats and therefore the valve maintains a very low leakage flow when closed. It is assumed that the pilot poppet is pressure balanced by the passage shown within the pilot poppet while being subjected to the pilot solenoid force, the feedback spring's force, viscous damping, and flow forces. In order to raise the main poppet off its seat current is applied to the pilot actuator solenoid which pushes the pilot poppet off its seat and allows fluid to exit the pilot control volume through its outlet orifice (2) restriction. Once the pilot poppet opens, the control volume inlet orifice 1 is effectively smaller than its outlet orifice creating a net outflow which allows the main poppet to lift off its seat. This opens the main metering orifice (3) restriction directly between supply and load, allowing flow to be metered. The upward movement of the main poppet will push the feedback spring and in turn push the pilot poppet back towards its seat until an equilibrium position is reached where the main poppet is open yet no longer moving. In order to close the main poppet, the actuator current is turned off allowing the feedback spring to push the pilot poppet back to its seat. The control volume outlet orifice is now closed while high pressure fluid from the inlet orifice fills the control volume and pushes the main poppet closed.

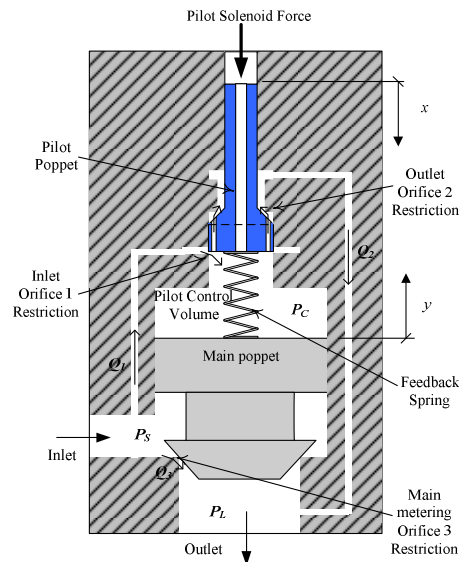**Figure 1 Diagram of the metering poppet valve**

The stability and performance of dynamic systems can define the success or failure of a manufactured system such as the MPV. The goal of this work is to find error models that account for a percentage of possible plants with random parameters. The variations in parameters such as spring rates and part geometry should serve as an input to this sort of

analysis since these characteristics can be obtained or are already known by the manufacturer. For a long time, manufactures have predicted the number of assembly failures due to the interference fit between parts that experience tolerance stack up (Stoll, 1999). In this work, statistical data about parameters of the metering poppet valve system is used to predict the probability of failure due to not achieving performance and stability requirements expressed in the frequency domain. A Monte Carlo method will be used to build an error model based on parameters that can be modeled as random numbers. The error model can be used to determine whether a system is stable or meets performance specifications with a given probability. The Monte Carlo approach used in this work provides a convenient way to solve a problem that is a function of potentially numerous random variables (Rubinstein, 1981).

Other researchers are working on probabilistic control design which is similar in concept to methods presented here but does not provide for predictions of failure rates but seeks to design controls such that success would be most likely given the statistical distribution of plant dynamics (Crespo and Kenny, 2005). There is also active research in the area of Probability Stability where one can predict the probability of stability based on the statistical distribution of dynamic equation parameters but these methods tend to be very cumbersome for all but the simplest low order systems (Jovanovic, 2004).

Some research has focused on the stochastic nature of plant uncertainty (i.e. uncertain parameters) which can be used to determine the stochastic root locus and probability of instability (Stengel, 1991). In addition, this work has been extended to determining the probability of achieving performance requirements and to nonlinear systems by developing indicator functions that are examined statistically to determine the probability of achieving specified behavior (Wang and Stengel, 2002). Further research in the area of probability stability showed that uniform distribution is the "right" way to estimate the probability densities for sampled parameters (Barnish, 1997).

The approach presented here provides a way to evaluate the new MPV system designs for probability of reliable stability and performance. Often, manufacturers do not use a systematic approach for analyzing robust stability and for predicting reliability and numbers of failures in multi component dynamic systems. However, manufactures of valves and other hydraulic components may have access to data which could be used to describe parameter variations statistically. For example, dynamically important parameters such as mass, spring rate, etc., can be described using a probability density function. This work focuses on the frequency response of the MPV system and its relationship to stability and performance. The model parameters affect dynamic performance and stability of a feedback control system in a way that can be seen by observing the frequency response of a transfer function model. The magnitude of the frequency response becomes random at each frequency if the parameters of the model are random. In addition, error models with random frequency responses are developed in this work. The random magnitude of the frequency response of generalized plant transfer functions and error models can then be analyzed to determine if performance objectives and/or stability are achieved using methods commonly used in robust control applications where the transfer functions do not have random magnitudes (Skogestad, 1996). Alternatively, one could analyze the systems by looking at variations in poles and zeros. However, it is often convenient to express performance specifications as a frequency response. Also, pole zero analysis does not lend itself to error models like frequency domain analysis does. The ability to model uncertainty in the frequency domain allows some change to the system (i.e. controller redesign) without reconstructing the uncertainty model.

2 UNCERTAINTY MODELING

In this section error models are discussed in general. Section 4 discusses the error model for the MPV. Let a plant transfer function, $G(j\omega)$, represent all possible perturbations of the plant due to model uncertainty such as uncertain parameters modeled as random numbers. A nominal plant transfer function, $G_{nom}(j\omega)$, can be chosen as an average or typical plant. At each frequency, the frequency response of $G(j\omega)$ can be calculated and the frequency response of the multiplicative model error,

$$l(j\omega) = \frac{G_{nom}(j\omega) - G(j\omega)}{G_{nom}(j\omega)},$$
(1)

can also be calculated. $l(j\omega)$ comprises a set of multiplicative errors generated using (1) and a set of perturbed plants $G(j\omega)$. If the plant response is uncertain, due to random uncertain parameters, then the frequency response of the multiplicative error magnitude will have a random distribution at each frequency with probability density function, $f_{l\omega}(\Theta)$, which depends on the plant transfer function. The plant transfer function may contain random parameters. Uncertainty can be modeled to account for modeling error due to a specified fraction of all possible plants if the distribution of magnitude of the plant frequency response is known. With an uncertainty model that describes the uncertainty for a large fraction of the possible plants, stability analysis can then be carried out. The resulting analysis would then only apply to the plants covered by the uncertainty model. This creates a way to avoid the typically conservative analysis that results from considering all possible plants in stability and performance analysis. Of course the drawback is that analysis using the new uncertainty models can only guarantee results for a portion of possible plants. Rather than finding a transfer function that bounds all $l(j\omega)$ at each frequency, we want to find a transfer function, $w_x(j\omega)$ with a magnitude frequency response that bounds a given fraction, x, of $l(j\omega)$ at each frequency. If $l(j\omega)$ has a random magnitude at each frequency, ω, then

$$P_{\omega}(|w_x(j\omega)| \geq |l(j\omega)|) = x \quad \forall\omega.$$
(2)

If $w_x(j\omega)$ satisfies (2), then $w_x(j\omega)$ is a model of the multiplicative uncertainty for a fraction, x, of the replications of $G(j\omega)$. Equation (2) can be satisfied by first finding $l^*(\omega)$ for each frequency in the following equation:

$$\int_0^{l^*(\omega)} f_{l\omega}(\Theta)d\Theta = x \quad \forall\omega$$
(3)

The symbol $f_{l\omega}(\Theta)$ stands for the probability density function of the magnitude of multiplicative error at a particular frequency. Note that the lower limit of the integral can be zero since the error magnitude is always greater than or equal to zero. Also note that both (2) *and* (3) must apply for all frequencies. This means that if we find a particular multiplicative error $l(j\omega)$ that has a magnitude less than $l^*(j\omega)$ at any frequency then it must be bounded by the uncertainty model, $w_x(j\omega)$, at *all* frequencies. If the multiplicative error frequency responses $l(j\omega)$ (found for each perturbation of the plant) do not overlap in magnitude, an error transfer function can be simply found such that $|w_x(j\omega)| \geq l^*(\omega)$, for all frequencies. However, if there is overlapping of the frequency responses of $l(j\omega)$ then the error model, $w_x(j\omega)$, must be found as an upper bound of the set of all $l(j\omega)$ for which

$|l(j\omega)| = l^*(\omega)$ at any frequency.   Let L ={all $|l(j\omega)|$ such that $|l(j\omega)| = l^*(j\omega)$ at any frequency} then $w_x(j\omega)$ can be chosen as an upper bound on L so that

$$| w_x(j\omega) | = \sup(L) \quad \forall \; \omega. \tag{4}$$

With this new error model, $w_x(j\omega)$, the model of the plant accounting for error is given in the multiplicative form as

$$G(j\omega) = (w_x(j\omega)\Delta(j\omega) + 1)G_{nom}(j\omega). \tag{5}$$

The symbol $\Delta(j\omega)$ stands for the set of all stable rational transfer functions with magnitude less than or equal to one. A block diagram describing the plant model including the nominal plant with the error model applied is given in Figure 2.
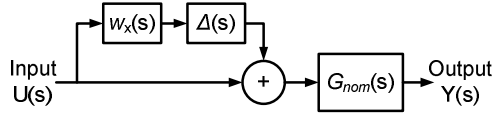

Figure 2 Plant model including an error model where $G_{nom}(s)$ is the nominal plant model

3. MPV MODEL

In this section, the model is briefly discussed. More detail can be found in previous works by the authors (Muller and Fales, 2008). The general model can be broken into four basic systems or governing equations: two spring mass damper systems with flow and pressure forces for each poppet, a pressure rise rate equation for the control volume, and a pressure rise rate equation for the load volume. The forces acting on the main poppet are represented by

$$M\ddot{y} = -b_y \dot{y} - k(y+x) - P_c A_c + P_s A_s + P_L A_L - 2\cos(\theta)C_d{}^2 h_3 y(P_s - P_L) \tag{6}$$

The force balance on the main poppet includes flow force, viscous friction, feedback spring, and, hydrostatic forces due to pressure at the inlet, outlet and pilot pressure. The pilot poppet has similar forces except for the hydrostatic forces since the pilot poppet is pressure balanced. Also, the solenoid force is present which actuates the valve. The pilot poppet dynamic equation is given as follows:

$$m\ddot{x} = -b_x \dot{x} - k(y+x) + f - 2\cos(\theta)C_d{}^2 h_2 x(P_c - P_L) + 2\cos(\theta)C_d{}^2 h_1 x(P_s - P_c) \tag{7}$$

The pressure in the pilot control volume is affected by main poppet movement, flow entering and exiting the control volume as follows:

$$\dot{P_c} = \frac{\beta}{V_{CO}}(Q_1 - Q_2 + A_c \dot{y}) \tag{8}$$

The load pressure (pressure at the outlet of the valve) can be given as,

$$\dot{P_L} = \frac{\beta}{V_L}(Q_2 + Q_3 - Q_4), \tag{9}$$

assuming that there is some load flow, Q_4, due to a load orifice for example. Later in this work, when experimental results are compared with simulations, P_L is simply an input to the

model rather than a simulated state. The flow terms, Q_1-Q_4, in Eq. 3 and Eq. 4 are modeled using the classic orifice equation.

$$Q = aC_d \sqrt{\tfrac{2}{\rho} \Delta P} \tag{10}$$

The orifice areas are functions of the position of the pilot poppet position for areas one and two and the main poppet for area three. The slopes for these area functions with respect to poppet displacement are h_1, h_2, and h_3.

The linearization of the model is discussed in previous work by the authors (Muller and Fales, 2008). The linearized model equations are given as follows:

$$M\ddot{y} = -b_y \dot{y} - k(y_n + x_n) - kfq_3 y_n - kfc_3(P_s - P_L) - P_c A_c +$$
$$P_s A_s + P_L A_L \tag{11}$$

$$\dot{P}_c = \frac{\beta}{V_{CO}} \left\{ \begin{array}{l} A_C \dot{y} + kq_1 x_n - kq_2 x_n - kc_1 P_C - \\ kc_2 (P_C - P_L) + kc_1 P_s \end{array} \right\} \tag{12}$$

$$m\ddot{x} = -B_x \dot{x} - k(y_n + x_n) - kfq_2 x_n + kfq_1 x_n - kfc_1 P_C -$$
$$kfc_2 (P_C - P_L) + f + kfc_1 P_s \tag{13}$$

The nonlinear model was linearized using Equations (11)-(13) about an operating point to study the dynamics of the system. A step response of the linearized model is given in Figure 3. The supply (valve inlet) pressure is approximately 3.2 MPa. The step increase in force is 8 Newtons (The solenoid actuator range is 60 Newtons). Even with the nonlinearities of the system, the linear model simulation follows the experimental data well. (Experimental data is given in Figure 3 and the experimental setup is shown in .) For this small step input, the linear and nonlinear models are nearly identical so the nonlinear simulation is not shown in Figure 3.
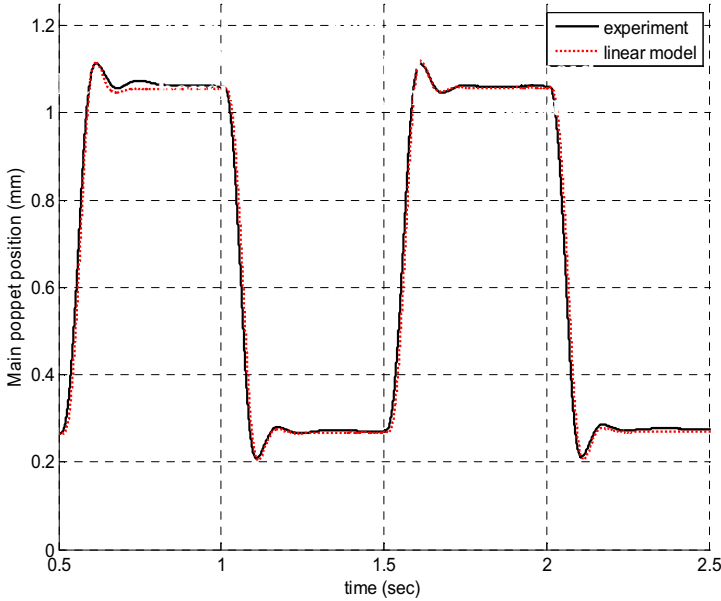

Figure 3 Experimental step response compared to a linear model

4 UNCERTIANTY MODEL FOR THE MPV

An uncertainty model can be used to predict stability and performance of a valve control system with consideration of uncertain parameters within the model. In this work, model uncertainty will refer to variations in the linear model used to create the simulation plot in Figure 3. Generally the higher the plant model uncertainty, the lower performance of a feedback control system must be to ensure robustness. In classical control terms, more plant model uncertainty means that a controller applied to create a closed loop system must have a greater gain margin. Greater gain margin typically is obtained by reducing performance. Therefore it is important to design components with the least amount of model uncertainty possible. Frequency domain uncertainty model can be used to analyze the robust stability of closed loop control systems (Skogestad, 1996).

There are several sources of uncertainty in the metering poppet valve model. Parameters can vary from valve to valve if the valve were to be mass produced or as the valve wears over time causing model uncertainty. The model linearization changes depending on operating conditions which can be treated as uncertain. This study will focus on three causes of uncertainty: pilot poppet damping, pilot poppet mass, and feedback spring rate (See Table 1). The uncertainty is considered in two cases corresponding to two different control designs, Design 1 and Design 2 listed in Table 2.

Table 1 Perturbed parameters for the uncertainty analysis of the MPV system

Perturbed Parameters	Nominal Values
k (N/m)	7355
b_X (N s/m)	1.4
m (kg)	0.0316

Table 2 Design parameters and uncertain parameters for each control design

Design Parameters	Design 1	Design 2
Low Frequency Error, a	0.01	0.1
High Frequency Error, M_p	2	2
Bandwidth (Hz), ω_b	3.2	3.2
Weight on Input (N), w_u	0.0001	0.0001
Perturbed Parameters Used	k, b_X	k, m

In this paper we will consider two error models cases with varying parameters: design 1, k and b_x ; and design 2, k and m_x. The random parameters are considered to be normally distributed with standard deviation equal to 10% of the nominal values. At this time the actual distributions of these parameters are unknown. The standard deviations have been chosen to be larger than might be expected to help illustrate the effects of the random parameters on the MPV.

In this Section an error model will be developed that satisfies (2) with x=0.94. This means that 94% of all possible plants will be accounted for in the error model. The system was linearized at steady state conditions with the parameters randomly varied. The frequency response plots are given in Figure 4 for design 1 where the spring rate and damping friction are varied. There is variation (error) in the frequency response over the entire frequency range shown. Note that the modeled error is smaller at high frequencies.

The error model was created using the technique described in Section 2. To do this, the distribution of the error at each frequency over a frequency range is needed. Histograms of the multiplicative error of the plant for a wide range of frequencies are given in Figure 5. One thousand replications of the plant and multiplicative error were created by using random samples of the spring and friction for design 1 and spring and mass for design 2 with parameters described in Table 1. The resulting magnitudes of the multiplicative error, $|l(j\omega)|$, were divided into 100 bins. Each of the histograms (one for each frequency) approximate the probability density function, $f_{l_\omega}(\theta)$, associated with the magnitude of the multiplicative error. These approximate density functions were numerically integrated to solve Equation (3) for $l^*(\omega)$ at each frequency. A transfer function, $w_x(j\omega)$ was found using a standard numerical algorithm available in MALAB ® known as fitmag() to find a stable minimum phase transfer function with a magnitude response that closely matches $l^*(\omega)$ at each frequency. Note that since there is no overlapping of the error frequency responses in Figure 6, (4) is satisfied by the chosen $w_x(j\omega)$ without having to check for multiplicative error cases that overlap the $l^*(\omega)$ boundary. The error transfer function, $w_x(s)$, along with all of the replications of the magnitude $|l(j\omega)|$ are plotted in Figure 6.
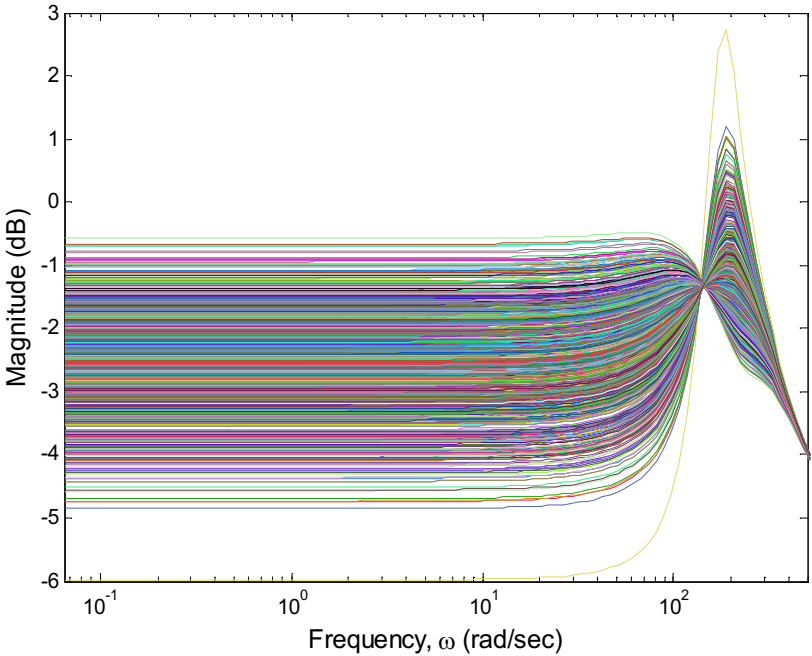

Figure 4 Magnitude responses of the perturbed plant, *G(jω)* (design 1 - *k* and *b*ₓ are the uncertain parameters considered)
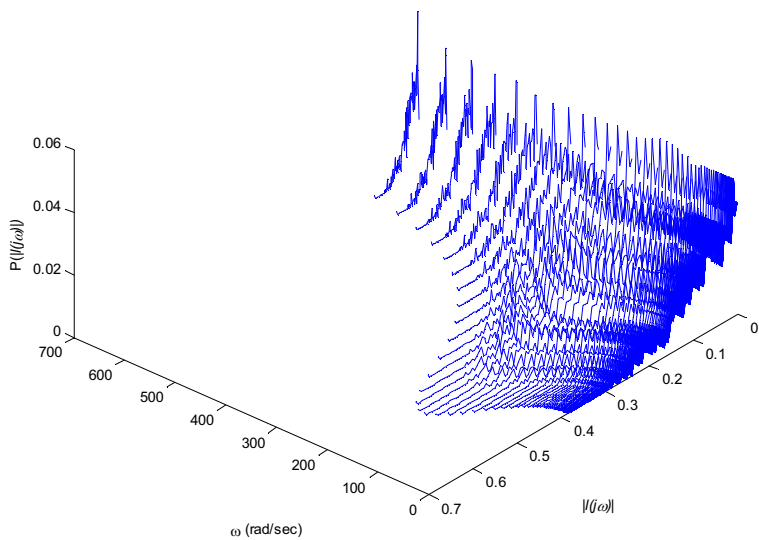
Figure 5 Multiplicative error distributions by frequency (design 1 - *k* and *b*ₓ are the uncertain parameters considered)
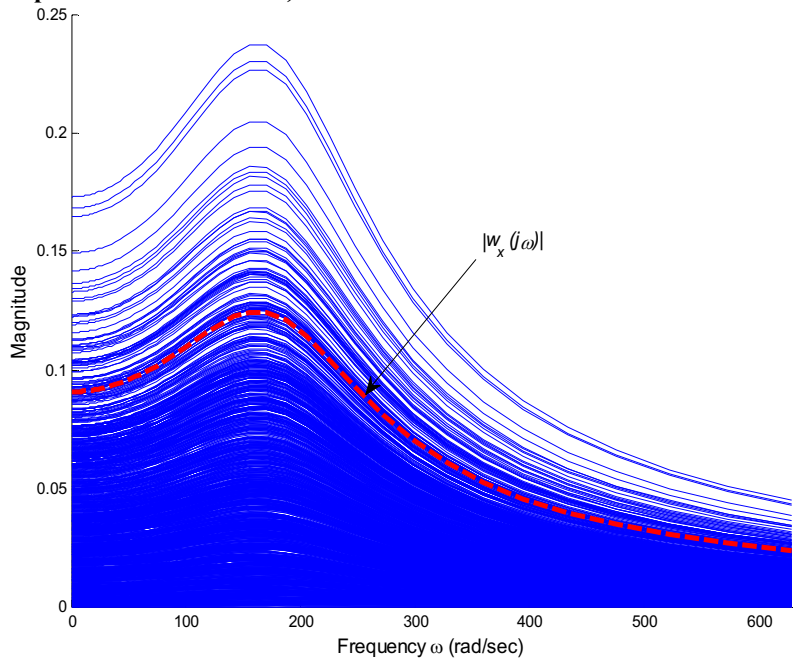
Figure 6 Multiplicative errors *l(jω)* for design 1 where *k* and *b*ₓ are the uncertain parameters considered – *w*ₓ(*jω*) bounds 94% of multiplicative error

Next, parameter uncertainty for design 2 in is considered. The same analysis is completed as in the analysis that led to the uncertainty model in Figure 6 for design 1. The results of the uncertainty analysis for design 2 are given in Figure 7. As can be seen in

Figure 7, there is a significant amount of overlapping of uncertainty $l(j\omega)$ frequency responses. Therefore it is important to apply Eq. (4) after determining L, the set of all $l(j\omega)$ the cross $l^*(\omega)$. The set L is shown in Figure 8. The results in Figure 7 and Figure 8 show that overlapping of the frequency responses of multiplicative error have a significant effect on the error model for the metering poppet valve. In design 2, the multiplicative error for 94 % of perturbed plants is nearly as large as the multiplicative error for 100 % of all the randomly sampled plants. However, in design 1, Figure 6 shows that there is a significant difference between the maximum error and the frequency response of the error model for 94% of all perturbed plants, $w_x(j\omega)$.

Figure 7 Multiplicative errors with three different bounds: upper bound of 100% of considered error, $l^*(\omega)$ which is the bound of 94% error computed at each frequency, $w_x(j\omega)$ which is the bound of 94% of all plant error (design 2 - k and m are the uncertain parameters considered)
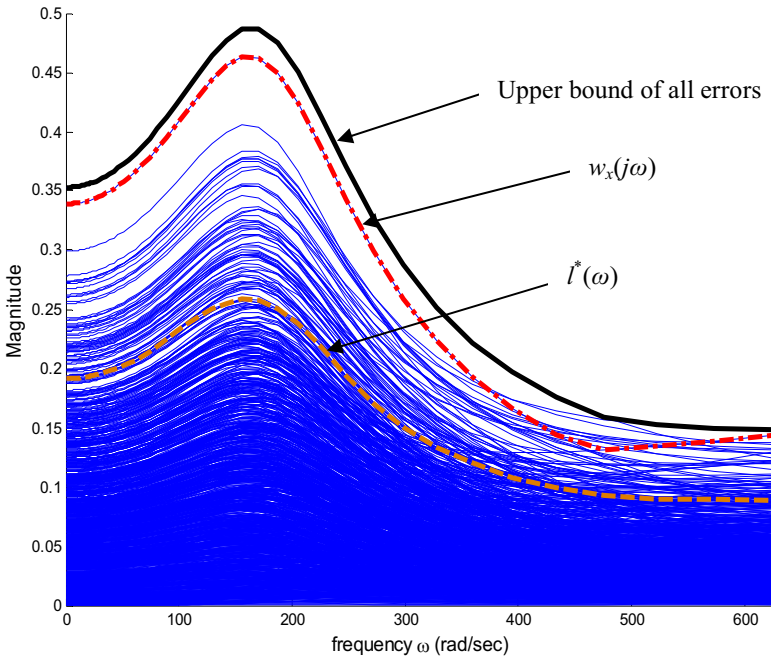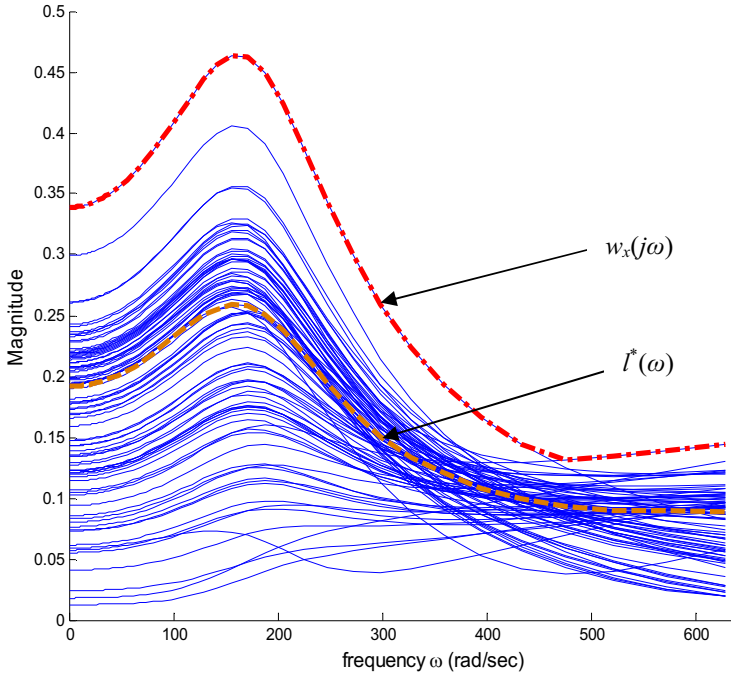
Figure 8 L, All multiplicative error frequency responses that cross over the line bounding 94% of error, l*(ω), computed at each frequency (design 2 - *k* and *m* are the uncertain parameters considered)

5. CONTROL DESIGN AND PERFORMANCE

In this section, two control system designs are presented which correspond to the two uncertainty models discussed in the previous section. The simple reference tracking control system structure which is the same for both design 1 and design 2 is given in Figure 9. Design 1 corresponds to the system where feedback spring rate and pilot poppet damping are considered as uncertain. Design 2 corresponds to the case where feedback spring rate and pilot poppet mass are considered as uncertain parameters. The control systems are each designed using a mixed sensitivity H-infinity design procedure. In the design parameters as well as the perturbed parameters for both control designs are given. In the mixed sensitivity H-infinity control design the frequency response of closed loop performance characteristics are optimized through design of the control gain $K(s)$. H-infinity optimization procedures can be found in texts such as Skogestad (1996).

In the control design for the MPV, it is desired to control tracking error of the main poppet position and to minimize control effort. A closed loop transfer function relating the input to the tracking error is given as $E(j\omega)/R(j\omega)=S(j\omega)=1/(1+G(j\omega)K(j\omega))$ (sensitivity transfer function). The performance objective is given as follows: $\left|s(j\omega)\right| < \dfrac{1}{\left|w_p(j\omega)\right|}$ for all frequencies. The transfer function, $w_p(j\omega)$, is a performance objective weighting function

the inverse of which can be chosen to be any frequency response desired. In this example, a typical tracking error performance weighting function is given as

$$w_p(j\omega) = \left. \frac{s/M_p + \omega_b}{s + A\omega_b} \right|_{s=j\omega} , \tag{14}$$

where M_p is the maximum high frequency error, ω_b is the desired bandwidth, and A is the maximum low frequency error. A similar weight can be applied to the control effort. The control effort weight on the plant input is w_u. The plant input weight is chosen as a constant. All of the parameters for the performance weights are given in Table 2.
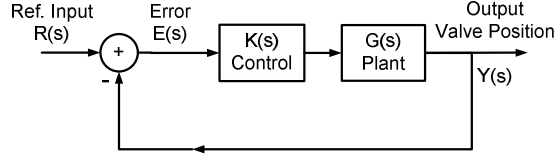
Figure 9 Control system diagram

As was stated earlier, control systems were designed using H-infinity optimization. The frequency responses of the resulting controller transfer functions are given in Figure 10 for design 1 and 2 respectively. As can be seen in the figures, the low frequency gain of the controllers differ by around 20 dB. Other than the low frequency gain the contollers were similar. The difference is due to having different performance weighting for each desing as listed in Table 2. The performance was varied between the two controllers in order to provide similar levels of robustness considering each set of uncertain parameters. Recall that design 1 and design 2 are subjected to different uncertain parameters.
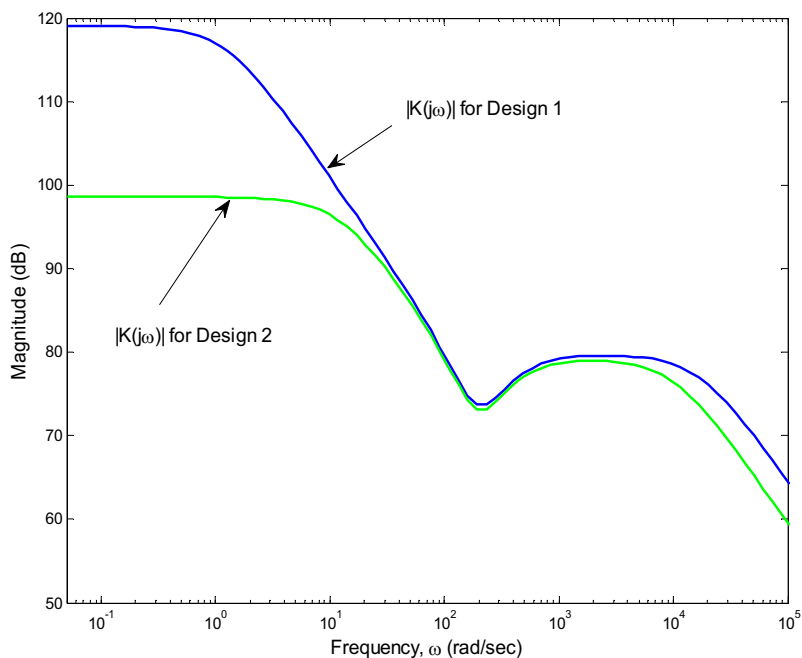
Figure 10 Frequency response of the controller, $|K(j\omega)|$ for design 1 and 2.

Next, robust performance tests can be completed using the error model, $w_x(j\omega)$, the tracking performance weight transfer function, $w_p(j\omega)$ and the control effort weight w_u. The block diagram of the system is given in Figure 11. The critical signals are labeled on the diagram.
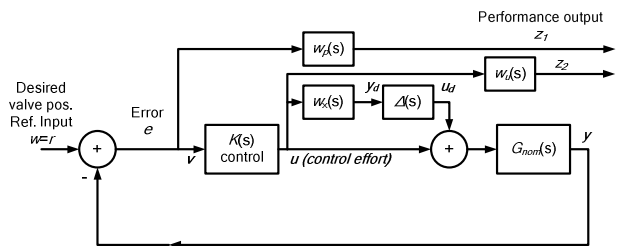
Figure 11 Control system with performance weights and error transfer functions included

A rearrangement of the block diagram in Figure 11 is a convenient way to look at a system with many of the blocks combined into a generalized plant, P (Skogestad, 1996). The system in terms of the generalized plant is given as follows with P partitioned into four parts:

$$\begin{Bmatrix} y_\Delta \\ z \\ v \end{Bmatrix} = \begin{bmatrix} P_{11} & P_{12} \\ P_{21} & P_{22} \end{bmatrix} \begin{Bmatrix} u_\Delta \\ r \\ u \end{Bmatrix}$$

$$P_{11} = \begin{bmatrix} 0 & 0 \\ -w_p G_{nom} & w_p \\ 0 & 0 \end{bmatrix} \qquad P_{12} = \begin{bmatrix} w_x \\ -w_p G_{nom} \\ w_u \end{bmatrix} \tag{15}$$

$$P_{21} = \begin{bmatrix} -G_{nom} & 1 \end{bmatrix} \qquad P_{22} = \begin{bmatrix} -G_{nom} \end{bmatrix}$$

$$z = \begin{bmatrix} z_1 & z_2 \end{bmatrix}^T$$

Once a system can be expressed in the standard form in (15) and the system can be transformed into a new transfer function matrix, $N(s)$, which includes the controller, $K(s)$, using a linear fractional transformation (LFT) with $N = P_{11} + P_{12}K(I - P_{22}K)^{-1}P_{21}$. After N is computed and partitioned, standard robustness analysis becomes a simple task using the following conditions on N for Nominal Stability (NS), Nominal Performance (NP), Robust Stability (RS), and Robust Performance (RP):

NS $\leftrightarrow N$ is stable

NP $\leftrightarrow \bar{\sigma}(N_{22}) = \mu_{\Delta p} < 1 \quad \forall \omega$

RS $\leftrightarrow \mu_\Delta(N_{11}) < 1 \quad \forall \omega$

RP $\leftrightarrow \mu_{\hat{\Delta}}(N(j\omega)) < 1 \quad \forall \omega$.

Also note that RP implies NS, NP, and RS.

The structured singular value, $\mu_{\hat{\Delta}}(N(j\omega))$, for the RP test is given in Figure 12 and Figure 12 for design 1 and design 2. Since the magnitude is less than one, both control system designs have robust performance for considered plant variations. Recall that the analysis applies to only 94% of possible plants. More information on the computation of the structured singular value can be found in texts that cover robust control such as those by Skogestad et al (1996) and Doyle et al (1992).

In Figure 12, the three structured singular values given are for robustness analysis using three different cases of an uncertainty model. The upper line corresponds to analysis with the uncertainty model bounding all $l(j\omega)$ (100 % of perturbed plant error). The lower line corresponds to the analysis with the error model with the frequency response of $l^*(\omega)$. The middle line corresponds to the robust performance analysis using the $w_x(j\omega)$ found according to (4). Note that the upper line is above 1 at some frequencies indicating that the control system does not have robust performance when considering 100% of all perturbed plants.
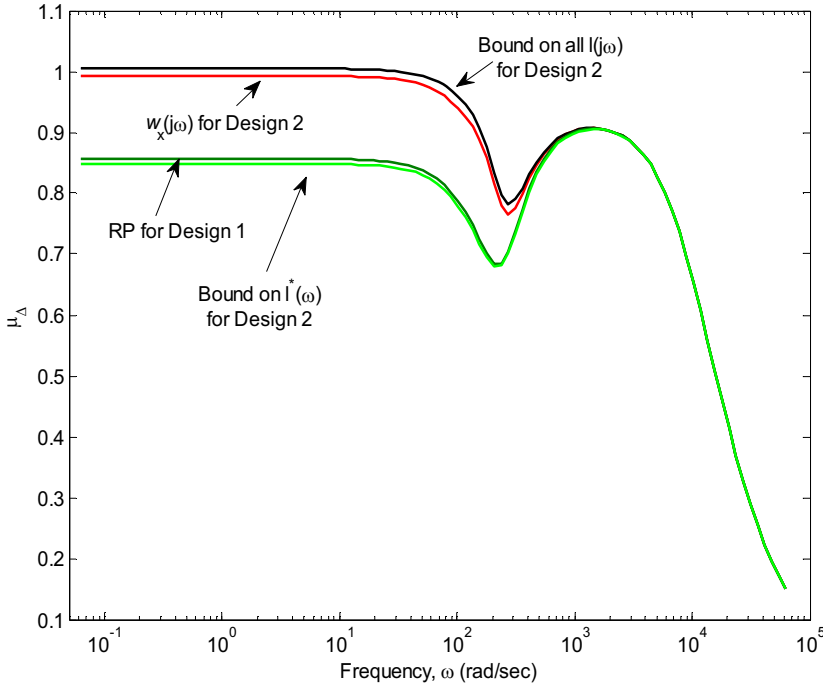
Figure 12 Robust performance analysis for controller design 1 (k and b_x are uncertain parameters) and the H-infinity control system applied to control design 2 (k and m are the uncertain parameters considered).

6. CONCLUSIONS

In this work, a technique for creating an error model for the MPV that contains the model error due to a given fraction of all possible plants with uncertain parameters. In general, the method can be used to predict the probability of a system achieving a performance objective described by a frequency response function.   Two cases of error models were presented. One of the cases showed that allowing the feedback spring and pilot poppet mass to be uncertain produced overlapping of the multiplicative error frequency responses.   This overlapping significantly increased the magnitude of the error model needed to account for 94% of all possible plant perturbations.

Using robustness analysis in the frequency domain, it was shown that two H-infinity control designs will perform according to performance specifications given in Table 1. Due to the differences in plant uncertainty considered it could be concluded that lower performance is possible when there is significantly large uncertainty in the pilot poppet mass (as in design 2 of parameter uncertainty). In both design 1 and 2, the performance specification in the frequency domain was achieved when considering 94% of all possible plants.

It should also be noted that the error model that bounds a known fraction of possible plant errors like the one presented in this work can be used for control synthesis. Standard techniques such as mu-synthesis can be carried out to design control systems that

are guaranteed to have robust performance in the presence of modeled error using transfer function error models. If the error model described in this work was used in a standard mu-synthesis design, the robustness would be guaranteed for the fraction of plant error described by the model. Thus, the error model described here leads to a helpful control synthesis technique.

Future work plans include testing the concept using data for a system that is made of mass produced components which exist in the market. This would require obtaining data on the variability in the parameters of these components. This data would need to include a model of the random distribution of the parameters. Theoretical models of the random distribution of the parameters of manufactured components could also be used.

7. NOMENCLATURE

A_C	Area of main poppet exposed to control pressure	[m^2]
A_L	Area of main poppet exposed to load pressure	[m^2]
A_S	Area of main poppet exposed to supply pressure	[m^2]
a_1	Area of the orifice from supply to control volume	[m^2]
a_2	Area of the orifice between control and load volumes	[m^2]
a_3	Area of the orifice from supply to load volume	[m^2]
a_4	Area of the orifice from the load volume to tank	[m^2]
b_X	Damping coefficient for the pilot poppet	[N s/m]
b_Y	Damping coefficient for the main poppet	[N s/m]
C_d	Orifice discharge coefficient	
f	Actuator input force	[N]
h_2	Slope of orifice 1 area vs. position curve	[m^2/m]
h_2	Slope of orifice 2 area vs. position curve	[m^2/m]
h_3	Slope of orifice 3 area vs. position curve	[m^2/m]
k	Feedback spring coefficient	[N/m]
$kc_{(1-4)}$	Pressure flow coefficient for orifices 1 – 4	[m^3/s/Pa]
$kfc_{(1-3)}$	Pressure flow force coefficient for orifices 1 - 3	[N/Pa]
$kq_{(1-3)}$	Flow gain for orifices 1 – 3	[m^3/s/m]
M	Mass of the main poppet	[kg]
m	Mass of the pilot poppet	[kg]
o	All o subscripts represent nominal conditions	
P_C	Control volume pressure	[Pa]
P_L	Load volume pressure	[Pa]
P_S	Fixed supply pressure	[Pa]
P_T	Fixed tank pressure	[Pa]
$Q_{(1-4)}$	Flow rate across orifices 1 - 4	[m^3/s]
θ	Jet angle for flow force	[rad]
V_C	Volume of the control volume above the main poppet	[m^3]
V_L	Load volume	[m^3]
x	Position of the pilot poppet referenced from closed position (positive is down in Fig. 1)	[m]
x_n	Pilot poppet position referenced from the nominal opening	[m]
y	Position of the main poppet referenced from closed position (positive is up in Fig. 1)	[m]

y_n	Main poppet position referenced from the nominal opening	[m]
β	Fluid bulk modulus	[Pa]
ρ	Fluid density	[kg/m^3]

REFERENCES

[1] Aardema, J. A., 1997, "Pilot Valve for a Flow Amplifying Poppet Valve," U.S. Patent 5 645 263, Jul. 8, 1997.

[2] Barmish, B.R. and C.M. Lagoa, "The Uniform Distribution: A Rigorous Justification for Its Use in Robustness Analysis," Math. of Control, Signals, and Systems, Vol. 10, pp. 203-222, 1997.

[3] Crespo, L., S. Kenny. 2005. "Reliability-Based Control Design for Uncertain Systems". AIAA Guidance, Navigation, and Control Conference and Exhibit, 15-18 Aug. 2005, San Francisco, CA, United States.

[4] Chen, B.S., W. Zhang. "Stochastic H2/H infinity control with state-dependent noise", *IEEE Trans. Automatic Control*, 49(1), pp.45-57, 2004.

[5] Doyle, J., B. A. Francis, and A. R. Tannebaum, 1992. *Feedback Control Theory*, Macmillan Publishing Company, New York.

[6] Franklin, G. F., J. D. Powell, A. Emami-Naeini, 2007. Feedback Control of Dynamic Systems 5th ed. Pearson Prentice Hall, Upper Saddle River, New Jersey.

[7] Jovanovic, Z., B. Dankovic. 2004. "On the Probability Stability of Discrete-Time Control Systems." FACTA UNIVERSITATIS. SERIES: ELECTRONICS AND ENERGETICS. vol. 17, April 2004, 11-20.

[8] Fales, R., 2006. "Stability and Performance Analysis of a Metering Poppet Valve." International Journal of Fluid Power. Vol. 7, No. 6, Pages 11-18.

[9] Fales, R. and Chang Li. "Experimental Evaluation of a Metering Poppet Valve." Fluid Power and Motion Control Symposium (FPMC 2008). Bath, England. Sep 10-12, 2008.

[10] Funk, J. E., 1964. "Poppet Valve Stability," Journal of Basic Engineering, June 1964, pp. 207-212.

[11] Hayashi, S., 1995. "Instability of Poppet Valve Circuit," JSME International Journal Series C, Vol. 38, No. (3), pp. 357-366.

[12] Li, P. Y., 2002, "Dynamic Redesign of a Flow Control Servovalve Using a Pressure Control Pilot," Journal of Dynamic Systems, Measurement, and Control, Vol. 124, pp 428-434.

[13] Manring, N. D., 2005. Hydraulic Control Systems, Hoboken, NJ: John Wiley & Sons, pp. 224-228.

[14] Muller, M., and R. Fales. 2008. "Design and Analysis of a Two-Stage Poppet Valve For Flow Control." *International Journal of Fluid Power*. Vol. 9, No. 1, Pages 17-26. Mar. 2008.

[15] Opdenbosch, P., Sadegh, N., Book, W., 2004. "Modeling and Control of an Electo-hydraulic Poppet Valve." ASME International Mechanical Engineer-ing Congress and Exposition, Anaheim, CA.

[16] Rubinstein, R. Y. 1981. *Simulation and the Monte Carlo Method* . New York: John Wiley & Sons.

[17] Schexnayder, L. F., 1995. "Poppet Valve with Force Feedback Control," U.S. Patent 5 421 545, Jun. 6, 1995.

[18] Skogestad, S., and Postlethwaite, I., 1996. *Multivariable Feedback Control: Analysis and Design*, John Wiley and Sons, New York.

[19] Stengel, R.F. and L.R. Ray, "Stochastic Robustness of Linear Time-Invariant Control Systems," *IEEE Trans. on Automatic Control*, Vol. 36, No. 1, 1991.

[20] Stoll, Henry W., 1999, *Product Design Methods and Practices*, Marcel Dekker, New York.

[21] Suyama, K., G. Apostolakis. 2000. "A new direction of reliable control: a context-based approach." Proceedings of the American Control Conference, Jun. 2000, Chicago, IL, United States.

[22] Wang, Q. and Robert F. Stengel, 2002. "Robust control of nonlinear systems with parametric uncertainty", *Automatica*, Volume 38, Issue 9, September 2002, Pages 1591-1599.

[23] Yang, X., Stephenson, D. B., Paik, M. J., 2005. "Hy-draulic Poppet Valve with Force Feedback," U.S. Patent 6 869 060, Mar. 22, 2005.

[24] Zhang, R., Alleyne, A. G., Prasetiawan, E. A., 2002. "Performance Limitations of a Class of Two-Stage Electro-Hydraulic Flow Valves," International Journal of Fluid Power, Vol. 3, 2002, No. (1).

[25] Zhang, W., B. S. Chen, C. S. Tseng. "Robust H infinity filtering for nonlinear stochastic systems", *IEEE Trans. Signal Processing*, 53(2), pp. 289-298, 2005.

Reevaluation of ideal nozzle flow

Jan Elvers
Hubertus Murrenhoff
RWTH Aachen University, Germany
Institute for Fluid Power Drives and Controls (IFAS)

ABSTRACT

Current simulation software for pneumatic systems like AMESim, DSHplus and SimulationX, has deficiencies in correctly computing mass flow through resistances. The resistance model is based on the flow from a container through an ideal nozzle. The model neglects kinetic energy upstream and downstream of the resistance. At this point a new project funded by Fluid Power Association of the German Engineering Federation (VDMA) will reevaluate the current model.

In this paper the first results of the evaluation of mass flow through ideal nozzles will be presented and a new mass flow model shall be introduced. This model considers the geometric properties of the connecting elements of the nozzle, thereby computing the flow velocity. Accounting for the velocity results in a lower static pressures and temperatures in the flow which influences mass flow. The new model is a first step for including inertia in the description of mass flow through a resistance. Correction of the error of the current model is especially important for serial connections of resistances in pneumatic systems.

Nomenclature

κ	isentropic exponent	$[\,-\,]$
Ψ	flow function	$[\,-\,]$
ρ	density	$[\,\text{kg/m}^3\,]$
A	area	$[\,\text{m}^2\,]$
b	critical pressure ratio	$[\,-\,]$
c_p	specific heat capacity at constant pressure	$[\,\text{J/kg K}\,]$
C	sonic conductance	$[\,\text{m}^3\text{/s Pa}\,]$
D	diameter	$[\,\text{mm}\,]$
h	specific enthalpy	$[\,\text{J/kg}\,]$

$\dot{m}$	mass flow	[kg/s]
p	pressure	[N/m^2]
R	ideal gas constant of air	[J/kg K]
T	temperature	[K]
v	velocity	[m/s]

1 Mass Flow through an ideal nozzle

The basis for the calculation of mass flow through an ideal nozzle is the first law of thermodynamics. The following assumptions are used for the calculation of mass flow: The Flow is isentropic, the nozzle is well-rounded, no work is added and the influence of height differences is neglected. Additionally, there is no friction.
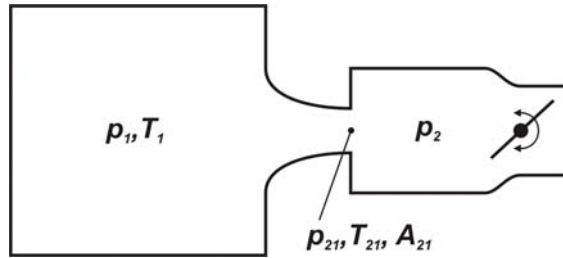

Figure 1   Container with nozzle and adjustable pressure p_a

Figure 1 shows a graphic representation for the current mass flow model. It consists of a container which is closed with an ideal nozzle. The second part behind the nozzle is necessary to adjust the pressure p_2. Basically, it is a representation of the measuring equipment.

The basis for the calculation of mass flow through an ideal nozzle is the first law of thermodynamics for stationary flow [1].

$$h_1 + \frac{v_1^2}{2} = h_{21} + \frac{v_{21}^2}{2} \tag{1}$$

At this point a first simplification is introduced: The velocity of the gas flow before the nozzle is set to zero.

$$\frac{v_{21}^2}{2} = h_{21} - h_1 = c_p(T_{21} - T_1) \tag{2}$$

Using the isentropic state equation, the properties of the specific heat capacities and the ideal gas law, results in the following equation.

$$v_{21} = \sqrt{2 \frac{\kappa}{\kappa-1} \frac{p_1}{\rho_1} \left[1 - \left(\frac{p_{21}}{p_1} \right)^{\frac{\kappa-1}{\kappa}} \right]} \qquad (2)$$

In the next step we utilise the definition of mass flow and the isentropic relation between density and pressure.

$$\dot{m} = v_{21} \cdot A_{21} \cdot \rho_{21} \qquad (3)$$

$$\frac{\rho_{21}}{\rho_1} = \left(\frac{p_{21}}{p_1} \right)^{\frac{1}{\kappa}} \qquad (4)$$

After conversion of (3) with equations (4) and (5) the description of mass flow reads [3]:

$$\dot{m} = A_{21} \sqrt{\frac{\kappa}{\kappa-1} \left[\left(\frac{p_{21}}{p_1} \right)^{\frac{2}{\kappa}} - \left(\frac{p_{21}}{p_1} \right)^{\frac{\kappa+1}{\kappa}} \right]} \sqrt{2 \cdot p_1 \cdot p_1} = A_{21} \cdot \Psi \cdot \sqrt{2 \cdot \rho_1 \cdot p_1} \qquad (5)$$

The function Ψ reaches its maximum for the critical pressure ratio p_{21}/p_1 [4].

$$\left(\frac{p_{21}}{p_1} \right)_{crit} = \left(\frac{2}{\kappa+1} \right)^{\frac{\kappa}{\kappa-1}} = b = 0.528 \qquad (6)$$

The critical pressure ratio is obtained by finding the maximum of Ψ with respect to p_2/p_1. For pressure ratios smaller than b the function Ψ keeps at its maximum of 0.484. Choked flow occurs which means that the mass flow can only be increased by increasing the pressure upstream of the nozzle. For pressure ratios greater than b, mass flow is calculated by stetting p_{21} to p_2 (subsonic conditions). In case of pressure ratios smaller than b, the pressure p_{21} is set to $b \cdot p_1$ (sonic conditions).

2 New mass flow model considering velocities before and after the resistance

Neglecting the kinetic energy of the flow before the nozzle poses some problems. Pneumatic systems possess several in-line resistances which are modelled using the nozzle model described before. Therefore the kinetic energy of the mass flow between the resistances is neglected at every element. This impreciseness leads to an accumulating error.

A new approach was chosen to enhance the mass flow model. **Figure 2** shows the expanded model. The dynamic pressure is taken into account which leads to the influence of the geometric properties of the connections attached to the resistance on the mass flow. For steady-state flows the geometric properties determine the velocities of the mass flow before and after the resistance, thereby influencing the static pressures p_{1*} and p_{2*}, respectively. A_{1*} and A_{2*} are the cross sectional areas of the two pipe sections connected to the nozzle. In the two sections there exist the flow velocities v_{1*} and v_{2*} beside the static pressures p_{1*} and p_{2*}. The variables at the smallest cross section of the nozzle are styled with subscripts 21.
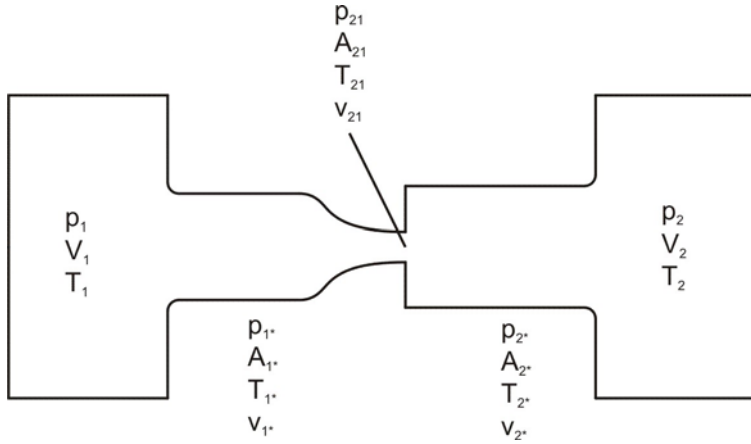

Figure 2   Container with pipe sections attached to a nozzle

Using the same approach as for the current model,

$$h_{1*} + \frac{v_{1*}^2}{2} = h_{21} + \frac{v_{21}^2}{2} \tag{7}$$

the following equation is deduced

$$v_{21} = \sqrt{2 \frac{\kappa}{\kappa - 1} \frac{p_{1*}}{\rho_{1*}} \left[1 - \left(\frac{p_{21}}{p_{1*}} \right)^{\frac{\kappa - 1}{\kappa}} \right] + v_{1*}^2} \tag{8}$$

By adapting and inserting the continuity equation (3) and the isentropic relation between density and pressure (4), we deduce the following equation for the proposed mass flow through an ideal nozzle.

$$\dot{m} = A_{21} \cdot \sqrt{2\frac{\kappa}{\kappa-1}\left[1-\left(\frac{p_{21}}{p_{1*}}\right)^{\frac{\kappa-1}{\kappa}}\right]\frac{p_{1*}}{\rho_{1*}}\rho_{1*}^2\left(\frac{p_{21}}{p_{1*}}\right)^{\frac{2}{\kappa}} + v_{1*}^2 \cdot \rho_{1*}^2\left(\frac{p_{21}}{p_{1*}}\right)^{\frac{2}{\kappa}}} \qquad (9)$$

After converting and arranging the new form of equation (9) reads as follows.

$$\dot{m} = \sqrt{\frac{\kappa}{\kappa-1}\left(\frac{p_{21}}{p_{1*}}\right)^{\frac{2}{\kappa}} - \frac{\kappa}{\kappa-1}\left(\frac{p_{21}}{p_{1*}}\right)^{\frac{\kappa+1}{\kappa}} + \frac{v_{1*}^2 \cdot \rho_{1*}}{2 \cdot p_{1*}}\left(\frac{p_{21}}{p_{1*}}\right)^{\frac{2}{\kappa}}} \cdot A_{21} \cdot \sqrt{2 \cdot \rho_{1*} \cdot p_{1*}} \qquad (10)$$

An additional conversion utilising the law for ideal gases and the continuity equation is helpful.

$$\rho_{1*} = \frac{p_{1*}}{R \cdot T_{1*}} \qquad (11)$$

$$\dot{m} = v_{1*} \cdot A_{1*} \cdot \rho_{1*} \qquad (12)$$

This leads to a new formulation of mass flow.

$$\dot{m} = A_{21}\sqrt{\frac{\kappa}{\kappa-1}\left(\left(\frac{p_{21}}{p_{1*}}\right)^{\frac{2}{\kappa}} - \left(\frac{p_{21}}{p_{1*}}\right)^{\frac{\kappa+1}{\kappa}}\right) + \left(\frac{\dot{m} R T_{1*}}{A_{1*} \; p_{1*}}\right)^2 \frac{1}{2RT_{1*}}\left(\frac{p_{21}}{p_{1*}}\right)^{\frac{2}{\kappa}}}\sqrt{\frac{2\; p_{1*}^2}{R\; T_{1*}}} \qquad (13)$$

In the next step the formula is converted into the following form

$$\dot{m} = A_{21} \cdot \sqrt{\frac{2 \cdot p_{1*}^2}{R \cdot T_{1*}}}\sqrt{\frac{\dfrac{\kappa}{\kappa-1}\left(\left(\dfrac{p_{21}}{p_{1*}}\right)^{\frac{2}{\kappa}} - \left(\dfrac{p_{21}}{p_{1*}}\right)^{\frac{\kappa+1}{\kappa}}\right)}{1-\left(\dfrac{A_{21}^2}{A_{1*}^2}\left(\dfrac{p_{21}}{p_{1*}}\right)^{\frac{2}{\kappa}}\right)}} \qquad (14)$$

Analogous to the current model the right term is abbreviated with Ψ.

$$\Psi = \sqrt{\dfrac{\dfrac{\kappa}{\kappa-1}\left(\left(\dfrac{p_{21}}{p_{1*}}\right)^{\frac{2}{\kappa}} - \left(\dfrac{p_{21}}{p_{1*}}\right)^{\frac{\kappa+1}{\kappa}}\right)}{1 - \dfrac{A_{21}^2}{A_{1*}^2}\left(\dfrac{p_{21}}{p_{1*}}\right)^{\frac{2}{\kappa}}}} \qquad (15)$$

For pressure ratios greater than b, mass flow is calculated by stetting p_{21} to p_{2*}. This means that the downstream fluid velocity and static pressure in cross-section A_{2*} have an influence on the flow function. Therefore the cross-section A_{2*} is not a direct part of the equation, but determines p_{21} in the case of subcritical flow.

The critical pressure ratio is identified by the same method used for the current model. The method is applied to the centre term of equation (13).

$$\frac{d\Psi}{d\left(\dfrac{p_{21}}{p_{1*}}\right)} = 0 \qquad (16)$$

This method leads to the following expression:

$$b = \left(\frac{2\,\kappa\,R\,T_{1*} + (\kappa-1)\,v_{1*}^2}{\kappa(\kappa+1)R\,T_{1*}}\right)^{\frac{\kappa}{\kappa-1}} = \left(\frac{2\,\kappa\,R\,T_{1*} + (\kappa-1)\left(\dfrac{\dot{m}\,R\,T_{1*}}{A_{1*}\,p_{1*}}\right)^2}{\kappa(\kappa+1)R\,T_{1*}}\right)^{\frac{\kappa}{\kappa-1}} \qquad (17)$$

For a velocity of zero the proposed equation for the critical pressure ratio simplifies to the following expression and leads (with $\kappa = 1.4$) to the same result as published previously in the literature, e.g. by Murrenhoff [1].

$$b = \left(\frac{2\,\kappa\,R\,T_{1*}}{\kappa(\kappa+1)R\,T_{1*}}\right)^{\frac{\kappa}{\kappa-1}} = \left(\frac{2}{\kappa+1}\right)^{\frac{\kappa}{\kappa-1}} = 0.528 \qquad (18)$$

In a real system with occurring flow velocities, the critical pressure ratio is far from constant. High flow velocities and lower temperatures which may develop behind upstream resistances influence critical pressure ratios.
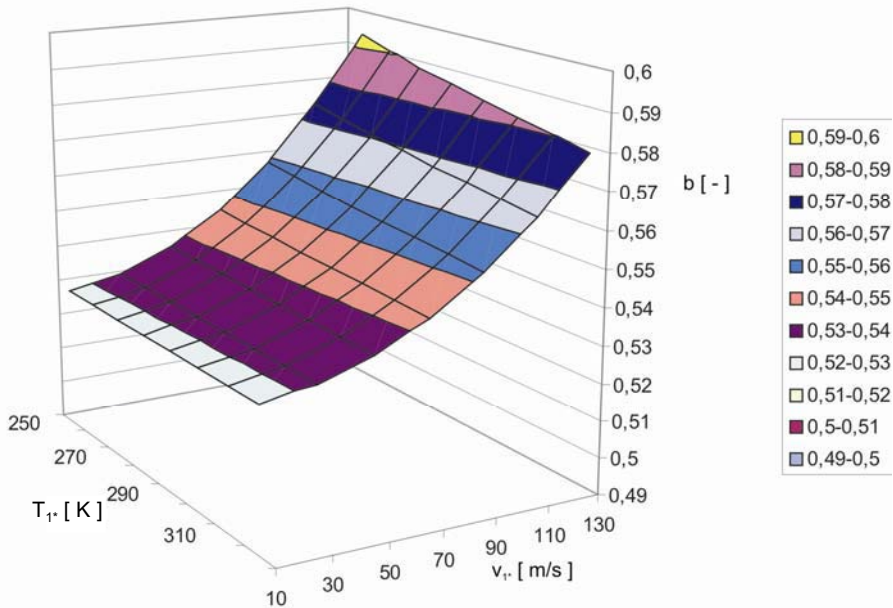
Figure 3   Critical pressure ratios for different temperatures and flow velocities

In common conditions (e.g. $v_{1*} = 15$ m/s, $T_{1*} = 293.15$ K) the deviation from the currently known critical pressure ratio is negligible, but for series connections of resistances the conditions may change to extremes which will have a serious impact on the behaviour of the resistances.

A model has been implemented in commercial math software that calculates the flow function and the critical pressure ratio dependent on the cross-section areas of pipes upstream and downstream of the nozzle. The cross-section areas A_{1*} and A_{2*} were varied while A_{21} and T_1 stayed constant ($D_{21} = 3.6$ mm, $T_1 = 293.15$ K). The results are shown in **Figures 4** and **5**. Equations (14) and (17) are used to calculate the mass flow. p_1 and p_2 are the total pressures for varying cross- sectional areas. Iteratively pressures p_{1*} and p_{2*} and the mass flow are calculated until the change of the mass flow is below a given error. The calculated results of Ψ and b are shown over the ratio of the total pressure in Volume 1 and the total pressure in Volume 2, analogue to the currently used model. Therefore it is possible to show the differences between the currently used model and the new proposed model in a single diagram. It is evident that smaller diameters before the resistance lead to values for b and Ψ_{Max} that are higher than previously published ones. The critical pressure ratio also depends on the pressure ratio itself. For smaller pressure ratios the critical pressure ratio increases and reaches values of more than 0.56.
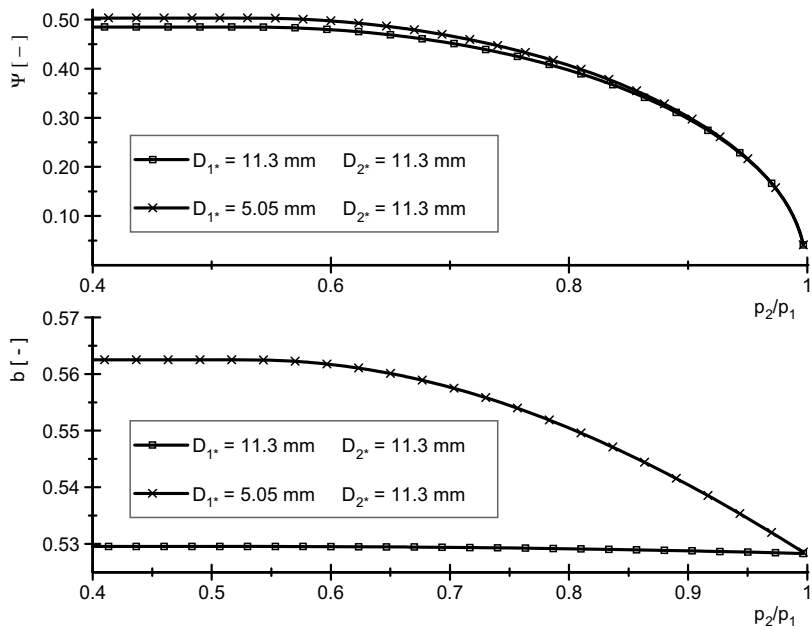
Figure 4   Variations of the inlet geometry: Flow function and critical pressure ratio

In Figure 5 a variation of inlet and outlet geometry is shown. For a small diameter of the inlet the flow function Ψ differs from that of the current model over the whole range of b. For a small diameter of the outlet the flow function Ψ differs only in the range of subcritical conditions where p_{21} equals p_{2*}. In critical condition p_{21} equals $b \cdot p_{1*}$.
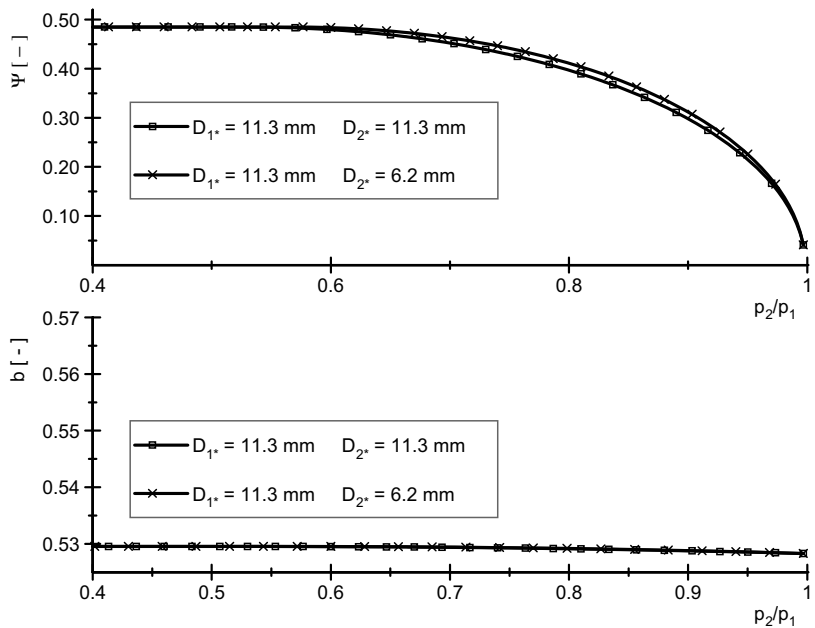
Figure 5   Variation of outlet geometry: Flow function and critical pressure ratio

Comparisons between a system with small inlet and small outlet ($D_{1*} = D_{2*} = 6.2$ mm) and a system with big inlet and outlet ($D_{1*} = D_{2*} = 35.7$ mm) result in a calculated difference in the mass flow of up to 5 %, as shown in **Figure 6**.
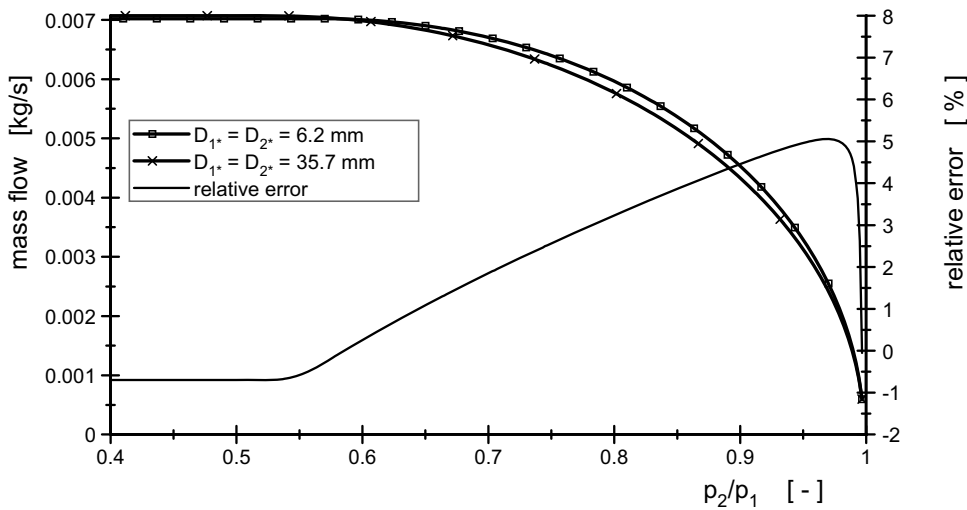

Figure 6   Variation of the in- and outlet geometry: Mass Flow

Table 1 gives an overview over the influence of the inlet and outlet size. Small geometries before the resistance result in maximum values of the flow function that are greater than the commonly accepted boundary of 0.484. For small outlet geometries a deviation of Ψ can be observed, but the maximum value of Ψ and the critical pressure ratio remain the same as in the original model of nozzle mass flow.

Table 1   Influences of in- and outlet size on Ψ and b

D_{1*}	D_{2*}	Ψ_{max}	b	Range of pressure ratio for deviations of Ψ from current model
huge	huge	0.484	0.528	-
small	small	0.492	0.543	1 to 0
huge	small	0.484	0.528	1 to b
small	huge	0.496	0.549	1 to 0

3 Conclusion

In this paper a reevaluation of the classical model for mass flow through an ideal nozzle has been presented. It was shown that neglecting the kinetic energy of the flow leads to an oversimplification. Therefore the critical pressure ratio b and the sonic conductance C, or the flow function Ψ, respectively, as they are defined by ISO 6358 [2], fail to adequately describe mass flow through a resistance. Especially b depends on the value of the temperature in front of the resistance and not only on the constancy of the temperature as has been published until now. Furthermore, the importance of the cross-sections of the connecting pipes has been presented.

This leads to the conclusion that besides the sonic conductance C, Ψ respectively, and the critical pressure ratio b, there is the temperature and the geometry of the connections before and after the nozzle that has to be considered. Otherwise the computed flow through in series connected resistances shows considerable deviation from measured results. Therefore use of the new model is proposed for describing connected resistances like throttle check valves, direction control valves, relief valves and other resistances.

4 Acknowledgements

5 References

1.   **Murrenhoff, H.**, Grundlagen der Fluidtechnik Teil 2. Pneumatik, Shaker Verlag Aachen, 2006

2.   Pneumatic fluid power – Components using compressible fluids – Determination of flow rate characteristics, ISO 6358 : 1989

3.   **Barber, A.**, Pneumatic Handbook, 7th ed., The Trade & Technical Press, Surrey, 1989

4.   **Potter, M.; Wiggert, D.**, Mechanics of Fluids, 3rd Edition, Wadsworth Group. Brooks/Cole, Pacific Groove, 2002

Efficient applications of fluid power

Development and Implementation of an Advanced Power Management Algorithm for Electronic Load Sensing on a Telehandler

Rico H. Hansen, Torben O. Andersen and Henrik C. Pedersen
Aalborg University, Department of Energy Technology, DK-9210 Aalborg East, Denmark

ABSTRACT

The relevance of electronic control of mobile hydraulic systems is increasing as hydraulic components are implemented with more electrical sensors and actuators. This paper presents how the traditional Hydro-mechanical Load Sensing (HLS) control of a specific mobile hydraulic application, a telehandler, can be replaced with electronic control, i.e. Electronic Load Sensing (ELS). The motivation is the potential of improved dynamic performance and power utilization, along with reducing the mechanical complexity by moving traditional hydro-mechanical implemented features such as pressure control, flow-sharing, prioritization of steering, anti-stall and high pressure protection into electronics. In order to implement these features, the paper presents and tests a general power management algorithm for a telehandler. The algorithm is capable of implementing the above features, while also handling the dynamics of the system, taking into account saturation phenomena as flow limitation and cylinder endstops. The development of control for a variable-displacement axial piston pump using a three-way servo valve is also treated.

Keywords: Mechatronics, Hydraulics, Fluid Power, Control, Electronic Load Sensing, Power Management

1. INTRODUCTION

Today the most common solution for open circuit hydraulics on mid and higher end mobile machinery is a hydro-mechanical adaptable flow and pressure control system known as Hydraulic Load Sensing (HLS). In HLS the pump pressure is continuously controlled to be a preset margin higher (LS-margin) than the highest load pressure. The control is realized by controlling the displacement of a variable pump using a system of pilot-lines, pressure compensators and shuttle valves. A typical HLS system is seen in Fig. 1. Features such as over pressure protection, load-independent flow-control of actuators, prioritization of steering etc., are also implemented using these hydro-mechanical components.

The wide usage of HLS systems is due to an implementation using robust components, and that HLS systems have improved energy efficiency compared to constant pressure and/or

constant flow systems. The disadvantage of HLS systems is a high commissioning effort as poorly designed HLS systems tend to become oscillatory or unstable. This originates in the complex dynamics invoked when implementing a pressure feedback, see e.g. (1), (2) and (3). Due to the dynamical complexity of HLS systems, the tuning approach is also limited to experience and trial-and-error, and the tuning itself is cumbersomely performed by adjusting or changing springs, orifices, spool design, hose volumes, etc.
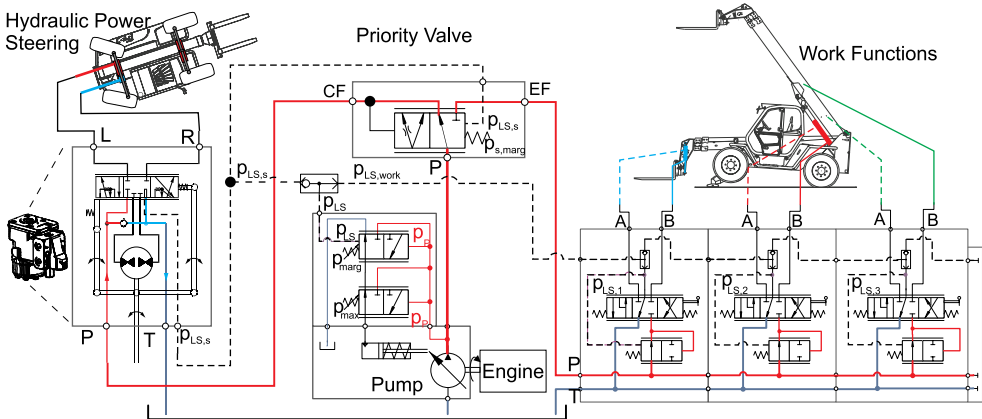

Figure 1: A typical HLS system on a telehandler.

To overcome the dynamical challenges, HLS systems are traditional designed with a power overhead in form of a larger LS-margin than staticly required. The large LS-margin is also due to the pump pressure being controlled locally at the pump. Hence, to ensure sufficient pressure across a valve stack it is necessary to conservatively set the system's LS margin according to the worst case pressure loss from pump to valve.

To reduce cost in HLS systems, steering and work functions are often supplied by a common pump. However, if the valve consumes flow while steering, this can lead to an undersupplied steering, yielding a hazardous situation. Consequently, a priority valve is installed to prioritize steering, see Fig. 1. If the supply pressure drops below required steering pressure (CF port), the priority valve reduces the excess flow (EF port) to the work functions by throttling, ensuring sufficient steering supply. Unfortunately, the priority valve introduces extra pressure drop from pump to valve, even during an inactive steering. Furthermore, all pump flow has to flow through the priority valve, resulting in a priority valve placed far away from the steering unit and designed with a large compensator spool. This degrades the response time and stability of the steering, as the priority valve also functions as a compensator for the steering unit to ensure a constant pressure across it.

This paper explores how the shortcomings of HLS can be solved by introducing computer controlled components into the open circuit. The solution should lead to better power utilization and management, and improved dynamic performance, along with a faster commissioning, as tuning control in software is less cumbersome. The potential of electronic control in open circuit systems is also becoming recognized, and is supported by more stand-alone electronic controlled components being introduced into the market.

When moving to computer controlled components, a range of control concepts is available, from making an electronic analogy of the current HLS system to using a different control topology. The research conducted in electronic open circuit control mainly falls into three groups, Electronic Load Sensing (ELS), Sum-of-Flow control (SummenStromRegelung, SSR) and Electronic Flow Matching (EFM).

The ELS control topology is explored by Esders in (4) and Langen in (5), and is the electronic analogy to HLS. The LS pressure is electronically sensed and a pump pressure controller operates an electrical controllable pump. Regarding valve control, Esders found that by using the pressure measurements, electronic pressure compensation could be performed by the the valve's main spools, removing the need for pressure compensators for providing load independent proportional flow-control.

In the SSR control topology the pump is operated without pressure feedback, but controlled to provide the sum of the requested flows. This can be performed in either open or closed loop. The closed loop SSR control is treated by Zähe in (6), where actuator velocity is the main feedback for pump and valve control. An open loop version of SSR is investigated in (7), where pressure sensors are equipped on all valve ports. The pump is set to give the sum of flow references, the control valve of the highest loaded consumer is completely opened and the flow to the lower loaded functions are controlled by their control valves using electronic pressure compensation. Hence, the pump is operated in open-loop flow mode. The SSR-solutions have the highest possible efficiency as no LS margin is present.

The EFM control scheme is closely related to SSR, but is oriented towards using a minimum of electronics. The pump is operated in feed-forward mode to deliver the sum of flow demands. A traditional flow-sharing valve distributes the flow. The concept is covered in (8), (9) and (10). The flow-sharing valve prevents an unstable pressure build up, as any flow oversupply is mutually distributed amongst the active consumers. EFM using a non-flow-sharing valve is investigated in (11) and (12). However, secondary compensators and/or spool position sensors are added to provide feedback for stabilizing the system.

Regarding steering, common for all the mentioned research is that either the steering unit is not included, or it is prioritized using a traditional priority valve.

In the work presented in this paper, the goal is to obtain complete electronic control of open circuit systems in mobile hydraulics. The control philosophy is to:

- Transfer as much as possible of the hydro-mechanical control to electronic control, reducing the mechanical complexity to a minimum.
- Do system control with intelligent machine power management utilizing engine information.
- Have a general control structure applicable for mobile hydraulic systems, which is designed and tuned using system information.

The work uses principles from both the ELS and the open loop SSR, but with added overall system control and power management. Additional, this work shows how the priority of steering can be performed electronically, removing the need for a priority valve. The developed distributed control structure is tested on a mobile machine, a telehandler, with electronic controlled open circuit components.

2. ELS SYSYEM DESCRIPTION

The application used for ELS feasibility testing is a Merlo P 35.11 EVS telehandler from 1997. Its traditional HLS circuit illustrated in Fig. 1, has been upgraded to ELS in Fig. 2. The machine has been re-equipped with electronic controlled open circuit components and a diesel engine with CAN interface. The engine transmits engine speed ω_e and current torque load τ_{actual} every 20 ms.

All the control is handled by a central computer from Speedgoat with CAN and analog I/O interface. The software platform used on the Speedgoat for implementing control is the xPC Target™ environment for MATLAB/SIMULINK by The MathWorks. The control sample rate is 1 ms.
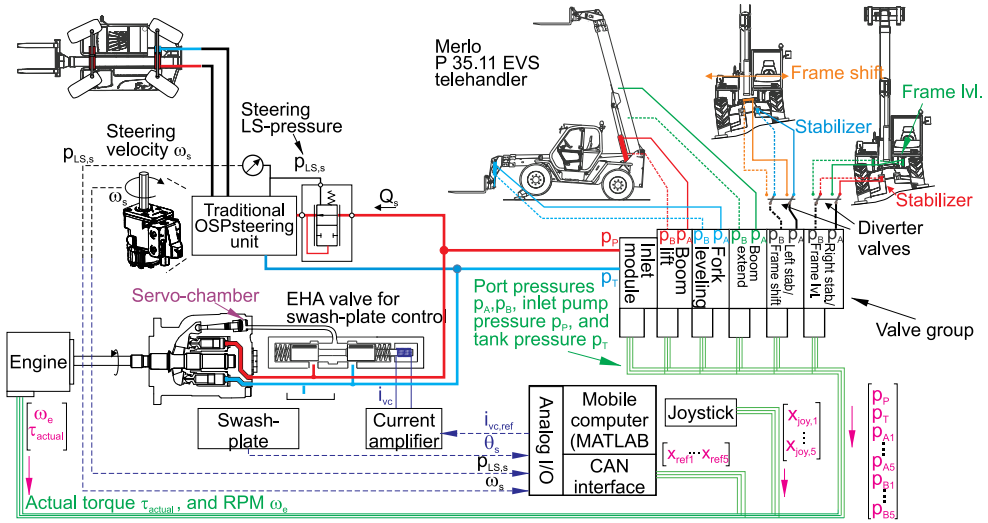

Figure 2: Telehandler with ELS.

The valve-group is equipped with pressure sensors on all ports, and electronic pressure compensation is implemented for load-independent flow control. A fluid temperature sensor, a pump pressure sensor and a tank pressure sensor are mounted at the valve-inlet. The valve-group receives reference spool position on the CAN bus from the Speedgoat. The steering unit is an OSPC 250cc/rev from Sauer-Danfoss equipped with a pressure compensator to maintain a constant pressure drop across it. The steering wheel speed ω_s and steering LS-pressure $p_{LS,s}$ are measured by the Speedgoat. Note that no priority valve is present, as prioritization will be performed electronically.

Flow reference signals from the operator are received from a CAN joystick transmitting every 20 ms. The pump is a modified Sauer-Danfoss Series 45 J-frame 60cc variable-displacement axial-piston pump. The pump has been equipped with a swash-plate position sensor, and the traditional hydro-mechanical LS-control housing has been replaced with an electronically actuated three-way valve (EHA-valve). The EHA valve is utilized for providing electronic swash-plate control, where the developed control algorithm is described in the following.

3. SWASH-PLATE CONTROL

The voice-coil actuated 3-way valve (EHA-valve) used for controlling the pump is based on the valve used in (13) for exploring electronic control of a Sauer-Danfoss Series 45 H-frame pump. The voice-coil actuator produces a force proportional to the applied current. In (13) the resulting control was a cascade control, consisting of a current loop PI-controller, a spool positioning loop with a PID-controller for the EHA valve, and a PID-controller for the swash-plate positioning loop.

In this paper, a swash-plate control algorithm not requiring the measurement of the EHA spool position is developed. In (13) the EHA positioning loop is added for increasing the bandwidth of the spool and to suppress the disturbance from flow forces. To replace the position feedback, the strategy is to implement a spool observer. In the system setup in Fig. 2 a current amplifier with internal current controller is utilized. Note that the EHA valve is equipped with a spool position sensor for identification and verification purposes.

If flow-forces on the spool are decoupled, which will be described shortly, and the spool friction is dominantly of viscous type, being valid as a dither signal is applied to the spool, the following linear second-order model is obtained for the spool position x_{EHA},

$$\frac{x_{\text{EHA}}}{i_{\text{ref}}} = \frac{\frac{k_{\text{f}}}{m_{\text{s}}}}{s^2 + \frac{\mu}{m_{\text{s}}}s + \frac{k_{\text{s}}}{m_{\text{s}}}} \tag{1}$$

where k_{f} is the voice-coil force-factor, m_{s} is the spool mass, μ is the viscous friction coefficient and k_{s} is the equivalent spring stiffness of the two springs.

To identify the coefficient μ, a ramped square-wave current is applied to the valve at no pressure, i.e. no valve flow. The response is seen in Fig. 3, where μ has been identified, yielding the second-order characteristics of $\omega_{\text{n}} = 317\,\frac{\text{rad}}{\text{s}}$, $\zeta = 6$ and a DC-gain of $K = 4.6\,\frac{\text{mm}}{\text{A}}$.
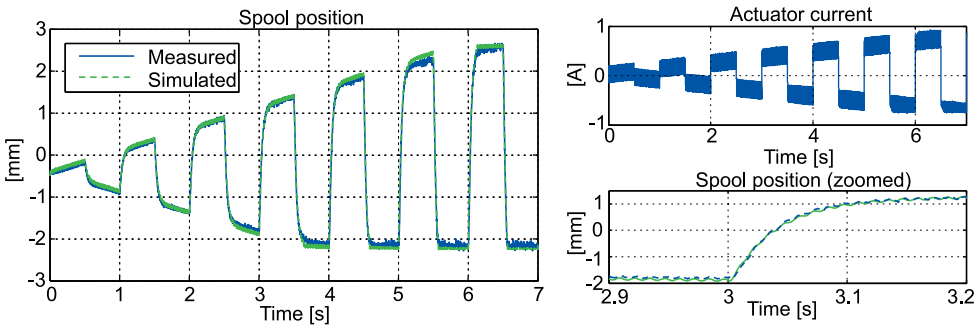

Figure 3: Measured valve dynamics and simulated valve dynamics.

The spool is over-dampened with a rise-time of approximately 80 ms. In comparison traditional LS-pumps have swash-plate dynamics with rise-times in the range of $50\,\text{ms}$ to $150\,\text{ms}$. This states that the EHA valve is too slow to be operated in open loop. To increase the bandwidth of the EHA valve, Eq.1 is synthesized to provide a spool feedback signal. Equation Eq.1 is however an open-loop estimator unable to compensate for flow-forces. Measurements have showed that flow-forces are able to pull the spool up to $1.5\,\text{mm}$ away

from the position estimated by Eq.1, degrading the value of the estimator as the maximum spool movement is 4.5 mm. However, if the flow-forces are estimated, a disturbance feed-forward could be given to suppress it.

To estimate the flow force, the flow is essential. Differentiating the swash-plate position yields the swash-plate velocity ω_s, which is approximately proportional to a flow through the EHA-valve $Q_{EHA} = \omega_s A_{DP} L_{DP}$, as the transient of pressure build-up in the small servo-chamber volume can be neglected. The area A_{DP} denotes the servo-piston area and L_{DP} is the piston's moment-arm on the swash-plate. By mapping how the flow-forces make the spool position divert from Eq.1 for different flows and pressure, a map from Q_{EHA} to F_{Ff} has been made and implemented in the controller, see Fig. 4. The flow-force estimate F_{Ff} is used as a feed-forward to suppress the flow-force. Resultantly, only the dynamics of Eq.1 remains, making it a valid estimator.

A EHA spool feed-back controller is implemented using the estimator, along with a feed-forward part to give the steady-state current for a given spool position. As the spool is very over-dampened, a simple P-controller can be used to increase the bandwidth. Using Eq.1, a proportional gain $k_{p,EHA}{=}1.5\,\frac{A}{mm}$ has been determined, yielding a bandwidth of $100\,Hz$ and a rise-time of $10\,ms$, while providing a damping factor of $\zeta \approx 2$. With this setup, the EHA-controller can handle steps up to approximately $0.5\,mm$ without actuator saturation.
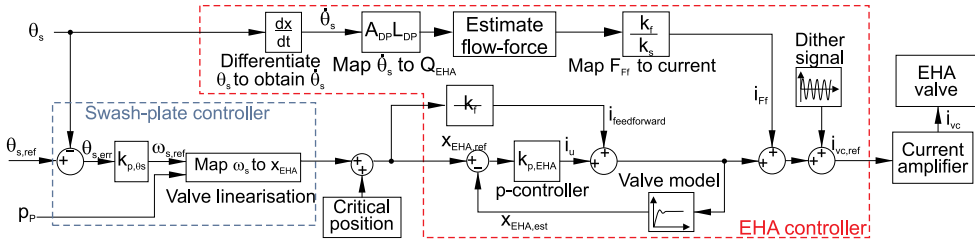

Figure 4: Swash-plate controller.

The developed EHA-controller is used as an inner loop for the swash-plate controller, see Fig. 4. As the EHA-valve is critical lapped, a natural integrator is always present from spool reference to swash-plate position. Consequently, no integrator-term is required in the swash-plate controller. The gain from spool reference $x_{EHA,ref}$ to swash-plate velocity ω_s is non-linear dependent on the pump pressure p_P and the pressure in the servo-chamber p_{DP} according to the orifice equation. Furthermore, a greater pressure loss is present across the spool when de-stroking due to the pump geometry, which approximately gives the static relation $p_{DP}{=}\frac{1}{3}p_P$. As the area characteristic of the spool is known and the pump pressure is measured, these can be used to statically cancel out the non-linearities by implementing an inverse orifice equation as in electronic pressure compensation by (4). Hence, a mapping is performed from a flow Q_{EHA} to a spool position x_{EHA}.

As the flow Q_{EHA} corresponds to a swash-plate velocity $\omega_s = \frac{Q_{EHA}}{A_{DP} L_{DP}}$, the control input to the system actually becomes a swash-plate velocity reference $\omega_{s,ref}$. Thus, the last loop of the swash-plate controller reduces to a P-controller, sending out a swash-plate velocity reference $\omega_{s,ref}$. This also emphasizes that no integrator is required in this control loop. The complete swash-plate controller is seen in Fig. 4.

4. SYSTEM CONTROL

The main control topology chosen for the electronic open circuit control is ELS, as pump pressure control is considered a basic and required functionality. For example, the open-loop SSR solutions has its limitation if consumers with unknown flow consumption are present, or highest loaded consumers have similar pressure levels.

The ELS control principle is to identify the LS-pressure, add it with a margin and use it as a reference signal for a pump pressure controller, in this case a PID, as seen in Fig. 5. Note that pump pressure feedback is measured at the valve inlet. This gives the advantage that the controller compensates for the pressure loss from pump to valve-group, making a less conservative choice of LS-margin possible compared to HLS. The gain of the pump increases with engine speed, as a smaller swash-plate angle is required to deliver the same amount of flow. To statically cancel out this non-linearity, the pump pressure controller always sends out a flow reference, which is then mapped into a swash-plate angle using the engine speed, along with compensating for the volumetric efficiency of the pump. A volumetric efficiency map is implemented in the control.

The flow consumed by the valve and steering can be viewed as a disturbance to the pressure controller, which has to continuously adapt to the flow consumption based on a pressure error, which is also the principle of HLS. However, the flow disturbance is known in advance from the operator's joystick inputs and the steering wheel velocity. These can be summarized into a feed-forward signal Q_{FF} to the pump, thereby decoupling the disturbance. Resultantly, the pressure control loop only has to make small flow corrections $\tilde{Q}_{ref}$ to maintain the correct pump pressure. A similar approach was used in (14). An extra advantage of electronic pump pressure control is that over pressure protection in the system is simply implemented as a saturation limit on the pump pressure reference, and the standby-pressure is determined by a the lower limit saturation. Note that in ELS the standby pressure is separated from the LS-margin setting, where these are traditionally equal in HLS due to the hydro-mechanical implementation.

The above constitutes the basics of the controller. The following sections describes how flow saturation, prioritization of steering, power saturation and actuator endstops are handled.

4.1 Flow and Power Saturation, and Electronic Prioritization of Steering

Flow saturation occurs when the operator request more flow than the pump can deliver. If this occurs in an HLS system where only the valve group is active, the highest loaded consumer would be starved and the LS-margin lost. If the HLS is equipped with flow-sharing valves, the available flow would be mutually distributed, but with reduced LS-margin, and hence reduced control precision. If the steering and valve is active simultaneously in an HLS system, the priority valve would reduce the flow to the valve group, such that steering always receives its required flow. In the ELS system no priority valve or flow sharing valves are present. To implement these features electronically, the engine speed is used for estimating the available flow. Hence, if the operator's flow request exceeds the available flow, a prioritized scaling is performed on the valve flows by a flow-sharing block, such that the sum is equal to the available flow. These scaled references are send to the valve-group. Note that the flow required by the steering Q_S is known from the steering wheel speed. This flow is used for calculating the flow available for the valve group.
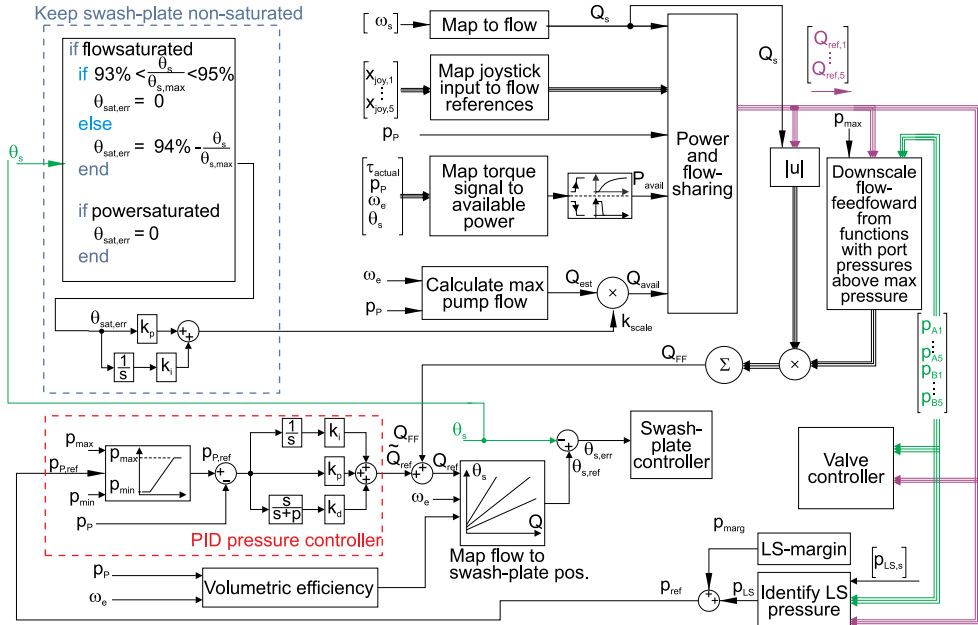
Figure 5: ELS control structure.

However, the sum of inaccuracies of estimated available flow, valve-group flow and steering flow can still result in trying to use more flow than available, thereby making the system fail to maintain the LS-margin, risking a starved steering. To deal with this, two control strategies can be used for the pump pressure control during flow saturation. The first strategy is to disable the normal pressure controller, force the swash-plate to maximum angle, and then control the pump pressure by adjusting the flow consumption of the valve-group using Q_{avail}. This requires shifting between controllers, and the gain from Q_{avail} to p_P is very dependent on the changing valve dynamics. It might also give ripples in the valve flows.

The second strategy is to realize that the system has two control inputs, the swash-plate θ_s and the flow-consumption of the valves Q_{avail}, to control one output, the pump pressure. For such control problems mid-range control, see e.g. (15), is often effective, which consists of two controllers: A main controller, controlling the output with one of the inputs, and a secondary controller, keeping the main controller out of saturation using the second input, i.e. keeping the main control signal in mid-range. Applied to this case, the swash-plate is used for controlling pump pressure, such that the same pressure controller is always active. The secondary controller scales the valve-group's flow-consumption Q_{avail}, such that the swash-plate is kept non-saturated, i.e. in mid-range. As it is important to utilize the pump's capacity, the secondary controller is set to keep a swash-plate angle between 93% to 95% of maximum during flow saturation. The implemented "skewed" midrange strategy is seen in Fig. 5. As the secondary controller is implemted as a PI, the sytems also obtains the ability to continuously adapt to changing flow charteristics of valves and pump due to e.g. fluid temperature. As the swash-plate never saturates, the pressure controller ensures the required pressure and thereby guarantees sufficient supply to the steering unit. Hence a robust electronic prioritization of steering has been implemented.

Power-saturation might also occur, giving a risk of engine stall. To avoid stall, the engine continuously transmits its current torque load to the ELS controller, which is used for calculating the available power P_{avail}. Using the pump pressure, the maximum allowed pump flow without exceeding P_{avail} can be calculated as $Q_{max} = P_{avail}/p_P$. Using the previous flow-sharing algorithm, flow references are scaled such that their sum never exceeds Q_{max}. Note that in case of simultaneous power and flow saturation, the midrange-controller does not attempt to force the swash-plate to 95% of maximum. Finally, a non-linear filter is added to the P_{avail} to avoid limit cycles with the engine by ramping P_{avail} slowly up. Regarding steering, it is consider safer to let the steering stall the engine, rather than denying it supply. Hence, the steering flow request bypasses the flow-sharing block.

4.2 Intelligent Over Pressure Control

When one of the telehandler's functions, for example boom lift, reaches its endstop, the LS-pressure rises until the pump-pressure limit is reached by the pump-pressure controller. In this case, the flow-feed forward Q_{FF} from the joystick to the pump ceases to be valid, as the flow reference to the function in endstop is not consumed. Thus, the pump-pressure controller now has to remove this excessive flow by integration. To improve the performance, the functions in endstop or otherwise blocked, can be identified by their port pressure reaching p_{max}. Consequently, the flow feed-forward from these functions is scaled down when it approaches p_{max}, making the flow feed-forward to the pump pressure controller valid again, and improves its performance. This is also implemented in Fig. 5. This control feature completes the control design, which is implemented on the telehandler.

5. RESULTS

In Fig. 6 a test of the swash-plate control algorithm is performed, where the load is a relief valve with a 50 bar setting. The swash-plate is initially tracking a 10 Hz sine-wave, and afterwards stepped from minimum to 95% of maximum stroke and back again. The destroke happens in 80 ms and the on-stroke is in 150 ms. Note that the on-stroke is from zero pressure. The swash-plate tracks the sine-wave with a phase lack of 45°, but with full amplitude as seen in the zoomed view in Fig. 6. The plot also shows the control signals and the spool position. Notice that the estimated spool position shows the same dynamics as the estimated, and that the swash-plate velocity reference given out of the controller resembles the actual velocity, as the controller was designed for.

In Fig. 7a a stabilizer is operated with the engine idling. The stabilizer is lowered to lift the machine, and then retracted to its initial position. The controller is configured to maintain an LS-margin of 20 bar which is maintained, and the swash-plate tracks the reference signal. At 8 s and 16 s the stabilizers reaches mechanical endstop, forcing the pump pressure to maximum. It is seen that the flow feed-forward Q_{FF} is reduced due to the intelligent high pressure protection, and that the pump pressure is maintained at its maximum pressure setting of 210 bar. At 11 s the machine is almost stalling, which can be seen by the engine speed dropping to 700 rpm and the available power P_{avail} going to zero. As a result, the flow feed-forward is eliminated by the system and the swash-plate de-stroked. Afterwards the system ramps up again as the engine recovers and P_{avail} rises.

In Fig. 7b multiple consumers are operated simultaneously (boom, extension and fork), where the requested flow exceeds the available. As seen, the system scales down the flow
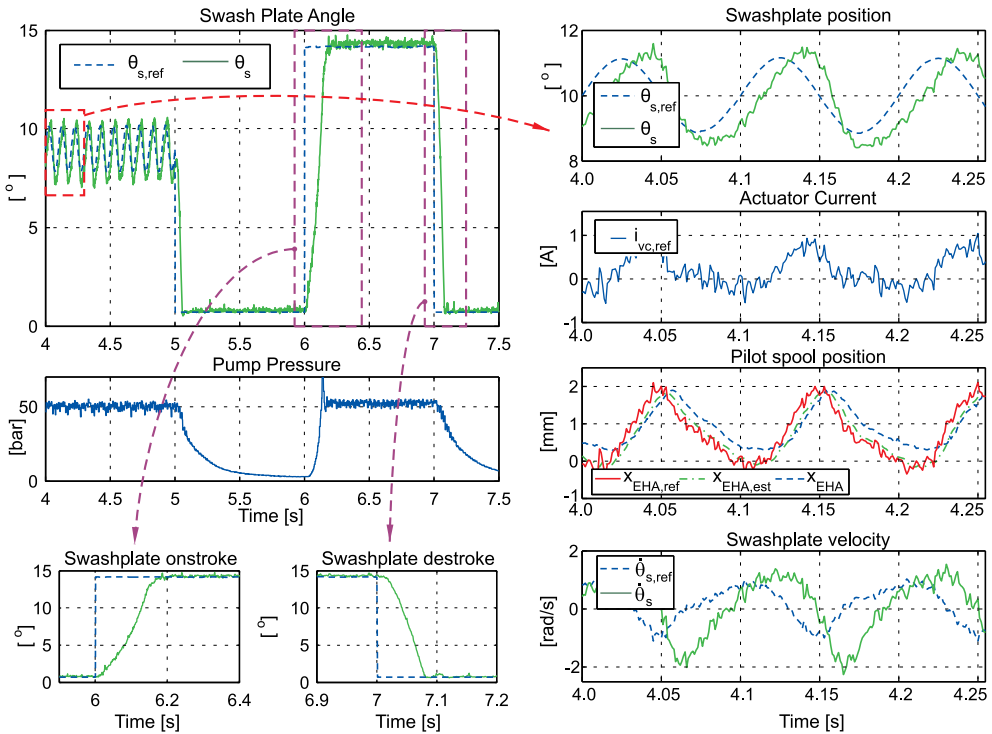
Figure 6: Swash-plate control test.

references (the black curves in the three topmost plots), such that the flow feed-forward Q_{FF} is almost constant, except when the engine speed is increased at 8.5 s. The swash-plate is kept at 95%, which enables the pump pressure controller to maintain the LS-margin of 20 bar at all time. The flow adaption graph shows the output of the mid-range controller for scaling the valve flow, such that the swash-plate is kept non-saturated.

In Fig. 5.a the boom is operated, where the LS-margin has been lowered to 7 bar, while still having a standby pressure of 20 bar. As seen, the system is able to maintain the LS-margin and standby pressure, while providing a well-damped swash-plate control. In Fig. 5.b the response time of the system is shown. The system is in standby, when a joystick flow reference is given. It is seen that the joystick flow-reference is directly feed-forwarded to a swash-plate reference, and the swash-plate has settled in 90 ms.

In Fig. 5. the steering respons and electronic prioritization of steering is tested. In Fig. 5.a the boom is lifted to consume all the available flow, i.e. a reference of 120 L/min. The steering is activated at 7.3 s and at 9.3 s. Resultantly, the flow to the boom Q_{Boom} is reduced, such that the flow Q_S can be provided to the steering. That sufficient supply is indeed given to the steering, is seen by the pump pressure always being 20 bar above the steering pressure p_S. As the load pressure of the boom p_{Boom} is lower than the steering pressure p_s, the steering would have been starved if no prioritization was performed. The flow adaption is running continuously, ensuring a non-saturate pump. In Fig. 5.b, the prioritization is tested by having an active steering while the engine is idling, and then suddenly at time
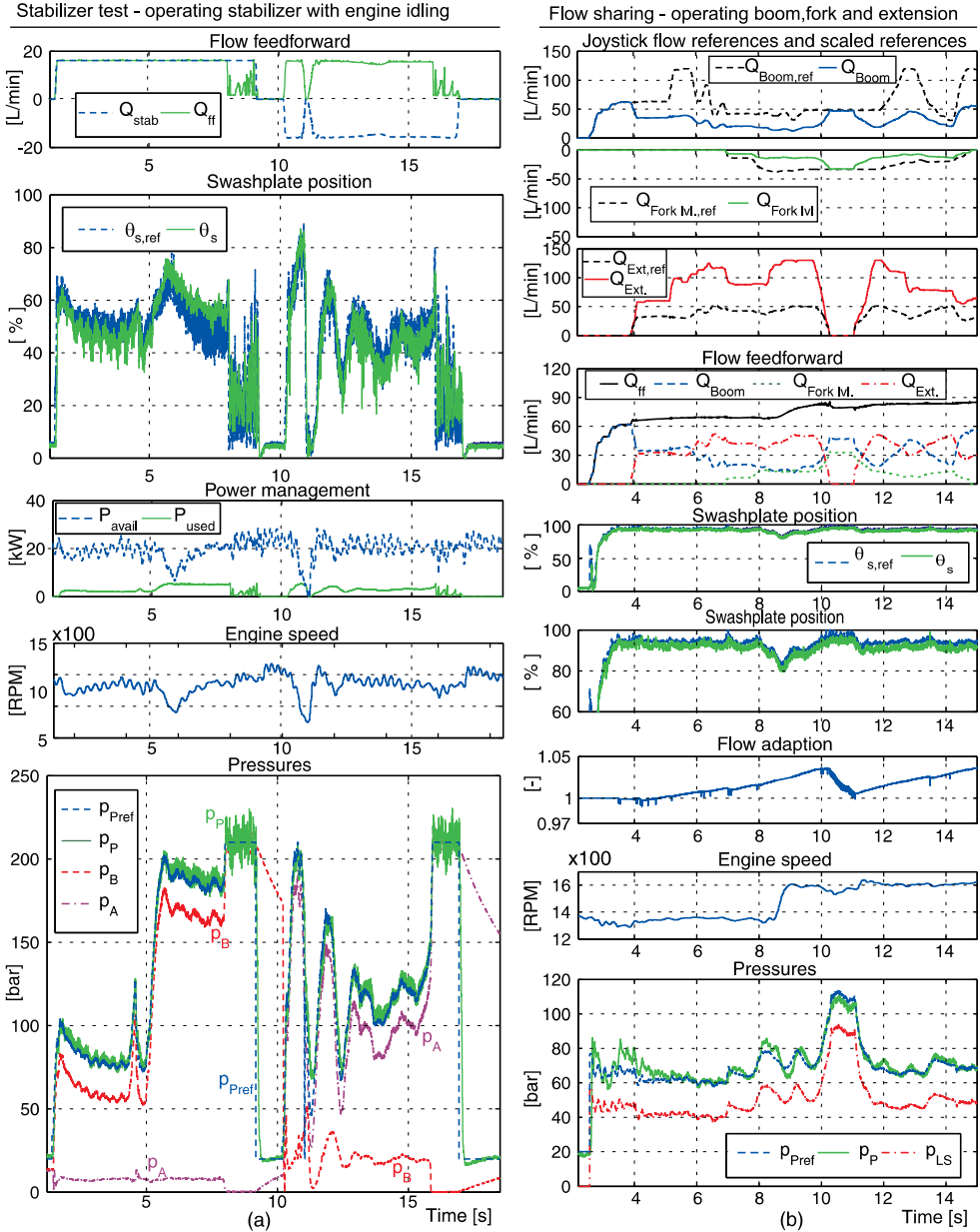
Figure 7: Operating stabilizer with engine idling (a), and a flow-sharing test (b).

29.6 s request full flow for the boom, which has a lower load pressure than the steering unit. It is seen that the flow to the boom is reduced to the available flow, and that the pressure margin for the steering is maintained. When the flow saturation is entered at time 29.4 s the flow adaption algorithm becomes active, ensuring that the swash-plate is at approximately 95% of maximum. Hence, the elctronic prioritization of steering is working as intended.
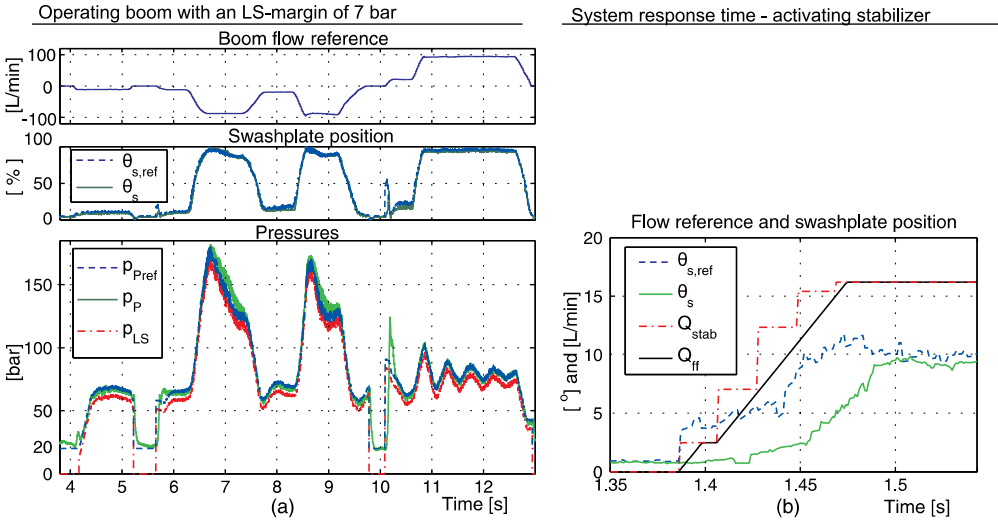
Figure 8: In (a), a boom trajectory is executed with 7 bar LS-margin. In (b), the system response time is tested with a flow step to a stabilizer.
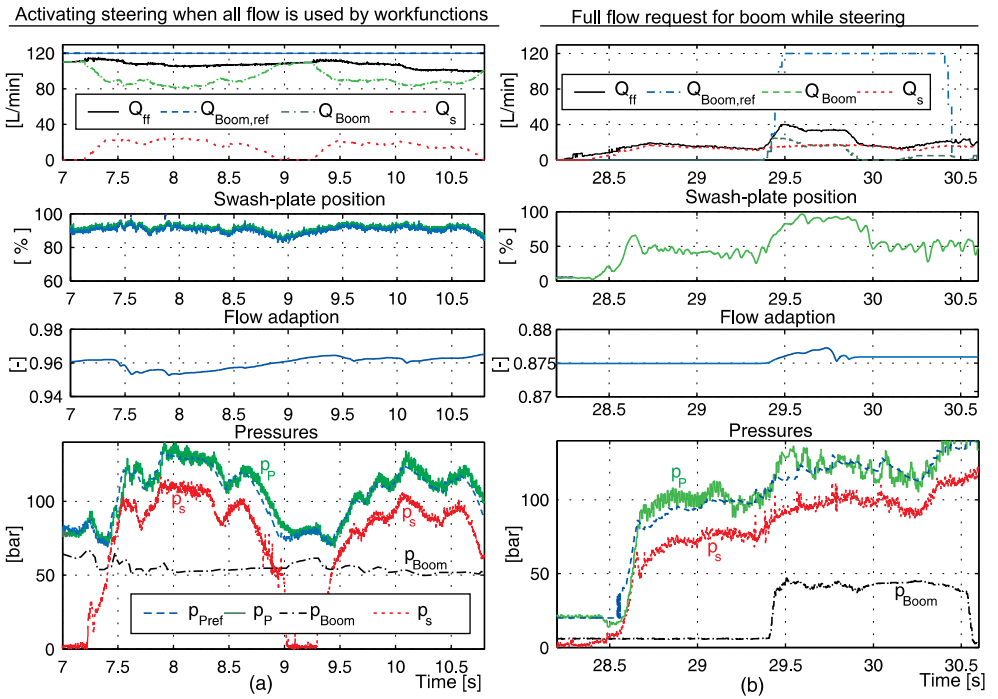

Figure 9: In (a) the boom is consuming all flow when steering is activated. In (b) the steering is operated, when a large boom flow is suddenly requested.

6. DISCUSSION AND CONCLUSION

Overall the developed ELS system shows that it is possible to move features as pressure control, flow-sharing, anti-stall, power sharing, high pressure protection and prioritization of steering from hydro-mechanical control to electronic control.

The developed swash-plate controller for actuation of a pump using a three-way valve shows a bandwidth of at least 10 Hz, validating the control concept. This concludes that it is possible to replace the spool position sensor of the EHA valve with an estimator, and that the valve flow-forces can be decoupled by the controller based on estimating flow through the valve using the swash-plate measurement. Based on the system's performance, it is concluded that the obtained bandwidth and on-stroke and de-stroke times of the electronic controlled pump are sufficient for the chosen electronic load sensing control principle.

The results verify that the prioritization of steering can be performed electronically with good dynamic performance, as the required steering pressure is alway supplied during flow saturation. Hence, the priority valve used in HLS system, see Fig. 1, may be omitted using this strategy. The pressure losses, extra hosing and reduced dynamic behavior caused by a priority valve can thus be avoided. Another advantage is the increased flexibility for improving a steering response. For example, to stabilize a system or improve steering responsiveness in HLS systems, designers may choose to raise the overall standby pressure of the system, or include a check-valve in parallel with an orifice in the steering unit's LS hose. The latter will make the steering LS pressure decay slower, which helps decoupling steering and pump pressure dynamics, and also gives faster re-steering response. In electronics, this can be simply implemented as non-linear filters on the steering LS-signal. To improve the response in cold fluids, a temperature dependent margin could also be defined.

Overall the developed control structure validates the effectiveness of an ELS control topology with a flow feed-forward from the joystick to the pump. This reduces the pump pressure controller to making small adjustment to the swash-plate in-order to maintain the desired pump pressure. The idea of eliminating the flow feed-forward from consumers reaching pressure limitation has also been shown to be a valid solution for maintaining the integrity of the flow feed-forward, and enhance the dynamic performance of the over-pressure protection functionality.

To elegantly handle flow-saturation and increase the control robustness, the skewed-midrange topology used during flow saturation has been validated. It ensures that the swash-plate never saturates, and that 93%-95% of maximum flow capacity is alway utilized during flow-sharing. As a result, the same pump pressure controller is aways operational, thereby ensuring that the LS-margin is always maintained. Also, the system continuously adapts to the flow characteristic of the pump and valves, which for example changes with fluid temperature. The strategy also gives a very robust prioritization of the steering, as the skewed-midrange topology function will continue to close down the valves groups until the swash-plate in under 95%, i.e. able to maintain steering pressure.

Regarding the implemented control, one of the overall results of the paper is the usefulness of canceling out non-linearities using system information to create appropriate coordinate shifts, for example from flow references to spool positions.

Finally, the results show that using ELS the system can be operated with an LS-margin down to 7 bar, while having a standby-pressure setting of 20 bar. This indicates that it is possible to improve efficiency of open circuit system by moving to electronic control. Also note, that standby-pressure and LS-margin are traditionally equal in HLS due to the hydro-mechanical implementation, but can be separated in electronic control.

The generality of the developed control structure makes it reasonable to expect that it is applicable for other mobile hydraulic applications than a telehandler.

References

(1) P. Krus, T. Persson and J. Palmberg. Dynamic Properties of Load Sensing Systems with Complex Mechanical Loads. Proc. of Int. Conf. on Fluid Power, Tampere, 1987.

(2) P. Krus, J. Palmberg and D. Kangzhi. Dynamic Response Characteristics of Pressure Control Pumps. First International Conference on Fluid Power Transmission and Control, Zhejiang University, Hangzhou, China, 1985.

(3) B. Lantto, P. Krus and J. Palmberg. Dynamic Properties of Load-Sensing Systems with Interacting Complex Mechanical Loads. Journal of Dynamic Systems, Measurement and Control, Transaction of the ASME, 115(3), Sep. 1993.

(4) H. Esders. Elektrohydraulisches Load Sensing für Mobile Anwendungen. PhD thesis, Teachnischen Universität Braunschweig, Germany, 1995.

(5) A. Langen. Experimentelle und Analytischen Untersuchungen an Vergesteuerten Hydraulisch-Mechanischen und Elektro-Hydraulischen Pumpenregulungen. PhD thesis, Rheinisch-Westälishen Technischen Hochschule Aachen, Germany, 1986.

(6) B. Zähe. Energiesparende Schaltungen Hydraulischer Antrieb mit Veränderlichem Versorgungsdruck und ihre Regelung. PhD thesis, Rheinisch-Westfälischen Technischen Hockschule Aachen, Germany, 1993.

(7) H. Jongebloed, D. Büren, U. Völkel and C. Jabs. Energy-Saving Valve System for Mobile Applications - Load-Control-System (LCS). 4th International Fluid Power Conference, Dresden, Vol.2, 2004.

(8) C. Latour. Electrohydraulic Flow Matching: The next generation of load-sensing controls. Off Highway March, 2007.

(9) R. Finzel and S. Helduser. Energy-Efficient Electro-Hydraulic Control Systems for Mobile Machinery/Flow Matching. 6th International Fluid Power Conf., Dresden, 2008.

(10) M. Djurovic and S. Helduser. Elektrohydraulisches Load-Sensing. Ölhydraulik und Pneumatik, 11, 2004.

(11) M. Djurovic and S. Helduser. New control strategies for electrohydraulic load-sensing. Power Transmission and Motion Control (PTMC), 2004.

(12) K. Mettälä, M. Djurovic, G. Keuper and P. Stachnik. Intelligent Oil Flow Management with EFM: The Potentials of Electrohydraulic Flow Matching in Tractor Hydraulics. The Tenth Scandinavian Int. Conf. on Fluid Power, SICFP'07, Tampere, Finland, 2007.

(13) M.R. Hansen, T.O. Andersen, H.C. Pedersen and F. Conrad. Feasibility Study of Electronic Load Sensing Concept for Hydraulic Variable Displacement Pump. , REM2006, KTH, Stockholm, Sweden, 2006.

(14) H.C. Pedersen. Automated Hydraulic System Design and Power Management in Mobile Applications. PhD thesis, Aalborg University, Denmark, 2007

(15) K.J. Åström, T. Hägglung. Advanced PID Control. ISBN: 978-1-55617-942-6, 2006.

Energy recuperation in working hydraulics of excavators

Martin Inderelst, Sebastian Sgro, Hubertus Murrenhoff
RWTH Aachen University, Germany, Institute for Fluid Power Drives and Controls

ABSTRACT

Decreasing fuel resources as well as increasing energy costs and stricter CO_2 regulations force engineers to research energy saving concepts for mobile working machines, especially for earth-moving machines like excavators. The optimisation of these machines is not only focused onto the drive train. Also, the supplementation of the working hydraulics by techniques for energy saving and recuperation is becoming more and more important. A comparatively easy possibility to meet the named criteria is controlling the hydraulic actuators of an excavator using hydraulic transformers.

Compared to a conventional load-sensing system which deals as the reference system in this study, a hydraulic control system using hydraulic transformers is introduced. After an explanation of both systems, they are analysed by means of hydraulic system simulations.

The energy consumption and losses are visualised by using Sankey Diagrams. Because throttling losses over control valves can be avoided in the transformer-controlled system and potential and kinetic energy can be recuperated easily, it is pointed out that the new system approach is more efficient. Simulated by using the same load and stroke cycles and modelled by the same level of detail, the energy consumption can be reduced by up to 70% of the reference system, using a hydraulic transformer controlled system in an excavator.

Keywords: working hydraulics, energy efficiency, energetic comparison, hydraulic transformer, load-sensing, system simulation, Sankey diagram, excavator

1 INTRODUCTION

Due to decreasing energy resources and rising energy costs, manufacturers of earth-moving machinery are forced to develop and offer new solutions for higher energy efficiencies. This trend is amplified by restrictions, imposed by governmental regulations such as the reduction of climate aggravating CO_2 production. But even for the customers, more efficient machines are gaining importance as they reduce fuel costs in comparison to pure acquisition costs. Thus, the manufacturers of earth-moving machinery are forced to satisfy this market requirement.

Until now, the main focus on reducing the energy consumption of construction vehicles has been the improvement of drive-train efficiency in general. An example for this is a hydro-static transmission with mechanical power split used in agricultural vehicles. However, manufacturers of earth-moving machinery increasingly focus on the improvement of efficiency of the working hydraulic system. Here, besides the energetic improvements of the control system, energy savings in the working equipment are possible by recuperation of potential and kinetic energies.

This paper deals with the potential of increasing energy efficiency in the working hydraulic system by means of hydraulic transformers for the control of linear and rotational actuators in comparison to an existing load-sensing system. As reference system, a 30 t hydraulic excavator with a 125 kW diesel engine was selected. The possibility to regain potential energy from the boom and kinetic energy from the swing drive is typical for this type of earth-moving machines.

2 SCOPE AND OBJECTIVES

There are different ways of installing additional energy saving and recuperation units in working hydraulics. Considering conventional valve-controlled systems, i.e. a load-sensing system of an excavator, there are some questions to be answered. What are the saving potentials during the main cycles, and how good is the efficiency of additionally installed components? Furthermore, do all additionally installed components and the need for more complex control justify these efforts?

An easier way is to control all linear and rotational actuators with hydraulic transformers (HT) out of a common high pressure rail which is directly connected to a hydraulic accumulator. The major advantage of such a system is the comparatively easy transmission of potential energy directly to the high pressure side. Using hydraulic transformers load pressure levels can be changed at the cost of energy-conversion losses which are depending on friction and internal oil leakage. Thus, throttling losses of balancing valves are expected to be reduced as well by such a system.

This paper compares the energetic consumption of two control systems for the working hydraulic system of a 30 t excavator by means of hydraulic simulations with the DSH*plus* software package. The control systems are selected as follows:

- Conventional load-sensing system with downstream pressure balancing valves
- Displacement control using hydraulic transformers without energy recuperation
- Displacement control using hydraulic transformers with energy recuperation

Typically, the load-sensing system to control the working hydraulics is utilised in European and American hydraulic excavators. It acts as the reference system in this paper.

In (1), hydraulic transformers used as pure control elements were analysed energetically in comparison to load-sensing systems and valve control systems. However, the study did not include swing drives in both of the systems and the load-sensing system was not built up with a second load-sensing circuit.

This study points out the energy saving potentials by use of hydraulic transformers in comparison to conventional valve controlled systems by regarding the whole system.

3 SYSTEM LAYOUT

3.1 Valve-controlled system

A load-sensing system as an example for a valve-controlled hydraulic system in construction vehicles is utilised to compare the presented systems by simulation (**Figure 1**). Not considered in this study are other valve-controlled systems, such as the Positive or Negative Control which are also typical for the kind of machinery being regarded (2). In the Negative Control system which is widely applied within the Asian market, the pump is swiveled back by an increasing stagnation pressure at a resistance in the bypass line. Stagnation pressure increases by a surplus volume flow supplied by the pump. A Positive Control system means that the pump is swiveled out by the highest pilot pressure of all control valves. Because Load-sensing systems are the most efficient designs of today, they are regarded as the reference system to give an impression about energy efficiency of the new approach using hydraulic transformers.
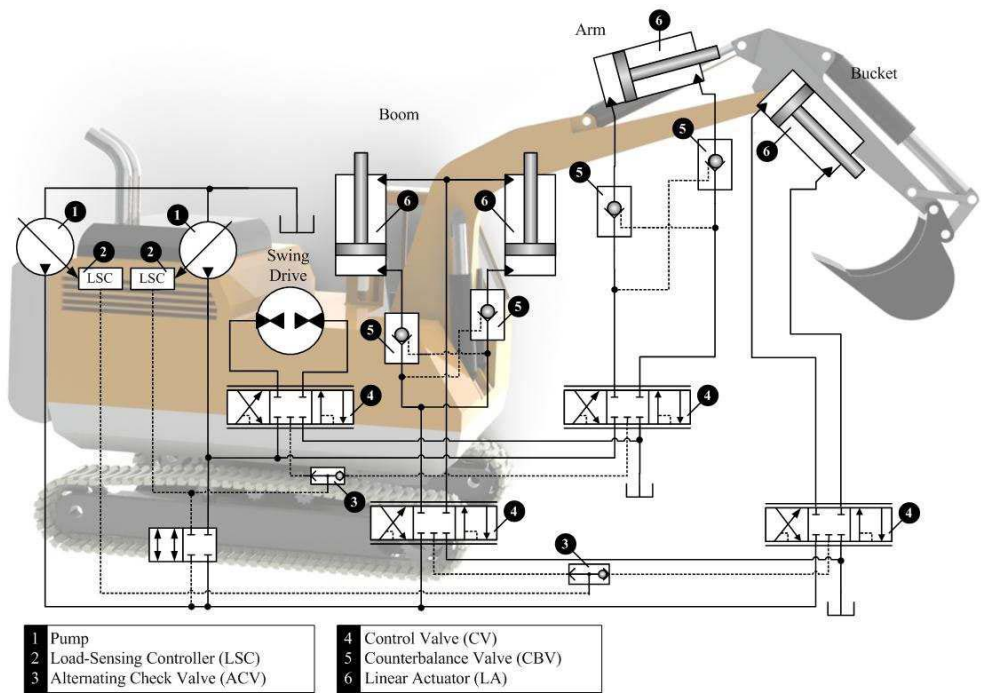

1	Pump	4	Control Valve (CV)
2	Load-Sensing Controller (LSC)	5	Counterbalance Valve (CBV)
3	Alternating Check Valve (ACV)	6	Linear Actuator (LA)

Figure 1   Load-sensing system

The observed load-sensing system is a hydraulic-mechanical control system using two pumps (3). Normally, one of them supplies the drives of the boom and the bucket while the other one supplies the cylinder of the arm and the swing drive. In case of fast movements of the arm, both circuits can be coupled by a valve. The control valves are actuated by the

operator, whereby the load pressure of the active axis is captured and transferred to the corresponding pump by the load-sensing controller. The pumps volume flow increases by swiveling of the swash plate until all attached loads are supplied sufficiently (4). To prevent velocity alternations while adding further loads, pressure balancing valves are arranged between the control valves and the corresponding drives. In this study, they are regarded as part of the control valves. Furthermore, the linear axes are equipped with counterbalance valves, in order to avoid uncontrolled movements in case of a pipe burst. In the hydraulic simulations, the counterbalance valves are implemented as hydraulic resistors in order to include their energy losses in the simulation. Alternating check valves are inserted to capture the maximum load pressure.

To optimise efficiency of current valve-controlled systems, a high complexity is necessary, because the pressures needed to move linear actuators and pressures of recuperation are not at the same level.

Due to throttling losses in valves, the obtainable pressure level in an additional accumulator is lower than the supply pressure. Hence, the recuperated energy in the cycle can only be used for lower pressure loads. For this, a complex control system is essential which continuously checks if recuperated energy can be used or not.

3.2 Hydraulic transformer-controlled system

The linear and rotational actuators of an excavator cannot only be controlled by using variable resistors, which cause high throttling losses, but also by using hydraulic transformers (HT). Hydraulic transformers use a constant pressure rail and accumulators optional to supply and control the linear actuators of the working hydraulic system. The pressure supply system, the load on the linear actuators and the hydraulic motors as well as the different work loads among each other are separated by this principle (5). In case of asymmetric loads, e.g. due to linear actuators, the load pressures can be adapted to the constant pressure rail without throttling losses.

In contrast to previous models, a new prototype of a hydraulic transformer using the Floating-Cup principle offers higher efficiencies, even in partial load conditions and high dynamics (6). A notable merit using hydraulic transformers in comparison to conventional load-sensing systems is the easy way of recuperating energy by feeding it into high pressure accumulators. The small and lightweight HT prototype is characterised by precise controllability and the possibility of its integration into the bottom of linear actuators. Further information about the HT and its functionality may be obtained from (5).

Figure 2 shows the hydraulic system of a 30 t excavator, which is supplied by a constant high-pressure rail and controlled by hydraulic transformers. For each linear actuator and the swing drive a separate hydraulic transformer is needed, because the constant pressure of the common pressure rail has to be adapted to each load pressure. Thus, the hydraulic transformers are arranged in two-quadrant-mode (5), because pressure level of the supplying pressure lines can not be switched. The operating direction of the differential cylinder is switched by a 4/2-way control valve (CV). One port of each linear actuator (LA) is connected via CV and counterbalance valve (CBV) to the corresponding hydraulic transformer, the other port to the constant low pressure rail. The counterbalance valves are integrated to get better performance and are opened by separated pilot pressures $p_{x,y}$.
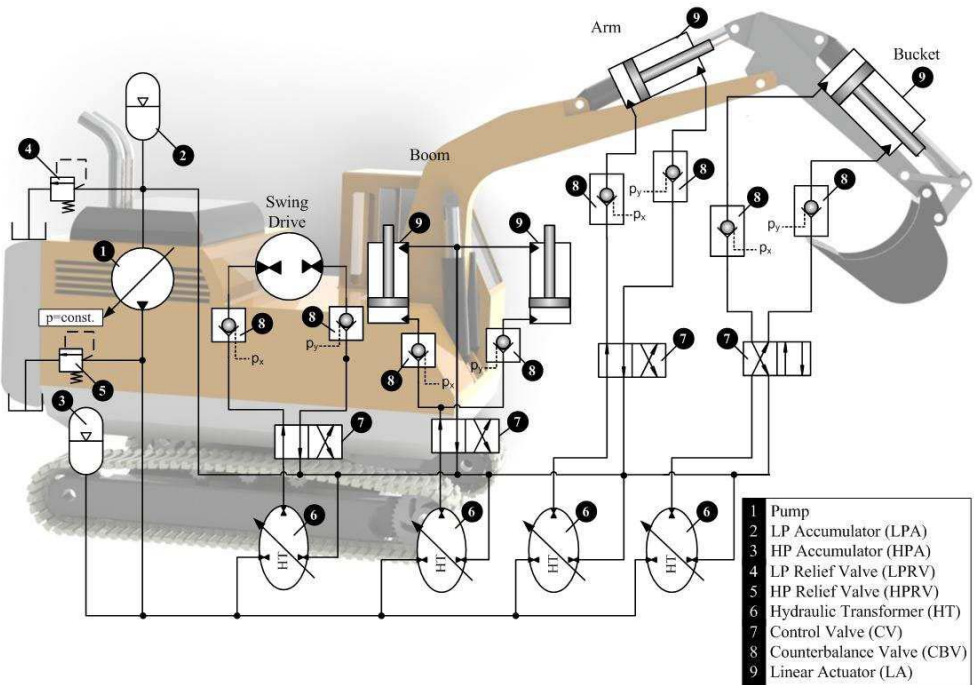
Figure 2 System using hydraulic transformers

4 SIMULATION

4.1 Model, cycle and boundary conditions

For a well founded comparison of both investigated systems an equivalent level of detail of both simulation system models using the same loads and stroke cycles is necessary. This is realised by using measured look-up-tables (e.g. pump and hydraulic transformers) and characteristic curves (e.g. cylinders and valves) for all of the components (7). In comparison to the load-sensing reference system, the control elements, the pump and the linear actuators of the transformer-controlled system have been exchanged or re-dimensioned. The look-up-tables and characteristic curves of the new components were extrapolated from measured data or provided by their manufacturers.

The reference system is a 30 t excavator equipped with a diesel engine with a power of 125 kW. The simulated excavator is equipped with a backhoe and conducts a standard excavation process, subdivided into four phases - excavating, swivelling and lifting, draining as well as swivelling back and lowering (3).

The load-sensing system of the reference excavator is driven by two hydraulic pumps with maximum displacements of $V_{P1} = 160$ ccm and $V_{P2} = 130$ ccm. The constant rotational speed of the diesel engine is set to $n = 2200$ rpm. The data used for this excavator is taken from (3).

The stroke cycles of each cylinder of the working hydraulics (boom, arm and bucket) nor-malised to their maximum values, and the angle of the swing drive are shown in **Figure 3**. These cycles are selected in order to research the particular controlling possibilities.
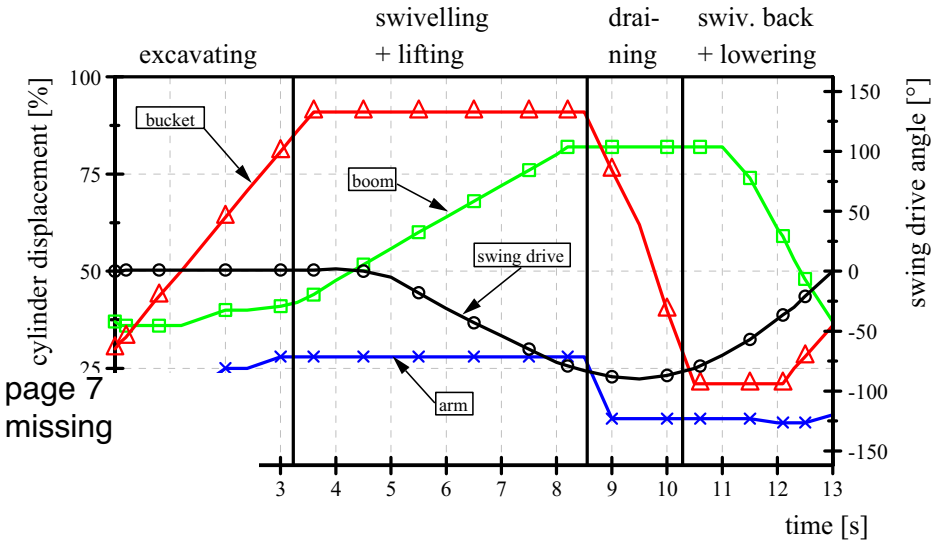

page 7
missing

Figure 3 Stroke cycles of linear and rotational actuators (3)

Loads on the working cylinders of the 30 t excavator are obtained from measured pressure signals, which are multiplied by the piston areas, and from the calculated balance of forces. The load cycles used in the simulations are displayed in **Figure 4**.
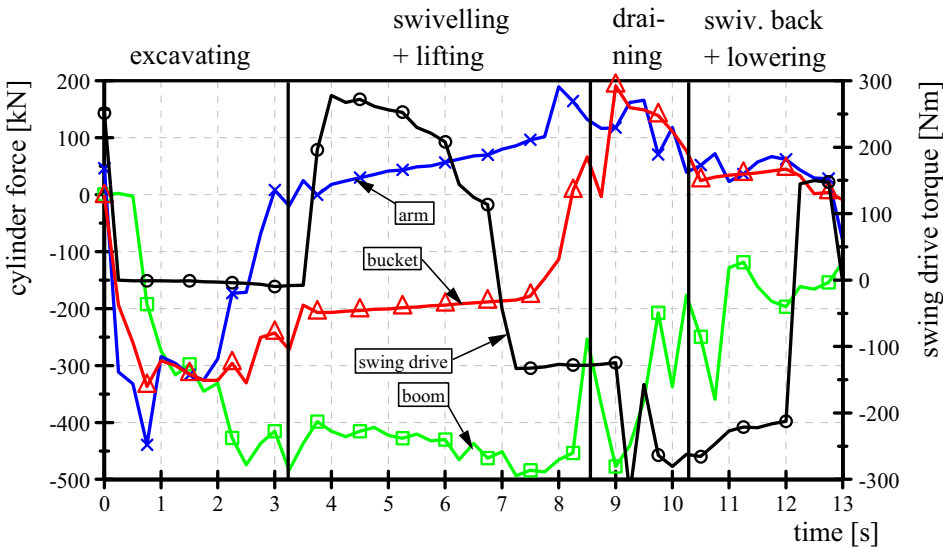
Figure 4 Load cycles of the actuators (3)

Load forces are defined as negative values if they are operating in extending direction of the cylinders and positive if the cylinders are retracting. Because the direction of the load forces does not depend on the moving direction, there are no indications for pulling and even pushing forces in the diagrams (cf. Figure 3 and Figure 4). The torque depends on the angle of the swing drive in the same way.

4.2 Control strategies

First, normal operation conditions are simulated for both systems. A possibility for energy recuperation does not exist for the load-sensing system and furthermore, there is no accumulator installed and thus no option to store recuperated energy in the transformer-controlled system. Nevertheless, an impression of the efficiencies of the controlling elements is given under these conditions.

Figure 5 shows the power requirements of all actuators against time during the introduced cycle. The curves are calculated from given data by multiplying load forces and velocities (3). A positive value means that the actuator is working in motor operating mode and power is consumed. Periods of negative values indicate possibilities for recuperating energy during the cycle, because forces and torques are operating in same direction of the corresponding actuator, which is running in pump mode under these conditions. Thus, Figure 5 indicates that energy can only be recuperated by lowering the boom and during braking of the swing drive.
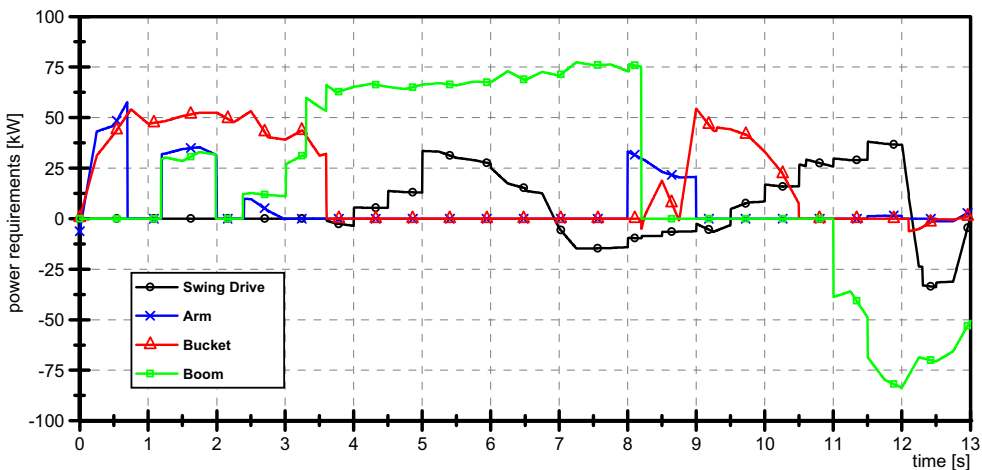

Figure 5 Power requirements of the actuators

In a second step, energy is recuperated during the cycle by modifying the control of the hydraulic transformers with comparatively low effort. Recuperated energy is being fed back into the constant high pressure rail. Thus, the pump works in a constant pressure control circuit.

5 RESULTS

The results of the simulations of each control concept modelled in DSH*plus* are compared on the basis of normalised energy values. The energy flows are displayed using Sankey diagrams. Although the primary energies of the internal combustion engines of both models are different, it is set to 100 % in each case for a better comparison. For this reason the percentaged primary energy compared to the primary energy of the load-sensing system is shown in brackets.

Figure 6 shows the Sankey diagram of the working hydraulics controlled by a conventional load-sensing system and the valve controlled system respectively. It can be found that 16% of the primary energy of the combustion engine is already lost in the hydraulic displacement pumps. Then, about one-third of the primary energy is used for the boom, another third is consumed by the bucket, 12% is used for the swing drive and at least 10% is consumed by the arm.

By sharing the same load-sensing circuit with the boom, which is working under higher pressure conditions, the highest throttling losses of all valves occur on the bucket side, because pressure differences between these actuators are discharged via the bucket pressure balancing valve which is integrated in the control valve.
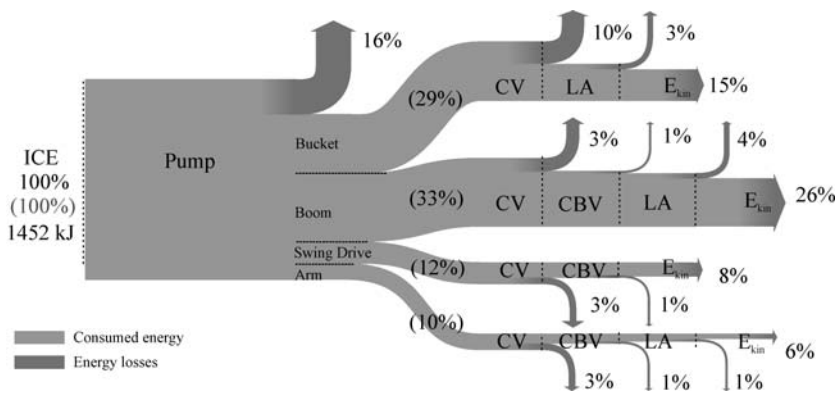

Figure 6 Sankey diagram of the Load-sensing system

Energy losses in the other load-sensing circuit for the swing drive and the arm are lower due to the lower power requirements (cf. Figure 5). Regarding the results in general, the overall efficiency of the hydraulic system is 55% for the cycle used in this study.

In comparison to the load-sensing system, **Figure 7** shows the energy flows of the hydraulic transformer system that has no possibility to store regenerated energy. The Sankey diagram shows that the efficiency of the main pump of 84.1% is in the same range of the two pumps of the load-sensing system. However the HT system consumes 25% less energy than the load-sensing system. This is caused by lower losses of the control components, i.e. the hydraulic transformers in comparison to the load-sensing valves. Especially the losses at the bucket load-sensing valve of 151 kJ (10% of primary energy) are significantly higher than the transformation losses in the hydraulic transformer at the bucket's side with only

30 kJ. Thus, throttling losses can be reduced by up to 120 kJ. Also, every transformer of the other linear actuators causes lower losses than the corresponding load-sensing valves.
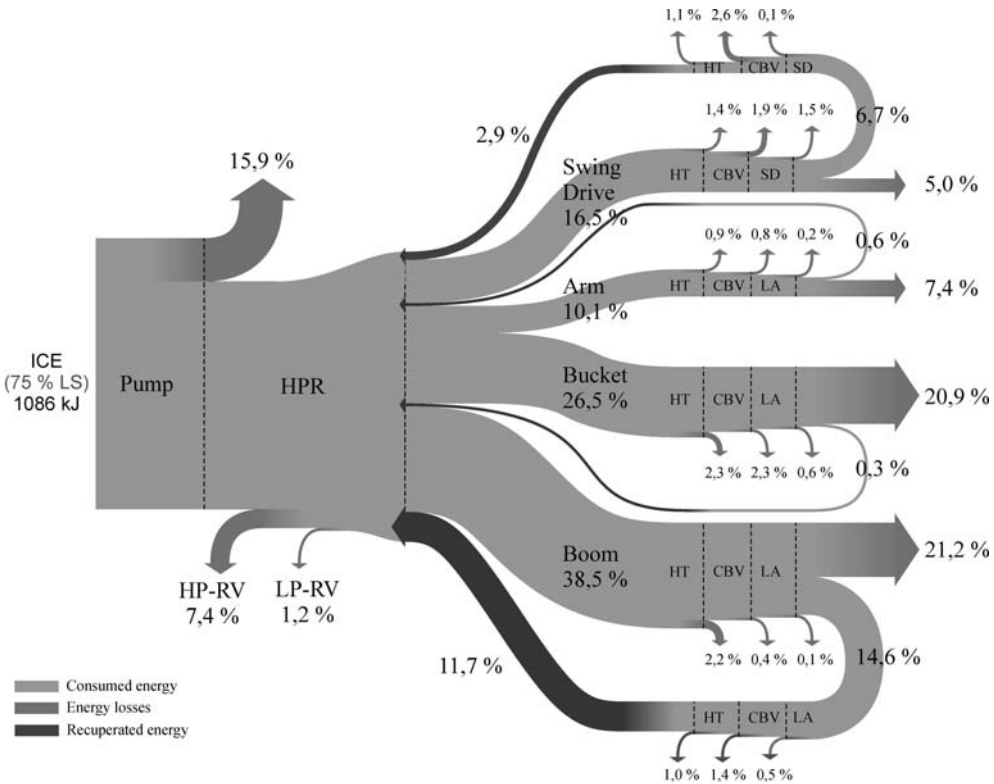

Figure 7 Sankey diagram of the HT system without storage of recuperated energy

The Sankey diagram also displays that about 168 kJ (16.8% of primary energy) of the load cycle could theoretically be regenerated, but there is no accumulator within this hydraulic circuit and therefore no possibility to store the regenerated energy exists to use it at a later occasion. That is why the regenerated energy is lost directly at the high-pressure relief valve of the common high pressure line.

It becomes obvious that it is only feasible to regenerate the potential energy of the boom and the kinetic energy of the swing drive, because the amount of regenerable energy of arm and bucket is too low to legitimate any technical efforts.

A reduction of the primary energy demand can be achieved by storing the recuperated potential energy of the boom and the kinetic braking energy of the swing drive through a hydraulic accumulator adapted to the common high pressure rail (cf. **Figure 8**).

About 123 kJ (12.4%) can be regenerated by refeeding the potential energy of the boom into the high-pressure accumulator. Furthermore, about 30 kJ of the kinetic braking energy of the swing drive can be recaptured.
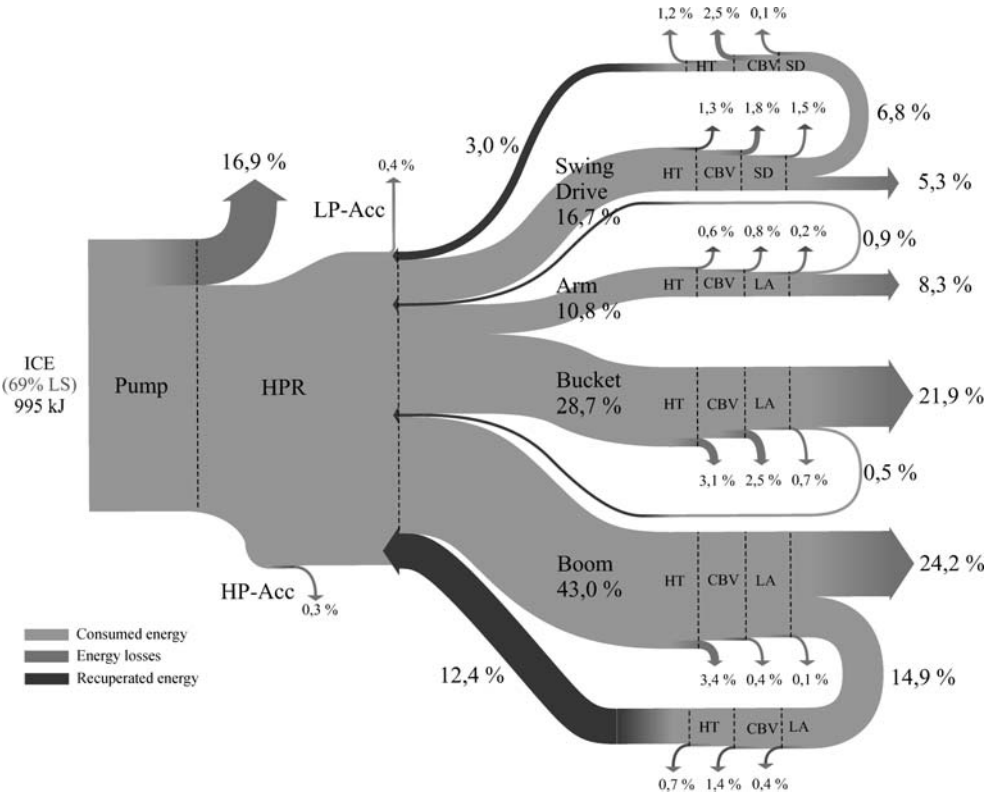
Figure 8 Sankey diagram of the HT system with storage of recuperated energy

The described procedures for energy regeneration lead to a reduction of the primary energy consumption by 31% in comparison to the conventional load-sensing system. Thus, an effective downsizing of the internal combustion engine and therefore a reduction of costs, energy demand and emissions can be realised.

Regarding costs for the whole life cycle of an excavator, fuel costs are as high as purchasing costs. Reducing energy consumption by up to 31% compared to the reference system by the new approach means that there is one-third of the fuel costs left for the components to be installed. Furthermore, the LS valves and the load detection hardware have to be taken out of the system. New prototypes of hydraulic transformers are designed for large-scale production (6) and therefore costs might not get higher. Anyway, the reduction of CO_2 emissions which is demanded by the government is the most important aim to be accomplished. Thus, more money and effort for changing the hydraulic system have to be accepted by the manufacturers.

6 CONCLUSION

In this paper, three systems for the control of the working hydraulics of an excavator have been introduced and compared: a load-sensing system and a hydraulic transformer system

with and without energy recuperation. It has become obvious that controlling linear actuators by hydraulic transformers requires less energy during the presented load cycle than controlling them by a conventional load-sensing system. This fact has been derived from simulation runs with real loss characteristics. The system is charged with a given load cycle. Energy losses of the load-sensing system have been compared to the HT system without storage of recuperated energy. The lower losses of 7.8% of the hydraulic transformers compared to 19% of the load-sensing system are caused by the pressure compensators of the load-sensing system. For a further reduction of the primary energy demanded from the combustion engine, it was suggested to add a hydraulic accumulator to the common high-pressure rail in order to store the recuperated potential energy of the boom. The simulations have shown that for the load cycle of the excavator only a regeneration of the boom's energy and the swing drive's energy is feasible because about 15.5% of the primary energy can be recuperated. The described procedures for the HT system lead to a total primary energy saving of 32% compared to a conventional load-sensing system.

The next step of research will be a comparison of the HT system to conventional primary control by displacement units and the HT system's evaluation on the basis of a simulation study. Furthermore, control algorithms for the internal combustion engine will be implemented. By these means the downsizing of the combustion engine for the HT system and possible reductions of fuel consumption and CO_2-production will be researched.

REFERENCES

(1)   **Sgro, S., Inderelst, M.**, Energy Efficiency of Mobile Working Machines, 7th International Conference on Fluid Power (IFK), Aachen, 2010, pp. 201-212

(2)   **Murrenhoff, H., Gies, S.**, Fluidtechnik für mobile Anwendungen, Lecture notes, Shaker Verlag, Aachen, Germany, 2008

(3)   **Holländer, C.**, Untersuchungen zur Beurteilung und Optimierung von Baggerhydrauliksystemen, Fortschrittberichte VDI Reihe 1 Nr. 307, VDI Verlag, Düsseldorf, Germany, 1998

(4)   **Zähe, B.**, Energiesparende Schaltungen hydraulischer Antriebe mit veränderlichem Versorgungsdruck und ihre Regelung, PhD thesis, RWTH Aachen University, Germany, 1993

(5)   **Achten, P., Potma, J., Vael, G.**, Cylinder Control with the Floating Cup Hydraulic Transformer, 8th Scandinavian International Conference on Fluid Power, Tampere, Finland, 2003

(6)   **Vael, G., Achten, P., Zhao, F.**, The Innas Hydraulic Transformer – The Key to the Hydrostatic Common Pressure Rail, Innas BV, 2000

(7)   **Kohmäscher, T.**, Modellbildung, Analyse und Auslegung hydrostatischer Antriebsstrangkonzepte, PhD thesis, RWTH Aachen University, Germany, 2008

Energy Dissipation Of The Hydraulic Circuit Of Remote Auxiliary Utilities Of An Agricultural Tractor

Massimo Borghi, Francesco Mancarella, Barbara Zardin
University of Modena and Reggio Emilia
Mechanical and Civil Engineering Department
Strada Vignolese 905, 41125, Modena, Italy

ABSTRACT

The aim of this work is to analyze the energy dissipation related to the hydraulic circuit which controls the remote auxiliary utilities of an agricultural tractor. This circuit is a typical hydraulic load sensing multi actuators system. This kind of system provides a good control strategy but it is characterized by quite high energy dissipation, especially when several actuators are working together under different variable loads. In this paper, the traditional load sensing system is modelled using a lumped parameter approach, and the energy dissipations are evaluated with reference to an actual duty measured on an agricultural tractor. Then, an alternative and more energy saving circuit architecture is introduced, based on an independent metering concept: in this architecture the single spool auxiliary valve is substituted with two electronically controlled proportional valves. The system has been also equipped with an electronically controlled variable pump; two strategies to control both the pump and the proportional valves are introduced. The energetic analysis is performed also for the alternative architecture using the same duty cycle, with the aim to identify the advantages, disadvantages and the critical features of this system with respect to the original one. Significant energy saving percentage characterizes the independent metering architecture, which seems to be a promising alternative to the standard hydraulic load sensing system.

Keywords: Energy saving, agricultural tractor, independent metering, duty cycle.

1. INTRODUCTION

The need to limit pollutant emissions of agricultural machines has become more and more pressing in the last years because TIER 4 in the US and StageIII/IV in the UE are becoming effective. Many researchers and manufacturers have focused their efforts on reducing the energy consumption in the system without compromising its functionality and its performance. From this point of view, the combined use of simulation tools and experimental testing represents the most promising way to develop alternative solutions

characterized by lower energy consumption. This work is part of a wider research project which aims to model the whole hydraulic circuit of a mid-size agricultural tractor, to study the energy consumption of the system modelled and to eventually suggest alternative and more convenient configurations. The hydraulic circuit of an agricultural tractor has to handle different users, such as the trailer brake valve, the hitch valve and the remote valves systems; it also manages the steering and feeds the low pressure line used to control all the electro-hydraulic valves and to lubricate the transmission. Every hydraulic subsystem will be modelled within the project and analyzed focusing on the dynamic behaviour and on the energy consumption. As a final step of the project, the alternative configurations studied will be integrated into the vehicle model and the interaction between the different hydraulic subsystems will be investigated in order to evaluate the total performance of the tractor.

This paper in particular is focused on the remote valves circuit of the tractor. This circuit can be classified as a standard hydraulic load sensing multi-actuators system: a variable displacement axial piston pump delivers flow to several actuators connected in parallel through as many again remote valves equipped with local pressure compensators; the pump displacement follows the pressure signal coming from the higher loaded actuator.

The load sensing concept has been introduced in the second half of the last century and it is still used in hydraulic applications because it has proved to be more efficient than the traditional hydraulic power system which entrusted power management to dissipative components (as the traditional pressure relief valve). At the same time, hydraulic load sensing systems are robust and reliable. The system dynamic behaviour depends on the pressure feedback which controls the pump displacement and stability of a load sensing system can be a critical issue in some operating conditions. A useful stability analysis is performed, for example, in (1) by means of linearized models and the results are compared with experiments, in order to provide information for the design and optimization of such system.

With the engagement of electronic controls in fluid power, the electronic load sensing concept has been adopted and the research has focused on designing control strategies to manage the pump displacement, demonstrating the feasibility, the optimization of dynamic behaviour of the system and the possibility of energy saving. A useful overview of the work done in this area can be found for instance in (2). Many authors have shown that the excessive time delay in the control of the pump displacement is critical, mainly when high dynamic flow transients occur in the system.

Regarding this aspect, an analysis of an electronic load sensing system can be found in (3): an electronic control of a variable displacement axial piston pump is realized using a 2-way pressure regulation proportional valve, electronically controlled, which can alter the load sensing pressure signal acting on the flow compensator of the pump. In this way the system can work as a pure traditional load sensing system or as a variable load sensing system, allowing maintaining a lower pressure difference between the pump pressure and the load pressure, in order to save energy when possible. It is shown by the authors that the performance of the system is strongly influenced by the electronic system control computational rate and by the sensors used. In (4), the concept of the variable load sensing electro-proportional valve to control the pump displacement is refined using an electro-proportional actuator which acts on the flow compensator spool, superimposing its action on the load sensing pressure signal; in this way the traditional hydraulic components are used and a better dynamic behaviour of the system is guaranteed.

The change to electronically control hydraulic components has allowed researchers to search for a better way to perform the control, maintaining good performances and saving energy.

For example, in (5) a general algorithm for power management of a single pump ELS-system was presented. The algorithm is based on an optimization approach, in order to minimize the power requirement in the system, having the possibility to electronically control the pump displacement, the proportional valves and the engine speed according to the optimal operating point.

However, a load sensing multi actuators system, being it hydraulically or electrically realized, is still characterized by a certain dissipation of energy mainly due to the following reasons: when more users are working together under different loads, relevant pressure drops are introduced by the local pressure compensators of the lower loaded actuators, in order to maintain the control; be it a meter-in type system, if a single spool proportional valve is used for the feeding of the actuators, energy dissipation is introduced by the meter-out section when partial flow is required by the user. A way to overcome these problems is to modify the architecture of the circuit; remembering that both the object of saving energy and maintaining good performance have to be pursued, the problem is which is the best approach to follow?

The use of independent metering valves seems promising for the system studied in this paper; in fact, this architecture allows saving energy in almost every operating conditions even if the remote actuators of an agricultural tractor are unknown. It should be noted that the remote valve circuit can serve a wide range of actuators, depending on the equipment connected at a particular moment on the tractor, for example a seeder, a loader or a harrow. The actuators can be both motors and cylinders and standardized duty cycles for this kind of circuit do not exist.

The independent metering concept has been analyzed by many authors in literature. For instance, in (6) and (7) a four independent metering configuration for the control of a cylinder is investigated highlighting the possibility to opportunely control the digital valves in order to regenerate energy otherwise dissipated at the outlet of the cylinder, control back pressure on the system, and manage overrunning loads. An optimal control of switching the valves has been investigated and the concept of Continuously Variable Modes against the simple discrete switching mode has been introduced: three of the four valves are always modulated to assure velocity control and this was the best way to guarantee a smoother movement of the cylinder and consequently allow energy savings to be achieved. The drawback is that the control of the valves is more complex.

In (8) the concept of independent meter-in and meter-out orifices has been applied to the case of a wheel loader of an earth moving machine obtaining an energy saving of 25%; it was also shown that the controller adopted to regulate the orifices is sensitive to the time delays in the valves. In (9) and (10) again four digital valves in different configurations are used to feed a cylinder and an algorithm to manage the valves is proposed; losses on a duty cycle of a 5 ton wheel loader are reduced 30-50%.

It is worth noting that independent metering proportional valves, where two spools substitute the traditional single spool, are already on market, for instance (16), (17). This configuration is easier to be realized and controlled than the solution which involves four

digital valves and can be integrated in the existing hydraulic circuit of a tractor without upsetting the original system.

Alternative regeneration systems applied to a multi actuator load sensing system have also been studied in literature; for instance, in (11) the combined use of electronically controlled discharge flow compensators and upstream compensators realizes the typical parallel or series or hybrid connections between the actuators, depending on the operating conditions. As a result of this flexibility, energy can be saved with regeneration or activating independent metering and moreover a better management of overrunning loads can be achieved.

For the analysis developed in this paper, an independent metering architecture was modelled as an alternative to the standard remote valves system analyzed, where two electronically controlled proportional valves have been introduced instead of the traditional remote valve. The system has been equipped with an electronically controlled variable displacement pump. This architecture may allow energy to be saved and can be integrated into the hydraulic circuit on an agricultural tractor, without compromising the integrity of the whole system.

Firstly, the control strategy adopted to control the pump and the valves has been developed as a typical electronic load sensing control.

Successively, the opportunity to save more energy using the concept of controlling the actuator position and velocity by directly adjusting the flow rate through a variable displacement pump, shown for instance in (12), (13), (14), has resulted in the authors testing an alternative control strategy. A flow controlled system is also described in (15) where the challenge to manage auxiliary functions without knowing the flow demands is discussed using a flow sharing pressure pre-compensator for each actuator.

According to the second strategy adopted, the flow demands of the users directly controls the pump displacement in order to deliver the flow to the actuators and the proportional valves are kept fully open, at least for the higher loaded actuator.

In this paper, the alternative independent metering architecture with the two control strategies defined has been modelled using again a lumped parameters approach; then, comparisons between the standard and alternative systems are performed with respect to simplified and actual duty cycles in order to value the energy saving percentage introduced by the use of independent metering and electronically controlled pump displacement.

2. HYDRAULIC STANDARD LOAD SENSING SYSTEM

The typical remote actuation hydraulic circuit of a mid-power agricultural tractor is a load-sensing system (manually, mechanically or electro-hydraulically controlled), which is designed to allow the hydraulic power modulation to multiple actuators (hydraulic motors and cylinders).

A load sensing hydraulic power generation system is shown in Figure 1, left side, where the displacement of pump P2 is controlled by a flow compensator V1. V1 modulates the

pressure in the control line, maintaining a constant difference between the pump pressure in line P and the load sensing pressure in line LS. This difference, called the pump pressure margin, depends on the cracking pressure given by the spring of V1 and it is typically equal to 20-30 bar; this value is determined in order to meet all the pressure drops in the circuit when the pump is at its maximum flow. V2 is a pressure compensator valve which only works when the pressure in the pump delivery line has reached a maximum value, set by the spring, which is typically the maximum pressure allowed in the system.

The circuit devoted to the remote actuators control presents a metering circuit designed to manage a parallel actuation, and each actuator is operated and controlled through a distribution block similar to the one shown in Figure 1, right side.

The core of the distribution block is represented by the proportional control valve 1. It is well known that metered power supplied to a hydraulic actuator corresponds to the opening condition of the proportional valve. The poppet lock check valves 2 introduces the piloted non-return control and valve 3 the local compensation control needed to manage the demands of multiple actuators, while the shuttle valve 4 selects the highest load-sensing piloting signal (LS). As shown by the functional description of the proportional control valve 1, the flow-rate modulation is of the meter-in type, which does not allow proper actuator control in the case of overrunning loads; under these particular operating conditions, the low pressure load-sensing signal selected by 4 reduces the pump displacement, the regulation exactly in opposition to the real need of the remote actuator.
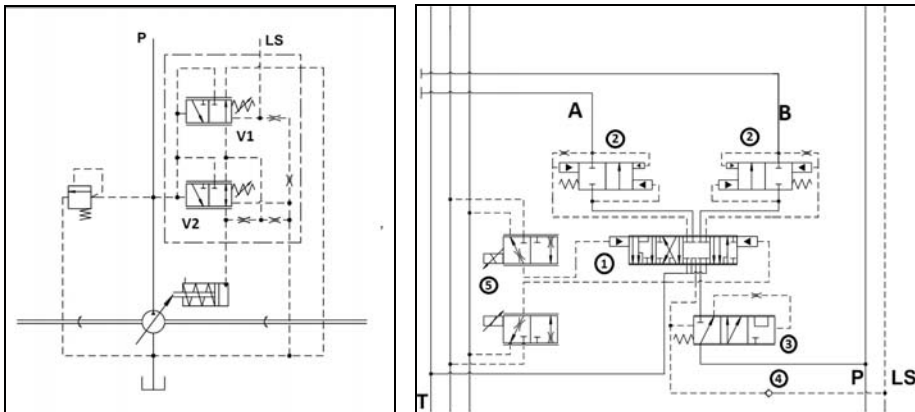

Figure 1 Hydraulic load sensing power generation system (left), hydraulic scheme of a proportional valve section (right).

The main advantage of this kind of system is that the excess flow, not directly used by the actuators, is only due to system leakages while a relatively small excess pressure, the pump pressure margin, is introduced to operate the actuator. In the case when a number of actuators operate simultaneously, the pressure compensators of the lower loaded actuators introduce an additional pressure drop in order to maintain control. With a pressure compensator located before the directional valves, as in the standard system adopted, a strategy has to be developed to contrast the reduction of flow going to the higher loaded user when the flow delivered by the pump saturates.

3. MODEL OF THE STANDARD LOAD SENSING HYDRAULIC SYSTEM

As a first step of the analysis, the standard architectural configuration of the load sensing system which feeds the actuators is modelled by means of a lumped parameter model developed in AMESim©.

The core of the model is represented by the proportional directional valves which convey the flow to the remote actuators (Figure 2).

Particular attention has been devoted to the description of the metering characteristics of the directional valve spools, because they determine the pressure drops across the passages and hence the energy dissipation introduced by the component itself. The same reason requires detailed models of the check valves and the local pressure compensator. To reach this level of detail, the Hydraulic Component Design Library of the software has been used; this tool allows a model to be generated where any single functionality of the actual component is represented through an element. For example, the flow passages determined by the metering edges of the spool of the proportional valve are described through elements which allow the flow area and hydraulic diameter to be defined using input files based on the spool actual geometry.
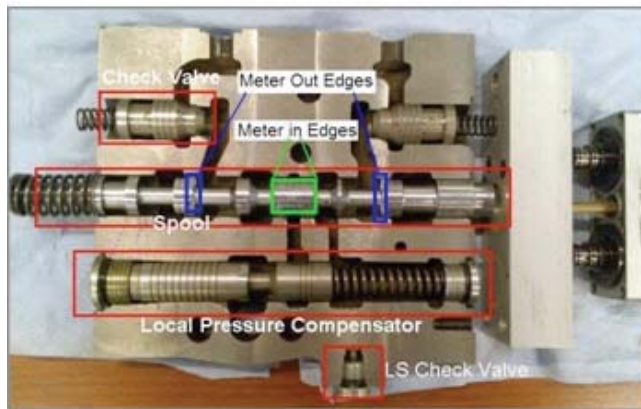
Figure 2 View of the proportional valve section.

Also the flow compensator of the variable displacement pump has been modelled using the Hydraulic Component Design Library. The pump flow compensator is composed by a proportional valve whose position depends on the balance between the pressure at the delivery of the pump and the pressure in the load sensing line. The pump pressure is higher than the load sensing pressure due to the pump pressure margin.

The position of the proportional valve controls the pressure in the control line and this pressure moves the actuator which determines the position of the swash-plate of the variable displacement axial piston pump.

Experimental validation of the model was performed by means of a comparison between the experimental and numerical pressure drops across different passages in the valve and

through a comparison of the metering characteristics. A hydraulic test rig equipped with a load sensing hydraulic power generator was used to perform the experimental analysis.

The model has been used to analyze the energy dissipation introduced by every single component in the hydraulic circuit of interest. This is particularly meaningful in order to identify possible alternative solutions to minimize the energy consumptions.

A steady state analysis developed in [18] using orifices as remote actuators has identified some critical features: first of all, even when a single user is activated, the presence of the local pressure compensator introduces a significant amount of energy dissipation, because the flow compensator may not be fully open especially in the case of a high flow rate request (the cracking pressure of the local pressure compensator is not sufficiently high). Relevant dissipations are introduced at the meter-in section if high flow is requested, while at partial flow the meter-out section also introduces high dissipation because it is partially closed. At high flow, the dissipations through the lock check valves and the quick-release couplings are also relevant. With more than one user active, the dissipation through the local pressure compensator of the lower loaded user is obviously high.

4. AN ALTERNATIVE ARCHITECTURE: INDEPENDENT METERING CONCEPT

An alternative to the hydraulic system previously described is represented by the well known independent metering architecture; in this work two control valves are used for each actuator and this allows the meter-in and meter-out sections to be controlled independently. The first clear advantage is that, if the meter-in section is partially open to meet the flow request, the meter-out section can be fully open and this avoids introducing a further pressure drop and, hence, energy consumption, in the system. The second advantage is that the local pressure compensators can be removed. The third advantage is that a proper control strategy to manage overrunning loads can be integrated, adjusting the meter-out section in an optimal way, in order to maintain actuator control without generating too much back pressure. Moreover, in this work an electronically controlled variable displacement pump was introduced.

Two strategies to control the flow delivered to the actuators with two independent proportional valves are adopted: the first strategy is again based on the load sensing concept, the second aims to control flow through the direct control of the variable displacement pump.

4.1 Electronic Load Sensing Strategy
As in the standard load sensing system, the pump displacement is controlled in order for the pump pressure to be higher than actuator pressure. This is achieved through the use of a PID controller, which continuously adjusts the pump displacement. The proportional valve at the meter-in section is directly regulated according to the flow required by a particular actuator, with the flow changing linearly as a function of the orifice area in the meter-in section. Moreover, the proportional valve at the meter-in section also performs the role of the local pressure compensator when two or more actuators are working together.

The control strategy adopted uses signals from the joysticks, i.e. the flow demand, the pressure at the inlet and outlet ports of the actuator, and the pressure at the delivery of the

pump. In particular, the signals coming from the joysticks directly control the meter-in section.

To explain the control strategy adopted, making reference to Figure 3, let's firstly consider one actuator working: from the sign of joystick signal is possible to understand the flow direction (from port A to port B or conversely). At this point it's possible to select the pressure determined by the actuator in the meter-in section (pressure A or pressure B). Using the equation of flow through an orifice, the area of the meter-in section can be defined if the pressure and flow requirements are known. In equation (1) Q is the flow demand, A the flow area, C_d the discharge coefficient, ρ the fluid density and Δp the pressure drop across the orifice. For simplicity, in this equation the value of the discharge coefficient is considered constant (0.7).

$$Q = C_d A \sqrt{\frac{2\Delta p}{\rho_i}} \Rightarrow A = \frac{Q}{C_d \sqrt{\frac{2\Delta p}{\rho_i}}} \qquad\qquad 1$$

In the case of a resistant load, the control valve in the meter-out section can be completely open with a significant improvement in energy efficiency.
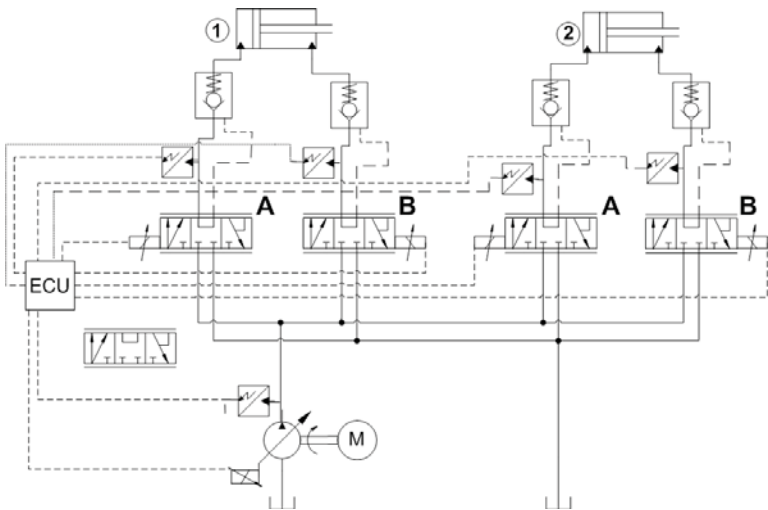
Figure 3 Hydraulic scheme of the independent metering system analyzed.

With two actuators, working under different loads, it is necessary to introduce a pressure drop equal to the difference between the two load sensing pressure values for the lower load actuator, thus ensuring the correct flow sharing between the actuators. In a standard load sensing system a local pressure compensator is used in each directional valve to perform this function. In this model, the control valve at the meter-in section of the lower load actuator is used to produce the additional pressure drop, so the system doesn't require any additional component. When two actuators are working together, the control algorithm selects the pressure at the higher load actuator and uses it to adjust the pump displacement; hence, the meter-in section of the higher load actuator is completely controlled by the

required flow demand, with the meter-in section of the lower load actuator determined in part by the flow demand and in part by the necessity of introducing pressure compensation.

It is worth noting that due to the presence of the PID controller, the variation in the pump global efficiency due to the operating conditions and the variation in displacement can be compensated. However, as evidenced by many authors in literature, closed loop control based on pump displacement, which involves the pump dynamic behaviour and the pressure dynamic behaviour in the delivery line of the pump, can produce instabilities in the systems, especially as the highest load pressure can vary considerably during the duty cycle.

4.2 Electronic Flow Matching Strategy

According to this strategy, the flow demand coming from the user directly controls the pump displacement. In this way, if only one user is working under a resistant load, both the meter-in and the meter-out sections can be fully open and additional pressure drops are not introduced in the system. When more than one user are working together, the pump delivers the total flow requested by the users, while the proportional valves at the meter-in section of the actuators working under the lower loads have to perform the local pressure compensation in order to maintain control of the users. Different cases can be analyzed in this situation; for simplicity, only two users working together are considered here. In equations 2, 3 and 4 p_p is the pressure at the pump delivery, p_{lmax} is the pressure at the higher load actuator, A_{max} is the maximum flow area and A_i is the adjusted area of the proportional valve at the meter-in section. Again, the equation of the flow through an orifice is used to derive the flow area.

- The two users require the same flow but are working at different loads:

$$Q_1 = Q_2 , F_1 \neq F_2 \qquad A_i = \sqrt{\frac{p_p - p_{l,max}}{p_p - p_i}} A_{max} , i = 1,2 \qquad\qquad 2$$

- The two users require different flows but are working at the same load:

$$Q_1 \neq Q_2 , F_1 = F_2 \quad A_i = \frac{Q_i}{Q_{max}} A_{max} , i = 1,2 \qquad\qquad 3$$

- The two users require different flows and are working at different loads:

$$Q_1 \neq Q_2 , F_1 \neq F_2 \qquad A_i = \frac{Q_i}{Q_{max}} \sqrt{\frac{p_p - p_{l,max}}{p_p - p_i}} A_{max} , i = 1,2 \qquad\qquad 4$$

Again, the control strategy adopted needs signals relating to the flow demands, the pressure at the inlet and outlet ports of the actuator, and the pressure at the delivery of the pump. In particular, the signals coming from the joysticks directly control the pump displacement. The pump flow rate can be expressed as in the following equation:

$$Q = \alpha \cdot V_{max} \cdot n \cdot \eta_{vol} \qquad\qquad 5$$

In equation 5 the coefficient α varies between 0 and 1 and modulates the pump displacement between the minimum and maximum value V_{max}. Actually, the volumetric efficiency η_{vol} is a function of the pump operating parameters, of the oil temperature and of the pump displacement itself. Given the fact that the displacement control is open loop,

there is no guarantee that the flow delivered by the pump exactly matches the requested flow rate. The open loop control provides a more stable but less accurate system. To overcome this problem, closed loop can be introduced using the pressure transducer signals at the inlet and outlet ports of the proportional valves in the meter-in section to determine the actual flow passing through the valve. This can be done once the flow area of the proportional valve is known, using, for instance, linear transducers to measure spool displacement. When the flow delivered does not match the requested flow, a correction has to be made to the pump displacement.

It is clear that the advantage of Electronic Flow Matching in comparison with the Electronic Load Sensing System is relevant mainly when a resistant load is acting on the user and in particular for the user working under the higher load; in this case, both the meter-in and the meter-out sections are fully open and the pump is directly controlled to deliver the exact flow to the actuator.

4.3 Strategy to Manage Overrunning Loads.

In the standard hydraulic load sensing system there is no guarantee that overrunning loads acting on the actuators will be controlled correctly. Only when the user is requiring partial flow will the flow area at the meter-out section be restricted to generate sufficient back pressure to control the actuator. Moreover, if the load is sufficiently high, the pressure at the inlet chamber reduces and the pump displacement decreases and the risk of cavitation occurring is increased.

A way to manage the overrunning loads to maintain actuator control has been introduced for both the control strategies adopted. Only in the case of overrunning loads, the proportional valve at the meter-out section is adjusted in order to determine a controlled pressure on the supply line to the actuator. When the control algorithm realizes that an overrunning load is acting on the actuator, a PID controller starts to work monitoring the pressure in the supply line and adjusting the proportional valve position at the meter-out section in order to keep this pressure at a value of a few bar. This guarantees the functionality of the system, avoiding the eventual occurrence of cavitation at the inlet of the actuator or maintaining a controlled back pressure on the system.

4.4 Actuator End Stops.

Using linear transducers at the actuators it is possible to add another important feature to the control strategy: when one actuator reaches its end stop, the pressure in the system will rise till the maximum value. In this situation, if another actuator is still working and the user doesn't set the flow demand to zero on the first actuator, a great amount of energy is wasted for pressure compensation in the second actuator, which forced to work at maximum pressure. In this scenario, the control algorithm is able to de-activate automatically the actuator that has reached its end stop, and the system can work at the pressure imposed by the load acting on the other actuator.

5. MODEL OF THE TWO INDEPENDENT METERING SYSTEMS AND ENERGETIC ANALYSIS.

The two systems previously described have been modelled within the AMESim© environment. The control strategies adopted have been developed through the use of a

specific library of signal and control components. The main simplifications of both models relate to the pump and the remote proportional valves. In particular, the dynamic behaviour of these components has, until now, been considered as ideal; the aim of this preliminary work was in fact to establish if the independent metering concept was a promising alternative to the traditional system in reducing the energy consumption of the remote actuation circuit fitted to an agricultural tractor. This particular section of the hydraulic circuit cannot be standardized because a wide range of actuators can be hydraulically connected to the remote valves on the tractor, each of them characterized by a particular and unique duty cycle. Hence, it is difficult to presume in advance if independent metering can introduce a significant reduction in the energy consumption in the case analyzed.

The two models have been used to perform a simplified energy analysis in order to compare the energy consumption of the traditional load sensing system (HLS-S), of the electronic load sensing independent metering system (ELS-IMS) and of the electronic flow matching independent metering system (EFM-IMS).

First of all two linear actuators were used for the analysis, working together under constant but different loads; each actuator extends and then retracts under the same load. The first duty cycle involves only resistant loads, whereas the second is characterized by resistant loads when extending strokes and overrunning loads when retracting. Simulations were performed at different actuator flow requirements with the same flow going to the two actuators, i.e. if the total flow is 60 l/min, 30 l/min is going to the actuator 1 and 30 l/min to actuator 2.
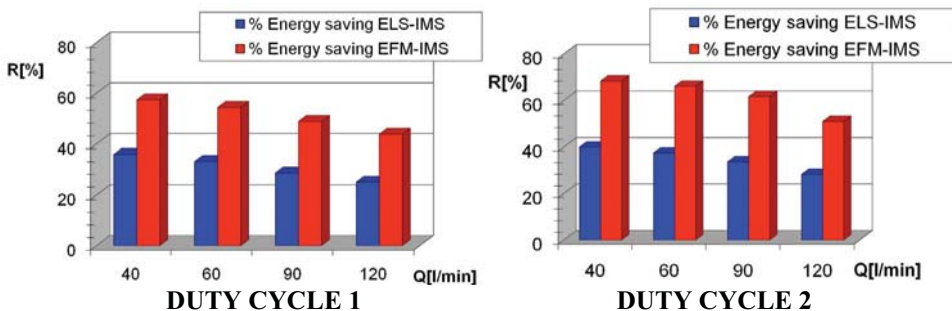
Figure 4 Percentage Energy saved of the ELS-IMS and EFM-IMS compared to the HLS-S.

In Figure 4 the energy percentage saved using the ELS-IMS and the EFM-IMS compared to the HLS-S energy consumption are represented as a function of the flow delivered by the pump.

The energy saved has been assessed with reference to the energy consumption of the pump and significant savings are obtained, particularly for the EFM-IMS. The energy saving reduces when the flow delivered is increased due to lower losses generated in the traditional HLS-S system, because the flow areas at the meter-in and meter-out sections increase with flow rate. It can be said that the alternative architectures are in this case compared with a "more efficient" system, so the percentage of energy recovered is reduced. The energy saved during duty cycle 2, involving both resistant and overrunning loads, is higher. During the second part of the cycle, when the loads on the actuators are both overrunning, the

hydraulic load sensing system wastes energy especially when the flow requested is low and the meter-out section is very restricted. As a consequence, the pressures at both actuators are increased and the pump is forced to work at a higher pressure. When the loads are overrunning in the alternative independent metering architectures, the meter-out section is adjusted in order to maintain a controlled pressure in the actuator inlet lines and this, in addition to preventing cavitation, saves energy.

However, these duty cycles, characterized by a constant flow and constant load, are far from the actual working condition of a remote actuation circuit. Considering the fact that the percentage of energy saved strongly depends on the duty cycle adopted, an energy analysis was undertaken based on an experimental duty cycle on an actual agricultural tractor, as explained in the next section.

6. EXPERIMENTAL DUTY CYCLE

A duty cycle was performed using a front loader installed on the remote distribution block of a mid size agricultural tractor, undertaking loading and unloading operations (Figure 5). In this application two remote valves are used simultaneously for boom and bucket movements of the loader. For both the boom and the bucket movements, two mechanically constrained cylinders are used.

The user flow requirements were recorded using the tractor CAN bus data, in particular the control state operations and the flow request percentages were monitored. In addition, four pressure transducers, located on the remote valves working ports, were used to record the pressure transients. The data post processing allows the position of the spools of each remote valves, and hence the flow passing through the valve and the loads on the actuators to be determined (Figure 6). These variables were then used as input data for the models of the standard and alternative architectures, so the actual duty cycle has been reproduced in the virtual environment to carry out the energy analysis.

Figure 5 Front loader used to perform the experimental duty cycle.

The duty cycle consists of the tractor first approaching the load, then the boom and bucket cylinders are moved to perform the pick-up operation, the tractor then backs up and when approaching the unloading zone the load is raised, the bucket is rotated to unload and, finally the bucket is lowered. From the non-dimensional boom and bucket cylinder flow transients represented in Figure 6 it can be seen that the actuators work together at different stages during the duty cycle.
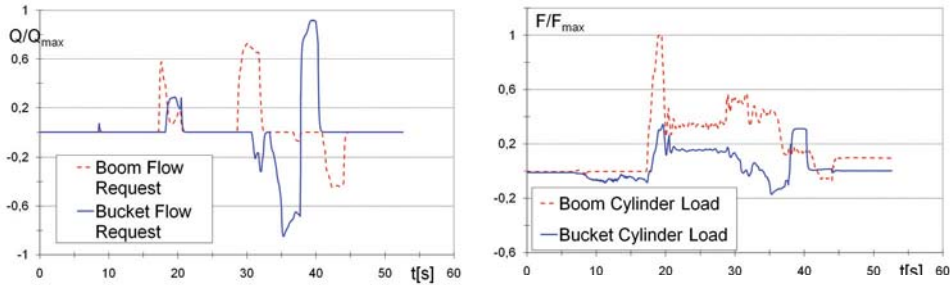

Figure 6 Left: Non-dimensional flow demand transients for the two actuators. Right: non-dimensional loads on actuators.

In Figure 7 the pump hydraulic power transients during the cycle are shown for the three different systems. A consistent reduction in the power characterizes all the main phases of the duty cycle, with energy savings equal to 25% for ELS-IMS and 36% for EFM-IMS. These results confirm that the independent metering approach coupled with an electronic control of the pump and a suitable strategy to control the operation of the proportional valves may save a consistent amount of energy during a working cycle of the auxiliary actuators of an agricultural tractor. However, the analysis does not take into account the dynamic behaviour of the variable displacement pump and of the proportional valves which can drastically influence the stability of the system and reduce the percentage of energy saved. For this reason, the next step of the research will be to include the dynamic behaviour of the components previously mentioned.
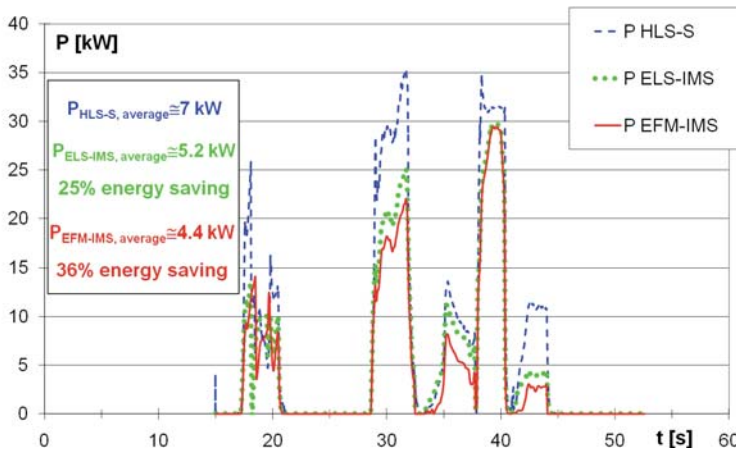
Figure 7 Power transients during the duty cycle for the three systems analyzed.

7. CONCLUSIONS

The research reported in this paper has been focused on the energy analysis of the remote valves hydraulic circuit of a mid size agricultural tractor. The circuit is a typical hydraulic load sensing multi actuators application. The main aim of the work has been to evaluate the energy losses in the standard architecture making reference mainly to an actual duty cycle performed with the tractor. The energy analysis undertaken on the circuit has highlighted that a certain margin of energy saving can be realized mainly resulting from the elimination of the pressure drops introduced by the meter-out flow area of the remote valves and by the pressure compensators acting at the inlet of the lower loaded actuators. Thus, alternative circuit architecture, based on the well known independent metering concept, has been introduced and modelled, where the single spool remote valves have been replaced by two digital valves. Moreover, given the chance to add functionalities and flexibility to the system and the possibility to save more energy, an electronically controlled variable pump has been used. Two control strategies to handle both the pump displacement and the proportional valves have been developed. With the aim of defining a term of comparison of the standard and alternative architectures, an actual duty cycle has been performed on a tractor using a front loader. The experimental data regarding loads and flow demands of the actuators involved, measured during the cycle, have been used as input data to the simulation models of the remote circuit. The main result obtained is that, making a comparison between the traditional and alternative architectures, a relevant percentage of energy can be saved due to the combined use of the independent metering concept and the electronic control of the pump displacement, and at the same time, the functionality of the system is preserved. However, a stability analysis of the system has to be performed and the influence of the eventual time delay in the pump displacement control and in the proportional valves on the percentage of energy saved has to be investigated.
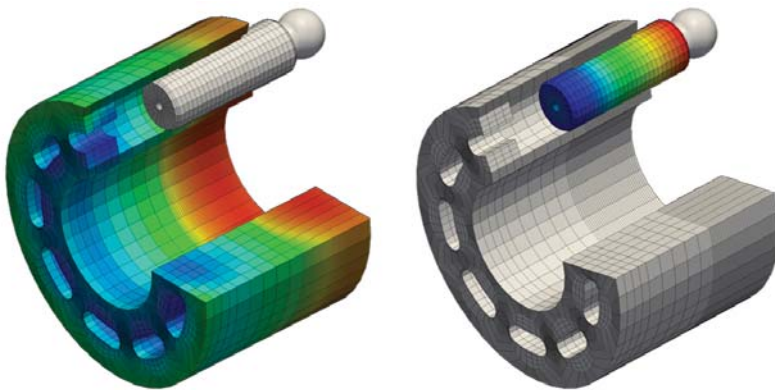
REFERENCES

1. **Wu, D., Schoenau, G., Burton, R., Bitner, D.,** 2005, Model and Experimental Validation of a Load Sensing System with a Critically Lapped regulator Spool, International Journal of fluid Power, Volume 6, Number 3, November 2005. ISSN 1439-9776.
2. **Pedersen, H., C., Andersen, T., O., Hansen, M., R.,** 2004, A Review of the Research Contributions throughout the last Decades, 4th International Fluid Power Conference, Dresden, 2004.
3. **Ruggeri, M., Guidetti, M.,** 2008, Variable Load Sensing and Anti-Stall Electronic Control with Sliding Mode and Adaptive PID, Proceedings of the 7th JFPS International Symposium on Fluid Power, TOYAMA 2008.
4. **Ruggeri, M., Martelli, M., Leati, E.,** 2010, Variable Load Sensing Electro-Proportional Valve with Torque, Power and Anti-Stall Control on Variable

Displacement Axial Piston Pumps, Workshop Proceedings of 7th International Fluid Power Conference, Aachen 2010. ISBN 978-3-950565-90-7.

5. **Pedersen, H., C., Andersen, T., O., Hansen, M., R.,** 2006, Power Management In Open Circuit Hydraulic Systems, Proc. of the 4th Ph.D. Symposium, Sarasota, Florida.

6. **Shenouda, A., Brook, W.,** 2005, Energy Saving Analysis using a four independent metering configuration controlling a hydraulic cylinder, SAE Paper 2005-01-3632, SAE Commercial Vehicle Congress and Exhibition, ISBN 0-7680-1678-9, 2005.

7. **Shenouda, A.,** 2006, Quasi-Static Hydraulic Control Systems and Energy Savings Potential Using Independent Metering Four-Valve Assembly, Ph.D. Thesis, Woodruff School of Mechanical Engineering, Georgia Institute of Technology, August 2006.

8. **Eriksson, B., Larsson, J., Palmberg, J.-O.,** 2006, Study on individual pressure Control in energy efficient Cylinder drives, Proc. of the 4th Ph.D. Symposium, Sarasota, Florida.

9. **Linjama, M., Huova, M., Vilenius, M.,** 2007, On Stability and Dynamic Characteristics of Hydraulic Drives with Distributed Valves, /ASME Symposium on Fluid Power and Motion Control.

10. **Huova, M., Karvonen, Ahola, V., Linjama, M., Vilenius, M.,** 2010, Energy Efficient Control of Multiactuator Digital Hydraulic Mobile Machine, Proceedings of 7th International Fluid Power Conference, Aachen 2010. ISBN 978-3-950565-90-7.

11. **Marani, P., Ansaloni, G., Paoluzzi, R**., 2008, Load Sensing with Active Regeneration System, Proceedings of the 7th JFPS International Symposium on Fluid Power, TOYAMA 2008.

12. **Rahmfeld, R., Ivantysynova, M., Weber, J.,** 2004, Displacement Controlled Wheel Loader - A Simple and Clever Solution, 4th International Fluid Power Conference - Dresden, 2004.

13. **Williamson, C., Zimmerman, J. and Ivantysynova, M**., 2008. Efficiency Study of an Excavator Hydraulic System Based on Displacement- Controlled Actuators, Bath/ASME Symposium on Fluid Power and Motion Control.

14. **Heybroek, K., Larsson, J., Palmberg, J.-O.,** 2006, Open Circuit Solution For Pump Controlled Actuators, Proc. of the 4th Ph.D. Symposium, Sarasota, Florida**.**

15. **Eriksson, B., Palmberg, J.-O.,** 2010, How to Handle Auxiliary Functions in Energy Efficient Single Pump, Flow Sharing Mobile Systems, Proceedings of 7th International Fluid Power Conference, Aachen 2010. ISBN 978-3-950565-90-7.

16. http://www.incova.com/index.php?option=com_content&task=view&id=55&Itemid=71

17. http://www.eaton.com/EatonCom/Markets/Hydraulics/ProductsCategory/Valves/MobileValves/ElectronicLoadSensingValve/index.htm

18. **Borghi, M., Zardin, B., Mancarella, F., Specchia, E.,** 2010, Energy Consumption of the Hydraulic Circuit of a Mid Size Power Tractor, Proceedings of 7th International Fluid Power Conference, Aachen 2010. ISBN 978-3-950565-90-7.

Authors' Index

Fluid Power and Motion Control (FPMC) 2010 comprises 39 papers presented at FPMC 2010 – the latest in a series of International Symposia held at the University of Bath. FPMC 2010 was co-organised by the American Society of Mechanical Engineers (ASME). This collection of papers reports on the latest research in the fields of hydraulic and pneumatic motion control worldwide.

The main theme of FPMC 2010 is 'Efficient Fluid Power'. Topics include:

- Digital hydraulics
- Energy efficiency and the environment
- Control
- Fluid dynamics and noise
- Hydraulic and pneumatic components and systems
- Modelling and simulation
- Condition monitoring and fault diagnosis
- Seals, friction and leakage
- Environmentally friendly and smart fluids
- Automotive and internal combustion engine applications
- Off-road, marine and industrial applications

This volume will be of particular interest to researchers and practitioners working in the fields of fluid power, motion control, hydraulics and pneumatics.